FACULTY OF SCIENCE
UNIVERSITY OF COPENHAGEN

Measuring the triple O_2 isotopic composition of air trapped in ice cores and quantifying the causes of $\delta^{18}O_{atm}$ millennial scale variations

PhD thesis

Corentin Reutenauer

Academic advisors:

Thomas Blunier
Centre for Ice and Climate, Niels Bohr Institute,
University of Copenhagen, Denmark

Amaëlle Landais
Laboratoire des Sciences du Climat et de l'Environnement,
UMR CEA/CNRS/UVSQ
Gif sur Yvette, France

This thesis has been submitted to the PhD School of
The Faculty of Science, University of Copenhagen, June 27th 2016

Haraka haraka haina baraka

Swahili Proverb

Abstract

Owing to its 1200 yr lifetime, atmospheric oxygen (O_2) is a global tracer of biological and hydrological processes. The dominant source of O_2 is located in the the low latitudes, where most of the O_2 production/uptake occurs. Atmospheric O_2 can therefore provide valuable information on the tropics, a region of the world which still lacks of climatic reconstructions and whose role is widely debated in the context of millennial-scale climate variations. Atmospheric O_2 is enriched in heavy isotopologues ($\delta^{17}O$, $\delta^{18}O$) relative to O_2 in ocean water, the ultimate source of O_2 for photosynthesis. The processes causing enrichment of $^{17}O/^{16}O$ and $^{18}O/^{16}O$ isotope ratios involve the biological cycle, the water cycle, global ice volume/sea-level variations, climatic conditions and stratospheric photochemistry. It is thus essential to estimate the relative importance of these processes to unleash the potential of O_2 isotopologues as global tracers of past changes in the climate system.

The evolution of the past atmosphere can be retrieved from the air bubbles occluded in polar ice cores back to 800 kyr. However, elemental and isotopic fractionation processes alter O_2 isotope ratios during the transport and entrapment of air in the porous layer (firn) on top of the ice sheets, during storage and during the experimental analysis. An understanding of these non-climatic mechanisms is a prerequisite for a correct interpretation of gases preserved in ice cores.

The work presented in this thesis focuses on the past evolution of stable isotopes of atmospheric oxygen from the technical aspects of the measurements of O_2 isotope ratios to the interpretation of their past variations. First, we present the O_2 cycle and describe the results of process-based modeling studies aiming at reproducing the observed enrichment in atmospheric $\delta^{18}O$ and $^{17}\Delta$ ($^{17}\Delta_{atm} = ln(\delta^{17}O_{atm} + 1) - 0.516 \cdot ln(\delta^{18}O_{atm} + 1)$. We review the current understanding of past orbital and millennial time-scale variations of atmospheric O_2 isotopes. We also give a description of air transport and associated processes in the firn, which alter the climatic signal preserved in ice core bubbles.

Second, a very high analytical precision and accuracy is required to measure the past variations of $\delta^{18}O_{atm}$ and especially $^{17}\Delta_{atm}$ preserved in ice core bubbles. One must primarily have the ability to measure variations as small as 10 permeg (0.01 ‰), corresponding to the millennial-scale changes observed in $^{17}\Delta_{atm}$. O_2 needs to be separated from other atmospheric constituents to achieve such a level of precision. This motivated us to develop a new method of O_2 separation, based on membrane

technology. We verify its 100 % selectivity to O_2 , and estimate its O_2 permeability. This method is currently not applicable to $^{17}\Delta_{atm}$ measurements due to sealing issues and variable isotope fractionation during O_2 permeation across the membrane.

Third, a semi-automated, offline experimental setup for $\delta^{18}O_{atm}$ and $^{17}\Delta_{atm}$ measurements was build up from scratch as an alternative, based on the conventional method relying on gas chromatograph (GC) separation of O_2 and nitrogen (N_2). It includes air extraction from ice, standard introduction and cryo-collection at 12 K (with a closed Helium cooler) of an O_2 /Argon (Ar) mixture, after separation from water (H_2O), carbon dioxide (CO_2) and N_2 . The GC unit can be bypassed for $\delta^{18}O_{atm}$ measurements in a dried and CO_2 -free air mixture. We give an overview of the units and controls of the experimental setup, and detail the developed procedure to extract, purify and collect atmospheric O_2 from ice core samples.

Fourth, the external precision of the setup, or the reproducibility of ice core $\delta^{18}O_{atm}$ measurements is estimated with 21 Late Holocene Neem (Greenland) ice core samples from the same depth. A melt-extraction method is applied on these large samples ($\simeq$ 30 g) and $\delta^{18}O_{atm}$, $\delta O_2/N_2$ and $\delta^{15}N$ are measured in an O_2 /N_2 /Ar mixture by isotope ratio mass spectrometry in Dual Inlet (DI) mode. We describe the automation of a measurement sequence of up to 10 ice core samples. The scatter observed in the raw $\delta^{18}O_{atm}$ and $\delta O_2/N_2$ underlines the occurrence of gas loss fractionation processes in ice core samples. We detail the method of data-processing, its associated uncertainty and the strategy employed to correct for non climatic effects. Based on zero-enrichment tests, the internal precision of DI measurements of $\delta^{18}O$ and $\delta^{15}N$ is 0.008 ‰ (1 σ) and 0.005 ‰ (1 σ). A similar precision is reached with individual ice core sample measurements. Based on the 21 Neem ice core samples, the ability of the analytical system to reproduce $\delta^{18}O_{atm}$ and $\delta O_2/N_2$ is estimated as 0.028 ‰ (1 σ) and 0.021 ‰ (1 σ), respectively.

Fifth, thanks to improving isotope measurement techniques, millennial scale variations of $\delta^{18}O_{atm}$ and $^{17}\Delta_{atm}$ preserved in polar ice cores have been revealed. In particular, a systematic $\delta^{18}O_{atm}$ increase is recorded during Heinrich stadials (Greenland stadials during which a Heinrich event occurs). Because of its global character, $\delta^{18}O_{atm}$ provides added value compared to the different local records of hydrological cycle variations in different continental and marine archives. However, until now, no quantitative, robust interpretation of past variations in $\delta^{18}O_{atm}$ has been established, which limits the use of $\delta^{18}O_{atm}$ as a quantitative indicator for past biospheric production or variations of the hydrological cycle. Here, we quantify the response of $\delta^{18}O_{atm}$ to such millennial events using a freshwater hosing simulation performed under glacial boundary conditions. Our O_2 isotope mass balance model takes into account the latest estimates of isotope fractionation factors for respiratory and photosynthetic processes, and makes use of atmospheric water isotope and vegetation changes obtained with the general circulation model IPSL-CM4. The atmospheric component of IPSL-CM4 is fitted with a water isotope module (LMDZ4), and its land component, the dy-

namic global vegetation model ORCHIDEE, is run offline. Our modeling approach reproduces the main observed features of a Heinrich stadial in terms of climatic conditions, vegetation distribution and $\delta^{18}O$ of precipitation. We use it to decipher the relative importance of the different processes behind the observed changes in $\delta^{18}O_{atm}$. Our results highlight the dominant role of hydrology on $\delta^{18}O_{atm}$ and confirm that $\delta^{18}O_{atm}$ can be seen as a global integrator of hydrological changes over vegetated areas. This work has been published in Climate of the Past in 2015 under the title **Quantifying molecular oxygen isotope variations during a Heinrich stadial**.

Resumé

Med sin atmosfæriske levetid på 1200 år er atmosfærisk ilt (O_2) en global markør, der hovedsagligt opstår på de lave breddegrader idet signalet integrerer biologiske og hdrologiske ændringer i områder med vegetation. Det kan derfor indeholde værdifulde oplysninger om klimaændringerne i troperne, en region som stadig mangler klimatiske rekonstruktioner, og hvis rolle i forbindelse med tusindårige klimavariationer ikke er klarlagt. Atmosfærisk O_2 er beriget i tunge isotopologer ($\delta^{17}O$, $\delta^{18}O$) i forhold til O_2 i havvand, der er den oprindelige kilde af O_2 fra fotosyntese. De processer, som forårsager en berigelse af $^{17}O/^{16}O$ og $^{18}O/^{16}O$-isotopforholdene er den biologiske cyklus, vandets kredsløb, ændringer i globalt is-mængde/hav-niveau, klimatiske forhold og fotokemiske processer i stratosfæren. For at benytte O_2 isotopologer til at sige noget om de klimatiske ændringer er det derfor vigtigt at kende den relative betydning af disse processer. Udviklingen i sammensætningen af fortidens atmosfære gennem de sidste 800.000 år kan bestemmes udfra luftbobler i de polare iskerner. Under transport og indeslutningen af luft i et porøst is-lag (firn) på iskappernes overflade, samt under lagring og analysering, foregår stof- og isotop-fraktionerings-processer, som ændrer isotopforholdet af O_2 . En forståelse af disse ikke-klimatiske processer er en forudsætning for in korrekt fortolkning af de gasser, som er bevaret i iskerneren.

Denne afhandling fokuserer på ændringerne af de stabile isotoper af atmosfærisk ilt, fra tekniske aspekter af måling af O_2 isotopforhold til klimatisk fortolkning af deres tidslige variationer. Først præsenteres cyklussen for O_2 , og vi beskriver resultater af proces-baserede modellerings-studier, som søger at reproducere den observerede berigelse af atmosfærisk $\delta^{18}O$ og $^{17}\Delta$. Vi gennemgår den nuværende forståelse af fortidens variation af atmosfæriske O_2 -isotoper. Vi beskriver også de processer forbundet med lufttransport i firnen, som ændrer det klimatiske signal i iskernernes luftbobler.

Det kræver meget høj analytisk præcision og nøjagtighed at måle fortidens variationer af $\delta^{18}O_{atm}$ og især $^{17}\Delta_{atm}$ bevaret i iskernernes luft-bobler. Dette gennemgås i del 2. Først og fremmest skal man kunne måle meget små variationer på ned til 10 permeg (0,01 ‰), hvilket svarer til de observerede ændringer i $^{17}\Delta_{atm}$ gennem de tusindårige klimaændringer. For at opnå denne grad af præcision er det nødvendigt at adskille O_2 fra de øvrige atmosfæriske bestanddele. Dette motiverede os til at udvikle en ny metode til O_2 -adskillelse, baseret på membranteknologi. Vi bekræftede, at membranen har 100 % selektivitet til O_2 , og vi har anslået dens O_2 -permeabilitet,

men metoden er endnu ikke anvendelig for $^{17}\Delta_{atm}$ -målinger grundet problemer med forsegling og variabel isotop-fraktionering under O_2 's bevægelse gennem membranen.

I afhandlingen tredje del gennemgås en semi-automatisk, offline forsøgsopstilling for $\delta^{18}O_{atm}$ og $^{17}\Delta_{atm}$ målinger, som vi byggede op fra bunden som en alternativ metode, baseret på den konventionelle metode der bygger på adskillelse af O_2 og kvælstof (N_2) i en gaskromatograf (GC). Metoden omfatter ekstraktion af luft fra is, introduktion af en standard og cryo-opsamling ved 12 K (med en lukket helium afkøler) af en O_2 -Argon (Ar) blanding, efter adskillelse fra vand (H2O), kuldioxid (CO_2) og N_2 . GC enheden kan bypasses for $\delta^{18}O_{atm}$ målinger i en tør og CO_2 -fri luftblanding. Vi giver et overblik af enhederne og kontrol af forsøgsopstillingen, og beskriver den udviklede procedure at udtrække, rense og indsamle den atmosfæriske O_2 fra iskerneprøverne.

I afhandlingens fjerde del bekræfter vi forsøgsopstillingens reproducerbarhed ved måling på 21 iskerneprøver fra NEEM iskernen (Grønland) taget fra den samme dybde, fra den sene del af Holocæn. Vi anvendte en smeltevands-ekstraktions metode på disse store prøver ($\simeq$ 30 g), og målte $\delta^{18}O_{atm}$, $\delta O_2/N_2$ og $\delta^{15}N$ i en O_2 -N_2 -Ar-blanding med isotopforholds massespektrometri i Dual Inlet (DI) tilstand. Vi beskriver automatisering af en målingssekvens på ten iskerneprøver. En vis spredning i de rå $\delta^{18}O_{atm}$ og O_2 /N_2 målinger understreger forekomsten af gastab ved fraktioneringsprocesser i iskerneprøverne. Vi beskriver metoden til databehandling, dens tilhørende usikkerhed og den strategi vi har anvendt til at korrigere for ikke-klimatiske effekter. Baseret på nul-berigelse tests findes den interne præcision af DI-målinger af $\delta^{18}O$ og $\delta^{15}N$ til at være 0.008 ‰ (1 σ) og 0.005 ‰ (1 σ). En tilsvarende præcision er nået med individuelle målinger af iskerneprøverne. Baseret på de 21 prøver fra NEEM iskernen anslås reproducerbarheden af $\delta^{18}O_{atm}$ og $\delta O_2/N_2$ af det analytiske system til at være henholdsvis 0.028 ‰ (1 σ) og 0.021 ‰ (1 σ).

Den forbedrede måleteknik for isotopmålinger har afsløret tusindårige variationer af $\delta^{18}O_{atm}$ og $^{17}\Delta_{atm}$ (del 5). Især ses en systematisk stigning i $\delta^{18}O_{atm}$ under Heinrich stadials. På grund af sin globale karakter giver $\delta^{18}O_{atm}$ en merværdi i forhold til lokale data-arkiver af de hydrologiske ændringer i forskellige kontinentale og marine arkiver. Men der findes endnu ikke nogen kvantitativ, robust fortolkning af fortidens variationer i $\delta^{18}O_{atm}$, hvilket begrænser anvendelsen af $\delta^{18}O_{atm}$ som en kvantitativ indikator for fortidige ændringer i den biosfæriske produktion eller den hydrologiske cyklus. Vi har her kvantificeret reaktionen af $\delta^{18}O_{atm}$ til sådanne tusindårige klima-begivenheder ved hjælp af en klimamodel med en ferskvands-spuling simulering under glaciale randbetingelser. Vores O_2 isotop-massebalance model tager højde for de seneste estimater for isotop-fraktioneringsfaktorer for respiratoriske og fotosyntetiske processer, og den gør brug af ændringerne i vegetation og atmosfærisk vandisotop-forhold fundet med den generelle cirkulationsmodel IPSL-CM4. Den atmosfæriske komponent i IPSL-CM4 er tilført et vandisotop-modul (LMDZ4), og dens

terrestriske komponent, den dynamiske globale vegetations model ORCHIDEE, køres offline. Vores modellering reproducerer de vigtigste observerede elementer i et Heinrich stadial, såsom de klimatiske forhold, vegetationsforhold og nedbørens $\delta^{18}O$. Vi bruger disse resultater til at afkode den relative betydning af de forskellige processer bag de observerede ændringer i $\delta^{18}O_{atm}$. Vores resultater påviser, at hydrologiske forhold er den dominerende faktor bag ændringerne i $\delta^{18}O_{atm}$, og de bekræfter, at $\delta^{18}O_{atm}$ kan ses som en globalt integreret markør af de hydrologiske ændringer i områder med vegetation. Dette arbejde er blevet publiceret i Climate of the Past (2015) under titlen **Quantifying molecular oxygen isotope variations during a Heinrich stadial**.

Contents

List of commonly-used abbreviations and physical constants

DI	Dual Inlet
CF	Continuous Flow
MS	Mass Spectrometer
IRMS	Isotope-Ratio Mass Spectrometry
GC	Gas Chromatograph
LIZ	Lock-in-zone
BFI	bubble-free ice
MIEC	mixed ionic/electronic conducting (ceramic membranes)
BCFZO	$BaCo_xFe_yZr_{1-x-y}O_{3-d}$
SST	stainless steel
IT	identical treatment
AC	alternating current
DC	direct current
NEEM	North Greenland Eemian Ice Drilling (Greenland, 77.4°N 51.1°W, 2484 m)
NGRIP	North Greenland ice core project (Greenland, 75.10°N and 42.32°W, 2917 m)
RICE	Roosevelt Island Climate Evolution (Antarctica, 79.21°S, 161.42 °W, 560 m)
EDC	EPICA Dome C (Antarctica, 75.1°S 123.4°E, 3233 m)
EPICA	European Project for Ice Coring in Antarctica
GS	Greenland stadial
GI	Greenland interstadial
HE	Heinrich event
HS	Heinrich stadial
DO	Dansgaard-Oeschger (event)
ITCZ	Intertropical convergence zone

e	$= 1.6022 \cdot 10^{-19}$ C	elementary charge
N_A	$= 6.02214179 \cdot 10^{23} mol^{-1}$	Avogadro number
R	$= 8.31451\,\mathrm{J} \cdot \mathrm{K}^{-1} \cdot \mathrm{mol}^{-1}$	gas constant
k	$= 1.3807 \cdot 10^{-23}\,\mathrm{J} \cdot \mathrm{K}^{-1}$	Boltzman constant
k	$= 8.6175 \cdot 10^{-5}\,\mathrm{eV} \cdot \mathrm{K}^{-1}$	Boltzman constant

1 Introduction

1.1 Preamble

This thesis focuses on the past variations of three stable isotopes of atmospheric oxygen preserved in polar ice cores, reflecting a global climatic signal. In order to retrieve the climatic information, the isotopic composition of O_2 occluded in ice core bubbles need to be measured with very high precision/accuracy and corrected for all the processes - in the firn, during coring, during storage and during the analytical measurements - that alter its composition and add uncertainties. The experimental part of my thesis focuses on these aspects and includes the building of an analytical system to extract and measure the three isotopes of O_2 in ice core samples. Once the "true" isotopic composition of ancient atmospheric O_2 is obtained, the interpretation of its past variations remains complex because the oxygen cycle includes various biological, hydrological and photochemical processes that cause oxygen isotope fractionation. It is therefore critical to estimate the relative contribution of these processes to give a correct interpretation of past oxygen isotope variations. The modeling part of this thesis quantifies the latter during abrupt climatic events of the last glacial period. OUTLINE

Disentangling of the measured O_2 isotopic signal ($\delta^{18}O_{atm}$, $^{17}\Delta_{atm}$) can thus be seen as the Ariadne's thread of this thesis: ARIADNE'S THREAD

- From an experimental standpoint, this implies (1) to design and build a high-purity O_2 extraction line, (2) to develop an analytical procedure in agreement with the international standards in isotope-ratio mass spectrometry (noted IRMS herafter) measurements, in particular in terms of precision and accuracy, (3) to correct for isotope fractionation caused by processes in the firn and gas loss processes during coring and storage, and (4) to correct for isotope fractionation processes occurring in the experimental setup during the handling, extracting, separating, collecting or measuring steps undergone by the ice core sample.
- From a modeling perspective, unraveling the signal requires (1) to understand the factors driving the isotopic composition of atmospheric oxygen, (2) to model the processes at play in the O_2 cycle, and (3) to quantify the relative contribution of these processes so as to give a consistent interpretation of the observed past variations.

The present PhD thesis is part of the Initial TRAining network on Mass Independent Fractionation (INTRAMIF) project (project No:237890). The scientific objectives of this European project were to "investigate processes which include signatures of Mass Independent Fractionation (MIF)" in several O-bearing compounds in the Earth's system. This was carried out in 13 individual Early Stage Researchers projects. INTRAMIF

My original project, ESR 11, was entitled **Mass independent fractionation in tropospheric O_2 : a tracer for past total oxygen production**. The initial goal of this thesis INITIAL PROJECT

was mainly experimental: it represented the development of a new method for oxygen separation (Chapter 2), along with the building of an improved extraction and collection system to measure the triple isotope composition of past oxygen in air bubbles occluded in ice cores (Chapter 3). The aim was to obtain a very high precision record of MIF over several glacial-interglacial cycles by extending measurements back to 850 kyr on Antarctic ice core, to track back the past global productivity of the vegetation. However, multiple challenges and delays faced throughout the PhD thesis on the experimental side required modifications to this approach. The oxygen line built during this thesis can currently measure $\delta^{18}O_{atm}$ with a reasonable ice reproducibility (Chapter 4), but has not been yet validated for $^{17}\Delta_{atm}$ analysis.

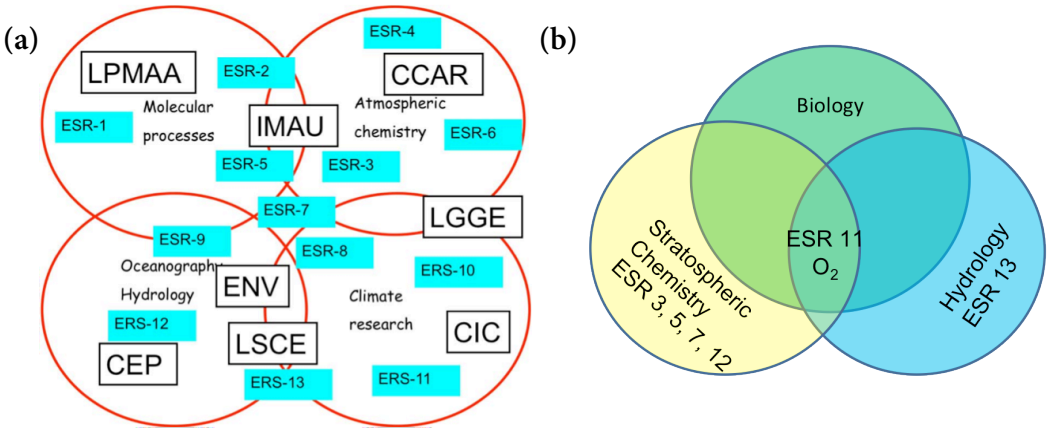

Figure 1.1 – The interdisciplinary character of the present thesis, ESR 11 project, is illustrated in this two graphs. **(a)** The different research centers involved in the INTRAMIF project. ESR 11 project is based at the Center for Ice and Climate (CIC), Denmark. **(b)** Interpreting the isotope composition of atmospheric O_2 is at the heart of the climate system (ocean, ice, atmosphere), requiring knowledge on the biospheric processes, the hydrological cycle and the stratospheric photochemistry.

ADJUSTMENT

Instead, a modeling part is included in my PhD, in collaboration with the Laboratoire des Sciences du Climat et de l'Environnement (LSCE). This work focuses on the millennial scale variations of atmospheric O_2 isotope composition over the last glacial period, and has been published in Climate of the Past in 2015 under the title "Quantifying molecular oxygen isotope variations during a Heinrich stadial" (Reutenauer et al., 2015). The paper is reproduced in Chapter 5.

Additionally to its interdisciplinary character (Fig. 1.1), a strong added value of this project was the opportunity to be involved in all the steps required to extract valuable climatic information from an ice core sample: from the ice sheet to the mass spectrometer (experimental side), and from the measured data to their interpretation, using models to disentangle the processes at play (modeling side). This section starts with an overview of the O_2 cycle, including a review of the processes influencing its isotope composition (Sect. 1.2). Section 1.3 describes the past variations of the three isotopologues of atmospheric O_2 over the last 800 kyr, documented by ice core archives, and

presents the current understanding of its orbital and millennial time-scale changes. To correctly interpret the past variations of atmospheric O_2 isotopologues preserved in air bubbles occluded in polar ice cores, it is critical to understand how the air is entrapped in the ice during the transformation of snow to ice, as these processes affect the elemental and isotope composition of O_2 (Sect. 1.4). Note that other artifactual gas loss processes cause isotope fractionation of O_2 , during ice core recovery, storage and/or during the ice core sample measurements, and they are discussed in Chapter 4. Finally, the organization of the manuscript is presented in Sect. 1.5.

1.2 The isotopic composition of atmospheric oxygen

Oxygen is the third most abundant element in the universe (with hydrogen and helium), and second most abundant species (with N_2) in atmospheric air (20.8 %). It is also abundant in surface waters, the mantle and the crust, and biological reservoirs. CO_2 plays an important role in the transfer of oxygen between these reservoirs (Thiemens, 2012). The cycle of O_2 represents the largest biogeochemical cycle on Earth, with $\simeq 3 \cdot 10^{16}$ moles of O_2 produced and consumed. As oxygen is produced by photosynthesis and consumed by respiration, a record of oxygen concentration in the past should help constrain these two major biospheric fluxes on Earth and potentially provide information on their link with the carbon cycle. Besides, gathering knowledge on the past vegetation is important, as biosphere - atmosphere interactions affect global climate through various feedbacks, via the role of the biosphere in the hydrological cycle or terrestrial albedo change, emission and consumption of greenhouse gases (Bender, 2003).

1.2.1 Focusing on O_2 isotopes rather than O_2 mixing ratio

Changes in the O_2 /N_2 ratio can be measured in air trapped in ice cores back to 800 kyr (Bender, 2002; Kawamura et al., 2007; Landais et al., 2012). Unfortunately the O_2 /N_2 ratio in ice cores does not provide a direct information on the true atmospheric variations because it is affected by permeation[1] through the ice lattice during bubble formation at pore close-off, roughly 100 m below the ice sheet surface, and by gas loss during ice core recovery and storage (Sect. 1.4). Orbital tuning of ice core chronologies has nonetheless been achieved based on the magnitude of $\delta O_2/N_2$ fractionation at bubble close-off, considered as a proxy for local summer insolation (Bender, 2002; Kawamura et al., 2007; Landais et al., 2010). While they affect the elemental composition of ice core samples, these processes have fortunately less impact on oxygen isotopologues ($\delta^{18}O$, $\delta^{17}O$), the diameter of which are of similar size (see Sect. 1.4.1.3). Oxygen isotope ratios have thus been explored as possible constraints on biospheric productivity (e.g. Luz et al., 1999).

[1]Permeation is the transport of a fluid through the interconnected pore space (interstitial space) of a porous medium.

1.2.2 Definitions

Molecular oxygen has three stable isotopologues, the most abundant being $^{16}O^{16}O$ (mole fraction: 0.99757(16)) and the two rarer $^{17}O^{16}O$ ($3.8(1) \cdot 10^{-4}$) and $^{18}O^{16}O$ ($2.05(14) \cdot 10^{-3}$). When dealing with oxygen isotopes, it is standard to use the isotope ratio, R, defined as the fraction of the abundance of the rare isotope over the dominant one in a substance:

$$^{i}R = R(^{i}O/^{16}O) = \frac{^{i}O}{^{16}O}, \tag{1.1}$$

where i can either be 18 or 17. Indeed, $^{34}R = 2 \cdot^{18} R$ and $^{33}R = 2 \cdot^{17} R$ are good approximations (Young et al., 2014). In this thesis, O_2 isotopologues are measured by IRMS, where the ratio of the ion currents, that is the number of ions collected in the Faraday cups (refer to chapter 4 for details), represents the quantity R (Coplen, 2011). For O_2 isotopologues, the ratio of the ion current measured on the $m/z34$ (mass (m) to charge (z) ratio) or $m/z33$ collector to the ion current measured on $m/z32$ collector is:

$$^{34}R = {}^{34/32}R = \frac{N(^{18}O^{16}O)}{N(^{16}O^{16}O)}, \tag{1.2}$$

and

$$^{33}R = {}^{33/32}R = \frac{N(^{17}O^{16}O)}{N(^{16}O^{16}O)}, \tag{1.3}$$

where $N(^{18}O^{16}O)$, $N(^{17}O^{16}O)$ and $N(^{16}O^{16}O)$ are, respectively, the $^{18}O^{16}O^{+}$, $^{17}O^{16}O^{+}$ and $^{16}O^{16}O^{+}$ number of ions collected on m/z 34, m/z 33 and m/z 32 collectors.

Since changes in isotope ratios through natural processes are very small, the *isotope delta*, or *relative difference in isotopic ratios* is expressed in relation to a standard using the δ notation. In the case of O_2 isotopes:

$$\delta^{i}O = \frac{^{i}R_{\text{sample}}}{^{16}R_{\text{standard}}} - 1, \tag{1.4}$$

where i can either be 18 or 17. As δ values are very small, it is standard to multiply them by a factor of 1000 and express them in ‰. Present-day atmospheric O_2 is used as a primary standard for atmospheric O_2 (e.g. Barkan and Luz, 2003) as it is spatially homogeneous because of its long residence time in the atmosphere ($\backsimeq$ 1200 yr) compared to the interhemispheric mixing time ($\backsimeq$ 1 yr). Additionally, its isotopic composition has not significantly changed over the last 50 years (corresponding to the period where it has been measured).

The partitioning of isotopes which occurs during most of physical and chemical processes on Earth is mass-dependent. It results from equilibrium and kinetic reactions between two substances (e.g. carbon dioxide into plant organic carbon), or phases (e.g. liquid water to water vapor). Isotopes of an element have indeed slight differences in

chemical and physical properties due to their mass difference (due to a different number of neutrons). As a result of fractionation processes, the isotope ratio of the considered substance is often unique and may inform on the source of the substance or the nature of the processes at play. The increased level of precision obtained through continuous improvements in IRMS measurements and analytical procedures enable at present to distinguish equilibrium and kinetic fractionation processes (Young et al., 2002).

EQUILIBRIUM FRACTIONATION

Equilibrium isotope fractionation is expressed with the isotope fractionation factor α. It is defined as the ratio of the isotope ratios between the two substances, or phases A and B at equilibrium. It is equivalent to the equilibrium constant between compounds A and B for the isotope substitution reaction $A + {}^{h}B \Longleftrightarrow {}^{h}A + B$, where h indicates the compound containing the heavy isotope (${}^{17}O$ or ${}^{18}O$ in the case of O_2):

$$K = \frac{[{}^{h}A][B]}{[{}^{h}B][A]} = \frac{[{}^{h}A]/[A]}{[{}^{h}B]/[B]} = \frac{{}^{h}R_A}{{}^{h}R_B} = {}^{h}\alpha_{A/B} = {}^{h}\alpha_{eq}. \tag{1.5}$$

For instance, let us consider equilibrium exchange of ${}^{18}O$ of H_2O between liquid (liq) and vapor (vap) phases, ${}^{i}R_A$ and ${}^{i}R_B$ are the oxygen isotope ratios ${}^{18}R_{liq}$ and ${}^{18}R_{vap}$, respectively. In that case, ${}^{18}\alpha_{eq}$ is greater than 1, in other words the O_2 isotopic composition of liquid water is heavier than the one of water vapor. Light isotopes have indeed a higher saturation pressure than heavy isotopes, and are therefore more abundant in the gas phase than in the liquid phase. The liquid phase is thereby enriched in heavy isotopes. In general, α decreases with temperature, as the isotopic difference in binding energies decreases with increasing temperature (Lennard-Jones, 1931).

KINETIC FRACTIONATION

Unlike reversible equilibrium reactions, where forward and backward reaction rates are identical, kinetic processes represent irreversible, one way reactions, such as respiration or evaporation. Such reactions are dependent on the ratio of the masses of the isotopologues. Light isotopologues indeed are more reactive according to their kinetic energy:

$$E_{kin} = kT = \frac{1}{2}mv^2, \tag{1.6}$$

where k is the Boltzmann constant, T the absolute temperature, m the mass and v the average molecular velocity. As shown by Eq. 1.6, the kinetic energy of a molecule is solely controlled by its temperature. This means that a heavier isotopologue will have a lower velocity than the light isotopologue. For atmospheric O_2 , the molecule containing a ^{18}O atom will move at $\sqrt{M_{OO}/M_{^{18}OO}} = \sqrt{32/34} = 0.94\%$ of the speed of the light isotopologue. This speed difference explains why light isotopologues will (1) diffuse faster, and (2) undergo more collisions with other molecules, thus reacting more often and thereby depleting the products (in heavy isotopologues) while enriching the reactants. Kinetic isotope fractionation is expressed with the fractionation factor α_{kin}.

The relation between the quantities isotope fractionation factor α, isotope fraction-

ation ε, and isotope delta δ of compounds A and B is expressed as:

$$\varepsilon_{A/B} = \alpha_{A/B} - 1 = \frac{\delta_{A/standard} - 1}{\delta_{B/standard} - 1}, \tag{1.7}$$

We've seen that the quantities ε and α can refer to a thermodynamic equilibrium process or a kinetic process. It can also define an "apparent" distribution of isotopes between substances or phases in complex biogeochemical systems, having unknown pathways or combining several reactions.

1.2.3 The oxygen cycle and its associated isotope fractionations

In this section, we describe the cycle of oxygen (Fig. 1.2) and its associated processes causing isotopic fractionation[2]. Not only biological processes, but also the hydrological cycle or the stratospheric photochemistry cause oxygen isotope fractionation, which makes the interpretation of atmospheric O_2 isotope variations complex.

1.2.3.1 Biological processes: oxygen production

photosynthesis Photosynthesis produces organic carbon from inorganic carbon (CO_2):

$$6CO_2 + 12H_2O + light \longrightarrow C_6H_{12}O_6 + 6O_2 + 6H_2O \tag{1.8}$$

Tropospheric oxygen is produced through terrestrial and marine photosynthesis. According to estimates from Bender et al. (1994), Luz et al. (1999), Hoffmann et al. (2004), marine production ranges from 7.61 to 12 $Tmol \cdot yr^{-1}$ of O_2 ($1 Tmol = 10^{15}$ mol), while terrestrial production causes O_2 fluxes from 16.7 to 20.4 $Tmol \cdot yr^{-1}$.

Land As photosynthesis produces O_2 from water, and ocean waters represents the ultimate source of oxygen, being the largest reservoir on Earth, one would not expect large differences between the isotopic composition of atmospheric O_2 and the one of ocean waters. At isotopic equilibrium between ocean water and air, $\delta^{18}O_{atm}$ would in fact be enriched by 6 ‰ (Urey and Greiff, 1935; Young et al., 2014). However, more than 80 years ago, Dole (1935) and Morita (1935) observed a very large difference in the atomic weight of oxygen in air and in water, with air enriched in ^{18}O. The review of Dole (1965) attributed this difference to isotope fractionation during photosynthesis (based on experiments of Dole and Jenks, 1944) and respiration (based on experiments from Lane and Dole, 1956). However, following observations (Guy et al., 1993) showed that no fractionation of oxygen isotopes occured during photosynthesis (on spinach thylakoids, cyanobacteria, and diatoms). Instead, Dongmann et al. (1972); Dongmann (1974) proposed that evapotranspiration of the substrate water for photosynthesis - at the site of oxygen production - would enrich newly produced O_2 by 8 ‰, a value refined since then (Sect. 1.2.3.3). This is an important contribution to

[2]An exhaustive review can be found in Luz et al. (2014), with a detailed description of the experimental studies done to determine isotope fractionation of biological processes

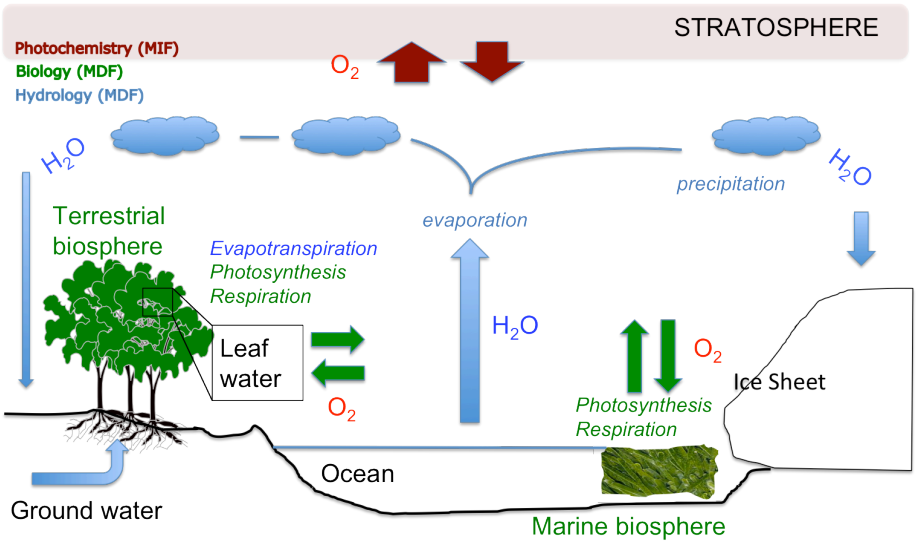

Figure 1.2 – Scheme of sources and sinks related to the oxygen cycle. Fluxes of water (blue), and fluxes of oxygen (green) are associated with mass-dependent fractionation, while fluxes of oxygen between the troposphere and the stratosphere (red) are associated with mass-independent fractionation. All these processes must be accounted for when calculating the isotopic balance of oxygen in the troposphere (Chapter 5).

the understanding of $\delta^{18}O_{atm}$ variations as $\delta^{18}O$ enrichment during photosynthesis on land is primary driven by hydrological processes (Sect. 1.2.3.3), rather than biological ones.

In the last 20 years, new experiments have confirmed that assuming no isotope fractionation during oxygen production (Guy et al., 1993) is likely to be correct for land photosynthesis (Luz and Barkan, 2005), but have also revealed that marine photosynthetic production of O_2 by phytoplancton causes enrichment of the produced O_2 up to 6 ‰ with respect to the substrate water (Eisenstadt et al., 2010), at the exception of cyanobacteria (Helman et al., 2005), where no fractionation is observed. Ocean

1.2.3.2 Biological processes: oxygen uptake

1.2.3.2.1 $^{18}\alpha_{resp}$

10 years later, Rabinowich (1945) first proposed that respiration was responsible for the isotopic enrichment observed in atmospheric O_2 . Indeed, respiratory processes consume preferentially light isotopologues of O_2 , leaving the remaining gas - the atmosphere - enriched in heavy isotopologues. Dole (1965) confirmed in a review that respiration by various organisms was causing isotopic fractionation.

In land, the isotope fractionation factor associated with oxygen uptake can be expressed in terms of dark (mitochondrial) respiration, Mehler reaction and photores-

piration fractions, each of these respiratory processes being associated with a specific fractionation:

$$
\begin{aligned}
{}^{18}\alpha_{\text{resp}} = {}^{18}\alpha_{\text{photo}} \cdot f_{\text{photo}} + {}^{18}\alpha_{\text{Mehler}} \cdot f_{\text{Mehler}} + {}^{18}\alpha_{\text{dark\_soil}} \cdot f_{\text{dark\_soil}} \\
+ {}^{18}\alpha_{\text{dark\_leaves}} \cdot f_{\text{dark\_leaves}},
\end{aligned}
\tag{1.9}
$$

The latest estimations - and associated references - of the isotope fractionation factors ${}^{18}\alpha_{\text{resp}}$, ${}^{18}\alpha_{\text{Mehler}}$, ${}^{18}\alpha_{\text{photo}}$, ${}^{18}\alpha_{\text{dark\_leaves}}$ and ${}^{18}\alpha_{\text{dark\_soil}}$ can be found in Table 1.1. Corresponding O_2 uptake fluxes are represented by f_{Mehler}, f_{photo}, $f_{\text{dark\_leaves}}$ and $f_{\text{dark\_soil}}$, whose sum equals 1. The Mehler reaction fraction, f_{Mehler}, is assumed to represent 10 % of global respiration (Badger et al., 2000). GCMs are required to precisely estimate the fraction of photorespiration (f_{photo}), (e.g. Hoffmann et al., 2004; Landais et al., 2007a; Reutenauer et al., 2015). The fractions $f_{\text{dark\_soil}}$ and $f_{\text{dark\_leaves}}$ can be estimated based on Schlesinger and Andrews (2000), who found that global carbon fluxes from soils represent 62 % of the global Gross Primary Production (GPP).

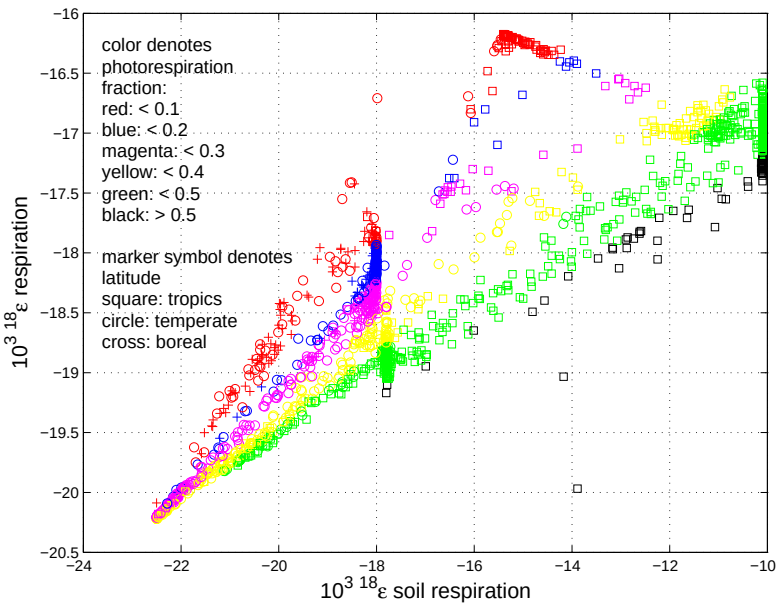

Figure 1.3 – The dependence of the isotope fractionation of terrestrial respiration on that of two of the main O_2 uptake processes, soil respiration and photorespiration. Values are calculated from GPP computed by the global dynamic vegetation model ORCHIDEE for the LGM Control simulation (refer to Chapter 5). Each value correspond to a grid cell in the model. While the fraction of photorespiration f_{photo} is variable but its associated isotope fractionation constant, the fraction of soil respiration $f_{\text{dark\_soil}}$ is almost constant but its associated isotope fractionation ${}^{18}\varepsilon_{\text{dark\_soil}}$ variable. The triangle shape is due to the fact that ε_{dark_soil} associated with temperate and boreal soils is of similar magnitude as ε_{photo}, such as variations of f_{photo} in mid to high latitudes have only a moderate impact. In contrast, ε_{dark_soil} is much weaker in tropical soils and compensates for the strong isotope fractionation of photorespiration.

Table 1.1 – Isotope fractionation $^{18}\varepsilon$ and mass-dependent fractionation slope λ ($\frac{ln(^{17}\varepsilon-1)}{ln(^{18}\varepsilon-1)}$) during O_2 uptake processes. Uncertainties are indicated if available

parameter	O_2 uptake process	$10^3 \cdot {}^{18}\varepsilon$	λ
$^{18}\varepsilon_{dark\_leaves}$	dark respiration in leaves (90 % COX, 10 % AOX)	19±1[a,b]	0.516±0.001[a,c]
	through		
	cytochrome oxidase pathway (COX)	17.4 to 19.9[e,f]	0.516[c,d]
	alternative oxidase pathway (AOX)	24.1 to 26.2[e,f]	0.514[c,d]
$^{18}\varepsilon_{dark\_soil}$	dark soil respiration	15.6±0.5[a]	0.516±0.001[a,c]
	including		
	tropical	10.1±1.5[c]	
	temperate	17.8±1.0[c]	
	boreal	22.5±3.6[c]	
$^{18}\varepsilon_{Mehler}$	Mehler reaction	10.8±0.2[g]	0.525±0.002[g]
$^{18}\varepsilon_{photo}$	Photorespiration	21.4[i]±1[g]	0.509±0.001[g]
	a two step process		
	rubisco oxygenase	21.3 to 21.8[g,h]	0.517[g]
	glycolate oxidase	21.5 to 22.7[g,h]	0.501[g]
$^{18}\varepsilon_{resp}$	global terrestrial respiration	17.4±1[a]	0.5145±0.0007[a]

[a] Landais et al., 2007a.
[b] Angert et al., 2003a.
[c] Angert et al., 2003b.
[d] Luz and Barkan, 2005.
[e] Guy et al., 1989.
[f] Guy et al., 1992.
[g] Helman et al., 2005.
[h] Guy et al., 1993.
[i] 21.5 is the average of the most recent values of rubisco oxygenase and glycolate oxidase measured by Helman et al. (2005).

1.2.3.2.2 *Dark respiration*

Mitochondrial respiration takes place in the cell of a living organism. It includes various pathways of substrate oxidations, involving glycolysis, Krebs' cycle and oxidative phosphorylation, that releases usable energy in the form of ATP. This process yields CO_2 and H_2O from oxygen and sugars:

$$6O_2 + C_6H_{12}O_6 \longrightarrow 6CO_2 + 6H_2O + ATP(energy), \tag{1.10}$$

Mitochondrial respiration is the dominant oxygen uptake mechanism, which is assumed to be similar under dark and light conditions (e.g., McCree and Amthor, 1982; van Iersel and Bugbee, 2000). It is also called dark respiration as it does not require sunlight to consume O_2 and release CO_2 , in contrast with photorespiration or the Mehler reaction. McCree et al. (1970) first proposed the empirical partitioning of dark respiration into two physiological components: a growth and a maintenance component. Growth respiration is dedicated to the synthesis of new biomass while maintenance respiration is defined as the respiration needed to provide the energy for all plant processes that do not result in a net gain in plant biomass, but maintain

existing organs and normal activities of living cells. Quantifying their contribution is essential as variations in their ratio may significantly alter the carbon balance of the plants. Indeed, the amount of carbon incorporated into dry matter represents 50% to 70% of the total amount of carbon fixed in the photosynthetic process (Amthor, 2012), which means that up to 50 % of the carbohydrates are respired by the plants.

Dark respiration occurs through two pathways, the cytochrome oxidase pathway (denoted COX hereafter) and the cyanide resistant alternative oxidase pathway (denoted AOX hereafter). In most of the plants, the COX pathway dominates, and a value for ${}^{18}\varepsilon_{\text{dark\_leaves}}$ of 0.981‰ (Landais et al., 2007a; Blunier et al., 2002) is estimated when assuming that only 10 % of dark respiration in leaves occurs through the AOX pathway, hence 90 % through the COX pathway.

1.2.3.2.3 *Dark respiration in soils*

A significant proportion of terrestrial respiration (30 to 40 %) occurs below the surface[3] (Raich and Potter, 1995) with varying fractionation values (Table 1.1). Indeed, isotope fractionation associated with tropical (10.1 ‰), temperate (17.8 ‰) and boreal soils (22.5 ‰) exhibit significant differences, due to different diffusion pathways (Angert et al., 2003a), increasing with colder temperatures, hence causing a high zonal contrast. The nature of the soils thus need to be considered to correctly estimate ${}^{18}\varepsilon_{\text{dark\_soil}}$ (Sect. 5).

Additionally to the nature of the soils, diffusion limitations in soils modify the magnitude of the effective ${}^{18}\alpha_{\text{dark\_soil}}$. This phenomenon was observed by Guy et al. (1989), who noted that when O_2 diffusion to the consumption site is slow, the effective ${}^{18}\varepsilon_{\text{dark\_soil}}$ is not only dependent on the isotope fractionation of the O_2 consuming process, but also on the isotope fractionation of the O_2 diffusion and the relative rate of diffusion and consumption (Angert et al., 2001). Farquhar et al. (1982) describes it for CO_2 uptake by leaves:

$$ {}^{18}\varepsilon_{eff} = {}^{18}\varepsilon_{diff} + ({}^{18}\varepsilon_{uptake} - {}^{18}\varepsilon_{diff})\frac{Ci}{Ca}, \tag{1.11} $$

where ε_{eff}, ε_{diff}, ε_{uptake} are respectively the effective, diffusion, uptake isotope fraction-

[3] It is interesting to mention here the role of soil respiration in Biosphere 2, an enclosed (airtight) experimental ecosystem located in southern Arizona, occupied by a few humans (e.g Broecker, 2000; Severinghaus, 1995): a sharp decrease in O_2 concentration (from 21 % to 14 %) was experienced within Biosphere 2 over the first 16 month. The O_2 loss was higher during winter, as photosynthesis was reduced at time of low luminosity. It turned out that soils were too rich in organic matter, causing respiration fluxes to be two times higher than photosynthetic ones. It took some time to validate this hypothesis because the increase in CO_2 concentration was too low with respect to the O_2 loss. Indeed, during microbial oxidation of organic matter, one mole of CO_2 is produced for each mole of O_2 consumed. The mystery was unfold when Severinghaus (1995) proved that uptake of carbon by concrete (walls material) to form calcium carbonate was responsible for the discrepancy. This story illustrates the important contribution of soil respiration to total respiration, but an analogy to the real world is not possible, as these soils were extremely rich in organic matter, in particular compost (Severinghaus, 1995).

ation, and Ca and Ci are the substrate concentrations in the ambient air and in the reaction site, respectively. In the case of very slow diffusion, any O_2 reaching the site of respiration is entirely consumed, and the effective O_2 soil isotope fractionation is only due to diffusion. When diffusion is rate limiting, higher clay content or water content in soils weakens the effective ${}^{18}\varepsilon_{\text{dark\_soil}}$ by switching the mode of O_2 diffusion from diffusion in gas to diffusion in liquid phase, much lower (Farquhar and Lloyd, 1993). Consequently, water saturated soils are very poor at transmitting oxygen from the sites of respiration back to the atmosphere (Angert et al., 2001), while dry soils, well aerated, have an effective isotope fractionation similar to the one of the O_2 uptake process. In other words, a high-moisture content in soils, by preventing or dampening the back flux of isotopically enriched O_2 , the residual left over after partial respiratory consumption, to the atmosphere, weakens the effect of ${}^{18}\varepsilon_{\text{dark\_soil}}$ on ${}^{18}\varepsilon_{\text{resp}}$.

In the context of millennial scale variability during the last glacial period, soil aeration is of great importance. Indeed, during HSs, NH tropical soils generally became less waterlogged, as inferred from the lower atmospheric nitrous oxide concentration and its isotopic composition during HS1 (Schilt et al., 2014). This should cause a stronger ${}^{18}\varepsilon_{\text{dark\_soil}}$, which could play a role in the $\delta^{18}O_{atm}$ increase over HSs. A rough attempt to account for soil water content variations on millennial time scale can be found in Chapter 5. Additionally, the influence of soil moisture on ${}^{18}\varepsilon_{\text{dark\_soil}}$ strengthens the link between $\delta^{18}O_{atm}$ and the low latitude hydrological cycle, as already proposed by e.g. Bender et al. (1994) and Severinghaus et al. (2009) on orbital and millennial time scale, respectively.

1.2.3.2.4 Photorespiration

Photorespiration is associated with a strong isotope fractionation, with ${}^{18}\varepsilon_{\text{photo}} = 21.4‰$ (Helman et al., 2005). It is therefore important to estimate the variations of its associated O_2 uptake flux as even small changes can significantly affect $\delta^{18}O_{atm}$ (Fig. 1.3). Photorespiration fraction f_{photo} is calculated from the proportion of C4 vs C3 plants, the Plant Functional Type (noted PFT heareafter, see Table 1 of Chapter 5 for details), the temperature and CO_2 level as depicted in the biochemical model of photosynthesis from Farquhar et al. (1980), and already implemented in the studies of Hoffmann et al. (2004) and Landais et al. (2007a). Low CO_2 level, high temperature, conditions of hydric stress lead to an increased rate of photorespiration.

In the following, we describe the parameters controlling f_{photo}. All types of C3 plants photorespire, but in different proportions, while C4 plants do not, owing to a CO_2 concentration mechanism allowing them to operate at high chloroplast CO_2 partial pressures and thereby to inhibit the oxygenation reaction (Von Caemmerer, 2000). As CO_2 assimilation rate and evapotranspiration rate are linked through stomatal conductance (Eq. 1.19), C4 plants resist better to hydric stress than C3 plants. Indeed, they do not need to open their stomata as much as C3 plants do to compensate for the low CO_2 level, and thereby limit their evapotranspiration. During photosynthesis, in

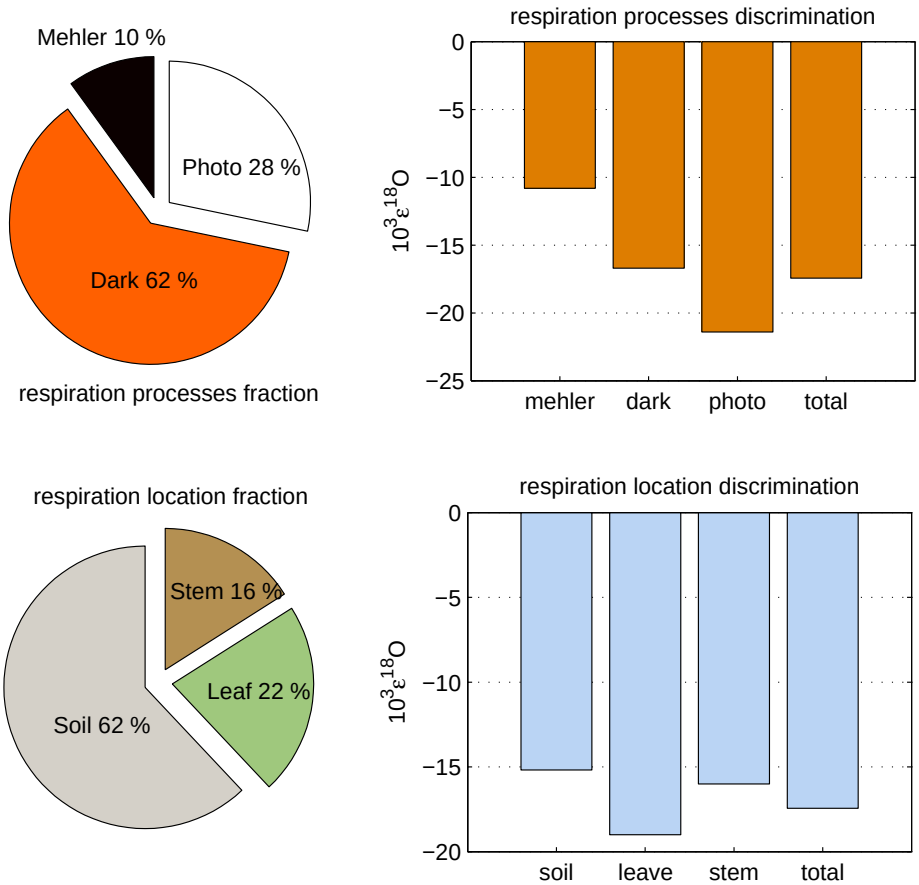

Figure 1.4 – Isotopic fractionation and location of various respiratory pathways involved in the oxygen cycle. This graphic is intended to give a qualitative overview of the processes to consider when calculating the global terrestrial isotope fractionation during oxygen uptake. Fractions and isotope fractionation can vary depending on vegetation distribution and climate conditions, in particular the fraction of photorespiration and ${}^{18}\varepsilon_{\text{dark}}$ through its soil contribution ${}^{18}\varepsilon_{\text{dark\_soils}}$. Please refer to text for details and Table 1.1 for references. **(a)** Fraction of respiratory processes. Photorespiration fraction primary depends on the C3/C4 ratio (Sect. 1.2.3.2.4) and thus requires the use of vegetation models. Here f_{photo} has been estimated under Last Glacial Maximum conditions with outputs of the global dynamic vegetation model ORCHIDEE (Sect. 5). **(b)** The total ${}^{18}\varepsilon_{\text{resp}}$ represents the O_2 consumption weighted average of ${}^{18}\varepsilon_{\text{Mehler}}$, ${}^{18}\varepsilon_{\text{photo}}$ and ${}^{18}\varepsilon_{\text{dark}}$. **(c)** This figure represents the soil, dark and stem fraction of dark respiration, that is without considering photorespiration and Mehler reaction, which do not occur in soils as they require sunlight. Note that in Reutenauer et al. (2015), stem respiration (Angert et al., 2012) is not considered as the estimation of both its fraction and associated isotope fractionation are uncertain.

the chloroplast stroma of C3 plants, there is competition between carboxylation and oxygenation of the Ribulose-1,5-biphosphate- carboxylase-oxygenase (Rubisco), the enzyme responsible for carbon fixation during the Calvin cycle (Tamiya and Huzisige,

1949; Bowes and Ogren, 1972). The rate of carboxylation, Vc, and of oxygenation, Vo, are related by $\eta = \frac{Vo}{Vc}$. During the photosynthetic carbon reduction (PCR) cycle, 1 mol of CO_2 consumed produces 1 mol of O_2 . During the photorespiratory carbon oxidation (PCO) cycle, 0.5 mole of CO_2 is released for 1 mol of O_2 consumed. In terms of carbon production and oxygen production:

$$C_{prod} = Vc - 0.5 \cdot Vo = Vc(1 - 0.5 \cdot \eta) \tag{1.12}$$

and

$$O_{2prod} = Vc + Vo = Vc(1 + \eta). \tag{1.13}$$

From the stoechiometry of the photorespirative reaction, it follows that P_{photo} for C3 plants, expressed in terms of carbon and oxygen production (Von Caemmerer, 2000; Hoffmann et al., 2004):

$$P_{photo} = f_{photo} + 1 = Vc(1 + \eta)/Vc(1 - 0.5 \cdot \eta). \tag{1.14}$$

From Eq. 1.12 it can be seen that the CO_2 compensation point τ (Laisk, 1977; Laisk and Oja, 1998), defined as the chloroplast CO_2 partial pressure when carboxylation equates oxygenation in absence of dark respiration or, in other words, when there is no net CO_2 assimilation, is reached when $\eta = 2$. Equations (2.16) and (2.17) from Von Caemmerer (2000) show that:

$$\eta = \frac{Vo}{Vc} = \frac{1}{S_{c/o}} \cdot \frac{Oi}{Ci}, \tag{1.15}$$

where $S_{c/o}$ is the relative specificity of Rubisco, and Oi and Ci are the leaf intercellular mixing ratio - or chloroplastic partial pressure - of O_2 and CO_2 , respectively. At CO_2 compensation point, Eq 1.15 becomes:

$$2 = \frac{1}{S_{c/o}} \cdot \frac{Oi}{\tau}, \tag{1.16a}$$

hence

$$S_{c/o} = \frac{Oi}{2 \cdot \tau}. \tag{1.16b}$$

Rearranging Eq. 1.15 using Eq. 1.16,

$$\eta = \frac{Vo}{Vc} = 2\frac{\tau}{Ci}. \tag{1.17}$$

Rearranging Equation 1.14 by substituting η with $2\frac{\tau}{Ci}$:

$$P_{photo} = \frac{Ci + 2\tau}{Ci - \tau}, \tag{1.18}$$

In their study, Lloyd and Farquhar (1994) estimate $\tau = 2 \cdot T_p$, where T_p is the temperature at the time of photosynthesis.

The dependence of P_{photo} on PFT is due to Ci, as detailed in the following. Indeed, each PFT optimizes its stomatal behaviour (Cowan, 1977; Cowan and Farquhar, 1977) by varying its stomatal conductance in order to keep constant Λ ($mol.mol^{-1}$) the PFT specific biome marginal water cost of plant carbon gain (Lloyd and Farquhar, 1994). Λ is expressed as follows: PFT DEPENDENCE

$$\Lambda = \frac{\frac{\partial E}{\partial gs}}{\frac{\partial A}{\partial gs}} = \frac{\partial E}{\partial A}, \tag{1.19}$$

where E is the transpiration rate, A the rate of carbon assimilation, gs the stomatal conductance. Ci calculates to:

$$Ci = Ca - \sqrt{\frac{1.6 \cdot D \cdot (Ca - \tau)}{\Lambda}}, \tag{1.20}$$

where 1.6 relates to how much faster than CO_2 water vapor pass through stomata pore, Ca denotes ambient CO_2 mixing ratio and D the leaf to air vapour mole fraction deficit during photosynthesis (biome values can be found in Lloyd and Farquhar, 1994). Ci depending on Λ, it follows that f_{photo} is PFT dependent. A detailed simulated vegetation cover is therefore required to assess f_{photo}, hence the global terrestrial biosphere's oxygen fluxes.

From Eq. 1.28 (Sect. 1.2.4) and Eq. 1.18, we can extract the following relationship relating photorespiration fraction to T, Ci, and C4 fraction, f_{C4}[4]:

$$f_{photo} = (1 - f_{C4})(1 - f_{Mehler})(1 - \frac{Ci - 2T_p}{Ci + 4T_p}), \tag{1.21}$$

The first term shows that an increased C4/C3 ratio will decrease f_{photo}, while the third term expresses both the positive relationship between f_{photo} and T_p (Fig. 1.5), and the relationship between f_{photo} and Ci, controlled by PFT, Ca and T_p (Eq. 1.20). Obviously CO_2 also has an impact on photorespiration. Increase in CO_2 would reduce the photorespiration fraction, thus lowering $^{18}\varepsilon_{\text{resp}}$, but replacement of C4 plants by C3 plants favored by higher CO_2 level would lead to an opposite effect. It is thus complex to assess the impact of a change in CO_2 concentration on the photorespiration fraction.

1.2.3.2.5 *Mehler reaction*

Like photorespiration, the Mehler reaction can be seen as an alternative electron sink during plant photosynthesis. During the Mehler reaction (Mehler, 1951), O_2 is ultimately reduced to H_2O using light. First, superoxide O_2^-, which results from the reduction of O_2 in the photosystem 1 complex, is dismutated to H_2O_2, which is subsequently reduced to H_2O by ascorbate peroxidase in the chloroplast (Rebeiz et al., 2010). Despite the weak contribution of the Mehler reaction to global O_2 uptake fluxes, $\backsim$10%

[4] such as $f_{C3} + f_{C4} = 1$

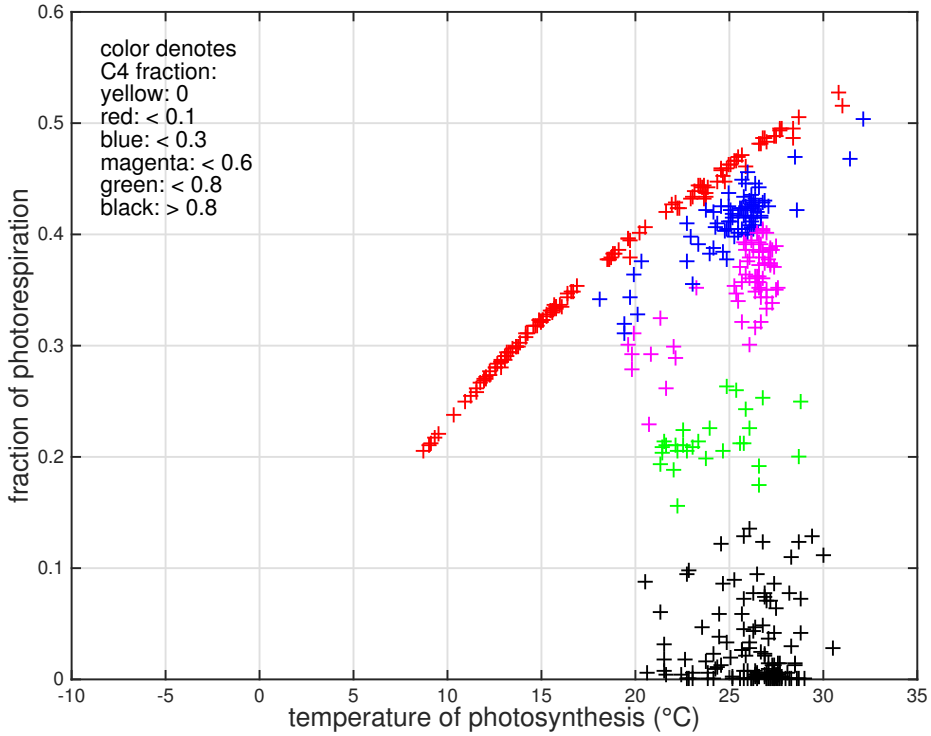

Figure 1.5 – The control of temperature and C3/C4 ratio on the fraction of photosynthesis f_{photo} based on Equation 1.21. A decrease in C4 fraction as well as an increase in temperature cause a higher f_{photo}. Below 15-20 °C, temperature controls f_{photo}, while above 20 °C, f_{photo} is strongly dependent on the C4 fraction, regardless of the temperature. Here outputs of the global dynamic vegetation model ORCHIDEE run under Last Glacial Maximum conditions are used (Sect. 5).

(Badger et al., 2000), interest in this respiratory pathway grew in recent years because in its role in the generation of reactive oxygen species, essential for the control of different cell processes, and in stress resistance, through the involvement of H_2O_2 in stomata closure and movement (Strizh, 2008). $^{18}\varepsilon_{\text{Mehler}}$ is very weak (10.8 ‰) relative to other respiratory processes (Helman et al., 2005) and therefore attenuates the magnitude of the global terrestrial respiratory isotope fractionation $^{18}\varepsilon_{\text{resp}}$ (Table 1.1).

1.2.3.2.6 *Uptake processes in the ocean*

Global respiratory isotope fractionation in the ocean $^{18}\varepsilon_{resp\_mar}$ is estimated in a global way as most of the O_2 uptake occurs in the euphotic zone ($f_{euph} \simeq 90\%$, Luz et al., 2014). Isotope respiratory fractionation in the euphotic zone, ε_{resp_euph}, is estimated to range from 20 ‰ to 26 ‰ (Kiddon et al., 1993; Quay et al., 1993; Luz et al., 2002; Hendricks et al., 2004). Marine respiration also occurs below the surface, associated with a weaker ε_{deep_resp} (Levine et al., 2009; Bender, 1990; Kroopnick and Craig, 1976; Rakestraw et al., 1951). As for soil respiration, ε_{resp_deep} is not only dependent on the isotope fractionation of the O_2 consuming process, but also on the isotope fractionation of the O_2 diffusion and the relative rate of diffusion and consumption (cf. Eq.

1.11). An effective respiratory isotope fractionation of 19.4 ± 0.5 in the subphotic zone has been derived by (Luz and Barkan, 2011) and can be taken as a representative value for ε_{resp_deep}. The fraction of respiration in the deep ocean f_{deep} is about 11%, according to the most recent estimation (Luz et al., 2014). Previous ones ranged from 5 % (Bender et al., 1994) to 20 % (Hoffmann et al., 2004) (Table 1.2).

1.2.3.3 Hydrological processes

The water consumed by the terrestrial biosphere serves as substrate water for photosynthesis and is largely responsible for isotope fractionation associated with oxygen production processes (Sect. 1.2.3.1). This substrate water, commonly called leaf water, is not homogenous worldwide and shows strong variations with the latitude and climate. Indeed, Rayleigh distillation associated with transport of meteoric water from the evaporative region to the source of precipitation causes a depletion of H_2O in ^{18}O and ^{17}O, increasing with latitude. Besides, changes in isotope composition of meteoric H_2O depends on the composition of the moisture source region, rainfall amount and the amount of evaporation, changes in past atmospheric circulation patterns and the ratio of summer to winter precipitations (Yuan et al., 2004; Johnson et al., 2006; Clemens et al., 2010; Dayem et al., 2010; Pausata et al., 2011; Tan, 2014). Integrating this combination of processes along air mass trajectories for each grid square can thus only be done with an AGCM (Risi et al., 2012).

In contrast, evapotranspiration at the site of land photosynthesis causes an enrichment of leaf water in heavy O_2 isotopes which is function of the relative humidity (Gonfiantini, 1965). The cause of the ^{18}O enrichment in leaf water is similar to that of evaporation from small water bodies and is controlled by the liquid-water isotopic equilibrium and the isotope fractionation during the diffusion of water vapor in air. Although measurements of $\delta^{18}O_{lw}$ have been used to calculate a global value of 6.5 ± 2.1‰ (West et al., 2008), it is complex to estimate the global isotopic composition of leaf water, because it is strongly affected by the spatial distribution and temporal variations of the isotopic composition of precipitation and of climate conditions (relative humidity and temperature) in the lowest layer of the atmosphere. GCMs fitted with water isotopes (Hoffmann et al., 2004; Landais et al., 2007a) are therefore required to model the worldwide isotopic composition of leaf water (See Chapter 5). The global isotopic composition of leaf water can be then computed from the spatial and temporal integration of local (grid cell in a model) $\delta^{18}O_{lw}$ and associated photosynthetic O_2 fluxes (e.g. Landais et al., 2007a). Local $\delta^{18}O_{lw}$ of leaf water is computed through the Craig and Gordon (1965) equation of evaporation from large bodies of water applied to leaf transpiration, including effects of diffusion through stomata and leaf boundary layer effects (Dongmann, 1974):

$$\delta^{18}O_{lw} = h \cdot (\delta^{18}O_{vap} +^{18} \varepsilon_{eq}) + (1-h) \cdot (\delta^{18}O_E +^{18} \varepsilon_{eq} +^{18} \varepsilon_{kin}), \qquad (1.22)$$

where h is the relative humidity at the site of photosynthesis, $^{18}\varepsilon_{eq}$ is the liquid vapor equilibrium isotope effect, temperature dependent, $^{18}\varepsilon_{kin}$ is the kinetic isotope effect occurring when humidity is below saturation, $\delta^{18}O_{vap}$ is the water vapor $\delta^{18}O$ in the

first layer of the troposphere, and $^{18}O_{gw}$ stands for soil water, but is stricto sensu the isotopic composition of the transpired water, that must be close to the one of the source (soil) water in steady state (Farquhar et al., 2007). $\delta^{18}O_{gw}$ and the $\delta^{18}O$ of meteoric waters at the site of O_2 production can be considered identical at first order. From Eq. 1.22, it follows that leaf water is usually ^{18}O enriched, as both equilibrium and kinetic fractionation tend to discriminate against heavy isotopologues. The former due to higher partial vapor pressure of the heavier isotopologue $H_2^{18}O$, the latter due to lower binary diffusivity in air for $H_2^{18}O$ water vapor (Farquhar et al., 2007). Under moist conditions, just after rain, $\delta^{18}O_{lw}$ enrichment will be very small, while the maximum isotope effect occurs when atmospheric humidity is very low, and can be approximated as the sum of kinetic and equilibrium fractionation terms (refer to Farquhar et al., 2007 for details).

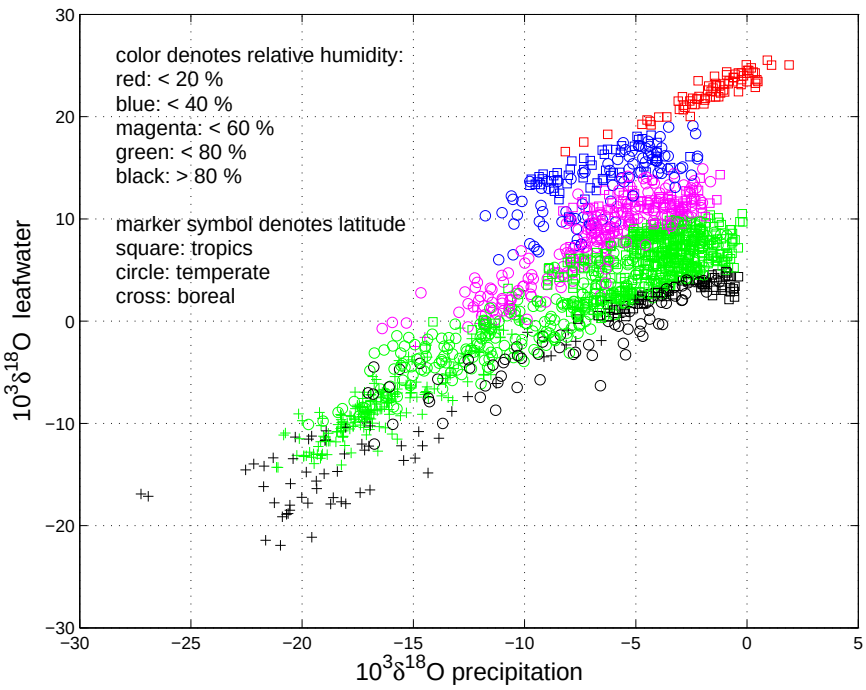

Figure 1.6 – Leafwater as a function of relative humidity and precipitation. Here outputs of the global dynamic vegetation model ORCHIDEE and LMDZ run under Last Glacial Maximum conditions are displayed (Chapter 5)

1.2.3.3.1 *Lower $\delta^{18}O_{lw}$ enrichment in observations*

Several studies have found that $\delta^{18}O_{lw}$ enrichment predicted by the Craig and Gordon equation (Eq. 1.22) was more enriched than observed $\delta^{18}O_{lw}$ (e.g. Allison et al., 1985; Bariac et al., 1989; Flanagan et al., 1994; Wang et al., 1998. Here we present a few hypothesis to explain why.

- A too strong kinetic fractionation at leaf surface?

$^{18}\varepsilon_{kin}$

Several values for the ratio $\frac{H_2^{16}O}{H_2^{18}O}$ can be found in the literature (Merlivat, 1978; Cappa et al., 2003; Luz et al., 2009), varying from 1.028 to 1.032. For leaf water transpiration, various studies suggest that kinetic fractionation is very heterogeneous (e.g. Yakir et al., 1989) and many of them have reported finding lower enrichment in $\delta^{18}O_{lw}$ than that predicted by Eq. 1.22. An explanation for the varying $^{18}\varepsilon_{kin}$ focused on the relative strength of either stomatal or boundary layer resistances (Farquhar et al., 2007). In 1989, Farquhar et al. suggested that kinetic fractionation at leaf surface could be expressed as:

$$^{18}\varepsilon_{kin} = \frac{32rs + 22rb}{rs + rb}/1000, \tag{1.23}$$

where rs and rb are the stomatal resistances (reciprocal of conductances gs and gb) of the stomata and the boundary layer to diffusion of water vapor, respectively. Here 32/1000 represents the fractionation during diffusion (Cappa et al., 2003), while 22/1000 comes from $1.032^{2/3}$ (Farquhar et al., 2007). In moist conditions, stomatal resistance rs is low. Thus fractionation caused by rb dominates, and it is follows from Eq. 1.23 that $^{18}\varepsilon_{kin}$ becomes weaker, closer from 22 ‰ than 32 ‰. Besides, stomatal opening and increased evapotranspiration increases the latent heat flux out of the leaves and thereby reduce leaf temperature, increasing relative humidity and in turn weakening $\delta^{18}O_{lw}$ enrichment (Farquhar et al., 2007). Accordingly, we have imposed a mean value of 20 ‰[5] for $^{18}\varepsilon_{kin}$ in the model presented in Chapter 5.

- How does plant transpiration relate to $\delta^{18}O_{lw}$ enrichment?

THE ROLE OF TRANSPIRATION

Plants must solve the dilemma of adjusting stomatal apertures to allow sufficient CO_2 uptake for photosynthesis while preventing excessive water loss, that is E (cf. Eq. 1.19). As pointed out by Farquhar et al. (2007),the relation between $\delta^{18}O_{lw}$ enrichment and the transpiration rate E is not straightforward. E is defined as:

$$E = gw \cdot v, \tag{1.24}$$

where gw is the conductance to diffusion of water vapor to the atmosphere from the sites of evaporation within the leaf, combining stomatal and boundary layer conductances, and v is the leaf-to-air water vapor concentration difference. According to Eq. 1.22, $\delta^{18}O_{lw}$ enrichment is increased with lower relative humidity h, thus with a higher E, while Eq. 1.23 shows that $^{18}\varepsilon_{kin}$, hence $\delta^{18}O_{lw}$, is increased with a stronger rs, thus with a lower E. It follows that estimating $\delta^{18}O_{lw}$ with the Craig and Gordon equation may be incomplete, as it only considers the positive relationship between $\delta^{18}O_{lw}$ and E.

[5] with the measured values from Merlivat (1978), $rs = 28‰ and rb = 19‰$.

- Spatial heterogeneity of $\delta^{18}O_{lw}$ within a single leaf.

  Applying Craig and Gordon model to leaves assumes two major assumptions, as noted by Helliker and Ehleringer (2002): one assumption is that the leaf is at isotopic steady-state, where the isotopic composition of the transpiration flux is identical to the one of the water entering the leaf through its bases (Helliker and Ehleringer, 2002), and the second one is that the leaf represents a single homogeneous pool of water from the base to the tip, with the substrate water entering from the petiole and exiting solely by evapotranspiration. Various studies have shown isotopic inhomogeneities in leaf water (e.g. Yakir et al., 1989, 1990), whose main feature is a progressive enrichment from the bases to the tips of the leaves (Farquhar et al., 2007). There have been two main approaches taken to represent this pattern. The "pools of water" model (Yakir et al., 1989) is based on isolated water pools in the leaf, a few of them - at least 10 % - with no enrichment, while the second model is based on $\delta^{18}O$ gradient within the leave, due to the opposing effect of convection of unenriched vein waters pumped from the roots and back diffusion of enriched evaporative water (the Peclet effect, Farquhar and Lloyd, 1993). According to the Peclet model, $\delta^{18}O_{lw}$ enrichment occurs if transpiration rate decreases.

1.2.3.3.2 *Link to $\delta^{18}O$ of CO_2*

The oxygen isotopic composition of CO_2 depends on interactions between CO_2 and ocean waters, soil water and leaf water (Francey and Tans, 1987; Farquhar et al., 1993). There is no exchange of O_2 isotopes with oxygen of water vapor. When CO_2 dissolves in liquid water, oxygen atoms are exchanged (Mills and Urey, 1940) through hydration/dehydration of CO_2 /HCO_3^-:

$$CO_2 + H_2O \longleftrightarrow H_2CO_3 \longleftrightarrow H^+ + HCO_3^-, \tag{1.25}$$

where H_2CO_3 is carbonic acid and HCO_3^- is bicarbonate. It takes $\simeq$ 30 s (up to a few minutes according to Luz et al. (2014)) for dissolved CO_2 to reach isotopic equilibrium with water, similar to the time required for hydration (Keeling, 1995). Exchange of O_2 isotopes of CO_2 with soil water is caused by diffusion into the atmosphere of CO_2 respired by the soils. It is assumed to vary with the $\delta^{18}O$ of precipitation, depleted polewards through Rayleigh fractionation. Exchange with ocean waters occurs through exchange of CO_2 across the air-sea interface (Keeling, 1995). As ocean is the dominant reservoir of water on Earth, it was long believed that $\delta^{18}O$ of CO_2 was driven by the $\delta^{18}O$ of ocean waters, until Francey and Tans (1987) found that the former was affected by $\delta^{18}O_{lw}$, despite the small size of the leaf water reservoir. Indeed, the CO_2 /H_2O equilibration is very fast in leaves, due to the presence of carbonic anhydrases (noted CA hereafter). CA are zinc-containing enzymes that catalyze the reversible reaction between carbon dioxide hydration and bicarbonate dehydration. Hence isotopic exchange occurs in spite of the small residence time (< 1 s) of CO_2 within the leaves (Keeling, 1995). Consequently, Farquhar et al. (1993) developed a global model

for $\delta^{18}O$ of atmospheric CO_2 including the rapid CO_2 /H_2O equilibration within leaves. To close the budget of $\delta^{18}O$ of CO_2 , their model calculated a value of 4.4 ‰ for global $\delta^{18}O_{lw}$, much weaker than the value of 8 ‰ needed by Dongmann (1974) or Bender et al. (1994) to balance their budget of the Dole Effect (Table 1.2).

The O_2 isotope composition of leaf water influences both $\delta^{18}O_{atm}$ and $\delta^{18}O$ of atmospheric CO_2 because at the time of photosynthesis, leaf water, that is the substrate water for the newly produced O_2 , instantaneously equilibrates with CO_2 , a fraction of which is not assimilated and diffuses back in the atmosphere (Keeling, 1995; Luz et al., 2014). The difference observed between the O_2 (e.g. Bender et al., 1994) and CO_2 (Farquhar et al., 1993) based $\delta^{18}O_{lw}$ may be due to an incomplete equilibration (≃80 %) between CO_2 and leaf water (Gillon and Yakir, 2001), resulting in an underestimation of $\delta^{18}O_{lw}$ in Farquhar et al.'s model. Another possibility arises from the fact that over night, if stomata are open, CO_2 can exchange isotopically with leaf water without involving photosynthesis (Cernusak et al., 2004).

1.2.3.4 Photochemistry in the stratosphere

Stratospheric CO_2 is enriched in heavy isotopes (e.g. Boering et al., 2004; Lammerzahl et al., 2002; Gamo et al., 1989). This results from mass-independent transfer of ^{18}O and ^{17}O from O_2 to ozone (O_3) and then to CO_2 (e.g.Thiemens, 1999). The stratospheric isotope exchange reaction can be described by the following set of reactions:

$$O_2 + h\nu \longrightarrow 2O, \tag{1.26a}$$

$$O + O_2 \longrightarrow O_3, \tag{1.26b}$$

$$O_3 + h\nu \longrightarrow O_2 + O(^1D), \tag{1.26c}$$

$$CO_2 + O(^1D) \longrightarrow CO_3, \tag{1.26d}$$

$$CO_3 \longrightarrow CO_2 + O, \tag{1.26e}$$

$$O + O \longrightarrow O2, \tag{1.26f}$$

Eq. 1.26a represents the ultraviolet photodissociation of O_2 , splitting the O_2 molecule in 2 atoms, while Eq. 1.26b describes the formation of O_3, whose ultraviolet photolysis produces $O(^1D)$ (Eq. 1.26c). The electronically excited oxygen atom reacts with CO_2 (Eq. 1.26d) to form carbon trioxide, which decays spontaneously to CO_2 and O_2 (Eq. 1.26e) (lifetime $<<$ 60s). The ^{17}O excess is transferred from O_3 to $O(^1D)$) and then to CO_2 (e.g. Shaheen et al., 2007)

From Eq. 1.26, we can thus see that stratospheric O_2 , the largest oxygen reservoir, is the ultimate source of oxygen in stratospheric CO_2 via the transfer of oxygen to O_3 then $O(^1D)$. Mass independent fractionation occurs during ultraviolet photolysis of O_3 (e.g. Thiemens and Jackson, 1987) producing O_2 and $O(^1D)$ (Eq. 1.26c). Bender et al. (1994) proposed that the mass-independent enrichment in heavy isotopes observed in stratospheric CO_2 should be accompanied by a mass-independent O_2 depletion in ^{18}O and ^{17}O, through an isotopic exchange between CO_2 and $O(^1D)$ (Eq. 1.26d and 1.26e). No CO_2 enrichment in the atmosphere is observed as the CO_2 turnover time is very short (1 yr), resulting from isotope exchange between CO_2 and liquid water in leaves (rapid exchange because of the presence of a catalyst, cf. Sect. 1.2.3.3.2) and ocean waters. In contrast, atmospheric O_2 has a long lifetime (1.2 kyr), and the ^{17}O depletion is only removed through respiration and photosynthesis. Bender et al. (1994) estimated that photochemical reactions in the stratosphere were causing a depletion of tropospheric $\delta^{18}O_{atm}$ of 0.4 ‰, refined to 0.3 ‰ (Luz et al., 1999), which is very small compared to the effect of hydrological and biological processes on $\delta^{18}O_{atm}$ (Table 1.2). However, the role of the stratospheric mass-independent fractionation has some important consequences when studying the past variations of the three stable isotopes of atmospheric O_2 (Sect. 1.2.5).

1.2.3.5 Estimating biospheric O_2 fluxes

To estimate the isotopic composition of atmospheric O_2 , on millennial to orbital timescales, at which the concentration of atmospheric O_2 remains almost constant, a system in biological steady state is considered, with equal fluxes of O_2 production and uptake (e.g. Bender et al., 1994; Hoffmann et al., 2004; Landais et al., 2007a):

$$F^{O_2}_{photosynthesis} = F^{O_2}_{resp}, \tag{1.27}$$

where $F^{O_2}_{resp}$ stands for O_2 respiratory fluxes. The terrestrial ($F^{O_2}_{terr}$) and marine ($F^{O_2}_{mar}$) components are estimated similarly, but separately.

Marine fluxes can be assessed with models computing the oceanic productivity. Terrestrial biospheric O_2 fluxes are usually derived from Gross Primary Production (GPP), computed for different PFTs by global vegetation models (e.g. Landais et al., 2007a). Simulated carbon molar fluxes ($molC \cdot m^{-2} \cdot yr^{-1}$) for each PFTs are converted to oxygen molar fluxes ($molO_2 \cdot m^{-2} \cdot yr^{-1}$), based on the biochemical model of photosynthesis from Farquhar et al. (1980). The model accounts for fraction of photorespiration, which is PFT and temperature dependent (Sect. 1.2.3.2.4), and the photosynthetic quotient (PQ), representing the net O_2 to CO_2 exchange with the ecosystem, and estimated as 1.1 ± 0.5 (Keeling, 1988; Severinghaus, 1995). Biospheric O_2 uptake fluxes for each PFT are expressed in terms of dark respiration, Mehler respiration and photorespiration:

$$F^{O_2}_{resp} = F^{O_2}_{Mehler} + F^{O_2}_{dark} + F^{O_2}_{photo} \tag{1.28a}$$

$$= \frac{GPP \cdot PQ \cdot (1 + f_{photo})}{1 - f_{Mehler}}, \tag{1.28b}$$

With,

$$F_{photo}^{O_2} = (1 - f_{Mehler}) \cdot (F^{O_2} - PQ \cdot GPP) \tag{1.28c}$$

$$F_{photo}^{O_2} = (1 - f_{Mehler}) \cdot PQ \cdot GPP \cdot f_{photo}, \tag{1.28d}$$

where f_{Mehler} represents 10 % of total respiration (Badger et al., 2000), that is $0.1 \cdot F_{resp}^{O_2}$. Underestimation of f_{photo} may arise from uncertainties related to the time of photosynthesis. In the real world, plants must reduce their CO_2 uptake under water stress, as stomata close to preclude water loss (See Eq. 1.19). This may lead to a higher proportion of photorespiration, not necessarily considered during experiments performed under ideal hydric conditions (pers. comm., Severinghaus, 2015), whose results are used in the classical Farquhar parameterization (Farquhar et al., 1980).

1.2.4 The global budget of $\delta^{18}O_{atm}$

1.2.4.1 The Dole Effect

Previous sections showed that $\delta^{18}O_{atm}$ is a complex signal, which results from biospheric (influenced by the hydrological cycle) and stratospheric fluxes associated with different isotope fractionations. Additionnally, $\delta^{18}O_{atm}$ is also dependent on the volume of ice sheets. Indeed, ice sheets are highly depleted in ^{18}O, due to Rayleigh distillation during transport and condensation of water vapor from the warm tropics to the cold poles. By storing more depleted H_2O , an increase of the ice sheet volume causes a sea-level decrease associated with an enrichment of ocean waters $\delta^{18}O$, to balance the water isotopic budget. Waelbroeck et al. (2002) estimated a 1 ‰ increase of ocean waters at the Last Glacial Maximum (LGM, 21 kyr B.P.) based on the isotopic composition of benthic foraminifera. As ocean is the substrate water for photosynthesis, variations in mean ocean waters $\delta^{18}O$ are transmitted to $\delta^{18}O_{atm}$. To remove the influence of sea level variations, it is common to use the difference between $\delta^{18}O_{atm}$ and mean ocean water's $\delta^{18}O$ (called $\delta^{18}O_{sw}$ hereafter), called the Dole Effect. The most recent estimate of the present-day DE measures to 23.88 ± 0.02‰ (Barkan and Luz, 2005). Note that for present-day, the DE and $\delta^{18}O_{atm}$ are identical, as the value of present-day $\delta^{18}O_{sw}$ is by convention 0 ‰ in the VSMOW scale.

Table 1.2 – evolution of the estimation of the DE budget in the last 20 years. It has been refined with new observations, more precise thanks to improvements in isotopic measurements. Bender et al. (1994) divided the DE in a marine and terrestrial component. It includes O_2 isotope fractionation during terrestrial photosynthesis (Dongmann, 1974), with a value of 4.4 ‰ for $\delta^{18}O_{lw}$ based on Farquhar et al. (1993). The budget takes account of new or more precise measurements on oxygen isotope fractionation associated with respiratory processes (Guy et al., 1989, 1993; Kiddon et al., 1993; Bender, 1990), and estimates of O_2 consumption on land and in the ocean (Farquhar et al., 1980; Guy et al., 1993; Keeling and Shertz, 1992). With respect to Bender et al. (1994), Hoffmann et al. (2004) obtain a higher $\delta^{18}O_{lw}$ but the increase in the terrestrial DE is counterbalanced by a decrease in the marine DE caused by a larger fraction of deep marine respiration (20 % against 5 % for Bender et al., 1994), which is associated with a weak isotope fractionation. Luz et al. (2014) additionally consider isotope fractionation in marine photosynthesis and attenuated fractionation in soil respiration in their work.

Variable	Bender et al. (1994)		Hoffmann et al. (2004)		Landais et al. (2007a)		Blunier et al. (2012)		Luz et al. (2014)	
	$10^3\delta^{18}O_{x/VSMOW}$, $(10^3)^{18}\varepsilon$ or 10^3DE_x	Fraction of global O_2 production	$10^3\delta^{18}O_{x/VSMOW}$, $(10^3)^{18}\varepsilon$ or 10^3DE_x	Fraction of global O_2 production	$10^3\delta^{18}O_{x/VSMOW}$, $(10^3)^{18}\varepsilon$ or 10^3DE_x	Fraction of global O_2 production	$10^3\delta^{18}O_{x/VSMOW}$, $(10^3)^{18}\varepsilon$ or 10^3DE_x	Fraction of global O_2 production	$10^3\delta^{18}O_{x/VSMOW}$, $(10^3)^{18}\varepsilon$ or 10^3DE_x	Fraction of global O_2 production
DE_{tot_meas}	23.5		23.5		23.5		23.88 ± 0.02		23.88 ± 0.02	
DE_{tot_calc}	20.8		23.5 ± 0.3						23.5 ± 2.5	
DE_{terr}	22.4	0.63	26.9 ± 0.3		$17.4 \pm 0.$			0.68	23.5 ± 2.3	0.63
DE_{mar}	18.9^b	0.37	16.97					0.32	24.4 ± 2.0	0.37
DE_{surf}, or ε_{up_surf}	20	0.35	model[d]	0.25			22	0.30	25.2 ± 1.9	0.33
DE_{deep}, or ε_{up_deep}	12	0.02	model[d]	0.06			12	0.02	23.2 ± 0.5	0.04
ε^a_{eq}	0.7								0.75 ± 0.05	
$\varepsilon_{photosynthesis\_mar}$	0		0		0		4		$\simeq 5$	
$\delta^{18}O_{lw}$	4.4		$6.1 - 6.8$		7.0 ± 1		6.791		5.75 ± 2.1	
ε_{strat}	0.4		0.4				$0.625 * 10^{-3}$		0.3 ± 0.1	

Details on respiratory processes

		Fraction of terrestrial production		Fraction of terrestrial production		Fraction of terrestrial production		Fraction of terrestrial production		Fraction of terrestrial production
ε_{Mehler}	15.1	0.1	15.3		10.9 ± 0.2	0.1	10.8	0.1		
ε_{Photo}	21.2	0.31	21.7		21.9 ± 1.0	0.3	21.4	0.38		
ε_{Dark}	18	0.59	20.35		19 ± 1.0	0.16	18	0.17	19.2	
ε_{Dark_soil}	nc		20.35		15.6 ± 0.5	0.44	15.6 ± 0.5	0.33	15.8	
$\varepsilon_{Dark\_leaves}$	nc		20.35		19 ± 1.0	0.16	18	0.17	19.2	
ε_{COX}	nc		19.2	0.95	30		30.	0.02		
ε_{AOX}	nc		30.8	0.05	30		30.	0.02		
ε_{resp_terr}	18^c	0.37			17.4 ± 1.0		17.998 ± 1.0		17.7 ± 1.0	
$Prod_{terr}$ $(Pmol \cdot yr^{-1})$	20.4	0.63	16.7 ± 1.7	0.69			23.4			
$Prod_{mar}$ $(Pmol \cdot yr^{-1})$	12	0.37	7.61 ± 1.7	0.31			10.9			

[a] equilibrium enrichment of O_2 in water with respect to air.

[b] $18.9 = 0.95 \cdot (20 - 0.7) + 0.05 \cdot 12$

[c] $18 = 18.7 - 0.7$

[d] ocean model calculates these quantities in an integrated way.

The Dole effect can be divided in a marine and terrestrial component (Bender et al., 1994):

$$DE = \delta^{18}O_{atm} - \delta^{18}O_{sw} = \frac{F^{O_2}_{terr}}{F^{O_2}_{tot}} \cdot DE_{terr} + \frac{F^{O_2}_{mar}}{F^{O_2}_{tot}} \cdot DE_{mar} -^{18} \varepsilon_{strat}, \qquad (1.29)$$

where $F^{O_2}_{tot} = F^{O_2}_{terr} + F^{O_2}_{mar}$. Air exchange between the troposphere and the stratosphere results in a $\delta^{18}O$ depletion of 0.3 *permil* ($^{18}\varepsilon_{strat}$) in tropospheric O_2 (Sect. 1.2.3.4). The latest estimations of DE_{terr} and DE_{mar} can be found in Table 1.2 for different studies. Most recent estimates of present-day DE_{terr} and DE_{mar} are 23.5 ± 2.3 and 24.3 ± 2.0, respectively (Luz et al., 2014).

1.2.4.2 DE_{mar}

DE_{mar} is estimated following Bender et al.'s (1994) approach:

$$DE_{mar} = f_{euph} \cdot DE_{euph} + f_{deep} \cdot DE_{deep}, \tag{1.30}$$

where f_{euph} (89 %) and f_{deep} (11 %) are the fraction of O_2 uptake in the euphotic zone and in the deep ocean, respectively (Sect. 1.2.3.2.6). DE_{euph} has been recently reestimated as 24.4 ± 1.1‰ (see Table 1.2) by (Luz and Barkan, 2011; Luz et al., 2014), after Eisenstadt et al. (2010) found photosynthetic enrichment up to 6 ‰ in marine phytoplancton. The combined effect of isotope fractionation due to photosynthesis and respiration ($^{18}\varepsilon_{bio\_euph}$) in the euphotic zone was estimated as 25.2 ± 1.9‰ from the mass balance of ^{18}O dissolved in O_2 (Luz et al., 2014). Additionally, the equilibrium isotope fractionation $^{18}\varepsilon_{eq}$ of dissolved O_2 in seawater with respect to atmospheric O_2 causes dissolved O_2 to be slightly enriched in ^{18}O by 0.75 ‰ with respect to $\delta^{18}O_{atm}$ (Benson and Krause, 1984). DE_{euph} is therefore calculated as:

$$DE_{euph} = {}^{18}\varepsilon_{bio\_euph} - {}^{18}\varepsilon_{eq} = 25.2 \pm 1.9‰ - 0.75‰ = 24.4‰, \tag{1.31}$$

1.2.4.3 DE_{terr}

DE_{terr} is estimated in the following way:

$$DE_{terr} = \delta^{18}O_{lw} + {}^{18}\varepsilon_{\text{resp}} - \delta^{18}O_{sw} \tag{1.32}$$

where $^{18}\varepsilon_{\text{resp}}$ is the respiratory isotope fractionation caused by terrestrial O_2 uptake (refer to Eq. 1.9 and Table 1.1), and $\delta^{18}O_{lw}$ the isotope composition of leaf water (refer to Eq 1.22). Last estimate of DE_{terr} by Luz et al. (2014) is 23.5 ± 2.3‰, 0.38 ‰ lower than the observed value of 23.88 ‰ (Barkan and Luz, 2005).

1.2.4.4 What processes influence $\delta^{18}O_{atm}$?

In this section we summarize all the factors that can cause a $\delta^{18}O_{atm}$ enrichment:

- a $\delta^{18}O_{sw}$ enrichment because of a sea level decrease/ ice sheet volume increase. Note that this would not affect the DE, by definition.
- a $\delta^{18}O_{lw}$ enrichment, driven by:
  - a decrease in relative humidity (due to increased temperature or reduced water vapor content), causing kinetic fractionation to dominate over equilibrium fractionation during plant transpiration.
  - a $\delta^{18}O$ enrichment of the meteoric water consumed by the plants
  - stomata closure and associated decrease of transpiration, according to the Peclet effect (Farquhar and Lloyd, 1993).
- an increase of the photorespiration fraction, driven by:

- a decrease of the ratio of C4/C3 plants, driven by a higher CO_2 concentration or more humid conditions
- a higher temperature at the site and time of photosynthesis
- a decrease in CO_2 concentration. Note that it is difficult to assess the net effect of a CO_2 decrease on $\delta^{18}O_{atm}$, as it also leads to replacement of C3 plants by C4 plants, hence to a reduction of the photorespiration fraction, causing $\delta^{18}O_{atm}$ depletion.

- a decrease in soil respiratory isotope fractionation, driven by:
  - an decrease in the fraction of tropical soils (with respect to temperate and boreal soils), associated with a weak isotope fractionation during O_2 uptake.
  - well-aerated soils, i.e. a lower water content in the soils, increasing the back flux from the site of respiration to the atmosphere of the remaining fraction of O_2 isotopically enriched after partial respiration. As explained in Sect. 1.2.3.2.3, the presence of water causes diffusion to be rate-limiting. As a result, instead of an effective soil respiratory fractionation reflecting the isotope fractionation of the O_2 uptake process (case of well-arerated soils), it reflects the isotope fractionation associated with diffusion of O_2 in water.

- a relative increase of the marine O_2 production (or uptake) $F_{mar}^{O_2}$, considering the latest estimations of DE_{terr} and DE_{mar} (Table 1.2). However, they are identical within the uncertainties ($\simeq$ 2‰) of their estimations. Luz and Barkan (2011) thus suggest that changes in the land-to-sea ratio O_2 production should not affect the global DE.

1.2.5 Three isotopes of oxygen

Numerous factors affect the DE (Sect. 1.2.4.4), so that even with a detailed quantitative approach (Chapter 5), it is difficult to assess the relative importance of the factors responsible for the DE. The triple isotope composition of atmospheric O_2 provides additional information on the O_2 cycle. Luz et al. (1999) indeed showed that past changes in global O_2 productivity could be inferred from the relation between $^{17}O/^{16}O$ and $^{18}O/^{16}O$ ratios. Moreover, studying the relative variations of the two heavy O_2 isotopologues through time should bring to light the driving processes of each isotopic change.

1.2.5.1 Definitions

On Earth, most of the isotopic variations observed in elements with at least three stable isotopes are strongly correlated with the isotopic mass differences. Let us consider the partitioning of O_2 isotopes between two compounds A and B. The mass-dependent relationship that relates isotope fractionation factors of $^{17}O/^{16}O$ and $^{18}O/^{16}O$

can be expressed as follows (Mook and De Vries, 2000):

$$^{17}\alpha_{A/B} = {}^{18}\alpha^{\lambda}_{A/B}. \tag{1.33}$$

In nature, most isotope fractionation processes cause the $^{17}O/^{16}O$ ratio of O_2 -bearing compounds to be approximately one half of the $^{18}O/^{16}O$ ratio, with a value of λ, the exponent relating the fractionation factors for two isotope ratios (the slope in the $^{17}O/^{18}O$ relationship), around 0.52. However, the improved analytical precision of stable isotope ratio measurements, allowing to determine λ with precision in the third decimal place (e.g. Barkan and Luz, 2003; Luz and Barkan, 2005) showed that on Earth, slight differences in the magnitude of the mass-dependent fractionation exist. In theory, isotope fractionation resulting from equilibrium or kinetic processes can explain such variations (Matsuhisa et al., 1978; Young et al., 2002). In the case of equilibrium exchange (depending solely on the atomic mass Young et al., 2002) of O_2 isotopes between two compounds A and B, λ is expressed such that:

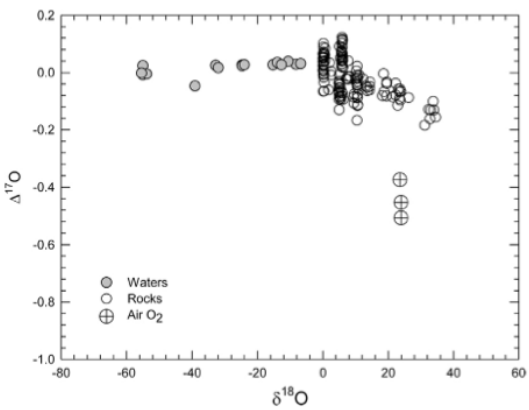

Figure 1.7 – Original Figure 1 from Young et al. (2014). Plot of $^{17}\Delta$ (as defined in Eq. 1.38, with $\lambda = 0.528$) vs. $\delta^{18}O$ (with respect to VSMOW) showing the pronounced depletion in ^{17}O of atmospheric O_2 relative to waters and rocks. Rock data: Rumble et al. (2007); Tanaka and Nakamura (2013). Water data: Barkan and Luz (2005); Schoenemann et al. (2013); Tanaka and Nakamura (2013). Air data: Barkan and Luz (2005, 2011); Young et al. (2014).

$$\lambda = \frac{(\frac{1}{16} - \frac{1}{17})}{(\frac{1}{16} - \frac{1}{18})} \backsimeq 0.5294. \tag{1.34}$$

In the case of a kinetic process:

$$\lambda = \frac{ln(\frac{M1}{M2})}{ln(\frac{M1}{M3})}, \tag{1.35}$$

where M1, M2 and M3 are atomic, molecular or reduced masses, and $M1 < M2 < M3$. Atomic or molecular masses apply for transport processes, while reduced masses apply for breaking bonds (Young et al., 2002). Using atomic or molecular masses bring a λ value of 0.5147 or 0.5076, respectively. Thus, according to theory, λ can vary between 0.501 (kinetic) and 0.531 (steady state) (e.g. Matsuhisa et al., 1978; Kaiser, 2008). As a matter of fact, various relations between $^{17}O/^{16}O$ and $^{18}O/^{16}O$ ratios have been observed in nature. λ has a value of 0.525 ± 0.001 in rocks (Miller, 2002), suggesting the domination of equilibrium processes during rock formation. The value of

0.528 ± 0.002 in meteoric waters (Meijer and Li, 1998; Landais et al., 2008; Luz and Barkan, 2010) can result from dominant equilibrium fractionation processes, but also from kinetic ones, as λ calculated with the reduced masses of H-OH bonds or O-H bonds varies from 0.5270 to 0.5286 (Young et al., 2002).

In Figure 1.7, atmospheric O_2 stands out among Earth's oxygen pools by its $^{17}\Delta$ signature, (calculated with $\lambda = 0.528$), or, in other words, by the low value of its slope λ compared to λ for rocks or λ for waters (e.g Young et al., 2014). The depletion is caused in part by the biologic origin of atmospheric O_2 . Indeed, close to the value predicted by theory for kinetic fractionation ($\lambda = 0.515$), Helman et al. (2005) and Luz and Barkan (2005) determined λ as 0.518 for dark respiration (the dominant respiratory process on Earth) in a number of organisms. Besides, as mentioned in Sect. 1.2.3.4 the deficit in ^{17}O in the atmosphere also originates from stratospheric photochemistry (Yung et al., 1991; Bender et al., 1994; Luz et al., 1999).

When studying the three stable isotopes of O_2 , the general practice (Miller, 2002; Luz and Barkan, 2005) is to use a modified δ, noted δ'. (Hulston and Thode, 1965):

$$\delta' = ln(\delta + 1) = ln(\frac{R}{R_{ref}}), \tag{1.36}$$

where R_{ref} refers to the isotope ratio of a reference state, another phase or to initial conditions. This "delta-prime" notation is convenient because of the linear relationship between $ln(^{17}\alpha)$ and $ln(^{18}\alpha)$ (Young et al., 2014):

$$\delta'^{17}O = \lambda \cdot \delta'^{18}O - (\delta'^{17}O_{ref} - \lambda \cdot \delta'^{18}O_{ref}), \tag{1.37}$$

Indeed, fractionation lines are straight in $\delta'^{18}O$ vs. $\delta'^{17}O$ plots, while they are curved in conventional $\delta^{18}O$ vs. $\delta^{17}O$ plots. In contrast, mixing lines are straight in a conventional three isotope plot but curved using the modified δ' space. Consequently, mixing laws are an approximation in this definition of $^{17}\Delta$ (Kaiser et al., 2004). Figure 1.8 illustrates the previous point for gaseous O_2 only affected by biologic fluxes, that is a system at steady-state between respiratory consumption and photosynthetic production: while respiratory fractionation processes, which can be determined with Rayleigh experiments (Luz et al., 2014), increase $\delta'^{18}O$ and $\delta'^{17}O$ along straight lines, photosynthesis leads to mixing of fractionated O_2 with new photosynthetic O_2 along curved lines (Luz and Barkan, 2005). Note that in general, the last term of Eq. 1.37, $\delta'^{17}O_{ref} - \lambda \cdot \delta'^{18}O_{ref}$, cancels out as the reference value can be taken to origin (Young et al., 2014).

$^{17}\Delta_{atm}$ represents the deviation from the specified mass-dependent isotopic fractionation relationship between $\delta'^{17}O_{atm}$ and $\delta'^{18}O_{atm}$, denoted as the anomaly $^{17}\Delta_{atm}$ (Luz et al., 1999) and expressed in per meg (10^{-6}) as variations are very small:

$$^{17}\Delta_{atm} = ln(\delta^{17}O_{atm} + 1) - \lambda \cdot ln(\delta^{18}O_{atm} + 1) = ln(^{17}\alpha_{atm}) - \lambda \cdot ln(^{18}\alpha_{atm}). \tag{1.38}$$

The standard of reference for O_2 gas is atmospheric O_2 . As the latter defines the origin of the isotopic scale, it follows that $\delta^{18}O_{atm}$, $\delta^{17}O_{atm}$ and $^{17}\Delta_{atm}$ have a value of 0 ‰. λ, as mentioned previously, is the slope of the mass-dependent isotopic fractionation line (or reference line) between the two heavy stable isotopologues of atmospheric O_2 . It should be mentioned that the value of λ is independent on the choice of isotopic reference (e.g. VSMOW or atmospheric O_2) (Miller, 2002). In contrast, Equation 1.38 shows that $^{17}\Delta_{atm}$ is strongly dependent on the chosen value of λ, but also on the choice of the standard of reference, as variations in $\delta^{18}O$ alone cause apparent variations in $^{17}\Delta$. A consistent selection of the two is therefore critical for a correct interpretation of $^{17}\Delta$ variations. We underline below why the choice of λ is critical, but the reader is invited to refer to Miller (2002); Young et al. (2014) or Luz and Barkan (2005) for more details on the selection of the optimal primary standard and relevant reference fractionation line with respect to the system under investigation.

1.2.5.1.1 *Choice of λ*

The symbol λ is empirically chosen to reflect a predicted or observed mass-dependent relationship between $^{17}O^{16}O$ and $^{18}O^{16}O$ isotope ratios (Meijer and Li, 1998; Li and Meijer, 1999). Because of the biologic origin of atmospheric O_2 , λ must be representative of equilibrium fractionation during O_2 uptake, whose most dominant process is dark respiration (Angert et al., 2003b; Helman et al., 2005). The dark respiration slope was determined by Helman et al. (2005) in closed-system experiments where only O_2 consumption took place, without O_2 production. In this case, the change in oxygen isotopic composition of the remaining fraction can be expressed with the Rayleigh fractionation equation (e.g. Young et al., 2014; Angert et al., 2003b; Helman et al., 2005):

$$\frac{^{i}R}{^{i}R_{init}} = f^{^{i}\varepsilon}, \tag{1.39}$$

where $^{i}R_{init}$ represents the initial isotope ratio $^{i}O^{16}O/^{16}O$, with i standing either for 17 or 18. f^{i} represents the remaining $^{16}O^{16}O$ fraction. This expression is equivalent to:

$$ln(\delta^{i}O + 1) - ln(\delta^{i}O_{init} + 1) = {}^{i}\varepsilon \cdot ln(f), \tag{1.40}$$

It follows that the fractionation law relating the two heavy isotopologues of O_2 in a Rayleigh process can be expressed as (e.g. Blunier et al., 2002; Helman et al., 2005):

$$\lambda = \gamma = \frac{ln(^{17}R/^{17}R_{init})}{ln(^{18}R/^{18}R_{init})} = \frac{ln(\delta^{17}O + 1) - ln(\delta^{17}O_{init} + 1)}{ln(\delta^{18}O + 1) - ln(\delta^{18}O_{init} + 1)} = \frac{^{17}\varepsilon}{^{18}\varepsilon}, \tag{1.41}$$

where γ represents the mass-dependent relationship between $^{18}O/^{16}O$ and $^{17}O^{16}O$ during a Rayleigh fractionation process. A value of $\gamma = 0.518$ was defined for dark respiration. Note that in this limiting case, the value of 0.518 represents the effective value of the three-isotope exponent γ, that is the effect of the process of interest (here O_2 consumption, characterized by its intrinsic fractionation) together with

Table 1.3 – Table describing the difference between the symbols β, β_{eff}, γ and η symbols used in literature for triple isotope exponent λ. Equations and terminology are based upon Young et al. (2014). Experimental conditions can differ: (i) steady-state or O_2 removal only (Rayleigh-type fractionation) in a closed system of 2 reservoirs, or (ii) a system where one reservoir provides an infinite amount of reactant (e.g. $\delta^{18}O_{sw}$ remains constant despite photosynthesis), its isotope composition thereby being not affected by a change of O_2 amount in the reservoir. Determination of λ from the best fit of a three isotope plot ($\delta'^{17}O$ vs $\delta'^{18}O$) does not necessarily represent the process at play, due to the fact that reservoirs influence each other in a closed system. As an illustration, applying Young et al.'s simple 2-box model for O_2 photosynthesis from H_2O and O_2 respiration, β_{eff} is given when ${}^{18}\alpha_{resp} = 17.4‰$, $\beta = 0.516$ and $k = F_{respiration}/F_{photosynthesis} = 0.9$. λ varies from 0.514 to 0.516, Note that in several studies, including this thesis and Reutenauer et al. (2015), θ corresponds to β.

λ	exponent	condition?	reservoir effects?	equation	$\frac{ln(\delta'^{18}O)}{ln(\delta'^{18}O)}$
β^a	intrinsic exponent		infinite reservoir	$\beta_{eff} = \beta$	0.516
η	steady-state exponent	steady-state	yes	$\beta_{eff} = \eta = \frac{ln(\frac{1+k}{1+{}^{18}\alpha^{\beta}\cdot k})}{ln(\frac{1+k}{1+{}^{18}\alpha\cdot k})}$	0.515
γ	Rayleigh exponent	O_2 removal alone	yes	$\beta_{eff} = \gamma = \frac{{}^{18}\alpha^{\beta}-1}{{}^{18}\alpha-1}$	0.514

[a]:called θ in this thesis as in e.g. Angert et al., 2003b; Helman et al., 2005; Landais et al., 2007a.
θ results only from the process of interest, and is not affected by mass balance considerations.

mass-balance effects (referred as "reservoir effects" by Young et al., 2014). The slope γ can be derived from the best fit of a $\delta'^{17}O vs. \delta'^{18}O$ plots.

The triple isotope exponent γ, characterizing a Rayleigh process, is not adapted for global mass balance calculations of triple isotope ratios of atmospheric O_2 in biological steady-state (combination of O_2 uptake and mixing with photosynthetic O_2), which is another limiting case where the mass-dependent relationship between ${}^{18}O/{}^{16}O$ and ${}^{17}O{}^{16}O$ can be predicted. A slope $\lambda = \theta$ of 0.516 (Table 1.4), which reflects the expected relationship between the two heavy O_2 isototopologues for dark respiration (most common respiratory process) fractionation in steady-state with production, is used instead and defined as (Blunier et al., 2002; Angert et al., 2003b; Helman et al., 2005; Luz and Barkan, 2005; Young et al., 2014):

$$\lambda = \theta = \frac{ln({}^{17}\alpha)}{ln({}^{18}\alpha)} = \frac{ln(\gamma \cdot {}^{18}\alpha - \gamma + 1)}{ln({}^{18}\alpha)} = \frac{ln(\gamma \cdot {}^{18}\varepsilon + 1)}{ln({}^{18}\varepsilon + 1)} \tag{1.42}$$

This equation is convenient as it enables calculation of θ from γ, which can be easily derived from a Rayleigh fractionation experiment. Note that according to Young et al. (2014), θ in Eq. 1.42 does not define a situation of steady-state, but the intrinsic triple isotope exponent β (see Table 1.3), obtained when reservoir effects are eliminated. Young et al. (2014) indeed shows that ${}^{18}\alpha$ and ${}^{17}\alpha$ are not modified when the exchange of isotopes between two reservoirs is not reciprocal, and in this case, the effective value of the slope λ is identical to the intrinsic value of the single process at play (as expressed in Eq. 1.35). Atmospheric O_2 can be considered free of reservoir ef-

fects because the ultimate source of atmospheric O_2 , seawater, represents an infinite reservoir of O_2 , and thereby its oxygen isotope composition, which mainly controls the one of the photosynthetic O_2 , is unaffected by the exchange between the reservoirs. On the contrary, in steady-state between respiration and photosynthesis in a closed system, isotope fractionation factors ${}^{18}\alpha$ and ${}^{17}\alpha$ arise from the weakening of the intrinsic fractionation in one direction (respiration) by the lack of fractionation in the other direction (photosynthesis), and the impact of isotopic exchange on both reservoirs (reciprocity) (Young et al., 2014).

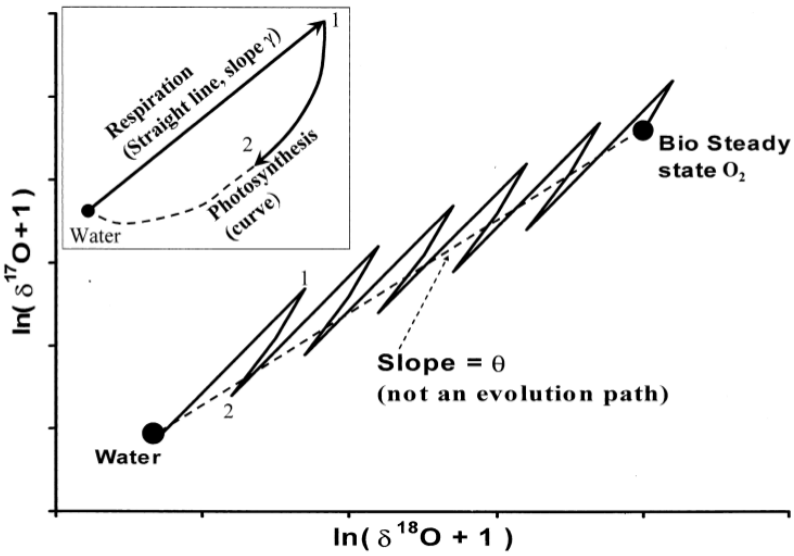

Figure 1.8 – Original Figure 2 from Luz and Barkan (2005). This figure schematizes the effect of biospheric fluxes on the triple isotope composition of gaseous O_2 at steady state (production = respiration). It depicts how the enrichment observed in gaseous O_2 compared to the substrate water is the product of two processes. Oxygen consumption through respiration, a one-way kinetic process, enriches gaseous O_2 as it tends to leave behind heavy isotopes, and appears as a straight line in a $\delta'^{18}O$ vs. $\delta'^{17}O$ plot. O_2 produced through photosynthesis, with the isotope composition of the substrate water (see below), depletes the enriched O_2 via mixing, whose graphical representation is a curved line. The dashed line connecting the points representing the isotopic composition of substrate water and gaseous O_2 in steady state, whose slope $\theta = 0.516$, does not represent a single fractionating process, but results from the combination of the two biologic processes (respiration and photosynthesis) (Luz and Barkan, 2005). The insert represents a zoom on the first cycle. Note that it is here assumed that photosynthesis does not fractionate O_2 isotopes, a view which has been recently challenged for marine photosynthesis in phytoplankton (Eisenstadt et al., 2010). Hence the newly produced O_2 bears the same isotopic composition as the substrate water.

1.2.5.2 Why is atmospheric O_2 depleted in ^{17}O relative to biological steady-state O_2 ?

In 1999, an experiment by Luz et al. (1999) revealed that atmospheric O_2 was depleted in ^{17}O versus biological steady state O_2 . The experiment took place in an airtight and illuminated terrarium containing Philodendron plants, soil and natural water (Luz et al., 1999). At the beginning of the experiment, the terrarium was filled with ambient air, with a $^{17}\Delta_{atm}$ value of 0 permeg by definition. Then mixing of fractionated O_2 by partial respiration[6] with newly produced photosynthetic O_2 caused $^{17}\Delta$ in the terrarium to increase over several weeks. Once all the O_2 in the terrarium was of biologic origin alone, $^{17}\Delta$ reached a stable value, denoted $^{17}\Delta_{bio}$ hereafter, enriched by $\simeq$155 permeg (updated to 166 permeg by Luz et al., 2014) relative to atmospheric O_2 , which conversely means that ambient O_2 is anomalously depleted in ^{17}O relative to O_2 of biological origin alone. Following (Bender et al., 1994) suggestion, they attributed this effect to stratospheric photochemistry (Sect. 1.2.3.4). Indeed, as CO_2 is preferentially enriched in ^{17}O, stratospheric isotope transfer reaction between O_2 and CO_2 via O_3 involves preferential depletion of atmospheric O_2 , the largest oxygen reservoir, in ^{17}O relative to biological steady state O_2 .

1.2.5.3 $^{17}\triangle_{atm}$, a tracer of past global O_2 productivity

Taking profit of the $^{17}\Delta$ stratospheric signal, Luz et al. (1999) and Blunier et al. (2002) interpreted $^{17}\Delta_{atm}$ measured in air preserved in ice cores as a tracer of past changes of global photosynthetic rate. Indeed, the triple isotope composition of tropospheric O_2 reflects the isotopic balance between (1) the oxygen flux between the biosphere and the troposphere associated with mass dependent fractionation, and (2) the oxygen flux between the stratosphere and the troposphere associated with mass independent fractionation (Luz et al., 1999):

$$F_{bio} \cdot ({}^{17}\Delta_{bio} - {}^{17}\Delta_{atm}) = F_{strat} \cdot ({}^{17}\Delta_{strat} - {}^{17}\Delta_{atm}), \tag{1.43}$$

where $^{17}\Delta_{strat}$ and $^{17}\Delta_{bio}$ are the deviations from the reference line of slope $\lambda = 0.516$ of the stratospheric O_2 flux (F_{strat}) and the biospheric O_2 flux (F_{bio}), respectively.

Knowing the stratospheric contribution thus enables in theory to access the past global productivity. To estimate the production rate of mass-independently fractionated O_2 in the stratosphere, $F_{strat} \cdot ({}^{17}\Delta_{strat} - {}^{17}\Delta_{atm})$, Luz et al. (1999) assume that it is proportional to CO_2 concentration. It is then possible to compare the O_2 productivity of the biosphere between two periods of time $t1$ and $t2$, with known $^{17}\Delta_{atm}$ and CO_2 concentration (Landais et al., 2007a):

$$\frac{F_{bio,t2}}{F_{bio,t1}} = \frac{[CO_2]_{t2} \cdot ({}^{17}\Delta_{bio,t1} - {}^{17}\Delta_{atm,t1})}{[CO_2]_{t1} \cdot ({}^{17}\Delta_{bio,t2} - {}^{17}\Delta_{atm,t2})}, \tag{1.44}$$

[6] if O_2 uptake is complete, respiration causes no fractionation as expected from a Rayleigh process

where $[CO_2]$ is the atmospheric concentration of CO_2. Based on Eq 1.44, the global oxygen biospheric productivity of the LGM was evaluated to be 60-85 % of the present value (Blunier et al., 2002; Landais et al., 2007a).

1.2.5.4 Evaluating $^{17}\triangle_{atm}$ budget

Rearranging Eq. 1.44, the temporal evolution of $^{17}\Delta_{atm}$ can be expressed as:

$$^{17}\Delta_{atm,t2} = {}^{17}\Delta_{bio,t2} - \frac{[CO_2]_{t2}}{[CO_2]_{t1}} \cdot \frac{F_{bio,t1}}{F_{bio,t2}} \cdot ({}^{17}\Delta_{bio,t1} - {}^{17}\Delta_{atm,t1}). \tag{1.45}$$

Equation 1.45 reveals that $^{17}\Delta_{atm}$ depends on $[CO_2]$, F_{bio} and $^{17}\Delta_{bio}$. It should be emphasized that a precise estimation of $^{17}\Delta_{bio}$ remains difficult as mass-dependent relationships between $^{18}O/^{16}O$ and $^{17}O^{16}O$ (i.e. λ) differ depending on the processes at play during the O_2 cycle (Table 1.4).

Table 1.4 – Mass-dependent fractionation slopes ($\gamma = \frac{^{17}\varepsilon}{^{18}\varepsilon}$ and $\theta = \frac{ln(^{17}\alpha)}{ln(^{18}\alpha)}$) during O_2 uptake processes and hydrologic processes. Values and uncertainties are indicated if available. The slope γ is optimal for describing the mass-dependent relationship between $^{18}O/^{16}O$ and $^{17}O^{16}O$ in a Rayleigh process system, where only uptake takes place (e.g. fractionation of water during the hydrological cycle, or respiration). To deal with a system at steady state (combination of O_2 uptake and mixing with photosynthetic O_2), θ is preferred (Luz and Barkan, 2005).

Process	$10^3 \cdot {}^{18}\varepsilon$	$10^3 \cdot {}^{17}\varepsilon$	γ	θ
Dark respiration in leaves	-19.0±1[a,b]	-9.84[d]	0.518±0.001[e]	0.516±0.001[a,c]
Dark respiration in soils	-15.60±0.5[a]	-8.08[d]	0.518±0.001[e]	0.516±0.001[a,c]
Mehler reaction	-10.80±0.2[e]	-5.68[d]	0.526±0.002[e]	0.525±0.002[e]
Photorespiration	-21.40±1[e]	-10.96[d]	0.512±0.001[e]	0.509±0.001[e]
Global Meteoric Water Line (GMWL)		0.528[f,g,h]		
Vapor-liquid equilibrium θ_{eq} (0 to 30 °C)	1.01182 to 1.00894[i]	1.00623 to 1.00472[h]		0.529±0.001[m]
Diffusive transport of water vapor in air θ_{diff}	9.6±1.8[h]	4.96± 1.8[j]		0.518±0.0002[m]
Evapotranspiration (λ_{transp})				$(-0.0078\pm0.0026) \cdot h^k + 0.5216\pm0.0008$[l]

[a] Landais et al., 2007a. [b] Angert et al., 2003a. [c] Angert et al., 2003b.
[d] derived from γ and $^{18}\varepsilon$ from Helman et al. (2005) such as $^{17}\varepsilon = \gamma \cdot {}^{18}\varepsilon$.
[e] Helman et al., 2005. [f] Meijer and Li, 1998. [g] Landais et al., 2008. [h] Luz and Barkan, 2010. [i] Horita and Wesolowski, 1994
[j] derived from λ and $^{18}\varepsilon$ such as $^{17}\varepsilon = (^{18}\varepsilon + 1)^{\lambda}$
[k] relative humidity at the site of photosynthesis
[l] Landais et al., 2006a. [m] Barkan and Luz, 2007

1.2.5.4.1 *Estimating $^{17}\Delta_{bio}$*

Similar to the approach taken to evaluate $\delta^{18}O_{atm}$ (Eq. 1.29), the marine $^{17}\Delta_{mar}$ and terrestrial $^{17}\Delta_{terr}$ contributions to $^{17}\Delta_{bio}$ are estimated separately, that is by considering the O_2 fluxes and associated isotope effect of marine (terrestrial) photosynthesis and respiration in a system at equilibrium between the atmosphere and the marine (terrestrial) component only. Here we summarize the current understanding of $^{17}\Delta_{bio}$

$^{17}\Delta_{terr}$ $^{17}\Delta_{terr}$ depends on the isotopic fractionation during O_2 uptake and on the isotopic

composition of leaf water, transferred to newly produced O_2 through photosynthesis. ${}^{17}\Delta_{terr}$ is expressed relative to atmospheric O_2 (Landais et al., 2007a):

$$ {}^{17}\Delta_{terr} = ln(\frac{{}^{17}R_{terr}}{{}^{17}R_{atm}}) - 0.516 \cdot ln(\frac{{}^{18}R_{terr}}{{}^{18}R_{atm}}), \tag{1.46} $$

where ${}^{17}R_{atm}$ and ${}^{18}R_{atm}$ represent the isotopic ratios of atmospheric O_2 (primary standard), and ${}^{17}R_{terr}$ and ${}^{18}R_{terr}$ the isotopic ratios of O_2 produced by the terrestrial biosphere, respectively. ${}^{i}R_{terr}$ is estimated as follows:

$$ {}^{i}R_{terr} = \frac{{}^{i}R_{lw}}{{}^{i}\alpha_{resp}}, \tag{1.47} $$

where i denotes either 17 or 18, and ${}^{i}R_{lw}$ stands for the global isotope ratio of leaf water. The global effective respiratory isotope fractionation factors ${}^{i}\alpha_{resp}$ are estimated as described in Eq. 1.9, with the fractionation factors ${}^{17}\alpha_{dark_{l}eaves}{}^{17}\alpha_{dark_{s}oils}$, ${}^{17}\alpha_{Mehler}$, ${}^{17}\alpha_{photo}$ calculated according to the fractionation law described by Eq. 1.33, i.e. ${}^{17}\alpha = {}^{18}\alpha^{\lambda}$, using the appropriate slope λ (refer to Table 1.4 for values and associated references) depending on the process at play (Landais et al., 2007a). The mass-dependent relationship between $\delta^{,18}O$ vs. $\delta^{,17}O$ can then be expressed as:

$$ {}^{17}\alpha_{resp} = {}^{18}\alpha_{resp}^{\lambda_{resp}}, \tag{1.48} $$

with:

$$ \lambda_{resp} = \frac{ln({}^{17}\alpha_{resp})}{ln({}^{18}\alpha_{resp})}. \tag{1.49} $$

where λ_{resp} is obtained by weighting it with the relative proportion of the various terrestrial respiratory processes. For instance, an increase of the photorespiration fraction, associated with a slope λ of 0.509, would lower ${}^{17}\alpha_{resp}$, hence ${}^{17}\Delta_{terr}$, the latter expressing the ${}^{17}O$ deviation from the biological steady-state fractionation line of slope $\lambda = 0.516$ (from D to E on Fig. 1.9 f). It is interesting to note that the opposite effect is observed on $\delta^{18}O_{terr}$, which is enriched with increasing fraction of photorespiration. This opposite sensitivity of $\delta^{18}O$ and ${}^{17}\Delta$ to the photorespiration fraction underscores the value of an additional tracer of the O_2 cycle as the relative variations of the two heavy isotopologues of O_2 should help constrain the processes at play.

$\delta^{18}O_{lw}$ is estimated following Eq. 1.22 and is enriched relative to $\delta^{18}O_{gw}$ (Sect. 1.2.3.3) while $\delta^{17}O_{lw}$ is evaluated as follows[7] (Landais et al., 2006a, 2007a):

$$ \delta'^{17}O_{lw} = \delta'^{17}O_{mw} + (\delta'^{18}O_{lw} - \delta'^{18}O_{mw}) \cdot \lambda_{transp}, \tag{1.50} $$

where λ_{transp} is the slope of the evapotranspiration process, measured by Landais et al. (2006a), and decreases linearly as relative humidity h increases, which may seem counterintuitive as a higher humidity causes less kinetic fractionation - associated with a

[7]Please remind that $\delta' = ln(\delta + 1)$

Table 1.5 – A few $^{17}\Delta_{atm}$ values calculated using the specified exponent λ and standard.

Symbol	$10^6 \cdot {}^{17}\Delta$	λ	standard	reference
$^{17}\Delta_{photo\_mar}$	26	0.518	VSMOW	Barkan and Luz, 2011
$^{17}\Delta_{mw}$	33	0.528	VSMOW	Barkan and Luz, 2011
$^{17}\Delta_{sw}$	223 ± 4	0.516	air O_2	Barkan and Luz, 2011
$^{17}\Delta_{mar}$	249 ± 15	0.516	air O_2	Luz and Barkan, 2000; Barkan and Luz, 2011
$^{17}\Delta_{terr}$	117 ± 35	0.516	air O_2	Landais et al., 2007a; Luz et al., 2014
$^{17}\Delta_{bio}$	166 ± 51	0.516	air O_2	Luz et al., 2014
$^{17}\Delta_{atm}$	0	0.516	air O_2	
$^{17}\Delta_{airO_2}$	-463^a	0.528	VSMOW	Kaiser, 2008
$^{17}\Delta_{airO_2}$	$-506^b \pm 4$	0.528	VSMOW	Barkan and Luz, 2011
$^{17}\Delta_{airO_2}$	$-453^c \pm 10$	0.528	VSMOW^d	Young et al., 2014

[a]value obtained by renormalizing prior values to VSMOW.
[b] -454 ± 10 permeg obtained with values from Barkan and Luz (2005).
[c]Adjusted value to accommodate for a $^{17}\Delta$ offset of -80 permeg in San Carlos olivine. Non corrected value is -373±5 permeg
[d]Indirect measurement, as they measured air O_2 against their rock reference, San Carlos olivine.

lower λ (0.518) than equilibrium fractionation (0.529) - hence a higher λ_{transp}, but the higher isotopic exchange between leaf water and surrounding atmospheric water vapor causes a decrease of λ_{transp} with higher humidity (see Fig. 1.9e and details in Landais et al., 2006a):

$$\lambda_{transp} = 0.522 - h \cdot 0.008, \tag{1.51}$$

when h ranges from 32 to 100 %, and λ_{transp} ranges from 0.5194 to 0.514 accordingly. When $h < 32\%, \lambda = 0.519$ (Landais et al., 2006a). A global value of 0.517 for λ_{trans} has been estimated by Landais et al. (2007a) for present-day. λ_{trans} being much lower than the global meteoric water line slope $\lambda_{mw} = 0.528$ (refer to Table 1.4 for references), the isotope effect of evapotranspiration causes a decrease of the $^{17}Oexcess$ of leaf water. However, as mentioned previously, a mass-dependent relationship between $\delta'^{17}O$ and $\delta'^{18}O$ with the slope $\lambda = 0.516$ must be used for evaluation of the global isotopic budget of atmospheric O_2 . As a result, plant transpiration only causes a slight increase in $^{17}\Delta_{terr}$, amplified in dry conditions.

In contrast, $^{17}\Delta_{terr}$ is much more affected by changes in the isotope composition of meteoric waters ($\delta^{17}O_{mw}$ and $\delta^{18}O_{mw}$) from the site of evaporation to the site of precipitation. These processes cause indeed a spatially heterogenous depletion in $^{18}O/^{16}O$ and $^{17}O^{16}O$ isotope ratios along the meteoric water line of slope $\lambda_{mw} = 0.528$. As mentioned previously, because of different fractionation slopes, shifts in $\delta^{18}O$ alone cause apparent shifts in $^{17}\Delta$ relative to the slope λ of reference. Consequently, as λ_{mw} is higher than 0.516, a decrease in $\delta^{18}O_{mw}$ of say 5 ‰ causes a $^{17}\Delta$ depletion of 60 permeg:

$$\Delta^{17}\Delta = (\lambda_{mw} - 0.516) \cdot ln(\Delta\delta^{18}O + 1) = 0.012 \cdot -0.005 = -0.0006 \tag{1.52}$$

Besides, Luz and Barkan (2010) observed a $^{17}O_{excess}$ of 33 per meg in meteoric waters (with respect to VSMOW) from various locations, such as:

$$\delta'^{17}O_{mw} = 0.528 \cdot \delta'^{18}O_{lw} + 0.000033. \tag{1.53}$$

The $^{17}O_{excess}$ is caused by (i) evaporation of ocean water into the atmosphere, increasing with decreasing humidity, hence more kinetic fractionation associated with a slope $\lambda = 0.518$ (from A to B on Fig. 1.9c) and (ii) by equilibrium fractionation between water vapor and precipitation, associated with a slope $\lambda = 0.529$ (from B to C on Fig. 1.9 d). By accounting for the combination of all the aforementioned terrestrial isotope effects, Landais et al. (2007a) estimated $^{17}\Delta_{terr}$ as 110±35 permeg with respect to atmospheric O_2 for present-day. This value was recently refined to 117±35 after accounting for (i) the correction of the value of $^{17}\Delta_{sw}$ (identical to VSMOW within the uncertainty of the measurements) with respect to atmospheric O_2 from 173 to 223 per meg (Barkan and Luz, 2011), and (ii) the $^{17}O_{excess}$ of 33 per meg in meteoric waters.

$^{17}\Delta_{mar}$ is estimated as 249 ± 15 permeg (Barkan and Luz, 2011) with respect to atmospheric O_2 . It consists of two components, $^{17}\Delta_{sw}$, the ^{17}O excess of seawater with respect to atmospheric O_2 , and $^{17}\Delta_{photo\_mar}$, the ^{17}O excess of photosynthetic O_2 with respect to its substrate water. $^{17}\Delta_{mar}$

- 15 years ago, Luz and Barkan (2000) obtained $^{17}\Delta_{mar}$ as 249 permeg from laboratory measurements of the isotopic composition of dissolved oxygen $^{17}\Delta_{diss}$, which depends on the rate of air-water gas exchange and the rate of in situ O_2 production through photosynthesis (Luz and Barkan, 2000). Respiration does not affect $^{17}\Delta_{diss}$ because it fractionates the two heavy isotopes of oxygen along a line of slope $\lambda_{diss} = 0.518$ (Fig. 1.9b), used for $^{17}\Delta_{diss}$ calculations (Barkan and Luz, 2011). Measurements were performed once the dissolved O_2 was solely of biological origin, the O_2 reservoir (overhead of the flask) being recycled through respiration and photosynthesis of various marine organisms in airtight flasks experiencing several dark-light cycles (without UV radiations). At this time, photosynthesis was believed to cause no O_2 isotopic fractionation of its substrate water, and the obtained $^{17}\Delta_{diss}$ was thus believed to represent $^{17}\Delta_{sw}$[8], but subsequent measurements on phytoplankton contradicted this assumption, at least for the marine realm (Eisenstadt et al., 2010). Isotope fractionation during photosynthesis was later confirmed by Barkan and Luz (2011), who found an average $^{17}\Delta_{photo\_mar}$ value of 26 permeg ($\lambda_{diss} = 0.518$) for photosynthetic O_2 with respect to the substrate water in experiments similar to the one carried out in 2000, even when respiration was prevented.

- Since 2005, the ability to measure at very high precision the triple isotope composition in water, using a method of water fluorination to produce O_2 (Barkan and Luz, 2005), made possible to measure the oxygen isotope composition of VSMOW (identical to the one of seawater within the experimental error, Luz

[8] or $^{17}\Delta_{mar}$ (of biological origin alone as as O_2 uptake processes do not modify $^{17}\Delta_{diss}$ and photorespiration was believed to causes no isotope fractionation back in 2000.

and Barkan, 2010) with respect to atmospheric O_2 . The most recent estimates of $\delta^{18}O_{sw}$ and $\delta^{17}O_{sw}$ are $-23.324‰$ and $-11.883‰$, respectively Barkan and Luz (2011). This translates into a $^{17}\Delta_{sw}$ of 223 permeg.

$^{17}\Delta_{bio}$ $^{17}\Delta_{terr}$ and $^{17}\Delta_{mar}$ ($\lambda = 0.516$) have been estimated as 117 ± 35 permeg and 249 ± 15 permeg, respectively. Depending on the relative proportion of terrestrial and marine O_2 production - for present-day conditions the various ocean and land biosphere models give an ocean to land O_2 production ratio that varies from 0.45 to 0.59 (Bender et al., 1994; Blunier et al., 2002; Hoffmann et al., 2004) -, the global Δ_{bio} calculates as 166 ± 51 permeg. Despite its large uncertainty, $^{17}\Delta_{bio}$ has been used with Eq. 1.44 to gain insight in past changes in biosphere productivity (e.g. Blunier et al., 2002, 2012; Landais et al., 2007a; Luz et al., 1999).

1.2.5.5 What processes influence $^{17}\triangle_{atm}$?

Figure 1.9 summarizes the various λ associated with the O_2 cycle. An increase of $^{17}\Delta_{atm}$ can be caused by:

- a $\delta^{18}O_{sw}$ enrichment as $\lambda_{sw} = 0.528$, because of a global ice volume increase
- a $\delta^{18}O$ enrichment of the meteoric water consumed by the plants
- an increase of λ_{trans}, driven by a decrease in relative humidity as shown by Eq. 1.51 (from C to D on Fig 1.9)
- a decrease of the CO_2 concentration, which scales the stratospheric depletion (causing I to move toward H on Fig 1.9).Young et al. (2014) details the possible stratospheric-related causes of $^{17}O/^{16}O$ and $^{18}O/^{16}O$ variations:
  - rates of O_3 formation and destruction in the stratosphere
  - rates of formation and quenching of excited-state atomic oxygen, $O(^1D)$, in the stratosphere
  - rate of transfer of O_2 isotopes from $O(^1D)$ to CO_2 in the stratosphere
  - AIR fluxes between stratosphere and troposphere
  - rate of CO_2 exchange with H_2O at the surface
- an increase of total photosynthetic and respiratory fluxes, as shown by Eq. 1.45, or a relative increase of O_2 oceanic production, associated with a higher $^{17}\Delta_{atm}$, with respect to the O_2 production on land (from E and G to H on Fig 1.9)
- a decrease of the photorespiration fraction, associated with a low $\lambda = 0.509$ (causing λ_{terr_resp} to increase from D to E on Fig 1.9). Note however that a reduced photorespiration fraction may be caused by an increased CO_2 concentration, which would lead to a decrease in $^{17}\Delta_{atm}$

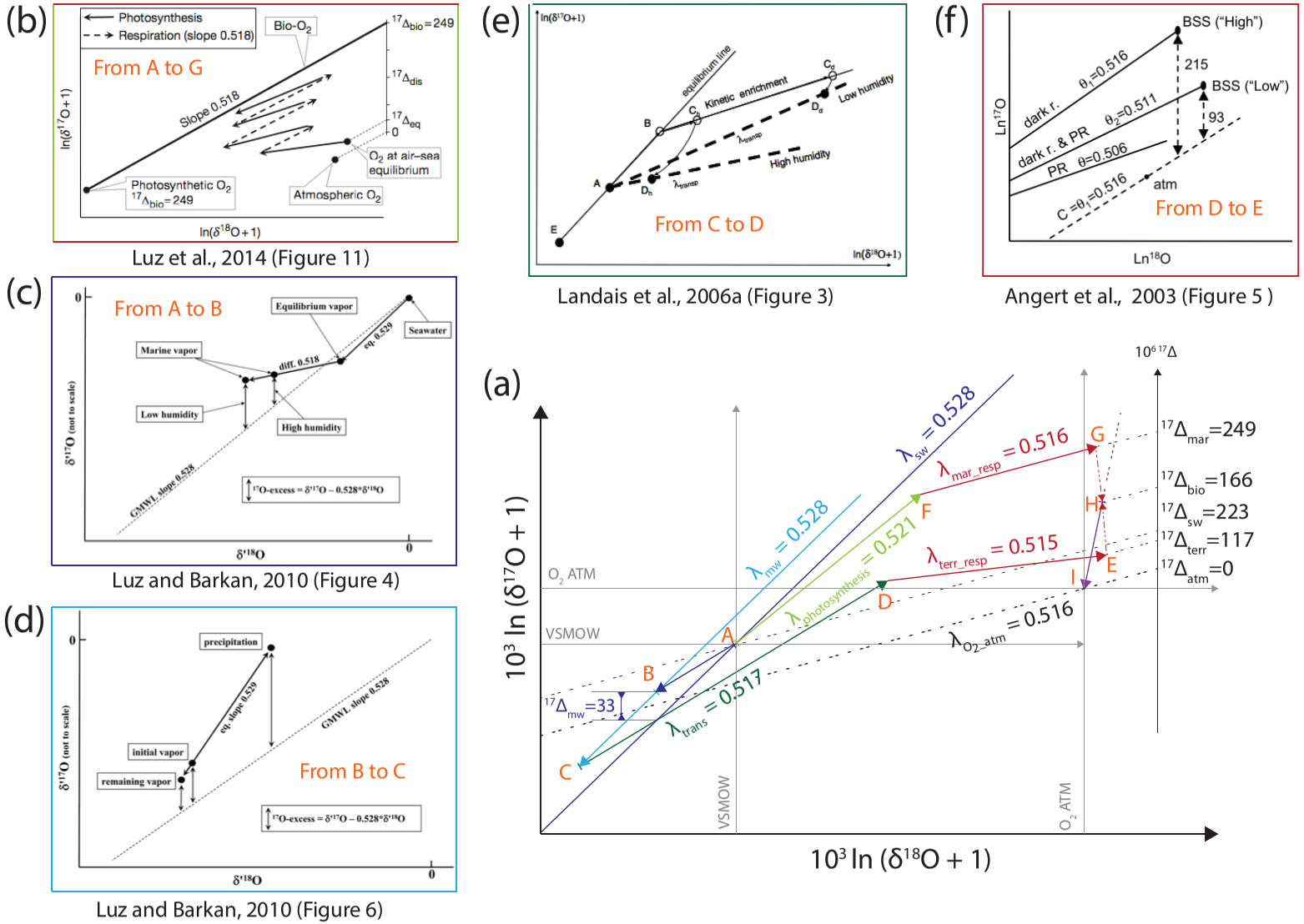

Figure 1.9 – A schematic representation of all the processes causing $^{17}\Delta_{atm}$ variations. Not to scale. Refer to text for details.

1.3 Past variations of the three O_2 isotopes in ice cores

Ice core archives represent the medium from which numerous tracers of the evolution of the climate in the past 800 kyr are retrieved. In particular, the past triple isotopic composition of atmospheric O_2 is obtained from fossil air preserved in ice core bubbles. This section describes the past orbital (Sect. 1.3.1) and millennial (Sect. 1.3.2) timescale variations of $\delta^{18}O_{atm}$ and $^{17}\Delta_{atm}$ over the last 800 kyr and 400 kyr, respectively, and the current understanding of these changes.

1.3.1 Orbital scale variations during the Quaternary Period

The Quaternary period, including the Pleistocene (from 2.588 Myr to 11700 yr B.P.) and Holocene period (from 11700 yrs), is characterized by a series of long-lasting glacial and shorter interglacial periods (Fig. 1.10). While ice started to accumulate in Antarctica over 20 Myr ago, major ice sheets in the Northern Hemisphere only started to build 2.5 Myr ago (e.g. Williams et al., 1997). During glacial periods, ice sheets covered an important part of Eurasia and North-America north of 40-50 °N, while only Antarctica and Greenland were ice covered during interglacial periods. These large-scale environmental changes caused a transfer of large amounts of water between oceans and ice sheets, leading to global sea level change up to ≃120 m (Waelbroeck et al., 2002; Lambeck et al., 2002; Bintanja et al., 2005). The Quaternary climate oscillations are recorded in archives like speleothems, marine or lake sediments (e.g. McDermott, 2004; Imbrie et al., 1984) and Antarctic ice cores (see Fig 1.10) for the last 800 kyr (e.g. Jouzel et al., 2007; Lüthi et al., 2008). Archives show that Pleistocene climatic oscillations varied with a period of 41 kyr until 1 Myr, then with a period of mean ≃100 kyr to present day. The reason of this frequency shift is still not fully understood. For instance, Ruddiman (2003) suggests that the 100 kyr cycle began 0.9 Myr ago because of a gradual global cooling trend allowing ice sheets to survive during weak precession insolation maxima and grow large enough during 41 kyr-ice-volume maxima to generate strong positive CO_2 feedback. As proposed by Milankovitch (1941), reduction of summer insolation in the mid-latitudes of the Northern Hemisphere causes onset of glaciations. Changes in insolation are driven by variations in the orbital parameters of the Earth, namely precession, obliquity and eccentricity (by modulating the precession signal). Milankovitch's hypothesis was that summer insolation in the NH at the periods of obliquity (41 kyr) and precession (23 kyr) directly forces NH ice sheets through changes in summer ablation. The response of the climate system to change in insolation is however more complex, because several processes interact and cause positive feedbacks. Indeed, a decrease in insolation is amplified by a weaker albedo feedback, and a decrease in greenhouse gases mixing ratios (which control the radiative surface forcing of the atmosphere), sea ice increase (Khodri et al., 2001), or biospheric changes (de Noblet et al., 1996). For instance, during the Last Glacial Maximum (noted LGM hereafter), 21 kyr ago, greenhouse gases concentration of CO_2 , CH_4 and N_2O reached a minimum of 185 ppm, 350 ppb et 200 ppb, resp. (Monnin et al., 2001; Dällenbach et al., 2000; Flückiger et al., 1999), while

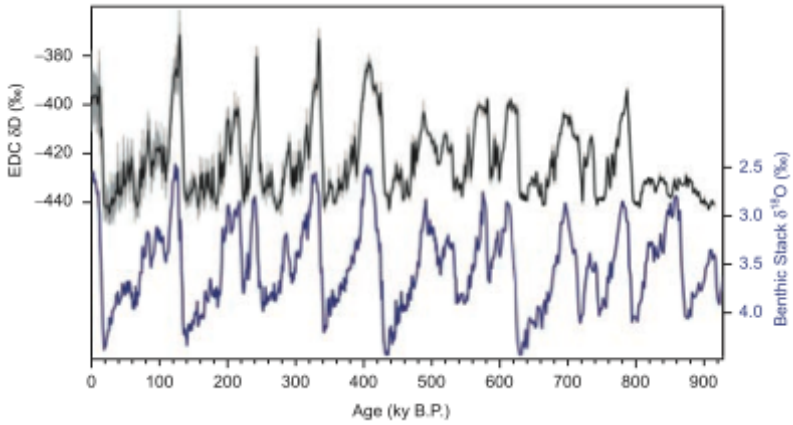

Figure 1.10 – Original figure from Jouzel et al. (2007). Comparison between two Late Pleistocene (last 800 kyr) records describing glacial interglacial cycles caused by orbital variations: the LR04 stack (benthic $\delta^{18}O$ records from 57 globally-distributed sites, Lisiecki and Raymo, 2005) on its own time-scale and δD from the EDC Antarctic ice core on EDC3 timescale (EPICA community members, 2004; Jouzel et al., 2007) present an excellent agreement. Benthic $\delta^{18}O$ is used as a proxy for global ice volume and deep ocean temperature, while δD variations indicate local surface temperature shifts.

reaching 280 ppm, 700 ppb et 270 ppb, resp., during the pre-industrial period (Fig. 1.11).

ICE ARCHIVES

The past atmospheric concentrations and isotope composition of ancient atmosphere are retrieved from air bubbles occluded in polar ice sheets. Indeed, in the firn to ice transition, close to the surface of the ice sheet, atmospheric air gets sealed into air bubbles (see Sect. 1.4.1.3). The air bubbles are then advected with the surrounding ice through the ice sheet. The deeper the ice layer, the older the retrieved climatic information. Ice cores drilled in Antarctica and Greenland have thus been analysed to reconstruct the past atmospheric composition up to 800 kyr (120 kyr in Greenland) back in time. For instance, ice core analysis show variations of greenhouse gases at orbital timescales (Lüthi et al., 2008; Loulergue et al., 2008; Petit et al., 1999; Schilt et al., 2010) synchronous with temperature reconstructions (see Fig.1.11), suggesting an amplifying role to orbital-scale climatic transitions as aforementioned. Not only past mixing ratios but also isotopic ratios of greenhouse gases and non-trace gases (e.g. O_2 , N_2 , Ar, Ne or Kr) are preserved in this irreplaceable natural archive, and provide valuable but complex information on the evolution of the past climate.

Precipitation in the form of snow falling each year is also preserved in the ice layers of the polar ice sheets. Water stable isotopes from Greenland (e.g NEEM members, 2013; NGRIP members, 2004) and Antarctic (e.g. Jouzel et al., 2007; EPICA community members, 2004; EPICA Community Members, 2006) ice cores are used to qualitatively define abrupt climatic transitions, while thermal fractionation of gases ($\delta^{15}N$, ^{40}Ar) in the diffusive column of the firn (Sect. 1.4.1.2) provides in Greenland a

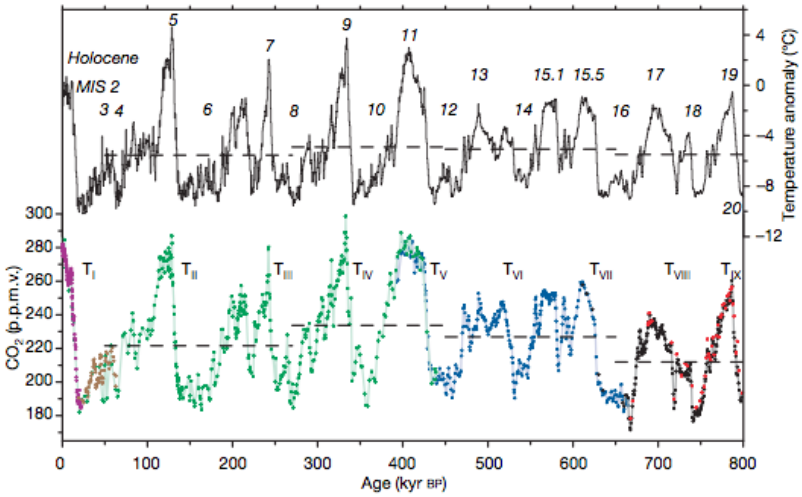

Figure 1.11 – Original figure from Lüthi et al. (2008). Original caption: Compilation of CO_2 records and EPICA Dome C temperature anomaly over the past 800 kyr. The Dome C temperature anomaly record with respect to the mean temperature of the last millennium (based on original deuterium data interpolated to a 500-yr resolution), plotted on the EDC3 timescale, is given as a black step curve. Data for CO_2 are from Dome C (circles in purple, blue, black,red), Taylor Dome (brown) and Vostok (green). All CO_2 values are on the EDC3_gas_a age scale. Horizontal lines are the mean values of temperature and CO_2 for the time periods 799-650, 650-450, 450-270 and 270-50 kyr BP. Glacial terminations are indicated using Roman numerals in subscript (for example TI); Marine Isotope Stages (MIS) are given in italic Arabic numerals

mean to quantify their amplitude (Landais et al., 2015; Severinghaus and Brook, 1999; Kindler et al., 2014).

1.3.1.1 Precession-driven variations of $\delta^{18}O_{atm}$

$\delta^{18}O_{atm}$ from ice samples has been measured for the period of the past 800 kyr (Bazin et al., 2016; Bender et al., 1985; Sowers et al., 1991; Jouzel et al., 1993, 1996; Malaize et al., 1999; Petit et al., 1999; Dreyfus et al., 2007) with a mean resolution of about 1000-1500 years (Landais et al., 2010 and references therein). Glacial-interglacial variation of $\delta^{18}O_{atm}$ mainly stems from $\delta^{18}O_{sw}$ variation (Bintanja et al., 2005), and reflects the role of ice sheet volume, forced by obliquity, on the ultimate source of atmospheric O_2 , seawater. Indeed, removing the signal of $\delta^{18}O_{sw}$ from $\delta^{18}O_{atm}$, that is the definition of the Dole effect (Dole, 1935; Dole et al., 1954), enables to remove the obliquity component (see Fig. 1.12b) common to both signals (Landais et al., 2010).

At the orbital scale, $\delta^{18}O_{atm}$ is depicting clear variations at a 23 kyr periodicity (Jouzel et al., 1996; Petit et al., 1999). Bender et al. (1994); Malaize et al. (1999) also revealed a strong precessional periodicity (23 kyr) in Dole Effect ($\delta^{18}O_{atm}$ - $\delta^{18}O_{sw}$) records, with a striking correspondence with summer insolation in the low latitudes

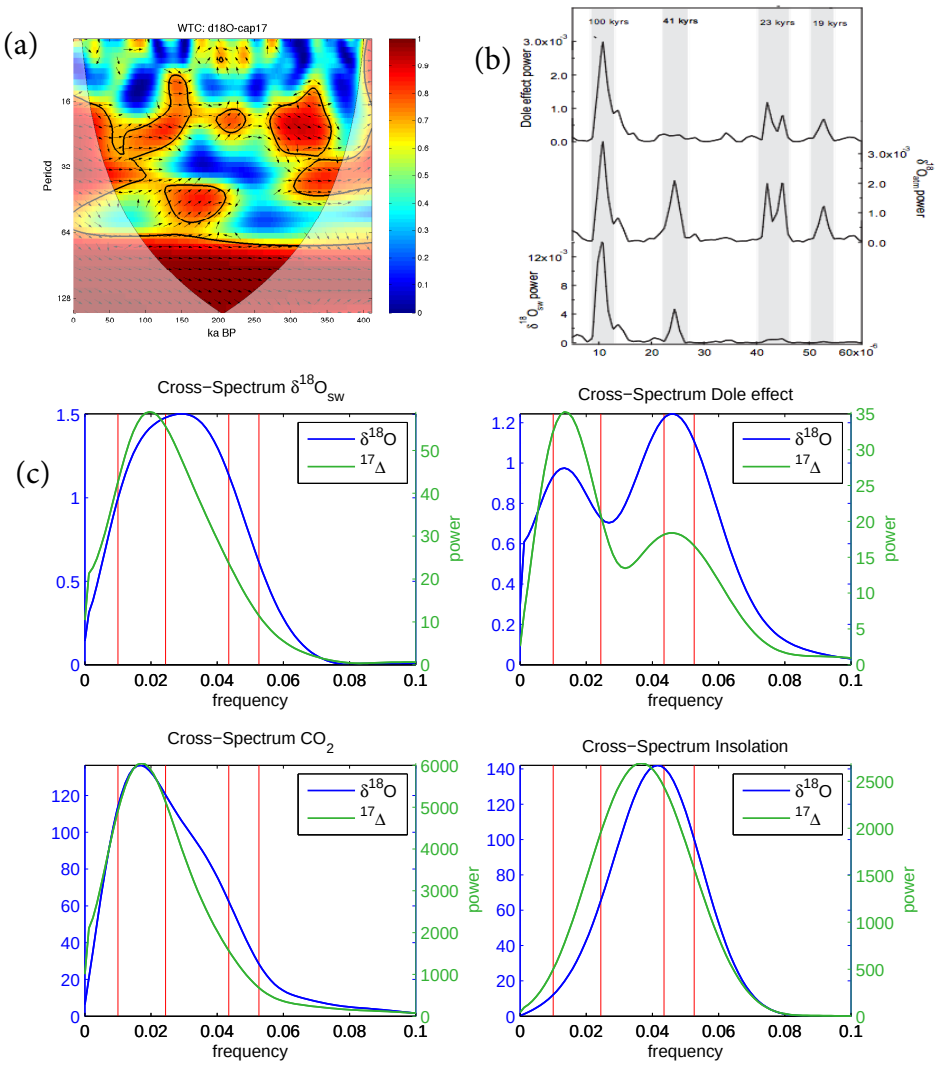

Figure 1.12 – **(a)** Coherence wavelet analysis using Wavelet Analysis (Grinsted et al., 2004) reveals a strong covariation of Vostok $\delta^{18}O_{atm}$ (Petit et al., 1999) and Vostok $^{17}\Delta_{atm}$ (Blunier et al., 2012) in the orbital frequencies. Both records were transferred to the orbitally tuned Vostok time scale from Suwa and Bender (2008). The most prominent feature is the variation of the coherence through time in the precession band. Covariation in obliquity mainly stems from $\delta^{18}O_{sw}$ signal. Black contours indicate significance on a 95% level assuming red noise. The transparent region outside the cone of influence should not be considered. **(b)** Figure from Landais et al. (2010) showing a spectral analysis of Dole effect (top), $\delta^{18}O_{atm}$ (Middle) and $\delta^{18}O_{sw}$ (Bottom) over the last 800 kyr with a 1000 kyr resolution. $\delta^{18}O_{atm}$ originates from EDC (Dreyfus et al., 2007) and Vostok (Sowers et al., 1991; Jouzel et al., 1993, 1996; Malaize et al., 1999; Petit et al., 1999) ice cores. Please note that according to the authors, the results do not depend on the chosen timescale (original timescales, or adjusted on precession (orbitally tuned)). Similar results are indeed obtained with the Vostok $\delta^{18}O_{atm}$ record in its original timescale GT4 (Glaciological Timescale 4 cycles), built through glaciological modeling (Petit et al., 1999). **(c)** Cross correlation spectra of $\delta^{18}O_{atm}$ and $^{17}\Delta_{atm}$ with $\delta^{18}O_{sw}$, Dole effect, CO_2 and insolation describe the influence of orbital parameters and associated mechanisms on the long term variations of those two records. Red bars represent the frequencies relevant for orbital parameters (from low to high frequency: excentricity (100 kyr), obliquity (41 kyr) and the two 23 kyr and 19 kyr peaks of precession).

.

of the Northern Hemisphere. This strong link with precession of both $\delta^{18}O_{atm}$ and the DE (Fig. 1.12b) is thus probably related to the variations of the hydrological cycle at low latitudes (Bender et al., 1994). Indeed, changes in precession, the timing of the seasons with respect to perihelion, affect the amplitude of the seasons and the intensity of the monsoons (Prell and Kutzbach, 1987). Variations related to the monsoon regime strongly imprint the isotopic composition of meteoric water as observed in speleothem records (e.g. Wang et al., 2008). They are easily transmitted to the isotopic composition of atmospheric oxygen because the major part of the biospheric productivity, hence photosynthesis, is occurring in the tropics and subtropics. Based on these observations, the DE is interpreted as a tracer of low latitude hydrological cycle on orbital timescale, hence of precession-driven monsoonal activity (e.g. Landais et al., 2010).

The dominant role of the low latitude hydrological cycle on $\delta^{18}O_{atm}$ orbital variations is corroborated by the striking correspondence between the calcite $\delta^{18}O$ record of a speleothem from Sanbao Cave (China, Wang et al., 2008) and $\delta^{18}O_{atm}$ from Vostok ice core. Indeed, both tropical speleothem's calcite $\delta^{18}O$, a tracer of monsoonal activity (e.g. Wang et al., 2001, 2008; Cruz et al., 2005), and $\delta^{18}O_{atm}$ bear a strong precession signal:

- Precession is believed to control the position of the InterTropical Convergence Zone (ITCZ) (Bender et al., 1994; Wang et al., 2008). During precession minima, the ITCZ and its associated tropical rain belt shift northwards, enhancing monsoonal activity on land. As a result, $\delta^{18}O_{mw}$ becomes depleted, through the amount effect, and it transmits the signal to $\delta^{18}O_{atm}$ through photosynthesis (Landais et al., 2010). The opposite effect occurs in the Southern Hemisphere, with less precipitation, characterized by enriched calcite $\delta^{18}O$ (e.g. Cruz et al., 2005). However, given the NH/SH land ratio, hence the biospheric O_2 production ratio, the imprint of the low latitudes of the NH on $\delta^{18}O_{atm}$ is dominant.

- The $\delta^{18}O$ of calcite, a local monsoon intensity tracer, is mostly influenced by land-sea thermal contrasts and local seasonal cycle, which are driven by precession. These processes influence $\delta^{18}O_{mw}$, hence calcite $\delta^{18}O$ (e.g. Braconnot and Marti, 2003).

PHASING Based on new $\delta^{18}O_{atm}$ and $\delta O_2/N_2$ (synchronous at first order with local summer insolation) records from EPICA Dome C (noted EDC hereafter, Fig 1.13), Bazin et al. (2016) recently confirmed the occurrence of large variations (1 to 6 kyr) in the phase delay between $\delta^{18}O_{atm}$ and precession. While previous studies observed a 5 to 6 kyr lag between $\delta^{18}O_{atm}$ and precession over Termination I (e.g. Dreyfus et al., 2007) and Termination II (e.g. Landais et al., 2013), Bazin et al. (2016) found similar lags over Termination II (-5.5 kyr), MIS 8 (-5 kyr) and MIS 16 (-2 kyr), but also minimal lags ($\simeq$ 1 kyr) during periods characterized by intermediate sea-ice extent and high eccentricity levels (MIS 6-7, end of MIS 9, the transition MIS 14-15 and the end of MIS 17). As Termination 2, MIS 8 and MIS 16 are associated with large destabilizations of the Northern Polar ice sheets, they hypothesize that changes in the low latitude hydrolog-

ical cycle caused by weak NH monsoonal activity (associated with large freshwater input causing a southwards ITCZ shift) delay the $\delta^{18}O_{atm}$ response to precession peak (Sect. 1.3.2). The variation of the lag has also serious implications for orbital datation of ice cores assuming a constant phase relationship between $\delta^{18}O_{atm}$ and the precession parameter (Dreyfus et al., 2007), or an insolation curve (e.g. Jouzel et al., 1996; Petit et al., 1999; Bender et al., 1994; Malaize et al., 1999), in terms of uncertainty, and this method should thus be used with caution. On the other hand, the change in the lag does not affect the potential of $\delta^{18}O_{atm}$ to synchronize ice cores, as the $\delta^{18}O_{atm}$ signal is global.

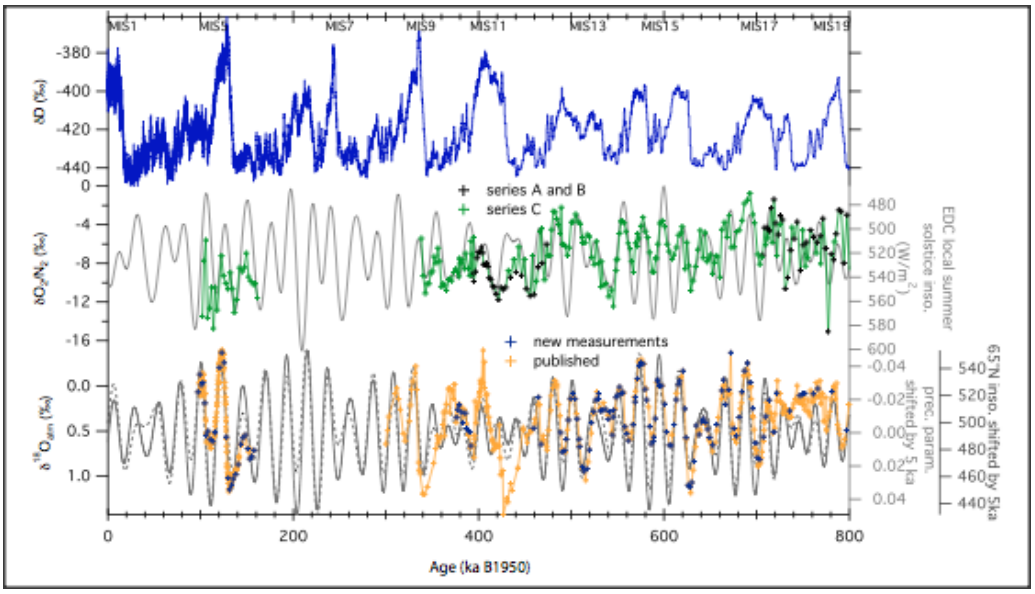

Figure 1.13 – *Original Figure from Bazin et al. (2016) with original caption: Top: EDC ice core record of water stable isotopes (δD, Jouzel et al., 2007). Middle: EDC record of $\delta O_2/N_2$ (black: Landais et al. (2012), green: Bazin et al. (2016)) and local summer solstice insolation (grey, reversed axis). Bottom: EDC record of $\delta^{18}O_{atm}$ (reversed vertical scale) (orange: Dreyfus et al. (2007, 2008); Landais et al. (2013), blue: Bazin et al. (2016)), precession parameter (grey, reversed axis) and 65 °N summer solstice insolation (dashed grey) both shifted younger by 5 kyr. All EDC records are presented on the orbitally tuned AICC2012 chronology (Bazin et al., 2013; Veres et al., 2013). The orbital parameters are calculated using the Laskar et al. (2004) solution, with the Analyseries software (Paillard et al., 1996).* This figure depicts the orbital variations of water stable isotopes, $\delta O_2/N_2$ and $\delta^{18}O_{atm}$ of the EDC ice core, back to 800 kyr During periods of weak eccentricity (e.g. around 400 kyr and before 720 kyr), there is no clear correspondence between the variations of $\delta^{18}O_{atm}$ and precession, and the variations of $\delta O_2/N_2$ with local summer solstice insolation (Bazin et al., 2016; Dreyfus et al., 2007; Landais et al., 2012).

1.3.1.2 Long-term variations of $^{17}\triangle_{atm}$

Owing to the low abundance of ^{17}O, accounting for 0.078 % of the total oxygen, and the subsequent very high precision required to obtain reliable datasets, only a few

studies have focused on past long term variations of ${}^{17}\Delta_{atm}$ (Luz et al., 1999; Blunier et al., 2002, 2012). ${}^{17}\Delta_{atm}$ has been measured back to 400 kyr with approximately 1000 years resolution (Blunier et al., 2002, 2012). ${}^{17}\Delta_{atm}$ also depict glacial-interglacial variation of around 40 permeg (Fig. 1.14), mainly driven by changes in CO_2 concentration. Such a strong dependence is mainly due to stratospheric photochemistry (Sect. 1.2.5.3) involving transfer of heavy isotopes of O_2 to CO_2 via O_3 (e.g. Thiemens, 1999), and scaling with CO_2 concentration. Timings of strong coherence between $\delta^{18}O_{atm}$ and ${}^{17}\Delta_{atm}$ occur during strong concomitant sea level and CO_2 variations, associated with a strong precession signal (Fig. 1.14).

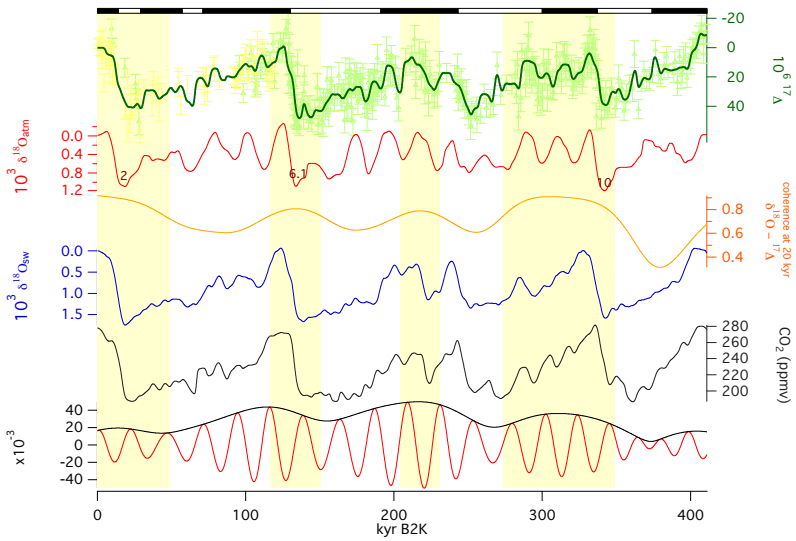

Figure 1.14 – Bottom-Up: Precession parameter and excentricity (Laskar et al., 2004) ; compiled CO_2 data from Vostok, Taylor Dome and Epica Dome C (Lüthi et al., 2008; Blunier et al., 2012) ; coherence in the precession band extracted from Fig. 1.12a ; $\delta^{18}O_{sw}$ curve from Bintanja et al. (2005) ; $\delta^{18}O_{atm}$ from Vostok (Petit et al., 1999) ; ${}^{17}\Delta_{atm}$ from Blunier et al. (2002). Vertical shaded bars indicates periods of strong coherence between $\delta^{18}O_{atm}$ and ${}^{17}\Delta_{atm}$; approximate MISs timings are indicated on top. Note that all records are displayed on their original timescale adjusted to start in 2000.

1.3.2 Millennial scale climate variability

Beyond the large and valuable climate information that can be retrieved from the polar ice sheets, ice core are unique archives as they also provide high temporal resolution (which is function of the accumulation rate) and accurate datation[9]. For instance, the fine yearly data resolution of NGRIP (Northern Greenland Ice Core Project, Greenland) ice core sample enables annual layer counting down to a depth of 2430 m, which

[9]With the new technological developments, speleothems nonetheless challenge ice archives in terms of absolute datation, because they can be dated in calendar years with a precision approaching $\pm 0.5\%(2\sigma)$ (McDermott, 2004). McDermott (2004) actually predicts that the chronology of the Greenland ice-cores records will be increasingly refined with speleothem records.

corresponds to an age of 60 kyr (Svensson et al., 2008).

Millennial-scale climate variability is perhaps best known from the Greenland ice cores, where it is manifested in the stable water isotopes of ice. During the last glacial period, these cores show 25 Dansgaard-Oeschger (DO) events (NGRIP members, 2004). A DO event typically exhibits a sawtooth pattern: (i) a cold phase (Greenland stadial, noted GS hereafter) lasting from centuries to millennia, followed by a warm phase (Greenland interstadial, GI) starting with (ii) a rapid transition (a few decades) with an amplitude of up to 16 ± 2.5°C (Landais et al., 2004a,b, 2006c; Huber et al., 2006b; Kindler et al., 2014), and ending with (iii) a gradual cooling before an abrupt decrease towards cold, stadial values. During the last glacial period, the presence of ice rafted debris (IRD, Ruddiman, 1977; Heinrich, 1988) in marine sediments from the North Atlantic region during the largest GS document episodes of massive iceberg release in the North Atlantic, mainly from the Laurentide and Fennoscandian ice sheets (Grousset et al., 1993; Guillevic et al., 2014 and references therein). Eventhough IRD are present in each GS (Elliot et al., 2002), not all GSs contain a Heinrich event. Only six major IRD, occurring within the Ruddiman band, between 40°N et 55°N, were defined as Heinrich events (Hemming, 2004). When a Heinrich event occurs during a GS, the latter is defined as a Heinrich stadial (HS) (Barker et al., 2009; Sanchez Goni and Harrison, 2010).

1.3.2.1 What drives abrupt climate changes?

Millennial-scale climate variations in Greenland are associated with abrupt climate changes in the mid to low latitudes as recorded in numerous terrestrial (speleothems, e.g. Fleitmann et al., 2009) and marine (e.g. Bond et al., 1993; Broecker, 2000) archives (read Clement and Peterson, 2008 for a review). As the tropics are the main source of heat and water vapor in the global climatic system (Clement and Peterson, 2008), and document major climatic impacts from millennial scale variability in terrestrial and marine paleoarchives (e.g. Voelker and workshop participants, 2002, and reference therein), hydrological reorganizations in low latitudes may have played a critical role (e.g. Peterson et al., 2000) in abrupt climatic events. Concomitant methane excursions in ice cores and variations in the isotopic composition of the calcite of speleothems in eastern Asia (e.g. Wang et al., 2001; Cheng et al., 2012) actually strongly support the fact that millennial scale variability is associated with major reorganization of the tropical water cycle and hence monsoon intensity in a relation with a shift in the ITCZ and its terrestrial equivalent, the tropical rain belt (Chappellaz et al., 2013; Wang et al., 2008; Pausata et al., 2011).

Each DO event has a corresponding Chinese Interstadial, as observed in $\delta^{18}O$ of calcite speleothems (e.g. Cheng et al., 2012). However, on shorter timescales, a decoupling is observed between the tropical and the polar regions. For instance, on-the-field continuous laser spectroscopy measurements of CH_4 , at a very high temporal resolu-

tion, unveiled sub-millennial scale variations with no signal in Greenland water stable isotopes (Landais et al., 2015; Chappellaz et al., 2013). Details of the link between tropical and high latitude climate is widely discussed and partly hampered by the difficulty to synchronize timescales of archives of different nature (speleothems, marine cores, ice cores). Guillevic et al. (2014) avoid interarchives datation discrepancies by developing a multi-proxy approach based on the identification in polar ice cores of the fingerprint of HEs in the mid-to-low latitudes. This study, based on direct comparison between various ice core proxies ($\delta^{18}O_{atm}$, CO_2, CH_4 mixing ratio, sulfuric acid (MSA)) sensitive to climate of different latitudes, also reveals a decoupling between Greenland temperatures and low latitude HE imprints (Heinrich event 4) during GS 9. These examples highlight the need for low latitude climate ice core proxies, on a common timescale and at high temporal resolution, for testing the mechanisms associated with millennial scale variability. Indeed, despite the variety of regional scale paleoarchives (ocean cores, lake sediments, speleothems, pollen, corals, paleosoils, tree rings) that unveil the imprint of climate instabilities at different latitudes in both hemispheres, assessing their spatial extent is challenged by (i) the dating uncertainties of low latitudes records, making difficult to obtain a precise chronology over archives of different types, and (ii) their spatial distribution, as most of the records are located in the North-Atlantic, with enormous spatial gaps elsewhere (Clement and Peterson, 2008; Voelker and workshop participants, 2002), and significance (Hemming, 2004; Wunsch, 2006; Severinghaus et al., 2009). Atmospheric O_2 helps address the spatial issue because it represents an integrated signal sensitive in particular to the low latitude hydroclimate.

1.3.2.2 Rapid changes in the composition of atmospheric O_2

$\delta^{18}O_{atm}$

At the millennial scale, $\delta^{18}O_{atm}$ is responding to the abrupt climate changes of the last glacial period. NGRIP $\delta^{18}O_{atm}$ high-resolution measurements(100 yrs step) covering MIS 4 and MIS 5 (Landais et al., 2007b, 2006c; Capron et al., 2008) and including 8 DO events indeed reveal a $\delta^{18}O_{atm}$ increase (decrease) over the cold (warm) phase of DO events (Fig. 1.15a). A clear illustration of this pattern can be found during DO 22 and 21. Superimposed to the general decreasing trend of $\delta^{18}O_{atm}$ by $-0.6‰$ (blue arrow on Fig. 1.15a), millennial scale variations, are observed (red arrows): during the warm phases of DO 22 and 21, $\delta^{18}O_{atm}$ decreases more abruptly, and remains stable during the cold stadial (Landais et al., 2010).

As mentioned in Sect. 1.3.1, among the cold phases (GSs) characterized by an increase in $\delta^{18}O_{atm}$ (Landais et al., 2007b; Severinghaus et al., 2009), some GSs are associated with major iceberg discharges and are designed as HSs. The $\delta^{18}O_{atm}$ signal is often stronger during the HSs than during the other GSs.

These GSs and/or HSs are associated with strong variations in the monsoon regime in the low latitudes through southward shift of the ITCZ, more pronounced during HS (GS associated with a HE) than GS, as suggested by speleothem growth rate and calcite $\delta^{18}O$ (Kanner et al., 2012; Wang et al., 2007; Mosblech et al., 2012). It has

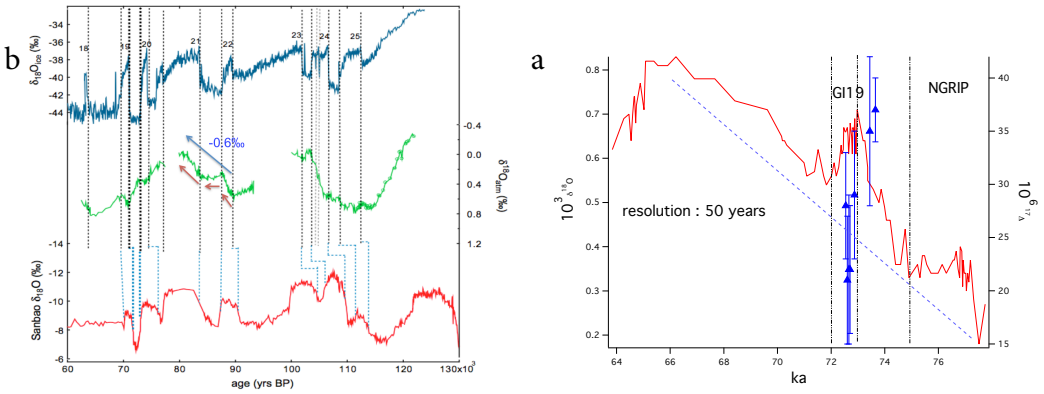

Figure 1.15 – **(a)** Based on Landais et al. (2010). Top: NorthGRIP water $\delta^{18}O$ is displayed on the EDML1 Antarctic timescale (Ruth et al., 2007; Capron et al., 2010). The DO events are indicated. Middle: millennial scale variations of $\delta^{18}O_{atm}$ on the EDML1 timescale (Landais et al., 2006a, 2007b; Capron et al., 2008) during MIS 5 and MIS4, increasing over GSs and decreasing over GIs. Are also shown in red variations of speleothem's calcite $\delta^{18}O$ from Sanbao, north-east Asia (Wang et al., 2008). Millennial forcings are superimposed to the precessional and/or ice-sheet-induced long-term $\delta^{18}O_{atm}$ trend. Vertical dotted lines indicate the correspondence between $\delta^{18}O_{atm}$, water $\delta^{18}O$ and calcite $\delta^{18}O$ records**(b)** Based on Landais et al. (2007b). Millennial scale variations of the three isotopes of O_2 over DO 19. NGRIP $\delta^{18}O_{atm}$ was measured at very-high resolution (50 years) resolution, not $^{17}\Delta_{atm}$. The blue dashed line symbolizes the sea-level gradual $\delta^{18}O_{sw}$ enrichment due to growing ice-sheet (e.g. Bintanja et al., 2005).

thus been suggested that the driver of the global $\delta^{18}O_{atm}$ millennial scale variations is the hydrological cycle of the low latitudes. For instance, Landais et al.'s study (2010) invokes changes in the low latitude hydrology and in terrestrial vegetation distribution, driven by ITCZ shifts, to explain $\delta^{18}O_{atm}$ millennial scale variations observed in ice cores. Besides, Severinghaus et al. (2009) found a striking anti correlation between Chinese speleothems calcite $\delta^{18}O$ (Wang et al., 2001, 2008) and $\delta^{18}O_{atm}$ derived ε_{land} from Siple Dome, highlighting too the importance of the NH tropical hydology. To summarize, these studies underscore the influence of NH monsoonal activity on $\delta^{18}O_{atm}$, driven by ITCZ shifts on millennial timescales. Quantifying its past variations should provide valuable information on the low latitude hydroclimate and this work represents the scope of Chapter 5.

To my knowledge, only one study hitherto has combined very high resolutions measurements of the three isotopes of atmospheric O_2 (Landais et al., 2007b). 96 $\delta^{18}O_{atm}$ measurements were performed over the period 80 to 60 kyr (DO 18, 19 and 20). In addition, $^{17}\Delta_{atm}$ measurements were done at 7 depth level over DO 19, where the largest temperature variation during MIS 4 occurs, to constrain the origin of the observed $\delta^{18}O_{atm}$ variations (Fig. 1.15b). As already observed for $\delta^{18}O_{atm}$ over other DO events, an imprint of millennial processes on the long-term trend of $\delta^{18}O_{atm}$ is observed. Indeed, $\delta^{18}O_{atm}$ should be steadily increasing from 76 kyr to 66 kyr B.P, driven by the increase in $\delta^{18}O_{sw}$ (symbolized by the dashed blue line in Fig. 1.15b) due to a decreasing sea level (and more voluminous ice sheet) (Landais et al., 2007b). Instead, $^{17}\Delta_{atm}$

it increases by more than 0.2 ‰ over GS 20 with respect to its long-term increase, and decreases by the same amount during GI 19 (considering that $\delta^{18}O_{atm}$ should get enriched) (Landais et al., 2007b). The mean $^{17}\Delta_{atm}$ decrease of 12 ± 10 permeg from GS 20 to GI 19 (Fig. 1.15) provides valuable information in the sense that the magnitude of its variation discards the possibility that rapid sea-level changes are driving $\delta^{18}O_{atm}$ variations over DO 19. Indeed, a 12 permeg decrease would require, according to Eq. 1.52, a 1 ‰ decrease of $\delta^{18}O_{sw}$, hence $\delta^{18}O_{atm}$ over GI 19, corresponding to the observed variations in mean $\delta^{18}O_{sw}$ between LGM and present-day (Waelbroeck et al., 2002), around 120 m (Bintanja et al., 2005). The inter-comparison of $\delta^{18}O_{atm}$ and $^{17}\Delta_{atm}$ relative variations over DO 19 by Landais et al. (2007b) confirms the view according to which the combined changes of hydrology and vegetation cover, rather than rapid sea-level changes, drives the triple isotopic composition of atmospheric O_2 on millennial time-scale.

The study of Landais et al. (2007b) illustrates the interest of combining very-high resolution measurements of $^{17}\Delta_{atm}$ and $\delta^{18}O_{atm}$ to constrain the origin of their variations. Still, $^{17}\Delta_{atm}$ measurements are challenging, requiring a very high precision (less than 10 permeg) to obtain a record with a reliable climatic signal. The quality of the record does not only depend on the quality of the analytical measurements, on the conditions of ice core recovery and storage, but also on our understanding of how the air is trapped in the ice. Indeed, the elemental and isotopic composition of the air occluded in ice core bubbles is different from the ancient atmosphere it represents, because of fractionating processes that occur in the firn, the porous top layer of the ice sheet where transformation of snow to ice occurs. Corrections are therefore unavoidable, and their quality reflects our understanding of these firn processes, which is reviewed in the next section.

1.4 Alteration of the composition of gases trapped in ice core bubbles

The previous section reviewed the current understanding of $\delta^{18}O_{atm}$ and $^{17}\Delta_{atm}$, described their orbital and millennial time-scale variations observed in ice cores, and focused on the processes that affect the triple isotope composition of atmospheric O_2 . In Chapter 5 we use a modeling approach to quantify the relative importance of the different processes behind the observed changes in $\delta^{18}O_{atm}$ over a Heinrich Stadial. However, this step requires first to reconstruct the original $\delta^{18}O_{atm}$, or $^{17}\Delta_{atm}$ record preserved in air bubbles entrapped in ice cores. To do so, leaving aside the building and validation of an analytical system able to measure with high precision the triple isotopic composition of O_2 from fossil air (Chapter 3), it is necessary to understand the processes of air trapping in the firn, and how they alter the elemental and isotope composition of fossil air. While this section introduces the firn processes, Chapter 4 will detail the strategy adopted to correct ice core measurements for these effects, but also for the effects of coring and post-coring fractionation.

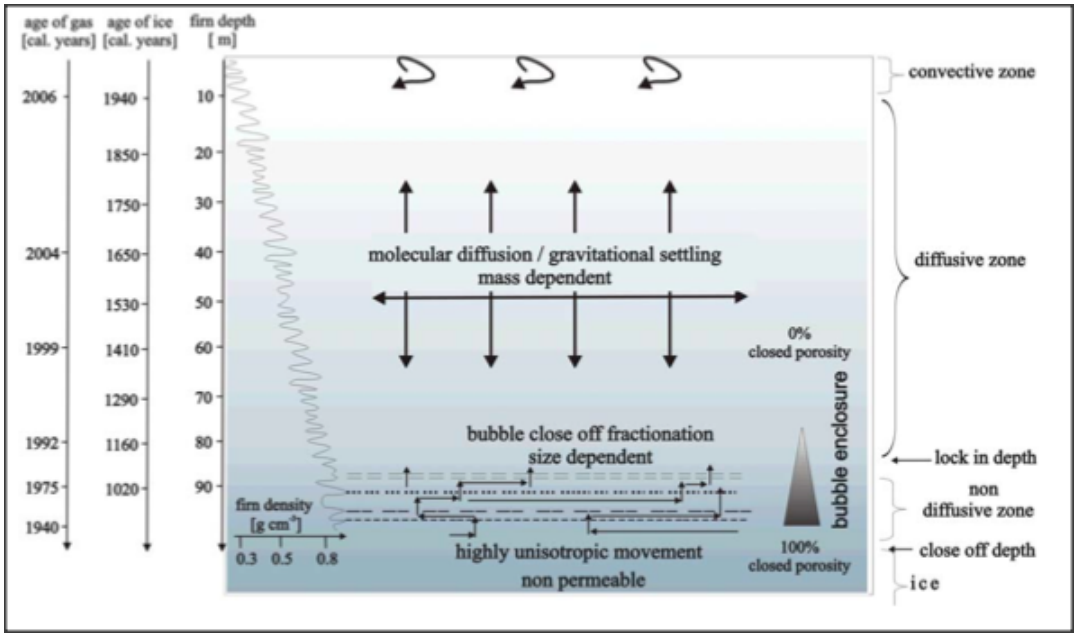

Figure 1.16 – Original figure 2-2 from Schmitt (2006). Scheme of physical processes occurring in the firn column with depth and age values for ice and gas representative for the drill site Kohnen station (Antarctica). This figure illustrates (1) the progressive compaction of snow to ice caused by the overburden pressure of successive precipitation, resulting in a gradual density increase from $\simeq 0.3 \pm 0.2\, g \cdot cm^3$ at the top to $0.8 \pm 0.05\, g \cdot cm^3$ ($\rho_{ice} = 0.92\, g \cdot cm^3$) at the bottom of the firn. (2) Firn densification causes the interstitial space between ice crystals, called porosity, to decrease with depth, and air to be gradually trapped in bubbles. (3) Firn can be divided in 3 distinct zones based on the mode of air transport: a convective zone, typically 1-15 m deep (Kawamura et al., 2006; Landais et al., 2006b) where the air has the same composition as the atmosphere due to rapid mixing; a diffusive zone characterized by molecular diffusion of gases, where mass dependent gravitational fractionation leads to enrichment of heavy isotopes with depth; and a lock-in-zone, or non diffusive zone, where air is advected with the ice matrix. Vertical diffusion stops at the lock-in-depth, on top of the locking zone. In other words, the lock-in-zone is isolated above from atmosphere, probably due to the presence of high density winter layers (Battle et al., 1996; Landais et al., 2006b) at the lock-in-depth that inhibit vertical gas transport (Buizert, 2011). The limit of the lock-in-zone is defined below by the firn to ice transition, where there are no more open pores. This zone is characterized by size-dependent fractionation, evidenced by e.g. Huber et al. (2006a); Severinghaus and Battle (2006), who observed strong enrichment of gas species with a small molecular diameter, such as He, Ar, Ne and O_2 (see text for details) (4) Finally, this figure shows how Δage (the ice age - gas age difference) increases with depth. This is due to the fact that air in the firn continuously exchanges with the atmosphere until the lock-in-zone is reached. As a result, the air occluded in bubbles is younger than the surrounding ice (Schwander and Stauffer, 1984). Note that in the lock-in-zone, the age of the air is substantially older than in the diffusive zone, as air is advected downwards at the same pace as the ice matrix. This offers the possibility to retrieve large ancient air samples without the need of extracting them from ice core bubbles(Severinghaus and Battle, 2006). However, it is challenging to isolate the climatic signal as the air composition of the lock-in-zone depends on several factors (Sect. 1.4.1.3.4).

1.4.1 DIFFUSIVE PROCESSES IN FIRN

Air bubbles trapped in ice cores have a different elemental and isotopic composition than the one of the past atmosphere they represent. This is caused by the presence of a 40-120 m thick porous snow layer at the top of the ice sheet (Fig. 1.16), called firn. Various processes modify the composition of the air traveling downwards until the air is occluded in the ice matrix at the bottom of the firn.

The firn column is usually divided in 3 zones, based on the $\delta^{15}N$ of N_2 (Sowers et al., 1992). Figure 1.17c shows that $\delta^{15}N$ has the same value as in the atmosphere in the upper 1-15 m of the firn column, where convective exchange (surface winds, thermal convection) with the atmosphere occurs. No diffusion occurs in this zone. The diffusive zone is mostly characterized by a gravitational enrichment of $\delta^{15}N$. In the lock-in-zone, the air is isolated from the atmosphere, which causes $\delta^{15}N$ enrichment to stop.

In the following sections we describe how the physical processes taking place in the firn column alter the elemental and isotopic composition of the air bubbles occluded in ice cores. Concentration gradients within the firn drive gas fluxes via molecular diffusion (Craig et al., 1988). They can originate from changes in the composition of the overlying atmosphere, gravitational settling (Craig et al., 1988) (Sect. 1.4.1.1), thermal diffusion (first observed in sand dunes, Severinghaus et al., 1996) (Sect. 1.4.1.2), and molecular size fractionation at close-off depth (Sect. 1.4.1.3), where all bubbles are closed Huber et al. (2006a).

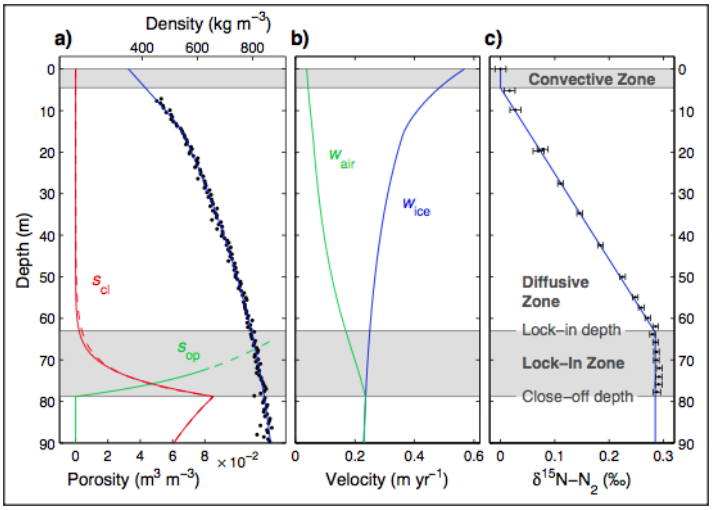

Figure 1.17 – Original caption and figure 2.3 from Buizert (2011). Firn characteristics at NEEM (North Eemian Drilling Project, Greenland, 77.4 °N, 51.1°W). **(a)** Firn density and porosity using the parameterizations of Schwander (1989) (solid line) and Goujon et al. (2003) (dashed line). **(b)** Downward velocity of firn layers (w_{ice}) and of air in the open porosity (w_{air}). **(c)** Zonal division based on gravitational enrichment of $\delta^{15}N$ of N_2 . Data are corrected for thermal fractionation.

1.4.1.1 Gravitational fractionation

Earth's gravity field causes heavy isotopes to accumulate at the bottom of the firn air column in diffusive equilibrium. Gravitational enrichment increases with depth and the absolute mass difference between a pair of elements, or isotopes. Equilibrium is reached when the gravitational force balances the molecular diffusion driven by the gradient of concentration in the firn. The isotopic enrichment at the lock in depth caused by gravitational settling can be expressed by the barometric equation (Craig et al., 1988):

$$\delta_{grav} = e^{\frac{\Delta_{mgz}}{RT}} - 1 \cong \frac{\Delta_m gz}{RT}, \tag{1.54}$$

with Δm being the mass difference between the two considered isotopologues, g the acceleration due to gravitation, z the depth of the diffusive zone, R the ideal gas constant, and T the mean firn temperature in K. Because gravitational fractionation scales with the mass difference Δ_m (Craig et al., 1988; Schwander, 1989), it is thus 2 times stronger for ^{18}O ($\Delta_m = 34 - 32 = 2$) than for ^{15}N ($\Delta_m = 29 - 28 = 1$).

1.4.1.2 Thermal fractionation

Thermal fractionation arises from temperature difference in the firn, leading to enrichment of heavy elements towards the bottom of the firn, colder than in the surface. This process is due to due to the sensitivity of intermolecular forces during collision of molecules and atoms (Severinghaus et al., 2001) and is determined empirically. To be significant, thermal gradients must be higher than 10 °C (Landais, 2004). Thermal fractionation is therefore stronger during abrupt climate changes, for instance during DO events: when a rapid temperature warming occurs at the surface, heavy isotopologues ($\delta^{15}N$, $\delta^{18}O$, ^{40}Ar) migrate towards the bottom of the firn. As diffusion of gases is $\backsim$ 10 times faster than diffusion of heat (Paterson, 1994), it will take hundreds of years before temperature homogenize in the firn, causing in turn $\delta^{15}N$ to reach back its initial value. It follows that the thermal diffusion signal can fully develop until warm temperatures reach the bottom of the firn. This also means that the temperature change indicated by air isotopes is recorded at the same level than changes in trace gases like CO_2 or CH_4 , while water isotopes register this change at the surface. As a consequence, a paleothermometry method based on $\delta^{15}N$ has been developed (see e.g. Severinghaus and Brook, 1999 or Kindler et al., 2014, who measured NGRIP $\delta^{15}N$ for the whole last glacial period from 10 to 120 kyr b2k (thousand years before 2000) including every DO event). This method offers the great advantage of avoiding the uncertainty caused by the depth difference Δ depth, hence age difference Δ age[10], between water isotopes and gas isotopes when interested in comparing temperature and greenhouse gases variations.

At equilibrium between thermal diffusion, in one direction, and molecular diffusion along a concentration gradient in the other direction, thermal fractionation can

[10]The error associated with Δ_{age} is $\backsim$ 10%, which corresponds to 100 yr in Greenland during the glacial period, and 1000 yr (or more) in Antarctica (Landais, 2004)

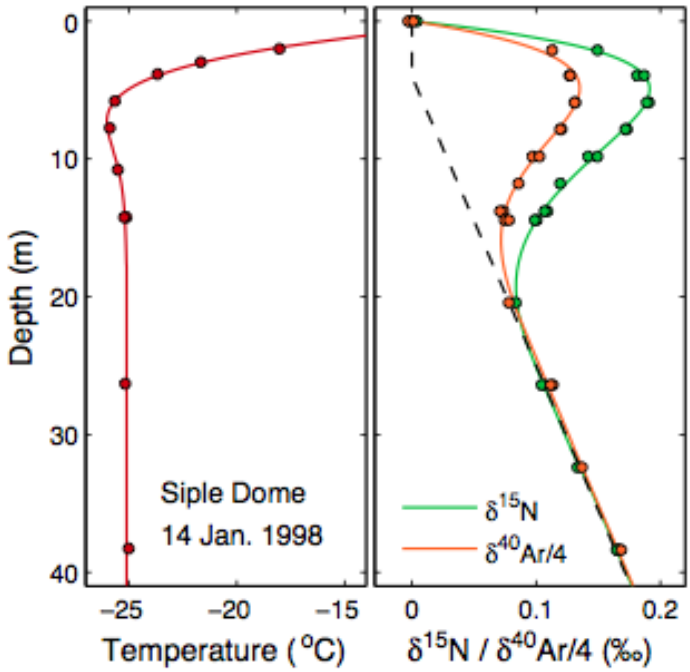

Figure 1.18 – Original figure 2.4 from Buizert (2011), using data from Severinghaus et al. (2001) and illustrating seasonal thermal fractionation in the upper layer of the firn. Indeed, in the shallow firn, large temperature gradients caused by the downward propagation of the seasonal surface temperature cycle, with a temperature minimum around 5 m depth here, lead to a local enrichment in heavy isotopes of N_2 and Ar. $\delta^{40}Ar$ is divided by 4 to display the gravitational enrichment in terms of unit of mass difference. Sampling was done in summer as the temperature is higher at the surface than in depth.

be expressed as (Severinghaus et al., 1998):

$$\delta_{therm} = ((\frac{T_t}{T_b})^{\alpha_T} - 1) \cong \alpha_T \cdot \frac{\Delta T}{T_b} \cong \Omega \Delta T, \tag{1.55}$$

where ΔT represents the temperature difference between the top (T_t) and the bottom (T_b) of the diffusive zone, α_T stands for the thermal diffusivity constant, Ω stands for the thermal diffusion sensitivity ($‰ \cdot K^{-1}$).

ΔT The influence of thermal diffusion can be corrected with isotope ratios of N_2 and Ar. The effect of gravitation can indeed be separated from thermal diffusion by using the thermal diffusion constants of considered gases (Severinghaus et al., 2001). These two effects can be quantified by N_2 and Ar isotope measurements on the same air sample. The gravitational signal of $\delta^{15}N$ and $^{40}Ar/4$ is identical, but their thermal diffusivities are different. Hence, the temperature gradient in the firn is proportional to:

$$\delta^{15}N_{excess} = \delta^{15}N - \delta^{40}Ar/4. \tag{1.56}$$

By measuring both parameters, $\delta^{15}N$ and $^{40}Ar/4$, on air extracted from Greenland ice

cores, the gradient of temperature in the firn can be estimated in the following way:

$$\Delta T = \frac{\delta^{15} N_{excess}}{(\alpha_{Ar} - 4 \cdot \alpha_N)} \tag{1.57}$$

To assess the magnitude of abrupt temperature changes at the surface, which are higher than ΔT, a firn model is needed to inverse the gradient of temperature ΔT, by accounting for the thickness and structure of the firn (Landais, 2004).

One prerequisite for applying Eq. 1.57 is the availability of accurate values for the thermal diffusion constants. This is the case since the thermal diffusion constants were precisely measured by Grachev and Severinghaus (2003b,a). In the laboratory, they experimentally determined the values of thermal diffusion constants of N_2 and Ar for temperatures spanning temperature gradients measured in the firn (−60 to −10 °C). For nitrogen ($^{15}N/^{14}N$) in atmospheric air:

$$\alpha_N \cdot 1000 = 8.656 - \frac{1232}{T_K}, \tag{1.58}$$

and for Argon ($^{40}Ar/^{36}Ar$) in atmospheric air:

$$\alpha_{Ar} \cdot 1000 = 26.08 - \frac{3952}{T_K}, \tag{1.59}$$

where T_K is the mean effective temperature defined as $T_K = T_1 \cdot T_2/(T_1 - T_2) \cdot ln(T_1/T_2)$, where T_1 is the warmest temperature of the gradient and T_2 the coldest.

1.4.1.3 Bubble close-off fractionation

Among the firn processes, bubble closure at the firn-ice transition is the least understood (e.g. Mitchell et al., 2015). It is however critical to understand its mechanism to correct for fractionation that occurs during air entrapment at the firn to ice transition, and correctly interpret ice core records of past atmosphere. Bubble close-off fractionation is for instance believed to play an important role in past $\delta O_2/N_2$ variations. Indeed, variations in the orbital scale of past atmospheric O_2 mixing ratio ($\delta O_2/N_2$) trapped in ice cores correlate strongly with local insolation changes (Bender, 2002; Kawamura et al., 2007; Suwa and Bender, 2008; Landais et al., 2012), and a suggested mechanism to explain this link is that changes in local summer insolation affect physical properties of the snow at the surface, properties which are maintained at the firn to ice transition and influence bubble close-off fractionation, hence $\delta O_2/N_2$ (Bender, 2002). In this section we describe the processes of bubble closure and air entrapment.

1.4.1.3.1 *Size dependent fractionation*

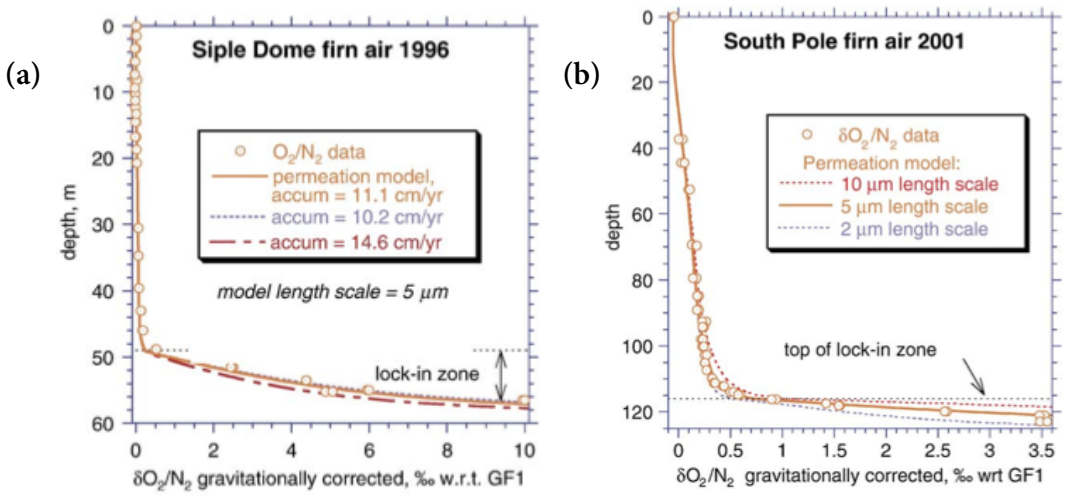

Figure 1.19 – **(a)** Original figure 4 from Severinghaus and Battle (2006). Firn $\delta O_2/N_2$ (gravitationally corrected) profile taken in 2001 at South Pole. By increasing the accumulation rate, the LIZ $\delta O_2/N_2$ enrichment obtained from the authors' permeation-related fractionation model becomes weaker. Indeed, with a higher accumulation rate, there is less time for the gas to escape, as the ice (and the advected air) moves faster in the LIZ, causing less enrichment in the LIZ. **(b)** Original figure 8 from Severinghaus and Battle (2006) Firn $\delta O_2/N_2$ (gravitationally corrected) profile taken in 1996 at Siple Dome. $\delta O_2/N_2$ was gravitationally corrected to isolate the close-off fractionation. These 2 figures show that the magnitude of $\delta O_2/N_2$ enrichment in the lock-in-depth caused by bubble close-off fractionation varies from site to site. The higher permeation of O_2 , 3 times higher than N_2 , causes a $\delta O_2/N_2$ enrichment in the lock-in-zone, confirming Ikeda-Fukazawa et al.'s prediction on selective permeability. Besides, one can see that the $\delta O_2/N_2$ enrichment is strongest in the LIZ, where gradual occlusion of bubble occurs. Finally, the gradient observed at the top of the lock-in-depth, in the diffusive column of the firn (on gravitationally corrected data) reveals an upward diffusive flux accross the lock-in depth (Severinghaus and Battle, 2006; Buizert, 2011): the O_2 loss to the atmosphere is balanced by a corresponding O_2 loss in bubble air, and provides thus a mean to estimate the isotope fractionation due to close-off fractionation.

SIZE-DEPENDENT A systematic elemental fractionation occurs within the lock-in-zone (Fig. 1.16), with small collision diameter gas molecules (Ne, O_2 , Ar) being preferentially excluded from the occluding bubbles during bubble close off, hence accumulating in the open firn pores (Severinghaus and Battle, 2006). Bubble closure occurs gradually and is strongly dependent on density (Schwander et al., 1993). Under the overlying pressure of the successive precipitation, closed bubbles are pressurized, which increases the gas partial pressure gradient between the bubbles and the open porosity. As a result, permeation occurs through the ice lattice, provided that the collision diameter

Table 1.6 – Mean annual temperature and ratio of enrichment R_{oe} of Ar and Ne (following notation of (Severinghaus and Battle, 2006) at different firn sites). Together with $\delta O_2/N_2$ measurements in the lock-in-zone (Sect. 4.6.3.3), these results suggest a temperature dependence of the fractionation process taking place during bubble occlusion (refer to text for details). Note that R_{oe}^{Ar} associated with gas loss handling and storage (usually in −25°C freezers) has a typical value of 0.5 ‰ · ‰$^{-1}$ (Bender et al., 1995).

Site	Mean annual temperature °C	R_{oe}^{Ar}, or Ar/N_2 /O_2 /N_2 ‰/‰	R_{oe}^{Ne}, or Ne/N_2 /O_2 /N_2 ‰/‰	R_{oe}^{Xe}, or Xe/N_2 /O_2 /N_2 ‰/‰	R_{oe}^{Kr}, or Kr/N_2 /O_2 /N_2 ‰/‰
South Pole	−51	0.15 ± 0.07^a	34 ± 1.5^a	0.08 ± 0.67^a	0.054 ± 0.081^a
Wais Divide	−31	0.27 ± 0.01^b	24.7 ± 0.4^b	0.16 ± 0.07^b	0.04 ± 0.03^b
Siple Dome	−25	0.33 ± 0.02^a			

[a] Severinghaus and Battle (2006)
[b] Battle et al. (2011)

of the molecules (c.f. 3.1) does not exceed 3.6 Å(Ikeda-Fukazawa et al., 2005), leading to an enrichment in O_2 , Ar, and other small species such as He or Ne within the lock-in-zone (e.g. Huber et al., 2006a; Severinghaus and Battle, 2006). The existence of a size-dependent fractionation process is corroborated by the fact that large molecules like N_2 , Kr or Xe are not escaping (or at a similar very low rate) from recently closed bubbles into open pores (e.g. Severinghaus and Battle, 2006; Battle et al., 2011). For instance, according to Ikeda-Fukazawa et al. (2005), the permeation rate of O_2 through the ice crystals is three times higher than the one of N_2 and has a value of $1.3 \cdot 10^{-20} mol \cdot m^{-1} \cdot s^{-1} \cdot Pa^{-1}$ at −25°C (Severinghaus and Battle, 2006).

Temperature dependence

Not only the magnitude of $\delta O_2/N_2$ depletion varies from site to site, but also the slopes of Ar/N_2 vs O_2 /N_2 and Ne/N_2 vs O_2 /N_2 ratios vary, probably due to a strong temperature dependence of the breaking of hydrogen bonds (Ikeda-Fukazawa et al., 2005; Battle et al., 2011). Large diameter molecules (but under 3.6 Å) like O_2 and Ar, in contrast with Ne (2.820 Å), are especially sensitive to temperature. (Severinghaus and Battle, 2006; Battle et al., 2011). Table 1.6 indicates the ratio of enrichment of various species vs. $\delta O_2/N_2$ within the lock-in-zone of 3 polar sites characterized by different mean annual temperature. The colder temperature at South Pole relative to WAIS-D (−51 vs. −31 °C) probably explains the higher ratio of enrichment R_{oe}^{Ne} (with a lower temperature, O_2 loss is reduced) and the slightly lower R_{oe}^{Ar} (larger in diameter, hence more dependent to the temperature-dependent mechanism, Ar loss is more reduced than O_2 loss at −51 °C). This is also consistent with the relatively large slope of R_{oe}^{Ar} at Siple Dome, but more measurements of Ar and Ne isotopes in the lock-in-zone are needed to confirm this hypothesis.

1.4.1.3.2 *Mass-dependent fractionation*

Recently, (Battle et al., 2011) found a mass-dependent enrichment of $\delta^{18}O$ within the lock-in-zone, in contradiction with a purely size-dependent permeation process.

They suggest that for gases with a collision diameter lower than 3.6 Å, permeation can occur through the ice lattice by breaking of hydrogen bonds (O_2 and Ar) (Ikeda-Fukazawa et al., 2004), but also via interstitial hopping, a velocity-dependent hence mass-dependent process, as suggested by Ikeda-Fukazawa et al. (2004) for Ne. Battle et al. (2011) suggest therefore that the depletion observed in $\delta^{18}O$ is due to permeation of O_2 through these two gas loss mechanisms.

1.4.1.3.3 *Depleted $\delta O_2/N_2$ in ice core samples*

This enrichment at the firn-ice transition is associated with a depletion in air bubbles entrapped in ice cores. Air in ice core bubbles is typically half as depleted in Ar/N_2 as in O_2/N_2 relative to atmospheric values (e.g. Battle et al., 1996; Sowers et al., 1992), and its O_2/N_2 ratio is typically around -4 to -10 ‰in well-preserved ice cores (Bender et al., 1995; Landais et al., 2010). It should be here emphasized that similar gas loss mechanisms as the one occurring at the firn-ice transition also cause size- and mass-dependent fractionation during coring and after coring (Sect. 4.6.4). Compelling evidences come from measurements of gases in ice cores (Ikeda-Fukazawa et al., 2005; Suwa and Bender, 2008; Bereiter et al., 2009; Vinther et al., 2009), showing in particular depleted $\delta O_2/N_2$ values (e.g. Bender et al., 1995; Suwa and Bender, 2008; Severinghaus et al., 2009; Landais et al., 2010). This can for instance result from long storage of ice in freezers at -25°C (Sect 4.6.4). Consequently, it is not possible to isolate the effects of air entrapment and bubble closure from coring and post-coring effects on the composition of gases trapped in ice core samples. Section 4.6.3.3 details the results of firn air sampling studies aiming at obtaining more direct information on fractionation during bubble close off, so as to precisely correct the composition of ancient air trapped in ice core bubbles from this effect.

1.4.1.3.4 *What factors influence close-off fractionation?*

The permeation of gases through the ice lattice at close-off depth can be seen as the combination of two gas-loss processes, permeation via breaking of hydrogen bonds, causing size-dependent fractionation, and permeation via interstitial hoping, causing mass-dependent fractionation. Large diameter molecules (but less than 3.6 Å) like Ar or O_2 permeate primarily through the first mechanism, which is strongly temperature-dependent as it is the hydrogen-bond breaking mechanism which limits the rate of diffusion, whereas small diameter molecules like Ne favor permeation via the second mechanism, only slightly affected by temperature.

The magnitude of the fractionation during bubble close-off is ultimately determined by the amount of gas loss across the lock-in depth (Buizert, pers. comm., 2016) (and not by the magnitude of the enrichment in the LIZ). For instance, if most of the fugitive O_2 were to escape from the LIZ to the diffusive zone (across the lock-in-depth) and then to the atmosphere, one would expect a relative small enrichment in the LIZ but a large depletion in the ice core samples. In Figure 1.19, the gravitationally cor-

rected $\delta O_2/N_2$ gradient observed in the diffusive zone reveals a diffusive flux from the deep firn to the atmosphere, which can be used to assess the average $\delta O_2/N_2$ depletion in ice core samples.

Accumulation rate also play an important role on the magnitude of close-off fractionation as it controls the amount of time an ice layer spends in the LIZ (air is advected with ice in the LIZ): in a site with a high accumulation rate, there is less time for the air to escape, hence a lower enrichment with depth in the LIZ (Fig. 1.19a), and a less depleted $\delta O_2/N_2$ in ice core bubbles.

Layering, that is cm-scale variations in density is an ubiquitous process in the firn whose origin is debated (refer to Mitchell et al., 2015 and references therein). It causes close-off fractionation to vary with depth, as revealed by high-resolution density of the LIZ together with CH_4 mixing ratio and total air content measurements of the LIZ closed porosity[11] at WAIS (Mitchell et al., 2015). An important implication for studies of trapped gases in ice cores (in particular for species with a short lifetime) is that the mean age of of gas samples from adjacent layers can vary by several years. For instance, quasi annual.scale variations observed in a continuous CH_4 record from a NEEM ice core (NEEM-2011-S1) are not of atmospheric origin but result from the stochastic nature of bubble close-off (Mitchell et al., 2015; Rhodes et al., 2013). This layering can also cause a scattering of $\delta O_2/N_2$ values in ice core bubbles.

Shallow and deep bubble close-off cause a highly contrasted $\delta O_2/N_2$ signature (Buizert, pers. comm., 2016), with a higher total air content when shallow trapping occurs (Mitchell et al., 2015). Bubbles/layers that close early/shallow in the LIZ are depleted in O_2 as O_2 escapes across the lock-in-depth, while bubbles/layers that close late/deep are enriched in O_2 as the O_2 permeate leaking out from occluding bubbles accumulates in the open porosity over time, and ultimately gets occluded in bubbles.

1.4.2 Fractionation due to clathrate hydrates

This process does not occur in the firn but deeper in the ice-sheet, but it can also be considered as a natural fractionating process. Fractionation due to clathrate hydrates is caused by the fact that O_2 is more easily dissolved in ice as gas hydrate than N_2 . In the transition zone of each ice core, extending over several hundred meters, for instance between 1000 m and 1700 m in GISP2 and between 800 m and 1000 m in Vostok (Suwa and Bender, 2008), highly positive values are observed. Because the dissociation pressure of O_2 (and Ar) is lower, it forms clathrate hydrates at a shallower depth than N_2 . There is thus more N_2 in the bubble air than O_2 within the transition zone, where both gas and solid phases coexist. After recovery of the ice, N_2 in buble air is preferentially lost relative to O_2 , because molecules in clathrate hydrates resist better post-coring fractionation (Suwa and Bender, 2008). Besides, gases exert a

[11] In the LIZ, the total porosity, the volume fraction not occupied by ice, is divided into open and closed porosity. Open pores can exchange with the atmosphere. Total porosity decreases with depth due to firn compaction, until all the air is occluded in bubbles

huge pressure on the ice, which becomes fractured during ice core recovery, and cause many fractures in the ice core samples (Kobashi et al., 2008; Bender et al., 1995).

1.5 Organization of the thesis

The work presented in this thesis focuses on the past evolution of stable isotopes of atmospheric oxygen. To unravel the climatic information they carry, the ancient atmospheric O_2 entrapped in polar ice core bubbles needs to be extracted, dried, purified, collected, measured and corrected. A new method of oxygen separation based on membrane technology was developed for the purpose of separating oxygen from all other air constituents such as N_2 and Ar, but proved not to be applicable for ${}^{17}\Delta_{atm}$ measurements (Chapter 2).

As an alternative, an analytical setup based on the classical method described in Barkan and Luz (2003) was build up from scratch. The developed setup and its associated analytical procedures (both for $\delta^{18}O_{atm}$ and ${}^{17}\Delta_{atm}$ measurements) are described in Chapter 3.

IRMS measurements of $\delta^{18}O_{atm}$ from air bubbles occluded in ice cores are the focus of Chapter 4. The chapter describes the automation of a sequence of up to ten ice core sample measurements with a Delta V mass spectrometer. It also focuses on the corrections applied to the raw data to retrieve the true climatic signal. The latter is indeed altered by processes in the firn, during coring and storage, and in the analytical setup. Finally, the ability of the analytical system to reproduce ice core $\delta^{18}O_{atm}$ measurements is assessed in this chapter based on 21 NEEM late Holocene ice core samples.

$\delta^{18}O_{atm}$ is a complex climatic proxy, involving global ice volume, the biosphere and the hydrosphere. Much work has already been devoted to orbital and millennial variation of $\delta^{18}O_{atm}$ (e.g. Landais et al., 2010; Severinghaus et al., 2009). Such a climatic proxy is indeed of great interest, as it is strongly influenced by low latitude climatic processes, and can therefore provide valuable information on the tropics, a region of the world which still lacks of climatic reconstructions and whose role is widely debated in the context of millennial-scale climate variations (e.g. reviews of Clement and Peterson, 2008; Seager and Battisti, 2007). Because of its global character, $\delta^{18}O_{atm}$ should provide added value compared to the different local records of hydrological cycle variations in different continental and marine archives. However, until now, no quantitative, robust interpretation of past variations in $\delta^{18}O_{atm}$ has been established, which limits the use of $\delta^{18}O_{atm}$ as a quantitative indicator for past biospheric production or variations of the hydrological cycle. The aim of the modeling study presented in Chapter 5 is thus to provide a quantitative interpretation for the systematic increase observed in $\delta^{18}O_{atm}$ over HSs. To reach this objective, we propose a global approach incorporating outputs from a water-isotope enabled general circulation model and focus on the millennial variability of the last glacial period. Following Hoffmann et al. (2004), we combine climatic parameters (temperature and humidity), isotopic com-

position of meteoric water, vegetation distribution and productivity simulated by different models with monthly mean temporal resolution. This work has been published in Climate of the Past in 2015 under the title *Quantifying molecular oxygen isotope variations during a Heinrich stadial* (Reutenauer et al., 2015) and is reproduced in Chapter 5.

Bibliography

Allison, G., Gat, J., and Leaney, F. (1985). The relationship between deuterium and oxygen-18 delta values in leaf water. *Chemical Geology: Isotope Geoscience section*, 58(1–2):145–156.

Amthor, J. S. (2012). *Respiration and crop productivity*. Springer Science & Business Media.

Angert, A., Barkan, E., Barnett, B., Brugnoli, E., Davidson, E. A., Fessenden, J., Maneepong, S., Panapitukkul, N., Randerson, J. T., Savage, K., Yakir, D., and Luz, B. (2003a). Contribution of soil respiration in tropical, temperate, and boreal forests to the ^{18}o enrichment of atmospheric o_2. *Global Biogeochemical Cycles*, 17(3):1089.

Angert, A., Luz, B., and Yakir, D. (2001). Fractionation of oxygen isotopes by respiration and diffusion in soils and its implications for the isotopic composition of atmospheric o2. *Global Biogeochemical Cycles*, 15(4):871–880.

Angert, A., Muhr, J., Negron Juarez, R., Alegria Munoz, W., Kraemer, G., Ramirez Santillan, J., Chambers, J. Q., and Trumbore, S. E. (2012). The contribution of respiration in tree stems to the dole effect. *Biogeosciences*, 9(10):4037–4044.

Angert, A., Rachmilevitch, S., Barkan, E., and Luz, B. (2003b). Effects of photorespiration, the cytochrome pathway, and the alternative pathway on the triple isotopic composition of atmospheric o2. *Global Biogeochemical Cycles*, 17(1):n/a–n/a. 1030.

Badger, M. R., von Caemmerer, S., Ruuska, S., and Nakano, H. (2000). Electron flow to oxygen in higher plants and algae: rates and control of direct photoreduction (mehler reaction) and rubisco oxygenase. *Philosophical Transactions of the Royal Society of London B: Biological Sciences*, 355(1402):1433–1446.

Bariac, T., Rambal, S., Jusserand, C., and Berger, A. (1989). Evaluating water fluxes of field-grown alfalfa from diurnal observations of natural isotope concentrations, energy budget and ecophysiological parameters. *Agricultural and Forest Meteorology*, 48(3–4):263–283.

Barkan, E. and Luz, B. (2003). High-precision measurements of 170/160 and 180/160 of o2 and o2/ar ratio in air. *Rapid Communications in Mass Spectrometry*, 17(24):2809–2814.

Barkan, E. and Luz, B. (2005). High precision measurements of 170/160 and 180/160 ratios in h20. *Rapid Communications in Mass Spectrometry*, 19(24):3737–3742.

Barkan, E. and Luz, B. (2007). Diffusivity fractionations of h2160-h2170 and h2160-h2180 in air and their implications for isotope hydrology. *Rapid Communications in Mass Spectrometry*, 21(18):2999–3005.

Barkan, E. and Luz, B. (2011). The relationships among the three stable isotopes of oxygen in air, seawater and marine photosynthesis. *Rapid Communications in Mass Spectrometry*, 25(16):2367–2369.

Barker, S., Diz, P., Vautravers, M. J., Pike, J., Knorr, G., Hall, I. R., and Broecker, W. S. (2009). Interhemispheric atlantic seesaw response during the last deglaciation. *Nature*, 457(7233):1097–1102.

Battle, M., Bender, M., Sowerst, T., Tansi, P., Butleri, J., Elkinsi, J., Ellis, J., Conwayt, T., Zhangt, N., Langt, P., et al. (1996). Atmospheric gas concentrations over the past century measured in air from firn at the south pole. *Nature*, 383:19.

Battle, M. O., Severinghaus, J. P., Sofen, E. D., Plotkin, D., Orsi, A. J., Aydin, M., Montzka, S. A., Sowers, T., and Tans, P. P. (2011). Controls on the movement and composition of firn air at the west antarctic ice sheet divide. *Atmospheric Chemistry and Physics*, 11(21):11007–11021.

Bazin, L., Landais, A., Capron, E., Masson-Delmotte, V., Ritz, C., Picard, G., Jouzel, J., Dumont, M., Leuenberger, M., and Prié, F. (2016). Phase relationships between orbital forcing and the composition of air trapped in antarctic ice cores. *Climate of the Past*, 12(3):729–748.

Bazin, L., Landais, A., Lemieux-Dudon, B., Kele, H. T. M., Veres, D., Parrenin, F., Martinerie, P., Ritz, C., Capron, E., Lipenkov, V., Loutre, M.-F., Raynaud, D., Vinther, B., Svensson, A., Rasmussen, S. O., Severi, M., Blunier, T., Leuenberger, M., Fischer, H., Masson-Delmotte, V., Chappellaz, J., and Wolff, E. (2013). An optimized multi-proxy, multi-site antarctic ice and gas orbital chronology (aicc2012): 120-800 ka. *Climate of the Past*, 9(4):1715–1731.

Bender, M. (2003). Climate-biosphere interactions on glacial-interglacial timescales. *Global Biogeochemical Cycles*, 17(3):n/a–n/a. 1082.

Bender, M., Labeyrie, L., Raynaud, D., and Lorius, C. (1985). Isotopic composition of atmospheric o2 in ice linked with deglaciation and global primary productivity. *Nature*, 318(6044):349–352.

Bender, M., Sowers, T., and Labeyrie, L. (1994). The dole effect and its variations during the last 130,000 years as measured in the vostok ice core. *Global Biogeochemical Cycles*, 8(3):363–376.

Bender, M., Sowers, T., and Lipenkov, V. (1995). On the concentrations of o2, n2, and ar in trapped gases from ice cores. *Journal of Geophysical Research: Atmospheres*, 100(D9):18651–18660.

Bender, M. L. (1990). The d18o of dissolved o2 in seawater: A unique tracer of circulation and respiration in the deep sea. *Journal of Geophysical Research: Oceans*, 95(C12):22243–22252.

Bender, M. L. (2002). Orbital tuning chronology for the vostok climate record supported by trapped gas composition. *Earth and Planetary Science Letters*, 204(1):275–289.

Benson, B. B. and Krause, D. (1984). The concentration and isotopic fractionation of oxygen dissolved in freshwater and seawater in equilibrium with the atmosphere1. *Limnology and Oceanography*, 29(3):620–632.

Bereiter, B., Schwander, J., Lüthi, D., and Stocker, T. F. (2009). Change in co2 concentration and o2/n2 ratio in ice cores due to molecular diffusion. *Geophysical Research Letters*, 36(5):n/a–n/a. L05703.

Bintanja, R., van de Wal, R. S., and Oerlemans, J. (2005). Modelled atmospheric temperatures and global sea levels over the past million years. *Nature*, 437(7055):125–128.

Blunier, T., Barnett, B., Bender, M. L., and Hendricks, M. B. (2002). Biological oxygen productivity during the last 60,000 years from triple oxygen isotope measurements. *Global Biogeochemical Cycles*, 16(3):3–1–3–13.

Blunier, T., Bender, M. L., Barnett, B., and von Fischer, J. C. (2012). Planetary fertility during the past 400 ka based on the triple isotope composition of o_2 in trapped gases from the vostok ice core. *Climate of the Past*, 8(5):1509–1526.

Boering, K. A., Jackson, T., Hoag, K. J., Cole, A. S., Perri, M. J., Thiemens, M., and Atlas, E. (2004). Observations of the anomalous oxygen isotopic composition of carbon dioxide in the lower stratosphere and the flux of the anomaly to the troposphere. *Geophysical Research Letters*, 31(3):n/a–n/a. L03109.

Bond, G., Broecker, W., Johnsen, S., McManus, J., Labeyrie, L., Jouzel, J., and Bonani, G. (1993). Correlations between climate records from north atlantic sediments and greenland ice. *Nature*, 365(6442):143–147.

Bowes, G. and Ogren, W. L. (1972). Oxygen inhibition and other properties of soybean ribulose 1,5-diphosphate carboxylase. *Journal of Biological Chemistry*, 247(7):2171–2176.

Braconnot, P. and Marti, O. (2003). Impact of precession on monsoon characteristics from coupled ocean atmosphere experiments: changes in indian monsoon and indian ocean climatology. *Marine Geology*, 201(1–3):23 – 34. Asian Monsoons and Global Linkages on Milankovitch and Sub-Milankovitch Time Scales.

Broecker, W. (2000). Abrupt climate change: causal constraints provided by the paleoclimate record. *Earth–Science Reviews*, 51(1–4):137–154.

Buizert, C. (2011). *The influence of firn air transport processes and radiocarbon production on gas records from polar firn and ice*. PhD thesis, Københavns Universitet'Københavns Universitet', Det Natur-og Biovidenskabelige FakultetFaculty of

Science, Niels Bohr InstitutetThe Niels Bohr Institute, Niels Bohr Institutet, Is og klimaThe Niels Bohr Institute, Ice and Climate.

Cappa, C. D., Hendricks, M. B., DePaolo, D. J., and Cohen, R. C. (2003). Isotopic fractionation of water during evaporation. *Journal of Geophysical Research: Atmospheres*, 108(D16):4525.

Capron, E., Landais, A., Lemieux-Dudon, B., Schilt, A., Loulergue, L., Buiron, B., Chappellaz, J., Masson-Delmotte, V., Dahl-Jensen, D., Johnsen, S., et al. (2008). Construction of a common timescale between northgrip and edml ice cores using 18o of atmospheric oxygen (18oatm) and ch4 measurements over mis 5 (80-123 ka). *Quaternary Science Reviews*.

Capron, E., Landais, A., Lemieux-Dudon, B., Schilt, A., Masson-Delmotte, V., Buiron, D., Chappellaz, J., Dahl-Jensen, D., Johnsen, S., Leuenberger, M., Loulergue, L., and Oerter, H. (2010). Synchronising {EDML} and northgrip ice cores using d18o of atmospheric oxygen (d18oatm) and {CH4} measurements over {MIS5} (80⊠123 kyr). *Quaternary Science Reviews*, 29(1–2):222 – 234. Climate of the Last Million Years: New Insights from {EPICA} and Other Records.

Cernusak, L. A., Farquhar, G. D., Wong, S. C., and Stuart-Williams, H. (2004). Measurement and interpretation of the oxygen isotope composition of carbon dioxide respired by leaves in the dark. *Plant Physiology*, 136(2):3350–3363.

Chappellaz, J., Stowasser, C., Blunier, T., Baslev-Clausen, D., Brook, E. J., Dallmayr, R., Faïn, X., Lee, J. E., Mitchell, L. E., Pascual, O., Romanini, D., Rosen, J., and Schüpbach, S. (2013). High-resolution glacial and deglacial record of atmospheric methane by continuous-flow and laser spectrometer analysis along the neem ice core. *Climate of the Past*, 9(6):2579–2593.

Cheng, H., Sinha, A., Wang, X., Cruz, F. W., and Edwards, R. L. (2012). The global paleomonsoon as seen through speleothem records from asia and the americas. *Climate Dynamics*, 39(5):1045–1062.

Clemens, S. C., Prell, W. L., and Sun, Y. (2010). Orbital-scale timing and mechanisms driving late pleistocene indo-asian summer monsoons: Reinterpreting cave speleothem d18o. *Paleoceanography*, 25(4):n/a–n/a. PA4207.

Clement, A. C. and Peterson, L. C. (2008). Mechanisms of abrupt climate change of the last glacial period. *Reviews of Geophysics*, 46(4). RG4002.

Coplen, T. B. (2011). Guidelines and recommended terms for expression of stable-isotope-ratio and gas-ratio measurement results. *Rapid Communications in Mass Spectrometry*, 25(17):2538–2560.

Cowan, I. (1977). Stomatal behaviour and environment. *Adv. Bot. Res.*, 4:117–128.

Cowan, I. and Farquhar, G. (1977). Integration of activity in the higher plant. *Stomatal function in relation to leaf metabolism and environment, Cambridge Univ Press, Cambridge*, pages 471–505.

Craig, H. and Gordon, L. (1965). Deuterium and oxygen 18 variations in the ocean and the marine atmosphere. In *Stable Isotopes in Oceanographic Studies and Paleotemperatures, July 26-30 1965, Spoleto, Italy*. Tongiorgi, E.

Craig, H., Horibe, Y., and Sowers, T. (1988). Gravitational separation of gases and isotopes in polar ice caps. *Science*, 242(4886):1675–1678.

Cruz, F., Burns, S., Karmann, I., Sharp, W., Vuille, M., Cardoso, A., Ferrari, J., Dias, P., and Viana, O. (2005). Insolation-driven changes in atmospheric circulation over the past 116,000 years in subtropical brazil. *Nature*, 434(7029):63–66.

Dällenbach, A., Blunier, T., Flückiger, J., Stauffer, B., Chappellaz, J., and Raynaud, D. (2000). Changes in the atmospheric ch4 gradient between greenland and antarctica during the last glacial and the transition to the holocene. *Geophysical Research Letters*, 27(7):1005–1008.

Dayem, K. E., Molnar, P., Battisti, D. S., and Roe, G. H. (2010). Lessons learned from oxygen isotopes in modern precipitation applied to interpretation of speleothem records of paleoclimate from eastern asia. *Earth and Planetary Science Letters*, 295(1–2):219 – 230.

de Noblet, N. I., Prentice, I. C., Joussaume, S., Texier, D., Botta, A., and Haxeltine, A. (1996). Possible role of atmosphere-biosphere interactions in triggering the last glaciation. *Geophysical Research Letters*, 23(22):3191–3194.

Dole, M. (1935). The relative atomic weight of oxygen in water and in air. *Journal of the American Chemical Society*, 57(12):2731–2731.

Dole, M. (1965). The natural history of oxygen. *The Journal of General Physiology*, 49(1):5–27.

Dole, M. and Jenks, G. (1944). Isotopic composition of photosynthetic oxygen. *Science*, 100(2601):409–409.

Dole, M., Lane, G., Rudd, D., and Zaukelies, D. (1954). Isotopic composition of atmospheric oxygen and nitrogen. *Geochimica et Cosmochimica Acta*, 6(2):65–78.

Dongmann, G. (1974). The contribution of land photosynthesis to the stationary enrichment of ^{18}o in the atmosphere. *Radiation and Environmental Biophysics*, 11(3):219–225.

Dongmann, G., Forstel, H., and Wagener, K. (1972). O-18 rich oxygen from land photosynthesis. *Nature-New Biology*, 240(99):127–&.

Dreyfus, G., Raisbeck, G., Parrenin, F., Jouzel, J., Guyodo, Y., Nomade, S., and Mazaud, A. (2008). An ice core perspective on the age of the matuyama⊠brunhes boundary. *Earth and Planetary Science Letters*, 274(1–2):151–156.

Dreyfus, G. B., Parrenin, F., Lemieux-Dudon, B., Durand, G., Masson-Delmotte, V., Jouzel, J., Barnola, J.-M., Panno, L., Spahni, R., Tisserand, A., Siegenthaler, U., and Leuenberger, M. (2007). Anomalous flow below 2700 m in the epica dome c ice core detected using δ^{18}o of atmospheric oxygen measurements. *Climate of the Past*, 3(2):341–353.

Eisenstadt, D., Barkan, E., Luz, B., and Kaplan, A. (2010). Enrichment of oxygen heavy isotopes during photosynthesis in phytoplankton. *Photosynthesis Research*, 103(2):97–103.

Elliot, M., Labeyrie, L., and Duplessy, J.-C. (2002). Changes in north atlantic deep-water formation associated with the dansgaard-oeschger temperature oscillations (60-10 ka). *Quaternary Science Reviews*, 21(10):1153 – 1165.

EPICA community members (2004). Eight glacial cycles from an Antarctic ice core. *Nature*, 429(6992):623–628.

EPICA Community Members (2006). One-to-one coupling of glacial climate variability in Greenland and Antarctica. *Nature*, 444(7116):195–198.

Farquhar, G., von Caemmerer, S. v., and Berry, J. (1980). A biochemical model of photosynthetic co2 assimilation in leaves of c3 species. *Planta*, 149(1):78–90.

Farquhar, G. D., Cernusak, L. A., and Barnes, B. (2007). Heavy water fractionation during transpiration. *Plant Physiology*, 143(1):11–18.

Farquhar, G. D., Ehleringer, J. R., , and T., H. K. (1989). Carbon isotope discrimination and photosynthesis. *Annual Review of Plant Physiology and Plant Molecular Biology*, 40(1):503–537.

Farquhar, G. D. and Lloyd, J. (1993). Carbon and oxygen isotope effects in the exchange of carbon dioxide between terrestrial plants and the atmosphere. In Farquhar, G. D., Ehleringer, J. R., and Hall, A. E., editors, *Stable Isotopes and Plant Carbon-water Relations*, pages 47–70. Academic Press, San Diego.

Farquhar, G. D., Lloyd, J., Taylor, J. A., Flanagan, L. B., Syvertsen, J. P., Hubick, K. T., Wong, S. C., and Ehleringer, J. R. (1993). Vegetation effects on the isotope composition of oxygen in atmospheric co2. *Nature*, 363(6428):439–443.

Farquhar, G. D., O'Leary, M. H., and Berry, J. A. (1982). On the relationship between carbon isotope discrimination and the intercellular carbon dioxide concentration in leaves. *Functional Plant Biology*, 9(2):121–137.

Flanagan, L. B., Phillips, S. L., Ehleringer, J. R., Lloyd, J., and Farquhar, G. D. (1994). Effect of changes in leaf water oxygen isotopic composition on discrimination against c180160 during photosynthetic gas exchange. *Functional Plant Biology*, 21(2):221–234.

Fleitmann, D., Cheng, H., Badertscher, S., Edwards, R. L., Mudelsee, M., Gktürk, O. M., Fankhauser, A., Pickering, R., Raible, C. C., Matter, A., Kramers, J., and Tüysüz, O. (2009). Timing and climatic impact of greenland interstadials recorded in stalagmites from northern turkey. *Geophysical Research Letters*, 36(19). L19707.

Flückiger, J., Dällenbach, A., Blunier, T., Stauffer, B., Stocker, T. F., Raynaud, D., and Barnola, J.-M. (1999). Variations in atmospheric n20 concentration during abrupt climatic changes. *Science*, 285(5425):227–230.

Francey, R. J. and Tans, P. P. (1987). Latitudinal variation in oxygen-18 of atmospheric co2.

Gamo, T., Tsutsumi, M., Sakai, H., Nakazawa, T., Tanaka, M., Honda, H., Kubo, H., and Itoh, T. (1989). Carbon and oxygen isotopic ratios of carbon dioxide of a stratospheric profile over japan. *Tellus B*, 41B(2):127–133.

Gillon, J. and Yakir, D. (2001). Influence of carbonic anhydrase activity in terrestrial vegetation on the 180 content of atmospheric co2. *Science*, 291(5513):2584–2587.

Gonfiantini, R. (1965). Some results on oxygen isotope stratigraphy in the deep drilling at king baudouin station, antarctica. *Journal of Geophysical Research*, 70(8):1815–1819.

Goujon, C., Barnola, J.-M., and Ritz, C. (2003). Modeling the densification of polar firn including heat diffusion: Application to close-off characteristics and gas isotopic fractionation for antarctica and greenland sites. *Journal of Geophysical Research: Atmospheres*, 108(D24):n/a–n/a. 4792.

Grachev, A. M. and Severinghaus, J. P. (2003a). Determining the thermal diffusion factor for 40ar/36ar in air to aid paleoreconstruction of abrupt climate change. *The Journal of Physical Chemistry A*, 107(23):4636–4642.

Grachev, A. M. and Severinghaus, J. P. (2003b). Laboratory determination of thermal diffusion constants for 29 n 2/28 n 2 in air at temperatures from- 60 to 0 c for reconstruction of magnitudes of abrupt climate changes using the ice core fossil–air paleothermometer. *Geochimica et Cosmochimica Acta*, 67(3):345–360.

Grinsted, A., Moore, J. C., and Jevrejeva, S. (2004). Application of the cross wavelet transform and wavelet coherence to geophysical time series. *Nonlinear processes in geophysics*, 11(5–6):561–566.

Grousset, F., Labeyrie, L., Sinko, J., Cremer, M., Bond, G., Duprat, J., Cortijo, E., and Huon, S. (1993). Patterns of ice-rafted detritus in the glacial north atlantic (40–55 n). *Paleoceanography*, 8(2):175–192.

Guillevic, M., Bazin, L., Landais, A., Stowasser, C., Masson-Delmotte, V., Blunier, T., Eynaud, F., Falourd, S., Michel, E., Minster, B., Popp, T., Prie, F., and Vinther, B. M. (2014). Multi-proxy fingerprint of heinrich event 4 in greenland ice core records. *Climate of the Past Discussions*, 10(2):1179–1222.

Guy, R., Berry, J., Fogel, M., Turpin, D., and Weger, H. (1992). Fractionation of the stable isotopes of oxygen during respiration by plants-the basis of a new technique to estimate partitioning to the alternative path. *Molecular, Biochemical, and Physiological Aspects of Plant Respiration*, pages 443–453.

Guy, R. D., Berry, J. A., Fogel, M. L., and Hoering, T. C. (1989). Differential fractionation of oxygen isotopes by cyanide-resistant and cyanide-sensitive respiration in plants. *Planta*, 177(4):483–491.

Guy, R. D., Fogel, M. L., and Berry, J. A. (1993). Photosynthetic fractionation of the stable isotopes of oxygen and carbon. *Plant Physiology*, 101(1):37–47.

Heinrich, H. (1988). Origin and consequences of cyclic ice rafting in the northeast Atlantic Ocean during the past 130,000 years. *Quaternary Research*, 29:142–152.

Helliker, B. R. and Ehleringer, J. R. (2002). Differential 18o enrichment of leaf cellulose in c3 versus c4 grasses. *Functional Plant Biology*, 29(4):435–442.

Helman, Y., Barkan, E., Eisenstadt, D., Luz, B., and Kaplan, A. (2005). Fractionation of the three stable oxygen isotopes by oxygen-producing and oxygen-consuming reactions in photosynthetic organisms. *Plant Physiology*, 138(4):2292–2298.

Hemming, S. R. (2004). Heinrich events: Massive late pleistocene detritus layers of the north atlantic and their global climate imprint. *Reviews of Geophysics*, 42:RG1005, doi:10.1029/2003RG000128.

Hendricks, M. B., Bender, M. L., and Barnett, B. A. (2004). Net and gross o2 production in the southern ocean from measurements of biological o2 saturation and its triple isotope composition. *Deep Sea Research Part I: Oceanographic Research Papers*, 51(11):1541 – 1561.

Hoffmann, G., Cuntz, M., Weber, C., Ciais, P., Friedlingstein, P., Heimann, M., Jouzel, J., Kaduk, J., Maier-Reimer, E., Seibt, U., and Six, K. (2004). A model of the earth's dole effect. *Global Biogeochemical Cycles*, 18(1). GB1008.

Horita, J. and Wesolowski, D. J. (1994). Liquid-vapor fractionation of oxygen and hydrogen isotopes of water from the freezing to the critical temperature. *Geochimica et Cosmochimica Acta*, 58(16):3425–3437.

Huber, C., Beyerle, U., Leuenberger, M., Schwander, J., Kipfer, R., Spahni, R., Severinghaus, J., and Weiler, K. (2006a). Evidence for molecular size dependent gas fractionation in firn air derived from noble gases, oxygen, and nitrogen measurements. *Earth and Planetary Science Letters*, 243(1–2):61–73.

Huber, C., Leuenberger, M., Spahni, R., Flückiger, J., Schwander, J., Stocker, T., Johnsen, S., Landais, A., and Jouzel, J. (2006b). Isotope calibrated Greenland temperature record over Marine Isotope Stage 3 and its relation to CH4. *Earth and Planetary Science Letters*, 243(3–4):504–519.

Hulston, J. R. and Thode, H. G. (1965). Variations in the s33, s34, and s36 contents of meteorites and their relation to chemical and nuclear effects. *Journal of Geophysical Research*, 70(14):3475–3484.

Ikeda-Fukazawa, T., Fukumizu, K., Kawamura, K., Aoki, S., Nakazawa, T., and Hondoh, T. (2005). Effects of molecular diffusion on trapped gas composition in polar ice cores. *Earth and Planetary Science Letters*, 229(3–4):183 – 192.

Ikeda-Fukazawa, T., Kawamura, K., and Hondoh, T. (2004). Mechanism of molecular diffusion in ice crystals. *Molecular Simulation*, 30(13–15):973–979.

Imbrie, J., Hays, J. D., Martinson, D. G., McIntyre, A., Mix, A. C., Morley, J. J., Pisias, N. G., Prell, W. L., and Shackleton, N. J. (1984). The orbital theory of pleistocene climate: Support from a revised chronology of the marine delta18 o record. In *Milankovitch and climate: Understanding the response to astronomical forcing*, volume 1, page 269.

Johnson, K. R., Hu, C., Belshaw, N. S., and Henderson, G. M. (2006). Seasonal trace-element and stable-isotope variations in a chinese speleothem: The potential for high-resolution paleomonsoon reconstruction. *Earth and Planetary Science Letters*, 244(1–2):394–407.

Jouzel, J., Barkov, N., Barnola, J., Bender, M., Chappellaz, J., Genthon, C., Kotlyakov, V., Lipenkov, V., Lorius, C., Petit, J., Raynaud, D., Raisbeck, G., Ritz, C., Sowers, T., Stievenard, M., Yiou, F., and Yiou, P. (1993). Extending the vostok ice-core record of palaeoclimate to the penultimate glacial period. *Nature*, 364(6436):407–412.

Jouzel, J., Masson-Delmotte, V., Cattani, O., Dreyfus, G., Falourd, S., Hoffmann, G., Minster, B., Nouet, J., Barnola, J. M., Chappellaz, J., Fischer, H., Gallet, J. C., Johnsen, S., Leuenberger, M., Loulergue, L., Luethi, D., Oerter, H., Parrenin, F., Raisbeck, G., Raynaud, D., Schilt, A., Schwander, J., Selmo, E., Souchez, R., Spahni, R., Stauffer, B., Steffensen, J. P., Stenni, B., Stocker, T. F., Tison, J. L., Werner, M., and Wolff, E. W. (2007). Orbital and millennial antarctic climate variability over the past 800,000 years. *Science*, 317(5839):793–796.

Jouzel, J., Waelbroeck, C., Malaize, B., Bender, M., Petit, J., Stievenard, M., Barkov, N., Barnola, J., King, T., Kotlyakov, V., Lipenkov, V., Lorius, C., Raynaud, D., Ritz, C., and Sowers, T. (1996). Climatic interpretation of the recently extended vostok ice records. *Climate Dynamics*, 12(8):513–521.

Kaiser, J. (2008). Reformulated 17o correction of mass spectrometric stable isotope measurements in carbon dioxide and a critical appraisal of historic absolute carbon and oxygen isotope ratios. *Geochimica et Cosmochimica Acta*, 72(5):1312–1334.

Kaiser, J., R⊠ckmann, T., and Brenninkmeijer, C. A. M. (2004). Contribution of mass-dependent fractionation to the oxygen isotope anomaly of atmospheric nitrous oxide. *Journal of Geophysical Research: Atmospheres*, 109(D3):n/a–n/a. D03305.

Kanner, L. C., Burns, S. J., Cheng, H., and Edwards, R. L. (2012). High-latitude forcing of the south american summer monsoon during the last glacial. *Science*, 335(6068):570–573.

Kawamura, K., Parrenin, F., Lisiecki, L., Uemura, R., Vimeux, F., Severinghaus, J. P., Hutterli, M. A., Nakazawa, T., Aoki, S., Jouzel, J., Raymo, M. E., Matsumoto, K., Nakata, H., Motoyama, H., Fujita, S., Goto-Azuma, K., Fujii, Y., and Watanabe, O. (2007). Northern hemisphere forcing of climatic cycles in antarctica over the past 360,000 years. *Nature*, 448(7156):912–U4.

Kawamura, K., Severinghaus, J. P., Ishidoya, S., Sugawara, S., Hashida, G., Motoyama, H., Fujii, Y., Aoki, S., and Nakazawa, T. (2006). Convective mixing of air in firn at four polar sites. *Earth and Planetary Science Letters*, 244(3–4):672 – 682.

Keeling, R. F. (1988). *Development of an interferometric oxygen analyzer for precise measurement of the atmospheric O2 mole fraction*. PhD thesis, Harvard University.

Keeling, R. F. (1995). The atmospheric oxygen cycle: The oxygen isotopes of atmospheric co2 and o2 and the o2/n2 ratio. *Reviews of Geophysics*, 33(S2):1253–1262.

Keeling, R. F. and Shertz, S. R. (1992). Seasonal and interannual variations in atmospheric oxygen and implications for the global carbon cycle. *Nature*, 358(6389):723–727.

Khodri, M., Leclainche, Y., Ramstein, G., Braconnot, P., Marti, O., and Cortijo, E. (2001). Simulating the amplification of orbital forcing by ocean feedbacks in the last glaciation. *Nature*, 410(6828):570–574.

Kiddon, J., Bender, M. L., Orchardo, J., Caron, D. A., Goldman, J. C., and Dennett, M. (1993). Isotopic fractionation of oxygen by respiring marine organisms. *Global Biogeochemical Cycles*, 7(3):679–694.

Kindler, P., Guillevic, M., Baumgartner, M., Schwander, J., Landais, A., and Leuenberger, M. (2014). Temperature reconstruction from 10 to 120 kyr b2k from the ngrip ice core. *Climate of the Past*, 10(2):887–902.

Kobashi, T., Severinghaus, J. P., and Kawamura, K. (2008). Argon and nitrogen isotopes of trapped air in the {GISP2} ice core during the holocene epoch (0⊠11,500 b.p.): Methodology and implications for gas loss processes. *Geochimica et Cosmochimica Acta*, 72(19):4675 – 4686.

Kroopnick, P. and Craig, H. (1976). Oxygen isotope fractionation in dissolved oxygen in the deep sea. *Earth and Planetary Science Letters*, 32(2):375 – 388.

Laisk, A. and Oja, V. (1998). *Dynamics of leaf photosynthesis: rapid-response measurements and their interpretations*. Number 1. Csiro Publishing.

Laisk, A. K. (1977). Kinetics of photosynthesis and photorespiration of c3 in plants.

Lambeck, K., Esat, T. M., and Potter, E.-K. (2002). Links between climate and sea levels for the past three million years. *Nature*, 419(6903):199–206.

Lammerzahl, P., R⊠ckmann, T., Brenninkmeijer, C. A. M., Krankowsky, D., and Mauersberger, K. (2002). Oxygen isotope composition of stratospheric carbon dioxide. *Geophysical Research Letters*, 29(12):23–1–23–4.

Landais, A. (2004). *Variabilité climatique rapide en Atlantique Nord: l'apport des isotopes de l'air piégé dans la glace du Groenland*. PhD thesis, Université Pierre et Marie Curie-Paris VI.

Landais, A., Barkan, E., and Luz, B. (2008). Record of d180 and 170-excess in ice from vostok antarctica during the last 150,000 years. *Geophysical Research Letters*, 35(2):n/a–n/a. L02709.

Landais, A., Barkan, E., Yakir, D., and Luz, B. (2006a). The triple isotopic composition of oxygen in leaf water. *Geochimica et Cosmochimica Acta*, 70(16):4105 – 4115.

Landais, A., Barnola, J.-M., Kawamura, K., Caillon, N., Delmotte, M., Van Ommen, T., Dreyfus, G., Jouzel, J., Masson-Delmotte, V., Minster, B., et al. (2006b). Firn-air $\delta 15n$ in modern polar sites and glacial–interglacial ice: a model-data mismatch during glacial periods in antarctica? *Quaternary science reviews*, 25(1):49–62.

Landais, A., Barnola, J. M., Masson-Delmotte, V., Jouzel, J., Chappellaz, J., Caillon, N., Huber, C., Leuenberger, M., and Johnsen, S. J. (2004a). A continuous record of temperature evolution over a sequence of dansgaard-oeschger events during marine isotopic stage 4 (76 to 62 kyr bp). *Geophysical Research Letters*, 31(22):n/a–n/a. L22211.

Landais, A., Caillon, N., Goujon, C., Grachev, A., Barnola, J., Chappellaz, J., Jouzel, J., Masson-Delmotte, V., and Leuenberger, M. (2004b). Quantification of rapid temperature change during {DO} event 12 and phasing with methane inferred from air isotopic measurements. *Earth and Planetary Science Letters*, 225(1–2):221 – 232.

Landais, A., Dreyfus, G., Capron, E., Jouzel, J., Masson-Delmotte, V., Roche, D., Prié, F., Caillon, N., Chappellaz, J., Leuenberger, M., et al. (2013). Two-phase change in co2, antarctic temperature and global climate during termination ii. *Nature Geoscience*, 6(12):1062–1065.

Landais, A., Dreyfus, G., Capron, E., Masson-Delmotte, V., ni, M. S.-G., Desprat, S., Hoffmann, G., Jouzel, J., Leuenberger, M., and Johnsen, S. (2010). What drives the millennial and orbital variations of $\delta^{18}o_{atm}$? *Quaternary Science Reviews*, 29(1–2):235 – 246.

Landais, A., Dreyfus, G., Capron, E., Pol, K., Loutre, M. F., Raynaud, D., Lipenkov, V. Y., Arnaud, L., Masson-Delmotte, V., Paillard, D., Jouzel, J., and Leuenberger, M. (2012). Towards orbital dating of the epica dome c ice core using delta o_2/n_2. *Climate of the Past*, 8(1):191–203.

Landais, A., Lathiere, J., Barkan, E., and Luz, B. (2007a). Reconsidering the change in global biosphere productivity between the last glacial maximum and present day from the triple oxygen isotopic composition of air trapped in ice cores. *Global Biogeochemical Cycles*, 21(1):n/a–n/a. GB1025.

Landais, A., Masson-Delmotte, V., Jouzel, J., Raynaud, D., Johnsen, S., Huber, C., Leuenberger, M., Schwander, J., and Minster, B. (2006c). The glacial inception as recorded in the northgrip greenland ice core: timing, structure and associated abrupt temperature changes. *Climate Dynamics*, 26(2–3):273–284.

Landais, A., Masson-Delmotte, V., Nebout, N. C., Jouzel, J., Blunier, T., Leuenberger, M., Dahl-Jensen, D., and Johnsen, S. (2007b). Millenial scale variations of the isotopic composition of atmospheric oxygen over marine isotopic stage 4. *Earth and Planetary Science Letters*, 258(1–2):101 – 113.

Landais, A., Masson-Delmotte, V., Stenni, B., Selmo, E., Roche, D., Jouzel, J., Lambert, F., Guillevic, M., Bazin, L., Arzel, O., Vinther, B., Gkinis, V., and Popp, T. (2015). A review of the bipolar see–saw from synchronized and high resolution ice core water stable isotope records from greenland and east antarctica. *Quaternary Science Reviews*, 114:18–32.

Lane, G. A. and Dole, M. (1956). Fractionation of oxygen isotopes during respiration. *Science*, 123(3197):574–576.

Laskar, J., Robutel, P., Joutel, F., Gastineau, M., Correia, A., and Levrard, B. (2004). A long-term numerical solution for the insolation quantities of the earth. *Astronomy Astrophysics*, 428(1):261–285.

Lennard-Jones, J. E. (1931). Cohesion. *Proceedings of the Physical Society*, 43(5):461.

Levine, N. M., Bender, M. L., and Doney, S. C. (2009). The d180 of dissolved o2 as a tracer of mixing and respiration in the mesopelagic ocean. *Global Biogeochemical Cycles*, 23(1):n/a–n/a. GB1006.

Li, W. and Meijer, H. (1999). The use of electrolysis for accurate delta o-17 and delta o-18 isotope measurements in water (vol 34, pg 349, 1998). *Isotopes in Environmental and Health Studies*, 35(1–2).

Lisiecki, L. E. and Raymo, M. E. (2005). A pliocene-pleistocene stack of 57 globally distributed benthic δ180 records. *Paleoceanography*, 20(1).

Lloyd, J. and Farquhar, G. (1994). 13c discrimination during co2 assimilation by the terrestrial biosphere. *Oecologia*, 99(3–4):201–215.

Loulergue, L., Schilt, A., Spahni, R., Masson-Delmotte, V., Blunier, T., Lemieux, B., Barnola, J.-M., Raynaud, D., Stocker, T. F., and Chappellaz, J. (2008). Orbital and millennial-scale features of atmospheric ch4 over the past 800,000 years. *Nature*, 453(7193):383–386.

Lüthi, D., Le Floch, M., Bereiter, B., Blunier, T., Barnola, J.-M., Siegenthaler, U., Raynaud, D., Jouzel, J., Fischer, H., Kawamura, K., et al. (2008). High-resolution carbon dioxide concentration record 650,000–800,000 years before present. *Nature*, 453(7193):379–382.

Luz, B. and Barkan, E. (2000). Assessment of oceanic productivity with the triple-isotope composition of dissolved oxygen. *Science*, 288(5473):2028–2031.

Luz, B. and Barkan, E. (2005). The isotopic ratios 17o/16o and 18o/16o in molecular oxygen and their significance in biogeochemistry. *Geochimica et Cosmochimica Acta*, 69(5):1099 – 1110.

Luz, B. and Barkan, E. (2010). Variations of 17o/16o and 18o/16o in meteoric waters. *Geochimica et Cosmochimica Acta*, 74(22):6276 – 6286.

Luz, B. and Barkan, E. (2011). The isotopic composition of atmospheric oxygen. *Global Biogeochemical Cycles*, 25(3):n/a–n/a. GB3001.

Luz, B., Barkan, E., Bender, M., Thiemens, M., and Boering, K. (1999). Triple-isotope composition of atmospheric oxygen as a tracer of biosphere productivity. *Nature*, 400(6744):547–550.

Luz, B., Barkan, E., Sagi, Y., and Yacobi, Y. Z. (2002). Evaluation of community respiratory mechanisms with oxygen isotopes: A case study in lake kinneret. *Limnology and oceanography*, 47(1):33–42.

Luz, B., Barkan, E., and Severinghaus, J. (2014). 5.14 - the stable isotopic composition of atmospheric o_2. In Holland, H. D. and Turekian, K. K., editors, *Treatise on Geochemistry (Second Edition)*, pages 363 – 383. Elsevier, Oxford, second edition edition.

Luz, B., Barkan, E., Yam, R., and Shemesh, A. (2009). Fractionation of oxygen and hydrogen isotopes in evaporating water. *Geochimica et Cosmochimica Acta*, 73(22):6697–6703.

Malaize, B., Paillard, D., Jouzel, J., and Raynaud, D. (1999). The dole effect over the last two glacial-interglacial cycles. *Journal of Geophysical Research-atmospheres*, 104(D12):14199–14208.

Matsuhisa, Y., Goldsmith, J. R., and Clayton, R. N. (1978). Mechanisms of hydrothermal crystallization of quartz at 250 c and 15 kbar. *Geochimica et Cosmochimica Acta*, 42(2):173–182.

McCree, K. and Amthor, M. (1982). Effect of diurnal variation in temperature on the carbon balances of white clover plants. *Crop Science*, 22(4):822–827.

McCree, K., Setliik, I., et al. (1970). An equation for the rate of respiration of white clover grown under controlled conditions. In *Prediction and measurement of photosynthetic productivity. Proceedings of the IBP-PP Technical Meeting, Trebon,[Czechoslovakia], 14–21 September, 1969*, pages 221–9. Wageningen PUDOC.

McDermott, F. (2004). Palaeo-climate reconstruction from stable isotope variations in speleothems: a review. *Quaternary Science Reviews*, 23(7):901–918.

Mehler, A. H. (1951). Studies on reactions of illuminated chloroplasts. ii. stimulation and inhibition of the reaction with molecular oxygen. *Archives of Biochemistry and Biophysics*, 34(2):339 – 351.

Meijer, A. J. and Li, W. J. (1998). The use of electrolysis for accurate d170 and d180 isotope measurements in water. *Isotopes in Environmental and Health Studies*, 34(4):349–369.

Merlivat, L. (1978). Molecular diffusivities of $h_2^{16}o$, $hd^{16}o$, and $h_2^{18}o$ in gases. *The Journal of Chemical Physics*, 69(6):2864–2871.

Milankovitch, M. M. (1941). *Canon of insolation and the ice–age problem*. Kongiglich Serbische Akademie, Beograd.

Miller, M. F. (2002). Isotopic fractionation and the quantification of 170 anomalies in the oxygen three-isotope system, an appraisal and geochemical significance. *Geochimica et Cosmochimica Acta*, 66(11):1881 – 1889.

Mills, G. A. and Urey, H. C. (1940). The kinetics of isotopic exchange between carbon dioxide, bicarbonate ion, carbonate ion and water1. *Journal of the American Chemical Society*, 62(5):1019–1026.

Mitchell, L. E., Buizert, C., Brook, E. J., Breton, D. J., Fegyveresi, J., Baggenstos, D., Orsi, A., Severinghaus, J., Alley, R. B., Albert, M., Rhodes, R. H., McConnell, J. R., Sigl, M., Maselli, O., Gregory, S., and Ahn, J. (2015). Observing and modeling the influence of layering on bubble trapping in polar firn. *Journal of Geophysical Research: Atmospheres*, 120(6):2558–2574. 2014JD022766.

Monnin, E., Indermühle, A., Dällenbach, A., Flückiger, J., Stauffer, B., Stocker, T. F., Raynaud, D., and Barnola, J.-M. (2001). Atmospheric co_2 concentrations over the last glacial termination. *Science*, 291(5501):112–114.

Mook, W. G. and De Vries, J. (2000). Volume i: introduction⊠theory, methods, review. *Environmental Isotopes in the Hydrological Cycle: Principles and Applications, IHP-V, Technical Documents in Hydrology*, 39.

Morita, N. (1935). The increased density of air oxygen relative to water oxygen. *Journal of the Chemical Society*, 56:1291.

Mosblech, N. A., Bush, M. B., Gosling, W. D., Hodell, D., Thomas, L., van Calsteren, P., Correa-Metrio, A., Valencia, B. G., Curtis, J., and van Woesik, R. (2012). North atlantic forcing of amazonian precipitation during the last ice age. *Nature Geoscience*, 5(11):817–820.

NEEM members (2013). Eemian interglacial reconstructed from a greenland folded ice core. *Nature*, 493(7433):489–494.

NGRIP members (2004). High-resolution record of Northern Hemisphere climate extending into the last interglacial period. *Nature*, 431(7005):147–151.

Paillard, D., Labeyrie, L., and Yiou, P. (1996). Macintosh program performs time-series analysis. *Eos, Transactions American Geophysical Union*, 77(39):379–379.

Paterson, W. (1994). *The physics of glaciers*. Butterworth-Heinemann.

Pausata, F. S., Battisti, D. S., Nisancioglu, K. H., and Bitz, C. M. (2011). Chinese stalagmite [delta] 180 controlled by changes in the indian monsoon during a simulated heinrich event. *Nature Geoscience*, 4(7):474–480.

Peterson, L. C., Haug, G. H., Hughen, K. A., and Röhl, U. (2000). Rapid changes in the hydrologic cycle of the tropical atlantic during the last glacial. *Science*, 290(5498):1947–1951.

Petit, J. R., Jouzel, J., Raynaud, D., Barkov, N. I., Barnola, J., Basile, I., Bender, M., Chappellaz, J., Davis, M., Delaygue, G., Delmotte, M., Kotlyakov, V. M., Legrand, M., Lipenkov, V. Y., Lorius, C., Pepin, L., Ritz, C., Saltzman, E., and Stievenard, M. (1999). Climate and atmospheric history of the past 420,000 years from the Vostok ice core, Antarctica. *Nature*, 399(6735):429–436.

Prell, W. L. and Kutzbach, J. E. (1987). Monsoon variability over the past 150,000 years. *Journal of Geophysical Research: Atmospheres*, 92(D7):8411–8425.

Quay, P. D., Emerson, S., Wilbur, D. O., Stump, C., and Knox, M. (1993). The d180 of dissolved 02 in the surface waters of the subarctic pacific: A tracer of biological productivity. *Journal of Geophysical Research: Oceans*, 98(C5):8447–8458.

Rabinowich, E. (1945). Photosynthesis and related topics vol i.

Raich, J. W. and Potter, C. S. (1995). Global patterns of carbon dioxide emissions from soils. *Global Biogeochemical Cycles*, 9(1):23–36.

Rakestraw, N. M., Rudd, D. P., and Dole, M. (1951). Isotopic composition of oxygen in air dissolved in pacific ocean water as a function of depth. *Journal of the American Chemical Society*, 73(6):2976–2976.

Rebeiz, C. A., Benning, C., Bohnert, H., Daniell, H., Hoober, J. K., Lichtenthaler, H. K., Portis, A. R., and Tripathy, B. C. (2010). *The chloroplast: basics and applications*, volume 31. Springer Science & Business Media.

Reutenauer, C., Landais, A., Blunier, T., Bréant, C., Kageyama, M., Woillez, M.-N., Risi, C., Mariotti, V., and Braconnot, P. (2015). Quantifying molecular oxygen isotope variations during a heinrich stadial. *Climate of the Past*, 11(11):1527–1551.

Rhodes, R. H., Fa⊠n, X., Stowasser, C., Blunier, T., Chappellaz, J., McConnell, J. R., Romanini, D., Mitchell, L. E., and Brook, E. J. (2013). Continuous methane measurements from a late holocene greenland ice core, atmospheric and in-situ signals. *Earth and Planetary Science Letters*, 368:9–19.

Risi, C., Noone, D., Worden, J., Frankenberg, C., Stiller, G., Kiefer, M., Funke, B., Walker, K., Bernath, P., Schneider, M., Wunch, D., Sherlock, V., Deutscher, N., Griffith, D., Wennberg, P. O., Strong, K., Smale, D., Mahieu, E., Barthlott, S., Hase, F., Garc⊠a, O., Notholt, J., Warneke, T., Toon, G., Sayres, D., Bony, S., Lee, J., Brown, D., Uemura, R., and Sturm, C. (2012). Process-evaluation of tropospheric humidity simulated by general circulation models using water vapor isotopologues: 1. comparison between models and observations. *Journal of Geophysical Research: Atmospheres*, 117(D5):n/a–n/a. D05303.

Ruddiman, W. F. (1977). Late quaternary deposition of ice-rafted sand in the subpolar north atlantic (lat 40 to 65 n). *Geological Society of America Bulletin*, 88(12):1813–1827.

Ruddiman, W. F. (2003). Orbital insolation, ice volume, and greenhouse gases. *Quaternary Science Reviews*, 22(15):1597–1629.

Rumble, D., Miller, M., Franchi, I., and Greenwood, R. (2007). Oxygen three-isotope fractionation lines in terrestrial silicate minerals: An inter-laboratory comparison of hydrothermal quartz and eclogitic garnet. *Geochimica et Cosmochimica Acta*, 71(14):3592 – 3600.

Ruth, U., Barnola, J.-M., Beer, J., Bigler, M., Blunier, T., Castellano, E., Fischer, H., Fundel, F., Huybrechts, P., Kaufmann, P., Kipfstuhl, S., Lambrecht, A., Morganti, A., Oerter, H., Parrenin, F., Rybak, O., Severi, M., Udisti, R., Wilhelms, F., and Wolff, E. (2007). "edml1": a chronology for the epica deep ice core from dronning maud land, antarctica, over the last 150 000 years. *Climate of the Past*, 3(3):475–484.

Sanchez Goni, M. F. and Harrison, S. P. (2010). Millennial–scale climate variability and vegetation changes during the last glacial: Concepts and terminology. *Quaternary Science Reviews*, 29(21–22):2823–2827.

Schilt, A., Baumgartner, M., Blunier, T., Schwander, J., Spahni, R., Fischer, H., and Stocker, T. F. (2010). Glacial–interglacial and millennial-scale variations in the atmospheric nitrous oxide concentration during the last 800,000 years. *Quaternary Science Reviews*, 29(1–2):182–192. Climate of the Last Million Years: New Insights from EPICA and Other Records.

Schilt, A., Brook, E. J., Bauska, T. K., Baggenstos, D., Fischer, H., Joos, F., Petrenko, V. V., Schaefer, H., Schmitt, J., Severinghaus, J. P., et al. (2014). Isotopic constraints on marine and terrestrial n2o emissions during the last deglaciation. *Nature*, 516(7530):234–237.

Schlesinger, W. H. and Andrews, J. A. (2000). Soil respiration and the global carbon cycle. *Biogeochemistry*, 48(1):7–20.

Schmitt, J. (2006). *A sublimation technique for high–precision d13C on CO2 and CO2 mixing ratio from air trapped in deep ice cores*. PhD thesis, Dissertation Universität Bremen.

Schoenemann, S. W., Schauer, A. J., and Steig, E. J. (2013). Measurement of slap2 and gisp d17o and proposed vsmow-slap normalization for d17o and 17oexcess. *Rapid Communications in Mass Spectrometry*, 27(5):582–590.

Schwander, J. (1989). The transformation of snow to ice and the occlusion of gases. *The environmental record in glaciers and ice sheets*, pages 53–67.

Schwander, J., Barnola, J.-M., Andri⊠, C., Leuenberger, M., Ludin, A., Raynaud, D., and Stauffer, B. (1993). The age of the air in the firn and the ice at summit, greenland. *Journal of Geophysical Research: Atmospheres*, 98(D2):2831–2838.

Schwander, J. and Stauffer, B. (1984). Age difference between polar ice and the air trapped in its bubbles.

Seager, R. and Battisti, D. S. (2007). Challenges to our understanding of the general circulation: abrupt climate change. In *Global Circulation of the Atmosphere*, pages 331–371. Princeton Univ. Press, Princeton, N. J.

Severinghaus, J. P. (1995). Studies of the terrestrial o_2 and carbon cycles in sand dune gases and in biosphere 2. Technical report, Oak Ridge Associated Universities, Inc., TN (United States).

Severinghaus, J. P. and Battle, M. O. (2006). Fractionation of gases in polar ice during bubble close-off: New constraints from firn air ne, kr and xe observations. *Earth and Planetary Science Letters*, 244(1–2):474–500.

Severinghaus, J. P., Beaudette, R., Headly, M. A., Taylor, K., and Brook, E. J. (2009). Oxygen-18 of o2 records the impact of abrupt climate change on the terrestrial biosphere. *Science*, 324(5933):1431–1434.

Severinghaus, J. P., Bender, M. L., Keeling, R. F., and Broecker, W. S. (1996). Fractionation of soil gases by diffusion of water vapor, gravitational settling, and thermal diffusion. *Geochimica et Cosmochimica Acta*, 60(6):1005 – 1018.

Severinghaus, J. P. and Brook, E. J. (1999). Abrupt climate change at the end of the last glacial period inferred from trapped air in polar ice. *Science*, 286(5441):930–934.

Severinghaus, J. P., Grachev, A., and Battle, M. (2001). Thermal fractionation of air in polar firn by seasonal temperature gradients. *Geochemistry, Geophysics, Geosystems*, 2(7):n/a–n/a. 1048.

Severinghaus, J. P., Sowers, T., Brook, E. J., Alley, R. B., and Bender, M. L. (1998). Timing of abrupt climate change at the end of the younger dryas interval from thermally fractionated gases in polar ice. *Nature*, 391(6663):141–146.

Shaheen, R., Janssen, C., and Rockmann, T. (2007). Investigations of the photochemical isotope equilibrium between o2, co2 and o3. *Atmospheric Chemistry and Physics*, 7(2):495–509.

Sowers, T., Bender, M., Raynaud, D., and Korotkevich, Y. S. (1992). $\delta^{15}n$ of n_2 in air trapped in polar ice: A tracer of gas transport in the firn and a possible constraint on ice age-gas age differences. *Journal of Geophysical Research: Atmospheres*, 97(D14):15683–15697.

Sowers, T., Bender, M., Raynaud, D., Korotkevich, Y. S., and Orchardo, J. (1991). The $\delta^{18}o$ of atmospheric o_2 from air inclusions in the vostok ice core: Timing of co_2 and ice volume changes during the penultimate deglaciation. *Paleoceanography*, 6(6):679–696.

Strizh, I. (2008). The mehler reaction as an essential link between environmental stresses and chloroplast redox signaling. In *Photosynthesis. Energy from the Sun*, pages 1343–1346, TIERGARTENSTRASSE 17, HEIDELBERG, GERMANY,D-69121. TIERGARTENSTRASSE 17, HEIDELBERG, GERMANY,D-69121.

Suwa, M. and Bender, M. L. (2008). O2/n2 ratios of occluded air in the gisp2 ice core. *Journal of Geophysical Research: Atmospheres*, 113(D11). D11119.

Svensson, A., Andersen, K. K., Bigler, M., Clausen, H. B., Dahl-Jensen, D., Davies, S. M., Johnsen, S. J., Muscheler, R., Parrenin, F., Rasmussen, S. O., Röthlisberger, R., Seierstad, I., Steffensen, J. P., and Vinther, B. M. (2008). A 60 000 year greenland stratigraphic ice core chronology. *Climate of the Past*, 4(1):47–57.

Tamiya, H. and Huzisige, H. (1949). Effect of oxygen on the dark reaction of photosynthesis. *Acta Phytochim*, 15:83–104.

Tan, M. (2014). Circulation effect: response of precipitation δ180 to the enso cycle in monsoon regions of china. *Climate Dynamics*, 42(3):1067–1077.

Tanaka, R. and Nakamura, E. (2013). Determination of 170-excess of terrestrial silicate/oxide minerals with respect to vienna standard mean ocean water (vsmow). *Rapid Communications in Mass Spectrometry*, 27(2):285–297.

Thiemens, M. H. (1999). Mass-independent isotope effects in planetary atmospheres and the early solar system. *Science*, 283(5400):341–345.

Thiemens, M. H. (2012). Oxygen origins. *Nature Chemistry*, 4:66.

Thiemens, M. H. and Jackson, T. (1987). Production of isotopically heavy ozone by ultraviolet light photolysis of o2. *Geophysical Research Letters*, 14(6):624–627.

Urey, H. C. and Greiff, L. J. (1935). Isotopic exchange equilibria. *Journal of the American Chemical Society*, 57(2):321–327.

van Iersel, M. and Bugbee, B. (2000). A multiple chamber, semicontinuous, crop carbon dioxide exchange system. design, calibration, and data interpretation. *Journal of the American Society for Horticultural Science*, 125(1):86–92.

Veres, D., Bazin, L., Landais, A., Toyé Mahamadou Kele, H., Lemieux-Dudon, B., Parrenin, F., Martinerie, P., Blayo, E., Blunier, T., Capron, E., Chappellaz, J., Rasmussen, S. O., Severi, M., Svensson, A., Vinther, B., and Wolff, E. W. (2013). The antarctic ice core chronology (aicc2012), an optimized multi-parameter and multi-site dating approach for the last 120 thousand years. *Climate of the Past*, 9(4):1733–1748.

Vinther, B. M., Buchardt, S. L., Clausen, H. B., Dahl-Jensen, D., Johnsen, S. J., Fisher, D., Koerner, R., Raynaud, D., Lipenkov, V., Andersen, K., et al. (2009). Holocene thinning of the greenland ice sheet. *Nature*, 461(7262):385–388.

Voelker, A. H. and workshop participants (2002). Global distribution of centennial-scale records for marine isotope stage (mis) 3: A database. *Quaternary Science Reviews*, 21:1185–1212.

Von Caemmerer, S. (2000). *Biochemical models of leaf photosynthesis*. Number 2. Csiro publishing.

Waelbroeck, C., Labeyrie, L., Michel, E., Duplessy, J., McManus, J., Lambeck, K., Balbon, E., and Labracherie, M. (2002). Sea-level and deep water temperature changes derived from benthic foraminifera isotopic records. *Quaternary Science Reviews*, 21(1–3):295–305.

Wang, X., Auler, A. S., Edwards, R. L., Cheng, H., Ito, E., Wang, Y., Kong, X., and Solheid, M. (2007). Millennial-scale precipitation changes in southern brazil over the past 90,000 years. *Geophysical Research Letters*, 34(23):n/a–n/a.

Wang, X.-F., Yakir, D., and Avishai, M. (1998). Non-climatic variations in the oxygen isotopic compositions of plants. *Global Change Biology*, 4(8):835–849.

Wang, Y., Cheng, H., Edwards, R. L., Kong, X., Shao, X., Chen, S., Wu, J., Jiang, X., Wang, X., and An, Z. (2008). Millennial- and orbital-scale changes in the east asian monsoon over the past 224,000 years. *Nature*, 451(7182):1090–1093.

Wang, Y. J., Cheng, H., Edwards, R. L., An, Z. S., Wu, J. Y., Shen, C.-C., and Dorale, J. A. (2001). A high-resolution absolute-dated late pleistocene monsoon record from hulu cave, china. *Science*, 294(5550):2345–2348.

West, J. B., Sobek, A., and Ehleringer, J. R. (2008). A simplified gis approach to modeling global leaf water isoscapes. *PLoS ONE*, 3(6):e2447.

Williams, M. A. J., Dunkerley, D. L., De Deckker, P., Kershaw, A. P., and Stokes, T. (1997). *Quaternary environments*. Science Press.

Wunsch, C. (2006). Abrupt climate change, an alternative view. *Quaternary Research*, 65(2):191–203.

Yakir, D., DeNiro, M. J., and Rundel, P. W. (1989). Isotopic inhomogeneity of leaf water: Evidence and implications for the use of isotopic signals transduced by plants. *Geochimica et Cosmochimica Acta*, 53(10):2769 – 2773.

Yakir, D., D., DeNiro, M. J., and Gat, J. R. (1990). Natural deuterium and oxygen–18 enrichment in leaf water of cotton plants grown under wet and dry conditions: evidence for water compartmentation and its dynamics. *Plant, Cell & Environment*, 13(1):49–56.

Young, E. D., Galy, A., and Nagahara, H. (2002). Kinetic and equilibrium mass-dependent isotope fractionation laws in nature and their geochemical and cosmochemical significance. *Geochimica et Cosmochimica Acta*, 66(6):1095 – 1104.

Young, E. D., Yeung, L. Y., and Kohl, I. E. (2014). On the d170 budget of atmospheric o_2. *Geochimica et Cosmochimica Acta*, 135:102 – 125.

Yuan, D., Cheng, H., Edwards, R. L., Dykoski, C. A., Kelly, M. J., Zhang, M., Qing, J., Lin, Y., Wang, Y., Wu, J., Dorale, J. A., An, Z., and Cai, Y. (2004). Timing, duration, and transitions of the last interglacial asian monsoon. *Science*, 304(5670):575–578.

Yung, Y. L., DeMore, W. B., and Pinto, J. P. (1991). Isotopic exchange between carbon dioxide and ozone via o(1d) in the stratosphere. *Geophysical Research Letters*, 18(1):13–16.

2 Science at risk: a new method of oxygen separation

2.1 INTRODUCTION

The INTRAMIF project was aiming at high-risk research. Accordingly, the primary goal of my PhD project was to develop a new method of O_2 separation to measure the triple isotope composition of atmospheric O_2 back to 800 kyr trapped in ice cores from Antarctica. Due to the small signal of $^{17}\Delta_{atm}$ anomaly ($\backsimeq$ 40 permeg from glacial to interglacial), the proposed measurements on ice cores are extremely challenging on both the extraction and measurement side. To reach the targeted precision (10 permeg), a quantitative separation of O_2 from other atmospheric constituents is crucial. To determine isotopic ratios of oxygen at high accuracy and precision, the sample must be introduced as pure O_2 into the MS (noted MS hereafter) (Sarma et al., 2003). However, with common chromatographic techniques, (i) a carrier gas (usually He, which is very expensive) is needed to transfer the sample through the GC and (ii) triple oxygen isotopic ratios are determined in a mixture of gases (O_2 -Ar, or O_2 -Ar-N2) by dual-inlet mass spectrometry. Corrections are applied to account for the resulting interferences, causing a loss of precision. IDEA, MOTIVATION

In order to obtain pure O_2 , membrane technology is an interesting alternative to the common method, as O_2 isotopologues are measured in a pure substance, avoiding the need for chemical slope correction (Sect. 4). A large part of my PhD was therefore dedicated to the development of this new technique. Many steps were involved, from prospecting, defining, designing and testing the new method. Unfortunately, membrane sealing issues, coupled to variable isotope fractionation during O_2 permeation across the membrane lead to an "early" stopping of the project. This chapter is structured as follows. Section 2.2 introduces the new method of oxygen separation, section 2.3 describes the experimental setups, Sect. 2.4 assesses the selectivity, permeability and isotope fractionation of the membrane, and discusses the application of such technology to ice core science.

2.2 Physical basis of measurements

The new method described here for oxygen separation relies on membrane-based technology. There are many existing oxygen selective membranes, as a wide range of application require generation or removal of oxygen, including production of high purity oxygen for medical applications, aqua-culture and combustion processes, control of oxygen partial pressure in industrial environments, production of power and chemicals, and removal of oxygen from enclosures and gas streams (Badwal and Ciacchi, 2001). However, such applications usually do require very-high purity O_2 , and research therefore focus on its permeation rate (e.g. Tablet, 2006; Wang et al., 2002) ORIGIN

rather than on its O_2 selectivity, whereas we would need the opposite characteristics for our application.

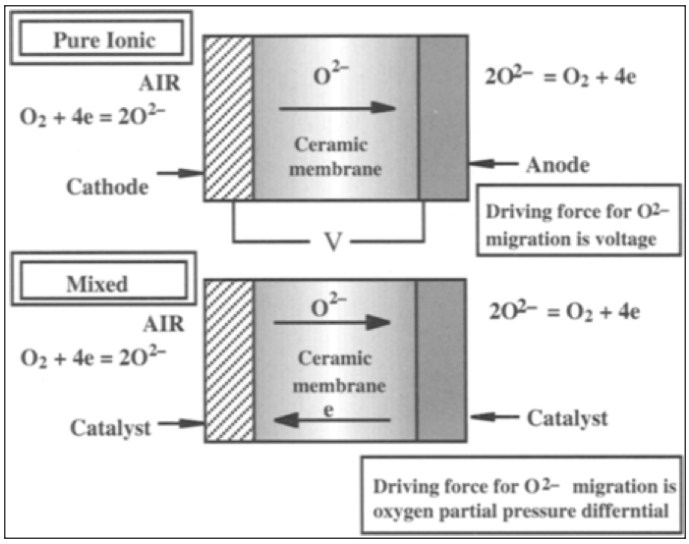

Figure 2.1 – Original figure from Badwal et al. (2003). Schematics of oxygen generation with pure ionic and mixed ionic/electronic conducting ceramic membranes. We are using the second type in this project.

PROSPECTION

Organic membranes were not considered during our prospection because they do not yield high purity oxygen. Indeed, transport in these membranes is based on molecular diffusion, and opportunity for higher oxygen selectivity is small as elemental gases like Ar have similar molecular sizes. We thus restricted our prospection to pure ionic and mixed ionic electronic conducting (noted MIEC hereafter) ceramic membranes, where permeation is based on ionic transport, enabling in theory higher O_2 selectivity.

There are two types of membranes based on solid electrolytes systems. The first one is based on pure or mainly oxygen-ion conducting transport. This consists in a solid electrolyte cell consisting of an ion-conducting electrolyte membrane coated with electrodes on both sides. The driving force for O^{2-} migration is voltage or current driven, and the rate of the oxygen ionic flux is directly proportional to the current flowing through the device. The second type is a mixed ionic/electronic conducting ceramic membrane, with high oxygen ion and electronic conductivities. The electrons in the membrane combine with O_2 in the air to create negatively charged oxygen ions. No electrodes are required and driving force for oxygen ion transport is provided by the temperature and the differential partial pressure of oxygen (chemical potential gradient) across the membrane (Fig.2.1).

The most promising (and available) membrane we found has been developed at the Fraunhofer-Institute for Interfacial Engineering and Biotechnology Inorganic Surfaces and Membranes (Germany). We therefore started a partnership (contact: Thomas

Schiestel and Marita Zipperle) and they provided us with a MIEC tubular perovskite membrane, characterized in theory by 100 % selective O_2 permeation and no correlation between selectivity and permeability.

2.2.1 Characteristics

- The dimensions of the membranes may differ between each other but only in a range between 1.10 and 1.18 mm for the outer diameter and between 0.80 and 0.88 mm for the inner diameter, the wall thickness measuring usually between 140 and 150 μ. The membrane consists in a hollow fiber, because the tubular design is more robust than the flat shaped one. Besides, it allows a sealing far from the permeation area, hence in the "cold zone". A disk-shaped membrane would indeed force the sealing to be located in the hot zone, which makes it extremely challenging. Finally, such a design should offer higher thermal cycling capabilities, as it is also subjected to low thermal stresses during its use. Badwal et al. (2003). As sealing of the membrane, even at moderate temperature, quickly turned out to be a major issue (Sect. 2.4.2), we obtained membranes with one closed end from the Fraunhofer-Institute, so that only one side of the membrane would need to be sealed, at cold temperature. GEOMETRY

- The ceramic membrane acts as a physical barrier to contaminants. STRUCTURE

- The oxygen transport through the membrane is based on a diffusion process, strongly temperature-dependent. For solid state materials, such as this membrane, diffusion takes place at high temperatures. At room temperature, no O_2 permeation occurs. The permeation process starts at around 750°C, with optimal working conditions from 850 to 1000 °C. High-temperature is important in practice because most membranes exhibit poor oxygen ion mobility at low temperature. Permeation through the perovskite membrane is driven by the oxygen partial pressure gradient between both sides of the membrane (Sect. 2.2.2). The rate of O_2 flow is proportional to the ratio of partial pressure of O_2 on the inlet side (S1) to the oxygen partial pressure on the output side (S2). PERMEATION

- The composition of the membrane material is protected for secrecy reasons since the Fraunhofer-Institute has an industrial project partner involved in the project. What is published is the following composition: $BaCo_xFe_yZr_{1-x-y}O_{3-d}$ (noted BCFZO hereafter). Important to bear in mind is that the amount of oxygen in perovskites differs, as shown by the "d" in the formula, with the composition of the atmosphere and with temperature. It is thus challenging to quantify the amount of oxygen in the membrane. COMPOSITION

2.2.2 Transport mechanisms

Transport mechanisms across perovskite membranes are briefly presented here, and the interested reader can find more details in e.g. Sunarso et al. (2008); Tablet (2006)

and ref. therein. Perovskite[1]-type (ABO_3) ceramic membranes have a high ionic and electronic conductivity, thereby a high oxygen permeability compared to other mixed-conducting ceramic membranes (Tablet, 2006). To fulfill the electric neutrality criteria, the flux of O_2 ions following the chemical potential gradient is charge compensated by a simultaneous flux of electrons in the opposite direction (Fig. 2.1). As shown in Fig. 2.2, O_2 transport across the membrane occurs in three steps (Sunarso et al., 2008; Tablet, 2006):

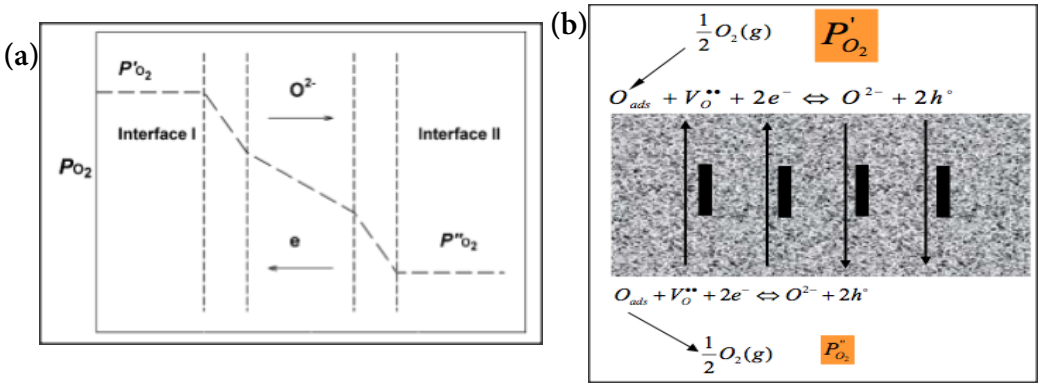

Figure 2.2 – **(a)** Original Figure 6 from From Sunarso et al. (2008). Schematics of O_2 transport through the perovskite membrane. The wall thickness of the membrane determines the limiting step of O_2 transport: it is bulk diffusion for thick membranes but surface reactions for thin ones (Sunarso et al., 2008). **(b)** Original Figure 1.2 from Tablet (2006) with original caption: Fluxes in mixed conducting membrane under a partial pressure gradient. P' is the higher O_2 partial pressure, P" is the lower O_2 partial pressure. Refer to text for details.

- At the surface exchange reaction on interface I (high O_2 partial pressure side). At the membrane surface, O_2 molecules adsorb and are reduced (gain in electron) to their ionic form.
- simultaneous counter diffusion of O_2 ions and electrons through the bulk of the membrane, driven by the O_2 partial pressure.
- reversed surface exchange on Interface II (low O_2 partial pressure side). O_2 ions recombine to form O_2 molecules.

Figure 2.2b reveals the presence of O_2 vacancies and electron holes in the membrane. They maintain local charge neutrality and may control the permeation rate, as the slowest moving species determine the net O_2 flux across the membrane. Indeed, the O_2 flux across the membrane mainly depends on (i) the diffusive rate in the bulk of the membrane of O_2 anions (O_2^-) and oxygen vacancies ($V_O{}^{**}$) and/or the simultaneous

[1]Perovskite is the most abundant ($\simeq$ 75%) solid phase of the lower mantle of the Earth and is called after Count Lev Aleksevich von Perovski. It was first found in the Ural in 1839. The general structure of the perovskite mineral is ABX3 where A (generally an alkali earth metal or a transition metal) and B (generally a transition metal or a rare earth metal) are cations and X oxygen anions (Tablet, 2006)

counter flux of electrons (e^-) and electron holes (h°) and (ii) the surface exchange at Interface I and II, which depends on several factors such as adsorption, dissociation, surface diffusion, charge transfer and incorporation in the surface layer (Tablet, 2006; Sunarso et al., 2008).

2.3 Experimental setup

In this section, we present the two experimental setups developed to asses O_2 isotope fractionation occurring during O_2 permeation. The reader is invited to refer to Chapter 4 for an introduction to the basics of mass spectrometry.

2.3.1 Setup A

The experimental setup presented in Fig. 2.3, called Setup A hereafter, was developed to estimate the permeation rate of the hollow perovskite fiber, and to assess the stability of the isotope composition of the permeated O_2 . While a constant supply of O_2 was provided to the feed side of the membrane, the permeated O_2 in the lumen was quickly flushed using He as carrier gas. The membrane was inserted in a 1/4" quartz tube heated to 700°C. The main advantage of this setup was to avoid sealing issues. Indeed, the permeating area of the membrane was isolated from lab air by a flow of atmospheric air or pure O_2 (working standards) introduced in the feed side of the membrane through a capillary[2]. Within the membrane (lumen), a He capillary inserted to the end was used as carrier gas to flush the permeated O_2 in order to keep a low O_2 partial pressure. This also ensured a pressure above atmospheric pressure, hence isolating permeated O_2 from lab air. Finally, in an attempt to measure O_2 permeating from areas where conditions are isothermal, the inlet of the capillary (sniffing point) connecting the lumen of the membrane to the MS (via a VICI 6-port valves and an open split) was located just before the hot zone (Fig. 2.3). Note that the coating of the capillaries inserted in the heated area was burned off prior introduction in the membrane unit to avoid contamination of the membrane surface.

[2]Note that this capillary also enables a stable high pressure in the feed side. When lab air was exposed to the membrane (without capillary), large fluctuations in permeation occurred.

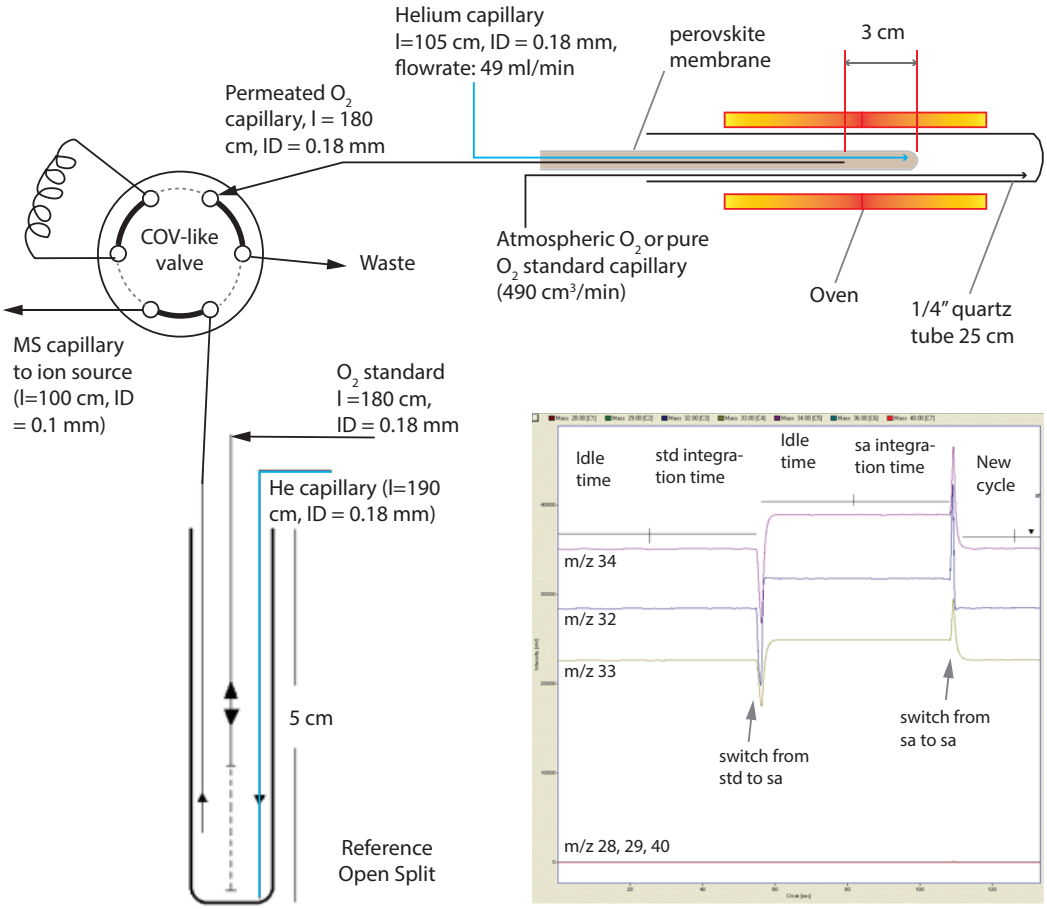

Figure 2.3 – Setup A including a O_2 permeation unit, a 6-port valve and an open split developed (i) to monitor the stability of O_2 permeation rate through the membrane, (ii) to determine isotope ratios of the permeated O_2 . In the initial configuration, no 6-port valve was installed, and measurements were done in CF mode. Because of the low precision of the measurements, a 6-port valve was added to micmic the changeover valve (COV) of the Dual Inlet (noted DI hereafter) mode of the MS. Refer to text for details.

Initially, measurements of O_2 isotope ratios were done in the Continuous Flow (CF) mode of the MS (Delta V and Delta V Advantage, ThermoFisher). Sample (permeated O_2) and standard (pure O_2) were introduced to the ion source of the MS through two capillaries connected to the needle valve of the MS. There were caveats associated with this method. Indeed, He flowing from the standard line's open split was diluting the sample (already diluted in He, see Fig 2.3) to such an extent[3] that size of sample and standards differed widely during the analysis (linearity, refer to Chapter 4), causing an important loss in precision. To improve the quality of the measurements, a pneumatically actuated 6-port valve[4] (Valco, USA) was added to the setup, and measurements

[3]in CF mode, the use of open splits as in Fig. 2.3 induces the use of a carrier gas which is constantly flowing to the ion source of the MS. Reference gas pulses are generated by moving the standard capillary upstream and downstream from the sniffing point (inlet of the capillary connected to the ion source).

[4]a 4-port valve would have worked perfectly too

performed in Dual Inlet (DI) mode.

In DI mode, the changeover valve (COV) enables the fast and repeated comparison of ion currents and ion current ratios, which minimizes instrumental effect Werner and Brand (2001). The COV diverts the sample to waste while the standard is introduced to the source and inversely. Therefore, in the final experimental setup, the COV is replaced by an automated six-port valve (into four-position), in the configuration shown in Fig. 2.3. To "trick" the Isodat software of the MS in order to measure in DI mode without using the COV valve, the Isodat function controlling the COV is modified so that the program controls the 6-port valve instead during the data acquisition.

N_2 (m/z 28) signal was measured with a magnetic scan to check for a possible contamination of the sample. Background values of m/z 28 with He only flowing to the ion source were about 3 mV. With pure O_2 and atmospheric O_2 introduced in the feed side of the membrane, they reached 10 and 30 mV, respectively, relative to a O_2 signal typically above 20 V (on the same cup). In Sect. 2.4.1, the O_2 /N_2 separation factor is quantified more precisely.

2.3.2 Setup B

A schematic of the membrane separation unit is described in Fig. 2.4. Unlike setup A, this setup, designed to separate O_2 from other atmospheric constituents in gases trapped in ice cores, requires to seal the membrane under vacuum (Sect. 2.4.2), as the lumen of the membrane is evacuated to cryogenically and quantitatively collect the permeated O_2 . As can be seen, the seal of the membrane is outside the heated area, which is critical as high temperature has proven to be extremely difficult, even for applications where high-purity O_2 is not required, and explains in part why tubular membranes are preferred over disk membranes (e.g. Badwal and Ciacchi, 2001; Sunarso et al., 2008) Obviously, the recovery will be limited by the decreasing O_2 pressure gradient across the membrane, due to a decrease of partial pressure of O_2 in the feeding side with permeation of O_2 , but the influence of the collection efficiency could not be tested as sealing issues quickly arise (Sect. 2.4.2). We present here the components of setup B.

Given the high operating temperature of the perovskite membrane, we chose a fused silica tube (melting point: 1700°C) to be inserted in our custom-made tubular furnace. The quartz tube was closed on one end and narrowed to $\frac{1}{2}''$ on the other by a glassblower (Pantmann Glassware, Denmark).The low thermal conductivity of quartz material allowed us to seal the quartz tube to a $\frac{1}{4}''$ welded stainless steel (noted SST hereafter) microvolume cross (SWAGELOK, USA) with a $\frac{1}{2}''$ Ultra-Torr nut and associated O-ring (70 durometer fluorocarbon FKM, wetted with a thin film of silicone vacuum grease), whose maximum temperature does not exceed 204°C. QUARTZ TUBE

Furnaces are commercially available, but are rather expensive. The custom-made OVEN

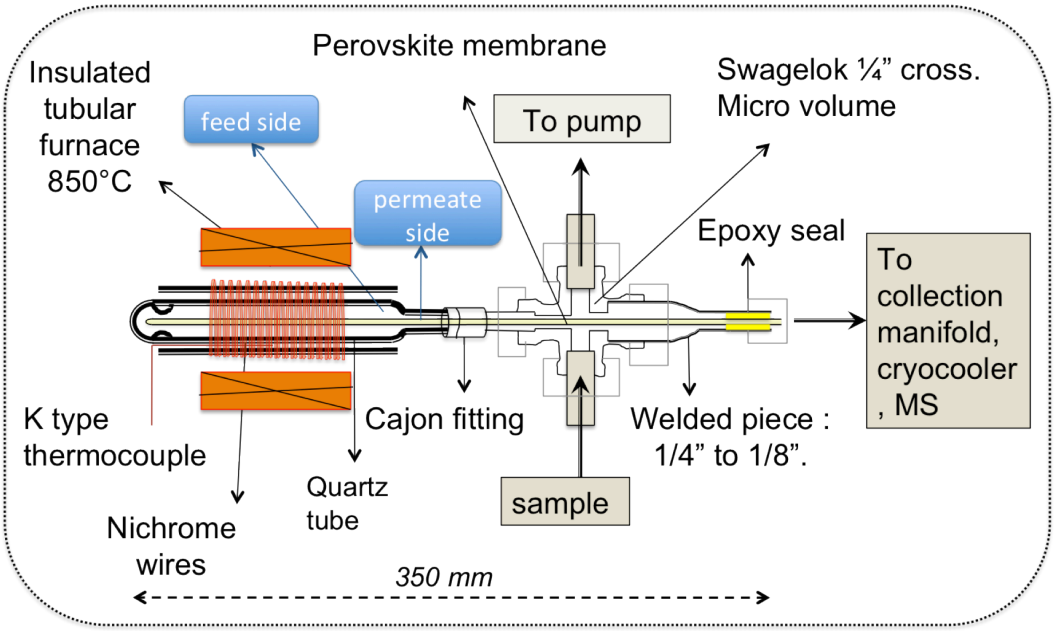

Figure 2.4 – Setup B: membrane separation unit. Refer to text for details on the experimental setup.

oven provides similar performances regarding maximum temperature, temperature stability, or width of the hot zone, where conditions are isothermal. The furnace consists in a 25 cm long quartz tube coated with nichrome (Nickel-Chromium, OMEGA, UK) wires[5] held in position with thermal paste. Voltage is adjusted with a Variac to control the temperature, monitored with a K-type thermocouple. The oven major requirements were (i) to reach at least 800°C and (ii) to provide an area with isothermal conditions (Fig 2.5). Indeed, given the lack of knowledge on O_2 isotopic fractionation through the perovskite membrane, the parameters controlling the permeability of the membrane need to be closely monitored. As O_2 partial pressure gradient and temperature are the driving force for O_2 transport across the membrane, ensuring isothermal conditions where permeation occurs is essential. The temperature profile of the oven at different temperature can be seen in Fig. 2.5. An area of 5 cm presents homogenous temperatures, and is referred as the "hot zone". To define the length of the hot zone, a K-thermocouple, instead of the membrane, is inserted across the microvolume cross and into the quartz tube, so as to micmic the conditions of the experiment as closely as possible.

CROSS The micro-volume SST 1/4" cross (SWAGELOK) across which the membrane passes minimizes dead volumes on the feed side of the membrane. On Fig. 2.4, one can see that one end of the cross is used to introduce the sample, another to evacuate the feed side of the membrane, the third end connects the cross to the separation unit thanks to a 1/2" SST welded tube fitting, and the fourth end consists in a 1/8" SST welded tube fitting, connecting the permeate side (lumen) of the membrane either to the collection

[5]same principle as e.g. a bread toaster

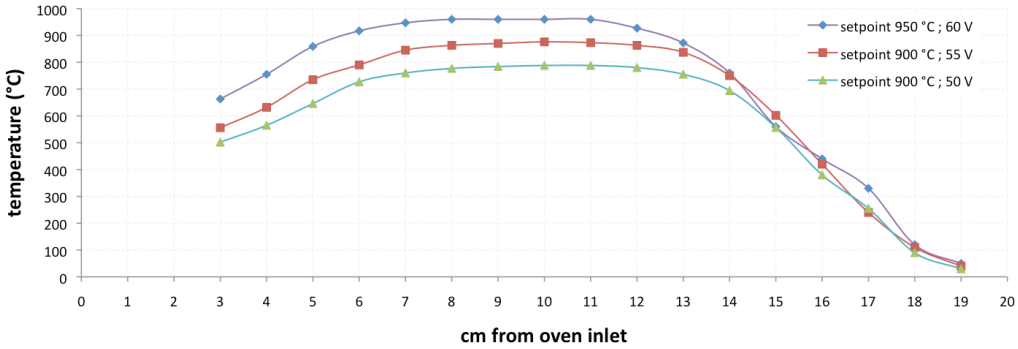

Figure 2.5 – Temperature profiles of the oven made out of a nichrome wire and a quartz. It can reach the optimal operating temperature of the membrane (850 °C), and has a homogenous hot zone of around 5 cm, 7 to 12 cm from the oven inlet.

manifold or directly to the MS (not shown on the setup is another cross offering the possibility to evacuate the lumen of the membrane). The membrane is sealed with Ultra-Torr (Accu-Glass Products, USA) to the 1/8" SST welded tube.

2.4 Characterization of the membrane

In this section we evaluate the selectivity, the sealing, the permeability and the isotope fractionation of the perovskite membrane.

2.4.1 Selectivity

Atmospheric air samples permeating across the membrane at operating temperature were collected in a 65 ml glass flask previously evacuated using setup B. The samples were then expanded into the bellows of the DI unit and a magnetic mass scan was performed (Fig. 2.6). Height and peak area are measured with both the peak detection tool from Isodat software from a Delta V Plus MS (please refer to Chapter 4 for an introduction to mass spectrometry) and results are checked with an independent software. The high value of the O_2 /N_2 ratio confirms the very high O_2 selectivity of the membrane, indicative of successive sealing and gas-tightness of the separation unit at the time of measurements. However, gas-tightness could not be maintained over period of times sufficiently long to reliably measure $^{17}\Delta$ (Sect. 2.4.2).

2.4.2 Sealing

Sealing of a tubular perovskite membrane is not trivial, as underlined by several studies (e.g. Li et al., 1999; Zhu et al., 2009; Sunarso et al., 2008), in particular at high temperature. In this case, the sealant must be flexible and gas-tight, have a thermal coefficient that corresponds to the one of the membrane and the supporting material, withstand thermal shock, and do not react with the surface of the membrane (Zhu et al., 2009). Even if the tubular geometry of the membrane requires minimal sealing

(a)

Experiment	Date	Figure	Instrument	Sample	Membrane temperature (°C)	Peak area (mV.steps)		Height (mV)		Blank area		Blank height		O2/N2 separation factor	
						O2	N2	O2	N2	O2	N2	O2	N2	area	height
membrane exposed to atmospheric air	02/2011	a	Delta V	Lab air	Operating temperature : 850 °C	468470.3	249.3	39733.1	22.56	44.9	36.7	3,9	3,4	1879	1761
Membrane exposed to atmospheric air	02/2011	not shown	Delta V	Lab air	Operating temperature : 850 °C	O2	N2	O2	N2	O2	N2	O2	N2	area	height
						408800.6	252,3	34008.1	22.56	44.9	36.7	3.9	3.4	1620	1507
Membrane at room temperature	03/2011	c	Delta Advantage	Lab air	Room temperature : 25 °C	O2	N2	O2	N2						
						103.3	75.1	9.8	7.4						
Source background	03/2011	d	Delta Advantage	MS Source		O2	N2	O2	N2						
						90,5	23,3	8,5	2,2						

(b)

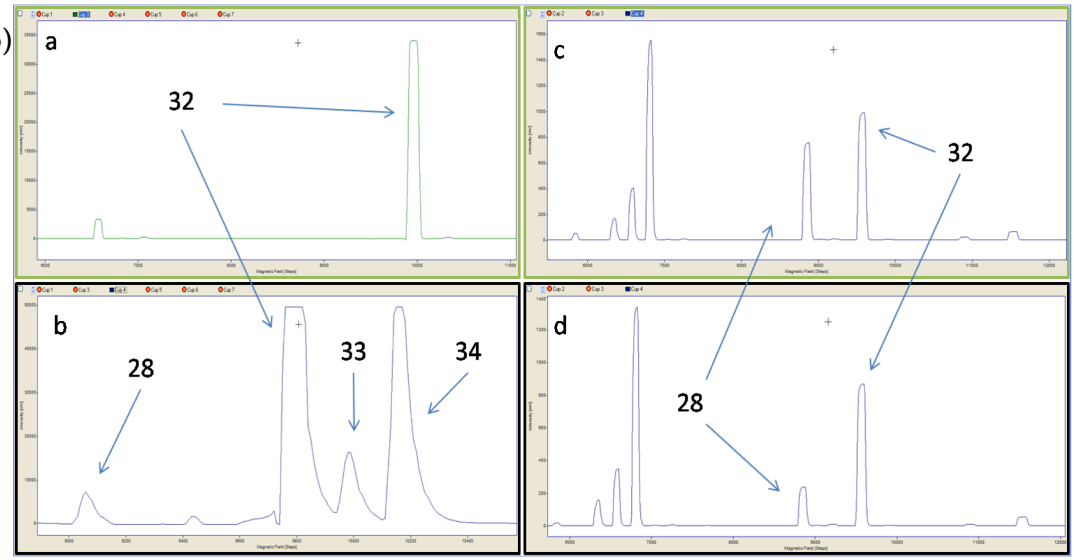

Figure 2.6 – Values of the scans and estimation of the O_2 /N_2 separation factor based on the magnetic scans displayed in **(b)**. **(b)** The selectivity of the membrane based on magnetic scans. Note the different scales. **a** 850°C : full scan after exposition of the membrane to atmosphere. **b**Zoom of **a** on m/z 28, 32, 33 and 34. **c** 25°C : absence of oxygen permeation when membrane exposed to atmosphere. **d** Background mass spectrum.

compared to a flat-shaped membrane (Badwal et al., 2003), and does not require a high-temperature sealing, we did not find a satisfactory solution to seal the membrane in this thesis. It needs to be underlined here that except for Zhu et al.'s study, production of very high-purity O_2 is not required for most of the applications described in literature, as the main industrial targets are the production of O_2 -enriched mixture of gases[6]. In other words, a successful sealing in these studies was likely to be a failure for the purpose of measuring air in ice cores. For instance, Wang et al. (2006) use silicon rubber O-rings to cold-seal the very same tubular BCFZO membrane, but this option does not provide the required gas tightness when applied here. In the same vein, fitting

[6]Often, O_2 permeation rates are calculated assuming leakage of O_2 through pores or cracks by Knudsen diffusion, where O_2 and N_2 fluxes are related by $J_{O_2}/J_{N_2} = \sqrt{32/28} = 4.02$. They therefore calculate the O_2 flux as $J_{O_2} = (C_{O_2} - C_{N_2}/4.02) \cdot F/S$, where C denotes concentration, F the measured total flow rate and S the effective permeation area of the membrane.

the membrane with silver plated ferrules or teflon ferrules (Valco, USA) would break the membrane. Besides, applied sealing techniques in some of these studies required elaborated procedures that could not be performed at CIC. As an illustration, Li et al. (1999) developed a ceramic binder, containing extra-fine alumina and some of the prepared perovskite type oxide. Consequently, we crushed in powder a broken membrane, mixed it with Ultra-Torr sealant, but without sucess. Other sealants are tested in the literature, including Pyrex glass rings, precious metal rings, ceramic binders, or even Cu(OH)2 binder in combination with phosphoric acid (see Li et al., 1999, and ref. therein). Tablet (2006) applies a gold coating on the surface of the membrane[7]. However, gas-tightness is a problem with Au paste. Usually, the seal needs to be reworked a few times to reach a gas-tight sealing because the paste looses a lot of volume during the annealing step and the shrinkage is very high (Zipperle, 2010, pers. comm.). In Zhu et al.'s study, a quartz cap is fixed to the membrane with a ceramic sealant (HT767A, Huitian Adhesive Enterprise Co. LTD. China), which can solidify at room temperature and remains hard at high temperatures. The ceramic sealant also holds the melted Ag (silver) used as a sealant. This high-temperature sealing technique was not tested, as it required to melt Ag, but inspired our most successful method, using Ultra-Torr (very fine epoxy resin with Magnesium Silicate Hydrate (talc)) as sealant. As shown in Sect. 2.4.1, this technique provides excellent results, but the sealant would quickly degrade over time. It is not likely that the leak is caused by a mismatch of thermal expansion coefficients of the Ultra-Torr paste and the perovskite membrane, as this part of the membrane does not undergo important thermal stress. Adding new layers of Ultra-Torr paste did not help.

To our view, the rough surface and tiny pores of the membranes are the main issues when it comes to sealing a membrane in the cold zone. The sealing material must be able to fill these pores, and without overcoming this problem, such a method of O_2 separation for ice core measurements is not feasible.

2.4.3 PERMEATION

The permeation rate (J_{O_2}) of perovskite membranes has been exhaustively studied for various conditions (e.g. Wang et al., 2002; Tablet, 2006). However, the O_2 pressure gradient across the membrane was much higher (in the 1 to 10 bar range) and sweep gases were used on both sides of the membrane with high flows, the purpose being to maximize J_{O_2}. For the purpose of measuring ice core samples, conditions are different: the gradient of O_2 partial pressure is much more reduced, and vacuum conditions are required[8]. As in other studies, we observed a fast increase of the permeation rate with increasing temperature (before reaching a plateau) and increasing O_2 partial pressure gradient. To calculate the O_2 permeation rate, we use setup A (Fig. 2.3). The modified

[7]sealing with Au is typically done when high-temperature sealing is required, but it should also work at cold temperatures

[8]Note that the setup used to estimate the permeation rate differs from the one built to separate O_2 from other gases trapped in ice cores, by the use of a career gas in the permeate side of the hollow fiber in the first case, while vacuum is maintained in the second case.

sniffing permeated O_2 capillary had a inner diameter of 0.1 mm.

ASSUMPTIONS

Calculating the permeation rate (J_{O2}) requires a few assumptions:

- J_{O_2} is based on the permeation rate of the most abundant O_2 isotopologue, $^{16}O_2$, neglecting the two heavier isotopologues.
- Permeation across the membrane is assumed to only occur in the hot zone of the oven, where conditions are isothermal. To ensure that permeation only occurs through the "hot zone", Tablet (2006) coated the ends of the membrane with Au paste. A dense Au film was obtained after sintering at 950 °C. As this method of high-temperature sealing could not be applied at CIC, we avoided to measure O_2 permeating from areas where conditions are not isothermal by ensuring that the sniffing point (inlet of the capillary that connects the lumen of the membrane to the sample open split of the MS) is located just before the hot zone (Fig. 2.3).
- the O_2 -He mixture of the ion source is well mixed and the Helium signal in the ion source is constant throughout experiments.

CALCULATIONS

J_{O_2} can be calculated from the measured permeated $^{16}O_2$ signal (beam voltage V^{32} of m/z 32) given by Isodat. The beam voltage of one block (V_b^{32}) is taken as the average of 8 cycles V_c^{32} (cycle defined as in Fig. 2.3). The ion current I^{32} (A) can be deduced from V^{32} (V) and the resistance of the cup where m/z 32 is collected (here $R_{cup} = 1 \cdot 10^9 \Omega$) ($U = RI$):

$$I^{32} = V_b^{32} \cdot R_{cup}. \tag{2.1}$$

Mol of O_2 ions per second (n_{ions}^{32}) can then be deduced, knowing Avogadro number $N_A = 6.02214179 \cdot 10^{23} mol^{-1}$, and the elementary charge ($e = 1.602176487 \cdot 10^{-19}$ C (or A · s)):

$$n_{ions}^{32} = \frac{I^{32}}{e \cdot N_A}. \tag{2.2}$$

Ionization efficiencies of O_2 (ζ_{O_2}, in molecules · ions^{-1}) and He (ζ_{He}) are required to deduce the amount of O_2 (n_{ms}^{32}) and He molecules (n_{ms}^{4}) reaching the ion source every second (the permeated O_2 is carried to the source with He, introduced in the lumen of the membrane (Fig 2.3). Ionization efficiency represents the number of molecules needed to form an ion. The Diagnosis Absolute Sensitivity tool of Isodat software (ThermoFisher) enables us to calculate the molecules to ions ratio : a defined micro-volume (0.145 cm^{-3}) located between the bellows of the MS (Refer to Chapter 4) and the inlet capillary to the ion source is filled with pure O_2 , adjusting the signal around 8 V. Based on this defined volume, it is possible to estimate the ion current as a function of the gas consumption over a defined time period. Integrating the ion current over this time period provides the number of ions, while the number of molecules is calculated from the O_2 signal drop using the ideal gas law (Delta V manual, ThermoFisher). Helium ionization efficiency (11037 molecules ion^{-1}) is a factor of 5 lower

than O_2 ionization efficiency (2033 molecules ion^{-1}) for the Delta V Plus used in this experiment. It follows that:

$$n^{32}_{ms} = n^{32}_{ions} \cdot \zeta_{O_2}. \tag{2.3}$$

He has a different ionization efficiency. The O_2 concentration in the source (C_{O_2},) can be expressed as:

$$C_{O_2} = \frac{n^{32}_{ms}}{n^{4}_{ions} \cdot \zeta_{He}}, \tag{2.4}$$

where the term $n^{4}_{ions} \cdot \zeta_{He}$ is assumed constant over the experiment (He, m/z 4)signal (V^4) is measured once at the start of the measurements on the same cup (collector) as m/z 32). Assuming a well mixed gas mixture (He and permeated O_2) in the lumen of the membrane, we can assume that the fraction of the gas mixture sniffed by the MS capillary and to the ion source (Fig 2.3) has the same O_2 to He ratio as the gas mixture in the lumen of the membrane. As the flow rate of He F_{He} in the lumen is known ($49cm^3 \cdot min^-1$), the flux of O_2 molecules F_{O_2} permeating (in $mol \cdot s^{-1}$ or $cm^3 \cdot s^{-1}$ according to the ideal gas law) through the membrane can be estimated as

$$F_{O_2} = C_{O_2} \cdot \frac{F_{He}}{60}, \tag{2.5}$$

The effective permeation area S (cm^2) of the membrane is calculated using the logarithmic mean diameter of the hollow membrane because the inner surface is smaller than the outer one:

$$S = \frac{\pi L(d_o - d_i)}{ln(d_o/d_i)}, \tag{2.6}$$

where d_o and d_i stand for the outer (0.1 cm) and inner (0.08 cm) diameter of the membrane, and L represents the length of the permeating area of the membrane, taken as the distance between the membrane closed end and the sniffing MS capillary (3 cm). Finally, by dividing Eq. 2.5 by Eq. 2.6, the permeation of O_2 J_{O_2} (in $cm^3 \cdot cm^{-2} \cdot s^{-1}$) across the membrane can be calculated:

$$J_{O_2} = \frac{F_{O_2}}{S}. \tag{2.7}$$

Fig. 2.7 summarizes results from the permeation experiment.

We observe a higher J_{O2} variability with atmospheric air than with pure O_2 , related to the lower O_2 partial pressure in air. The permeation rates found in these experiments are similar to those found in other experiments, though much less stable. Wang et al. (2002) reports for example values between 0.5 and 3.5 $cm^3/cm^{-2}/min^{-1}$ with increasing temperature and O_2 partial pressure gradient. The most striking figure is the important variability of the permeation. It may relate to variations of O_2 partial pressure in the feed side of the membrane, or to small temperature fluctuations (variations of $\simeq$3°C were observed in the hot zone). Alternatively, these large fluctuations may be due to changes in the location of the He and/or sniffing (permeated O_2) capillaries. However, the fact that the permeation oscillates around its mean before getting stable may also point to a equilibration time required for J_{O_2} to stabilize. This experiment would need to be reproduced in more stable conditions, so as to understand

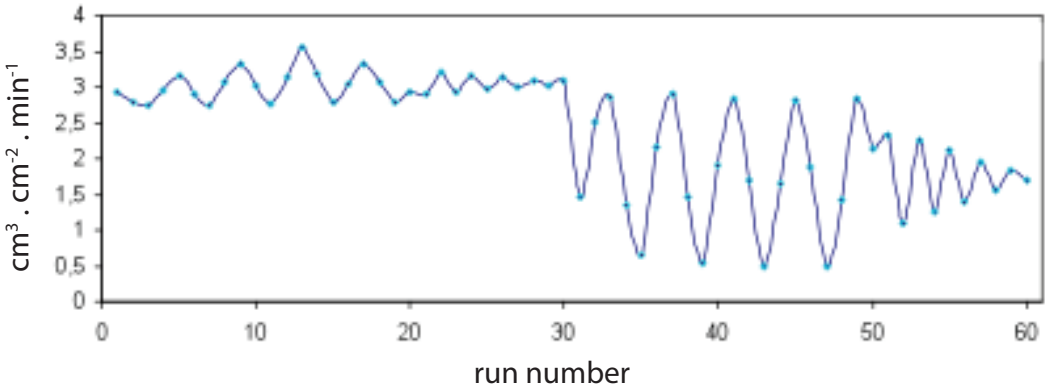

Figure 2.7 – Permeation rate of the membrane over 60 runs at ≃ 700°C. The permeation rate first describes large oscillations before reducing its variance around a mean value. The membrane was fed with pure oxygen for the first 30 runs, then with atmospheric air. With pure O_2 , the permeation rate varied from 2.75 and 3.55 $ml \cdot cm^{-2} \cdot s^{-1}$ with an average value of 3.03 $ml \cdot cm^{-2} \cdot s^{-1}$. With air, from run 31 to run 60, values oscillated between 0.48 and 2.90 $ml \cdot cm^{-2} \cdot s^{-1}$, with an the average calculated as 1.79 $ml \cdot cm^{-2} \cdot s^{-1}$.

if the variability observed in J_{O_2} is inherent to the membrane or arises from the experiment. However, the collection of discrete samples of permeated O_2 using setup B revealed excessive isotope fractionation during O_2 permeation, which sounded the death knell of the membrane-based method for O_2 separation (Sect. 2.4.4).

2.4.4 Isotope fractionation

A Rayleigh-type fractionation experiment in closed system was performed with the perovskite membrane to extract the three-isotope exponent γ from the experimental data. During the experiment, 7.2 cc of pure O_2 standards were introduced in the feed (sample) side of the membrane (setup B, Fig. 2.4) and were permeating through the membrane at operating temperature (850 °C). They were collected in a 65 ml glass flask after different permeation time (1 min to a 2 h). Collection of the sample was not quantitative as the samples (the permeated O_2) were collected by expansion under vacuum [9]. Only collection time was allowed to vary. Typically, ≃60 % of the sample was collected.

γ can be derived from the best fit of a $\delta'^{17}O$ vs. $\delta'^{18}O$ plots in experiments where only O_2 consumption (here permeation) takes place in a closed system, as explained in Sect. 1.2.5.1.1. The results, obtained with DI measurements, reveal that O_2 isotopes undergo mass-dependent fractionation when permeating through the membrane, with a slope $\lambda = 0.528$, at the high end of expected θ values that lie between 0.5010 and 0.5305 for kinetic and equilibrium (high temperature) isotope fractionations (Matsuhisa et al., 1978; Young et al., 2002; Kaiser et al., 2004). Indeed, the maximum value

[9] the He cryocooler was not available at the time of these experiments

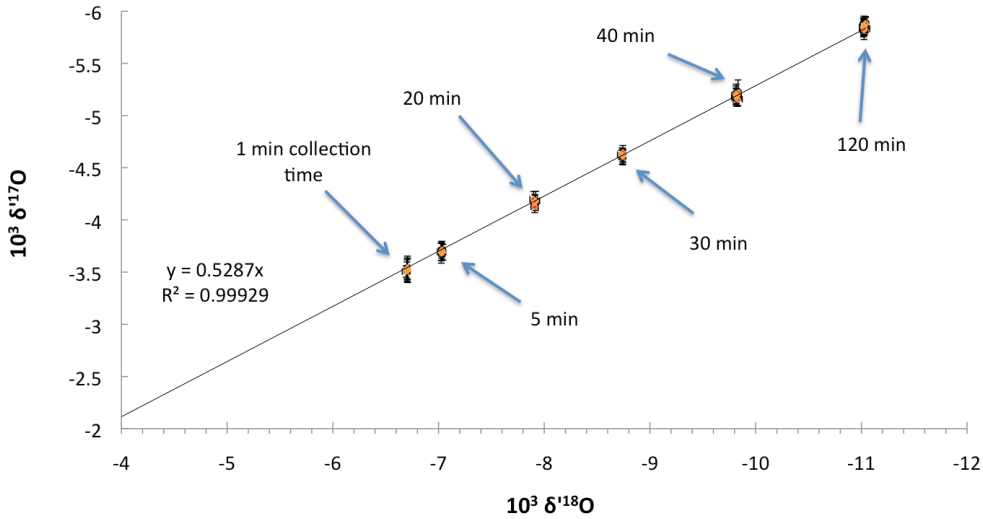

Figure 2.8 – Three-isotope plot of permeated O_2 resulting from a "Rayleigh" fractionation experiment (but it turned out Rayleigh conditions were not met, refer to text for details) at 850 °C. Abscissa and ordinate error bars (2 σ, drawn in black) enclose data points within the 95 % confidence level.

of θ, corresponding to equilibrium fractionation at high temperature, is 0.5305 (Matsuhisa et al., 1978; Kaiser, 2008).

The non quantitative collection of the samples questions however the assumption of Rayleigh fractionation. Indeed, given the high O_2 permeation rate across the membrane, permeation occurs quickly, and pressures on the feed side and the permeate side of the membrane are balanced after after less than a minute. This was verified by calculating back the pressures in both sides of the membrane based on the volume and pressure of the introducing and collecting flasks after collection. With the absence of O_2 pressure gradient across the membrane, exchange of O_2 between the two sides of the membrane may occur, which implies that Rayleigh fractionation conditions are not respected. Increasing collection time causes $\delta^{18}O$ depletion. This may be caused (i) by temperature gradients within the membrane separation unit, or (ii) by an increasing amount of O_2 segregated in the perovskite membrane.

- Important temperature gradients exist between the collection flask (room temperature, around 25 °C) and the membrane unit (850 °C), which can cause unmixing of gaseous mixtures Grachev and Severinghaus (2003). A rough estimation can be done: given that 2/3 of the sample is collected after permeation, and assuming a sensitivity of $\delta^{18}O$ to thermal diffusion of 0.03 ‰ $\cdot K^{-1}$ in air, the potential fractionation is $\frac{0.03}{3}800 = 8$‰, which is in the range of the observed enrichment. However, heavy O_2 isotopologues should migrate towards the cold end, and thus cause an enrichment of the measured mixture (and a depletion in the hot zone of the membrane) with increasing collecting time, while we observe the opposite pattern. Actually, on the feed side on the membrane,

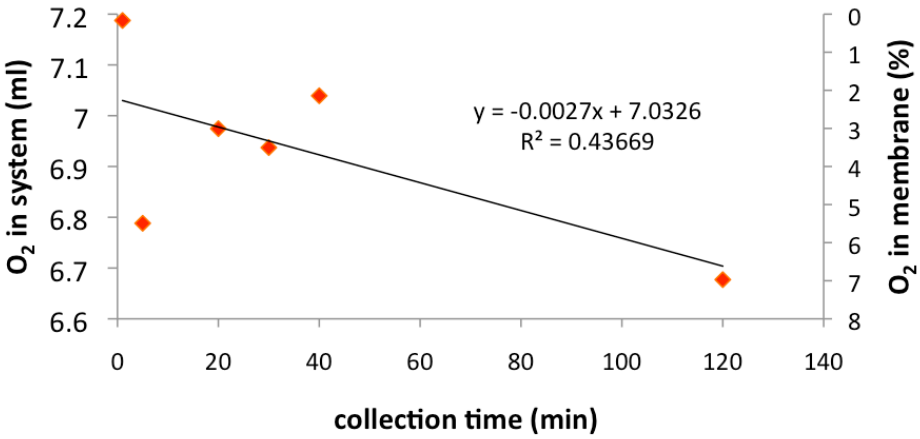

Figure 2.9 – Loss of O_2 in the membrane separation unit in function of the collection time during the "Rayleigh" experiment. Note that the membrane was extensively flushed with a pure standard mixture before the beginning of the experiments. A new standard was introduced for each collection time, after evacuation of both sides of the membrane. On the right axis the proportion of O_2 in the membrane is indicated. For reason that we do not understand, the loss of O_2 after a collection of 5 min is almost as important as after 2 h, and may be related to an operator error.

thermal diffusion causes a gradual $\delta^{18}O$ depletion in the hot zone relative to the introducing flask, which implies that O_2 permeating is depleted. In contrast, on the lumen side, permeated O_2 is artifactually depleted in $\delta^{18}O$ in the hot zone, but more enriched in the collection flask. It is therefore difficult to estimate the net effect of thermal diffusion, especially because we lack information on the O_2 exchange between the two reservoirs when there is no O_2 gradient across the membrane.

- Another explanation for the $\delta^{18}O_{atm}$ depletion with increasing collecting time is related to the perovskite membrane. It contains O_2 , as indicated in the formula (O_{3-d}), and the O_2 content of the membrane is adjusted by shifting the temperature and/or partial pressure (Sunarso et al., 2008). However, Yin and Lin (2007) shows that while the O_2 sorption kinetics are fast, desorption kinetics are complex and depend in part on the temperature and the sorbent structure. Our experiment seems to indicate a loss of O_2 with respect to collection time. Indeed, as shown in Fig. 2.9, assuming that all the O_2 is recovered from the membrane after 1 min of collection, 7 % are lost after a collection of 2 h, which corresponds to 0.5 ml for a 7.2 ml O_2 sample.

Such results demonstrate the need to repeat the experiment in conditions ensuring Rayleigh fractionation, which calls for a quantitative collection (Fig. 2.10) of the sample to confirm or not the segregation of O_2 in the membrane. Is it due to the absence of O_2 pressure gradients across the membrane at the end of the collection? Or is it due to thermal diffusion? The three-isotope plot displayed in Fig. 2.10 reveals excursions

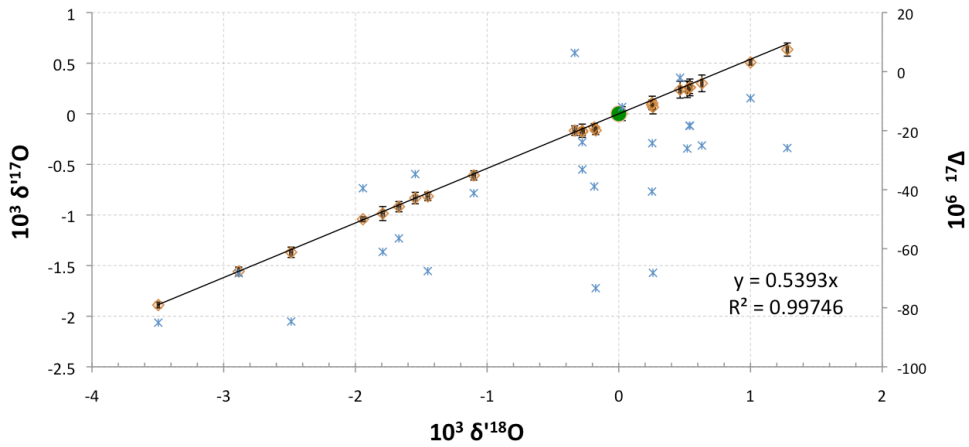

Figure 2.10 – Three-isotope plot of permeated O_2 collected at 12 K (Chapter 3) at 850°C. Also displayed are $^{17}\Delta$ values (right axis) calculated with $\lambda = 0.516$.

of $\delta^{18}O$ and $\delta^{17}O$ values of pure O_2 permeated across the membrane. Similar experiments (in terms of temperature conditions, sample size or collection time) completed other days reveal similar excursions (not shown), with γ oscillating between 0.49 and 0.54, which represents the full range of expected mass-dependent fractionation. Results underline the variable isotope fractionation occurring during O_2 permeation, which precludes high-precision isotope measurements as long as the origin of the variability has not been found.

The stability of the membrane was also assessed in a CF mode to circumvent the sealing issue and create conditions where one reservoir is infinite, so as to define directly the intrinsic fractionation from a three isotope plot (Young et al., 2014). In the setup, there was indeed no change in the isotope composition or the flow rate of either pure O_2 or air, flowing through a capillary to the sample (feed) side of the perovskite membrane. However, the experiment was too unstable to obtain reliable data. For instance, λ has a value of 0.414 with pure O_2 , and 0.601 with air, well beyond the predicted mass-dependent relationship.

2.5 Conclusion and perspectives

In this section we showed:

1. The high permeability of the membrane to O_2 is confirmed, ranging from 0.5 to 3.5 $ml \cdot cm^{-2} \cdot s^{-1}$.

2. The 100 % selectivity to O_2 was verified.

3. Variable mass-dependent fractionation is observed, even in the case of intense flushing before the measurements, probably because O_2 is not quantitatively released by the membrane during operation.

4. Based on the few experiments performed, fractionation of the membrane cannot be determined. Such unpredictable behavior precludes measurement of ${}^{17}\Delta_{atm}$.

5. Membrane's gas-tightness cannot be achieved.

To be applied to ice core science, the membrane requires a leak-tight sealing. Provided that an adequate sealant is found, the membrane can be used in applications where removal of O_2 is required, taking profit of its 100 % selectivity to O_2 . Additionally, pure O_2 standards can be produced in large amounts from atmospheric O_2 given the large permeability of the membrane.

Bibliography

Badwal, S., Ciacchi, F., Zelizko, V., and Giampietro, K. (2003). Oxygen removal and level control with zirconia⊠yttria membrane cells. *Ionics*, 9(5-6):315–320.

Badwal, S. P. and Ciacchi, F. T. (2001). Ceramic membrane technologies for oxygen separation. *Advanced materials*, 13(12-13):993–996.

Grachev, A. M. and Severinghaus, J. P. (2003). Determining the thermal diffusion factor for 40ar/36ar in air to aid paleoreconstruction of abrupt climate change. *The Journal of Physical Chemistry A*, 107(23):4636–4642.

Kaiser, J. (2008). Reformulated 170 correction of mass spectrometric stable isotope measurements in carbon dioxide and a critical appraisal of historic ⊠absolute⊠ carbon and oxygen isotope ratios. *Geochimica et Cosmochimica Acta*, 72(5):1312–1334.

Kaiser, J., R⊠ckmann, T., and Brenninkmeijer, C. A. M. (2004). Contribution of mass-dependent fractionation to the oxygen isotope anomaly of atmospheric nitrous oxide. *Journal of Geophysical Research: Atmospheres*, 109(D3):n/a–n/a. D03305.

Li, S., Qi, H., Xu, N., and Shi, J. (1999). Tubular dense perovskite type membranes. preparation, sealing, and oxygen permeation properties. *Industrial & engineering chemistry research*, 38(12):5028–5033.

Matsuhisa, Y., Goldsmith, J. R., and Clayton, R. N. (1978). Mechanisms of hydrothermal crystallization of quartz at 250 c and 15 kbar. *Geochimica et Cosmochimica Acta*, 42(2):173–182.

Sarma, V., Abe, O., and Saino, T. (2003). Chromatographic separation of nitrogen, argon, and oxygen in dissolved air for determination of triple oxygen isotopes by dual-inlet mass spectrometry. *Analytical chemistry*, 75(18):4913–4917.

Sunarso, J., Baumann, S., Serra, J., Meulenberg, W., Liu, S., Lin, Y., and Da Costa, J. D. (2008). Mixed ionic–electronic conducting (miec) ceramic-based membranes for oxygen separation. *Journal of Membrane Science*, 320(1):13–41.

Tablet, C. (2006). Dense hollow fiber perovskite membranes for oxygen separation and partial oxidation of light hydrocarbons. *PhD manuscript, University of Hannover*.

Wang, H., Cong, Y., and Yang, W. (2002). Oxygen permeation study in a tubular ba0.5sr0.5co0.8fe0.203-d oxygen permeable membrane. *Journal of Membrane Science*, 210(2):259 – 271.

Wang, H., Schiestel, T., Tablet, C., Schroeder, M., and Caro, J. (2006). Mixed oxygen ion and electron conducting hollow fiber membranes for oxygen separation. *Solid State Ionics*, 177(26–32):2255–2259. Solid State Ionics 1, Proceedings of the 15th International Conference on Solid State Ionics, Part {II}.

Werner, R. A. and Brand, W. A. (2001). Referencing strategies and techniques in stable isotope ratio analysis. *Rapid Communications in Mass Spectrometry*, 15(7):501–519.

Yin, Q. and Lin, Y. (2007). Beneficial effect of order⊠disorder phase transition on oxygen sorption properties of perovskite-type oxides. *Solid State Ionics*, 178(1–2):83–89.

Young, E. D., Galy, A., and Nagahara, H. (2002). Kinetic and equilibrium mass-dependent isotope fractionation laws in nature and their geochemical and cosmochemical significance. *Geochimica et Cosmochimica Acta*, 66(6):1095 – 1104.

Young, E. D., Yeung, L. Y., and Kohl, I. E. (2014). On the d170 budget of atmospheric o_2. *Geochimica et Cosmochimica Acta*, 135:102 – 125.

Zhu, X., Sun, S., Cong, Y., and Yang, W. (2009). Operation of perovskite membrane under vacuum and elevated pressures for high-purity oxygen production. *Journal of Membrane Science*, 345(1–2):47–52.

3 Building an extraction and collection line for oxygen isotopes

3.1 INTRODUCTION

In this chapter we present the experimental system developed at CIC to extract gases occluded in ice core bubbles and collect either pure O_2 for $^{17}\Delta$ measurements, or an O_2 -N_2 -Ar mixture for $\delta^{18}O_{atm}$ measurements, together with $\delta O_2/N_2$ ratio, $\delta^{15}N$ and $\delta^{40}Ar$. $\delta^{18}O$ measurements from the NEEM (North Eemian Drilling Project, Greenland) and RICE ice cores have been successfully performed on this experimental setup (Grzymala-Lubanski, 2015), with an acceptable precision ($\sigma = 0.028‰$ with error propagation, see Chap. 4). In contrast, ice core $^{17}\Delta$ measurements have not started at the time of writing this thesis as the accuracy and precision they require has not been reached.
The first section of this chapter presents the analytical requirements of the analytical system (Sect. 3.2). The second section presents an overview of the system based on Barkan and Luz (2003) (Sect. 3.3). A third section describes the building and implementation of the extraction, purification and collection units of the experimental setup (Sect. 3.4). Sect. 3.5 focuses on the gas chromatograph O_2 /N_2 separation unit.The fifth section describes the automation of the system and informs about the electrical characteristics of the setup (Sect. 3.6). Finally, Sect. 3.7 focuses on the development of the experimental protocols to measure stable oxygen isotopes ($\delta^{18}O$ or $^{17}\Delta$). The measurement sequence developed for IRMS measurements is described in Chapter 4.

3.2 ANALYTICAL REQUIREMENTS

To measure the triple isotope composition of atmospheric oxygen, the fundamental requirement of an analytical system resides in its ability to preserve and measure variations as small as 10 permeg (0.01 ‰), corresponding to millennial-scale variations observed in $^{17}\Delta_{atm}$. In order to meet this requirement, the experimental procedure should respect the following criteria for:

1. Identical Treatment
   The gas sample introduced in the MS must be representative of the air extracted from the ice core. In other terms, the fractionation involved by extraction, separation, purification, collection and introduction of the sample in the IRMS must be accounted for. It is however almost impossible to prevent fractionation to occur in a system as there may be adsorption processes, temperature fluctuations, different equilibration times, incomplete transfer, etc. We therefore try to follow the principle of Identical Treatment (Werner and Brand, 2001 of the sample and the standard as closely as possible. Instead of preventing fraction-

ation to occur, which is not realistic nor feasible, the IT principle requires to process samples and standards (reference material) in an identical manner, so that the setup-related alterations of the sample gas are canceled out by the standard ones.

2. Isobaric interference
   Ionized molecules with the same mass/charge ratio must be avoided in the source of the MS to prevent isobaric interferences. Therefore, for $^{17}\Delta_{atm}$ measurements, O_2 needs to be separated from N_2 , as these species react during ionization to form mass fragments, for instance $^{14}N^{18}O^+$ with a mass/charge ratio of 32 (like $^{16}O^{16}O^+$). Besides, $\delta^{18}O$ and $\delta^{17}O$ depend on the N_2 /O_2 ratio of the sample gas relative to the working reference gas (Barkan and Luz, 2003), causing further corrections and loss of precision. As precision of $\delta^{18}O_{atm}$ measurements is not as critical, $\delta^{18}O_{atm}$ can be measured in air and corrections applied for N_2 interference.

3. Flow regime
   The dimensions of the analytical setup must ensure a viscous flow regime. For instance. introduction of the standard in the system may lead to fractionation due to changes in physical principles of gas flow. Indeed, from a high pressure source to the vacuum area, 3 flow regimes appear with decreasing pressure: viscous flow, Knudsen flow and molecular flow 3.1. In Knudsen and molecular flow regime, diffusion of isotopocules with different masses causes fractionation of the gas species and their isotopes (Schmitt, 2006; Honig, 1945; Halsted and Nier, 1950). For instance, Knudsen diffusion causes fractionation that scales with the square root of the mass ratio while ordinary molecular diffusion scales as the proportional mass difference (Severinghaus and Battle, 2006). Viscous flow is required to avoid fractionation during transfer of the analyzed gases, as implemented for instance in a MS, where standard and sample are introduced with a narrow-bore capillary (0.1 mm ID) at pressures ensuring viscous flow conditions.

4. Precision
   The analytical error of the procedure should not exceed 10 permeg, which correspond to the variation in $^{17}\Delta_{atm}$ associated with e.g. DO 19 (Landais et al., 2007). A precision an order of magnitude higher (≃1 permeg) would be advantageous, but remains beyond the current analytical capabilities of IRMS measurements (5-10 per meg).

3.3 Overview of the system

3.3.1 General idea

VERSATILE SETUP

This experimental setup is primarily built for automated $^{17}\Delta$ measurements. It requires a very high precision that only DI IRMS measurements can provide hitherto.

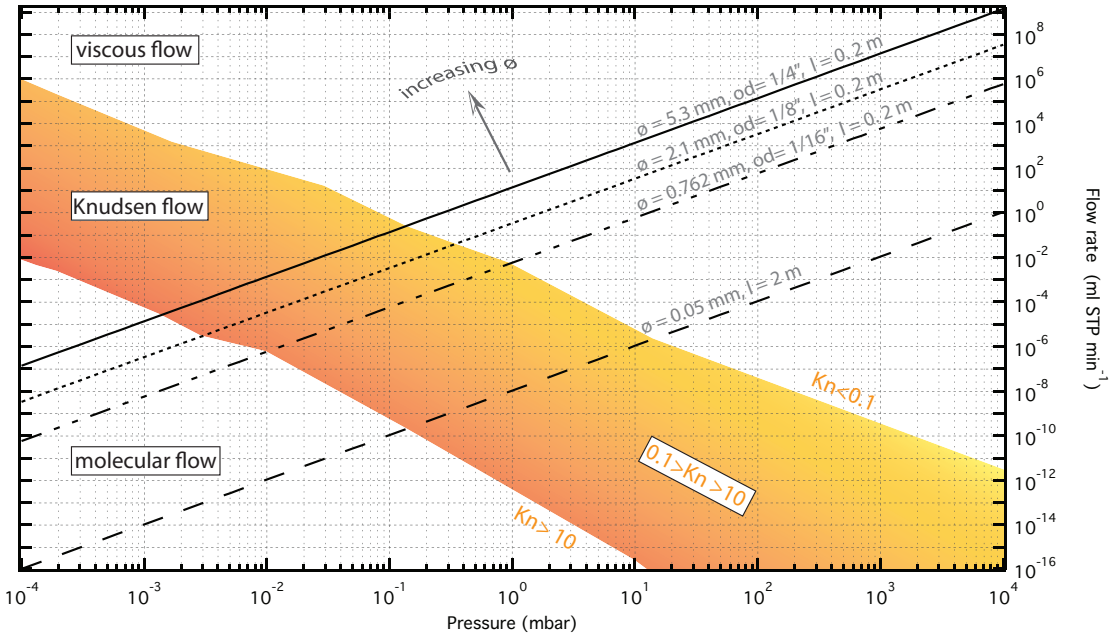

Figure 3.1 – Flow regimes and volumetric flow rate STP (log scale) according to pressure (log scale) and diameter of the pipe. The volumetric flow rates are calculated using Poiseuille's law, thereby assuming laminar flow. The x-axis represents pressure drop along the pipe. Lines describe flow rates with different diameters (from 0.05 to 1/4") corresponding to the characteristic dimensions of our setup. Except for the narrow bore capillary (0.05 mm id) which has a length of 2 m, calculations are done with tube length set to 20 cm. This graph shows for instance that viscous flow regime is only achieved with a pressure higher than 10 mbar in the narrow bore capillary.

Therefore we did not consider to develop a continuous extraction system as described for e.g. in Huber and Leuenberger (2004); Huber et al. (2003), but built an offline system. The "^{17}O line" is nonetheless versatile. Indeed, separation of oxygen and nitrogen is not needed for $\delta^{18}O$ measurements. In this case, the oxygen separation unit, consisting of 2 focusing traps and a chromatographic column, is bypassed, as it is possible to measure $\delta^{18}O$ with a reasonable precision and accuracy within a O_2 -N_2 mixture and correct for N_2 interference.

The experimental setup described on this chapter is based on the system developed by Barkan and Luz (2003) in Jerusalem and relies on chromatographic technique for oxygen separation. Indeed, as explained in Chapter 2, after almost two years of prospection, development and testing of the perovskite membrane, this new method of oxygen separation was proven unadapted for $^{17}\Delta$ measurements. Still, the design, building, automation and calibration of the system took several months, regardless of the time needed to adjust our measurement protocols to a different MS. Among changes to improve the system or adapt it to the working space and environment, a CLASSICAL METHOD

major modification in the design of the analytical setup relates to the sample collection unit. Indeed, to reduce operation costs, we cryogenically collect the samples with a Helium cryocooler instead of freezing the samples at 4 K in a SST tube lowered into a tank of liquid helium. The system was also thought to maximize sample throughput. It allows in theory the successive collection of 10 samples a day. However, 2 or more rods are in practice dedicated to standard measurements, to respect the principle of identical treatment (noted IT hereafter), by which samples and standards (reference material) are processed in an identical manner (Werner and Brand, 2001).

3.3.2 General layout of the experimental setup

The "^{17}O line" allows measurements of $\delta^{18}O$ in air or $^{17}\Delta$ in a O_2 /Ar mixture. The off-line system is schematically described in Fig. 3.2. It can be divided into 2 main sections:

- A section common to $\delta^{18}O$ and $^{17}\Delta$ measurements operated under vacuum (see Sect. 3.4). As mentioned earlier, $\delta^{18}O$ can be precisely measured in a N_2 -O_2 -Ar mixture, while $^{17}\Delta$ measurements require O_2 to be separated from N_2 . This section includes:
    1. a vacuum system (cf. box in fig 3.2)
    2. a standard introduction unit. Standard is introduced using a mass flow controller (MFC) or an aliquot equipped with two manual valves (SS-4H, SWAGELOK)
    3. an extraction unit
    4. a purification unit including a water trap (T1) and a CO_2 trap (T2)
    5. a collection unit, called "LynnOax", consisting of ten SST rods
- A separation unit which allows the separation between an O_2 -Ar mixture and N_2 , constantly flushed with high-purity He used as carrier gas. For $\delta^{18}O$ measurements, this section is bypassed with a 1/8" SST tubing connecting valves L2 and L7.This section includes:
    1. a Gas Chromatography column
    2. two focusing traps: a Full Air trap (T3) to focus the N_2 -O_2 -Ar mixture before introduction to the GC and a O_2 trap (T4)
    3. a He line providing the carrier gas needed for gas chromatography separation
    4. a Thermal Conductivity Detector (TCD, Vici, USA) to control the elution time of O_2 and N_2 .

Quality check — Stable temperature and pressure conditions are critical for quality measurements.

Two pressure gauges PG1 and PG2 (Pirani, Edwards) monitor the pressure in the system. PG1 is located between the extraction and purification section and PG2 between the separation and collection section. They are both located before a valve controlling the access to the pumping system. Typical measured vacuum background pressures are typically under range, with $P_{ur} < 10^{-3}$ Pa. All 4 traps, the extraction and GC units and a section of the line are equipped with K-thermocouples to monitor the temperature. Cooling elements (extraction unit, GC) and heating ropes (T2, T3, T4, GC, line) are connected to in-house PID controllers to ensure stability of temperature conditions (see details in section 3.4 and 3.5).

Inner surfaces and contamination

Almost all inner surfaces of the experimental line are made out of SST and are connected together either with Viton O-rings or SWAGELOK connections. A few wetted surfaces, typically the stem tips of some valves are however made in polytetrafluoroethylene (PTFE, commonly called Teflon).

3.4 Extraction, purification and collection units

3.4.1 Vacuum system

Vacuum background pressures are typically $< 10^{-5}$ mbar as measured on the two Pirani gauges (lower limit of detection: $< 2 \cdot 10^{-5}$ mbar). High vacuum ($< 10^{-5}$ mbar) is provided by a turbomolecular pumping station (HiCube, Pfeiffer, Germany) backed by a oil-free diaphragm pump integrated in the pumping station. This rough pump cannot be used to provide low vacuum (> 0.1 mbar) as the turbo pump would need to be switched off and on depending on the pressure in the system. Therefore, a rotary vane pump (EDM2, Edwards, USA) is connected to the vacuum line and is used whenever important amount of gases need to be rapidly removed from the analytical line[1]. Evacuation takes place through 1/4" or larger SST tubes. The pumping system is connected to the main analytical line (where the sample is processed) through the 2 valves P1 and P2. This allows pumping upstream and downstream of the separation unit.

3.4.2 Standard introduction unit

3.4.2.1 Respecting the principle of identical treatment

Werner and Brand (2001) pointed out the importance of respecting the IT principle for accurate isotope analysis. Not only the sample and the standard should go through the same steps during the collecting and measuring steps, but the standard also needs to closely resemble the samples to be measured against, with an isotopic ratio close to the one of the samples. In addition, it should be in a stable form, homogeneous, easy and safe to handle and transport. For ice core analysis, real ice with ≃10 % of air of known composition would be the perfect standard. As such a standard has not

[1] This rough pump is also used for evacuation of the vacuum casing of the cryocooler.

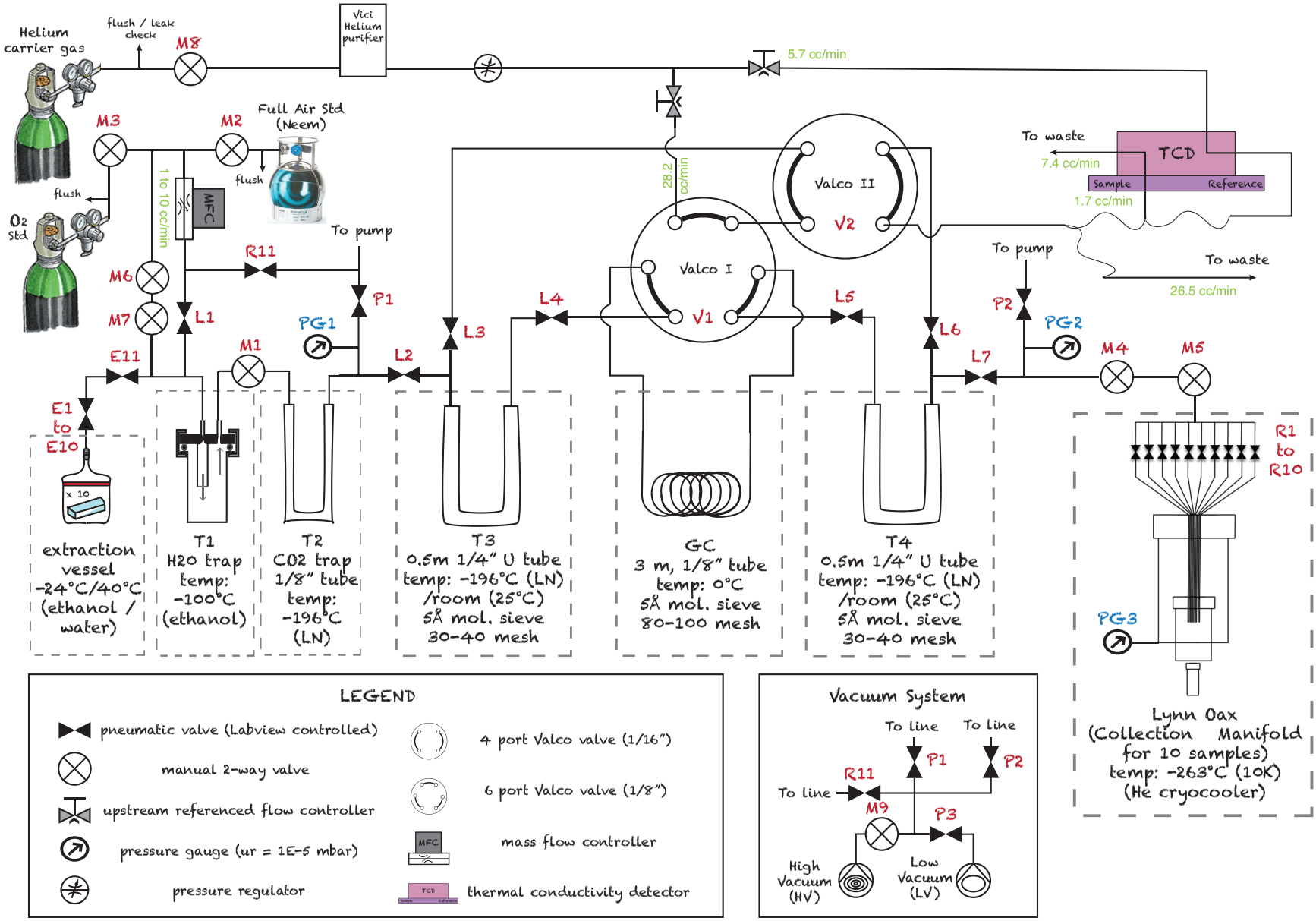

Figure 3.2 – Schematic representation of the analytical system for triple isotope oxygen collection built during this PhD thesis. It is based on Barkan and Luz (2003). The setup is semi automated and consists of an extraction, purification separation and collection section.

been produced hitherto, the next best reference strategy consists in introducing an air standard on top of bubble-free ice (noted BFI hereafter), i.e ice that contains no air at all. At CIC, we produce BFI by degassing milli-Q (ultrapure) water under vacuum through a water trap while heating and stirring it. The evacuated vessel is then closed and brought to a -15°C cold room. The vessel is wrapped into a heated blanket (heating wire wrapped around a copper sheet) to maintain a temperature of 4°C. Then the water is slowly frozen from the bottom up at a rate of $\simeq 10cm \cdot day^{-1}$ to ensure that dissolved gases can diffuse faster than the ice grows.To avoid supercooled water to form, some tapwater is added for the ice crystals to have a site to nucleate. It however turned out that the BFI we tested for standard measurements still contained too much air, despite the absence of visible bubbles, which lead to unreliable results when standard air (NEEM air) was introduced over BFI, and we describe in section 3.7 the strategy used to overcome this issue.

3.4.2.2 Gas standards

Reference materials consists of natural minerals or compounds with desired isotopic composition, chemical purity, stability and homogeneity (Gonfiantini et al., 1995). They are the primary reference materials (noted PRMs hereafter) against which raw data are expressed and enable inter-laboratory comparisons. PRMs are certified by the IAEA or NIST for different isotopes and do not have associated uncertainties. For instance, IAEA defines by consensus the origin of the δ scale such as the Vienna Standard Mean Ocean Water (VSMOW, with the NIST material code RM 8535a), thus with $\delta^{18}O_{\ VSMOW} = 0‰$ and $\delta^{17}O_{\ VSMOW} = 0‰$. As a matter of fact, VSMOW was a calibration standard that has become de facto the PRM to express hydrogen and oxygen water stable isotope variations in replacement of the PRM SMOW (Craig, 1961), which was never physically available (Gonfiantini et al., 1995). Note that VSMOW2 has recently become the new PRM to replace VSMOW, exhausted. Contrary to VSMOW, VSMOW2 has a combined standard uncertainty associated to δ^2H and $\delta^{18}O$ reference values (IAEA, 2009). REFERENCE MATERIALS

Dried atmospheric oxygen is the PRM for molecular oxygen isotopic ratio ($^{18}O/^{16}O$, $^{17}O/^{16}O$). $\delta^{18}O$ and $\delta^{17}O$ values are hence defined as 0 ‰. Its abundant availability and spatial homogeneity (due to the long residence time of oxygen (>1200 yrs) relative to the inter-hemispheric mixing time in the atmosphere (1 yr)) are the main advantageous characteristics of this PRM. ATMOSPHERIC O_2

The PRMs are often valuable materials of finite quantity that may not always be in an appropriate chemical form for simple isotope standardization or that are not sufficient to fix the scale expansion/contraction of the analytical methods employed (Berhanu, 2013). The calibration materials, or secondary reference materials, are carefully calibrated versus the PRMs, and the calibration values are internationally agreed and adopted (Gonfiantini et al., 1995). These calibration standards have been developed along the years to fill these gaps and their δ values and associated uncertainties CALIBRATION STANDARD

can be found here. Calibration standards can thus be accurately normalized to international scales as they are anchored to the primary standards.

WORKING STANDARDS

Another important distinction lays between primary and calibration standards on one hand, and working, or in-house standards, on the other hand. Primary or calibration standards are generally too rare to be used on a daily basis. Instead, working standards are calibrated against the formers. In the case of atmospheric O_2 , abundance is not an issue though. According to Carter and Barwick (2011), in-house standards must be homogeneous, easy and safe to store, handle and transport, stable during storage, abundant and easily replaceable and non hygroscopic.

NEEM AIR

A working standard thus needs to closely resemble the samples to be measured against, with an isotopic ratio close to the one of the samples. It should be in a stable form, homogeneous, easy and safe to handle and transport. An atmospheric air tank was sampled in the year 2008 at a clean-air site of the NEEM camp in northwest Greenland (Sperlich et al., 2013). For stable oxygen isotopes measurements, this dried atmospheric air from NEEM is used as a PRM standard but also as a working standard, owing to its abundance. It indeed respects all required criteria in terms of origin: NEEM is a remote source far from polluted areas, and its elemental (N_2 , O_2 , Ar) and isotopic composition is close to the one of the measured sample, given its long-term stability owing to the long residence time of O_2 in the atmosphere.

INTERMEDIATE STANDARD

To respect the principle of identical treatment as closely as possible, the working standard is treated as a sample, going through all the steps that the latter experiences. Collected samples and standards are then introduced in the sample bellow of the MS. They are then measured against an intermediate standard introduced in the standard bellow of the DI system. This intermediate standard is the same as the working standard for $\delta^{18}O_{atm}$ measurements (NEEM air), and an O_2 -Ar mixture (or pure O_2 when oxygen separation was achieved with the perovskite membrane) for $^{17}\Delta_{atm}$ measurements, so as to closely match the elemental and isotopic composition of the gas mixture introduced in the IRMS. It should be mentioned that this intermediate standard is only used as a transition step to relate the sample to the working standard (see Sect. 4.5.5), and it is therefore not necessary to know its isotopic composition.

3.4.2.3 Gas standard introduction unit

The full air working standard Neem_S1 is stored in a 3 l Silco can (Restek, USA) to ≃2.5 bar. It is filled from the high pressure tank Neem_C1. To check if fractionation occurs during the transfer, Neem_S1 is measured against Neem_C1 after filling[2]. If the oxygen stable isotopic ratios are identical between Neem_S1 and Neem_C1 within the uncertainty of measurements performed, the standard transfer is validated, and the Silco can is connected to the reference inlet of the experimental system (attached

[2]measurements are performed in DI mode, Neem_S1 being introduced to the sample bellow, and Neem_C1 to the standard bellow

to valve M2 in Fig. 3.2) and the line located between the Silco can valve and valve M2 is purged. Between measurements, the line upstream the MFC is conditioned by filling it with Neem_S1 standard.

Pure O_2 working standards are stored in a high pressure cylinder and permanently hooked up to the main line via valve M3 (Fig. 3.2). It should be mentioned that all high pressure cylinders are equipped with high purity regulators (Y13-C444A, single stage, stainless steel with Kel-F and Teflon seals, Airgas, USA).

STANDARD INTRODUCTION

In our setup, the standard is introduced in the glass flask under vacuum via a mass flow controller (MFC) set to 2 ml·min^{-1}. At this flowrate, no mass-dependent elemental or isotopic fractionation should occur as viscous flow conditions prevail, inlet pressure (the pressure upstream the cryoccoler) being higher than 2 bar. Knudsen or molecular diffusion would only be an issue at inlet pressures 4 orders of magnitude lower (Fig. 3.1). The line upstream the MFC is flushed 3 times prior each standard introduction. As the flow through the MFC is low, a high flow pathway (including valves M6 and M7) is used to evacuate the line upstream the MFC after flushing (Fig. 3.2). More details are given on Section 3.7.

3.4.3 Extraction Unit

EXTRACTION TECHNIQUES

Three main techniques exist for extracting gases from ice cores, all undertaken under vacuum. Melt-extraction is the oldest and most common technique, and have been used for gases such as O_2 , N_2 , Ar and CH_4 . In contrast, gas species like CO_2 require dry extraction techniques (needle-crusher[3], ball mill, ice mill, cheese-grater) due to their high solubility (see Table 3.1) in water caused by oxidation of organic acids or carbonate (CO_3^{2-}) dissolution (Leuenberger et al., 2002) in acidic ice, i.e. the hydration of CO_2 to form carbonic acid (H_2CO_3). A third technique is based on sublimation of ice to prevent chemical reactions between extracted gases and water, but this limits the sample throughput as the extraction process is much slower. A major difference between the 3 techniques relates to the extraction efficiency. The dry extraction does not allow 100 % of the sample to be collected, but fractionation can be avoided by careful conditioning of the extraction unit (Leuenberger et al., 2002). With melt-extraction or sublimation techniques, a close to 100 % extraction-efficiency theoretically prevents isotope fractionation as all the air is extracted.

MELT EXTRACTION

Melt-extraction is straightforward and was thus the first technique applied to extract fossil air occluded in ice core bubbles. It is still successfully used for $\delta^{18}O_{atm}$ measurements (e.g. Capron et al., 2010) . Several melt extraction methods have been developed, from simple melting, vigorous stirring of the meltwater, to melting with subsequent refreezing of the sample (melt-refreeze technique). Sometimes, the sample is refrozen 3 times from the bottom to force the dissolved air above the water body. The different methods of melt extraction all follow a similar goal, maximizing

[3] At CIC, CO_2 is extracted thanks to a indium sealed needle-crusher unit.

Figure 3.3 – The design of the extraction flask was chosen to minimize the volume of the extraction flask while keeping an easy access for ice samples. A bottom-rounded glass vessel was chosen to favor a higher exchange surface between the melt water and the headspace.

extraction efficiency. Indeed, a quantitative transfer implies no fractionation during the extraction process. Depending on the considered gas specie, a substantial fraction of the extracted gas dissolves in the melted water, and reducing this dissolved fraction explains most of the aforementioned developments in the melt extraction technique. The solubility of a gas specie is controlled by the temperature (T) of the water body and by the partial pressure of the gas specie over the water body. For instance, about twice as much oxygen ($14.6 mg \cdot l^{-1}$) dissolves at 0°C than at 20°C ($7.6 mg \cdot l^{-1}$) (Emsley, 2011). We varied several parameters to determine the optimal gas extraction conditions depending on the focus of the measurements ($\delta^{18}O$ only or the three O_2 stable isotopes). Refer to the protocol section 3.7 for details.

EXTRACTION VESSEL

Twelve identical glass vessels (Fig. 3.3) were made in the glassblowing workshop of IMAU, (Institute for Marine and Atmospheric Research, Utrecht, The Netherlands, contact: Wim Nieuwenhuis). The extraction vessel consists in a bottom-rounded 210 cm^3 borosilicate glass vessel. A Teflon centering ring (NW 50) with Viton O-ring and a clamp made out of high temperature plastic seals the bottom and upper part of the glass flask on its wider diameter (50 mm). The ice sample fits on the bottom part of the glass vessel. The upper part ends with a 6 mm glass tube, connected to the collection setup with a SWAGELOK1/4" Ultratorr fitting with Viton O-ring. Note that these unions are nickel-plated to prevent corrosion as they are often in contact with water. The Ultra-Torr fittings are attached to a 1/4" pneumatically actuated bellow-sealed valve (SS-4BK-1C, SWG), operated under Labview through dynamic link function libraries (noted DLL hereafter) of cheap (compared to Labview acquisition cards) but very functional control boards (PC-control, UK) (see Sect. 3.6).

Table 3.1 – Properties of main atmospheric gases. In general, the lower the boiling point, the higher the partial pressure of the considered gas at any given temperature. Solubility decreases with increasing temperature: the solubility of a gas at 0°C is thus close to its maximal value.

Gas	molar mass $g \cdot mol^{-1}$	concentration in air % (by vol)	melting point °C	boiling point °C	solubility at 0°C vol/vol (STP)	molecular size[a] 10^{-10}m
O_2	31.999	20.946	-218.79 (54.36 K)	-182.96 (90.19 K)	0.0489	3.467
N_2	28.013	78.084	-210.00 (63.15 K)	-195.80 (77.35 K)	0.02348	3.798
Ar	39.948	0.924	-189.37 (83.78 K)	-185.85 (87.30 K)	0.0537	3.542
CO_2	44.01	0.04	-56.57 (216.58 K)	-78.45 (194.70 K)	1.7163	3.941
CH_4	16.043	0.00018	-182.46 (90.69 K)	-161.48 (111.67 K)	0.054	3.758

[a] Severinghaus and Battle, 2006

SIMULTANEOUS EXTRACTION

A SST vessel, built by the CIC workshop, is filled either with cold ethanol or warm water. Ten extraction flasks can be simultaneously immersed in the vessel. The design allows its double wall evacuation thanks to a low vacuum (LV) rotary vane pump (Edwards, EDM2) to reduce heat exchange with the environment. 50 l of pre-cooled ethanol in a −25°C freezer are required to keep the samples frozen during overhead evacuation of the extraction flasks. Unfortunately, the available immersion cooler chiller (NESLAB CC-100 coldfinger) did not have the cooling capacity sufficient to keep such a mass of ethanol within the optimal temperature range (−22°C to −24°C). Additionally, the thermal gradient in the ethanol bath was too important between the 10 extraction flasks despite vigorous stirring. Finally, we were unable to prevent leakage to occur when many extraction flasks were simultaneously connected to the collection system. Resolving this issue remains critical to achieve a full automation of the collection system, as it requires some of the extraction vessels to remain sealed for a few hours.

SINGLE EXTRACTION

We thus opted for a one-by-one sample extraction system. During evacuation the bottom part of the extraction vessel is submerged in an ethanol dewar. Ethanol is kept between −22°C and −24°C with a temperature controlled NESLAB coldfinger. Within this temperature range, sublimation causes a water vapor flow to effectively remove any gases adsorbed onto the ice surface during the evacuation process (Severinghaus et al., 2003). Meanwhile, such a low temperature prevents the sublimation rate from being too high to cause substantial loss of the sample. Additionally, the sweep out of the extraction vessel becomes more efficient.

Temperature is measured with a K-thermocouple and regulated by a proportional-integral-derivative (noted PID hereafter) controller (CN7500, OMEGA), which switches on and of the NESLAB coldfinger. We chose a 4°C temperature range to minimize the on-off cycles undergone by the chiller while ensuring a reasonable sublimation rate (Fig. 3.4). Since the density of ethanol decreases monotonically with temperature, unlike water, vertical thermal gradient within the dewar can easily form.

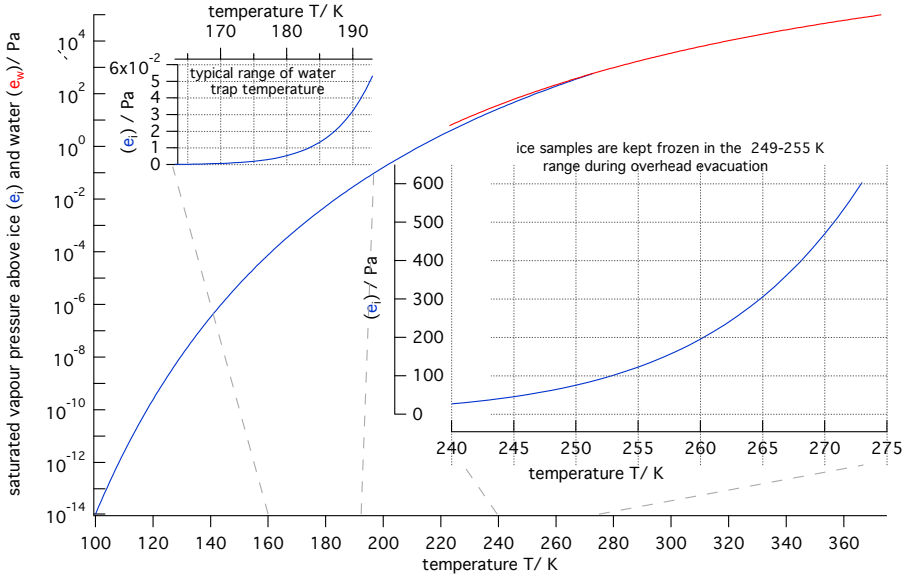

Figure 3.4 – Saturated vapor pressure (in *Pa*) above water (e_w) and ice (e_i) (log scale) vs temperature (in *K*), using Murphy and Koop (2005) formula for e_i and World Meteorological Organization No. 49, Technical Regulations, Basic Documents No. 2, Volume I, General Meteorological Standards and Recommended Practices, Appendix A formula for e_w. Note that the red curve extending below 273 K represents saturated vapor pressure over supercooled water, slightly higher than e_i. The stacked windows zoom on temperature ranges relevant for O_2 extraction and cryotrapping of H_2O .
(**lower right panel**) During the extraction process, saturated vapour pressure above the ice sample reaches up to 1 mbar at −20°C, creating a sublimation flux that helps cleaning of the ice sample surface and pumpdown time (Section 3.4.3). e_i is also used as a thermometer as its value is exclusively dependent on the temperature of the ice body above which it is measured. The temperature of the ice sample is thus more accurately estimated with e_i than with a thermocouple measuring the temperature of the ethanol bath, separated from the ice sample by a glass vessel.
(**upper left panel**) Water vapour is trapped in a SST cylinder kept at a temperature ranging from −85°C to −110 °C. At these temperatures, sublimation provides a few hundredths of Pa to the total pressure measured in the line.

At the bottom of the dewar, a waterproof fan (Trevor Popp recovered it from an antic experimental setup at CIC) prevents ethanol stratification.

3.4.4 Water trap

TEMPERATURE Water vapour is trapped in a SST cylinder (trap T1 in Fig. 3.2) kept at a temperature ranging from −85°C to −110 °C. The coolant consists of ethanol cooled down

to $-110°C$ with LN_2. When it gets close to its melting point ($-114°C$), ethanol turns to slush. The increased viscosity of ethanol at low temperatures combined with higher density further inhibits mixing in the dewar, which results in a thermal gradient along the water trap. Temperature is therefore measured with 2 K thermocouples at the bottom and the top of the ethanol-filled dewar, and manual stirring is performed when the temperature gradient exceeds 5 to 10°C.

Some water still remains in the extraction line even after the water trap, since the freeze out occurs at around $-90°C$ at which temperature e_i is 0.00969 Pa (10^{-4} mbar) using equation (7) [4] of Murphy and Koop (2005) (Fig. 3.4).

CLOGGING

The design of the water trap strongly evolved during the course of the PhD thesis. The initial water trap was a 1/4" tube filled with glass beads but the capacity was too low. A similar problem arose with the second water trap, similar to the current one but with a smaller height. The trap consisted of a one closed-end SST cylinder (40 mm ID) sealed with a blank flange (DN 40 ISO-KF, Pfeiffer vacuum, Germany) drilled all the way through and connected to a 1/2" SST tubing ending 2 cm above the bottom of the SST cylinder. The cylinder and the blank flange were sealed with a compression O-ring. The trap had a too low volume to allow more than one ice sample to be processed before clogging, because of water freezing within the inner 1/2" tube. The lower limits of the 2 SingleGauge Pirani Transmitter PG1 and PG2, located after the water trap, were quickly reached ($< 5 \cdot 10^{-5}$ mbar), the frozen water acting as a seal between the extraction unit and the remaining part of the system. The third water trap was similar in shape as the first one, but 7 cm longer to increase its volume, hence its capacity to collect water. However, it would either get clogged, a plug of ice forming at the end of the SST 1/2" inner tubing, or on the contrary too much water vapor would escape the water trap, when slightly lowering the ethanol level in the dewar. This resulted in high water levels in the collected samples.

DIAGNOSIS

To prevent water vapour from escaping the water trap, we filled the latter with glass beads (⌀2 mm). By increasing the distance the gas had to travel in the water trap, the probability of freezing the water vapour should increase. However the water trap would quickly clogged by a layer of frozen water right on top of the beads, suggesting that instead of capacity, it was rather (i) the rate of water vapour transferred at a time through the water trap that was too large, and (ii) the inlet (1/2" SST tubing) temperature of the water trap that was too low, freezing water vapour before it would reach the glass beads. To solve these issues, two changes were implemented:

- **Water flow.**
  The 1/4" SST tubing connecting the extraction unit to the water trap was reduced to 1/16". It aimed at reducing the amount of water vapour reaching the water trap at a time, hence lowering the probability that a ring of frozen water would form immediately at the water trap inlet. It turned out that it significantly

[4] $ln(e_i) = 9.550426 - 5723.265/T + 3.53068 \cdot ln(T) - 0.00728332 \cdot T$ Pa, with T in Kelvin and e_i in Pa.

reduced the transfer time of the sample too, the flow of water vapour through a 1/16" line acting efficiently as a carrier gas for the released fossil air (Severinghaus et al., 2003). This can be explained by the reduced ratio between free-mean path of a molecule and the cross-section diameter of the tube (Knudsen number), which implies an increasing number of collisions between air constituents and water vapour molecules. Additionally, this change minimized the risk of gas occlusion under the freezing water vapor that can occur when a large amount of water is transferred to the water trap (Headly and Severinghaus, 2007).

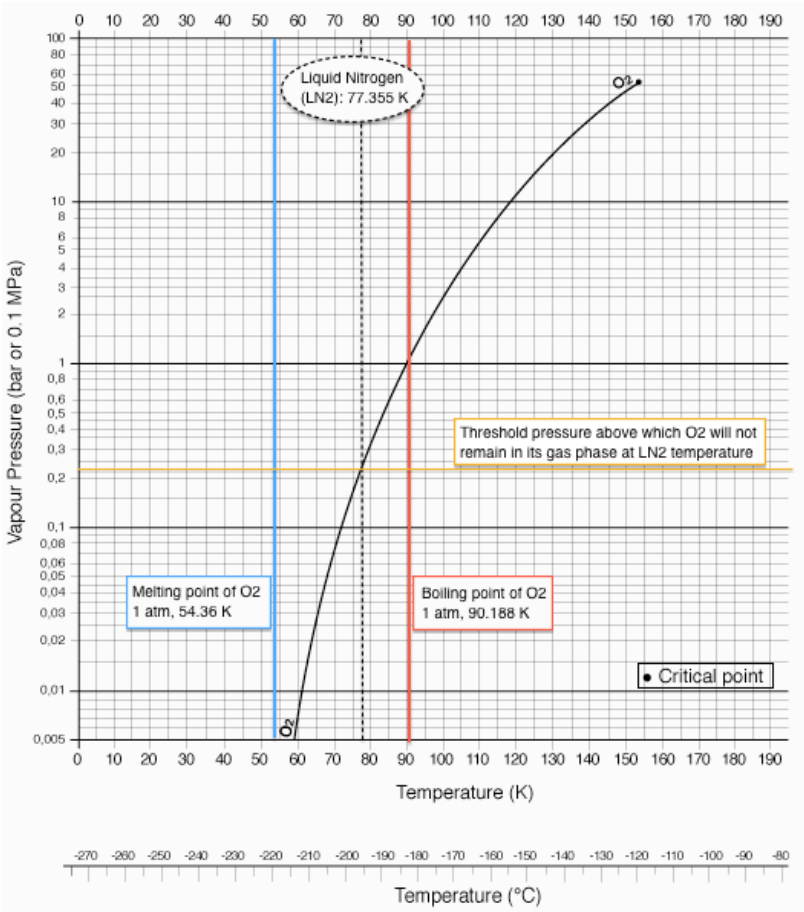

Figure 3.5 – (**black curve**)Oxygen vapor pressure curve from Air Liquid (http://encyclopedia.airliquide.com/images_encyclopedie/VaporPressureGraph/Oxygen_Vapor_Pressure.GIF). The critical point is indicated by a black spot on the liquid-vapor equilibrium curve.(**red line**) Boiling temperature of O_2 at atmospheric pressure. (**blue line**) Melting temperature of O_2 at atmospheric pressure. (**dashed black line**) Liquid Nitrogen (LN_2) temperature. At 77 K, O_2 would be liquid at atmospheric pressure. (**yellow line**) To ensure that O_2 remains in its gaseous phase at LN_2 temperature, the total pressure of the sample in the system must be kept below 0.2 atmosphere. This condition is largely met as the system has a volume of a few hundreds of cm^3, 2 orders of magnitude higher than the volume of any air sample (up to 4 cm^3).

- **Temperature.**
  The line connecting the extraction unit to the water trap was heated with a rope heater (FGR-060, Omegalux, UK) to the set temperature of 50°C, regulated by a PID controller (CN7500, Omegalux, UK). It ensured that freezing of the water vapour would not occur immediately after entering the water trap.

3.4.5 CO_2 TRAP

CO_2 needs to be excluded from the extracted air mixture:

- As for $^{17}\Delta$ measurements, the O_2 -Ar mixture needs to be separated from N_2 to obtain precise measurements. Indeed, measuring a pure gas avoids pressure effect and isobaric interferences in the MS. Besides, this separation step requires to remove CO_2 , as the material in the gas chromatography (GC) column used for N_2 -O_2 separation tends to trap CO_2 (Section 3.5).
- As for $\delta^{18}O_{atm}$ measurements in air, the presence of CO_2 in the MS can lead to isobaric interference with N_2 isotopes. Indeed, formation of $^{13}C^{16}O$ may affect the measurements of $\delta^{15}N$, measured on m/z 29. As for O_2 measurements, $^{14}N^{18}O$ can be created in the ion source and is isobaric with $^{1}6O_2$, but the error introduced is very small as $^{1}6O_2$ is abundant.

Just after the water trap, the trap T2 (Fig. 3.2) is set to LN_2 temperature and freezes out CO_2 . Indeed, with a boiling point at -78.45°C STP, CO_2 freezes out at LN_2 temperature[5], even at the low pressure of the operating system (a few tens of mbar).N_2 and Ar, with a boiling point close to the one of O_2 (Table 3.1), remain also in their gas phase at the system pressure (Fig. 3.5).

Besides its primary function, the CO_2 trap acts as a secondary trap in case water vapour remains in the system after the water trap. We are aware that gases may adsorb on ice at LN_2 temperature. However, at -100°C (temperature of the water trap), water vapour pressure only amounts to $\backsimeq 10^{-2}$ Pa (Fig. 3.4). Hence adsorption of the fossil gases on ice should be avoided given the extremely low water content.

3.4.6 COLLECTION UNIT

3.4.6.1 Closed cycle He cooler

3.4.6.1.1 Motivations

The reasons we decided to use a closed cycle refrigerator are manyfold[6]:

- Short sample tubes can be used (Kawamura, pers. comm, 2010).

[5] N_2O is also trapped at this temperature, as it has nearly identical physical properties

[6] We did not consider to trap O_2 with molecular sieve at LN_2 temperature as Barkan and Luz (2003) showed that the adsorption process is not complete, and found out that measured $\delta^{18}O$ and $\delta^{17}O$ are lower than true values. The same holds true for the O_2 /Ar ratio.

- It is more convenient than liquid helium as the only need is electricity. The reservoir of He within the compressor has not been refilled since its installation in 2010.
- It is safer as a helium cryocooler does not require handling of liquid helium.
- Cost of the product is reimbursed only after a few years of use, as no liquid He is required. Obviously, it varies according to the costs of electricity and liquid Helium, and recent years have shown how pricy the latter has gone.

3.4.6.1.2 Design

The cryogenic cold head (CH-204SFF) and water-cooled He compressor (HC-4E) were purchased at Sumitomo (SHI Cryogenics, Japan) together with the He gas lines for ≃ 8000 euros. The CH204SFF cold head is a two-stage cryogenic refrigerator that operates on the Gifford-McMahon refrigeration cycle. The cold head uses helium gas (99.995% purity) from a He compressor to produce the cold temperatures. Electricity to power the cold head's valve motor is supplied from the compressor by the cold head cable (Sumitomo manual). We exchanged closely with a cryogenic engineering company called AS Scientific (contact Colin Hillier) who have long experience with manufacturing systems specifically designed for a particular purpose. The design of the cryocooler needed to meet the following criteria:

- Trapping temperature: 12 K. Such a temperature is a good trade-off between performance and price. Cooling 10 tubes at 4 K is possible but requires huge power. A 12 K refrigerator is powerful enough for trapping gases like O_2 , and a lot less expensive. The performance of the refrigerator is determined by the power of cooling unit, the size of cooling chamber and the amount of heat intrusion from outside (radiation, conduction), and thus require specific design and dimensions (Fig. 3.6)
- Minimal volume for the collection tubes. The length of 1/4" tubes must be as short as possible, because the amount of O_2 trapped is further expanded into the 40 ml bellow of the MS. However, the longer the tubes, the less heat conducted from outside to the second stage cold station (see Sect. 3.4.6.1.4).
- Heat load. Dimension and volume of the tubes of the collection manifold control the heat transferred by conduction to the cryocooler (see Sect. 3.4.6.1.4). Furthermore, the mass of copper needs to be minimized to reduce cool down times. While the specified cooling time of the cold head to 20 K is 40 min, it takes 50 minutes more to reach 10-12 K.
- Cleanness. All 10 tubes were assembled in a copper block and vacuum brazed to ensure that the inside of the tube is kept clean.
- Mobility. A few cryocoolers allow the removal of a single sample tube while the cryocooler is still operating. This makes it significantly more functional (and

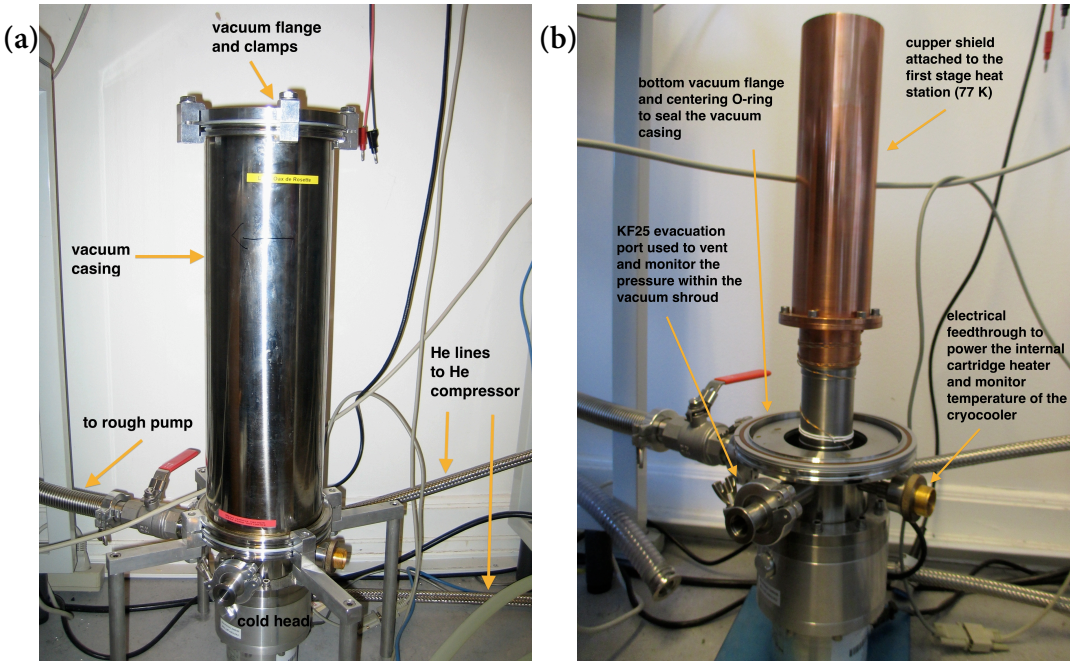

Figure 3.6 – **(a)**Vacuum casing in which the collection manifold (LynnOax) is cooled to 12 K. Vacuum flanges and clamps are used to connect LynnOax to the cryocooler. The vacuum shroud can be evacuated with a rough pump to 10^{-3} mbar. Also shown are the gas lines connecting the cold head to the water-cooled He compressor.**(b)** Similar as in **(a)** without the vacuum casing. A copper shield conducts cold from the first stage heat station (77 K) to the rods of the collection manifold. The polished copper (emissivity $\varepsilon = 0.03$) also acts as a radiation shield, which reduces radiation loss to the second stage cold station.

expensive) but is actually not necessary for our experiment. Indeed, mass spectrometry measurements require stable conditions, which are more likely to be respected if samples are measured within a short period of time. As extraction and collection of samples is time-consuming, it is preferable to first collect the samples offline and measure them together. On the first design, the copper block would be flanged to the 2nd stage cold station of the cooler. However, this option was discarded as it would prevent an easy removal of the collection manifold from the cryocooler. Rather, thermal grease is used to ensure a good thermal contact between the copper surround block of the collection manifold and the copper cup connected to the second stage cold station (Fig. 3.7a). Note that the pressure difference created during evacuation of the vacuum casing after LynnOax is inserted in the cryocooler helps connecting the 2 copper blocks.

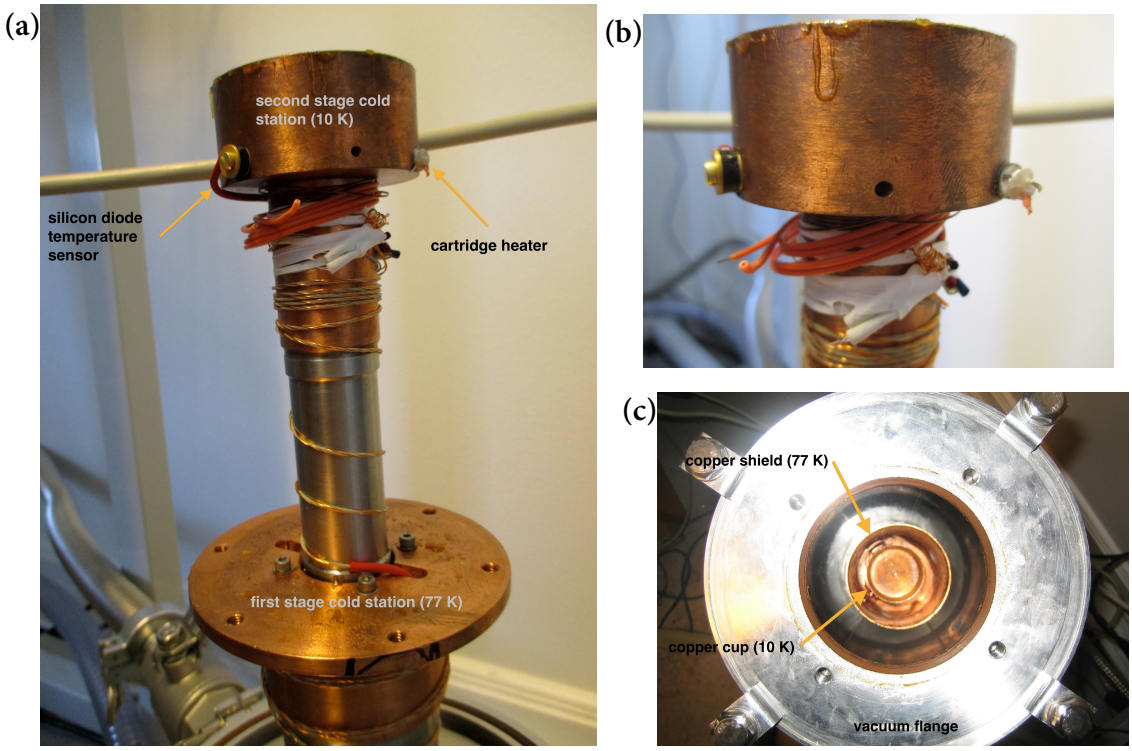

Figure 3.7 – **(a)**The copper cup connected to the second stage cold station (12 K) is reached by removing the copper shield flanged to the first stage cold station. The silicon diode temperature sensor and the cartridge heater attached to the copper cup are shown. Note however that they are not wired, the figure being taken after both cease to function due to mechanical stress. **(b)** Zoom on the second stage cold station where the damage caused on the leads can be seen. The failure occurred during the removal of the collection manifold by rotating it. Being still too cold, the solid thermal grease forced the copper cup, screwed to the cold station, to rotate together with the collection manifold. This lead to the breakage of the leads of the cartridge heater and silicon diode temperature sensor as they are wrapped around the the copper cup on which LynnOax's copper block is incrusted. The silicon diode leads could be soldered again but the cartridge heater needed replacement. It is thus very important to wait for the thermal grease to soften by allowing more warming time - and not to use an excessive amount. **(c)**Top-view on the vacuum flange through which LynnOax is inserted into the vacuum casing of the cryocooler. Also shown are the copper shield and copper cup.

- Thermal stability. The copper surround block (Fig. 3.8a) needs to have high purity to give thermal stability to the stainless tubes. To ensure homogeneous thermal distribution, each SST tube needs to be surrounded by copper to avoid contact between them, which however increases the copper block's mass, thus increasing the time needed to reach 12 K.

- Faster heating of the collection manifold to room temperature is achieved thanks to an internal cartridge heater fitted into the copper cup of the cryocooler (Fig. 3.7). Refer to Sect. 3.7.2.2 for details.

3.4.6.1.3 *Instrumentation collar*

The instrumentation collar includes thermometry devices, an electrical feedthrough and two KF25 evacuation ports. A rough pump is attached to one port via a manual on-off valve (red handle on Fig. 3.6). The pressure is monitored with a pressure gauge attached to the second KF25 port. This port is also used to vent the vacuum casing of the cryocooler. The thermometry is wired to the second stage heat station through an electrical feedthrough (Fig. 3.8b). It consists in a silicon diode temperature sensor (DT-470-CU-12A, Lakeshore) and cartridge heater (40V, 40 W). The silicon diode temperature sensor follows the Curve 10 standard temperature response curve, describing the relation between temperature and voltage output of the silicon diode when excited by a current source.

3.4.6.1.4 *Heat load*

The final design of the cryocooler is the following: the sample holder is mounted to the second-stage heat station and a radiant heat shield mounts to the first stage heat station (Fig. 3.6). According to the specifications provided by Sumitomo, the first stage heat station provides 13.5 W at 77 K and the second stage cold station provides 7 W at 12 K (50 Hz). It is essential that the heat intake to the second stage heat station is significantly lower than the cooling capacity of the cold head. Excluding gas load, heat load is essentially due to conduction of heat within the 10 sample tubes walls and infrared radiation from the vacuum shroud. Rapid calculations show that heat transfer from outside (298 K) to the first stage heat station (77 K) amounts at max to $\backsimeq$10 W, of which 5 W arise from radiation and $\backsimeq$3.5 W from conduction. The heat transfer from the first stage (77 K) to the second stage heat station (12 K) is reduced to 0.44 W by conduction of heat along the 304 SST tubes. Indeed, radiation can be neglected given the very low emissivity of the polished copper radiation shield. In conclusion, the heat transfer does not challenge the cooling capacity of the cryocooler, as observed during experiments.

3.4.6.1.5 *Installation setup*

The cryocooler (cold head and vacuum casing in which the collection manifold is inserted) can't be moved, and is therefore located close to the experimental line, so that the collection manifold can be connected with a 1/4" 30 cm long flexible SST tube (SS-FM4TA4TA4-12H, SWAGELOK). Two manual bellow-sealed valves (SS-4H, SWAGELOK) command the access to the main line and the collection manifold (3.8b). Gas lines filled with He connect the cold head to the He compressor. To operate, the latter needs to be cooled by a constant flow of water, which is currently provided by the cold water circuit of the building in which the experiment is located[7].

[7]This improvement is essential, as In the previous setup, an air-cooled water chiller (LC3500, ICS Cool Energy Ltd, UK) provided the cold water required for the He compressor to operate. The main drawback was caused by the fact that the operation of the air-cooled water-chiller would function only

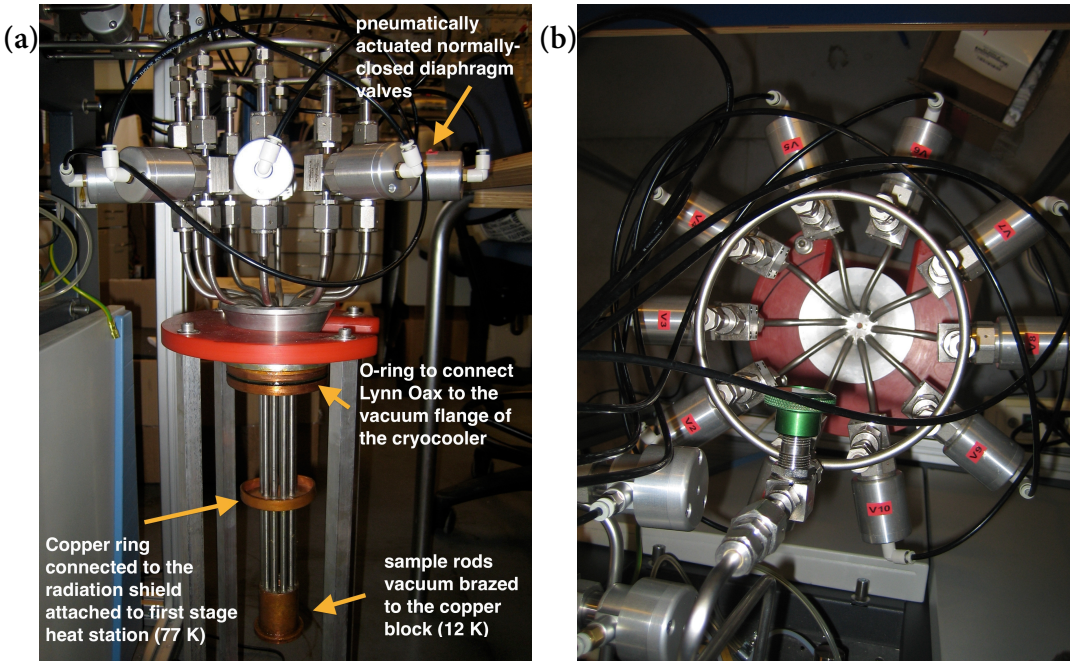

Figure 3.8 – **(a)** Profile view of the collection manifold (LynnOax). Visible are the 10 sample rods vacuum brazed to a copper block at their closed end. The copper block enables a good transfer of cold from the second stage heat station to the sample rods. An O-ring fitted in the groove of a copper block ensures a leak tight connection when LynnOax is attached to the vacuum casing of the cryocooler. **(b)** Top-view of LynnOax. A manual 1/4" valve (SS-4H, SWAGELOK) controls the access to the SST ring of the collection manifold. Pneumatically actuated normally-closed 1/4" diaphragm valves are attached to the sample tubes with VCR silver-plated gaskets.

3.4.7 Collection manifold

ORIGIN

The collection manifold can be seen on Fig. 3.8. The ten SST tubes vacuum brazed to the copper blocks were provided by AS Scientific. Bending of the tubes, connection to pneumatically actuated diaphragm valves (6LVV-DPVR4-P-C, SWAGELOK), design and building of the distributing 1/4" SST ring and welding took place at the CIC workshop (thanks to the great skills of Carsten). A manual bellow-sealed valve (SS-4H,SWAGELOK) seals the collection manifold from ambient air.

SAMPLE TUBE VOLUME

In general, 1/4" tubes ($ID = 5.3$ mm) are used but their length and volume differ widely in previous studies. When collection is achieved with liquid He, sample tubes can vary from 0.70 m ($V = 15$ ml) (Severinghaus et al., 2003) to 1.5 m ($V = 33$ ml) (Mani et al., 2008), for 4 ml of air and 2 ml of N_2 -Ar, resp. This length is required to expose a maximum of fresh surfaces to improve sample collection[8]. With a He cy-

with surrounding air colder than 25°C, which required a fan to bring cold air into the small corridor in which the water chiller was located...

[8] Severinghaus et al. (2003) lower the sample tube into the liquid helium in three stages over the course of the transfer to gradually expose fresh metal surfaces.

cle cooler, tubes can be much shorter (Kawamura, 2010, pers. comm). For instance, Kawamura et al. (2003) use 35 cm long tubes, i.e. a inner volume of 6 ml, to collect 30 ml of air. In sharp contrast, for O_2 -Ar samples (0.75 ml after N_2 separation), Barkan and Luz (2003) opted for 95 cm long 1/4" sample tubes (20 ml) to ensure a gas pressure lower than 50 mbar after warming to room temperature, observig that above 100 mbar, a significant amount of gas remains adsorbed on the walls after warming from liquid He temperatures when introduced to the inlet of the IRMS.

The samples tubes used in our experiment are 42 cm long, 1/4" in diameter (ID=5.3 mm). This corresponds to a volume of $\simeq$ 9 ml, planned to collect samples varying from 0.8 ml to 4 ml. This means that a pressure up to 500 mbar can build up in the sample tube at room temperature. By varying the size of the standards from 4 to 0.4 ml, we did not observe systematic differences in O_2 isotope ratios after conditioning of the rods, suggesting that the effect seen by Barkan and Luz (2003) does not occur on our analytical system. It should be mentioned that ice samples dedicated for $^{17}\Delta_{atm}$ measurements build up a total pressure of maximum 100 mbar after warming from 12 K, hence in the acceptable range according to Barkan and Luz (2003).

3.5 O_2 /Ar - N_2 separation unit

We rely on the classical gas chromatography method to separate O_2 and Ar from N_2 (Barkan and Luz, 2003). However, we use a different GC column to separate N_2 from the O_2 -Ar mixture, and we direct the carrier gas flow thanks to a combination of a 4-port and 6-port Valco valve (Fig. 3.2) rather than 4 three-way valves to minimize dead-volumes in the system.

3.5.1 Helium lines

High purity He ($\geq$ 99.999%, 50 l cylinder, Air Liquid, Denmark), additionally purified by a getter (Gas Purifier, VICI, Valco Instruments Co. Inc, USA), is permanently provided to the O_2 /Ar - N_2 separation unit. The total He consumption of the system amounts to $\simeq$34 cc.min^{-1} in operation, and 5.7 cc.min^{-1} at rest. Similar to the analytical system, all lines are made out of SST . He flow is regulated with a pressure controller and 2 upstream-referenced flow controllers (Bronkhorst) to provide $\simeq$28 cc.min^{-1} to the GC column and $\simeq$6 cc.min^{-1} to the reference side of the TCD (see Fig. 3.2).

3.5.2 Focusing traps

3.5.2.1 full air trap T3

Prior introduction to the GC column, the O_2 -Ar-N_2 mixture is focused on a molecular sieve trap. The full air trap T3 consists of a $\simeq$40 cm 1/4" SST U-tube filled with molecular sieve (5A, 30-40 mesh size) over 10 cm, i.e. 1.25 g of trapping material.

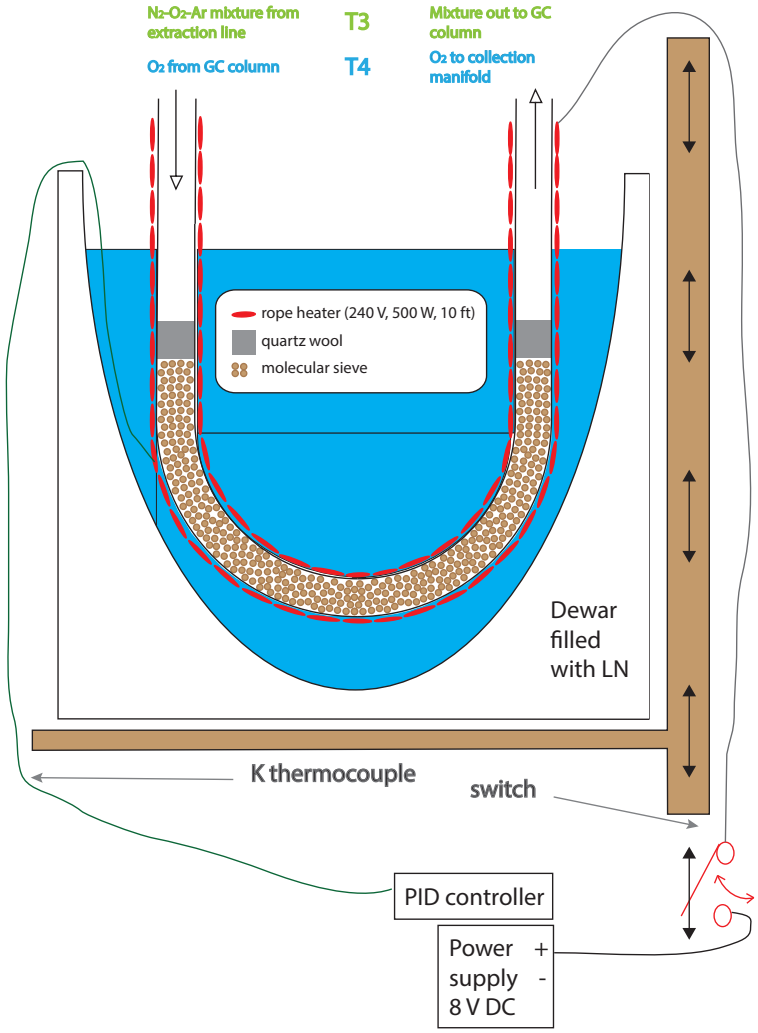

Figure 3.9 – focusing traps prior and after introduction to the GC column. Not to scale. After removal of H_2O and CO_2 , the remaining extracted gases, mainly N_2 , O_2 and Ar are focused in the trap T3 at LN temperature. The gas mixture is released by heating the trap to room temperature.

The trap is similar to the trap developed by Barkan and Luz (2003), consisting in a SST U-tube, 0.45 m x 1/4" o.d., filled to one-third of its height with molecular sieves (5 Å, 100-140 mesh). Two quartz wool's plugs (≃2 cm) hold the trap into place (Fig. 3.9). A rope heater (FGR100, 240 V, 500 W, 10 ft, Omegalux, UK) enables a fast heating to room temperature. The heating starts as soon as the LN dewar is removed, as the dewar hits a push for "on" electrical switch which enables supply of current to the rope heater (Fig. 3.9). The heating procedure is temperature controlled with a PID controller tuned to avoid temperature overshooting. It takes 30 s to reach a stable temperature after warming the trap. The molecular sieve trap is regenerated after each serie of measurements by heating it to 200°C and flushing the traps with a stream of He.

3.5.2.2 O_2 -Ar trap T4

trap T4 is identical to trap T3, in terms of design, dimensions and amount of trapping material, but is used to focus an O_2 -Ar mixture (instead of dry air) at the GC outlet.

3.5.3 Gas Chromatograph unit

3.5.3.1 GC column

The packed chromatographic column (88014-800, Restek, USA) used to separate the O_2 -Ar mixture from N_2 consists of 10 feet (≃ 3.1 m) of a 2 mm ID (1/8" OD) SST tubing[9], packed with molecular sieve material (5A, 80-100 mesh size), synthetic forms of zeolite packing. We selected a packed rather than a capillary GC column because it enables a baseline separation between N_2 and O_2 at positive temperatures with a relatively short length (3 m in our case). For comparison, Barkan and Luz (2003) also used a packed GC column with fine 5 Åmolecular sieves (45-60 mesh), but much shorter (20 cm · 2 mm ID), requiring the GC column to be cooled to −85°C to operate, which we find not practical. Note that to separate O_2 and Ar, a much longer column would be needed. PACKED GC

The basis of the separation process relies on molecular size and shape difference of analyzed gases. We selected 5A (pore size: 5 Å) instead of 13X (pore size: 10 Å) packing as the 5A packing provides greater retention, which improves the separation of O_2 -Ar and N_2 . The retention time represents the time for a compound to travel through the GC column (here defined as the time between the sample's release from trap T3 and its detection on the TCD.). Retention time is controlled by the stationary phase (molecular sieve material), the flow rate of the carrier gas (He in our case), the dimensions (length and ID) and the temperature of the GC column. The GC column's ID is constrained by the balance between separation efficiency (narrow peak) and sample capacity. RETENTION TIME

At normal temperatures, CO_2 is permanently adsorbed in molecular sieve material, and can lead to loss of O_2 -N_2 resolution. Similarly, H_2O may be trapped in the GC column and affect the retention time of the analyzed gases. Fortunately, the process is reversible, and the GC column can be reconditioned by baking it to 200°C for several hours. To avoid GC column contamination, as mentioned earlier in this chapter, trapping of water and CO_2 occurs prior to the sample introduction in the GC column in our experiment. PURIFICATION

3.5.3.2 GC box

The temperature of the GC column needs to be closely controlled, as it determines TEMPERATURE CONTROL

[9] at the beginning of the experiments, we used a shorter (1 m) GC column, but we replaced it due to a too low resolution between O_2 -Ar and N_2 .

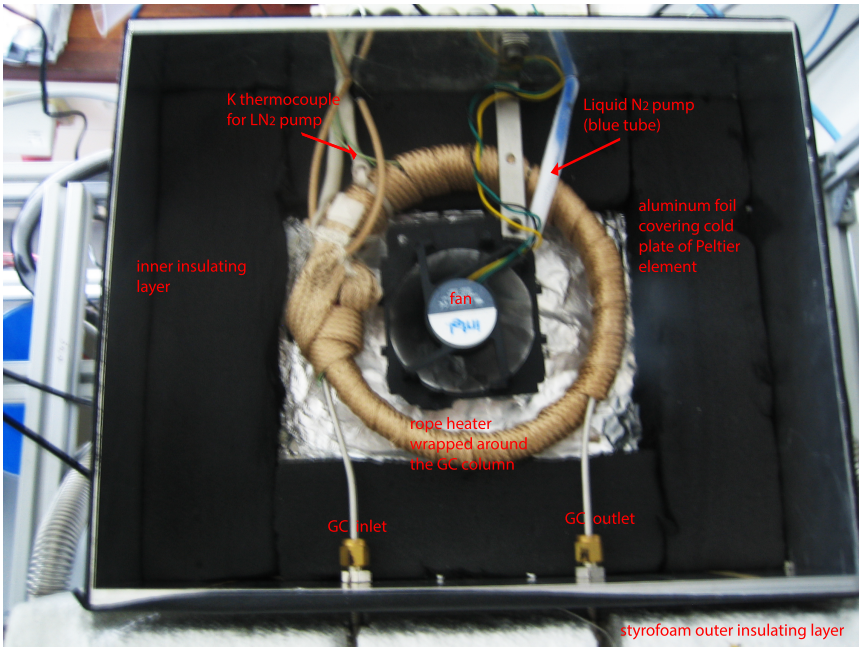

Figure 3.10 – GC column

the elution of the gases through the column. The GC column is kept at a constant temperature of 0°C. This is achieved by combining a heat pump and a LN pump.

3.5.3.2.1 *Peltier unit*

HEAT PUMP

The GC column is cooled with a thermo-electric cooler, also known as peltier element. A peltier element[10] typically consists of several thermocouples in series mounted between two thermally conductive plates. When a voltage is applied to a thermocouple, it causes a temperature difference between the 2 junctions. This is called the Peltier effect, inverse of the Seebeck effect (basis for thermocouple thermometers).

THERMO-ELECTRIC ASSEMBLY

In our setup, the peltier unit consists of the peltier element itself, a massive heat sink blown by a fan (24 V, 0.35 A) to improve the dissipation of heat, and an insulated SST box (built at the CIC workshop) sitting on the cold anodised aluminium plate of the peltier element (Fig. 3.10). An advanced programmable PID temperature controller (PR-59 Series, Supercool, Sweden) enables a precise temperature control of the GC box by comparing the temperature measured by a platinum resistance temperature (PT1000) with the targeted temperature (≃ 0°C) and regulating the power applied to the peltier element (maximum load: 240 W, 30 V, 8A).

[10]The main advantage of a peltier element is its ability to cool below ambient temperature. However, peltier element's efficiency drops off as the input power rises, often consuming more power than they transport (hence the need of a massive heatsink).

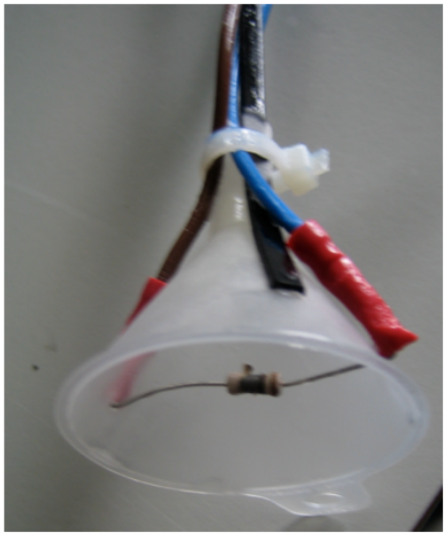

Figure 3.11 – An electric current passes through the 10 Ω resistance immersed in a LN dewar. The hot heating element, thanks to the Leidenfrost phenomenon, enables LN droplets at −196°C to be carried in their own vapour cushion through a plastic tubing at near ambient air temperature to the GC box without vaporizing within the tubing.

3.5.3.2.2 *LN_2 pump*

Besides the peltier unit, a LN_2 pump provides additional cooling to the GC box (Fig. 3.10). This LN_2 pump significantly reduces the time needed to cool the GC box. It was added while the former GC column was still in use for 3 main reasons. MOTIVATION

- To improve cooling efficiency of the peltier unit. Indeed, the cold plate is very sensitive to change of air temperature. Once exposed to warm and moist lab air, it takes a long time to cool the GC box down. By lowering the air temperature within the GC box, the targeted temperature is reached quickly.
- To reach negative temperatures that the peltier element could not reach alone. Indeed, condensation of water vapour trapped in the insulated GC box releases latent heat during cooling, which increases significantly the time needed to reach negative temperature. It takes up to 1 h for the temperature of the GC box to reach below 0°C.
- To homogenize the temperature within the GC box. The GC column sits on the cold plate, but its geometry and the heavy heating tape (FGH052-060, 240V, 310W, Omegalux, UK) wrapped around (for baking purposes) reduces the flow of heat energy by conduction from the GC column to the the cold plate. A fan located within the GC box ensures that the vaporized LN cools homogeneously the GC box.

The pumping device consists of a LN dewar, a resistance (10 Ω), a funnel, a power supply (Lascar, PSU130, 0-30 V, 1 A), a PID controller (CN7500, Omegalux, UK) and a plastic tubing (ID 6 mm). The resistance is attached to a funnel immersed in a LN dewar (see Fig. 3.11). When a current (6 V, 3.6 W) flows through the resistance, electrical energy is converted into heat energy. The temperature measured by a K-thermocouple sitting on the GC column is compared with the set-point temperature (0°C). A PID controller allows an electric current to flow through the heating element SETUP

to trigger the LN_2 pump until the set-point temperature is reached: a stream of LN droplets is then automatically carried in their gas phase from the LN dewar to the GC box.

LEIDENFROST PRINCIPLE

Heat dissipated by the 10 Ω resistance creates a high temperature gradient between the resistance and LN. If the temperature difference exceeds 100°C (Leidenfrost point), LN droplets are hold up by an insulated layer of N_2 vapor forming at the hot suface. As thermal conductivity of vapor is low, heat transfer from the resistance's surface to LN droplets is greatly reduced, which enables LN droplets to remain liquid and be carried in their own vapour cushion (Linke et al., 2006; Schmitt, 2006) through a plastic tubing to the GC box. This physical phenomenon is called the Leidenfrost principle.

3.5.3.3 Separation validation

3.5.3.3.1 *Thermal Conductivity Detector*

FLOW

A thermal conductivity detector (TCD, Vici, USA) measures the difference in thermal conductivity between the sample flow eluting from the GC column and the reference flow. Changes in conductivity are measured only by the change in current required to keep the filament at a constant temperature. The sample flow consists in a mixture of air and carrier gas (He), while only carrier gas flows through the reference channel. The measured difference is proportional to a voltage and a typical output signal is shown in Fig. 3.12. The two gas streams are switched over the filament at a rate of 5 times per second.

CONFIGURATION

The TCD filament can be permanently damaged if gas flow through the detector cell is interrupted while the filament is operating. As shown in Fig 3.2, the total sample flow out of the TCD amounts to 7.4 cc.min^{-1}, of which 5.7 cc.min^{-1} originate directly from the reference flow. Such a configuration efficiently discards this possible source of damage.

3.5.3.3.2 *Chromatograms*

ELUTION

Fig. 3.12 presents chromatogram showing retention time of O_2 (and Ar), and N_2 . Temperature of the GC column is set to 0°C. Carrier gas is He, with a flow rate of $\simeq$28 mL.min^{-1}. After release of the sample from the full air trap (T3) to the GC column, O_2 elutes after 345 s an ends at 580 s, and N_2 elution starts after 825 s. With 4 min between the end of O_2 elution and the start of N_2 elution, there is enough time for O_2 to divert the N_2 flow towards the TCD (Fig. 3.12) and out to waste while O_2 is being trapped in T4 (refer to section 3.7).

BASELINE

The baseline variability is mainly due to the communication between the TCD and the computer. At best, the TCD output signal ranges from 0 to 10 V. As the analog

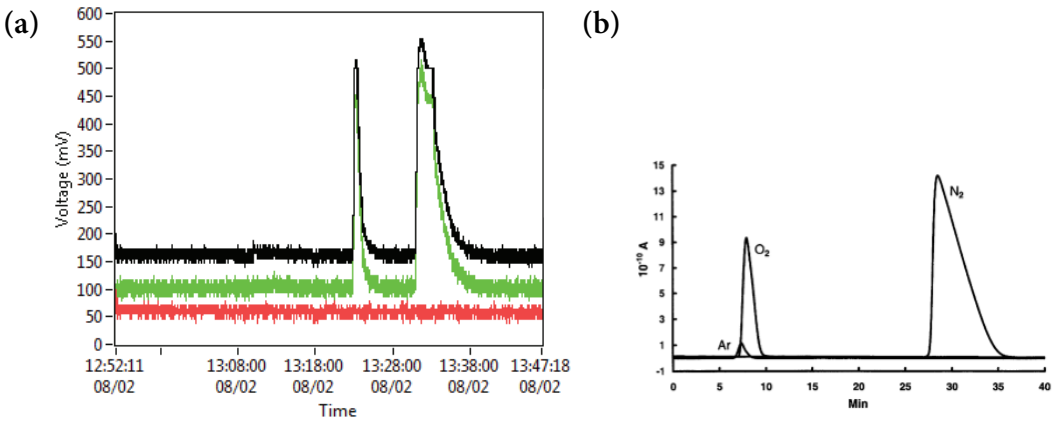

Figure 3.12 – **(a)** Chromatogram as it appears on the Labview Visual Interface (VI) developed during this thesis. The first peak represents O_2 and elutes from 5 min 45 s to 9 min 40 s and the second peak represents N_2 eluting at 13 min 45 s. The green curve represent the difference in thermal conductivities between the gases flowing in the sample channel (black line) and the reference channel (red line), fed by He alone. The output signals (mV) are provided by the TCD every 0.2 s and show elution time for O_2 and N_2 through the GC column used in our setup.**(b)** Fig. 2 from Barkan and Luz (2003), original caption: chromatogram showing separation of N_2 from O_2 -Ar mixture. He flow rate is $\backsim 25mL \cdot min^{-1}$. In their system, 13 minutes separate O_2 and N_2 elution.

input of the electronic board ("Wasp", PC-control Ltd, UK) used to transmit the signal to Labview doesn't accept values higher than 2.0 V, we chose to use the 0-1 V output signal of the TCD. As a result, only 128 steps are available to represent the TCD output signal's variations (see Section 3.6), with ΔV between 2 steps reaching $\backsim$ 7.8mV. In Fig 3.12, the apparent high variability of the baseline actually translates a ± 1 step variation, caused by the chip card precision. The baseline has typically a standard deviation $\sigma < 5$ mV.

ARTIFACT

The recording chart of the TCD signal remains systematically blocked for a short while at 500 mV, which is clearly seen in Fig. 3.12. All the TCD measurements show a similar pattern, and suggest an artifact most likely due to a electronic deficiency in the transmission of the TCD output signal to Labview through the WASP electronic card.

TCD USAGE

The very high precision needed for $^{17}\Delta$ measurements requires N_2 to be removed despite its interest[11]. In our setup, the TCD is essential for setting up the GC system, choosing the optimal temperature and carrier gas flow to obtain a excellent separation between O_2 and N_2 . During the collection of a sample, the TCD informs on the elution time of N_2 , but no O_2 peak can be detected. Indeed, to avoid a possible contamination/loss of the sample, the possibly-leaky TCD is not included in the high purity line. The O_2 /N_2 mixing ratio of a sample can not thus be retrieved from the TCD in

[11]Isotopic composition of N_2 ($\delta^{15}N$) is used for thermal fractionation corrections (Sect. 1.4.1.2) and picks up rapid temperature changes in Greenland that can be linked to other gas archives like $\delta^{18}O_{atm}$, CO_2 or CH_4 on a common gas time scale.

our configuration. The TCD also helps us to monitor the stability of the GC unit. A valve switch, a flow variation, or a slight temperature change in the path (GC column or the traps T3 and T4) of the carrier gas indeed modifies the thermal conductivity of the sample flow measured in the detector cell.

3.6 AUTOMATION

This setup was built with the ultimate objective of fully automating the system so that samples and standards can be collected in an identical manner and without the need of an operator. A few steps are missing to complete this goal, from the replacement of a few manual valves by pneumatically-actuated valves, to the implementation and testing of the automated procedure from extraction to collection.

The experimental setup is therefore semi-automated curently, in the sense that it can be remotely controlled under Labview environment (Fig. 3.14), at the exception of (i) a few valves that only need to be opened at the start of the measurements (valves M1, M4, M5 in Fig. 3.2, and (ii) essentially the manual valve that commands the access to the turbo molecular pump[12].

Instead of relying on acquisition cards from Labview, device/computer communication is achieved with electronic board from PC-control. They are connected to a USB port of the computer and considered as human interface device, making it easy to install. Dynamic linked libraries containing all the available functions are used to control the board with Labview. The real advantage of this library is that it gives the possibility to combine several boards of different types and build a custom and flexible control system, which is needed for the experimental setup.

Details on the control system of the experimental setup run with Labview can be seen in figures 3.13. The 11 pneumatically actuated valves of the extraction unit (E1 to E11 on Fig. 3.2) are controlled via 11 high voltage capable DC switching outputs of a "Mini-Bee" type board (supplied with 24V DC power supply (PSU130, 30 V, 30 W, Lascar)), that supply/interrupt a current flow to the solenoid valves (24 V, 30 mA DC) enabling/interrupting the flow of compressed air to the pneumatic valves.
Another "Mini-Bee" board is connected in a similar way to control the 10 valves of the collection manifold (R1 to R10) and R11 (for evacuation of the standard introduction unit). It should be mentioned that the connection is slightly modified as the valves of the collection manifold need to be controlled both by Labview (when collecting the samples) and the MS (when releasing the sample):

1. The switching outputs of the "Mini-Bee" board are soldered to a female 24 pins D-sub socket.

2. The MS provides 24 V DC external switching outputs (controlled with Isodat,

[12] at pressures higher than 0.1-1 mbar, the primary pump is preferably used to avoid any damage to the turbo pump

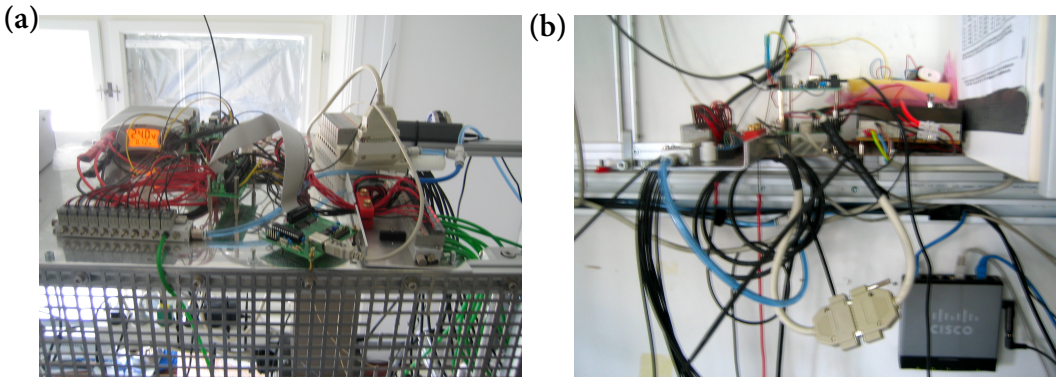

Figure 3.13 – **(a)** A part of the control system is located on top of the setup. Electronic boards, block valves and power supplies can be seen. **(b)** The collection manifold block valve with its D-sub cable connected to the "Mini-Bee" board controlled with LabvieW.

the MS software) that one can physically access at the back of the MS with D-sub cables (24 pins). 2 D-sub cables are connected to the MS sockets JO520 and JO521[13]. These cables are cut and the relevant leads are soldered to the pins of a female D-sub adapter in the same pin configuration as in (1).

3. The leads of the solenoid valves controlling the yield of compressed air are soldered to the pins of a male D-sub adapter with the pin configuration matching (1) and (2).

This design enables a simple switching between the two setups. The block valve (consisting of the 12 solenoid valves) is moved together with LynnOax and it only requires to connect it either to the female D-sub socket attached to the MS or to the Mini-Bee board.

A Digi-Bee card is used to control the remaining valves of the experimental line, including the 4 and 6-port position Valco valves V1 and V2.

Labview communicates with the two pressure gauges PG1 and PG2 (Pirani, Edwards) thanks to a RS232 serial port.

As seen in Sect. 3.5.3.3.2, the 0-1 V output signal of the TCD is transmitted to an analog input of a "Wasp" electronic board ("Wasp", PC-control Ltd, UK). This analog input is converted to a digital output which is transmitted to Labview using DLLs.

The silicon diode temperature sensor is connected in the same way as the TCD to an analog input of the "Wasp" board to communicate with Labview via DLLs.

[13] 2 different D-sub cables are needed to control 12 valves (the 10 of the collection manifold and 2 for the standard introduction) as only 8 pins per MS socket provide 24 V DC.

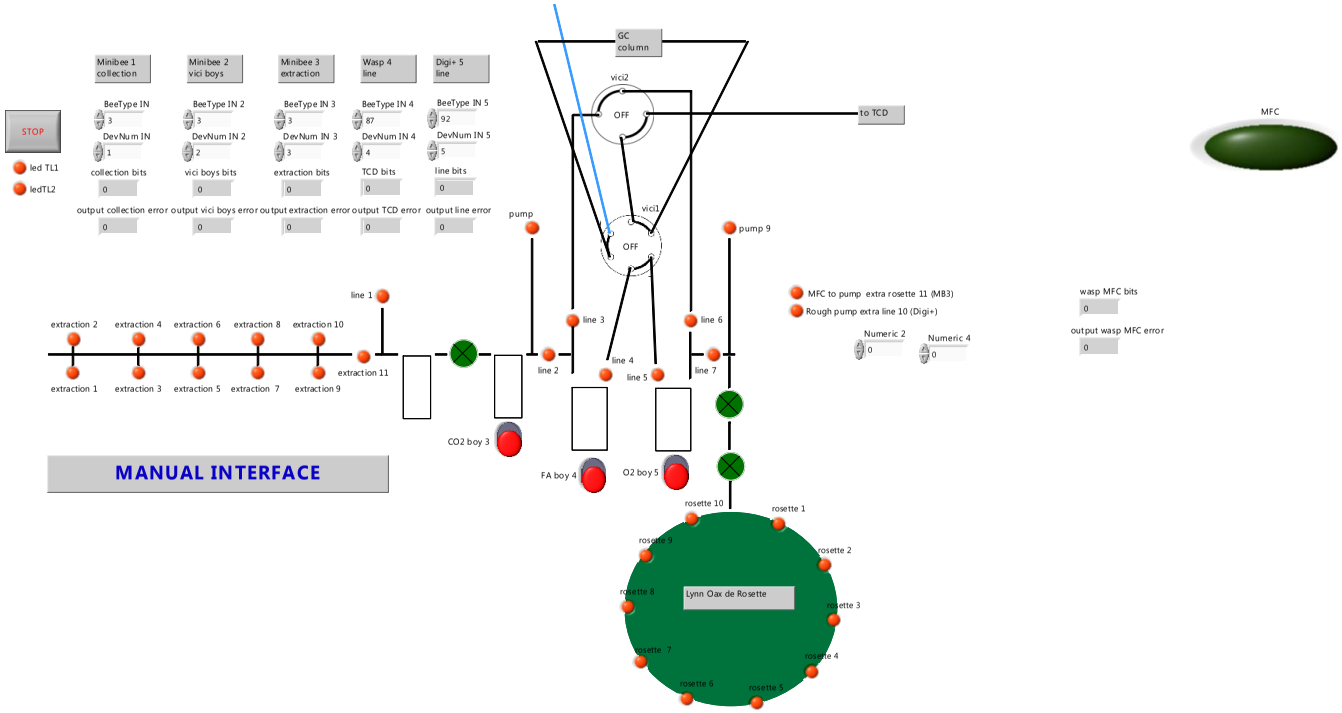

Figure 3.14 – The O_2 line is controlled with Labview. The figures displays the manual interface used to control the opening/closing of the MFC and the pneumatically-actuated valves and cylinders of the system. The upper left part displays the status of the different electronic boards. A value of 0 corresponds to no error.The large green dot on the right controls the opening of the MFC. Note that in another screen are constantly monitored the TCD signal, the temperature of the cryocooler (e.g. Fig 3.15) and the pressure measured at PG1 and PG2.

3.7 Procedure for extraction and collection of O_2 isotopologues

This section describes the two methods used to collect stable oxygen isotopes from trapped gases in ice cores, with the aim of measuring $\delta^{18}O_{atm}$ only, or $^{17}\Delta_{atm}$, hence the three isotopes of O_2 . Extraction, purification and collection are similar for both methods, the only difference relating to the separation unit (Sect. 3.7.6). Indeed, when measuring $\delta^{18}O_{atm}$, this step is bypassed as it can be measured in air. However, when it comes to $^{17}\Delta_{atm}$ measurements, the very high precision needed requires to separate N_2 from the O_2 /Ar mixture. This section therefore describes the method applied for $^{17}\Delta_{atm}$ measurements, as it covers all the steps of the procedure. The full procedure excluding extraction takes ≃45 min, similar to the procedure of Barkan and Luz (2003). Note that except the Sect. 3.7.6 on the GC unit, all other sections also apply to $\delta^{18}O_{atm}$ measurements.

3.7.1 Ice core samples

3.7.1.1 Ice core storage

Ice samples are usually stored in a cold chamber at a maximal temperature of −25°C. The δ O_2 /N_2 of air trapped in ice core samples is known to decrease with storage time because the O_2 molecule preferentially leaks through the ice lattice (Kawamura, 2000). Craig et al. (1988) and Severinghaus and Battle (2006) found that small atoms Ar, Ne and O_2 were leaking out, contrary to Kr, Xe and N_2 , suggesting a size-dependent fractionation during leakage from overpressured air bubbles. This gas loss process appears temperature dependent, as samples stored at lower temperatures (−50°C) experience less gas loss (Ikeda-Fukazawa et al., 2005), similar to gas-loss fractionation observed in the LIZ (Sect. 1.4.1.3). It is therefore crucial to keep the storage temperature as low as possible to preserve the air entrapped in ice core bubbles. Consequently, our ice samples dedicated to $^{17}\Delta$ measurements, not measured yet, are stored below −50°C to minimize gas loss. Details on gas loss fractionation during storage can be found in Sect 4.6.4 . TEMPERATURE

3.7.1.2 Ice sample preparation

Ice samples typically weight 40 g after cutting. Dimensions of the piece are ≃ 2.5·2.5·7.5 cm, with the long axis oriented parallel to the ice core so as to average over several annual layers (Severinghaus et al., 2003). With 10 % of fossil air, this sample size yields around 4 cc of gas, hence 0.8 cc of O_2 . This amount of O_2 is reduced during expansion of the sample from the SST rod of the collection manifold to the bellows of the MS, but the loss of gas caused by expansion of the sample to the MS bellow is minimized by setting the bellow to its maximum volume (≃40 cc). In the case of $\delta^{18}O$ ($^{17}\Delta$) measurements, this sample size corresponds to ≃40 mbar (8 mbar) in the bellow in full expansion, i.e. ≃1.6 cc (0.3 cc) STP. The bellow is then compressed to reach a range of pressure that ensures viscous flow conditions throughout the full measurement cycle. SAMPLE SIZE

ICE SAMPLE TRIM

The outer layer (1 to 3 mm) of the sample is cut with a bandsaw in a cold chamber at −15°C, adjacent to the storage chamber at −25°C. This minimizes risks of drilling fluid contamination for deep ice cores and fractionation due to gas loss processes by exposing fresh surface. The sample is then cleaned with a synthetic bristle brush and smoothed with a scalpel to remove surface cracks and irregularities. Care is taken to minimize glove contact with the ice sample as handling may weaken the ice (by warming it on the surface before it has annealed) and create fractures causing mass-dependent fractionation (Bender et al., 1995; Bender, 2002; Severinghaus et al., 2009). After cutting and cleaning, the ice sample is put in an pre-cooled (−25°C) extraction flask (Sect. 3.4.3). This step is usually performed in the morning just before the start of the measurements.

3.7.2 Pre-operation

3.7.2.1 Conditioning of the analytical line

LYNNOAX CONDITIONING

The extraction line and the 10 rods of the collection manifold are filled with a pure O_2 standard to 300 mbar ($^{17}\Delta$ measurements) or with Neem_S1 standard (for $\delta^{18}O$ measurements) when not in operation. This step was added to the procedure because of the systematic poor accuracy observed at the start of a measurement period, and a gradual improvement with successive collections.

MOLECULAR SIEVE

Before each use, molecular sieve traps T3 and T4, as well as the GC column (after removal of insulating material that would melt at this temperature) are heated to 200°C for some hours while flushed with the carrier gas (He). This baking step ensures that no water remains within the molecular sieve and enables its regeneration. After the baking step, the He flow is maintained until the start of the measurements to condition the separation unit. In addition, following Barkan and Luz (2003), traps T3, T4 and GC column are baked at 200°C while pumping whenever the molecular sieves are in contact with ambient air.

3.7.2.2 Collection unit

CRYOCOOLER

In general, the day prior to measurements, LynnOax is inserted to the cryocooler. A vacuum flange and O-ring mounted on a centering ring are used to connect LynnOax to the vacuum casing of the cryocooler. 4 small clamps fitted with screws ensure a leak-tight connection. Thermal grease (Apiezon N-grease) is added on the copper block of the collection manifold to ensure a good thermal contact with the cryocooler cold station. Without grease, the lowest temperature reached by the cryocooler exceeds 15 K, thus reducing its trapping power. However, too large amount of grease bends LynnOax to the cold station, and make it very difficult to disconnect the collection manifold from the cryocooler after warming to room temperature.

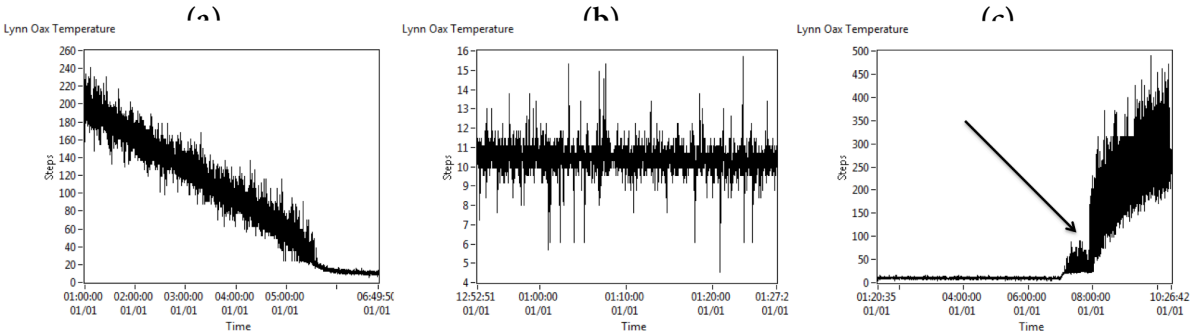

Figure 3.15 – **(a)** Cooling of LynnOax as recorded on the Labview interface. **(b)** The operating temperature of the cryocooler is ≃12 K. **(c)** LynnOax heating. Note the transition in the heating process (shown by the black arrow) when cartridge heater (40 V, 40 W) is switched on. Note that the DT-470-CU-12A silicon diode temperature sensor (Lakeshore cryotronics, USA) sensitivity ($S = dV/dt$) is much larger in the 10-25 K temperature range, which explains the sudden decrease in the variability of the signal in this temperature range. The larger variability during warming is due to interferences caused by the operation of the internal cartridge heater

Once the collection manifold is attached to the cryocooler, LynnOax is connected with a 1/4" VCR meshed gasket to the main line. One hour before the start of the measurements, all sample tubes are evacuated from the standard mixture simultaneously through P2.

PRECAUTION ISSUES

It is critical to ensure a good vacuum within the vacuum casing before starting the He cryocooler primarily for safety reasons. Indeed, at 12 K, N_2 and O_2 would freeze in the vacuum casing, then build in an enormous pressure and probably a burst while heating the unit. The volume of the gas phase of O_2 , for instance, is ≃840 times more important than the volume of the solid phase.

Once the pressure in the vacuum casing reads below $4 \cdot 10^{-2}$ mbar on the pressure gauge PG3, the vacuum shroud is isolated, and a rapid leak check is performed. If no rise in pressure is observed, the He compressor is switched on and cooling of the cold head starts. It takes 90 minutes for the cryocooler to reach 12 K, temperature at which the samples are cryotrapped (Fig. 3.15a). When 12 K is reached, the pressure in the vacuum casing is typically in the $2.9 \cdot 10^{-4} - 4.5 \cdot 10^{-4}$ mbar range. This is due to the fact that the remaining O_2 and N_2 after vacuum casing evacuation freeze at these temperatures. While the cryocooler always reaches its minimum temperature in 90 min, the latter may vary depending on the initial vacuum pressure within the vacuum casing or, most frequently, on the quality of the thermal contact between the second stage cold station and the collection manifold. The optimal thermal contact is observed when only a thin and smooth layer of grease is added on the copper block. The grease indeed becomes solid at low temperatures, and rough surfaces then probably reduce the area of the copper block in physical contact with the cold station.

3.7.2.3 Extraction unit

EXTRACTION DEWAR

While the cryoccoler is cooling to 12 K, the extraction dewar filled with ethanol is cooled down to −24°C thanks to the PID controlled NESLAB coldfinger. To fasten the cooling process, ethanol is stored beforehand in a cold room at −15°C. Temperature is homogenized thanks to a fan located at the bottom of the dewar[14]. The temperature of the cold bath is allowed to vary between −22°C and −24°C to limit the on-off cycles undergone by the coldfinger. In practice, the temperature of the cold bath vary by less than 2°C for each sample.

3.7.2.4 Separation unit

This pre-operating step is only necessary for $^{17}\Delta_{atm}$ measurements, as $\delta^{18}O_{atm}$ measurements do not require separation of O_2 from N_2 . The GC column is cooled down to 0°C with the Peltier element and droplets of LN carried in their vapor cushion (see Sect. 3.5.3.2.2) 2 h before the start of the first gas separation to let time for the temperature to stabilize. Traps T3 and T4 are kept in room temperature. The 2 Valco valves V1 and V2 are set to "load" mode, and the carrier gas flows through the GC column at ≃28 ml·min^{-1} out to waste. Typical flow rates can be found on Fig. 3.2.

3.7.2.5 Initial configuration

The initial configuration can be seen in details in Fig. 3.16. Water trap T1 is cooled to −100°C with a slush of ethanol and liquid N_2 . It should be mentioned that the water trap is disconnected from the system after a day of measurement, and dried overnight in an oven set to 150°C. The CO_2 trap T2 is immersed in a LN dewar (−196°C) using a double actuated pneumatic cylinder (CD85N20–250B, SMC, Denmark). The entire system, including traps T1, T2, T3 and T4 and the collection manifold, is evacuated through P1 and P2. Once the pressure in the system reaches $5 \cdot 10^{-5}$mbar on PG1 and PG2, a static leak-check is performed and validated if no rise in pressure is observed for 2 min after closing P1 and P2.

3.7.3 Considerations on working standard introduction

Whenever trapped gases in ice cores are collected in LynnOax, two rods are dedicated to working standards collection. Both samples (Sa) and working standards are then measured against an intermediate standard by IRMS as described in Sect. 4.5.5. Working standards are also use for system characterization, stability assessment and daily calibration. Section 3.4.2.3 describes the purging and flushing steps before introducing the standards in the extraction flask. To respect the IT principle and micmic the steps experienced by the ice core sample in the analytical setup, the standard is introduced at a flow rate of 2 ml·min^{-1} above BFI after overhead evacuation. The in-

[14]Note that the fan needs to be switched on simultaneously with the coldfinger. Indeed, the viscosity of ethanol at low temperature prevents the fan from starting below −20°C

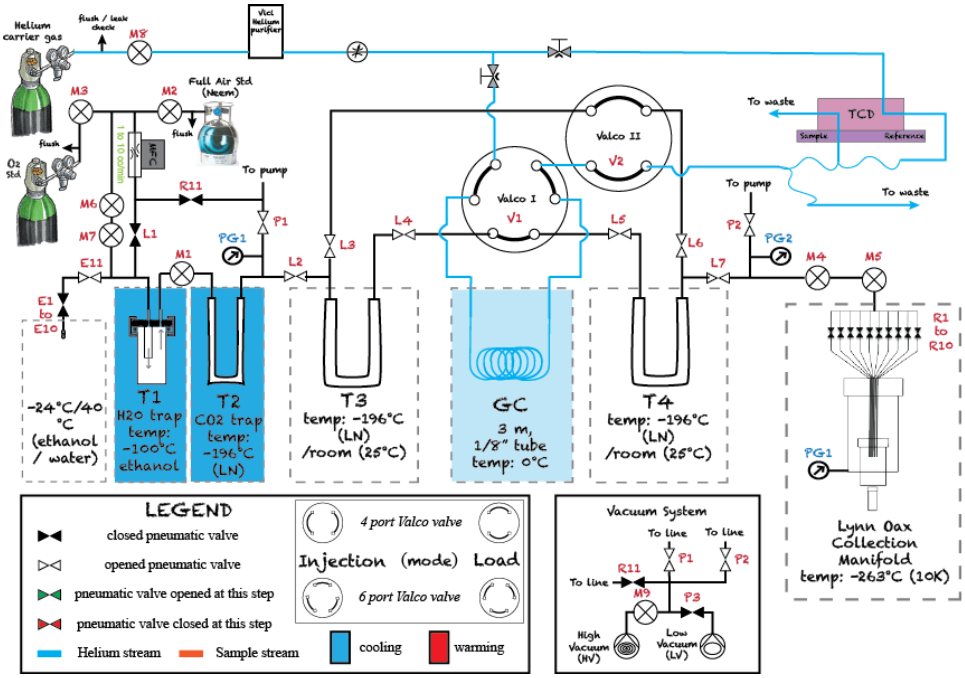

Figure 3.16 – Step: initial configuration. Valves E11, L2 to L7, M1, M4 and M5 are opened, enabling evacuation of traps T1, T2, T3 and T4 and the collection manifold, is evacuated through P1 and P2 until the pressure in the system reaches the limit of detection of the pressure gauges ($P < 5 \cdot 10^{-3}$Pa)

troduction is performed as follows: the gas standard is allowed to flow through the MFC out to waste (valve R11 opened and L1 closed) for 2 min (more if the flow rate is not stable). Access to pump is then closed and valve L1 opened for standard introduction. After a variable amount of time, depending on the desired standard size (e.g. 2 min for 4 ml), valve L1 is closed.

Different procedures have been tested to assess the fractionation caused by the gas standard introduction, from (1) direct collection in LynnOax after standard introduction, to (2) expansion in the extraction vessel over BFI, via (3) expansion in the glass flask without ice and (4) change in the flow-rate of standard introduction. Introduction (1) and (3) at different flow-rates (4) gave satisfactory results, but it turned out that standard measurements with introduction over BFI (2) were not reliable, possibly due to the presence of dissolved air in the blank ice, as observed by Bock et al. (2010). Sperlich et al. (2013) showed that the presence of dissolved gases in BFI (a different batch produced at CIC too) affected CH_4 measurements (in CF mode) during the melting process of BFI. In contrast, the stability of consecutive extraction of standard gas above melted BFI showed that BFI was fully degassed. A simple test of this effect in our setup would be to collect and measure successive Neem_S1 standards injected first over frozen BFI, then over the same melted BFI, and should be performed in the future to closely follow the IT principle.

Instead of relating the isotope composition of ice core samples to the working standard Neem_S1 over BFI because of the aforementioned considerations, Grzymala-Lubanski (2015) chose to reference the samples to Neem_C1 standard (introduced in the standard bellow of the DI system), measuring NEEM Holocene ice core samples from the same depth to control the accuracy of the RICE measurements. Such a "choice" (which was forced by the large $\delta^{18}O$ variability of the standards introduced over BFI), came with pros and cons. On one hand, as pointed out by Schmitt (2006), the best, but utopic standard hitherto, would be artificial ice with $\simeq$ 10% air inclusions of known composition formed in the same way as air bubbles form during ice formation. One could thus argue that this procedure would respect even more closely the IT principle than the standard introduction over BFI, as the process of air entrapment within the ice would be similar for both sample and NEEM quality standards. On the other hand, this choice obviously meant that besides the uncertainties in the true value of the standard itself, fractionation processes associated with transport in firn, bubble close-off, ice core recovery and ice core storage are modifying O_2 isotope ratios and need to be corrected for, causing a loss in precision and accuracy.

3.7.4 Sample overhead evacuation

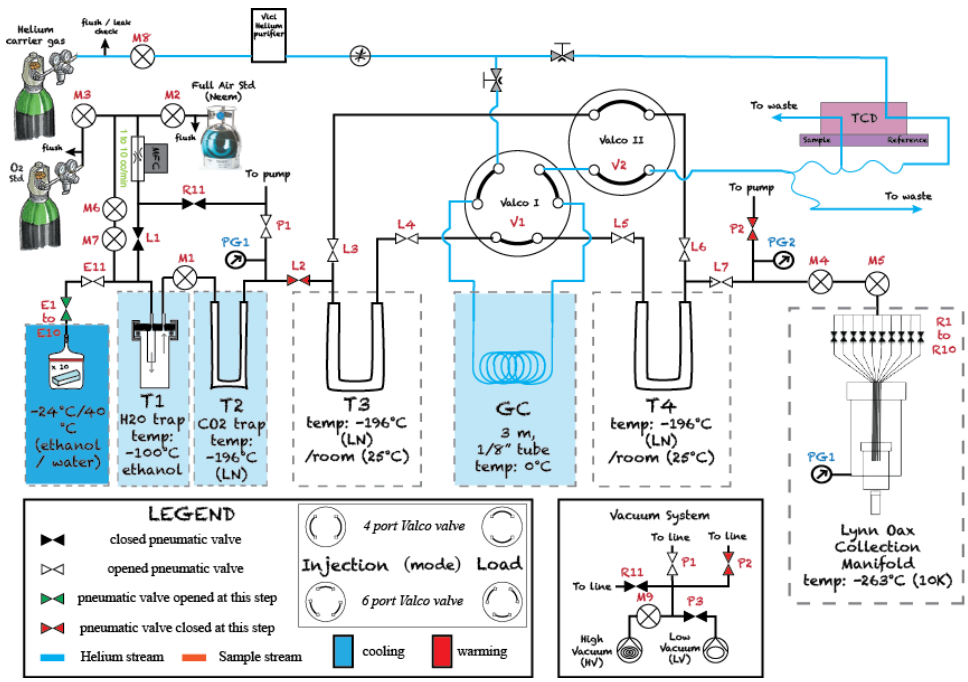

Figure 3.17 – Step: sample overhead evacuation. Valves L2 and P2 are closed once vacuum in the system is established, monitored by PG1 and PG2. Valve E1 is opened to enable sample overhead evacuation.

GLASS FLASK CONNECTION

Just before the start of the measurements, the pre-flanged glass flask containing the ice sample is brought from the cold room to the lab freezer, both at −25°C. As soon as the system evacuation is completed, the 6 mm glass tube of the flask is connected

to the 1/4" nickel plated UltraTorr fitting attached to valve E1 of the extraction line with a Viton O-ring. The glass flask is then immediately immersed in the pre-cooled ethanol dewar (3.7.2.3), whose temperature is stabilized to $\simeq -23 \pm 1$°C by the PID controlled NESLAB coldfinger. The temperature of the extraction bath must be stable as it controls the sublimation rate of the ice sample (Fig. 3.4). Indeed, at this temperature, saturated vapour pressure above the ice sample, e_i, reaches up to 1 mbar, creating a sublimation flux that helps cleaning of the ice sample surface and improves pump-down time during sample overhead evacuation (Sect. 3.4.4).

EVACUATION

Figure 3.17 describes the system configuration during sample overhead evacuation. Once vacuum is reached in the system in its initial configuration (Fig. 3.16), the separation unit and collection unit are isolated and sample overhead evacuation starts through the cold water and CO_2 trap (through P1).

3.7.5 Ice core sample extraction

MELTING

Overhead evacuation is complete when the pressure read on PG1, located after the water trap, where all water vapor should removed from the gas stream, reduces to $5 \cdot 10^{-5}$ mbar. Then the glass flask is isolated, and the cold ethanol dewar is replaced by a warm bath heated to 40°C. The warmer the warm bath, the higher the flux of water vapor, and the the more efficient the gas extraction. Note however than a too high flux of water may clog the water trap or cause fractionation in the water trap due to occlusion of gases within the frozen ice (Sect. 3.4.4). Moreover, less dissolved O_2 , N_2 and Ar should remain in the water as solubility of these gases decreases with increasing temperature (at least in this 280-320 K temperature range), thereby improving extraction efficiency.

$\delta^{18}O$

Regarding $\delta^{18}O$ measurements, the next step of the analytical procedure is described in Sect. 3.7.7. Indeed, the separation umit is bypassed by connecting valves L2 to L7, as the dry and CO_2 free O_2 -N_2 -Ar gas mixture is directly cryotrapped in the sample rod of the collection manifold.

3.7.6 O_2 -Ar / N_2 separation

3.7.6.1 Focusing the sample in full air trap T3

Once the extraction vessel is immersed in the water bath, molecular sieve trap T3 is isolated from the main line by closing valves L3 and L4. Trap T3 is then immersed in a LN dewar. Note that the LN level in the dewar is carefully check to ensure similar conditions for all the samples. Then, after checking that pressure read in PG1 is under-range, extraction valve E1 and valve L2 are opened to start transfer of the sample to trap T3. At this temperature, molecular sieve acts as a cryo-pump that drives the pressure gradient from the extraction vessel to trap T3. The trapping process takes $\simeq$8 min and trapping is considered complete when pressure read on PG1 reaches 3

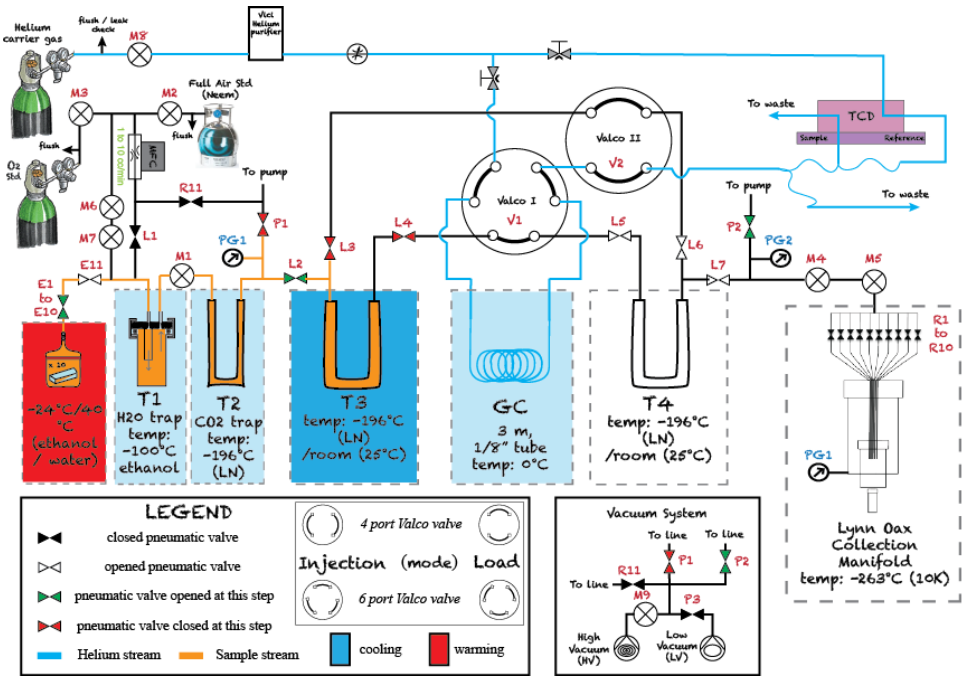

Figure 3.18 – Step: focusing the sample in the molecular sieve full air trap T3. After sample overhead evacuation is completed (PG1 needs to reach under-range values), valve E1 is closed and the cold ethanol bath is replaced by a warm water bath at 40°C. Then trap T3 is immersed into LN by lifting the LN dewar using a pneumatic cylinder after isolating the trap by closing L3 and L4 (note that L2 is already closed). Evacuation of the transfer line is stopped by closing P1, and the sample is transferred to trap T3 while melting by opening E1 and L2. Meanwhile, trap T4 and collection unit are evacuated through P2 to ensure vacuum conditions in the rest of the system.

Pa (0.03 mbar) for 4 ml STP of moist air (timing not available for an ice sample).

3.7.6.2 Switching sequence from load to injection mode

After trapping is complete, residual air is evacuated through P1. Then valves L2 and L7 are closed to isolate the separation unit and valve L3 and L4 are opened. At this time, He flows through the GC column at ≃28 ml·min^{-1} out to waste while T3 (at LN temperature) and T4 (at room temperature) are under vacuum. The next step consists in switching successively (as fast as possible) Valco valves V2 and V1. Figure 3.19 describes the effect of switching V1 before V2 and inversely.

V1 THEN V2 By switching V1 first, He from the GC column is simultaneously sucked into the outlet of T3 and the inlet of T4, both traps being under vacuum (Fig. 3.19B1). With this switching sequence, the carrier gas flows directly from V2 out to waste. As soon as V2 is switched to injection mode (Figure 3.19C), the carrier gas is directed towards T3 inlet. With this switching sequence, the carrier gas needs to fill T3 and T4 before the reverse flow established into the waste line is stopped. At a rate of 28 ml·min^{-1},

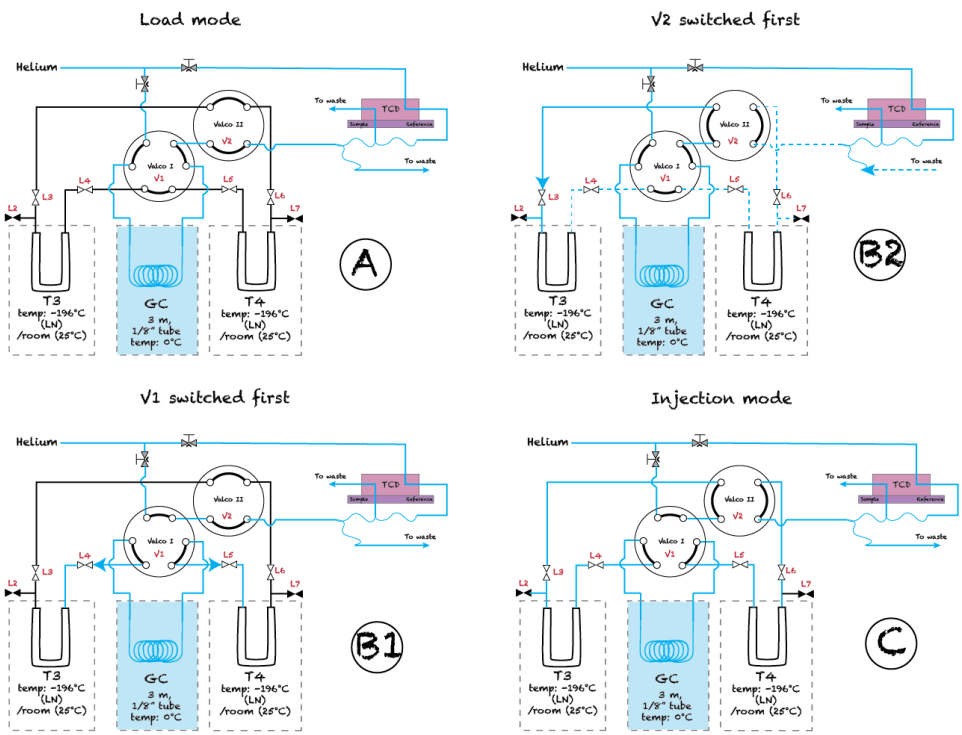

Figure 3.19 – Switching the separation unit from load to injection (to the GC column) mode. See text for details.

it takes a bit less than 1 min to fill both T3 and T4 traps (≃12.5 cm^3 volume each accounting for the volume of the valve), time during which ambient air could potentially contaminate the line.

By switching V2 first (Fig. 3.19B2), the He flow is directed through the GC column, T3 then T4. Instead of creating a reverse flow of He towards T3 outlet (other switching sequence), trap T3 starts immediately to be filled with He from its inlet. This enables a faster stabilization of the carrier gas flow. Once V2 is switched to injection mode, the path of the carrier gas goes from GC column-T3-T4 to T3-GC column-T4 and out to waste. Similar to the other sequence, a reverse flow in the waste line occurs as long as the carrier gas has not reached trap T4. The change in the flow is confirmed by the decrease of the He flow in the sample channel of the TCD. Indeed, the TCD configuration ensures that a flow of 5.7 $ml{\cdot}min^{-1}$ of He from the reference channel outlet feeds permanently the sample side of the TCD, in addition to a flow of 1.7 $ml{\cdot}min^{-1}$ from the separation unit (Fig. 3.2). After switching, the sample flow rate decreases by 1.7 $ml{\cdot}min^{-1}$, from 7.4 to 5.7 $ml{\cdot}min^{-1}$, strongly suggesting that no more He flows through the capillary connecting the separation unit to the sample channel of the TCD. The following paragraph describes how to overcome this issue.

V2 THEN V1

To summarize, we selected the B2 switching sequence because it prevents a reverse flow of He from the GC column to T3, enabling a faster carrier gas flow stabilization. However, both switching sequences B1 and B2 (from load of the sample into T3 to

INJECTION MODE

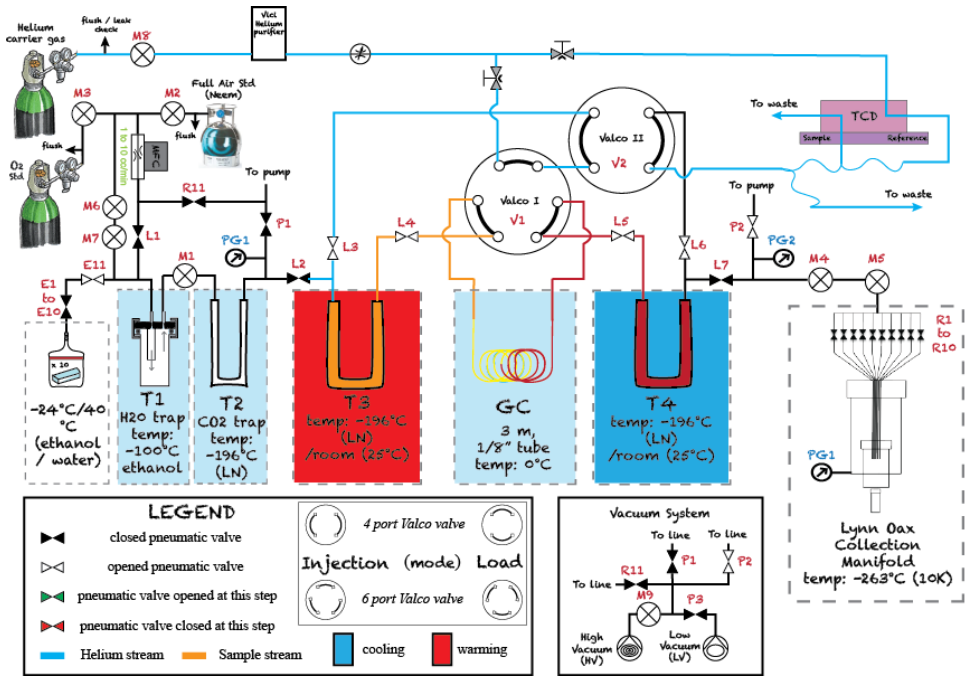

Figure 3.20 – Step: Separation of N_2 from the O_2 -Ar mixture. Trap T3 is warmed to room temperature while T4 is cooled down to LN temperature. As a result, the gas mixture desorbed from the molecular sieve is injected into the GC column, where separation takes place. The O_2 -Ar mixture is then adsorbed in trap T4.

its injection in the GC column) have the common caveat of causing a reverse flow into the waste line (a flow meter located at the outlet of the waste line sees the flow rate drop to 0 ml·min^{-1}) and thereby contaminating the system with ambient air, as already noted by Barkan and Luz (2003). Therefore it is critical for the waste line to have a large volume (>50 cm^3) to ensure that only He would be sucked into T4 by its outlet after switching the Valco valves. By precaution, valve L6 is closed immediately before switching V2 and V1 to injection mode, so that no gas can enter into trap T4 from its outlet. Besides, the reverse flow in the waste line is also reduced as there is not a 12.5 cm^3 evacuated volume to fill anymore. The valve is reopened after $\simeq$ 2 min, once the He pressure within the trap exceeds the pressure in the waste line. It then takes a couple of minutes until the flow of carrier gas stabilizes to its equilibrium value. At this point, injection of the sample into the GC column can start.

3.7.6.3 Desorption (T3), separation (GC) and adsorption (T4)

The dry air mixture adsorbed into the molecular sieve trap is desorbed by heating T3 to room temperature. Warming of the trap is automatically controlled thanks to a push-for "on" switch closed mechanically during removal of the LN dewar from trap T3 (see Fig. 3.9 for details). Meanwhile, trap T4 is cooled to −196°C by immersing the latter in a LN dewar. When T3 reaches room temperature, the gas mixture is injected together with the carrier gas in the GC column. After elution, the O_2 -Ar mixture is

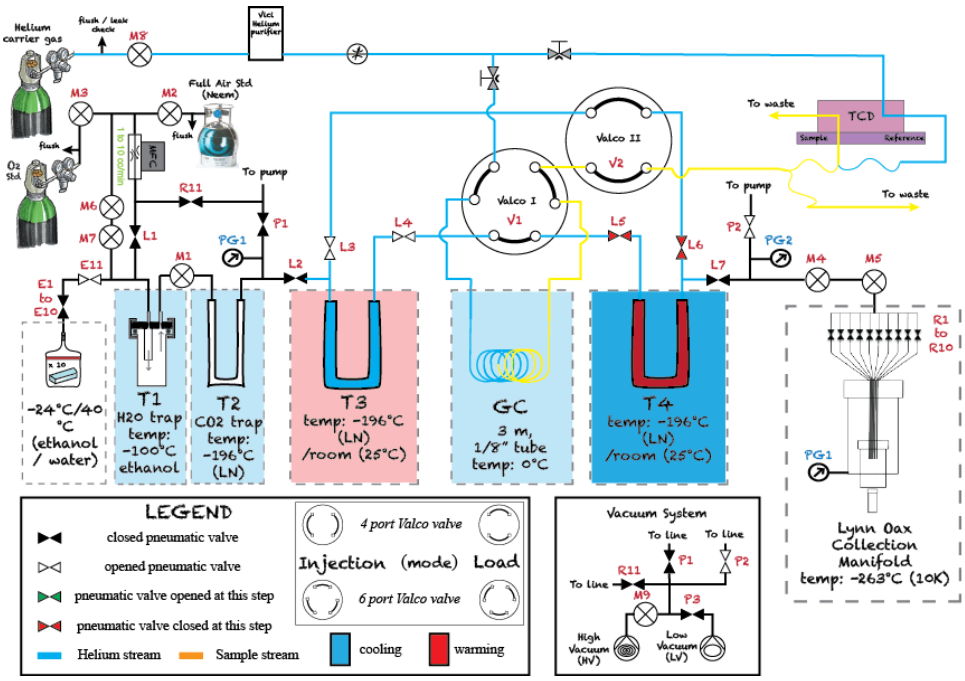

Figure 3.21 – Step: Diverting N_2 stream. Once the O_2 -Ar mixture is trapped in T4, the separation unit is switched over to load mode to divert the N_2 stream out to waste. After the elution mid-term point (after the O_2 -Ar peak tail returns to baseline), valves L5 and L6 are closed just before switching V1 then V2. Closing L5 and L6 avoids potential introduction of residual air in T3 directly from T4 after switching.

trapped in trap T4 (Fig. 3.20). Once O_2 -Ar elution is complete, Valco valves V1 and V2 are switched back to load mode to divert the N_2 flow out to waste (Fig. 3.21).

As described in Sect. 3.5.3.3.2, the O_2 -Ar mixture elutes after 345 s and ends at 580 s, while N_2 elution starts after 825 s. With 4 min between the end of O_2 elution and the start of N_2 elution, there is enough time to divert the N_2 flow towards the TCD and out to waste while O_2 is still being adsorbed in trap T4. Valves V1 and V2 are switched once the elution mid-term point is reached so that the N_2 stream is diverted from the GC column out to waste. The success of the separation process can be rapidly assessed with the TCD signal. Indeed, if the switch were to occur too early, the tail of the O_2 -Ar peak would be detected by the TCD; if it were to occur too late, no N_2 peak would be recorded. The chromatogram shown in Fig. 3.12 represents a typical successful O_2 -Ar separation from N_2 .

3.7.7 Sample collection

3.7.7.1 $\delta^{18}O$

The trapping time is consistent between collections rods and days of measurements. air samples

Typically, for a dry air sample of $\backsim$4cm^3, it takes 10 min to reach a pressure (as read on PG2) of 10^{-2} mbar (efficiency of sample collection: 99.9%) and 15 min to reach $2 \cdot 10^{-3}$ mbar (99.99%).

ICE SAMPLES

The fossil air samples dedicated to $\delta^{18}O$ measurements are collected in a sample rod of the collection manifold while melting the sample. During transfer the pressure in the main line reaches an equilibrium of about 3 to 5 mbar between the gas released from the melting ice and the pumping power of the rod. Collection lasts until the pressure gauges PG1 and PG2 show $\backsim$ 1% of the equilibrium pressure value, in order to collect up to 99% of the extracted sample gas.

COLLECTION TIME

A potential source of error, resulting from sample fractionation, can be caused by an incomplete collection of the sample in the collection tube. To investigate this the working standard freezing time was increased to collect up to 99.999 % of the extracted air (collection stopped when the pressure in the system is below $5 \cdot 10^{-4}$ mbar), which did not modify the measured $\delta^{18}O$ values. This suggests that there were no fractionation effect caused by an incomplete collection.

3.7.7.2 $^{17}\triangle$

Before the transfer of the O_2 -Ar mixture to the sample rod of the collection manifold, residual He in T4 trap is pumped away while maintaining T4 at LN temperature. The access to pump (P2) is then closed, while L7 and one of the valve of the collection rod (R1 to R10) are opened. Meanwhile, T4 is warmed to room temperature (30 s) to release the sample. The pressure read on PG2 immediately after sample release typically lies the 5-8 mbar range then decreases until a threshold pressure is reached around 0.3 mbar after $\backsim$ 5 min. The role of water vapor was quickly discarded as it would have frozen at these temperatures. Besides, no water vapor is present in this part of the system, as it is located after the H_2O trap. To understand what causes this threshold pressure, 2 different experiments were performed. First, two collection rods were used to collect a sample. The pressure in the system in this configuration was similar, suggesting that the high pressure was not due to a lack of pumping power of the cryocooler. This was further confirmed by a blank experiment, where the same threshold pressure was observed at the end of the collection. Based on these tests, we concluded that the pressure plateau is probably due to residual He in the trap T4 and transferring line, which is not trapped at 12 K.

3.7.8 Warming the collection manifold to room temperature

VENTING THE CRYOCOOLER

Once collection of samples and standards is completed, the He cryocooler is switched off. Then, with the help of the internal heater (40W, 40 V), the collection manifold is warmed to 25 °C. Once room temperature is reached according to the temperature sensor of the cryocooler, a delay of 30 min is observed before venting the vacuum casing. Indeed, the cartridge heater is inserted within the copper cup on which the

temperature sensor is attached. Thereby, transfer of heat to the temperature sensor (and the copper block of the collection manifold) is efficient given the high thermal conductivity of copper, but the temperature of the vacuum casing itself is still much lower, vacuum acting as an insulator and only allowing weak radiative heat transfer from the cartridge heater.

If the vacuum casing is vented too early, massive condensation of water vapor occurs on the wall of the vacuum casing. As a matter of fact, even after the 30 min delay, water vapor condensation occurs on the walls, but to a lesser extent.

In summary, the collection manifold can be disconnected from the cold head of the cryocooler after $\simeq$ 2 h. This may seem long, but note that a more efficient heating of the cryocooler would not shorten the period of time needed between the end of the collection and the start of IRMS measurements, as a couple of hours are usually required for sample rod homogenization in the sample tube after warming. Note however that this step can vary from 40 min (Barkan and Luz, 2003; Landais et al., 2012) to a full night[15] (Kawamura et al., 2003).

HEAT TRANSFER

As mentioned above, the silicon diode sensor attached to the copper cup of the cold station is not representative of the temperature of the vacuum casing. Therefore we monitor its pressure for additional control. We observe systematic patterns during the heating (cooling) procedure, for instance a sudden rise (drop) of pressure occurring when N_2 and O_2 trapped in the vacuum shroud reach their gas phase. From this time on only, the warming procedure could be fastened by venting the vacuum casing with dry N_2 , or dry air, thereby allowing efficient heat transfer by conduction.

3.7.9 LynnOax transfer to the mass spectrometer

LynnOax is transferred to the MS and attached to the the sample bellow of the DI system with the usual UltraTorr fitting with Viton O-ring. From this point, the measuring sequence is fully automated and described in Chapter 4.

[15] the sample consists of 300 g of ice, vs 40 g in Landais et al., 2012's study.

Bibliography

Barkan, E. and Luz, B. (2003). High-precision measurements of 170/160 and 180/160 of o2 and o2/ar ratio in air. *Rapid Communications in Mass Spectrometry*, 17(24):2809–2814.

Bender, M., Sowers, T., and Lipenkov, V. (1995). On the concentrations of o2, n2, and ar in trapped gases from ice cores. *Journal of Geophysical Research: Atmospheres*, 100(D9):18651–18660.

Bender, M. L. (2002). Orbital tuning chronology for the vostok climate record supported by trapped gas composition. *Earth and Planetary Science Letters*, 204(1):275–289.

Berhanu, T. (2013). *Caracterisations isotopiques des voies de formation du nitrate atmospherique et de la photochimie du nitrate dans la neige*. PhD thesis, Grenoble.

Bock, M., Schmitt, J., Behrens, M., M⊠ller, L., Schneider, R., Sapart, C., and Fischer, H. (2010). A gas chromatography/pyrolysis/isotope ratio mass spectrometry system for high-precision dd measurements of atmospheric methane extracted from ice cores. *Rapid Communications in Mass Spectrometry*, 24(5):621–633.

Capron, E., Landais, A., Lemieux-Dudon, B., Schilt, A., Masson-Delmotte, V., Buiron, D., Chappellaz, J., Dahl-Jensen, D., Johnsen, S., Leuenberger, M., Loulergue, L., and Oerter, H. (2010). Synchronising {EDML} and northgrip ice cores using d18o of atmospheric oxygen (d18oatm) and {CH4} measurements over {MIS5} (80⊠123 kyr). *Quaternary Science Reviews*, 29(1–2):222 – 234. Climate of the Last Million Years: New Insights from {EPICA} and Other Records.

Carter, J. and Barwick, V. (2011). Good practice guide for isotope ratio mass spectrometry. *FIRMS Network*.

Craig, H. (1961). Standard for reporting concentrations of deuterium and oxygen-18 in natural waters. *Science*, 133(3467):1833–1834.

Craig, H., Horibe, Y., and Sowers, T. (1988). Gravitational separation of gases and isotopes in polar ice caps. *Science*, 242(4886):1675–1678.

Emsley, J. (2011). *Nature's building blocks: an AZ guide to the elements*. Oxford University Press.

Gonfiantini, R., Stichler, W., and Rozanski, K. (1995). Standards and intercomparison materials distributed by the international atomic energy agency for stable isotope measurements.

Grzymala-Lubanski, I. (2015). $\delta^{18}o$ of o_2 in rice ice core. Master's thesis, Centre for Ice and Climate.

Halsted, R. and Nier, A. O. (1950). Gas flow through the mass spectrometer viscous leak. *Review of Scientific Instruments*, 21(12):1019–1021.

Headly, M. A. and Severinghaus, J. P. (2007). A method to measure kr/n2 ratios in air bubbles trapped in ice cores and its application in reconstructing past mean ocean temperature. *Journal of Geophysical Research: Atmospheres*, 112(D19):n/a–n/a. D19105.

Honig, R. E. (1945). Gas flow in the mass spectrometer. *Journal of Applied Physics*, 16(11):646–654.

Huber, C. and Leuenberger, M. (2004). Measurements of isotope and elemental ratios of air from polar ice with a new on-line extraction method. *Geochemistry, Geophysics, Geosystems*, 5(10):n/a–n/a. Q10002.

Huber, C., Leuenberger, M., and Zumbrunnen, O. (2003). Continuous extraction of trapped air from bubble ice or water for on-line determination of isotope ratios. *Analytical chemistry*, 75(10):2324–2332.

IAEA (2009). Reference sheet for vsmow2 and slap2 international measurement standards. page 5.

Ikeda-Fukazawa, T., Fukumizu, K., Kawamura, K., Aoki, S., Nakazawa, T., and Hondoh, T. (2005). Effects of molecular diffusion on trapped gas composition in polar ice cores. *Earth and Planetary Science Letters*, 229(3–4):183 – 192.

Kawamura, K. (2000). *Variations of atmospheric components over the past 340000 years from Dome Fuji deep ice core, Antarctica*. PhD thesis, Univ.

Kawamura, K., Nakazawa, T., Aoki, S., Sugawara, S., Fujii, Y., and Watanabe, O. (2003). Atmospheric co2 variations over the last three glacial⊠interglacial climatic cycles deduced from the dome fuji deep ice core, antarctica using a wet extraction technique. *Tellus B*, 55(2):126–137.

Landais, A., Dreyfus, G., Capron, E., Pol, K., Loutre, M. F., Raynaud, D., Lipenkov, V. Y., Arnaud, L., Masson-Delmotte, V., Paillard, D., Jouzel, J., and Leuenberger, M. (2012). Towards orbital dating of the epica dome c ice core using delta o_2/n_2. *Climate of the Past*, 8(1):191–203.

Landais, A., Masson-Delmotte, V., Nebout, N. C., Jouzel, J., Blunier, T., Leuenberger, M., Dahl-Jensen, D., and Johnsen, S. (2007). Millenial scale variations of the isotopic composition of atmospheric oxygen over marine isotopic stage 4. *Earth and Planetary Science Letters*, 258(1–2):101 – 113.

Leuenberger, M., Bourg, C., Francey, R., and Wahlen, M. (2002). Extraction of trapped gases in ice cores for isotope analysis. *Stable isotope measurement techniques for atmospheric greenhouse gases*, page 59.

Linke, H., Alemán, B., Melling, L., Taormina, M., Francis, M., Dow-Hygelund, C., Narayanan, V., Taylor, R., and Stout, A. (2006). Self-propelled leidenfrost droplets. *Physical review letters*, 96(15):154502.

Mani, F. S., Dennis, P., Sturges, W., Mulvaney, R., and Leuenberger, M. (2008). An improved method for delta 15 n measurements in ice cores. *Climate of the Past Discussions*, 4(1):149–171.

Murphy, D. M. and Koop, T. (2005). Review of the vapour pressures of ice and supercooled water for atmospheric applications. *Quarterly Journal of the Royal Meteorological Society*, 131(608):1539–1565.

Schmitt, J. (2006). *A sublimation technique for high–precision d13C on CO2 and CO2 mixing ratio from air trapped in deep ice cores.* PhD thesis, Dissertation Universität Bremen.

Severinghaus, J. P. and Battle, M. O. (2006). Fractionation of gases in polar ice during bubble close-off: New constraints from firn air ne, kr and xe observations. *Earth and Planetary Science Letters*, 244(1–2):474–500.

Severinghaus, J. P., Beaudette, R., Headly, M. A., Taylor, K., and Brook, E. J. (2009). Oxygen-18 of o2 records the impact of abrupt climate change on the terrestrial biosphere. *Science*, 324(5933):1431–1434.

Severinghaus, J. P., Grachev, A., Luz, B., and Caillon, N. (2003). A method for precise measurement of argon 40/36 and krypton/argon ratios in trapped air in polar ice with applications to past firn thickness and abrupt climate change in greenland and at siple dome, antarctica. *Geochimica et Cosmochimica Acta*, 67(3):325 – 343.

Sperlich, P., Buizert, C., Jenk, T., Sapart, C., Prokopiou, M., Röckmann, T., and Blunier, T. (2013). An automated gc-c-gc-irms setup to measure paleoatmospheric δ13c-ch4, δ15n-n2o and δ18o-n2o in one ice core sample. *Atmospheric Measurement Techniques*, 6:2027–2041.

Werner, R. A. and Brand, W. A. (2001). Referencing strategies and techniques in stable isotope ratio analysis. *Rapid Communications in Mass Spectrometry*, 15(7):501–519.

4 Mass spectrometry

4.1 INTRODUCTION

The $\delta^{18}O_{atm}$, $\delta O_2/N_2$ and $\delta^{15}N$ of twenty-one shallow NEEM ice core samples from the same depth (331±1 m) were extracted with the experimental line presented in Chap. 3 by Grzymala-Lubanski (2015), used as quality control standards for RICE (Roosevelt Island Climate Evolution) ice core samples (Sect. 4.5.5). They were subsequently measured by IRMS. The NEEM shallow samples provide valuable information on the stability of the system and its ability to reproduce ice core measurements. In this chapter, we thus take benefit of the NEEM ice core measurements to assess the performance of the analytical system, which includes the extraction line and mass spectrometry measurements. We also show that NEEM samples were affected by gas loss processes, as inferred from $\delta^{18}O_{atm}$, $\delta O_2/N_2$ and $\delta^{15}N$ variations of the 21 replicates. After corrections for gravitational (Sect. 4.6.3.1), thermal (Sect. 4.6.3.2) and gas loss (Sect. 4.6.3.3) fractionation, the precision of ice core measurements with the analytical system is estimated as $\sigma = 0.021‰$ with error propagation ($\sigma = 0.008‰$ without).

This chapter introduces the principle of IRMS in Sect. 4.2, with a focus on the DI mode (Sect. 4.4). Section 4.5 focuses on the development of the protocol and the automation of IRMS measurements, while Sect.4.6 details data post-processing, i.e. the sequence of corrections applied to the measured δ values. Finally, Sect. 4.6.7 assesses the quality of the analytical system based on 21 late Holocene NEEM ice core samples from the same depth.

4.1.1 LASER SPECTROMETERS VS MASS SPECTROMETERS

LASER SPECTROSCOPY

Ideally, ice core gases analysis should take place in the field, in the science trench just where the ice core is drilled, thereby avoiding possible contamination, partial melting and/or gas loss during ice core transport and storage. This is happening nowadays with laser spectroscopy techniques[1], allowing for instance high-resolution online measurements of greenhouse gases mixing ratios (Chappellaz et al., 2013) and water isotopic ratios (e.g. Gkinis, 2011) from ice cores in a field-based setting, with the analyzed gas stream originating directly from a continuously melting rod. However this technique cannot be applied to molecular O_2 isotopic measurements, as the O_2 molecule does not absorb in the near-infrared region.

CF VS DI

Instead, measurements of O_2 isotopes described in this thesis are made with a Delta V Plus Advantage (ThermoFisher) IRMS. IRMS usually enables two operating modes,

[1]The operating principle is described briefly: vibrational or rotational motions of all molecules with three or more atoms, thus including CO_2 , CH_4 , N_2O or H_2O isotopocules, induce a net change in the dipole moment of the molecule, allowing absorption of IR energy at wavelengths that correspond to the transition energy between two quantum mechanical energy states, called absorption lines (Balslev-Clausen, 2011). The absorption spectrum at these long wavelengths is unique for each isotopocule as the energy states depend on the masses, configurations and binding energy of the atoms in the molecule. Isotopologues of a same molecule can thus be distinguished based on their mass differences.

DI and continuous flow. In CF mode, the IRMS is alternatively fed by a stream of standard or sample gas, with the help of a carrier gas and an open split. This offers a higher temporal resolution but lower precision compared to measurements of discrete samples in DI mode, as the sample is measured several times against the standard to achieve a very high precision.

4.2 Mass spectrometry basics

The MS enables the separation of isotopologues according to their mass, and consists essentially of three parts: a ion source, a mass analyser and a detector (Fig. 4.1). The sample and reference gases are introduced in the sample and standard bellow, resp., of the MS. Thanks to the changeover valve, sample and standard gases are alternatively introduced into the ion source of the MS or diverted to waste through a capillary, ensuring stable flow conditions. Gas molecules are ionized in the ionization chamber by an electron beam produced by a heated tungsten filament. The ionized molecules (charge q) are then focused with focusing plates and accelerated to several kV by a voltage difference (V, in volts). The kinetic energy of a charged particle can be expressed as the product of Vq such as:

$$\frac{1}{2}mv^2 = Vq, \tag{4.1}$$

where v is the velocity of the charged isotopologue. The ionized molecules are then deflected by a magnetic field according to their mass to charge ratio (noted m/z hereafter) and their velocity. Indeed, the radius of curvature r of the charged particle's trajectory can be expressed as follows:

$$r = \sqrt{\frac{2mV}{qB^2}}, \tag{4.2}$$

where B (gauss) is the magnetic field. Equation 4.2 shows that a heavier isotopologue will move along a curved trajectory having a longer radius than a lighter one. it also shows that increasing the high voltage and/or decreasing the magnetic field leads to a higher r, i.e. a weaker deflection. In a MS, it is possible to control both V and B, which thereby enables a large selection of masses to be measured. However, during a set of measurements, V and B are kept constant and stored in the gas configuration corresponding to the gas to be measured, e.g. O_2 , N_2 , or CO_2 isotopologues. The detector consists in an array of Faraday cups located along the focal place of the MS to allow a simultaneous collection of isotopologues, e.g. m/z 32, 33 and 34 for O_2 . The ions hitting the Faraday cup are neutralized by electrons flowing from ground to the cup. This flow of electron generate a current, which is first amplified then attenuated in an amplifier. It is the attenuation of the amplified current, controlled by a resistance, which gets converted into pulses in a voltage-to-frequency converter. The pulses are counted over a preset integration time, the result of which is collected by a processor and sent to the software of the MS, Isodat, as a signal in Volt, used to calculate isotope ratios. The amplifiers collecting the rare ionized isotopologues (e.g. m/z 33 or 34 for O_2) are equipped with low resistances while high resistances are used for the abundant isotopologues so as to match natural isotopic abundances (Sect. 4.3).

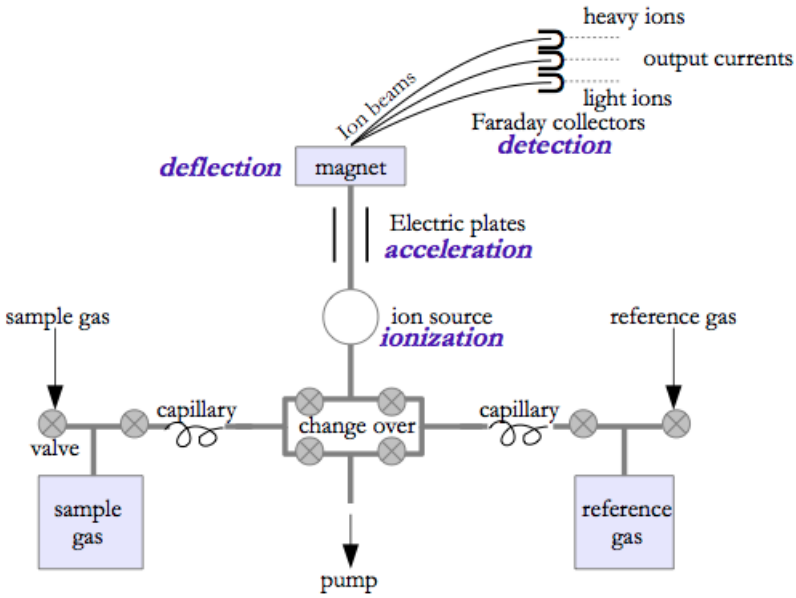

Figure 4.1 – Original Figure 1.8 from Guillevic (2013). Schematic of a MS including the DI system (bellows, source capillaries and changeover valve). In DI mode, sample gas (left bellow) and reference gas (right bellow) are alternatively flowing into the ion source or into a waste line of the MS through two capillaries. The fast switching between sample and standard gas is performed with the changeover valve.

4.3 Delta V Advantage Isotope Ratio Mass Spectrometer

Delta V Plus

During the first years of this PhD thesis, oxygen isotope ratios were measured on a Delta V Plus (Thermo Fisher) IRMS, equipped with 7 Faraday cups enabling the measurement of atmospheric air (masses over charge (m/z) 28, 29, 32, 33, 34, 36 and 40), N_2 (m/z 28, 29 and 30) or CO_2 (m/z 44, 45 and 46). This 7-cups configuration was advantageous as this enabled simultaneous collection of O_2 isotopologues together with $^{14}N^{14}N$, $^{15}N^{14}N$ and ^{40}Ar, which are needed for correcting the measured O_2 isotope ratios (see Sect. 4.6).

A new birth

After a couple of years, we decided to exclusively dedicate the Delta V Plus to CO_2 measurements, and another IRMS, a Delta V Advantage (Thermo Fisher) to O_2 measurements. This IRMS, originally dedicated for H_2O measurements, needed maintenance:

- the DI system was contaminated with oil that had been introduced through the pumping system, probably after a power outage. Indeed, if the MS is not vented before shutdown, oil from the rough pump can be sucked in the DI system, driven by the high vacuum in the DI line. The whole pumping system, the DI block valves and tubings were consequently unmounted and ultrasonic cleaning of SST parts was applied to remove grease and oil traces.
- the O-rings of half of the block valves that control the DI system, including the

change-over valve, had become stiff. As a result, cracks in the O-ring caused massive internal leakage within the DI system, as the compressed air pressure was too low to properly close the pneumatically-actuated valves of the IRMS, which are normally open. Besides, a few gold ring and gold gaskets of the block valves had to be replaced too, as they were causing external leakage

Cup settings

The Delta V Advantage is equipped with 5 Faraday cups. In this collector configuration (universal triple collector + HD), 2 cups (1 and 5) are dedicated to m/z 2 and 3, that is the two stable isotopes of molecular hydrogen, ($^{1}H^{1}$) and deuterium ($^{2}H^{1}H$). Their large relative difference in mass to charge ratio requires these 2 cups to be distant from each other. As a result, they can only be used for hydrogen isotope measurements. Depending on the selected gas configuration, the 3 remaining cups can simultaneously collect[2]:

- N_2 isotopologues, $^{14}N^{14}N^{+}$ (m/z 28) and $^{15}N^{14}N^{+}$ (m/z 29) or CO isotopologues, $^{12}C^{16}O^{+}$ (m/z 28), $^{13}C^{16}O^{+}$ (m/z 29) and $^{12}C^{18}O^{+}$ (m/z 30).
- CO_2 isotopologues, $^{12}C^{16}O^{16}O^{+}$ (m/z 44), $^{13}C^{16}O^{16}O^{+}$ and $^{12}C^{17}O^{16}O^{+}$ (m/z 45), $^{12}C^{18}O^{16}O^{+}$ (m/z 46).
- O_2 isotopologues, $^{16}O^{16}O^{+}$ (m/z 32), $^{17}O^{16}O^{+}$ (m/z 33), $^{16}O^{18}O^{+}$ (m/z 34).

The main drawback of this collector configuration, compared to the one of the Delta V Plus, is caused by its inability to measure simultaneously O_2 , N_2 and Ar. They can nonetheless be measured separately by "peak jumping", where the magnetic field is modified while the high voltage is kept constant. However, this procedure lengthens the sequence of measurements and imposes more data processing. Besides, the ionization efficiency of the Delta V Advantage is lower (1200-1500 molecules·ions^{-1}) than the Delta V Plus (800-1100 molecules·ions^{-1}), which translates into a lower sensitivity.

The ionized molecule hitting a Farraday cup transmits an electric charge that is then amplified in order to balance the abundance of the isotopes collected in the different cups. Because of a too small amplification of the electric signal associated with O_2 isotopologues, especially $^{17}O^{16}O^{+}$ (m/z 33), resistors were replaced. Following this change, resistors of $10^{9}\Omega$, $10^{12}\Omega$ and $3 \cdot 10^{11}\Omega$ are associated with the Faraday cups tuned to collect m/z 32, m/z 33 and m/z 34 in the O_2 gas configuration, respectively.

4.4 Dual Inlet system

Dual Inlet System

The DI system of a IRMS is an ultra-clean device consisting of SST tubes, capillaries, connectors, gauges, and valves, of all metal design, with wetted surfaces being either from SST (body and membranes) or gold (gaskets, seals). Stable isotope measurements in DI mode are performed by often and quickly comparing the ion current ratio of a sample with the one of a standard and by reporting the relative deviation to the

[2] here we do not distinguish between charged isotopomers such as $^{17}O^{16}O^{+}$ and $^{16}O^{17}O^{+}$

standard in the usual delta notation. IRMS are indeed designed to compare ion current ratios rather than absolute ion currents in order to achieve a very high precision Brand1996. The core of the DI system consists in the changeover valve and the variable volume of the sample and standard reservoirs (Werner and Brand, 2001). Together, they allow an identical treatment of the sample and the standard during the analysis, in line with the IT principle.

CHANGEOVER VALVE

The changeover valve enables an uninterrupted flow of sample and standard gas by alternatively diverting the flow to the ion source of the IRMS or to the waste line, both maintained under very high vacuum (2 to $6 \cdot 10^{-8}$ mbar). This fast switching, repeated several times, between the sample and the standard (a cycle) during a measurement run cancels out instrumental effects like temperature drifts or fluctuations of sensitivity over time (McKinney et al., 1950; Werner and Brand, 2001), and thereby enables high-precision measurements.

VARIABLE VOLUME

The transfer of gas from the variable volume to the changeover valve occurs through 2 thin capillaries (≃1.5 m, 0.1 mm ID). A pressure higher than 15 mbar at the capillary inlet, obtained by adjusting the variable volumes of the sample and standard reservoirs, ensures viscous flow conditions[3]. Such conditions are critical to avoid isotopic fractionation in the reservoir during the gas transfer to the ion source of the IRMS. Ensuring viscous flow thus imposes a minimal sample size as the amount of air (or pure O_2) in the DI bellows (after full compression) must be sufficient to reach 15 mbar even at the end of the measurement cycle. With these variable volumes, the standard and sample ion beams (corresponding to the most abundant isotopologue, e.g. $^{16}O^{16}O$ for O_2) can be precisely balanced, thereby minimizing the loss of precision due to the "linearity" of the MS[4]. However, the sample and standard major ion beams usually get unbalanced with time, requiring correction (Sect. 4.6.1).

4.4.0.1 Sensitivity versus linearity

Adjusting the source parameters and focusing the beam is performed every time the ion source is opened, usually after a filament replacement[5]. There are two optimal settings, one favoring the linearity, the other the sensitivity of the IRMS. Linearity focusing requires a high extraction voltage in order to efficiently extract the ions out of the ionization housing. This leads to less collisions between molecules and ions in the ion source and to a higher isotope ratio linearity. Usually, linearity is favored in CF mode, where large differences in sample and standard beam voltages can occur. On the other hand, sensitivity is favored in DI mode. Indeed, linearity corrections are minimized (but still exist) in this mode, as sample and standard voltages are balanced by adjusting the pressure of the variable volumes before the measurements. Sensitivity focusing requires a low extraction voltage to maximize the time spent by the ions

[3] As a rule of thumb, the mean free path of a gas molecule should not exceed $1/10^{th}$ of the capillary dimensions to be in viscous flow conditions

[4] Linearity can be seen as the dependence of the delta value to the intensity of the signal.

[5] a batch of THERMOFISHER filaments proved to be faulty

in the ionization housing. This setting aims at optimizing ionization efficiency. For our measurements performed in DI mode, we chose however to favor linearity over sensitivity to minimize corrections caused by pressure imbalance. Besides, linearity settings also reduce the chemical slope corrections (Sect. 4.6.2), as already observed by Severinghaus et al. (2003).

4.5 Measurements

This section focuses on the protocol associated with measurements of $\delta^{18}O$ and $^{17}\Delta$ in DI mode. It includes the minor changes made on the MS to improve precision (Sect. 4.5.2), a typical ice core measurement sequence, as well as the automated procedures developed under ISL (language from the IRMS software Isodat) to measure the collected samples (Sect. 4.5.3).

4.5.1 Dual Inlet measurements: cycle, block and run

The ionized molecules hitting a Farraday cup transmit an ion current signal (nA) that is then amplified in order to balance the natural abundance of the isotopes collected in the different cups (see Sect. 4.4). To the ion current signal corresponds a voltage between 0 and 50 V (with a Delta V Advantage MS). In the following V^m_{sa} and V^m_{std} represent the sample and standard beam voltage, resp., on mass (m/z) m.

BACKGROUND The electronic noise on each Faraday cup is measured once before a period of measurements and kept constant over this period. This is a tiny contribution, denoted B^m for background of the Faraday cup collecting mass m/z m.

In DI mode, the $\delta^{18}O$ value of a cycle is calculated by Isodat in the following way:

$$\delta^{18}O = \frac{\delta^{18}O_a + \delta^{18}O_b}{2}, \tag{4.3}$$

where

$$\delta^{18}O_a = \left(\frac{(V^{34}_{sa1} - B^{34})/(V^{32}_{sa1} - B^{32})}{(V^{34}_{std1} - B^{34})/(V^{32}_{std1} - B^{32})} - 1\right), \tag{4.4}$$

$$\delta^{18}O_b = \left(\frac{(V^{34}_{sa1} - B^{34})/(V^{32}_{sa1} - B^{32})}{(V^{34}_{std2} - B^{34})/(V^{32}_{std2} - B^{32})} - 1\right), \tag{4.5}$$

The two standard measurements of a cycle (std1 and std2 for cycle 1, then std2 and std3 for cycle 2, etc) are averaged to normalize for instrument drift (Severinghaus et al., 2003).

CYCLE A measurement cycle consists in 3 steps: simultaneously integrating V^{34}_{std1} and V^{32}_{std1} for 16 s, then V^{34}_{sa1} and V^{32}_{sa1}, and finally V^{34}_{std2} and V^{32}_{std2}. An idle time of 16 s enables the flow to stabilize after every switch between the sample and the standard. The cycle sequence is repeated 16 times, defining a block. Idle time, integration time and number of cycles are chosen based on zero-enrichment tests to optimize measurement precision.

The $\delta^{18}O$ value of a block represents the average of 16 cycle $\delta^{18}O$ values, excluding outliers, i.e. cycle $\delta^{18}O$ values that don't lie within two σ of the mean block value (Dixon outlier test performed by Isodat). This block $\delta^{18}O$ value corresponds to the evaluated data of Isodat. BLOCK

The $\delta^{18}O$ value of a run is defined as the average of 3 blocks, that is 48 cycles (or less if there are outliers). The standard deviation of the 3 $\delta^{18}O$ block values defines the precision of the run. RUN

4.5.2 Changes on the mass spectrometer

A few changes were done on the IRMS in order to better monitor the vacuum in the DI system and as an attempt to improve the precision of the measurements:

- The pressure gauge (noted PG hereafter) of the DI system is installed by default in the fore vacuum pumping line, which means that pressure in the DI system can only be monitored while pumping with the rough pump. In order to monitor the pressure in the line at any time, the pressure gauge location has been modified. It lies therefore just before the block valve controlling the access to the high vacuum or low vacuum line. The real advantage of this modification arises from the possibility to use a pressure threshold instead of a time threshold to control the quality of the vacuum in the automated measurement sequence. It would be advantageous to replace the PG (limit of detection at 10^{-3} mbar) with a more sensitive one to be able to detect very small leaks as the pressure in the DI line is usually well below 10^{-3} (as high vacuum is provided by a turbomolecular pump).

- In the original configuration, the two bellows of the DI system are connected together with a 1/4" SST line. This line is also connected to the low and high vacuum pumps of the DI system. As a consequence, every time the DI system sees atmosphere (e.g. when connecting a device to the sample inlet), moist lab air containing trace gases is evacuated through this line. Besides, with the aforementioned modification, a potential contamination may occur through the pressure gauge. To avoid using this potentially "dirty" line when transferring standards from the right (standard) inlet of the MS to the left bellow (e.g. for zero-enrichment tests), a "clean" 1/4" SST line has been installed which connects the sample cross to the standard cross of the DI system. This clean line is kept closed when lab air is introduced in the DI line and is only used to transfer standard gas from one side to the other.

- As suggested by Severinghaus et al. (2003), we wrapped the bellows, block valves and DI lines with insulating material to limit the effect of short term temperature fluctuations and minimize thermal fractionation during the transfer of the sample from LynnOax collection rod to the sample bellow of the IRMS.

4.5.3 Automation of IRMS measurements

The principle of identical treatment (IT principle) by which samples and reference materials (RMs) are processed in an identical manner calls for an automated measuring sequence of O_2 isotopologues, which reduces operator-related errors (but not programming ones). Mass spectrometry measurements are performed with the software Isodat, and the script developed to control the automated sequence is thus written with the programming language from Isodat (isl).

4.5.3.1 Sequence and method

SEQUENCE

Fig. 4.2 represents an example of sequence of ice core measurements run automatically. The sequence starts with 2 zero-enrichment runs. These runs do not only estimate the internal precision and stability of the MS, but also condition the DI lines of the MS with standard gas (Neem_C1 for $\delta^{18}O_{atm}$ measurements). Besides, this allows the samples collected in LynnOax multiport to have a sufficient time to equilibrate after warming from 12 K. The zero-enrichment tests at the end of the sequence (usually 2 runs but 1 row is missing in Fig. 4.2) are not systematically performed, but can be useful to check whether a drift of the isotopic composition of the standard occurred during the ice core sample measurements.

O_2 isotope ratios (1 run of 3 blocks) and N_2 isotope ratio (1 block) of samples collected in rod 3, 2, 1, 7, 8, 9, 10 are successively measured in this sequence[6], resulting in 28 sample blocks. To each block (or row) correspond one method file, defined in the rightmost column of the sequence. In Fig. 4.2, two methods files are used throughout the whole sequence. One (LynnOax_automated_d18O2N2.met) dedicated to O_2 isotopologues (and $\delta O_2/N_2$ via "peak jumping"), the other (LynnOax_automated_d29N2.met) to N_2 isotopologues. Cycle numbers, idle and integration times are defined in the method file, as well as the standard parameters (like its delta-value w.r.t. the isotope scale of reference, see Sect. 3.4.2.2) and settings for the pressure adjustment (called PA hereafter), background and peak center procedures (Sect. 4.5.3.2). Besides, an isl script is attached to each method.

The flow diagram presented in Fig. 4.3 describes the successive actions performed before, during and after a block of O_2 isotope ratio measurements. The different columns of the sequence (Fig. 4.2) represent parameters that the operator must set for each measuring block before the start of the automated sequence as they are interpreted by the isl script. Depending on their values, different actions are performed during the block, as described in Sect. 4.5.3.2.

[6]The number of rods measured and their order may differ according to the experiments. A few rods were permanently discarded, because of internal leakage occurring probably through the pneumatic valves to the ring of LynnOax

Row				AmountBellow	Sample Intro	Standard Intro	Measurement Type	O2 separation	Standard Injection	Checks	Pleft+	Pright+	Magnet!	MonitorM	Evacuate Sa	Evacuate Std	Lynn Oax Inle	
1	✓	✓	✓	0.6	DI Ext Right automated	DI Ext Right automated	Corrections	none	separate filling	zero enrichment					✓	✓	none	LynnOax_automated_d18O2N2.met
2	✓		✓	0.6	DI Ext Right automated	DI Ext Right automated	Corrections	none	separate filling	zero enrichment							none	LynnOax_automated_d18O2N2.met
3	✓		✓	0.6	DI Ext Right automated	DI Ext Right automated	Corrections	none	separate filling	zero enrichment							none	LynnOax_automated_d18O2N2.met
4	✓		✓	0.6	DI Ext Right automated	DI Ext Right automated	Corrections	none	separate filling	zero enrichment					✓	✓	none	LynnOax_automated_d18O2N2.met
5	✓		✓	0.6	DI Ext Right automated	DI Ext Right automated	Corrections	none	separate filling	zero enrichment							none	LynnOax_automated_d18O2N2.met
6	✓		✓	0.6	DI Ext Right automated	DI Ext Right automated	Corrections	none	separate filling	zero enrichment			✓				none	LynnOax_automated_d18O2N2.met
7	✓		✓	0.6	LynnOax DI Ext Left automated	DI Ext Right automated	Sample	none	separate filling	zero enrichment					✓	✓	sample 3	LynnOax_automated_d18O2N2.met
8	✓		✓	0.6	LynnOax DI Ext Left automated	DI Ext Right automated	Sample	none	separate filling	zero enrichment							sample 3	LynnOax_automated_d18O2N2.met
9	✓		✓	0.6	LynnOax DI Ext Left automated	DI Ext Right automated	Sample	none	separate filling	zero enrichment			✓				sample 3	LynnOax_automated_d18O2N2.met
10	✓		✓	0.6	LynnOax DI Ext Left automated	DI Ext Right automated	Sample	none	separate filling	zero enrichment							sample 3	LynnOax_automated_d29N2.met
11	✓		✓	0.6	LynnOax DI Ext Left automated	DI Ext Right automated	Sample	none	separate filling	zero enrichment					✓		sample 2	LynnOax_automated_d18O2N2.met
12	✓		✓	0.6	LynnOax DI Ext Left automated	DI Ext Right automated	Sample	none	separate filling	zero enrichment							sample 2	LynnOax_automated_d18O2N2.met
13	✓		✓	0.6	LynnOax DI Ext Left automated	DI Ext Right automated	Sample	none	separate filling	zero enrichment			✓				sample 2	LynnOax_automated_d18O2N2.met
14	✓		✓	0.6	LynnOax DI Ext Left automated	DI Ext Right automated	Sample	none	separate filling	zero enrichment							sample 2	LynnOax_automated_d29N2.met
15	✓		✓	0.6	LynnOax DI Ext Left automated	DI Ext Right automated	Sample	none	separate filling	zero enrichment					✓		sample 1	LynnOax_automated_d18O2N2.met
16	✓		✓	0.6	LynnOax DI Ext Left automated	DI Ext Right automated	Sample	none	separate filling	zero enrichment							sample 1	LynnOax_automated_d18O2N2.met
17	✓		✓	0.6	LynnOax DI Ext Left automated	DI Ext Right automated	Sample	none	separate filling	zero enrichment			✓				sample 1	LynnOax_automated_d18O2N2.met
18	✓		✓	0.6	LynnOax DI Ext Left automated	DI Ext Right automated	Sample	none	separate filling	zero enrichment							sample 1	LynnOax_automated_d29N2.met
19	✓		✓	0.6	LynnOax DI Ext Left automated	DI Ext Right automated	Sample	none	separate filling	zero enrichment					✓		sample 7	LynnOax_automated_d18O2N2.met
20	✓		✓	0.6	LynnOax DI Ext Left automated	DI Ext Right automated	Sample	none	separate filling	zero enrichment							sample 7	LynnOax_automated_d18O2N2.met
21	✓		✓	0.6	LynnOax DI Ext Left automated	DI Ext Right automated	Sample	none	separate filling	zero enrichment			✓				sample 7	LynnOax_automated_d18O2N2.met
22	✓		✓	0.6	LynnOax DI Ext Left automated	DI Ext Right automated	Sample	none	separate filling	zero enrichment							sample 7	LynnOax_automated_d29N2.met
23	✓		✓	0.6	LynnOax DI Ext Left automated	DI Ext Right automated	Sample	none	separate filling	zero enrichment					✓		sample 8	LynnOax_automated_d18O2N2.met
24	✓		✓	0.6	LynnOax DI Ext Left automated	DI Ext Right automated	Sample	none	separate filling	zero enrichment							sample 8	LynnOax_automated_d18O2N2.met
25	✓		✓	0.6	LynnOax DI Ext Left automated	DI Ext Right automated	Sample	none	separate filling	zero enrichment			✓				sample 8	LynnOax_automated_d18O2N2.met
26	✓		✓	0.6	LynnOax DI Ext Left automated	DI Ext Right automated	Sample	none	separate filling	zero enrichment							sample 8	LynnOax_automated_d29N2.met
27	✓		✓	0.6	LynnOax DI Ext Left automated	DI Ext Right automated	Sample	none	separate filling	zero enrichment					✓		sample 9	LynnOax_automated_d18O2N2.met
28	✓		✓	0.6	LynnOax DI Ext Left automated	DI Ext Right automated	Sample	none	separate filling	zero enrichment							sample 9	LynnOax_automated_d18O2N2.met
29	✓		✓	0.6	LynnOax DI Ext Left automated	DI Ext Right automated	Sample	none	separate filling	zero enrichment			✓				sample 9	LynnOax_automated_d18O2N2.met
30	✓		✓	0.6	LynnOax DI Ext Left automated	DI Ext Right automated	Sample	none	separate filling	zero enrichment							sample 9	LynnOax_automated_d29N2.met
31	✓		✓	0.6	LynnOax DI Ext Left automated	DI Ext Right automated	Sample	none	separate filling	zero enrichment					✓		sample 10	LynnOax_automated_d18O2N2.met
32	✓		✓	0.6	LynnOax DI Ext Left automated	DI Ext Right automated	Sample	none	separate filling	zero enrichment							sample 10	LynnOax_automated_d18O2N2.met
33	✓		✓	0.6	LynnOax DI Ext Left automated	DI Ext Right automated	Sample	none	separate filling	zero enrichment			✓				sample 10	LynnOax_automated_d18O2N2.met
34	✓		✓	0.6	LynnOax DI Ext Left automated	DI Ext Right automated	Sample	none	separate filling	zero enrichment							sample 10	LynnOax_automated_d29N2.met
35	✓		✓	0.6	DI Ext Right automated	DI Ext Right automated	Corrections	none	separate filling	zero enrichment					✓		none	LynnOax_automated_d18O2N2.met
36	✓		✓	0.6	DI Ext Right automated	DI Ext Right automated	Corrections	none	separate filling	zero enrichment							none	LynnOax_automated_d18O2N2.met
37	✓		✓	0.6	DI Ext Right automated	DI Ext Right automated	Corrections	none	separate filling	zero enrichment			✓	✓			none	LynnOax_automated_d18O2N2.met
38	✓		✓	0.6	DI Ext Right automated	DI Ext Right automated	Corrections	none	separate filling	zero enrichment							none	LynnOax_automated_d29N2.met
39	✓		✓	0.6	DI Ext Right automated	DI Ext Right automated	Corrections	none	separate filling	zero enrichment					✓	✓	none	LynnOax_automated_d18O2N2.met

Figure 4.2 – An example of sequence dedicated to $\delta^{18}O$ measurements of ice core samples overnight. The sample measurements are bracketed by 2 runs of 3 blocks of zero-enrichment tests. For each measuring block (row), columns of the sequence provide parameters required by the isl script (Fig. 4.3). Refer to text for details.

4.5.3.2 Protocol for $\delta^{18}O_{atm}$ IRMS measurements

Once the samples have been collected to the collection manifold (LynnOax) and allowed to warm, LynnOax is hooked up to the sample inlet of the MS, and the standard line (Neem_C1) is purged 3 times. Then, the "O2_gaslab" gas configuration is set to ensure that high voltage, magnetic field, focus and cup settings allow measurements of O_2 isotope ratios.

Peak centering[7] is either determined once before the start of the sequence and "passed" to the O_2 gas configuration, or determined before each block, as in Fig. 4.2. The latter option can be very time-consuming. However, zero-enrichment tests showed that performing a peak center only at the start of a run (i.e. 1 peak center every 3 blocks) leads to a loss of accuracy, as the peak center determined at the start of the run is not preserved at the end of the first block, but replaced by the peak center defined in the O_2 gas configuration for the 2 next ones. We therefore usually choose to perform a peak center for each block in the case where only a few samples have to be measured. Finally, the background value (Sect. 4.5.1) is measured once before a set of measurements.

From this point, an isl script (refer to Annex i for the main script and to Annex ii for the developed isl functions) schematically described in Fig. 4.3 allows a complete automation of standard and sample introductions, pressure adjustment, oxygen ratio measurements, mass monitoring and peak jumping (called PJ hereafter) procedure to measure m/z 28 and m/z 32 so as to obtain $\delta O_2/N_2$ value.

The script described in Fig. 4.3 is run for every blocks of the automated sequence, at the exception of the block dedicated to N_2 isotope ratios. It allows the measurement of $\delta^{18}O$, and $\delta O_2/N_2$ by peak jumping for successive samples. The action of the script can be divided in 3 main parts: (1) sample and standard introduction, (2) pressure adjustment procedure, and (3) measurements (Fig: 4.3).

4.5.3.2.1 Sample and standard introductions

Regarding the sample and standard introduction in the DI bellows, the requirements of the program are to (i) introduce (or not) a standard in the right bellow (RB) and check whether the standard pressure in the RB is high enough to ensure viscous flow conditions (>5000 mV with Neem_C1 as standard) throughout the considered block; and (ii) introduce or not a standard or a sample to the left bellow at the start of a block:

- A standard is introduced to the RB if the flag state "Evacuate Std" in Fig. 4.2 is checked in the considered block (row). If no standard needs to be introduced, the pressure of the RB is still measured and a new standard is reintroduced if

[7] peak centering is the action of varying the accelerating high voltage of the ion source to center the peak at the center of the narrowest Faraday cup, collecting m/z 33 in the "O2_gaslab" gas configuration. The optimal value of the high voltage is then used for the block, only.

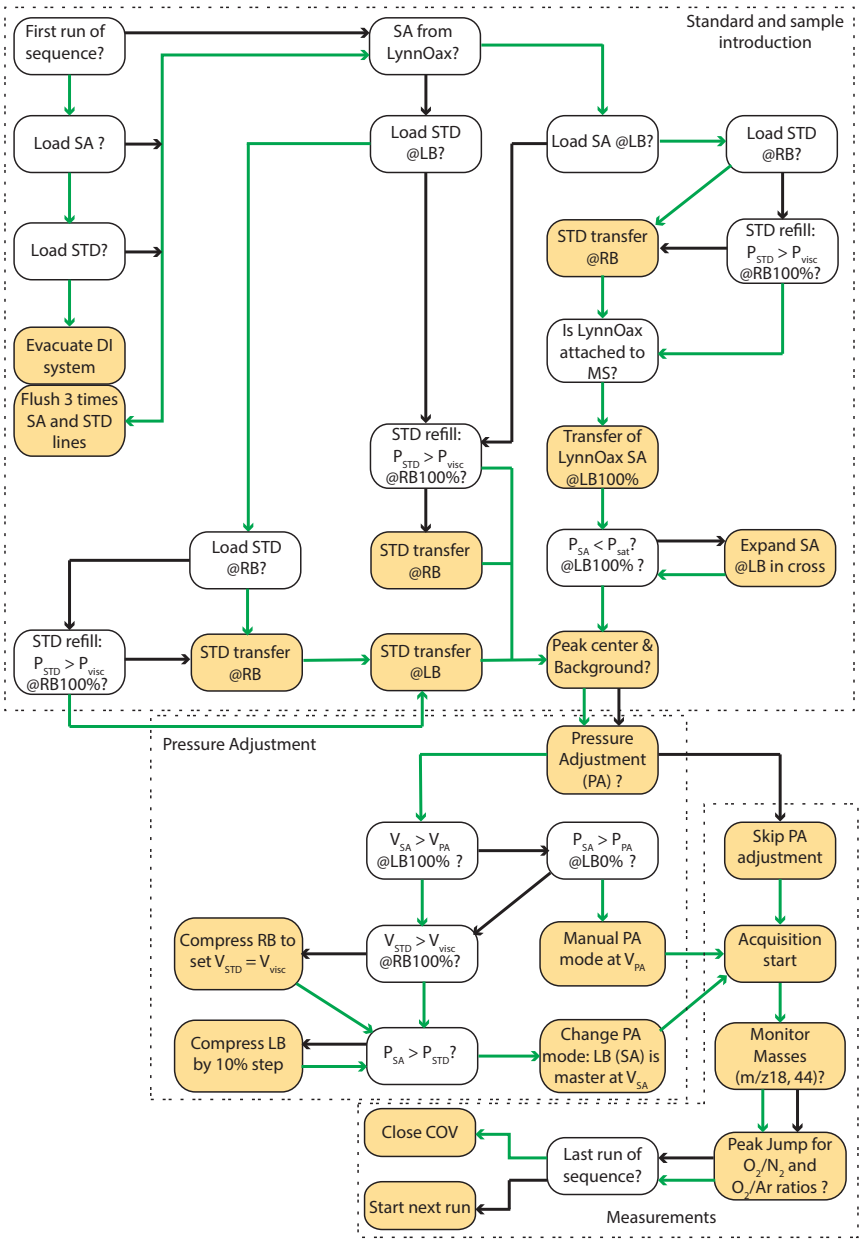

Figure 4.3 – Schematic representation of the automated IRMS measurements program written with ISL scripts. The script was written to enable overnight measurements of up to 10 air/O_2 samples and is used for every block (a row in the sequence described in Fig. 4.2) of the automated sequence (except for $\delta^{15}N$ measurements). White boxes represent boolean conditions, where a green (black) arrow means that the condition is (not) met. The colored boxes represent actions. Note that a few actions, performed or not, lead to the same step (green and black arrow lead to the same box). For instance, the PA procedure will always follow peak centering and background steps.

Table 4.1 – Definitions of abbreviations used in Figure 4.3. Note that the threshold pressure and beam voltages can be found in the isl script in Annex A

Abbreviation	Name
SA	sample
STD	standard
DI	Dual Inlet
LynnOax SA	SA in a rod of the collection manifold
PA	pressure adjustement
LB	left bellow (SA is always introduced in LB in our setup)
RB	right bellow (STD is always introduced in RB in our setup)
@RB	towards, or in RB
@LB	towards, or in LB
@RB100%	towards, or in RB expanded to 100 %
@LB100%	towards, or in LB expanded to 100 %
@LB0%	towards, or in LB compressed to 0 %
P_{STD}	pressure of STD in RB
P_{SA}	pressure of SA in LB
P_{visc}	$P_{viscous}$, minimal pressure ensuring viscous flow conditions for the coming block
P_{sat}	$P_{saturated}$, maximal pressure above which V^{34}_{SA} is saturated (> 50 volts)
P_{PA}@LB0%	pressure in LB at 0 % corresponding to V_{PA}
V	V^{32}, beam voltage associated with m/z 32
V_{visc}	$V^{32}_{viscous}$, minimal beam voltage value to ensure viscous flow conditions
V_{PA}	V^{32}_{PA}, beam voltage value at which both LB and RB are adjusted (manual PA)
COV	ChangeOver valve

viscous flow conditions are not met.

- If the flag state "Evacuate Sa" is checked, column "Lynn Oax Inlet" is used by the isl script to distinguish between a zero-enrichment test or a sample block. Neem_C1 standard is introduced from the right inlet of the MS to the LB in the first case, whereas a sample collected in LynnOax is introduced from the left inlet of the MS to the LB in the second case[8]. It should be mentioned that LynnOax needs to be physically connected to the MS for the sample transfer to happen, which avoids possible contamination of the DI line with ambient air. If "Evacuate Sa" is not checked, a new sample or standard is not reloaded.

- In case the sample contains too much air, the sample is expanded to the cross of the MS until the pressure of the LB at 100 % ensures no saturation in the O_2 beam voltages.

4.5.3.2.2 *Pressure adjustment*

Depending on the sample beam voltage V^{32}_{sa}, either a manual pressure adjustment (PA) is performed at 10 V or at the sample beam voltage level. Manual PA is favored but in case of a too high V^{32}_{sa} in the fully expanded LB or a too low pressure in the fully compressed LB, the program changes of PA mode and performs a PA at the sample beam voltage V^{32}_{sa}. If too low, the standard beam voltage V^{32}_{std} is set to a value that ensures viscous flow conditions by compressing the RB. Then the sample pressure is set above the standard pressure (in case it was not the case) by compressing the LB by 10

[8]Note that the columns "Sample Intro" and "Standard Intro" in Fig. 4.2 inform from which MS inlet samples and standard are introduced, but are not used by the isl script.

% steps. This pre-PA procedure was added to ensure that V^{32}_{std} could be adjusted to V^{32}_{sa} by compressing the RB. Typically, the amount of sample gas is lower than the amount of standard gas at the beginning of the 10 sample measurements, which leads to a higher rate of pressure decrease on the sample side, but this ratio gets inverted with time. To correct for this beam voltages difference, a pressure imbalance correction is applied (Sect. 4.6.1).

4.5.3.2.3 O_2 *isotope ratio measurements*

We've seen in Sect. 4.5.1 that 16 cycles per block were optimal for O_2 isotope ratio measurements. Therefore, one run of three blocks of 16 cycles is performed for each sample (and each zero-enrichment test) with the "O2_gaslab" configuration to measure $^{18}O/^{16}O$ and $^{17}O/^{16}O$ ratios. The $\delta^{18}O$ of a run represents the average of 3 $\delta^{18}O$ ($\delta^{17}O$) blocks, and the precision of the run is defined by the standard deviation of 3 $\delta^{18}O$ ($\delta^{17}O$) block values. This step corresponds to the box "Acquisition start" in Fig. 4.3.

4.5.3.2.4 *Measuring* $\delta O_2/N_2$ *by peak jumping*

The collector configuration of the MS (Sect. 4.3) does not enable a simultaneous collection of m/z 28 and m/z 32, necessary to calculate $\delta O_2/N_2$:

$$\delta\frac{O_2}{N_2} = (\frac{(V^{32}_{sa} - B^{32})/(V^{28}_{sa} - B^{28})}{(V^{32}_{std} - B^{32})/(V^{28}_{std} - B^{28})} - 1), \tag{4.6}$$

where V^{28} is the beam voltage on m/z 28 ($^{14}N^{14}N$). Note that B^{28} and B^{32} have identical values, as both m/z 28 and m/z 32 are measured on the same cup (see below). Instead, $\delta O_2/N_2$ is measured by peak jumping (called PJ hereafter) at the end of the third block of a sample run. PJ is done in the same gas configuration as O_2 ("O2_gaslab") by jumping forth and back the magnetic field B between the O_2 and N_2 peaks.

PJ is performed only if "MagnetScan" is checked in the sequence displayed in Fig. 4.2. For this procedure, we adapted a script (refer to Annex A) that was developed by Severinghaus et al. (2003) to improve the PJ precision of $^{84}Kr/^{36}Ar$ measurements[9]. The gain in precision is mostly linked to a faster PJ procedure, which minimizes instrumental drift and saves time by avoiding a reset of the magnet between each measurement (Severinghaus et al., 2003). Note that $\delta O_2/Ar$ can not be measured easily in our automated sequence because of the impossibility to switch between high and low amplification with isl (probaly related to an issue with the Isodat version used), as detailed in Sect. 4.6.5.

As the amount of sample and standard gas generally differs, their beam voltages are characterized by a different decrease rates. As the peak jumping procedure requires

[9]The script from Severinghaus et al. (2003) is based itself on the Interfering Masses program from Isodat (accessible from the method file), corresponding to the box "MonitorM" in Fig. 4.3. This program is called during a block if "Magnet" is checked in the sequence (Fig. 4.2)

to reset the magnet after each peak jump to account for hysteresis effect, and as integration and idle times are set to 16 s, sample and standard voltage beams can be too unbalanced to obtain reliable $\delta O_2/N_2$ values. O_2 and N_2 sample and standard beam voltages are therefore measured 6 times and the individual decrease rate for each beam voltages except V_{sa}^{32} is obtained by fitting their measured beam voltages with a linear function over time (Fig. 4.4). The individual decrease rates are used to interpolate all beam voltages to the times where V_{sa}^{32} was measured:

$$V_n^i(T_{sa}^{32}) = V_n^i(T_n^i) + \Delta \cdot (T_{sa}^{32} - T_n^i), \tag{4.7}$$

where ΔV is the decrease rate, T the time of measurement,n stands either for sample or standard and i for 28 or 32. Voltage beams were measured 6 times instead of 3 to ensure a good fit (in case of outliers). A Python script was developed by Grzymala-Lubanski (2015) to automate the calculation of $\delta O_2/N_2$ value from the exported text file produced by the peak jumping isl program (Severinghaus et al., 2003) and can be found in the Annex B.

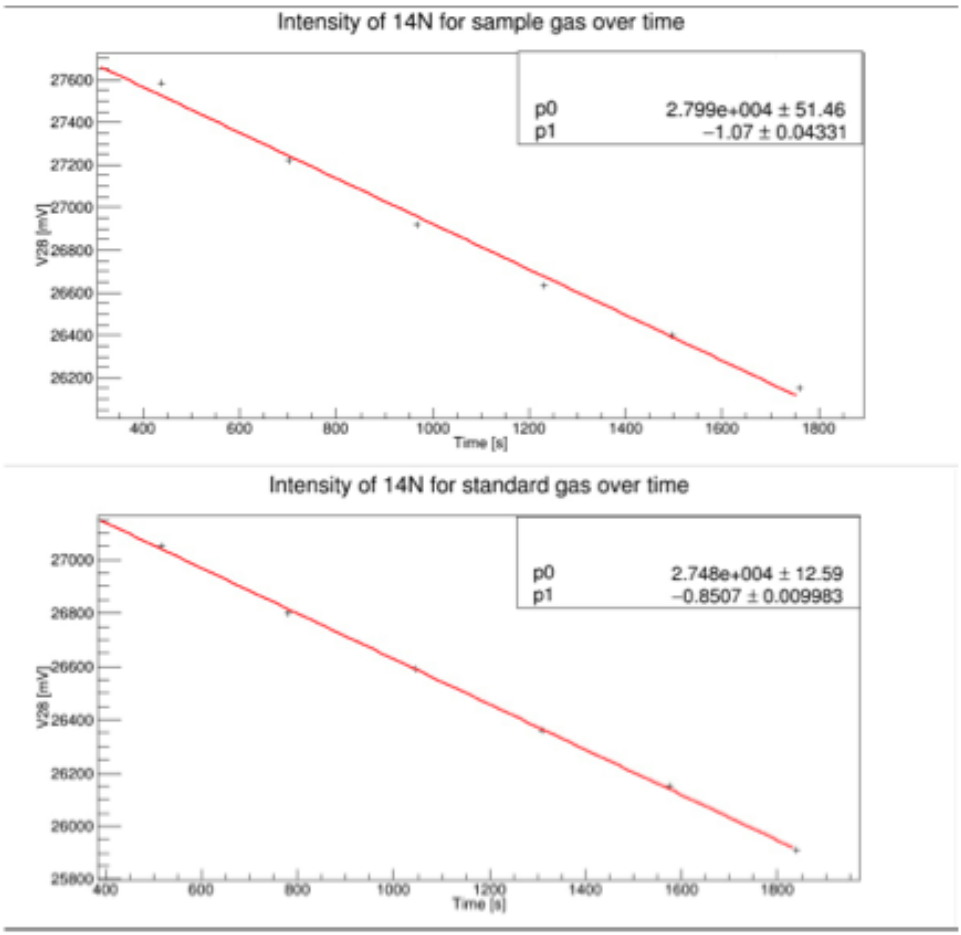

Figure 4.4 – Original figure from Grzymala-Lubanski (2015). Quality of the linear regression (in a limited range, the exponential decrease of the beam voltages can be considered to be linear) for V_{sa}^{28} (top) and V_{std}^{28} (bottom).

4.5.4 IRMS INTERNAL PRECISION AND ACCURACY

The IRMS stability was checked with zero-enrichment experiments. These tests were performed daily during ice core measurements periods, and after a change in the focus settings of the MS, mostly caused by a filament replacement. These tests consist in expanding the same standard gas (NEEM air for $\delta^{18}O$ measurements, O_2 -Ar mixture for $^{17}\Delta$ measurements[10]) in both sample and standard bellows. The standard is transferred from a 50 l cylinder to a 1/4" SST aliquot located between 2 pneumatically-actuated bellow valves (controlled under Isodat). The pressure of the standard line is adjusted so that the standard size is in the range of the measured samples. A zero-enrichment test reflects any fractionation of sample or reference occurring during transfer to the source, informs about the conditioning of the DI line and assesses any leaks in the inlet system during a measurement sequence. As mentioned earlier, zero-enrichment tests are performed before and after a sequence of sample measurements to ensure that the IRMS is stable, at least over a sequence of measurements. Over the time period of NEEM measurements, results for Neem_C1 ($\delta^{18}O = 0.001 \pm 0.005$, $\delta^{15}N = 0.0005 \pm 0.008$) are identical within the uncertainty associated with the measurements.

Zero-test enrichments can be slightly modified over time, with a change of filament or focus settings, and typically show anomalous values if the DI system and ion source has not been conditioned to air or O_2 (depending on the measurements), as observed by Bender et al. (1994c)[11].

4.5.5 Referencing to the isotope scales

As mentioned in Sect. 3.4.2.2, the isotope ratios of ice core samples are referenced against present-day atmospheric air, as it is commonly done when measuring molecular O_2 (e.g. Barkan and Luz, 2003; Severinghaus et al., 2009). An atmospheric air tank was sampled in the year 2008 at a clean-air site of the NEEM camp in northwest Greenland (Sperlich et al., 2013) and is referred to as Neem_C1 air. We use it as a working standard (Neem_S1) but also as a reference material (PRM) as it is available in large amount and the isotopic composition of $\delta^{18}O$, $\delta^{15}N$ and $\delta O_2/N_2$ was stable in the last 50 years.

In order to fulfill the IT-principle, and gain in precision, both the sample and the

[10] we use an O_2 -Ar mixture when O_2 is separated with the GC method, as the sample still contains Ar. In contrast, both N_2 and Ar were separated from O_2 with the perovskite membrane, that was hence measured against a pure O_2 mixture in the standard bellow.

[11] Bender et al. (1994c) also observed that reversing capillaries was not affecting the value of zero-enrichment tests. We observed similar results. However, balancing sample and standard flows in the ion source capillaries proved to be difficult, because a differential drift in ion beam voltages between the sample and the standard was systematically observed in the day following crimping adjustment. Non-balanced beam voltages lead to a larger pressure imbalance over a block of measurements despite an identical amount, which requires corrections (Sect. 4.6.1).

working standard against which the sample is measured must be introduced in theory through the sample side of the IRMS. This means that the isotopic content of the intermediate standard in the standard bellow does not need to be known with precision. However, it needs to be of similar nature, and in the isotopic range of the sample and working standard to be measured (Werner and Brand, 2001). Unfortunately, as mentioned in Sect. 3.7.3, introduction of the working standard Neem_S1 over BFI caused isotope fractionation of O_2 . The RICE ice core samples measured by Grzymala-Lubanski (2015) were thus referenced against the intermediate standard Neem_C1 (which is also the PRM for O_2 measurements and has a $\delta^{18}O$ and $^{17}\Delta$ value of 0 ‰ by definition) introduced in the standard (right) bellow of the MS. To assess the stability of the extraction line, 21 late Holocene NEEM ice core samples were run together with the RICE ice core samples and displayed a remarkable stability around -0.05 ± 0.03 ‰ (Sect. 4.6.7) after usual corrections (Sect. 4.6). Such results, from ice core samples that were collected in different rods and at different days, give us confidence that the conditions of the analytical system are similar at least during a sequence of ice core measurements. Summarizing, we are aware that referencing ice core samples against the intermediate standard NEEM_C1 does not fully respect the IT principle, and introduction of Neem_S1 above BFI should be implemented in the future to fulfill this condition. However, the stability of the measured $\delta^{18}O_{atm}$ of 21 NEEM shallow ice core samples from the same depth, that can thus be considered as replicates, underline the ability of the system to reproduce measurements of gas trapped in ice core bubbles. Concretely, this means that the measured RICE $\delta^{18}O_{atm}$ values may be offset relative to the true value on the $O2_{atm}$ isotopic scale, but their relative variations are real and not the result of random artifactual fractionation during the experiment.

4.6 Corrections

This section describes data post-processing for $\delta^{18}O$. Several corrections need to be applied to the raw delta values calculated by Isodat. There are 4 main sources of error that need to be accounted for:

1. biases associated with mass spectrometry measurements: internal stability of the MS, pressure imbalance, chemical slope. These biases depend on the settings of the IRMS ion source, and vary with time.

2. biases associated with the experimental setup, which can be reduced by referencing the samples agains a standard that was treated the same way.

3. processes occurring in the firn, associated with the transition of snow to ice: gravitative settling, thermal diffusion, and ordinary diffusion.

4. processes associated with the drilling, retrieval and storage of the ice core samples: coring and post coring processes

These corrections significantly improve the precision of the measurements. The standard deviation of 21 ice samples from the same sampling site (Neem) and depth

(337 m) improves from 0.09 ‰ to 0.03 ‰ after data post-processing. The corrections are presented in the same way as they are done, that is (1) pressure imbalance correction, (2) chemical slope correction, (3) corrections associated with molecular diffusion processes in the firn and (4) gas loss corrections.

4.6.1 PRESSURE IMBALANCE

A difference of pressure between the sample and standard bellows slightly affects the measured $\delta^{18}O$ values, requiring a small correction.

Avoiding differences in pressure in the bellows would be ideal. With a similar amount on both sides, the decreasing pressure with measurement time would indeed be similar in both bellows, implying a similar gas flow decrease through the transfer capillaries, and therefore balanced beam voltages throughout the run. However, as the amount of gas always slightly differ from one ice core sample to another (many causes can be invoked: various dimensions of the cleaned samples after chiseling off their external layers, various total air content, small changes in the fossil air extraction and collection efficiencies, etc), ensuring an (almost) identical amount in both sample and standard bellows would require to first measure the amount of sample gas introduced in the bellow, and then adjust the volume of the standard bellow so that the amount of expanded standard gas matches the amount of expanded sample gas, as recommended by e.g. Bender et al. (1994a) for O_2 /N_2 analysis.

Actually, as $\delta^{18}O$ is measured in a mixture of gases (N_2 -O_2 -Ar), with grossly 4 times more N_2 than O_2 , an identical amount in both bellows is not sufficient to ensure balanced O_2 beam voltages throughout the run if the O_2 mixing ratio differs between the sample and standard gas mixtures. Indeed, when measuring O_2 isotope ratios, the Isodat function "press adjust" (PA) balances the major O_2 beam voltages (m/z 32), hence the O_2 partial pressure, just before the start of the measurement sequence.

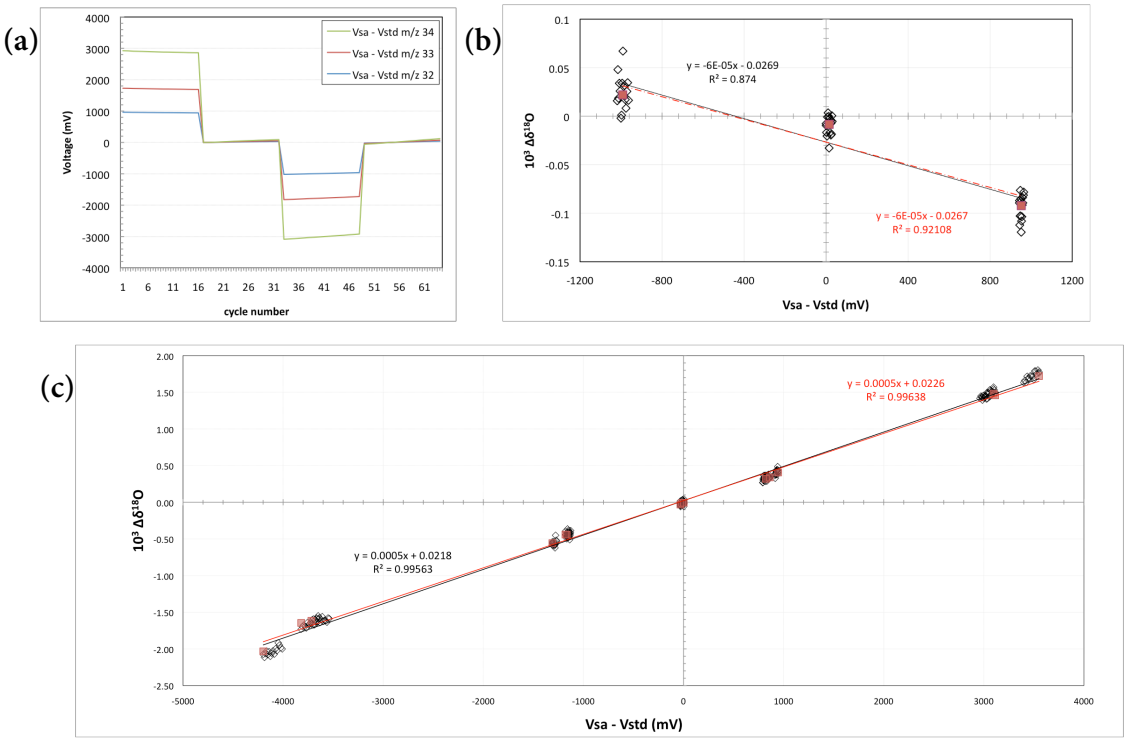

Figure 4.5 – **(a)** Voltage difference between a sample and a standard ($\Delta V = V_{sa} - V_{std}$) for m/z 32, 33 and 34 over a typical automated sequence of 3 blocks of 16 cycles each (the 4th block, including cycles 49 to 64, is corresponds to a zero-enrichment test). The pressure in the sample bellow is first increased to obtain a difference of ≃ 1000 mV between the 2 bellows during the first block, and the opposite is done during the third block. Sample and standard pressures are balanced over the second block. **(b)** Pressure imbalance determination (Feb. 2014) using a pure O_2 working standard (Tank_1b). Black diamonds correspond to the $\delta^{18}O$ values of 48 individual cycles and their associated $\Delta V = V_{sa} - V_{std}$. Red squares correspond to the mean $\delta^{18}O$ values of the 3 blocks versus ΔV. The slope of the linear regression line represents the sensitivity of $\delta^{18}O$ to pressure imbalance im $‰ \cdot mV^{-1}$. **(c)** Similar as in **(b)** (July 2015) but with an atmospheric air working standard (Neem_C1). The PI sensitivity is an order of magnitude higher in air than in pure O_2 , and the PI slopes are of opposite sign. Values of the PI slope during RICE and NEEM ice core measurements can be found in Table 4.2. It should be mentioned that the ion source had to be opened between the 2 experiments, so the source parameters and focus settings are slightly different between **(a)** and **(b)**.

But it is the total pressure in the bellow that controls the flow of gas through the transfer capillary, not the O_2 partial pressure. As a result, even with an identical amount of gas, the sample and standard beam voltages will become unbalanced over time, the bellow with the lower O_2 partial pressure being more compressed after the PA procedure, that is with a higher total pressure at the start of the measurements and consequently loosing more gas per unit of time.

In our fully automated DI measurement sequence, the standard bellow is not refilled after each sample introduction, but only when it reaches a threshold pressure under

which isotope ratios can't be precisely measured, as viscous flow conditions are not met. Refilling the bellow with a new standard after each sample introduction would be too time-consuming. Besides, as explained in this section, introducing a similar amount in both bellows does not ensure balanced beam voltages throughout the run. Finally, we favor a manual "PressAdjust" (cf Sect. 4.5.3), by which both sample (V^{32}_{sa}) and standard (V^{32}_{std}) major O_2 beam voltages are balanced to a preset value (≃7000mV on m/z 32) after each block, so that measurements are performed in similar conditions.

Typically, the amount of sample gas is lower than the amount of standard gas after a standard refill, which leads to a higher rate of pressure decrease on the sample side, but this ratio gets inverted with time. As shown by Grzymala-Lubanski (2015) for ice core measurements, during a block of 16 cycles, the sample and standard beam voltages can differ by up to 200 mV despite being balanced at start. SA

To correct for this pressure imbalance, a run of 3 blocks of 16 cycles is included at the start of the measuring sequence (Fig. 4.5a) and is run every week of measurements. An aliquot of the standard gas Neem_C1 is successively introduced in both bellows from the standard inlet of the IRMS. The first (third) block is run with the sample (standard) major O_2 beam voltage unbalanced by ≃ 5 to 10 %, and the second block with both beam voltages balanced, as in a zero-enrichment test. A typical chart used to determine the sensitivity of $\delta^{18}O$ to pressure imbalance is shown in figure 4.5b. The slope of the linear regression line represents the sensitivity of $\delta^{18}O$ to pressure imbalance im ‰ $\cdot\, mV^{-1}$. This correction thus assumes a linear relationship between $\Delta\delta$ (the PI-related δ deviation from its true value) and ΔV (pressure imbalance expressed as the beam voltage difference between sample and standard) (Severinghaus et al., 2003), as observed by e.g. Bender et al. (1994b). PI SENSITIVITY

Table 4.2 demonstrates the stability of the PI slope, determined in an air mixture, Neem_C1, over the 4 weeks of RICE core measurements (Grzymala-Lubanski, 2015), with a typical value of $5 \cdot 10^{-4}$‰ $\cdot\, mV^{-1}$. A difference of 200 mV thus causes a shift of 0.1 ‰ in the measured value.

Once the PI slope is determined, the raw $\delta^{18}O$ value calculated by Isodat can be corrected. We choose to correct every cycle rather than the mean block value, obtaining a better precision with this method:

$$\delta_{PI\,corrected} = \delta_{measured} - PI\,slope \cdot \Delta V, \tag{4.8}$$

where $\delta_{measured}$ corresponds to the cycle δ values as calculated by Isodat, and $\Delta V = V_{sa} - V_{std}$, with V_{sa} and V_{std} representing the sample and standard beam voltage of the most abundant isotope of the measured gas (e.g. m/z 28 for N_2 , m/z 32 for O_2), resp. Please keep in mind that a beam voltage corresponds to the amplified ion current signal produced by hitting of ionized molecules in the Faraday cup.

Typical corrections of ≃ 0.03-0.07 ‰ are applied to $\delta^{18}O$ values, which are in the high range of other studies measuring O_2 isotopes in fossil air. For instance, Capron

Table 4.2 – Pressure Imbalance slope during the 4 weeks of RICE core measurements. Gas standard: Neem_C1. Original Table 5.1 from Grzymala-Lubanski (2015)

PI slope ($‰ \cdot mV^{-1}$)	R^2 of linear regression	week number
0.000498	0.982	1
0.000556	0.999	2
0.000536	0.958	2
0.000559	0.997	2

(2010) corrects $\delta^{18}O$ for PI imbalance by ≃ 0.02 to 0.03 ‰. The PI correction on cycle $\delta^{18}O$ is useful as the standard deviation of the PI corrected block $\delta^{18}O$ is reduced.

Given the small effect of PI on $\delta^{15}N$, and the fact that a χ^2 test demonstrates that the goodness of the linear fit is not significantly better than the one of a horizontal line, Grzymala-Lubanski (2015) does not apply PI corrections on $\delta^{15}N$.

4.6.2 CHEMICAL SLOPE

A better precision is achieved when measuring isotope ratios in a pure substance[12]. This gain in precision is due to the fact that in a mixture of gases, the variations of elemental ratios have an influence on the measure of the isotopic ratios of a single element: $\delta O_2/N_2$ influences $\delta^{18}O$ and $\delta^{15}N$ measurements, $\delta^{15}N_2/Ar$ affects δ^{40}Ar (Severinghaus et al., 2001, 2003; Landais et al., 2003; Capron, 2010). Different causes have been invoked, like molecules-ions interactions in the source that affect the relative ionization efficiencies of light and heavy isotopologues, hypothesis which is supported by the fact that the chemical slope is reduced when source parameters are tuned to optimize linearity. Indeed, linearity settings are likely to reduce ion-molecule interactions in the ion source as the ions are quickly extracted (Sect. 4.4.0.1). However, the process is not really well understood and varies between MSs. We apply an empirical correction to account for these interfering masses as done by Severinghaus et al. (2003). We assume this correction to be linear in the range of our measurements. This chemical slope correction for $\delta^{18}O$ is done before a set of measurements by adding increasing amounts of high-purity N_2 in aliquots of standard gas (here Neem_C1), and measuring it against the standard gas alone. A mass flow controller is used to introduce increasing amounts of N_2 to the standard gas line.

The figure 4.6a presents the chemical slope characterization performed by Grzymala-Lubanski (2015) on the Delta V Advantage. The quality of the fit is not excellent, and its intersection with the y-axis ($\delta^{18}O\ (0,0) = -0.053 \pm 0.021‰$) does not lie within the measurement uncertainty of a zero-enrichment test (while it should in theory, as it corresponds to the measurements of the standard gas versus itself). The uncertainty associated with the chemical slope can be due to large pressure imbalance observed

[12]this gain in precision is the mian motivation to separate N_2 from O_2 for $^{17}\Delta$ measurements, requiring a very high precision (≃10 permeg) to gain climatic information from the small signal (≃ 40 permeg between glacial and interglacial)

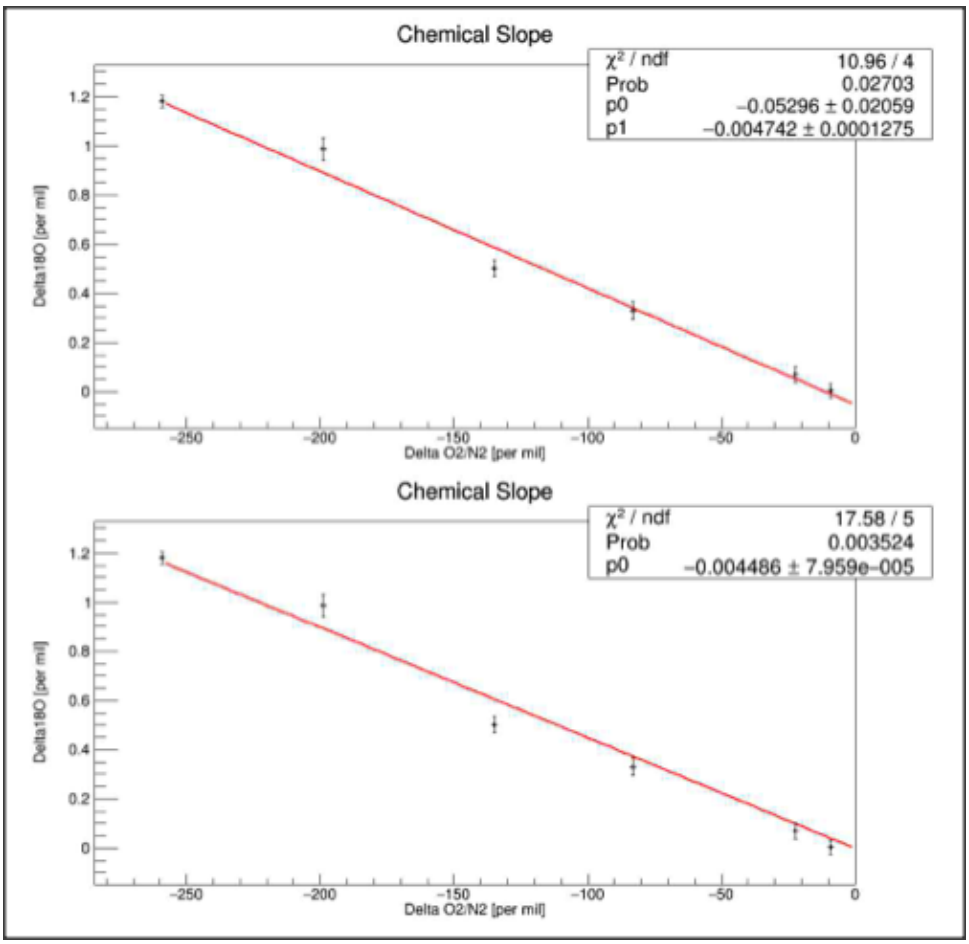

Figure 4.6 – Original figure from Grzymala-Lubanski (2015) **(a)** Empirical determination of the chemical slope characterization performed by Grzymala-Lubanski (2015) on the Delta V Advantage. Increasing amounts of pure N_2 were progressively added to the standard gas (Neem_C1) and measured against itself, as in a zero-enrichment test. Resulting $\delta^{18}O$ values are plotted against $\delta O_2/N_2$ values. The red line represents the linear fit corresponding to the chemical slope. p0 gives the intercept of the linear regression with the y-axis and its associated error, while p1 stands for the slope of the linear fit and its associated error **(b)** Chemical slope when forced through (0,0). p0 stands for the slope of the fit. A χ^2 test is used to evaluate the goodness of the fit for both plots. χ^2 is the squared difference between the measured δ values and their theoretical predictions given by the fit weighted by the expected errors of measurements (Barlow, 1989), set to the standard deviation of a zero enrichment test.

$$\chi^2 = \sum_i \frac{(y_i - f(x_i))^2}{\sigma_i^2} = \sum \left(\frac{\delta_i^{measured} - \delta_i^{theoretical}}{expected\ error} \right)^2 \tag{4.9}$$

The closer χ^2 divided by the number of degrees of freedom is closed to 1, the better the fit matches the measurements.

for samples highly enriched in N_2 (up to $\delta V = 400mV$, Grzymala-Lubanski, 2015), so that the PI corrections applied on $\delta^{18}O$ became significant. The large imbalance arises from the fact that Neem_C1 (atmospheric air) already contains ≃80 % N_2 . Indeed, to obtain 90 % N_2 in the final gas mixture, the size of the standard had to be doubled (2 ml of N_2 added to 2 ml of Neem_C1). It should also be reminded that the $\delta O_2/N_2$ ratio cannot be measured simultaneously (because of the Universal Triple collector configuration of the IRMS, Sect. 4.3), which requires further data treatment and possible loss of precision. Based on the aforementioned considerations, the fit is forced to (0,0) (Fig. 4.6b). The quality of the fit is reduced, but the slope is only slightly affected. Indeed, with a $\delta O_2/N_2$ of -10‰, taking a different slope does not affect $\delta^{18}O$ by more than 0.003 ‰, which is lower than the internal precision of the MS (Sect. 4.5.4).

More measurements will be needed in the future to determine more precisely the chemical slope, especially in the range $\delta O_2/N_2 \in [-30‰, 0‰]$, where most of our measurements lie. This is important as the uncertainty of the fit affects the final $\delta^{18}O$ values. The chemical slope correction is applied to $\delta^{18}O_{\,PI\,corrected}$ in the following way:

$$\delta^{18}O_{CS\,corrected} = \delta^{18}O_{PI\,corrected} + chemical\,slope \cdot \delta O_2/N_2, \tag{4.10}$$

where $\delta O_2/N_2$ is measured by peak jumping (Sect. 4.5.3.2.4). Despite the uncertainty associated with the chemical slope, the correction makes sense, as demonstrated by the pooled standard deviation of the 21 NEEM ice core samples from the same sampling depth (337 m), which reduces from 0.077 ‰ ($\delta^{18}O_{\,PI\,corrected}$) to 0.068 ‰ after chemical slope correction ($\delta^{18}O_{\,CS\,corrected}$).

4.6.3 Corrections due to diffusive processes in the firn

The firn alters the elemental and isotopic composition of the air bubbles trapped in ice cores (Sect. 1.4.1). It is therefore required to apply corrections to retrieve the true atmospheric signal.

4.6.3.1 Gravitational fractionation

To separate the firn and atmospheric fractionation processes, the influence of gravitational fractionation in the firn is removed from corrected $\delta^{18}O$ of O_2 using the $\delta^{15}N$ measurements. In Sec. 1.4.1.1, we describe how gravitational fractionation scales with Δm. Following Bender et al. (1994c), Sowers and Bender (1995), Severinghaus et al. (2009), $\delta^{18}O$ is corrected in the following way:

$$\delta_{gravcorr} = \delta_{CS\,corrected} - \Delta m \cdot \delta^{15}N, \tag{4.11}$$

where the mass difference $\Delta m = 2$ for $\delta^{18}O$ and $\Delta m = 4$ for $\delta O_2/N_2$. This correction assumes that $\delta^{15}N$ enrichment is only of gravitational origin (Fig. 4.9), which is a fair assumption here as explained in the next section. Note that fractionation processes that scale with the absolute mass difference Δm, that can occur for instance during the experiment, will be also removed by this correction (Sect. 4.6.6).

4.6.3.2 Thermal fractionation

Difference in O_2 and N_2 coefficients of thermal diffusion leads to a thermal fractionation 1.6 times larger for $\delta^{18}O$ than for $\delta^{15}N$ (Severinghaus et al., 2001). However, in general, correction for thermal fractionation can be neglected. Indeed, large and rapid temperature changes (Sect. 1.4.1.2) are necessary to affect isotope ratios. In East Antarctica, firnification and temperature changes are too slow to create large transient temperature gradients in the firn (Goujon et al., 2003). Furthermore, the thermal equilibration evolves as the square of the firn thickness, which is only 40-60 m in Antarctic coastal zones (Paterson, 1994; van den Broeke, 2008), where the RICE ice core measured by Grzymala-Lubanski (2015) originates. As a consequence, no correction for thermal fractionation is applied to RICE ice core samples in Grzymala-Lubanski (2015). RICE

In contrast, large millennial scale temperature changes (DO events) occurred during the last glacial period in Greenland. Resulting temperature gradients in the firn are much larger than in Antarctica, and modify substantially the isotopic composition of the bubbles (Landais et al., 2010). As explained in Sect. 1.4.1.2, the effect on $\delta^{18}O$ can be corrected for by combining $\delta^{15}N$ and ^{40}Ar measurements. The NEEM (and Eurocore, drilled at Summit drilling station) ice core measurements presented in this thesis are dated from the late Holocene, where temperature variations were low. Indeed, reconstructed surface temperature histories (from 2000 to 0 yrs A.D.) based on borehole temperature measurements performed at GRIP (Greenland, 72.4°N, 37.4°W) do not vary by more than ± 1°C (Dahl-Jensen et al., 1998). It is thus reasonable to assume that the effect of thermal fractionation can be neglected. As a consequence, no correction for thermal fractionation is applied to NEEM and Eurocore standards. NEEM

4.6.3.3 Bubble close-off fractionation

While gravitational and thermal fractionation are mass-dependent diffusive processes occurring in the gas phase, bubble close-off fractionation combines size-dependent and mass-dependent diffusive process occurring in the ice matrix (Sect 1.4.1.3). As mentioned in Sect. 1.4.1.3 and developed in Sect. 4.6.4, artifactual gas loss from the ice can also occur during coring and storage, making difficult to estimate solely the effect of bubble close-off fractionation on $\delta O_2/N_2$ and $\delta^{18}O_{atm}$. We present here the alternative strategies adopted to quantify the effect of bubble close-off fractionation on the elemental and isotopic composition of gases trapped in ice core bubbles, with a focus on $\delta O_2/N_2$, required to correct $\delta^{18}O_{atm}$.

One could imagine that pumping firn air directly in the LIZ would help estimate bubble close-off fractionation. As shown in Fig. 1.19, a gradual $\delta O_2/N_2$ enrichment with depth occurs in the lock-in-zone. However, the observed $\delta O_2/N_2$ enrichment in the LIZ found by firn air studies (e.g. Severinghaus and Battle, 2006) is due to the fact that the sampling of deep firn air is incomplete, accessing only the open porosity, FIRN AIR SAMPLING

but not macropores or the closed porosity (Severinghaus, pers. comm., 2016). Hence the observed enriched $\delta O_2/N_2$ is not representative of the average $\delta O_2/N_2$ in ice core bubbles. At the close-off-depth, the very limited open porosity actually even precludes the extraction of firn air samples (Battle et al., 2011). In the following, we detail the cause of $\delta O_2/N_2$ enrichment in the LIZ.

SUMMER VS WINTER LAYERS

Large differences in $\delta O_2/N_2$ are observed between summer and winter layers, the former being consistently less depleted than the latter[13]. Summer layers are less depleted because bubbles in summer layers close later/deeper than bubbles in winter layers:

1. O_2 permeating 3 times faster than N_2 through the ice lattice, the permeate, that is the air expelled from closing bubbles) is highly enriched in O_2 (with a $\delta O_2/N_2$ of $\backsimeq$ 2000‰) and accumulates in the high open porosity of the summer layers.

2. As explained in Sect. 1.4.1.3.4 for layering, the O_2 enriched air cannot escape to the atmosphere from the open pores of the deep summer layers of the LIZ, because of the formation of quasi impermeable horizontal layers in the LIZ (e.g. denser winter layers, whose open porosity is low, as bubbles are already mostly closed off), and ultimately gets trapped in bubbles.

It follows that the pumping of air from the LIZ is mostly originating from the $\delta O_2/N_2$ enriched open pores of the summer layers, which explains, as aforementioned, the observed gradual enrichment in $\delta O_2/N_2$ (Severinghaus, pers. comm., 2016). It should be underlined that the difference in $\delta O_2/N_2$ of summer and winter layers probably explain a large part of the scattering of $\delta O_2/N_2$ values observed in replicate ice core samples. This also explain why the long axis of the samples need to be orientated parallel to the ice core so as to average over several (depending on the accumulation rate) seasonal layers.

We've seen in Sect. 1.4.1.3.4 that close-off fractionation is ultimately depending on the amount of gas-loss across the lock-in-depth. A method to estimate the average $\delta O_2/N_2$ depletion solely due to bubble close-off in ice core samples consists in estimating the upward O_2 loss flux to the atmosphere from the observed O_2 /N_2 gradient in the diffusive zone, above the lock-in-depth, applying Fick's second Law[14], and assuming steady state after correcting for anthropogenic atmospheric O_2 change (Severinghaus and Battle, 2006). At NEEM, this method only requires precise $\delta O_2/N_2$ firn air measurements, as D at NEEM is well-known (Buizert et al., 2012). This method was applied at Siple Dome and South Pole by Severinghaus and Battle (2006). They estimated that the upward flux of O_2 accross the LIZ should leave the air bubbles in ice depleted with an average $\delta O_2/N_2$ of $\backsimeq -2$‰. However, $\delta O_2/N_2$ from South Pole ice core samples was consistently depleted by $\backsimeq -8$‰ (Severinghaus, pers. comm.,

[13] a careful study of this was done at Siple Dome, where it was possible to visually identify the summer layers in shallow mature ice (90 m depth, vs. a close-off around 60 m) (Severinghaus, pers. comm., 2016)

[14] $\frac{\partial c}{\partial t} = D \cdot \frac{\partial c}{\partial z^2}$, where c stands for gas concentration, t stands for time, D is diffusivity and z is depth.

2016). This difference between the two $\delta O_2/N_2$ values evidences artifactual gas loss caused by coring and post coring processes, as detailed in Sect. 4.6.4.

4.6.4 Coring and post-coring gas loss fractionation

This section focuses on the two processes altering the elemental and isotope composition of ice core samples during ice core recovery and storage. Observations indeed show that artifactual gas loss can be divided into two categories, which may be difficult to distinguish: gas loss associated with size-dependent fractionation and gas loss associated with mass-dependent fractionation, similar to the one observed for close-off fractionation (Sect. 1.4.1.3). This section also describes the different correction strategies, which widely differ between studies, applied to samples affected by gas loss fractionation. It finally focuses on the NEEM late Holocene ice core samples measured by Grzymala-Lubanski (2015) on the analytical line built during this thesis and present the empirical correction applied to $\delta O_2/N_2$ and $\delta^{18}O_{atm}$ for gas loss fractionation.

4.6.4.1 Size-dependent fractionation

Similar to the gas-loss mechanism during the bubble close-off, size-dependent diffusion from overpressured air bubbles through the ice lattice takes place during storage. STORAGE Suwa and Bender (2008) remeasured $\delta O_2/N_2$ of well preserved deep GISP2 samples after 12 years of storage at −35 °C. Figure 4.7 presents the evolution of $\delta O_2/N_2$ for 7 samples with a similar depth. A constant depletion of 7.3 ‰ is observed, suggesting that the loss of O_2 is correlated with the storage duration, as already observed by Ikeda-Fukazawa et al. (2005). $\delta^{18}O$ remains almost unaffected in this study, with a $\delta^{18}O$ depletion by 0.021 ± 0.074‰ during storage. The fact that the isotope composition of molecular O_2 remains unaffected while elemental O_2 /N_2 ratio gets depleted calls against a mass dependent fractionation process.

Ikeda-Fukazawa et al. (2005) explains that no mass-dependent fractionation occurs because it is not the velocity of the molecules but the rate of gas diffusion through the ice lattice that is controlled by the rate of hydrogen-bond-breaking (cf. Sect. 1.4.1.3). This view is supported by the fact that gas loss is strongly dependent on temperature (Kawamura et al., 2007; Ikeda-Fukazawa et al., 2005). These observations are in agreement with the hypothesis of Bender et al. (1995), who proposed that gas loss during and after coring is caused by a process fractionating elements in a size-dependent way (depending on the molecular diameter) rather than in a mass-dependent way (depending on the diffusivity). Severinghaus et al. (2009) suggests that the absence of mass-dependent fractionation can be explained by the absence of cracks, due to the low stress associated with annealing of the ice core over a long time during storage, in spite of gas constantly leaking out of overpressured bubbles in ice.

Available observations suggest that size-dependent fractionation also occurs in CORING

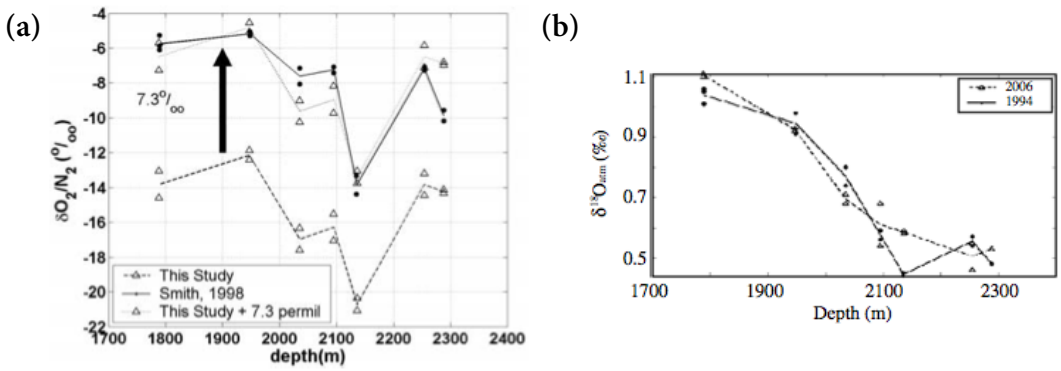

Figure 4.7 – **(a)** Original Figure 2 from Suwa and Bender (2008). $\delta O_2/N_2$ of GISP2 samples of similar depth measured after 11 years (2006) of storage at −35°C are depleted by 7.3 ‰. **(b)** Original Figure 11 from Kobashi et al. (2008), based on measurements performed by Suwa and Bender (2008). $\delta^{18}O$ of same GISP2 samples as in **(a)** shows quasi no changes (0.021 ± 0.074‰ depleted) after storage.

highly-fractured ice. Fractures can be caused by drilling an ice core without pressure-compensating the borehole with drilliing fluid. As described in Sect. 1.4.1.3, small gas molecules like O_2 and Ar diffuse much faster than N_2 through the ice lattice, causing loss of O_2 and Ar in roughly equal proportions (Severinghaus et al., 2009). No isotope fractionation should occur through this process as isotopologues have an identical molecular diameter. However, replicate pairs of ice core samples affected by artifactual gas loss present a characteristic signature in which Ar is half as much depleted as O_2 (Bender et al., 1995; Severinghaus et al., 2009), while one would expect a similar depletion of O_2 and Ar with size-dependent fractionation only. This discrepancy arises from the fact that mass-dependent fractionation also occurs during coring and post-coring (Sect. 4.6.4.2).

4.6.4.2 Mass-dependent fractionation

STORAGE In contrast with observations presented in the previous section, fractionation of Ar isotopes has been evidenced on samples stored at −20°C for more than 5 years by Severinghaus et al. (2003), Grachev (2004) and Kobashi et al. (2008), in apparent contradiction with above-mentioned results. Several studies revealed that a loss of O_2 ($\delta O_2/N_2$ depletion) is associated with an increase in $\delta^{18}O$ during ice core storage. In her thesis, Landais (2004) also found a $\delta^{18}O$ enrichment associated with an increasing loss of O_2 from the inner core to the periphery of a NorthGRIP sample drilled in 1992. Bender et al. (1995) found that samples with highly anomalous O_2 /N_2 ratios with respect to modern air were enriched in $\delta^{18}O$ by 0.1-0.2 ‰. Similarly, GRIP ice core samples remeasured after 6 years of storage were affected by a preferential loss of O_2 on the order of 3 %, associated with an increase of $\delta^{18}O$. The depletion of $\delta O_2/N_2$ and fractionation of $\delta^{18}O$ were shown to correlate linearly by measuring replicate samples (Landais et al., 2003). Several other studies revealed a similar constant slope of 0.01‰ · ‰$^{-1}$ between $\delta O_2/N_2$ variations and $\delta^{18}O$ variations for Antarctic

ice cores - Vostok (Suwa and Bender, 2008), EDC (Dreyfus et al., 2007), Siple Dome (Severinghaus et al., 2009).

Artifactual gas loss associated with mass-dependent fractionation is often associated with poorly-preserved or highly-fractured ice core samples and is called "core-cracking fractionation" (Bender, 2002; Severinghaus et al., 2009). Cracking can occur during handling, as non annealed ice can weaken if warmed on the surface (Bender et al., 1995; Bender, 2002; Severinghaus et al., 2009), or during ice core recovery, caused by high stresses in the ice after depressurization as the ice is brought to surface pressures. Fractures in the ice are often created during recovery of ice belonging to the gas-clathrate transition zone. Indeed, in this "brittle" zone, long of several hundred meters, gases in ice cores transform their state from gas to solid (clathrate) owing to the overlying pressure which increases with depth (Shoji and Langway, 1982). The air entrapped in the ice coexists in both states, gas and solid (clathrate). During ice recovery, the important pressure exerted by the gas fraction on the surrounding ice leads to many fractures in the ice sample. Kobashi et al. (2008) propose that the presence of cracks in the ice leads to gas loss by viscous flow, molecular or Knudsen diffusion, the two latter causing mass-dependent fractionation. CORING

Summarizing, gas-loss processes involve a mix of size- and mass-dependent fractionation that can be caused by bubble close-off, coring and post-coring processes. It is therefore difficult to distinguish between these mechanisms.

4.6.5 Gas-loss corrections applied to NEEM ice core samples

In this section we first present the strategies employed in literature for gas-loss corrections (Sect. 4.6.5.1), then present the strategy adopted for the NEEM ice core samples (Sect. 4.6.5.2).

4.6.5.1 Existing gas-loss correction strategies

We've seen that gas-loss fractionation can occur (i) through two different mechanisms described in the previous sections. Both size and mass-dependent mechanisms are caused by gas leaking out of overpressured bubbles in ice (Severinghaus et al., 2009), and (ii) are not limited to post coring (sample handling, transport and storage), but also fractionate gases during bubble close-off or ice core retrieval[15]. It follows that applying a specific gas loss correction for each of these steps is hardly possible, and prior work circumvent this issue by applying a empirical correction accounting for all gas-loss processes.

As mentioned earlier, fossil air in fractured ice core samples that suffered gas loss typically present an elemental composition half as depleted in Ar as in O_2 (Bender $\delta O_2/N_2$ AND ^{40}Ar

[15]here we do not consider gas loss fractionation associated with the bubble-clathrate transition zone, as measured NEEM samples were coming from much shallower depths.

et al., 1995; Severinghaus et al., 2009). Severinghaus et al. (2009) suggest that this typical gas loss signature results from the combination of diffusion in the ice lattice (size-dependent fractionation) then through cracks (mass-dependent fractionation). Indeed, the apparent slope of 0.5 between $\delta Ar/\delta^{15}N$ and $\delta O_2/N_2$ can be obtained by combining a size-dependent fractionation mechanism, in which O_2 and Ar are affected in similar proportions (slope of 1), and a mass-dependent process, where Ar is 3 times as much enriched as O_2 relative to N_2 , owing to the relative mass difference (Fig. 4.8). If this assumption holds true, it is then possible to separate the size-dependent from the mass-dependent process by combining $\delta Ar/\delta^{15}N$ and $\delta O_2/N_2$ measurements. Adopting this logic, Severinghaus et al. (2009) correct Siple Dome $\delta^{18}O$ in the following way:

$$\delta^{18}O_{atm} = \delta^{18}O_{gravcorr} + 0.0136 \cdot (\delta O_2/N_{2gravcorr} + 2.1‰) - 0.0130 \cdot \delta Ar/N_{2gravcorr} \tag{4.12}$$

Note the typical slope of ≃ 0.01 between $\delta^{18}O$ and $\delta O_2/N_2$ associated with gas-loss processes, as well as the 2.1 ‰ value which is an adjustable parameter tuned to force the mean of the last 1000 yrs of $\delta^{18}O_{atm}$ to 0 ‰.

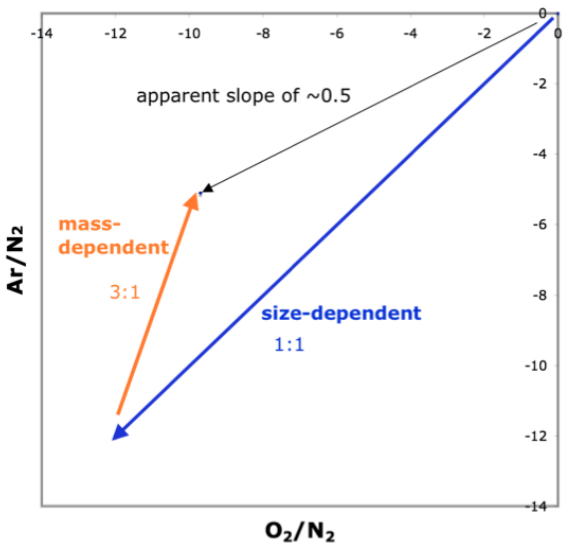

Figure 4.8 – Original figure S4 and caption from Severinghaus et al. (2009). *Schematic of proposed dual-mechanism gas loss. Lattice diffusion causes loss of argon and O_2 in roughly equal proportions, based on their smaller molecular diameters than N_2 , without mass dependence. Transport along fractures to the exterior of the ice sample then causes mass-dependent fractionation, which strongly favors retention of argon due to its 3-fold greater mass difference than O_2 . The net result is an apparent slope of 0.5, but with large scatter due to the fact that varying amounts of each process cause the data to populate a plane in 3-D rather than a line.*

$\delta O_2/N_2$ ONLY

Various empirical corrections based solely on $\delta O_2/N_2$ for artifactual gas loss are described in literature. (Landais et al., 2003) applied a correction to measured GRIP $\delta^{18}O_{atm}$ depending on the time of storage, as observed by Ikeda-Fukazawa et al. (2005): in their study, given the rough dependence of $\delta O_2/N_2$ and $\delta^{18}O$ ($R^2 = 0.6$), the $\delta^{18}O_{atm}$ correction consisted of discarding samples with an O_2 loss higher than 5 ‰ and decreasing valid $\delta^{18}O_{atm}$ by 0.07 ‰ based on the storage effect (over 14 yrs) observed in $\delta^{18}O_{atm}$ of 6 duplicate Vostok ice core samples.

Temperature of storage is crit-

ical to minimize gas-loss: $\delta O_2/N_2$ of EDC ice core samples stored at $-50°C$ were associated with a standard deviation of 0.32 ‰ while EDC samples stored at $-25°C$ had a standard deviation of 10‰ (Landais et al., 2012). Consequently they only corrections were only applied to samples stored at $-25°C$.

4.6.5.2 Gas-loss correction applied to NEEM ice core samples

The gas-loss correction applied to NEEM ice core samples' $\delta^{18}O_{atm}$ is adapted from the correction applied by (Landais et al., 2010) for NGRIP ice core samples. They found the typical slope of $0.01‰ \cdot ‰^{-1}$ between $\delta O_2/N_2$ variations and $\delta^{18}O_{atm}$ variations (4.6.4.2), and corrected $\delta^{18}O_{atm}$ for this effect. As NGRIP ice core samples measured immediately after the recovery of the ice core had a mean $\delta O_2/N_2$ value of $-10‰$ relative to atmospheric air (Landais et al., 2010). The authors concluded that a natural process (i.e. not occurring during shipping, storage or handling of the ice core) had depleted the elemental composition of the ice bubble air and needed to be corrected for. $\delta O_2/N_2$ was thus corrected for gas-loss fractionation during close-off by adding 10‰ to the measured $\delta O_2/N_2$ values. However, the assumption that no artifactual gas loss occurred may be incorrect, because of core-cracking fractionation: an ice core undergoes enormous stress while being brought to the surface (Sect. 4.6.4.2). Small cracks open up during depressurization and may later re-heal, giving the appearance of a well-preserved ice sample without cracks at the surface. This has been shown by shining certain wavelengths of light at the core, which cause drilling fluid trapped in re-healed cracks to fluoresce (Severinghaus, pers. comm., 2016). However, not accounting for core-cracking fractionation does not affect the quality of the $\delta^{18}O_{atm}$ corrections, because natural and artifactual gas loss cause similar fractionation of the trapped gases in ice. In other words, it is not necessary to know the relative contribution of bubble close-off, coring and post-coring processes to the total gas loss fractionation as a general empirical correction is applied correct for these effects without distinguishing between them.

Our mass spectrometry procedure (Sect. 4.5) developed to measure $\delta^{18}O_{atm}$ did not include $\delta^{40}Ar$ measurements, in spite of its potential to correct $\delta^{18}O_{atm}$ from thermal fractionation and to distinguish between mass-dependent and size-dependent gas-loss processes (e.g. Severinghaus et al., 2009). The resistors attached to the Universal triple collector of the Delta V plus MS were such that m/z 40 was saturated in the most sensitive Faraday cup (devoted usually to m/z 33) in the "O2_gaslab" configuration. Switching off high amplification proved to be impossible to program with ISL scripts in an automated sequence, requiring a change of configuration to obtain a measurable m/z 40 ion voltage. Grzymala-Lubanski (2015) did the choice to significantly reduce measurement time at the expense of $\delta^{40}Ar$ measurements. As ^{40}Ar was not measured, the correction for NEEM ice core samples presented here is solely based on $\delta O_2/N_2$.

$\delta O_2/N_2$ was measured with an improved peak jumping procedure, based on Sever-

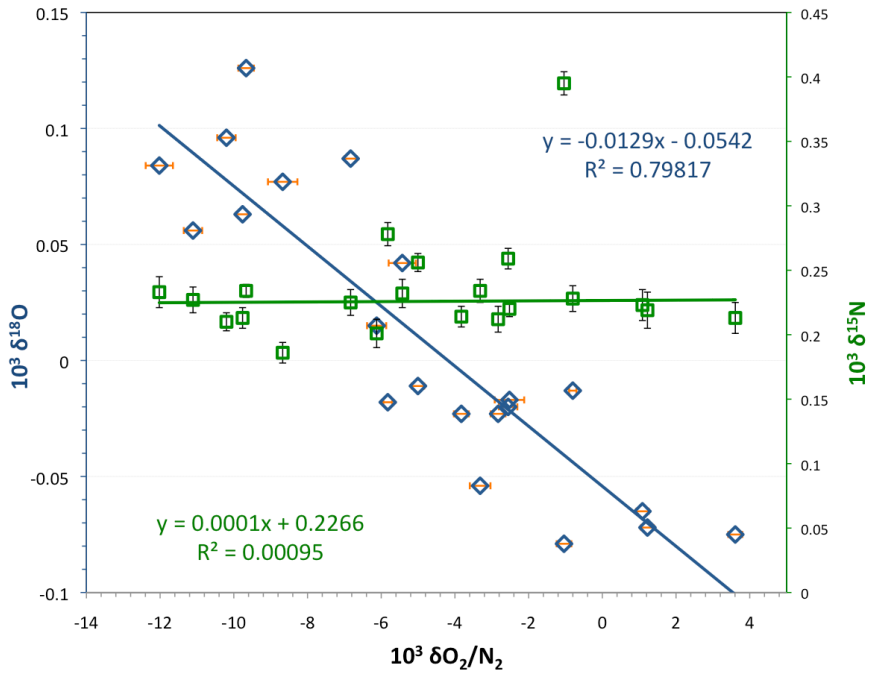

Figure 4.9 – NEEM $\delta^{18}O_{atm}$ or NEEM $\delta^{15}N$ versus $\delta O_2/N_2$. Both NEEM $\delta^{18}O_{atm}$ and $\delta O_2/N_2$ ice core samples are gravitationally corrected based on $\delta^{15}N$. Text in blue (green) gives the slope and intercept of the regression line and its associated R^2. Intercepts of the linear fits only reflect the choice of the O_2 /N_2 standard. Note that $\delta^{15}N$ is insensitive to gas-loss fractionation in our experiments, which confirms that $\delta^{15}N$ can be used with confidence to correct $\delta^{18}O_{atm}$ for gravitational fractionation. The enriched $\delta^{15}N$ results probably from pressure-gradient driven fractionation during the experiment (scaling with the absolute mass-difference as gravitational fractionation), as $\delta^{18}O_{atm}$ from the same sample is identical to other NEEM replicates after gravitational correction (Sect. 4.6.6).

inghaus et al. (2003), as described in Sect. 4.5.3.2.4, as the collector configuration of the IRMS did not enable the simultaneous measurements of masses m/z 32 (O_2) and 28 (N_2). The mean corrected $\delta O_2/N_2$ value of the 21 well preserved NEEM Holocene ice core samples is -3.9 ± 4.4‰. When plotting $\delta^{18}O$ against $\delta O_2/N_2$ of the 21 NEEM late Holocene ice core samples, we find a slope of $0.0129‰ \cdot ‰^{-1}$ between the $\delta O_2/N_2$ variations and $\delta^{18}O$ variations (Fig. 4.9), similar to the one found in other studies, and therefore correct $\delta^{18}O$ measurements from gas loss through the following equation:

$$\delta^{18}O_{atm} = \delta^{18}O_{gravcorr} + 0.0129 \cdot (\delta O_2/N_{2gravcorr} + 4.2), \tag{4.13}$$

where 4.2 is a adjustable parameter used to force the mean $\delta^{18}O$ of the 21 late Holocene NEEM ice core samples to 0‰. Here we follow the approach from Severinghaus et al. (2009), who applied such a correction to $\delta O_2/N_2$ to account for a poorly understood O_2 consumption process occurring during the experiment, which could be caused by oxidative reactions with SST surface. We also indicate in Table 4.3 $\delta^{18}O_{gaslosscorrected}$,

which is defined as follows:

$$\delta^{18}O_{gaslosscorrected} = \delta^{18}O_{CScorrected} + 0.0129 \cdot (\delta O_2/N_{2gravcorr}), \tag{4.14}$$

4.6.6 Correction synthesis

This section summarizes the data processing of NEEM $\delta^{18}O_{atm}$ and details how error propagation is evaluated. The uncertainty of the fully-corrected data is estimated with error propagation.

4.6.6.1 Ensemble of corrections applied to NEEM $\delta O_2/N_2$

We present in Fig. 4.10 the results of gas-isotopic analyses of NEEM ice core samples. Precise values of $\delta^{18}O_{atm}$, $\delta^{15}N$ and $\delta O_2/N_2$ at different stages of the correction process, together with their average and standard deviation can be found in Table 4.3.

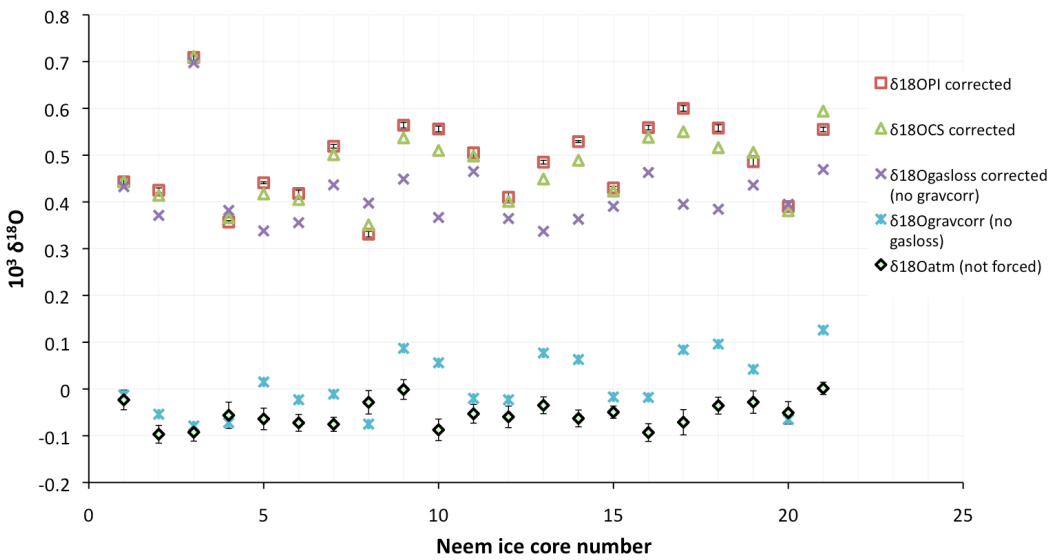

Figure 4.10 – Synthesis of all the corrections applied to Late Holocene NEEM ice samples. The loss of precision of individual ice core samples from the pressure-imbalanced corrected data ($\delta^{18}O_{PIcorrected}$) to the fully corrected data ($\delta^{18}O_{atm}$), resulting from error propagation as described in Sect. 4.6.6.2, is illustrated by the increase of the error bars. In parallel, the pooled standard deviation of the 21 NEEM ice core $\delta^{18}O_{atm}$ decreases from 0.077 to 0.028 ‰, validating the applied corrections (refer to Table 4.3 for precise values). Note that $\delta^{18}O_{atm}$ is not forced to 0 ‰ by adding a constant offset to $\delta O_2/N_2$ values.

Pressure-gradient fractionation during evacuation of the frozen ice sample sitting in the extraction flask may be responsible for $\delta^{15}N$ and $\delta^{18}O_{atm}$ enrichment observed in NEEM ice core sample number 3 (measurement from 26/08/2015, with $\delta^{15}N$=0.395 ‰) (Severinghaus et al., 2009; Kobashi et al., 2008). Indeed, the presence of micro-

cracks, from which lighter isotopes would preferentially escape during evacuation, could explain an isotopic enrichment. Alternatively, an internal leak from the collecting rod through the valve of the collection manifold after collection of the sample may also cause an isotopic enrichment. Pressure-gradient fractionation scales as the absolute mass difference, which would enrich $\delta^{18}O_{atm}$ twice as much as $\delta^{15}N$. As revealed in Fig. 4.10, $\delta^{18}O_{gasloss\,corrected}$ of the anomalous NEEM sample is enriched by 0.28 ‰ compared to the mean $\delta^{18}O_{gasloss\,corrected}$ value, roughly twice as much as the enrichment observed in $\delta^{15}N$. Besides, once corrected for gravitational fractionation, which is a particular case of pressure-gradient fractionation, where the pressure gradient results from hydrostatic equilibrium (Severinghaus and Battle, 2006), $\delta^{18}O_{atm}$ of the anomalous NEEM ice core sample is identical to the mean $\delta^{18}O_{atm}$ within the uncertainty associated with the experiment.

4.6.6.2 Estimation of uncertainty

Assuming that errors are statistically independent, the error propagation formula for $f(x, y, z)$ reduces to:

$$\sigma \cdot f = \sqrt{\left(\frac{\partial f}{\partial x}\sigma x\right)^2 + \left(\frac{\partial f}{\partial y}\sigma y\right)^2 + \left(\frac{\partial f}{\partial z}\sigma z\right)^2} \tag{4.15}$$

Simple expressions can be employed (Barlow, 1989) to propagate the uncertainty to the sequence of corrections applied to $\delta^{18}O_{atm}$:

$$f = aA \rightarrow \sigma_f^2 = a^2 \cdot \sigma_A^2 \tag{4.16a}$$

$$f = A + B \rightarrow \sigma_f^2 = \sigma_A^2 + \sigma_B^2 \tag{4.16b}$$

$$f = AB \rightarrow \sigma_f^2 = B^2 \cdot \sigma_A^2 + A^2\sigma_B^2 \tag{4.16c}$$

Applied to $\delta^{18}O_{atm}$ correction procedure, the total uncertainty of a block of $\delta^{18}O_{atm}$ measurements is calculated as follows[16] using equations 4.16 . First:

$$\sigma^2_{\delta^{18}O_{CScorrected}} = \sigma^2_{\delta^{18}O_{PIcorrected}} + \delta\frac{O_2}{N_2} \cdot \sigma_{chemical\,slope} + (chemical\,slope)^2 \cdot \sigma^2_{\delta\frac{O_2}{N_2}}, \tag{4.17}$$

And:

$$\sigma^2_{\delta^{18}O_{gaslosscorrected}} = \sigma^2_{\delta^{18}O_{CScorrected}} + 0,0129 \cdot \sigma^2_{\delta\frac{O_2}{N_2}}, \tag{4.18}$$

Besides:

$$\sigma^2_{\delta^{18}O_{atm}} = \sigma^2_{\delta^{18}O_{gaslosscorrected}} + 2 \cdot \sigma^2_{\delta^{15}N}. \tag{4.19}$$

Inserting Eq. 4.18 into Eq. 4.19:

$$\sigma^2_{\delta^{18}O_{atm}} = \sigma^2_{\delta^{18}O_{CScorrected}} + 0,0129 \cdot \sigma^2_{\delta\frac{O_2}{N_2}} + 2 \cdot \sigma^2_{\delta^{15}N}. \tag{4.20}$$

[16]Note that the gravitational fractionation correction applied to $\delta O_2/N_2$ was neglected given that $\delta O_2/N_2$ uncertainty is 20 times higher than $\delta^{15}N$ uncertainty.

Table 4.3 – Summary of $\delta^{18}O_{atm}$ measurements of NEEM Late Holocene ice core samples and applied corrections. Note that NEEM ice core sample number 3 (measurement from 26/08/2015), in red in the table, is considered as an outlier due to its anomalously enriched $\delta^{15}N$ (0.395 ‰), and is therefore not included in average and standard deviation calculations.

Date	Depth m	Rod #	$\delta^{18}O_{PI\,corrected}$ ‰	$\delta^{15}N$ ‰	$\delta O_2/N_2$ ‰	$\delta^{18}O_{CS\,corrected}$ ‰	$\delta^{18}O_{gasloss\,corrected}$ ‰	$\delta^{18}O^{a}_{gravcorr}$ ‰	$\delta^{18}O_{atm}$ (not forced[b]) ‰	$\delta^{18}O_{atm}$ ‰
26/08/2015	337	1	0.443 ± 0.006	0.228 ± 0.01	0.11 ± 0.1	0.443	0.433	−0.013	−0.0233	0.0308 ± 0.021
26/08/2015	337	2	0.425 ± 0.005	0.234 ± 0.009	−2.38 ± 0.28	0.414	0.371	−0.054	−0.0968	−0.0426 ± 0.019
26/08/2015	337	3	0.709 ± 0.007	0.395 ± 0.009	0.54 ± 0.2	0.711	0.698	-0.079	-0.0924	-0.0382 ± 0.019
26/08/2015	337	7	0.357 ± 0.003	0.219 ± 0.014	2.1 ± 0.17	0.366	0.382	−0.072	−0.0562	−0.0020 ± 0.028
28/08/2015	337	1	0.441 ± 0.002	0.201 ± 0.011	−5.32 ± 0.26	0.417	0.338	0.015	−0.0640	−0.0098 ± 0.023
28/08/2015	337	2	0.418 ± 0.007	0.214 ± 0.008	−2.97 ± 0.2	0.405	0.356	−0.023	−0.0725	−0.0182 ± 0.018
28/08/2015	337	3	0.519 ± 0.004	0.256 ± 0.007	−3.98 ± 0.17	0.501	0.436	−0.011	−0.0756	−0.0214 ± 0.015
28/08/2015	337	7	0.331 ± 0.006	0.213 ± 0.012	4.46 ± 0.19	0.351	0.398	−0.075	−0.0285	0.0257 ± 0.025
31/08/2015	337	1	0.564 ± 0.006	0.225 ± 0.01	−5.93 ± 0.16	0.537	0.449	0.087	−0.0011	0.0531 ± 0.021
31/08/2015	337	2	0.556 ± 0.006	0.227 ± 0.01	−10.2 ± 0.25	0.51	0.367	0.056	−0.0873	−0.0331 ± 0.023
31/08/2015	337	3	0.505 ± 0.012	0.259 ± 0.008	−1.52 ± 0.25	0.498	0.465	−0.02	−0.0530	0.0012 ± 0.02
31/08/2015	337	7	0.41 ± 0.01	0.212 ± 0.01	−1.98 ± 0.2	0.401	0.365	−0.023	−0.0595	−0.0053 ± 0.023
31/08/2015	337	8	0.485 ± 0.004	0.186 ± 0.008	−7.93 ± 0.4	0.449	0.337	0.077	−0.0349	0.0193 ± 0.018
02/09/2015	337	1	0.529 ± 0.002	0.213 ± 0.008	−8.91 ± 0.16	0.489	0.363	0.063	−0.0629	−0.0087 ± 0.018
02/09/2015	337	2	0.43 ± 0.003	0.22 ± 0.006	−1.64 ± 0.4	0.423	0.390	−0.017	−0.0495	0.0047 ± 0.013
02/09/2015	337	3	0.559 ± 0.005	0.278 ± 0.009	−4.71 ± 0.12	0.538	0.463	−0.018	−0.0931	−0.0389 ± 0.019
02/09/2015	337	7	0.6 ± 0.006	0.233 ± 0.012	−11.09 ± 0.37	0.55	0.395	0.084	−0.0711	−0.0169 ± 0.027
02/09/2015	337	8	0.558 ± 0.007	0.21 ± 0.007	−9.36 ± 0.25	0.516	0.384	0.096	−0.0356	0.0186 ± 0.018
10/09/2015	337	na	0.486 ± 0.009	0.232 ± 0.011	−4.5 ± 0.37	0.506	0.436	0.042	−0.0280	0.0262 ± 0.024
10/09/2015	337	na	0.39 ± 0.002	0.223 ± 0.012	1.98 ± 0.17	0.381	0.395	−0.065	−0.0510	0.0032 ± 0.024
14/09/2015	337	na	0.555 ± 0.005	0.234 ± 0.005	−8.73 ± 0.21	0.594	0.469	0.126	0.0013	0.0555 ± 0.013
Mean			**0.478**	**0.226**[c]	**-3.90**	**0.464**	**0.400**	**0.013**	**-0.0540**	$2 \cdot 10^{-3}$
Std dev 1σ			**0.077**	**0.021**[d]	**4.40**	**0.068**	**0.042**	**0.061**	**0.028**	**0.028**

[a] No gas loss correction applied (Fig. 4.10).
[b] No constant offset is added to the gravitationally corrected $\delta O_2/N_2$ so as to force the mean of the 21 $\delta^{18}O_{atm}$ NEEM samples to be 0 ‰.
[c] calculated excluding the outlier $\delta^{15}N$ value in red in the table (Fig. 4.11). Mean is 2.234 ‰.
[d] $\sigma = 0.042$‰ when the outlier $\delta^{15}N$ value (Fig. 4.11) is not excluded (red value).

Finally, inserting Eq. 4.17 into Eq. 4.20 provides the uncertainty associated with corrected $\delta^{18}O_{atm}$:

$$\sigma^2_{\delta^{18}O_{atm}} = \sigma^2_{\delta^{18}O_{PIcorrected}} + \delta\frac{O_2}{N_2}\cdot\sigma_{chemical\,slope} + (chemical\,slope)^2\cdot\sigma^2_{\delta\frac{O_2}{N_2}} + 0,0129\cdot\sigma^2_{\delta\frac{O_2}{N_2}} + 2\cdot\sigma^2_{\delta^{15}N}. \tag{4.21}$$

4.6.7 Reproducibility of $\delta^{18}O_{atm}$ ice core measurements

The external precision of the setup associated with $\delta^{18}O_{atm}$ ice core measurements is assessed with the 21 late Holocene NEEM ice core samples measured over the 3 weeks during which RICE ice core measurements were performed by Grzymala-Lubanski (2015). Indeed, the usual procedure, where standard gas (Neem_S1) is injected on top of BFI, resulted in a depletion and a large scatter of measured $\delta^{18}O$ and $\delta^{15}N$ values, which is probably due to the presence of dissolved gases in BFI, even in the absence of visible inclusion, in line with the description of Bock et al. (2010). Using shallow ice core samples as quality control standard allows us to take into account potential fractionation of NEEM in our analytical system. They are also used to check the stability of the experimental set-up and estimate the uncertainty associated with ice core sample measurements.

As pointed out by Severinghaus et al. (2003), it is reasonable to expect that samples cut from around the same depth of an ice core should have the same true isotope composition. It is especially true for molecular O_2 , whose signal is quasi constant over the Holocene. Here these 21 NEEM ice core samples, measured at different days, collected in different rods, are associated after corrections with a standard deviation of 0.028‰ for $\delta^{18}O$ and 0.021‰ for $\delta^{15}N$ after excluding one outlier (Fig. 4.11).

NEEM $\delta^{15}N$ measurements are depleted by $\simeq$ 0.11‰ compared to the published measurements. Indeed, the mean 5 NEEM Holocene samples from the depths 396-416 m and ages 1846-1957 yr b2k, measured at LSCE, have a mean $\delta^{15}N$ value of 0.34 $\pm$ 0.02 ‰ (NEEM members, 2013), while the mean $\delta^{15}N$ of NEEM ice core samples measured by Grzymala-Lubanski (2015) is enriched by 0.23 $\pm$ 0.021 ‰. This offset might be due to an undetected artifact during the experiment. Atmospheric air leaking-in, maybe associated with the sealing of the air samples in the extraction flasks, would cause a $\delta^{15}N$ depletion of the sample, which should also be observed in $\delta^{18}O_{atm}$, but this is not clear from NEEM ice core measurements. As the background of water (m/z 18) was consistently low, and no anomalous increase in sample amount was observed while measuring the samples, this hypothesis is not favored. The offset could express the isotopic signature of the analytical setup, as NEEM ice core samples are referenced again Neem_C1 introduced in the standard bellow of the MS (Sect. 4.5.5).

4.7 Conclusions and perspectives

In this chapter we described mass spectrometry measurements in DI mode of atmospheric O_2 and N_2 isotope ratios:

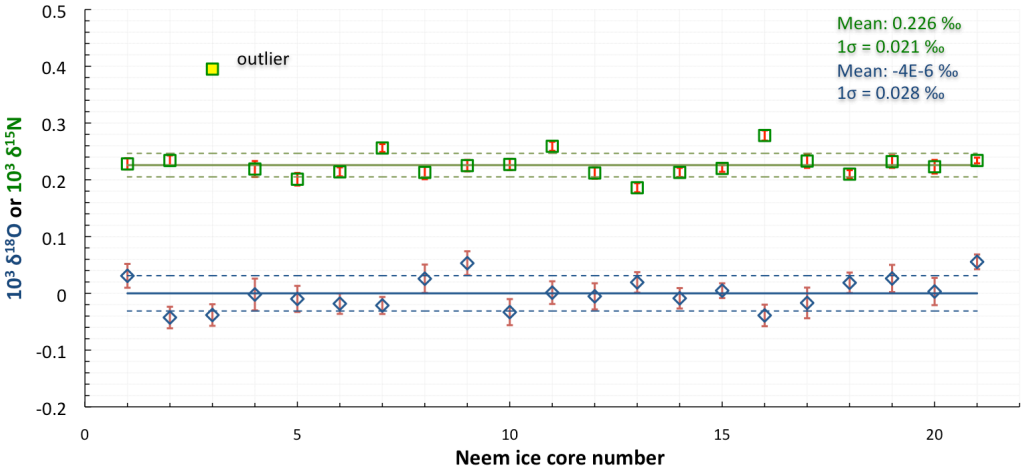

Figure 4.11 – $\delta^{18}O$ or $\delta^{15}N$ obtained from the Late Holocene NEEM ice samples. Both NEEM $\delta^{18}O$ and $\delta O_2/N_2$ are gravitationally corrected using $\delta^{15}N$. Text in blue (green) gives the average (represented by the line of the same color) and standard deviation (represented by the dashed lines) associated with $\delta^{18}O$ ($\delta^{15}N$) after routine (pressure imbalance, chemical slope, gravitational fractionation) and gas loss corrections.

- We developed a custom-based script to fully automate high-precision DI ice core sample measurements of $\delta^{18}O$, $\delta^{17}O$, $\delta^{15}N$ and $\delta O_2/N_2$, including samples (collected in a collection manifold connected to the sample inlet of the MS (Chapter 3)) and standard introduction, adjusted pressure adjustment and peak-jumping procedures. The peak-jumping procedure for $\delta O_2/N_2$ measurements is based on the script developed by Severinghaus et al. (2003) for Kr/Ar measurements.

- We made minor changes and major maintenance on the MS to minimize artifactual fractionation during DI measurements.

- The measured 21 NEEM ice core samples from the same depth display large variations in their $\delta O_2/N_2$ and $\delta^{18}O$ ratio, not representative of a true atmospheric change as they should carry the same signal. The scatter underlines the occurrence of gas loss processes causing varying O_2 isotope ratios, with a dependence of $\delta^{18}O_{atm}$ on $\delta O_2/N_2$ (0.0129 ‰ · ‰$^{-1}$) similar to the one described in literature. Improvements for the future should include "δAr/N_2 measurements to evaluate, in combination with $\delta O_2/N_2$, the relative contribution of mass-dependent and size-dependent fractionation components to gas loss processes. Besides, the NEEM science trench, where the ice cores were stored, was significantly too warm during the first years of the ice core drilling campaign, likely to have caused a fair amount of gas loss in ice core samples stored on the field.

- Pressure-gradient fractionation during extraction flask evacuation may be responsible for $\delta^{15}N$ and $\delta^{18}O_{atm}$ enrichment observed in the outlier NEEM ice

core sample, due to the presence of microcracks. Once corrected for gravitational fractionation, the anomalous NEEM ice core sample is identical to the mean $\delta^{18}O_{atm}$ within the uncertainty associated with the experiment.

- Based on 21 NEEM ice core samples from the same depth, collected over a time period of 3 weeks over different rods, we proved the ability of the analytical system (including extraction line and mass spectrometry) to reproduce ice core sample measurements of corrected $\delta^{18}O_{atm}$ and $\delta^{15}N$ with an external precision of 0.028 ‰ and 0.021 ‰, respectively.

- Using the peak jumping procedure of Severinghaus et al. (2003), $\delta O_2/N_2$ is measured with a precision ranging from 0.1 to 0.4 ‰ for an individual ice core sample. The 21 NEEM samples exhibit the expected large scatter (*pm* 4.40) caused by a varying amount of mass-dependent and size-dependent fractionation during gas loss processes.

- Based on zero-enrichment tests, the internal precision of DI measurements of $\delta^{18}O$ and $\delta^{15}N$ is 0.008 ‰ (1 σ) and 0.005 ‰ (1 σ). As seen in Table 4.3, individual ice core sample measurements have a similar precision. This level of precision is similar to the one found in other studies.

- We detail the data-processing method , its associated uncertainty and the strategy employed to correct for non climatic effects, including effects of sample and standard beam voltage imbalance on the measured $\delta^{18}O_{atm}$ ratio (pressure imbalance), of variations of the O_2 /N_2 ratio on $\delta^{18}O_{atm}$ (chemical slope), of gravitational fractionation, and of gas loss processes associated with bubble close-off and air entrapment, coring and post-coring processes.

The work presented in this chapter can be further developed by:

- Referencing the ice core samples to the working standard[17] Neem_S1 introduced over BFI so as to fully respect the IT principle and enable confident comparison with other $\delta^{18}O_{atm}$ records measured in other laboratories. Such standard measurements involving BFI were not reproducible hitherto, and may arise from the fact that Neem_S1 was introduced before melting the BFI. To circumvent this problem, the adopted strategy in this thesis is to reference the sample against Neem_C1 introduced in the right bellow of the MS, and to check the reproducibility and accuracy of the measurements by measuring real ice core samples with known[18] unknown[19] O_2 isotope ratios.

- The setup is built for three-oxygen isotope measurements, but the precision required for ice core $^{17}\Delta_{atm}$ measurement is three times better than the precision

[17] which is also the PRM for atmospheric O_2 measurements

[18] we know what the true atmospheric signal should be for a given period of time as it is the same in all ice cores owing to the long lifetime of O_2 in the atmosphere relative to the inter-hemispheric mixing time.

[19] we know that the signal preserved in ice cores is different than the true atmospheric signal

obtained in this thesis for $\delta^{18}O_{atm}$ measurements in ice cores. To obtain such a precision, reproducible measurements of standard gas introduced over BFI are required, as well as a complete automation of the extraction line to respect an identical extraction/collection procedure for each ice core sample and enhance precision.

.

Bibliography

Balslev-Clausen, D. M. (2011). *Application of cavity ring down spectroscopy to isotopic bio-geo and climate-sciences and the development of a mid-infrared CRDS analyzer for continuous measurements of N2O isotopomers*. PhD thesis.

Barkan, E. and Luz, B. (2003). High-precision measurements of 170/160 and 180/160 of 02 and 02/ar ratio in air. *Rapid Communications in Mass Spectrometry*, 17(24):2809–2814.

Barlow, R. J. (1989). *Statistics: a guide to the use of statistical methods in the physical sciences*, volume 29. John Wiley & Sons.

Battle, M. O., Severinghaus, J. P., Sofen, E. D., Plotkin, D., Orsi, A. J., Aydin, M., Montzka, S. A., Sowers, T., and Tans, P. P. (2011). Controls on the movement and composition of firn air at the west antarctic ice sheet divide. *Atmospheric Chemistry and Physics*, 11(21):11007–11021.

Bender, M., Sowers, T., and Labeyrie, L. (1994a). The dole effect and its variations during the last 130,000 years as measured in the vostok ice core. *Global Biogeochemical Cycles*, 8(3):363–376.

Bender, M., Sowers, T., and Lipenkov, V. (1995). On the concentrations of 02, n2, and ar in trapped gases from ice cores. *Journal of Geophysical Research: Atmospheres*, 100(D9):18651–18660.

Bender, M. L. (2002). Orbital tuning chronology for the vostok climate record supported by trapped gas composition. *Earth and Planetary Science Letters*, 204(1):275–289.

Bender, M. L., Sowers, T., Barnola, J.-M., and Chappellaz, J. (1994b). Changes in the 02/n2 ratio of the atmosphere during recent decades reflected in the composition of air in the firn at vostok station, antarctica. *Geophysical Research Letters*, 21(3):189–192.

Bender, M. L., Tans, P. P., Ellis, J., Orchardo, J., and Habfast, K. (1994c). A high precision isotope ratio mass spectrometry method for measuring the 02n2 ratio of air. *Geochimica et Cosmochimica Acta*, 58(21):4751 – 4758.

Bock, M., Schmitt, J., Behrens, M., M⊠ller, L., Schneider, R., Sapart, C., and Fischer, H. (2010). A gas chromatography/pyrolysis/isotope ratio mass spectrometry system for high-precision dd measurements of atmospheric methane extracted from ice cores. *Rapid Communications in Mass Spectrometry*, 24(5):621–633.

Buizert, C., Martinerie, P., Petrenko, V. V., Severinghaus, J. P., Trudinger, C. M., Witrant, E., Rosen, J. L., Orsi, A. J., Rubino, M., Etheridge, D. M., Steele, L. P., Hogan, C., Laube, J. C., Sturges, W. T., Levchenko, V. A., Smith, A. M., Levin, I., Conway, T. J., Dlugokencky, E. J., Lang, P. M., Kawamura, K., Jenk, T. M., White,

J. W. C., Sowers, T., Schwander, J., and Blunier, T. (2012). Gas transport in firn: multiple-tracer characterisation and model intercomparison for neem, northern greenland. *Atmospheric Chemistry and Physics*, 12(9):4259–4277.

Capron, E. (2010). *L'air piégé dans les glaces polaires: contraintes chronologiques et caractérisation de la variabilité climatique rapide*. PhD thesis, Université de Versailles-Saint Quentin en Yvelines.

Chappellaz, J., Stowasser, C., Blunier, T., Baslev-Clausen, D., Brook, E. J., Dallmayr, R., Faïn, X., Lee, J. E., Mitchell, L. E., Pascual, O., Romanini, D., Rosen, J., and Schüpbach, S. (2013). High-resolution glacial and deglacial record of atmospheric methane by continuous-flow and laser spectrometer analysis along the neem ice core. *Climate of the Past*, 9(6):2579–2593.

Dahl-Jensen, D., Mosegaard, K., Gundestrup, N., Clow, G. D., Johnsen, S. J., Hansen, A. W., and Balling, N. (1998). Past temperatures directly from the greenland ice sheet. *Science*, 282(5387):268–271.

Gkinis, V. (2011). *High resolution water isotope data from ice cores*. PhD thesis, CIC.

Goujon, C., Barnola, J.-M., and Ritz, C. (2003). Modeling the densification of polar firn including heat diffusion: Application to close-off characteristics and gas isotopic fractionation for antarctica and greenland sites. *Journal of Geophysical Research: Atmospheres*, 108(D24):n/a–n/a. 4792.

Grachev, A. M. (2004). *Laboratory-determined air thermal diffusion constants applied to reconstructing the magnitudes of past abrupt temperature changes from gas isotope observations in polar ice cores*. PhD thesis.

Grzymala-Lubanski, I. (2015). $\delta^{18}o$ of o_2 in rice ice core. Master's thesis, Centre for Ice and Climate.

Guillevic, M. (2013). *Characterisation of rapid climate changes through isotope analyses of ice and entrapped air in the NEEM ice core*. PhD thesis, Versailles-St Quentin en Yvelines.

Ikeda-Fukazawa, T., Fukumizu, K., Kawamura, K., Aoki, S., Nakazawa, T., and Hondoh, T. (2005). Effects of molecular diffusion on trapped gas composition in polar ice cores. *Earth and Planetary Science Letters*, 229(3–4):183 – 192.

Kawamura, K., Parrenin, F., Lisiecki, L., Uemura, R., Vimeux, F., Severinghaus, J. P., Hutterli, M. A., Nakazawa, T., Aoki, S., Jouzel, J., Raymo, M. E., Matsumoto, K., Nakata, H., Motoyama, H., Fujita, S., Goto-Azuma, K., Fujii, Y., and Watanabe, O. (2007). Northern hemisphere forcing of climatic cycles in antarctica over the past 360,000 years. *Nature*, 448(7156):912–U4.

Kobashi, T., Severinghaus, J. P., and Kawamura, K. (2008). Argon and nitrogen isotopes of trapped air in the {GISP2} ice core during the holocene epoch (0⊠11,500

b.p.): Methodology and implications for gas loss processes. *Geochimica et Cosmochimica Acta*, 72(19):4675 – 4686.

Landais, A. (2004). *Variabilité climatique rapide en Atlantique Nord: l'apport des isotopes de l'air piégé dans la glace du Groenland*. PhD thesis, Université Pierre et Marie Curie-Paris VI.

Landais, A., Chappellaz, J., Delmotte, M., Jouzel, J., Blunier, T., Bourg, C., Caillon, N., Cherrier, S., Malaize, B., Masson-Delmotte, V., Raynaud, D., Schwander, J., and Steffensen, J. P. (2003). A tentative reconstruction of the last interglacial and glacial inception in greenland based on new gas measurements in the greenland ice core project (grip) ice core. *Journal of Geophysical Research: Atmospheres*, 108(D18):n/a–n/a. 4563.

Landais, A., Dreyfus, G., Capron, E., Masson-Delmotte, V., ni, M. S.-G., Desprat, S., Hoffmann, G., Jouzel, J., Leuenberger, M., and Johnsen, S. (2010). What drives the millennial and orbital variations of $\delta^{18}o_{atm}$? *Quaternary Science Reviews*, 29(1–2):235 – 246.

Landais, A., Dreyfus, G., Capron, E., Pol, K., Loutre, M. F., Raynaud, D., Lipenkov, V. Y., Arnaud, L., Masson-Delmotte, V., Paillard, D., Jouzel, J., and Leuenberger, M. (2012). Towards orbital dating of the epica dome c ice core using delta o_2/n_2. *Climate of the Past*, 8(1):191–203.

McKinney, C. R., McCrea, J. M., Epstein, S., Allen, H., and Urey, H. C. (1950). Improvements in mass spectrometers for the measurement of small differences in isotope abundance ratios. *Review of Scientific Instruments*, 21(8):724–730.

NEEM members (2013). Eemian interglacial reconstructed from a greenland folded ice core. *Nature*, 493(7433):489–494.

Paterson, W. (1994). *The physics of glaciers*. Butterworth-Heinemann.

Severinghaus, J. P. and Battle, M. O. (2006). Fractionation of gases in polar ice during bubble close-off: New constraints from firn air ne, kr and xe observations. *Earth and Planetary Science Letters*, 244(1–2):474–500.

Severinghaus, J. P., Beaudette, R., Headly, M. A., Taylor, K., and Brook, E. J. (2009). Oxygen-18 of o2 records the impact of abrupt climate change on the terrestrial biosphere. *Science*, 324(5933):1431–1434.

Severinghaus, J. P., Grachev, A., and Battle, M. (2001). Thermal fractionation of air in polar firn by seasonal temperature gradients. *Geochemistry, Geophysics, Geosystems*, 2(7):n/a–n/a. 1048.

Severinghaus, J. P., Grachev, A., Luz, B., and Caillon, N. (2003). A method for precise measurement of argon 40/36 and krypton/argon ratios in trapped air in polar ice with applications to past firn thickness and abrupt climate change in greenland and at siple dome, antarctica. *Geochimica et Cosmochimica Acta*, 67(3):325 – 343.

Shoji, H. and Langway, C. C. (1982). Air hydrate inclusions in fresh ice core.

Sowers, T. and Bender, M. (1995). Climate records covering the last deglaciation. *Science*, 269(5221):210–214.

Sperlich, P., Buizert, C., Jenk, T., Sapart, C., Prokopiou, M., Röckmann, T., and Blunier, T. (2013). An automated gc-c-gc-irms setup to measure paleoatmospheric δ13c-ch4, δ15n-n20 and δ180-n20 in one ice core sample. *Atmospheric Measurement Techniques*, 6:2027–2041.

Suwa, M. and Bender, M. L. (2008). O2/n2 ratios of occluded air in the gisp2 ice core. *Journal of Geophysical Research: Atmospheres*, 113(D11). D11119.

van den Broeke, M. (2008). Depth and density of the antarctic firn layer. *Arctic, Antarctic, and Alpine Research*, 40(2):432–438.

Werner, R. A. and Brand, W. A. (2001). Referencing strategies and techniques in stable isotope ratio analysis. *Rapid Communications in Mass Spectrometry*, 15(7):501–519.

5 Quantifying molecular oxygen isotope variations during a Heinrich stadial

C. Reutenauer[1], A. Landais[2], T. Blunier[1], C. Bréant[2], M. Kageyama[2], M-N. Woillez[2a], C. Risi[3], V. Mariotti[2], P. Braconnot[2]

[1] Centre for Ice and Climate, Niels Bohr Institute, University of Copenhagen, Copenhagen, Denmark
[2] Institut Pierre Simon Laplace (IPSL), Laboratoire des Sciences de Climat et de l'Environnement (LSCE), UMR8212 (CEA-CNRS-UVSQ), CE Saclay, Orme des Merisiers, Bat. 701, 91191 Gif-sur-Yvette Cedex, France
[3] Laboratoire de Météorologie Dynamique UMR 8539, IPSL/CNRS/UPMC, 4, place Jussieu, 75252 Paris Cedex 05, France
[a] now at: IFPEN, 14 avenue de Bois Préau, 92852 Rueil-Malmaison Cedex

correspondence to: C. Reutenauer (creuten@nbi.ku.dk)

Received: 22 May 2015 - Published in Clim. Past Discuss.: 23 June 2015
Revised: 1 November 2015 - Accepted: 5 November 2015 - Published: 19 November 2015

5.1 Abstract

δ^{18}O of atmospheric oxygen ($\delta^{18}O_{atm}$) undergoes millennial-scale variations during the last glacial period, and systematically increases during Heinrich stadials (HSs). Changes in $\delta^{18}O_{atm}$ combine variations in biospheric and water cycle processes. The identification of the main driver of the millennial variability in $\delta^{18}O_{atm}$ is thus not straightforward. Here, we quantify the response of $\delta^{18}O_{atm}$ to such millennial events using a freshwater hosing simulation performed under glacial boundary conditions. Our global approach takes into account the latest estimates of isotope fractionation factor for respiratory and photosynthetic processes and make use of atmospheric water isotope and vegetation changes. Our modeling approach allows to reproduce the main observed features of a HS in terms of climatic conditions, vegetation distribution and δ^{18}O of precipitation. We use it to decipher the relative importance of the different processes behind the observed changes in $\delta^{18}O_{atm}$. The results highlight the dominant role of hydrology on $\delta^{18}O_{atm}$ and confirm that $\delta^{18}O_{atm}$ can be seen as a global integrator of hydrological changes over vegetated areas.

5.2 Introduction

Oxygen is one of the most abundant species in atmospheric air. As oxygen is produced by photosynthesis and consumed by respiration, a record of oxygen concentration in the past should help us to constrain these two major biospheric fluxes on Earth and potentially provide information on their link with the carbon cycle.

Changes in the O_2 / N_2 ratio can be measured in air trapped in ice cores back to 800 kyr (Bender, 2002; Kawamura et al., 2007; Landais et al., 2012; Bazin et al., 2014). Unfortunately the O_2 / N_2 ratio in ice cores does not provide a direct information on the true atmospheric variations because it is affected by permeation through the ice lattice during bubble formation at pore close-off, roughly 100 m below the ice sheet surface, and by gas loss during ice core storage. These effects have less impact on the isotopic composition of oxygen. These isotopic compositions have thus been explored as possible constraints on biospheric productivity (Luz et al., 1999).

When dealing with isotopes, it is standard to use the isotope ratio, R, defined as the fraction of the abundance of the rare isotope over the dominant one in a substance. Since changes in isotope ratios through natural processes are very small, they are expressed in relation to a standard (recent air and Vienna Standard Mean Ocean Water (VSMOW) being used for O_2 and H_2O , respectively) using the δ notation,

$$\delta^{18}O = \frac{{}^{18}R_{\text{sample}}}{{}^{18}R_{\text{standard}}} - 1. \tag{5.1}$$

$\delta^{18}O$ and $\delta^{17}O$ of atmospheric oxygen have been measured for the period of the past 800 kyr with a mean resolution of about 1500 years (e.g., Landais et al., 2010, and references therein; Blunier et al., 2012). As shown by Bender et al. (1994), $\delta^{18}O$ of atmospheric oxygen, noted $\delta^{18}O_{atm}$ hereafter, cannot easily be related to biospheric productivity through photosynthesis and respiration fluxes. $\delta^{18}O_{atm}$ variations actually reflect for a large part the isotopic composition of the meteoric water. The latter is transmitted to the plant through its roots and stems to the leaves, where photosynthesis produces oxygen with an isotopic composition close to the isotopic composition in leaf water. Respiration modifies the isotopic composition of atmospheric oxygen in a complex way. While the processes consuming oxygen enrich atmospheric oxygen through a preferential consumption of the lightest molecules, individual biological pathways are associated with a wide range of oxygen fractionations (Helman et al., 2005).

Based on fractionation factors available at the time, Bender et al. (1994) established that the relative proportion of oceanic vs. terrestrial biospheric productivities together with the difference in isotope fractionation over land and ocean were driving the $\delta^{18}O_{atm}$ budget. Several studies have built on this idea and interpret the $\delta^{18}O_{atm}$ variations mainly as variations in the oceanic vs. terrestrial biospheric productivities (Hoffmann et al., 2004; Ciais et al., 2012). However, recent measurements have revealed that, overall, fractionation associated with oceanic productivity is very similar to its terrestrial counterpart (Hendricks et al., 2004; Eisenstadt et al., 2010), questioning the interpretation of $\delta^{18}O_{atm}$ as an indicator of the relative proportion of oceanic vs. terrestrial biosphere productivity (Luz and Barkan, 2011).

Despite the complex interpretation of $\delta^{18}O_{atm}$, several robust features have already been observed that highlight the potential of these measurements. At the orbital scale, $\delta^{18}O_{atm}$ is showing clear variations at a 23 kyr periodicity (Dreyfus et al., 2007).

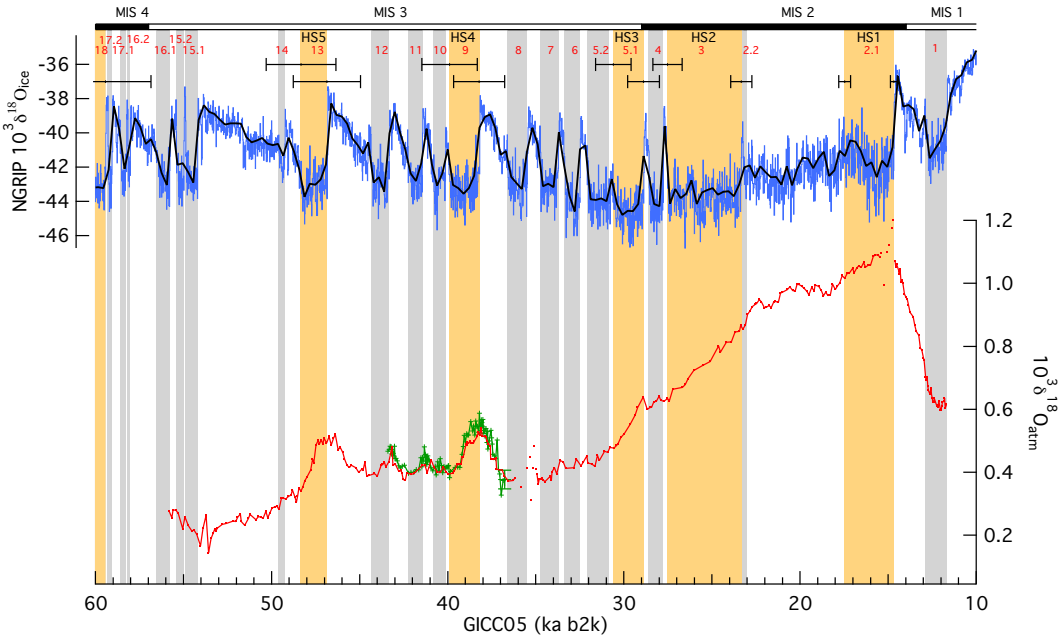

Figure 5.1 – Greenland stadials and Heinrich stadials during the last glacial period. Red numbers indicate GSs and black labels HSs. **(a)** Black line: NGRIP $\delta^{18}O$, ‰, on the GICC05 timescale back to 60 ka b2k. **(b)** Red line: Siple Dome atmospheric $\delta^{18}O$ (Severinghaus et al., 2009) on GICC05 timescale. Red dots denote intervals in the core where deep air convection or cracked firn layer may have thermally fractionated these samples, as shown by anomalous $\delta^{15}N$ in Figs. S1 and S8 of Severinghaus et al. (2009). The transfer of Siple Dome atmospheric $\delta^{18}O$ on the GICC05 chronology is achieved by using the Siple Dome gas age scale compatible with the GICC05 chronology (Guillevic, 2013), based on match points between Siple Dome methane variations (Brook et al., 2005; Ahn et al., 2012; depth point) and NEEM methane variations (Chappellaz et al., 2013; GICC05 gas age point). A linear interpolation is then performed between match points to calculate the Siple Dome gas age. Green line: NEEM atmospheric $\delta^{18}O$, ‰ (±0.03 ‰; Guillevic et al., 2014). Colored areas: GSs. Grey: GS with no major Heinrich event. Orange: HS1, HS2, HS3, HS4, HS5 and end of HS6 – GSs with a major Heinrich event. Black error bars indicate HS onset and end uncertainty (2σ), based on the Rasmussen et al. (2013) maximum counting error (MCE). Top (right to left): black and white horizontal bar indicate Marine Isotope Stage 1 to 4.

This strong link with precession is probably related to the variations in the hydrological cycle at low latitudes (Bender et al., 1994). Indeed, variations related to the monsoon regime strongly imprint the isotopic composition of meteoric water as observed in speleothem records (e.g., Wang et al., 2008). They are easily transmitted to the isotopic composition of atmospheric oxygen because the major part of the biospheric productivity, and hence photosynthesis, is occurring in the tropics and subtropics.

At the millennial scale, it has recently been shown that $\delta^{18}O_{atm}$ is responding to the abrupt climate changes of the last glacial period (Landais et al., 2007a; Severinghaus et al., 2009). Millennial-scale climate variability is perhaps best known from the

Greenland ice cores, where it is manifested in the stable water isotopes of ice. During the last glacial period, these cores show 25 Dansgaard–Oeschger (DO) events (NGRIP members, 2004). A DO event typically exhibits a sawtooth pattern: (i) a cold phase (Greenland stadial, noted GS hereafter) lasting from centuries to millennia, followed by a warm phase (Greenland interstadial, GI) starting with (ii) a rapid transition (a few decades) with an amplitude of up to 16±2.5°c (Landais et al., 2004; Huber et al., 2006; Kindler et al., 2014), and ending with (iii) a gradual cooling before an abrupt decrease towards cold, stadial values.

During the last decade, mechanisms of glacial abrupt events have been investigated using coupled ocean–atmosphere models of varying complexity (e.g., Kageyama et al., 2010, 2013; Stouffer et al., 2006). Recent hypotheses often invoke internal variability (Kleppin et al., 2015; Dokken et al., 2013), involving sea ice–atmosphere interactions (e.g., Li et al., 2005, 2010), through ice–albedo feedback and the impact of sea ice cover on regional temperatures by preventing heat exchange between the ocean and atmosphere. There remains robust evidence from multiple lines of paleoceanographic information and modeling that millennial-scale variability is linked to changes in the Atlantic meridional overturning circulation (AMOC) intensity (e.g., Mc Manus et al., 1998), potentially initiated by large freshwater input in the North Atlantic (e.g., Broecker et al., 1990). The presence of ice rafted debris (IRD; Ruddiman, 1977; Heinrich, 1988) in marine sediments from the North Atlantic region during the largest GS document episodes of massive iceberg discharge in the North Atlantic (Heinrich events) mainly from the Laurentide (H2, H4, H5) and Fennoscandian (H3, H6) ice sheets (Grousset et al., 1993; Guillevic et al., 2014 and references therein). Even though IRD is present in each GS (Elliot et al., 2002), not all GSs contain a Heinrich event. Heinrich stadials (noted HSs hereafter) are GSs associated with a Heinrich event (Barker et al., 2009; Sanchez Goni and Harrison, 2010).

Several aspects of the observed patterns during DO events can be captured through the response of the Earth system to imposed freshwater perturbations in the North Atlantic (Liu et al., 2009; Otto-Bliesner and Brady, 2010; Kageyama et al., 2010; Roche et al., 2010), mimicking Heinrich events. Depending on the background state of the climate (glacial or interglacial, orbital context) and the AMOC, as well as on the magnitude of the freshwater forcing, these models produce a complete shutdown of the AMOC (HS-like state) or a reduction of the strength of the AMOC (GS-like state; e.g., Menviel et al., 2014). The injection of freshwater produces in all models a significant cooling of the North Atlantic region. The amplitude of the associated temperature change is probably affected by the simulated change in sea ice extent and feedbacks between sea ice and temperature that vary in the different models (Kageyama et al., 2013). These hosing experiments also produce an interhemispheric see-saw temperature pattern, associated with a southward shift of the Intertropical Convergence Zone (ITCZ) (e.g., Dahl et al., 2005; Broccoli et al., 2006; Krebs and Timmermann, 2007; Swingedouw et al., 2009; Cvijanovic and Chiang, 2013). Abrupt climate variation associated with the Greenland signal is found down to low latitudes in numerous ter-

restrial and marine archives (e.g., Clement and Peterson, 2008). Its climatic impact is recorded in large parts of the North Atlantic region, both in marine cores (e.g., Bond et al., 1993; Broecker, 2000) and in speleothems (Fleitmann et al., 2009). Concomitant methane excursions and variations in the isotopic composition of the calcite of speleothems in eastern Asia (e.g., Wang et al., 2001; Cheng et al., 2012) strongly support the fact that these DO events are associated with major reorganization of the tropical water cycle and hence monsoon intensity through a shift in the ITCZ and its terrestrial equivalent, the tropical rain belt (Chappellaz et al., 2013; Wang et al., 2008; Pausata et al., 2011).

For this period of millennial-scale variability, high-resolution measurements of $\delta^{18}O_{atm}$ have been obtained in Greenland and Antarctic ice cores (e.g., Guillevic et al., 2014; Landais et al., 2007a, 2010; Severinghaus et al., 2009). In Fig. 5.1 we present a synthesis of $\delta^{18}O_{atm}$ evolution from the Siple Dome ice core over HSs displayed on Greenland Ice Core Chronology 2005 (GICC05) timescale, using definitions of Rasmussen et al. (2013) of the onset of GS. The $\delta^{18}O_{atm}$ records show a systematic increase in a few thousand years following the onset of a HS (Fig. 5.2) by around 0.13 ‰, from +0.08 ‰ (HS1) to +0.18 ‰ (HS5). The difference in the slope inflection at the onset of HS4 and HS5, more pronounced that for HS1, HS2 and HS3, may be due to the long-term trend observed in $\delta^{18}O_{atm}$. Indeed, from 35 to 15 kyr, $\delta^{18}O_{atm}$ exhibits a constant increase, consistent with the build-up of polar ice sheet, and hence enrichment of ocean water in ^{18}O, but remains relatively stable over MIS3 (Fig. 5.1).

Because of its global character, $\delta^{18}O_{atm}$ should provide added value compared to the different local records of hydrological cycle variations in different continental and marine archives. However, until now, no quantitative, robust interpretation of past variations in $\delta^{18}O_{atm}$ has been established, which limits the use of $\delta^{18}O_{atm}$ as a quantitative indicator for past biospheric production or variations in the hydrological cycle. The aim of this

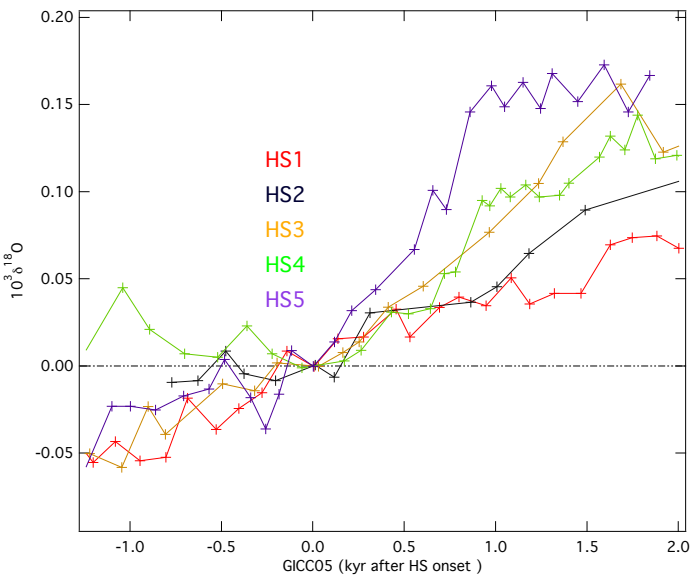

Figure 5.2 – Evolution of Siple Dome atmospheric oxygen $\delta^{18}O$ (Severinghaus et al., 2009) during Heinrich stadials on the GICC05 timescale.

modeling study is thus to provide a quantitative interpretation for the systematic increase in $\delta^{18}O_{atm}$ over HSs. To reach this objective, we propose a global approach incorporating outputs from a general circulation model implemented with water isotopes and focus on the millennial variability in the last glacial period. We follow a modeling approach already developed by Hoffmann et al. (2004). We combine climatic parameters (temperature and humidity), isotopic composition of meteoric water, vegetation distribution and productivity simulated by different models with monthly mean temporal resolution.

In the following section, we describe the general method used to simulate a global $\delta^{18}O_{atm}$ signal. Section 5.4.1 is dedicated to model validation and Section 5.4.2 proposes to quantify the different contributions (hydrology, vegetation, climatic conditions) to the $\delta^{18}O_{atm}$ signal over a HS equivalent.

5.3 Method

According to Landais et al. (2007a, 2010) and Severinghaus et al. (2009), the millennial variations in $\delta^{18}O_{atm}$ during the last glacial period are driven by shifts in the tropical rain belt modifying the relative humidity distribution and the isotopic composition of meteoric water consumed by terrestrial biosphere. The isotopic content of atmospheric oxygen is controlled by numerous processes, so we must consider (i) the worldwide meteoric water isotopic composition, from which ground water is derived; (ii) the worldwide temperature and humidity, from which evaporative enrichment of leaf water $\delta^{18}O$ is calculated; (iii) the worldwide vegetation cover and gross primary productivity, defining the photosynthetically and respiratory active areas that contribute to $\delta^{18}O_{atm}$; and (iv) respiratory processes.

5.3.1 Oxygen isotopes mass balance model

Oxygen is exchanged with the terrestrial and marine biospheres as well as with the stratosphere. Assuming a steady state, $\delta^{18}O_{atm}$ can thus be expressed as follows:

$$\delta^{18}O_{\text{atm}} = \frac{(F_{\text{terr}} \cdot \delta^{18}O_{\text{terr}} + F_{\text{mar}} \cdot \delta^{18}O_{\text{mar}})}{(F_{\text{terr}} + F_{\text{mar}})} - {}^{18}\varepsilon_{\text{strat}}, \tag{5.2}$$

where ${}^{18}\varepsilon_{\text{strat}}$ represents the stratospheric isotope fractionation caused by photochemical reaction in the stratosphere involving O_2 , O_3 and CO_2 . F_{terr} and F_{mar} denote O_2 fluxes of gross terrestrial and oceanic productivity, respectively. $\delta^{18}O_{\text{terr}}$ and $\delta^{18}O_{\text{mar}}$ are the isotopic composition arising from the terrestrial and oceanic realms, respectively. ${}^{18}\varepsilon_{\text{strat}}$ is a small term, 0.4 ‰ compared to $\simeq$ 23.8 ‰ for $\delta^{18}O_{atm}$ with reference to V-SMOW (Luz et al., 2014) and is not assumed to change significantly over a HS because CO_2 level remains relatively stable. We assume a constant CO_2 level between the LGM and HS in our study. Ahn and Brook's (2014) study shows that variations over HSs are small (increase of less than 20 ppm). Effect of isotopic exchange between CO_2 and O_2 in the stratosphere on $\delta^{18}O_{atm}$ is expected to be proportional to CO_2 mixing ratio. Following the calculation of Bender et al. (1994), which estimates a $\delta^{18}O_{atm}$

depletion of 0.4 ‰ for a CO_2 concentration of 353 ppm, we can estimate that a 20 ppm increase between the LGM and HS can modify $\delta^{18}O_{atm}$ by -0.023 ‰. The sign of this change is actually opposite to the sign of the observed $\delta^{18}O_{atm}$ signal. We focus mainly on the millennial-scale variations in the terrestrial contribution to $\delta^{18}O_{atm}$ signal, i.e., $F_{\text{terr}} \cdot \delta^{18}O_{\text{terr}}/(F_{\text{terr}} + F_{\text{mar}})$.

We do not consider the marine influence, in this first approach, for the following reasons. First, our aim is to test the hypothesis of Landais et al. (2007b) and Severinghaus et al. (2009) that $\delta^{18}O_{atm}$ millennial-scale variations are largely driven by changes in the low-latitude hydrological cycle through changes in the $\delta^{18}O$ of precipitation. Second, Hendricks et al. (2004) and Luz and Barkan (2011) have shown that the difference between $\delta^{18}O_{\text{terr}}$ and $\delta^{18}O_{\text{mar}}$ is not significant. Finally, the spatial and temporal variations in water $\delta^{18}O$ and respiration pathways in the ocean are expected to be relatively small compared to the variations on land, which renders their integration for $\delta^{18}O_{atm}$ modeling less crucial, as illustrated in the study of Hoffmann et al. (2004).

5.3.2 Calculation of $\delta^{18}O_{terr}$

The major source of atmospheric oxygen from the terrestrial biosphere is the oxygen produced during photosynthesis. The fractionation associated with photosynthesis is small (Guy et al., 1993; Eisenstadt et al., 2010). The oxygen produced by this process thus has almost the same isotopic composition as the leaf water. Consumption of oxygen is also associated with biosphere productivity through different pathways (dark respiration, photorespiration, Mehler reaction). $\delta^{18}O_{\text{terr}}$ thus results from isotope fractionation associated with photosynthesis and oxygen uptake. Following Bender et al. (1994), Blunier et al. (2002), Hoffmann et al. (2004), and Landais et al. (2007b), we assume a steady state, where photosynthesis equals respiration. $\delta^{18}O_{\text{terr}}$ calculates as

$$\delta^{18}O_{\text{terr}} = \frac{(\delta^{18}O_{\text{lw}} + 1)}{{}^{18}\alpha_{\text{resp}}} - 1, \tag{5.3}$$

where $\delta^{18}O_{\text{lw}}$ is the global production-weighted average isotopic composition of leaf water and ${}^{18}\alpha_{\text{resp}}$ is the global apparent respiratory isotope fractionation factor associated with global oxygen uptake, i.e., oxygen consumption weighted average of fractionation factors associated with specific respiratory pathways.

5.3.3 Photosynthetic oxygen

As classically done, we estimate the value of $\delta^{18}O$ of leaf water, hereafter $\delta^{18}O_{\text{lw}}$, based on the Craig and Gordon (1965) equation (C&G) of evaporation applied to leaf transpiration (Dongmann, 1974; Flanagan et al., 1991b). It is thus calculated in the following way:

$$\delta^{18}O_{\text{lw}} = h \cdot (\delta^{18}O_{\text{vap}} +^{18} \varepsilon_{\text{eq}}) + (1 - h) \cdot (\delta^{18}O_{\text{gw}} +^{18} \varepsilon_{\text{eq}} +^{18} \varepsilon_{\text{kin}}),$$

where h is the relative humidity at the site of photosynthesis, ${}^{18}\varepsilon_{\text{eq}}$ is the temperature-dependent liquid–vapor equilibrium isotope effect (Majoube, 1971), ${}^{18}\varepsilon_{\text{kin}}$ is the ki-

netic isotope effect occurring when humidity is below saturation, $\delta^{18}O_{gw}$ is the isotopic composition of soil water and $\delta^{18}O_{vap}$ is the water vapor $\delta^{18}O$ near the surface. ${}^{18}\varepsilon_{kin}$ is deduced from the ratio of the diffusion coefficient associated with $H_2^{16}O$ (D) and $H_2^{18}O$ (D*). Several values for the ratio D/D^* can be found in the literature (Merlivat, 1978; Cappa et al., 2003; Luz et al., 2009), varying from 1.028 to 1.032. For leaf water evaporation, many studies have reported lower enrichment in $\delta^{18}O_{lw}$ than that predicted by Eq. (5.4a) with ${}^{18}\varepsilon_{kin} = D/D^* - 1$ as classically assumed (e.g., Allison et al., 1985; Bariac et al., 1989; Walker et al., 1989; Walker and Brunel, 1990; Yakir et al., 1990; Flanagan et al., 1991b,a, 1993, 1994). Farquhar et al. (1989) suggested that ${}^{18}\varepsilon_{kin}$ depends on the importance of either stomatal or boundary layer resistances. In moist conditions, stomata resistance is low and boundary layer resistance high, leading ${}^{18}\varepsilon_{kin}$ to values as low as 19 ‰ when using the Merlivat (1978) value for D/D^*. In this study, we have imposed a mean value for ${}^{18}\varepsilon_{kin}$ of 20 ‰ because higher values led to too high a global value for $\delta^{18}O_{atm}$.

The calculation of $\delta^{18}O_{lw}$ using Eq. (5.4a) requires spatial and temporal variations in temperature and relative humidity as well as the variations in the isotopic composition of water vapor and meteoric water, from which $\delta^{18}O_{gw}$ will be deduced (Sect. 5.3.3.2). These variables are obtained from outputs of modeling experiments.

5.3.3.1 Simulated climatic variations over an abrupt cooling

Temperature and relative humidity variations over a HS are inferred from simulations with the atmosphere–ocean general circulation model (AOGCM) IPSL_CM4 (Marti et al., 2010) with a horizontal resolution for the atmosphere grid of 3.75 °× 2.5 °(latitude × longitude) and with a 19 vertical layer atmosphere. To model the $\delta^{18}O_{atm}$ variations over a HS, we have used a glacial simulation perturbed by a freshwater hosing experiment. We will compare in the following the outputs of two simulations: one for the Last Glacial Maximum (LGM_ctrl) and one for the Heinrich stadial (HS_exp).

The LGM_ctrl boundary conditions are as follows (see Kageyama et al., 2009, for a detailed presentation of the climate setup): orbital parameters for 21 ky BP, CO_2 , CH_4 and N_2O levels set to 185 ppm, 350 and 200 ppb, respectively (Monnin et al., 2001; Dällenbach et al., 2000; Flückiger et al., 1999), ICE-5G ice sheet reconstruction and land–sea mask (Peltier, 2004).

The first experiment is an equilibrated glacial run (LGM_ctrl) used as a reference run (see LGMb in Kageyama et al., 2009). The second experiment (HS_exp) is a water hosing experiment, where an additional freshwater flux of 0.1Sv (1Sv = $10^6 m^3 s^{-1}$) is imposed instantaneously in the Atlantic north of 40°N and the Arctic (see LGMc in Kageyama et al., 2009) from year 150 for 400 years. The input of freshwater in HS_exp, mimicking a Heinrich event, leads to an AMOC collapse in 250 years (see Fig. 1 in Kageyama et al., 2009). We selected this HS_exp experiment since the most efficient way to simulate the climate state during an Heinrich event with a model is to add

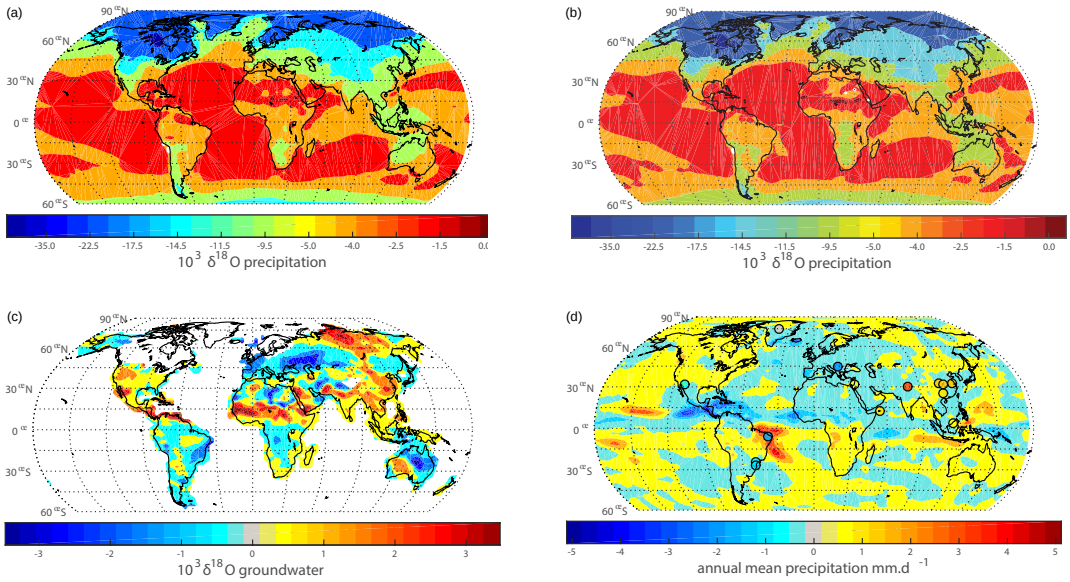

Figure 5.3 – Amount-weighted annual-mean $\delta^{18}O$ of precipitation for **(a)** LGM_ctrl and **(b)** HS_exp experiments obtained with LMDZ-iso. Note that the anomaly can be seen in Fig. 5.4a. **(c)** HS_exp–LGM_ctrl annual-mean anomaly of groundwater $\delta^{18}O$. Groundwater $\delta^{18}O$ represents the isotopic value of the substrate water for photosynthesis (see text for details). **(d)** HS_exp–LGM_ctrl annual-mean anomaly of rainfall amount.

freshwater in the high latitudes of the Atlantic ocean, even though results from recent studies (Marcott et al., 2011; Guillevic et al., 2014; Rhodes et al., 2015; Alvarez-Solas et al., 2013) suggest that this does not satisfactorily explain the observed sequences of events (freshwater discharges from ice sheets might not be the initial trigger of Heinrich events) and especially the decoupling between Greenland and low latitudes. We therefore center our study on the mean state of two contrasted periods rather than investigate the dynamics of the transition from the LGM to HS. It also explains why we only focus on HSs and not DO events.

The climate response to the AMOC collapse in the HS_exp is of global extent and qualitatively agrees with paleoarchive reconstructions for the North Atlantic cooling, southwards Atlantic ITCZ migration and weakening of Indian and African monsoons (Kageyama et al., 2009, 2013). However, the model does not simulate an Antarctic warming or weakened East Asian monsoon (Kageyama et al., 2009). In the following we used the monthly averaged spatial fields of temperature (Tm) and humidity calculated on the first layer of the atmosphere grid. From these data we followed the Lloyd and Farquhar (1994) approach to link leaf temperature during photosynthesis, Tp, to Tm, through $\mathrm{Tp} = 1.05 \cdot (\mathrm{Tm} + 2.5)$. An additional 2.5°C is added to Tm to account for the daytime increase in air temperature at the time of photosynthesis. The 5 % increase allows for net canopy to air heat fluxes (Farquhar and Lloyd, 1993). The relative humidity from the first layer is not modified (Farquhar et al., 2007).

5.3.3.2 Modeling of $\delta^{18}O$ of meteoric water and groundwater

For our estimate, we also need the distribution of the oxygen isotopic composition of meteoric water. We extract it from the isotopic version of the atmospheric general circulation model developed at the Laboratoire de Météorologie Dynamique (LMDZ4; Risi et al., 2010). LMDZ is the atmospheric component of the IPSL-CM4 model used above. The physical package is described in detail by Hourdin et al. (2006). It includes in particular the Emanuel convective parameterization (Emanuel, 1991; Grandpeix et al., 2004) coupled to the Bony and Emanuel (2001) cloud scheme. Each grid cell is divided into four subsurfaces: ocean, land, ice sheet and sea ice (Risi et al., 2010). The monthly sea surface temperature and sea ice fields obtained from the two aforementioned experiments at equilibrium (LGM_ctrl and HS_exp) have been used as surface boundary conditions for the isotopic simulations. Monthly mean outputs of the IPSL-CM4 are imposed to the LMDZ4 model, so there is no coupling between ocean and atmosphere, and nonlinear submonthly scale processes are thus not taken into account here. This choice should not alter our results. Indeed, LeGrande and Schmidt (2008) analyze changes in water isotopes following the 8.2 ka event's meltwater pulse (meltwater $\delta^{18}O: -30$ ‰) in a fully coupled AOGCM (Goddard Institute for Space Studies ModelE-R) and show that the effect of the freshwater impulse on $\delta^{18}O$ of precipitation, noted $\delta^{18}O_p$ hereafter, can be neglected because the signal is very short-lived, only a few decades, before the climatic component dominates. Furthermore, the main changes are constrained to the northern North Atlantic and its surrounding regions (Fig. 6 of LeGrande and Schmidt, 2008). Those regions only have a limited contribution to the $\delta^{18}O_{atm}$ signal, as most of the terrestrial photosynthesis occurs in the tropics. Figure 7 of LeGrande and Schmidt (2008) shows that two decades after a meltwater pulse, the ensemble mean (five simulations) anomaly of $\delta^{18}O_p$ calculates to -0.01 ‰, confirming the small impact of $\delta^{18}O$ depleted meltwater.

Figure 5.3 shows the mean annual $\delta^{18}O_p$, simulated for the LGM_ctrl and the HS_exp experiments. The $\delta^{18}O_p$ distribution for the LGM_ctrl experiment has already been confronted to observations of water isotopes in vapor and precipitation (Risi et al., 2010) and seasonal patterns are well captured. For validation purposes, $\delta^{18}O_p$ changes from the LGM to HS are compared with changes in (i) calcite $\delta^{18}O$ in speleothems, noted $\delta^{18}O_c$ hereafter, and in (ii) ice $\delta^{18}O$ in Greenland ice cores over Heinrich events (Sect. 5.4.1.2; see Fig. 5.4a for $\delta^{18}O_p$ anomaly).

Finally Eq. (5.4a) also requires an estimate of $\delta^{18}O_{gw}$. Groundwater pumped through the plant's roots represents a mixture of stored water and incoming precipitation water (McGuire et al., 2002). Indeed, during spring/summer, when maximal productivity occurs, the groundwater is composed of significant amounts of fall/winter precipitation. In order to take the mixing into account we use amount-weighted annual-mean $\delta^{18}O$ of precipitation. This approach has been shown to be realistic in a field experiment in Kenya (Wang et al., 2012) and has been implemented in a global coupled climate model of intermediate complexity (Caley et al., 2014). When implementing

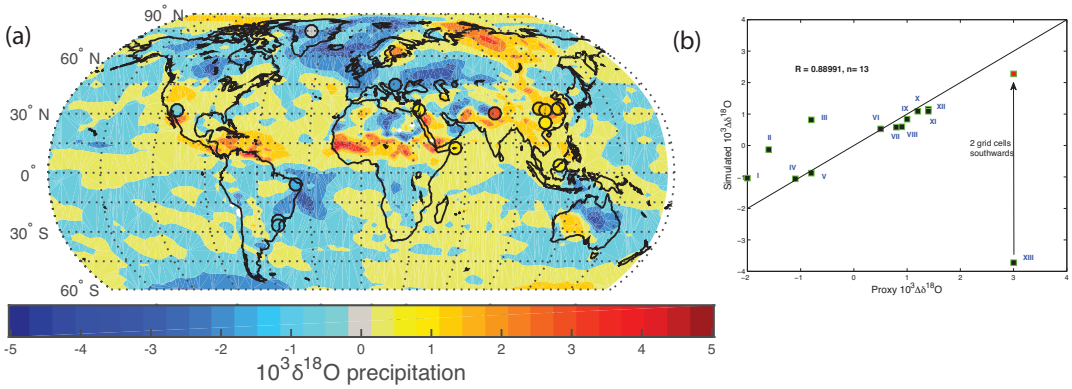

Figure 5.4 – **(a)** Model–data comparison of $\delta^{18}O$ precipitation anomaly during HS compared to the LGM. Data represent speleothem's calcite $\delta^{18}O$ from various locations (see Table 5.3 for details). **(b)** Comparison of reconstructed HS precipitation anomaly $\Delta\delta^{18}O$ from selected proxies shown in **(a)** and simulated $\Delta\delta^{18}O_p$ anomaly ($R = 0.89$, $n = 13$). Note that the correlation is done with point XIII corrected, as we assume a bias in the model. Refer to Table 5.3 for details on reconstructed precipitation. Points falling on the line depict the same anomaly in the reconstruction and the simulation. Note that Timta and Dongge (Wang et al., 2005) Cave $\delta^{18}O_c$ values were estimated from the Younger Dryas excursion, sometimes called Ho and characterized by a large freshwater input in the North Atlantic (Pausata et al., 2011).

this, we neglect the fractionation effects that can significantly affect the soil water isotopic composition, especially in dry regions (Kanner et al., 2014).

5.3.4 Oxygen uptake in respiratory processes

5.3.4.1 Global oxygen production

The geographical distribution of respiratory O_2 fluxes (noted GPP_O_2 hereafter from the hypothesis of equilibrium between oxygen production and consumption) is computed from the vegetation cover and gross primary productivity (GPP) distribution provided by the ORCHIDEE model, which simulates the vegetation distribution of 10 natural plant functional types (PFTs) and bare soil (Krinner et al., 2005). ORCHIDEE is the land surface component of the IPSL-CM4 model. It is used here with the same spatial resolution as the aforementioned models (latitude $\times$ longitude $3.75° \times 2.5°$) and is run in offline mode, forced by the high-frequency outputs from IPSL-CM4 for the two experiments LGM_ctrl and_HS_exp. The prescribed forcing has a 6 h time step temporal resolution, and thus takes into account daily variability and diurnal cycle simulated by the IPSL model (Woillez, 2012). Each grid cell simulates the vegetation cover by splitting the cell into fractions of 10 PFTs (see Table 5.1 for names) and provides GPP fluxes ($gCm^{-2}yr^{-1}$) for each PFT. Validation of the vegetation cover can be found in Woillez et al. (2011) for LGM_ctrl and Woillez et al. (2013) for HS_exp over western Europe. Here we extend this work and compare the LGM

Table 5.1 – Plant functional types (PFT) in ORCHIDEE, abbreviation used and mega-biome assignment in this study.

PFT	Abbreviation	Mega-biome
Bare soil	Bare soil	Bare soil
Tropical broadleaf evergreen trees	TrBE	Tropical trees
Tropical broadleaf raingreen trees	TrBR	Tropical trees
Temperate needleleaf evergreen trees	TempNE	Temperate trees
Temperate broadleaf evergreen trees	TempBE	Temperate trees
Temperate broadleaf summergreen trees	TempBS	Temperate trees
Boreal needleleaf evergreen trees	BoNE	Boreal trees
Boreal broadleaf summergreen trees	BoBS	Boreal trees
Boreal needleleaf summergreen trees	BoNS	Boreal trees
C3 grass	C3 grass	C3 grass
C4 grass	C4 grass	C4 grass

and HS simulation with worldwide vegetation reconstructions selected from marine (coastal) and terrestrial paleoarchives with high temporal resolution (Sect. 5.4.1.3).

In this study, following Hoffmann et al. (2004), we calculate the terrestrial biosphere's O_2 fluxes in three steps. First, the outputs from ORCHIDEE provide the GPP expressed in $\mathrm{gCm^{-2}yr^{-1}}$ for each of the 10 PFTs on each model grid point. Second, simulated carbon molar fluxes for each PFT are converted to oxygen molar fluxes, based on the biochemical model of photosynthesis from Farquhar et al. (1980). The model accounts for the fraction of photorespiration and the photosynthetic quotient (PQ) – measured by Keeling (1988) and Severinghaus (1995) as $\backsim$ 1.1. Third, GPP_O_2 for each PFT is expressed in terms of dark respiration (mitochondrial), Mehler respiration and photorespiration, each of these respiratory uptake processes being associated with a specific fractionation (refer to Table 5.2 for values):

$$\begin{aligned}\mathrm{GPP\_O_2} &= \mathrm{GPP\_O_2\_Mehler} + \mathrm{GPP\_O_2\_dark} \\ &+ \mathrm{GPP\_O_2\_photo} = \frac{\mathrm{GPP} \cdot \mathrm{PQ} \cdot (1 + f_{\mathrm{photo}})}{1 - f_{\mathrm{Mehler}}},\end{aligned} \tag{5.4a}$$

with

$$\mathrm{GPP\_O_2\_Mehler} = f_{\mathrm{Mehler}} \cdot \mathrm{GPP\_O_2}, \tag{5.4b}$$

$$\mathrm{GPP\_O_2\_dark} = (1 - f_{\mathrm{Mehler}}) \cdot \mathrm{PQ} \cdot \mathrm{GPP}, \tag{5.4c}$$

$$\begin{aligned}\mathrm{GPP\_O_2\_photo} &= (1 - f_{\mathrm{Mehler}}) \cdot (\mathrm{GPP\_O_2} - \mathrm{PQ} \cdot \mathrm{GPP}) \\ \mathrm{GPP\_O_2\_photo} &= (1 - f_{\mathrm{Mehler}}) \cdot \mathrm{PQ} \cdot \mathrm{GPP} \cdot f_{\mathrm{photo}},\end{aligned} \tag{5.4d}$$

where f_{Mehler} denotes the fraction of Mehler reaction, and accounts for 10 % of the total respiration (Badger et al., 2000) and f_{photo} represents the fraction of photorespiration.

5.3.4.2 Photorespiration

All types of C3 plants photorespire, but in different proportions. In contrast, C4 plants do not photorespire, because of a CO_2 concentration mechanism allowing them to operate at high chloroplast CO_2 partial pressures and thereby inhibit the oxygenation reaction during photosynthesis (Von Caemmerer, 2000). The proportion of photorespiration is calculated from the proportion of C4 vs. C3 plants, temperature and CO_2 level (assumed constant in our study) as depicted in the biochemical model of photosynthesis from Farquhar et al. (1980) and already done in the studies of Hoffmann et al. (2004) and Landais et al. (2007a). Increasing photorespiration modifies ${}^{18}\varepsilon_{\text{resp}}$, as photorespiration is associated with a high discrimination and in turn affects $\delta^{18}O_{\text{terr}}$. Details on equations used in our offline model for $\delta^{18}O_{\text{terr}}$ calculation can be found in Hoffmann et al. (2004).

5.3.4.3 Soil respiration

We have assigned fractionation factors for each soil using the soil type discrimination proposed by Angert et al. (2003). For this, we relate the Angert soil types to the type of vegetation cover over the considered soil in the ORCHIDEE model. As an example, we have assigned tropical soils (fractionation coefficient of -10.1 ‰) to soil covered by dominant the PFT tropical broadleaf evergreen trees and the PFT tropical broadleaf raingreen trees. Tropical soils (-10.1 ‰) discriminate significantly less than temperate (-17.8 ‰) or boreal soils (-22.4 ‰) following Angert et al. (2003). The global respiratory isotope fractionation for the control run calculates as -15.895 ‰, much weaker than the common value (-18 ‰) used for terrestrial ecosystems. As soil respiration only occurs where vegetation exists, a shift of the latter modifies the spatial distribution of soils where dark respiration takes place. In our model, the change in vegetation cover from the LGM to HS leads to a very slight weakening of soil respiration isotope fractionation using fractionation values of Angert et al. (2003). We present in Sect. 5.4.2.2 a sensitivity test to assess the magnitude of the uncertainty in soil respiration isotope fractionation that is introduced by not taking into account the effect of soil aeration, i.e. the weakening of respired O_2 back-diffusion in waterlogged soils.

5.3.4.4 Global terrestrial fractionation factor

Uptake of oxygen by respiration discriminates against heavy isotopes, leaving the substrate oxygen, atmospheric O_2 , enriched in ${}^{18}O$. Each of the oxygen uptake processes is affected by a specific, spatially and temporally constant fractionation (Table 5.2) and the global terrestrial isotope fractionation factor ${}^{18}\alpha_{\text{resp}}$ is expressed as follows:

$$\begin{aligned} {}^{18}\alpha_{\text{resp}} = {}^{18}\alpha_{\text{photo}} \cdot f_{\text{photo}} + {}^{18}\alpha_{\text{Mehler}} \cdot f_{\text{Mehler}} \\ + {}^{18}\alpha_{\text{dark\_soil}} \cdot f_{\text{dark\_soil}} + {}^{18}\alpha_{\text{dark\_leaves}} \cdot f_{\text{dark\_leaves}}, \end{aligned} \tag{5.5}$$

The latest estimations of ${}^{18}\alpha_{\text{Mehler}}$, ${}^{18}\alpha_{\text{photo}}$ and ${}^{18}\alpha_{\text{dark\_leaves}}$ can be found in Table 5.2. A significant proportion of terrestrial respiration (30 to 40 %) occurs below the sur-

face (Raich and Potter, 1995) with varying fractionation values. Respiration below surface ($^{18}\alpha_{\text{dark\_soil}}$) thereby needs to be considered for the different types of soils (boreal, temperate, tropical), as each soil type is associated with a specific fractionation factor because of different diffusion pathways (Angert et al., 2003). The Mehler fraction, f_{Mehler}, represents 10 % of global respiration (Badger et al., 2000) and f_{photo} is calculated from the outputs of the ORCHIDEE and IPSL-CM4 models. The dark respiration fraction is composed of leaf (38 %) and soil (62 %) respiration, following Landais et al. (2007b).

5.4 Results

5.4.1 Simulation of regional climate, vegetation and isotopic pattern during a HS

We propose here a model–data comparison on a regional scale to evaluate the model performances, as the climatic and water cycle responses during a HS are not spatially homogeneous. Climatic outputs of the HS experiments are already discussed in Kageyama et al. (2009) and Woillez et al. (2013). In the following we thus mainly discuss the simulated change in relative humidity (Sect. 5.4.1.1) since the latter has an important influence on the $\delta^{18}O_{\text{lw}}$ and hence $\delta^{18}O_{\text{terr}}$. Then, we further compare the modeled change in $\delta^{18}O$ of precipitation over a HS with changes in speleothems calcite $\delta^{18}O$ (Sect. 5.4.1.2) and modeled fraction of vegetation with vegetation reconstructions (Sect. 5.4.1.3).

5.4.1.1 Simulated humidity validation

According to climate reconstructions, during HS, wet periods in northeastern Brazil are synchronous with periods of weak East Asian summer monsoons (Wang et al., 2001) and with cold periods in Greenland (Grootes and Stuiver, 1997) and Europe (Genty et al., 2003). Reorganization in tropical rainfall patterns leads to wetter conditions in southwestern North America (Asmerom et al., 2010) and southern South America (Kanner et al., 2012), and to dryer conditions in the Australian–Indonesian monsoon region (Mohtadi et al., 2011), wide parts of Asia (Wang et al., 2008), northern South America (Peterson and Haug, 2006), Mediterranean region (Fleitmann et al., 2009), and equatorial western Africa (e.g., Weldeab, 2012).

During HS, the model simulates similar humidity patterns as reconstructed ones, with dryer conditions over Europe, the Mediterranean region, northern and equatorial Africa, southern and eastern Asia, Middle East, India, southern Australia and parts of Indonesia. In South America, a region of particular interest, where major simulated changes in vegetation and oxygen production occur, the model captures well the observed contrast with increased moisture in northeastern Brazil, and drying in northern South America and Central America.

Table 5.2 – Parameters involved in the calculation of $\delta^{18}O_{atm}$. Uncertainties are given for most of the parameters except for those derived from the ORCHIDEE model.

Parameter	Unit	Definition	LGM_ctrl	HS_exp
CO_2	ppm	carbon dioxide mixing ratio in the troposphere	190	190
t	°C	temperature at the site of photosynthesis	21.08	21.41
h	%	relative humidity at the site of photosynthesis	66.09	66.12
GPP_C	$PmolCyr^{-1}$	gross photosynthetic molar carbon flux from the terrestrial biosphere	6.758	6.450
GPP_O_2	$PmolO_2yr^{-1}$	gross photosynthetic molar oxygen flux from the terrestrial biosphere	11.768	11.410
f_{C_4}	%	C4 fraction (in terms of GPP_C)	36.92	35.59
f_{photo}	%	fraction of photorespiration	28.55	29.52
$f_{\text{soil\_dark}}$	%	soil fraction of dark respiration	62[a]	62[a]
$f_{\text{dark\_soil}}$	%	fraction of soil respiration	38.10	37.50
$f_{\text{dark\_leaves}}$	%	fraction of leaf respiration	23.35	22.98
f_{Mehler}	%	fraction of Mehler respiration	10[b]	10[b]
${}^{18}\varepsilon_{\text{dark\_soil}}$	‰	global isotopic fractionation associated with dark soil respiration	16.242 ± 0.5[c]	16.056 ± 0.5[c]
${}^{18}\varepsilon_{\text{dark\_leaves}}$	‰	mitochondrial (AOX + COX) isotopic fractionation in leaves	19 ± 1[c]	19 ± 1[c]
${}^{18}\varepsilon_{\text{Mehler}}$	‰	global Mehler respiration isotopic fractionation	10.8 ± 0.2[d]	10.8 ± 0.2[d]
${}^{18}\varepsilon_{\text{photo}}$	‰	global photorespiration isotopic fractionation	21.4 ± 1[d]	21.4 ± 1[d]
${}^{18}\varepsilon_{\text{resp}}$	‰	global terrestrial respiration isotopic fractionation	17.83	17.80
$\delta^{18}O_{\text{p\_amount}}$	‰	global precipitation water isotope delta	−6.689	−6.781
$\delta^{18}O_{\text{p}}$	‰	global photosynthesis precipitation water isotope delta	−5.530	−5.289
$\delta^{18}O_{\text{vap\_amount}}$	‰	global water vapor isotope delta	−12.648	−12.653
$\delta^{18}O_{\text{vap}}$	‰	global photosynthesis water vapor isotope delta	−12.483	−12.295
$\delta^{18}O_{\text{leafwater}}$	‰	global leaf water isotope delta	5.164 ± 1[e]	5.301 ± 1[e]
$\delta^{18}O_{\text{terr}}$	‰	global terrestrial tropospheric isotope delta	23.407 ± 1	23.516 ± 1
$\delta^{18}O_{\text{mar}}$	‰	global marine tropospheric isotope delta	25.3 ± 2[f]	25.3 ± 2[f]
$\delta^{18}O_{atm}$	‰	global tropospheric isotope delta	23.88 ± 2	23.95 ± 2

[a] (Schlesinger and Andrews, 2000). Note that this estimation is for present day, and here we assume it was similar during the last glacial period.
[b] (Badger et al., 2000).
[c] (Landais et al., 2007a).
[d] (Helman et al., 2005).
[e] (Gillon and Yakir, 2001).
[f] Note that the increase of 1‰ compared to the Luz et al. (2014) value accounts for the 1 ‰ enrichment of the glacial ocean (Waelbroeck et al., 2002).

These rapid comparisons show that there is a good general agreement between modeled changes in humidity over an HS and climatic reconstructions over the different regions.

5.4.1.2 Simulated amount-weighted $\delta^{18}O_p$ validation

5.4.1.2.1 *Tropics*

Comparisons of modeled hosing-driven amount-weighted $\Delta\delta^{18}O_{\text{p}}$ anomalies with reconstructed $\Delta\delta^{18}O$ of speleothem's calcite during HSs are presented in Table 5.3 and Fig. 5.4. Thirteen Heinrich $\Delta\delta^{18}O_p$ proxy reconstructions arise from Lewis et al. (2010) ($n = 11$) and Pausata et al. (2011) ($n = 4$). They are located in the eastern Mediterranean, and in the regions of the South American monsoon, East Asian monsoon, Indian summer monsoon, North American monsoon and the Australian–Indonesian monsoon. Those regions represent the most productive ones and therefore carry a substantial part of the $\delta^{18}O_{\text{terr}}$ signal. Although reconstructed $\Delta\delta^{18}O_{\text{p}}$ anomalies from Lewis et al. (2010) and Pausata et al. (2011) studies were estimated differently, they are consistent and common reconstructed $\Delta\delta^{18}O_{\text{p}}$ estimates (for Hulu and Songjia Cave) are similar in both studies (Table 5.3, this study; method section of Pausata et al., 2011).

The dominant hydrological controls on reconstructed $\delta^{18}O_p$ are site-specific and are

Table 5.3 – Comparison of isotopic proxy records (speleothem's calcite $\delta^{18}O$) with annual average modeled amount-weighted $\delta^{18}O_p$. Note that anomalies from Pausata et al. (2011) are calculated from H1 and YD, while anomalies from Lewis et al. (2010) arise from all identifiable $\delta^{18}O_c$ excursions.

Core	ID	Region	Latitude	Longitude	Data $\Delta\delta^{18}O$	Model $\Delta\delta^{18}O$	Reference
Hulu Cave	XI	China	32.5	119.2	1.4	1.1	Pausata et al. (2011); Lewis et al. (2010)
Songjia Cave	XII	China	32.3	107.2	1.4	1.1	Pausata et al. (2011); Lewis et al. (2010)
Dongge Cave	IX	China	25.3	108.8	1	0.8	Pausata et al. (2011)
Timta Cave	XIII	India	29.8	80.0	3	−3.7	Pausata et al. (2011)
Sanbao Cave	X	China	31.7	110.5	1.2	1.1	Lewis et al. (2010)
Borneo	VII	Indonesia	4.0	114.0	0.8	0.6	Lewis et al. (2010)
Moomi Cave	VIII	Yemen	12.5	54.3	0.9	0.6	Lewis et al. (2010)
Soreq Cave	VI	Israel	31.5	35.0	0.5	0.5	Lewis et al. (2010)
Rio Grande do Norte	II	northeastern Brazil	−5.7	−37.7	−1.6	−0.1	Lewis et al. (2010)
Santana Cave	V	southern Brazil	−24.5	−48.7	−0.8	−0.9	Lewis et al. (2010)
Botuvera Cave	IV	southern Brazil	−27.2	−49.2	−1.1	−1.1	Lewis et al. (2010)
Cave of the Bells	III	North America	31.7	−110.8	−0.8	0.8	Lewis et al. (2010)
Poleva Cave	I	Europe	44.7	21.8	−2	−1.0	Lewis et al. (2010)

described by Lewis et al. (2010). Figure 5.4 demonstrates the ability of the AOGCM LMDZ-iso to reproduce the observed $\Delta\delta^{18}O_p$ spatial pattern for most of the sites, particularly in regions strongly affected by ITCZ (and its land extension) variations and hence by changes in the water cycle, regardless of the processes at play. There are two regions where the model does not properly reproduce the observed signal over HS. The first one occurs in the Indian summer monsoon domain (Timta Cave). Model and observation would reconcile two grid cells south of Timta Cave, as it is located just at the transition between a positive and negative simulated $\delta^{18}O_p$ anomaly. This disagreement can be due to a model bias. The IPSL model indeed does not simulate the monsoonal signal at the right place, with an Indian monsoon located too far south even for modern climate (Marti et al., 2010). In the LGM simulation also, the IPSL model predicts that it mostly takes place over the ocean (-0.5 to -2 mm $\cdot day^{-1}$ is only simulated over the ocean; see Fig. 9 (lower panel) of Kageyama et al., 2009), while there is evidence for a monsoonal signal over land. In northern India, i.e., the Timta Cave site, the model does not simulate any significant rainfall change between the two periods. A more intense weakening of the Indian monsoon over land in the HS run, and hence less rainfall, would have helped in reconciling the model and data at Timta Cave, since $\delta^{18}O_p$ would have been enriched through the amount effect. Pausata et al. (2011) recently suggested that change in rainfall amount associated with Indian monsoon rather than in southeastern Asia explains changes observed in calcite $\delta^{18}O$ in Chinese stalagmites (in southeastern Asia). As in Pausata et al. (2011), a freshwater impulse was applied to the control simulation with LGM background climate. Rainfall amount drops in eastern Asia and northwestern India, mostly over the ocean, but increases in southeastern India, as shown in Fig. 5.3d. Values of -0.17 and -0.13mm $\cdot day^{-1}$ are simulated at Hulu and Songjia Cave during HS, respectively. The enrichment in $\delta^{18}O_p$ observed in Chinese caves is reproduced by the model, but the latter fails to capture the enrichment in Timta Cave. Overall, $\delta^{18}O_p$ is enriched over the whole of India (with an abrupt change south of Timta Cave) and southern Asia. The possible role of the Indian monsoon in the oxygen isotopic enrichment of Chinese stalagmites is limited in our simulation, probably because the monsoonal signal is lo-

cated too far south in the IPSL model. The increase in $\delta^{18}O$ over southeastern Asia is consistent with local amount effect.

Another mismatch occurs in the North American monsoon domain (Cave of the Bells), where the observed $\Delta\delta^{18}O_{\mathrm{p}}$ (-0.8‰) and the modeled $\Delta\delta^{18}O_{\mathrm{p}}$ (0.9‰) are of opposite sign. The elevation of the site (1700 m a.s.l.) might explain the disagreement between model and data, in a region where the coarse model resolution does not allow for the role of orography to be properly represented. At Timta Cave and Cave of the Bells, our model fails to capture the calcite $\delta^{18}O$ anomaly recorded in speleothems. These two sites are located at high altitude and do not correspond to the regions where most of the oxygen is produced.

As shown in Table 5.3, the modeled increase in $\delta^{18}O_p$ quantitatively agrees with data $\delta^{18}O_{\mathrm{c}}$ increase during HS in most of the compared sites (Fig. 5.4). In conclusion, the key features of HS precipitation inferred from speleothem's $\delta^{18}O_{\mathrm{c}}$, i.e., a low-latitude interhemispheric see-saw pattern (Cheng et al., 2012), are generally well captured by the LMDZ model.

5.4.1.2.2 *High latitudes*

In Greenland, HS can hardly be distinguished from the GS or from the mean LGM state. The only clear $\delta^{18}O_{\mathrm{ice}}$ signal is observed from GI to GS (or HS) with an approximately 4 ‰ decrease in central Greenland sites (GRIP, GISP2, NGRIP). The depletion simulated in Greenland, with a 1.6 ‰ decrease at the GRIP site, by the model for a HS compared to a glacial background state does not compare well with available data. However, it is difficult to compare the $\delta^{18}O$ change simulated by a freshwater input (the most efficient way to model a Heinrich event, as mentioned in Sect. 5.3.3.1) and the $\delta^{18}O$ depletion between a GI and a GS. Indeed, there is more and more evidence that the $\delta^{18}O_p$ depletion at the end of a GI is not due to the same freshwater discharge than the one associated with a Heinrich event. It can well be due to a threshold in the extent in sea ice or an atmospheric heat transport. Therefore our choice of modeling approach may potentially explain some of the discrepancies observed in the low latitudes, but our approach is the best we can realize today.

5.4.1.3 Validation of simulated vegetation

In order to compare model and data easily, simulated PFTs are gathered into five mega-biomes (boreal, temperate and tropical trees, C3 and C4 grasses) as well as bare soil. We distinguish between C3 and C4 plants as their partitioning has a strong impact on photorespiration fraction. The simulated dominant vegetation fraction is shown for LGM_ctrl (Fig. 5.5) and HS_exp (Fig. 5.6), together with pollen-based reconstructed mega-biomes. Given its domination, we display bare soil fraction only if it covers more than 80 % of a grid cell.

Table 5.4 – Comparison of mega-biomes during Heinrich stadials between pollen reconstructions (references are included in the table) and simulated vegetation (compiled from HS_exp using the ORCHIDEE vegetation model). Note that simulated C3 and C4 grasses are merged into one mega-biome because pollen-based biome reconstructions do not allow us to distinguish between the two PFTs.

Core	ID	Region	Latitude	Longitude	Resolution[a] (yr/sample)	Which HS?	Mega-biome distribution: pollen data: flora	pollen data: biome(s) designation	model results dominant, subdominant biome	Agreement	Reference
Kashiru Bog	1	equatorial Africa	−3.47	29.57	410	HS1	grassland and dry shrubland, savannah and xerophytic scrubland	grasses	tropical forest, grasses	fair	Hessler et al. (2010); Handiani et al. (2012)
Lake Tanganyika	2	equatorial Africa	−8.5	30.85	610	HS1	warm temperate mixed forest, savannah and xerophytic scrubland	temperate forest, grasses	grasses, tropical forest	fair	Hessler et al. (2010); Handiani et al. (2012)
Lake Masoko	3	equatorial Africa	−9.33	33.75	550	HS1	warm temperate mixed forest, savannah and xerophytic scrubland	temperate forest, grasses	grasses, tropical forest	fair	Hessler et al. (2010); Handiani et al. (2012)
Lake Malawi	4	equatorial Africa	−11.29	34.44	200	HS1	savannah and xerophytic scrubland, tropical forest	grasses, tropical forest	grasses	good	Hessler et al. (2010); Handiani et al. (2012)
Barombi Mbo	5	equatorial Africa	4.51	9.4	590	HS1	savannah and xerophytic scrubland, tropical forest	grasses, tropical forest	grasses, tropical forest	good	Hessler et al. (2010); Handiani et al. (2012)
KS 84-063	6	equatorial Africa	4.4	−4.18	450	HS1	tropical forest, warm temperate mixed forest	tropical forest, temperate forest	tropical forest, grasses	good	Hessler et al. (2010); Handiani et al. (2012)
ODP 1078-C	7	equatorial Africa	−11.92	13.4	140	HS1	warm temperate mixed forest, temperate montane forest	temperate forest, boreal forest	bare soil, tropical forest	bad[b] (soil > 90 %)	Hessler et al. (2010); Handiani et al. (2012)
GEOB 1023 – Cunene River Mouth	8	equatorial Africa	−17.15	11.02	185	HS1	savannah and xerophytic scrubland, grassland and dry shrubland	grasses	none	none	Hessler et al. (2010); Handiani et al. (2012)
Lake Caco	9	South America	−2.97	−43.42	80	HS1	warm temperate mixed forest, tropical forest	temperate forest, tropical forest	bare soil, tropical forest	moderate	Hessler et al. (2010); Handiani et al. (2012)
Colonia	10	South America	−23.87	−46.71	710	HS1	savannah and xerophytic scrubland, grassland and dry shrubland	grasses	grasses, temperate forest	good	Hessler et al. (2010); Handiani et al. (2012)
La Laguna, Bogota	11	South America	4.92	−74.03	670	HS1	savannah and xerophytic scrubland, grassland and dry shrubland	grasses	bare soil	bad (soil = 100 %)	Hessler et al. (2010); Handiani et al. (2012)
Fuquene	12	South America	4.92	−74.03	520	HS1	savannah and xerophytic scrubland, temperate montane forests	grasses, temperate forest	bare soil	bad (soil = 100 %)	Hessler et al. (2010); Handiani et al. (2012)
GEOB 3104	13	South America	−3.67	−37.72	670	HS1	temperate montane forest, warm temperate mixed forest	temperate forest	tropical forest, bare soil	bad[b]	Hessler et al. (2010); Handiani et al. (2012)
GEOB 3910-2	14	South America	−4.15	−36.21	125	HS1	savannah and xerophytic scrubland, warm temperate mixed forests	grasses, temperate forest	tropical forest, bare soil	bad[b]	Hessler et al. (2010); Handiani et al. (2012)
MD03-2622	15	South America	10.71	−65.17	420	HS3, HS4, HS5	montane forest, semi-deciduous forest, savannah (except HS4)	temperate forest, grasses	none	none	Hessler et al. (2010); Handiani et al. (2012)
17 962	16	Australasia	7.18	112.08	370	HS4	tropical forest	tropical forest	tropical forest, grasses	good	Harrison and Goni (2010)
18 300	17	Australasia	4.35	108.65	526	HS4	tropical forest	tropical forest	tropical forest, grasses	good	Harrison and Goni (2010)
18 323	18	Australasia	2.78	107.88	420	HS4	tropical forest	tropical forest	tropical forest, grasses	good	Harrison and Goni (2010)
Lake Wangoom	19	Australasia	−38.35	142.6	362	HS4	herbaceous and shrublands	grasses	temperate forest, tropical forest	bad	Harrison and Goni (2010)
Tyrendarra Swamp	20	Australasia	−38.2	141.76	337	HS4	herbaceous and shrublands	grasses	temperate forest, tropical forest	bad	Harrison and Goni (2010)
Lake Surprise	21	Australasia	−38.06	141.92	345	HS4	herbaceous and shrublands	grasses	temperate forest, tropical forest	bad	Harrison and Goni (2010)
Kohuora	22	Australasia	−36.57	174.52	375	HS4	herbaceous and shrublands	grasses	temperate forest, tropical forest	bad	Harrison and Goni (2010)
Native Companion Lagoon	23	Australasia	−27.68	153.41	655	HS4	tropical forest and open forest, woodland	tropical forest, temperate forest	bare soil, temperate forest	moderate	Harrison and Goni (2010)

Table 5.4 – Continued.

Core	ID	Region	Latitude	Longitude	Resolution[a] (yr/sample)	Which HS?	Mega-biome distribution: pollen data: flora	pollen data: biome(s) assignation	model results dominant, subdominant biome	Agreement	Reference
Ioannina 284	24	Europe	39.75	20.85	325	HS4	grassland and dry shrubland	grasses	boreal forest, grasses	fair	Fletcher et al. (2010)
Megali Limni	25	Europe	39.1	26.32	150	HS4	grassland and dry shrubland with 40 % xerophytic steppe elements	grasses	grasses, boreal forest	good	Fletcher et al. (2010)
Lago Grande di Monticchio	26	Europe	40.93	15.62	210	HS4	grassland and dry shrubland with 40 % xerophytic steppe elements	grasses	boreal forest, grasses	fair	Fletcher et al. (2010)
MD04-2845	27	Europe	45.35	−5.22	540	HS3	grassland and dry shrubland	grasses	none	none	Fletcher et al. (2010)
MD99-2331	28	Europe	41.15	−9.68	390	HS4	grassland and dry shrubland	grasses	none	none	Fletcher et al. (2010)
MD95-2039	29	Europe	40.58	−10.35	300	HS4	grassland and dry shrubland	grasses	none	none	Fletcher et al. (2010)
MD95-2042	30	Europe	37.8	−10.17	360	HS4	grassland and dry shrubland with 40 % xerophytic steppe elements	grasses	none	none	Fletcher et al. (2010)
ODP site 976	31	Europe	36.2	−4.3	240	HS4	grassland and dry shrubland with 40 % xerophytic steppe elements	grasses	bare soil, boreal forest	bad (soil > 90 %)	Fletcher et al. (2010)
MD95-2043	32	Europe	36.13	−2.62	260	HS4	grassland and dry shrubland with 40 % xerophytic steppe elements	grasses	bare soil, boreal forest	bad (soil > 90 %)	Fletcher et al. (2010)
Khoe	33	Japan	51.34	142.14	750	HS4	cold deciduous and evergreen conifer forest	boreal forest	boreal forest, grasses	good	Takahara et al. (2010)
Kenbuchi	34	Japan	44.05	142.38	250	HS1, HS2	cold deciduous forest	boreal forest	boreal forest, grasses	good	Takahara et al. (2010)
MD01-2421	35	Japan	36.02	141.77	150	HS4	cold evergreen conifer forest	boreal forest	boreal forest, temperate forest	good	Takahara et al. (2010)
Lake Nojiri	36	Japan	36.83	138.22	100	HS4	increase in cold evergreen conifer forest within cool conifer forest	temperate forest, boreal forest	none	none	Takahara et al. (2010)
Lake Biwa	37	Japan	35.22	136	300	HS4	increase in cool conifer forest within temperate conifer forest	temperate forest	boreal forest, temperate forest	fair	Takahara et al. (2010)
Kamiyoshi Basin	38	Japan	35.1	135.59	800	HS4	increase in cool conifer within temperate conifer forest, and deciduous broadleaf forest	temperate forest	boreal forest, temperate forest	fair	Takahara et al. (2010)
Toushe Basin	39	Japan	23.82	120.88	300	HS4	temperate deciduous or warm temperate evergreen forest	temperate forest	boreal forest, temperate forest	good	Takahara et al. (2010)
Fargher Lake	40	North America	45.88	−122.58	270	HS4	boreal forest	boreal forest	none	none	Jimenez-Moreno et al. (2010)
Carp Lake	41	North America	45.91	−120.88	630	HS4	open temperate and pine forest	temperate forest	none	none	Jimenez-Moreno et al. (2010)
Little Lake	42	North America	44.16	−123.58	260	HS4	boreal–temperate forest	boreal forest, temperate forest	none	none	Jimenez-Moreno et al. (2010)
W8709A-13PC	43	North America	42.25	−127.66	430	HS4	boreal forest with decrease in heterophyla	boreal forest	none	none	Jimenez-Moreno et al. (2010)
EW-9504-17PC	44	North America	42.23	−125.81	460	HS1, HS2, HS3	warm temperate	temperate forest, tropical forest	none	none	Jimenez-Moreno et al. (2010)
ODP 893A	45	North America	34.28	−120.03	220	HS4	open temperate forest	temperate forest	temperate forest, bare soil	good	Jimenez-Moreno et al. (2010)
Bear Lake	46	North America	41.95	−111.3	680	HS4	xerophytic shrubland	grasses	grasses	good	Jimenez-Moreno et al. (2010)
Camel Lake	47	North America	30.26	−85.01	300	HS4	temperate forest with increase in southeastern pine forest	temperate forest	boreal forest, temperate forest	fair	Jimenez-Moreno et al. (2010)
Lake Tulane	48	North America	27.58	−81.5	480	HS4	southeastern pine forest, florida scrub	grasses, temperate forest	bare soil, temperate forest	moderate	Jimenez-Moreno et al. (2010)

[a] Sampling resolutions of the MIS where vegetation changes occur. Mean sampling resolution is 393 years. [b] Similar to Handiani et al. (2012) model results.

5.4.1.3.1 *Global oxygen production*

Present-day carbon and oxygen productions amount to 10.5 $PmolC \cdot yr^{-1}$ and 17.95 $PmolO_2 \cdot yr^{-1}$ (taking into account photorespiration) in the ORCHIDEE model, respectively. This is in line with other estimates, e.g., Angert et al. (2003) or Welp et al. (2011), estimating 8 to 13 $PmolC \cdot yr^{-1}$ and 12.5 to 14.2 $PmolO_2 \cdot yr^{-1}$, respectively. For the LGM and HS, land carbon production estimates from the ORCHIDEE model are rather low, 6.8 and 6.5 $PmolC \cdot yr^{-1}$, which translates into 11.8 and 11.4 $PmolO_2 \cdot yr^{-1}$ for the LGM and HS, respectively. This is up to a factor of 2 lower than model-based LGM estimates from Joos et al. (2004), Hoffmann et al. (2004) or Bender et al. (1994), ranging from 23 to 16.7 $PmolO_2 \cdot yr^{-1}$.

The ORCHIDEE model is known to underestimate LGM productivity at both low latitudes (too low productivity in tropical forests, especially Amazonia) and high latitudes (too low productivity in the absence of permafrost modeling).

Photorespiration fraction (see Sect. 5.3.4.2) may also be invoked to explain part of the model–data discrepancy for the LGM and HS. Underestimation of photorespiration may arise from uncertainties related to the time of photosynthesis. In the real world, plants must reduce their CO_2 uptake under water stress, as stomata close to preclude water loss. This leads to a higher proportion of photorespiration, not necessarily considered during experiments performed under ideal hydric conditions, whose results are used in the classical Farquhar parameterization (Farquhar et al., 1980).

The classical scaling factor between carbon uptake and oxygen production (Keeling, 1988) of 1.07 used in our study may also have been underestimated. Indeed, plants can produce oxygen without involving carbon uptake during times of stress, which is not considered in experiments run under ideal conditions. The oxygen production calculated here from the ORCHIDEE model seems to be biased toward too low values for the LGM. The same bias is true for HS. Still, it should be noted that the $\delta^{18}O_{\text{terr}}$ calculations of our study and hence the final results do not depend on the absolute value of oxygen production at the LGM and HS.

5.4.1.3.2 *LGM_ctrl vegetation*

The main features of the glacial vegetation are correctly reproduced by the ORCHIDEE model, as briefly presented by Woillez et al. (2011): reduced fractions of tropical forest, particularly in Amazonia, and high grass fractions in Siberia, Alaska, and western North America. Main biases are an overestimation of the tree fractions over western Europe, eastern Eurasia and eastern North America, as well as an overestimation in bare soil fractions over India, southern Africa, Siberia and South America (Woillez et al., 2011), leading to an underestimation of the global carbon production, as mentioned in the previous section.

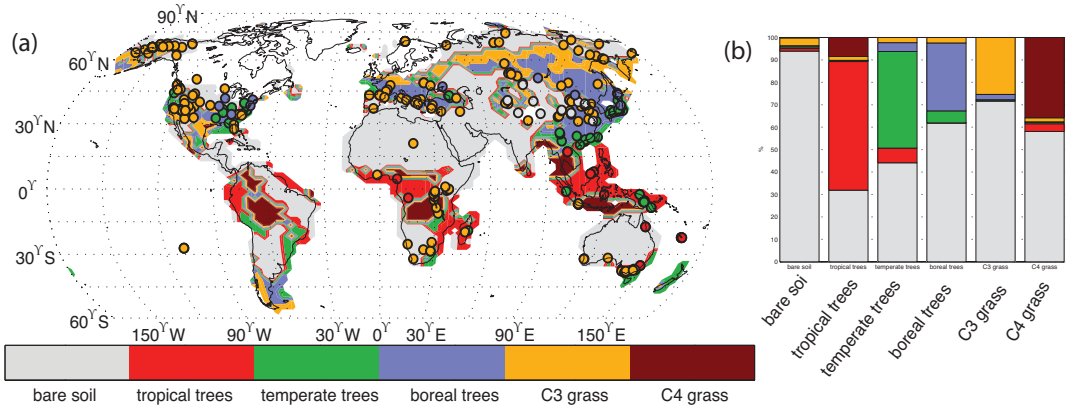

Figure 5.5 – **(a)** Model–data comparison of mega-biome distribution for LGM_ctrl based on dominant PFT type simulated by ORCHIDEE. For each grid cell, the fraction of bare soil, tropical forests, temperate forests, boreal forests, and C3 and C4 grasses is considered. The type covering the greatest cell fraction is the dominant type. Note that dominant bare soil fraction denotes more than 80 %. Circles denote LGM mega-biomes inferred from pollen and plant macrofossil records compiled by the BIOME6000 project. Refer to Table 5.4 to see how PFTs simulated by ORCHIDEE have been assigned to the mega-biomes mapped in this figure. **(b)** Detail of the averaged vegetation composition in grid cells occupied by a dominant mega-biome for LGM_ctrl.

The model simulates temperate trees in southeastern Asia (Vietnam, southern China, Cambodia), tropical trees and grasses over the western pacific warm pool (Malaysia, Thailand, Indonesia) and over southern Africa, in agreement with BIOME6000 reconstructions (Prentice et al., 2000). The model underestimates temperate trees in Asia and overestimates bare soil in South Africa.

A more detailed comparison shows that the important (boreal) tree fraction over southwestern Europe differs from palynological reconstructions depicting an important grass fraction, but this bias mainly comes from the overestimation of Boreal broadleaf summergreen trees, which is a common feature in the version of ORCHIDEE used here, also found in present-day vegetation simulations. The bias might also be the sign that the LGM climate simulated by IPSL-CM4 over western Europe is too warm and wet (Woillez et al., 2011). In a few regions, ORCHIDEE correctly simulates the presence of forest, but the dominant type of tree disagrees with pollen reconstructions: tropical trees over Papua New Guinea and western Indonesia, while reconstructions reveal the presence of temperate trees over these regions. Simulated forests over southern Australia (a thin coastal band in the southeast) are composed of temperate and tropical trees, while reconstructions rather indicate the presence of a few tropical trees. The model simulates mixed vegetation composed of grasses, boreal and temperate trees in eastern North America, consistent with pollen data, but the spatial distribution is incorrect.

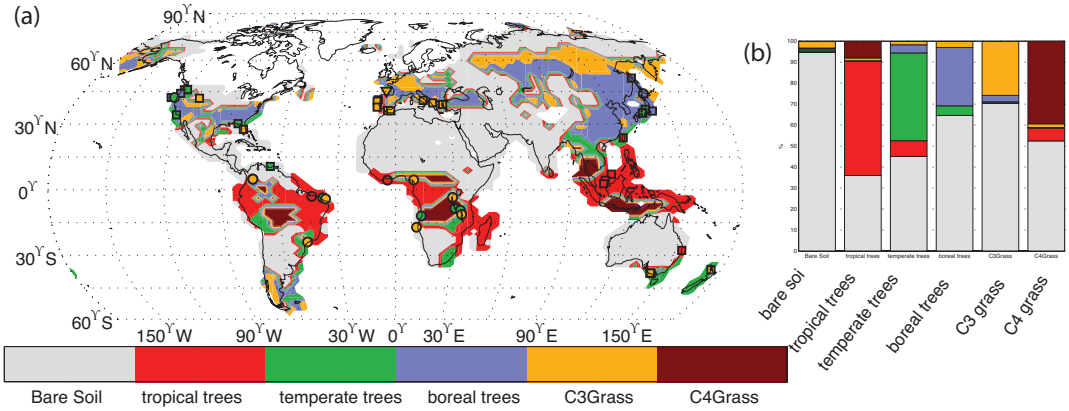

Figure 5.6 – **(a)** Model–data comparison of mega-biome distribution for HS_exp based on dominant PFT type simulated by ORCHIDEE. For each grid cell, the fraction of bare soil, tropical forests, temperate forests, boreal forests, and C3 and C4 grasses is considered. The type covering the greatest cell fraction is the dominant type. Note that dominant bare soil fraction denotes more than 80 %. Circles denote HS_exp mega-biomes inferred from pollen and plant macrofossil records compilation. Refer to Table 5.4 to see how PFTs simulated by ORCHIDEE and reconstructed vegetation have been assigned to the mega-biomes mapped in this figure. **(b)** Detail of the averaged vegetation composition in grid cells occupied by a dominant mega-biome for HS_exp.

It is important to keep in mind that model–data comparison of vegetation can only remain qualitative given the coarse resolution of the vegetation model, related to the model resolution of the climatic forcing fields. Furthermore, pollen records represent the surrounding vegetation distribution at different altitudes, while the ORCHIDEE model does not account for elevation changes within a grid cell (Woillez et al., 2013).

5.4.1.3.3 *HS_exp vegetation*

To validate the simulated HS vegetation, we compare the millennial-scale changes in selected high-resolution ($<$ 800 years; mean resolution is 400 years) pollen records of 48 sites described for HS1-GS2 ($n = 16$) in South America and southern Africa (Hessler et al., 2010; Handiani et al., 2012), and for HS4–GS9 ($n = 31$) in Europe (Fletcher et al., 2010), North America (Jimenez-Moreno et al., 2010), Japan (Takahara et al., 2010) and Australasia (Harrison and Goni, 2010). Figure 5.7 displays the location of paleorecords discussed in this study. Table 5.4 summarizes the model–data comparison at a grid cell level and provides additional information revealed by palynological reconstructions. The sampling resolution for the analyzed period (MIS2 for HS1, MIS3 for HS4), the other biomes represented for a given site, and the potential occurrences of similar reconstructed vegetation changes over other HSs are presented.

The model–data comparison has been performed as follows: the two dominant re-

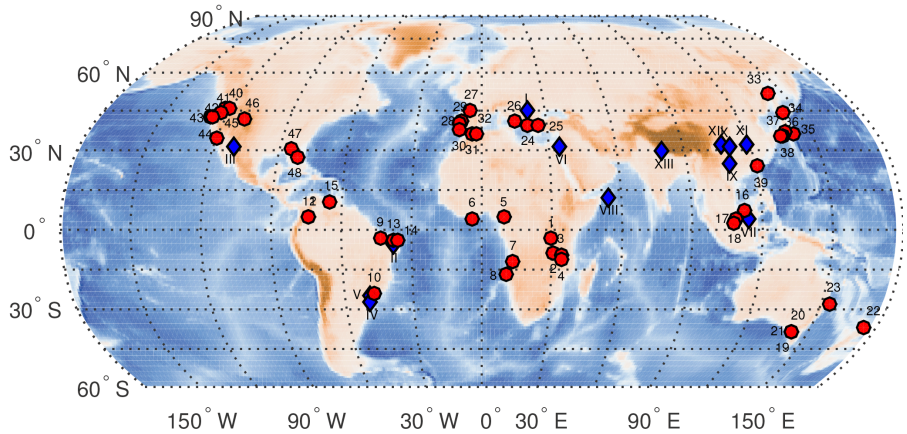

Figure 5.7 – Location of marine and terrestrial paleoarchives sites included in the model–data comparison. Blue diamonds denote speleothem's calcite $\delta^{18}O$ and red circles denote pollen records. Arabic numbers and Roman numerals displayed on the map identify the location of the paleoarchives listed in Tables 5.3 (hydrology) and 5.4 (vegetation) for site names, references and further details.

constructed biomes are compared with the two dominant simulated biomes over the grid cell covering the site where the proxy originates. Among the 48 sites with pollen reconstructions, 12 were discarded because of absence of vegetation on the considered grid cell. Among the remaining 36 terrestrial and coastal sites, 11 disagree (30 %) and 25 (70 %) display moderate to good agreement (Table 5.4). Good agreement ($n = 13$) is obtained when reconstructed and simulated dominant biomes are alike, fair agreement ($n = 9$) when a subdominant biome agrees with a dominant one, and moderate agreement ($n = 3$) when subdominant biomes only are similar.

Simulated vegetation in regions associated with high oxygen productivity agrees well with pollen reconstruction. This is the case for South America, where a strong increase in tropical forest at the expense of bare soil is simulated in eastern Brazil, and in the West Pacific Warm Pool region, where tropical forest represents the dominant biome. The slight southward shift of the southern border of desert areas in equatorial Africa is also well captured by ORCHIDEE. In the Indian summer monsoon region, the simulated weakened monsoon (Kageyama et al., 2009) leads to the appearance of desert areas south and east of India, consistent with a dryer climate revealed by a core from the Indus region (Deplazes et al., 2014).

From this analysis it appears that sites showing a disagreement between model and data are coastal sites and/or have a very high bare soil fraction. Coastal sites do not necessarily only represent the vegetation in the coastal region, but they offer numerous records and allow high-resolution analysis thanks to their high sedimentation rate, so it is crucial to include them for millennial-scale analysis. Five (50 %) of the sites showing no agreement present a very high simulated bare soil fractions (> 90 %). Woillez et al. (2013) already pointed out the overestimation of the bare soil fractions by the ORCHIDEE model. We argue that this bias might partly explain the observed

discrepancy between model and data. Furthermore, the other sites showing a disagreement, over Europe and Australia, underestimate grass fraction. For Europe, the bias is already present in the LGM simulation and is probably partly due to the systematic overestimation of forest by ORCHIDEE in this region (Woillez et al., 2011). Given the scarcity of data offering a time resolution high enough to catch millennial-scale vegetation variability, further testing of the simulated vegetation remains challenging. In conclusion, HS_exp vegetation agrees reasonably well with available pollen-based vegetation reconstruction.

Finally, based on the reasonable agreement of the simulated changes in vegetation, humidity and precipitation with observations depicted in this section, we can rely on the validity of the model to simulate $\delta^{18}O_{\text{terr}}$ over a HS.

5.4.2 Global increase in $\delta^{18}O_{\text{terr}}$ during a HS

The model calculates $\delta^{18}O_{\text{terr}}$ for LGM_ctrl and HS_exp as 23.41 and 23.52 ‰, respectively (Table 5.2). This average $\delta^{18}O_{\text{terr}}$ value is coherent with the $\delta^{18}O_{atm}$ value of 23.8 ‰ with respect to V-SMOW and the finding that terrestrial and marine contribution to $\delta^{18}O_{atm}$ are similar (Luz et al., 2014). Moreover, the global increase in $\delta^{18}O_{\text{terr}}$ of 0.11 ‰ (Fig. 5.8) can quantitatively explain most of the 0.1 ‰ $\delta^{18}O_{atm}$ increase over HS (Severinghaus et al., 2009; Guillevic et al., 2014; Fig. 5.1). In the following, we use the different model outputs to decipher the main influences on $\delta^{18}O_{\text{terr}}$ and hence on $\delta^{18}O_{atm}$.

By construction (Eq. 5.3), $\delta^{18}O_{\text{terr}}$ is linearly dependent on both $\delta^{18}O_{\text{lw}}$ and ${}^{18}\varepsilon_{\text{resp}}$; we discuss these two effects below. Figure 5.8 (upper panel) details the different contributions to $\delta^{18}O_{\text{terr}}$ change over a HS and demonstrates the dominant role of $\delta^{18}O_{\text{lw}}$ (Sect. 5.4.2.1) compared to ${}^{18}\varepsilon_{\text{resp}}$ (Sect. 5.4.2.2). Indeed, the 0.11 ‰ increase in $\delta^{18}O_{\text{terr}}$ exclusively stems from $\delta^{18}O_{\text{lw}}$ increase (+0.14 ‰ over HS_exp), while respiratory fractionation leads to a negative anomaly (−0.03 ‰) over HS_exp. We explore in more details below the origin of the relative changes in ${}^{18}\varepsilon_{\text{resp}}$ and $\delta^{18}O_{\text{lw}}$ as calculated by our modeling approach. In particular, we look at the different regional contributions to the global ${}^{18}\varepsilon_{\text{resp}}$ and $\delta^{18}O_{\text{lw}}$ signals since low-latitude regions are associated with the largest GPP_O_2 (Fig. 5.9a for the whole latitudinal range and Fig. 5.10a for a closeup of the tropics) and hence have the strongest influence on the global $\delta^{18}O_{\text{terr}}$ signal (Fig. 5.9c).

5.4.2.1 Leaf water

We find global $\delta^{18}O_{\text{lw}}$ values of 5.16 and 5.30 ‰ for LGM_ctrl and HS_exp, respectively. The 0.14 ‰ difference is similar to the $\delta^{18}O$ increase observed in ice cores during HS (Fig. 5.2). The increase in $\delta^{18}O_{\text{lw}}$ is clearly visible in the low-latitude regions. It corresponds to an increase in $\delta^{18}O_p$ and a decrease in GPP_O_2 weighted relative humidity, both effects leading to a global $\delta^{18}O_{\text{lw}}$ increase (Fig. 5.9b).

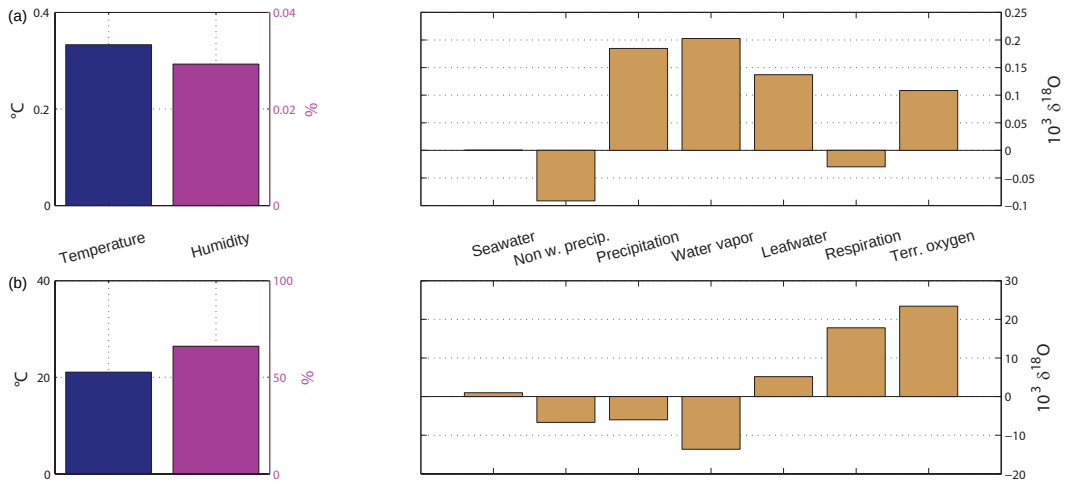

Figure 5.8 – Evolution of the main simulated factors controlling atmospheric $\delta^{18}O$. Note that all variables are oxygen-production-weighted, i.e., integrated over vegetated areas, if not stated with "non w.". **(a)** Left panel: HS_exp – LGM_ctrl anomalies of temperature and relative humidity. Right panel: (left to right) HS_exp – LGM_ctrl anomalies of seawater $\delta^{18}O$, amount-weighted precipitation $\delta^{18}O$, precipitation $\delta^{18}O$ ($\delta^{18}O_p$), water vapor $\delta^{18}O$, leaf water $\delta^{18}O$ ($\delta^{18}O_{\mathrm{lw}}$), respiratory isotope fractionation ($-{}^{18}\varepsilon_{\mathrm{resp}}$) and terrestrial contribution to atmospheric $\delta^{18}O$ ($\delta^{18}O_{\mathrm{terr}}$). **(b)** LGM_ctrl values of same relevant factors as in **(a)** in $\delta^{18}O_{\mathrm{terr}}$ budget. Note that plotted respiratory isotope fractionation anomaly is inverted as respiration is an oxygen uptake process. Note also that the $-{}^{18}\varepsilon_{\mathrm{resp}}$ anomaly totals 0.02 ‰ when soil aeration influence on soil respiratory isotope fractionation is considered. $\delta^{18}O_{\mathrm{lw}}$ is controlled by $\delta^{18}O_{\mathrm{p}}$, temperature and relative humidity as described by Eq. (5.4a). Combined with ${}^{18}\varepsilon_{\mathrm{resp}}$ as described in Eq. (5.3), one obtains $\delta^{18}\mathrm{O}_{\mathrm{terr}}$.

Still, when looking at the whole latitudinal range, the GPP_O_2 weighted relative humidity is not significantly different in HS and in LGM state. This is due to the decrease in relative humidity during HS in the extratropical regions (Fig. 5.9b). The net effect of relative humidity on $\delta^{18}O_{\mathrm{lw}}$ is thus zero. As a consequence, the main driver of $\delta^{18}O_{\mathrm{lw}}$ (and hence $\delta^{18}O_{\mathrm{terr}}$) increase is the increase in GPP_O_2 -weighted $\delta^{18}O_p$ (Fig. 5.9b) by 0.18 ‰ (Fig. 5.8). This increase is linked to the southward shift of the tropical belt occurring during HS, as suggested from the speleothem data compilation (see Sect. 5.4.1.2).

Figure 5.10 clearly shows how rainfall amount and $\delta^{18}O_p$ are anticorrelated as expected on most of the intertropical band. During a HS, $\delta^{18}O_p$ is enriched in the Northern Hemisphere down to 14°s. A particular pattern occurs between the Equator and 14°s, where oxygen production is most enhanced at HS, as precipitation is more abundant but also heavier in $\delta^{18}O_p$.

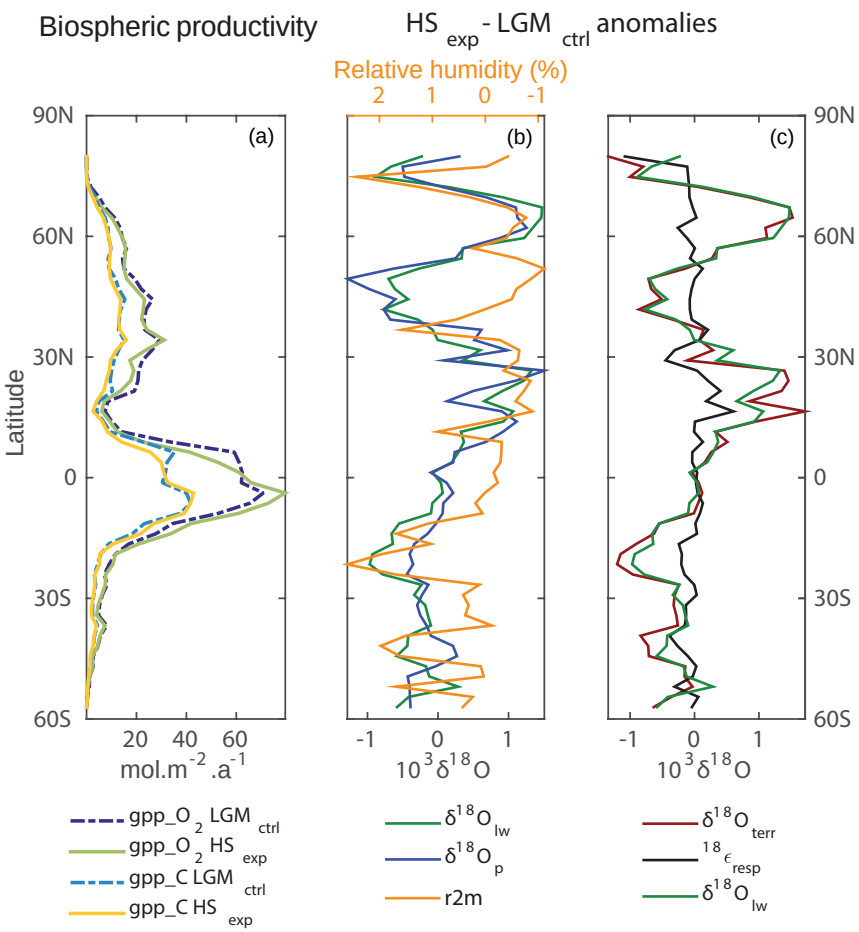

Figure 5.9 – **(a)** Zonal annual mean of gross primary productivity expressed in terms of carbon (GPP_C) and oxygen (GPP_O_2) annual molar fluxes for LGM_ctrl and HS_exp, respectively. **(b)** Zonal annual-mean anomalies of $\delta^{18}O_{\text{lw}}$, $\delta^{18}O_p$ and relative humidity (note its inverted x axis). **(c)** Zonal annual-mean anomalies for $-{}^{18}\varepsilon_{\text{resp}}$, $\delta^{18}O_{\text{lw}}$ and $\delta^{18}O_{\text{terr}}$. Note that all variables of panels **(b)** and **(c)** are oxygen-production- (GPP_O_2) weighted.

5.4.2.2 Respiration

Respiratory processes lead to a 0.03 ‰ decrease in $\delta^{18}O_{\text{terr}}$ in HS_exp compared to $\delta^{18}O_{\text{terr}}$ in LGM_ctrl (Fig. 5.8a). This variation is too small to challenge $\delta^{18}O_{\text{terr}}$ enrichment caused by hydrological processes, but the sign of its anomaly raises questions. Here we explain the stability of ${}^{18}\varepsilon_{\text{resp}}$ on millennial timescales by a compensatory effect taking place between the main respiratory pathways. We then carry out a simple sensitivity experiment to get a better understanding of the causes of ${}^{18}\alpha_{\text{dark\_soil}}$ negative anomaly during HS.

${}^{18}\varepsilon_{\text{resp}}$ is classically separated into four contributions as given in Eq. (5.5): soil respiration, leaf respiration, photorespiration and Mehler reaction.

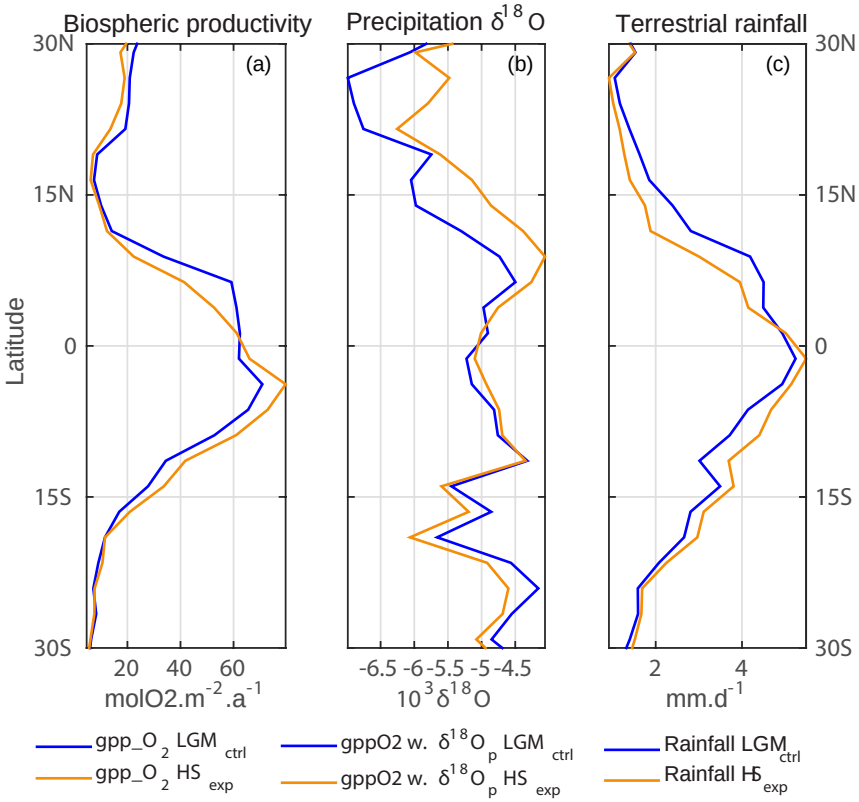

Figure 5.10 – Intertropical profiles of **(a)** zonal annual mean of gross primary productivity expressed in terms of oxygen (GPP_O_2) annual molar fluxes for LGM_ctrl and HS_exp. **(b)** Zonal annual mean of oxygen-production-weighted $\delta^{18}O_p$ for LGM_ctrl and HS_exp. **(c)** Zonal annual mean of rainfall amount for LGM_ctrl and HS_exp.

Soil respiration with associated fractionation factor ${}^{18}\alpha_{\text{dark\_soil}}$ represents 63 % of dark respiration (Schlesinger and Andrews, 2000). It represents 39 % of global terrestrial respiration in our simulation, in agreement with estimates from Raich and Potter (1995) of 30 to 40 %. ${}^{18}\alpha_{\text{dark\_soil}}$ is temperature-dependent (Angert et al., 2003), with higher fractionation associated with colder soils, causing a high zonal contrast. This temperature effect leads to a change in ${}^{18}\alpha_{\text{dark\_soil}}$ by 0.19 ‰ at HS, increasing ${}^{18}\varepsilon_{\text{resp}}$ by 0.12 ‰ and in turn depleting $\delta^{18}O_{\text{terr}}$.

The photorespiration fraction, strongly discriminative against ${}^{18}O$ (${}^{18}\alpha_{\text{photo}} = -21.4$ ‰), represents 28.56 % of the global terrestrial oxygen uptake in LGM_ctrl. The proportion of photorespiration is mainly linked to the change in the C3 vs. C4 plant proportions and in temperature during photosynthesis (Von Caemmerer, 2000; Hoffmann et al., 2004). During HS_exp, photorespiration fraction increases by 1 % (29.52 %), driven by a slight decrease in C4 grass (1.3 %) and a slight photosynthesis temperature increase (0.3°C). As a result, change in photorespiration fraction and soil respiration lead ${}^{18}\varepsilon_{\text{resp}}$ to decrease by 0.03 ‰ in HS_exp, thus causing $\delta^{18}O_{\text{terr}}$ enrichment.

In summary, in our model, a weaker ${}^{18}\alpha_{\text{dark\_soil}}$ during HS cancels out the effect of increased photorespiration on ${}^{18}\varepsilon_{\text{resp}}$. Note that this compensation between the two main respiratory processes explains not only the temporal stability of ${}^{18}\varepsilon_{\text{resp}}$ but also its zonal stability. Indeed, in high latitudes, cold temperatures lead to a weak photorespiration but strong soil isotope fractionation. In low latitudes, despite a weak soil isotope fractionation, high temperatures and variable C4 fraction lead to a highly variable photorespiration.

The 0.19 ‰ increase in ${}^{18}\alpha_{\text{dark\_soil}}$ during HS needs to be considered carefully. Indeed, following the southward migration of the tropical rain belt during HS, tropical soils generally dry out during HSs, as inferred from the lower atmospheric nitrous oxide concentration and its isotopic composition during HS1 (Schilt et al., 2014). Well-aerated soils are associated with a strong discrimination (Angert et al., 2003). Well-aerated tropical soils of the Northern Hemisphere should thus lead to a stronger ${}^{18}\alpha_{\text{dark\_soil}}$, owing to the greater area of the northern vs. southern tropics. We perform a sensitivity study to assess the effect of soil moisture content on ${}^{18}\alpha_{\text{dark\_soil}}$ by allowing the latter to vary in the intertropical band according to the amount of precipitation simulated by the IPSL model, used as a proxy for soil aeration. Concretely, ${}^{18}\alpha_{\text{dark\_soil}}$ is allowed to vary from its initial value (e.g., −10.2 ‰ for tropical waterlogged soils) up to a factor of 2 (−20.2 ‰ for well-aerated tropical soils). Note that not only tropical but also temperate soils are simulated in the 30°S–30°N latitudinal band, as the type of soil is related to the vegetation cover in our model (Sect. 5.3.4.3).

${}^{18}\alpha_{\text{dark\_soil}}$ totals −22.36 ‰ in the modified run, 6.12 ‰ stronger than in the LGM control run (−16.24 ‰). $\delta^{18}O_{\text{terr}}$, increases subsequently by 2.91 ‰ The picture is similar for HS_exp run, where ${}^{18}\alpha_{\text{dark\_soil}}$ strengthens by 6.17 ‰ from −16.06 to −22.23 ‰, leading $\delta^{18}O_{\text{terr}}$ to increase by 2.96 ‰ at HS.

While the absolute values of ${}^{18}\alpha_{\text{dark\_soil}}$, ${}^{18}\varepsilon_{\text{resp}}$ and $\delta^{18}O_{\text{terr}}$ are significantly modified by accounting for tropical soil aeration, this does not modify the sign of ${}^{18}\alpha_{\text{dark\_soil}}$ anomaly between the LGM and HS. However, its magnitude is slightly reduced by 0.05 ‰, which causes the ${}^{18}\varepsilon_{\text{resp}}$ anomaly to vary from −0.03 to +0.02 ‰. As a result, $\delta^{18}O_{\text{terr}}$ is enriched by 0.16 ‰ during HS. This 0.05 ‰ increase in $\delta^{18}O_{\text{terr}}$ anomaly may give an estimate of the magnitude of the uncertainty associated with ${}^{18}\alpha_{\text{dark\_soil}}$ when considering soil wetness. This sensitivity test does not fundamentally affect the conclusion of the present study, as the ${}^{18}\varepsilon_{\text{resp}}$ anomaly, although becoming positive, remains very small (+0.02 ‰) but underlines the limitations of our approach. Why does a ${}^{18}\alpha_{\text{dark\_soil}}$ negative anomaly persist when soil aeration is considered? First, in our sensitivity test, we use the amount of precipitation as an index for soil aeration. This approach may be too simple and could be improved by quantitatively relating the soil aeration to the model's rainfall amount and land surface slope by using existing parameterizations employed in models that predict nitrous oxide production (e.g., LPX-Bern, which is a state-of-the-art bottom-up dynamic global vegetation and

land surface process model; Stocker et al., 2013). Second, soil respiration is closely linked to the vegetation cover in our model, as types of soil (boreal, temperate, tropical) and their associated fractionation factor are related to PFTs rather than land area (Sect. 5.3.4.3). Third, aboveground oxygen productivity controls the rate of soil respiration. As Southern Hemisphere tropics dominate over Northern Hemisphere tropics in terms of GPP_O_2 for both LGM and HS runs, ${}^{18}\alpha_{\text{dark\_soil}}$ anomaly remains negative even when considering soil aeration. The distribution of vegetation simulated by ORCHIDEE, favoring Southern Hemisphere tropics, combined with the GPP_O_2 weighting of soil respiration, explains why the drying-out of the Northern Hemisphere soils, albeit covering a greater land area, does not lead to a stronger ${}^{18}\alpha_{\text{dark\_soil}}$ during HS in our model.

5.5 Discussion

Our results suggest a strong control of tropical hydrology on $\delta^{18}O_{terr}$ through changes in $\delta^{18}O_p$. It suggests that $\delta^{18}O_{atm}$ is related to tropical hydrology and may be a good tracer for global monsoon signal. The aim of the following discussion is to evaluate these results by (i) providing some insights on $\delta^{18}O_{\text{mar}}$ estimate and (ii) testing the robustness of our conclusion on the driver of $\delta^{18}O_{\text{terr}}$ changes through three sensitivity experiments separating the different parameters (hydrology, climate and vegetation).

5.5.1 Estimate of $\delta^{18}O_{\text{mar}}$ over a Heinrich stadial

$\delta^{18}O_{\text{mar}}$ has been recently estimated as 24.3 ± 2.0 ‰ for present day (Luz et al., 2014). In order to estimate $\delta^{18}O_{\text{mar}}$ for the LGM and HS, we assumed that fractionation during oxygen uptake by marine biosphere remained constant between the LGM/HS and present day and used a mean ocean $\delta^{18}O$ enriched by 1 ‰ at the LGM (Waelbroeck et al., 2002). This results in a value of $\delta^{18}O_{\text{mar}}$ of 25.3 ± 2.0 ‰ for the LGM and HS. It is important to note that a rise in sea level during a HS would lead to a depleted mean ocean $\delta^{18}O$, as polar ice sheets accumulate ${}^{16}O$, and can therefore not explain the increased $\delta^{18}O_{atm}$ observed during stadials.

Because of the spatial limitation of paleorecords to provide a global picture of marine primary productivity, we have estimated the marine productivity for the LGM and HS using the Pelagic Interaction Scheme for Carbon and Ecosystem Studies (PISCES) model. The PISCES model is a biogeochemical model of the global ocean including a simple representation of marine ecosystem and forced offline by the AOGCM IPSL-CM4 (Aumont and Bopp, 2006; Mariotti et al., 2012). The model PISCES has already been compared under glacial conditions with observations (Mariotti et al., 2012; Tagliabue et al., 2009; Bopp et al., 2003) and reproduces roughly the paleoproductivity reconstruction of Kohfeld et al. (2005). Using the same forcings as for our simulations, Mariotti et al. (2012) simulate a global decrease in oceanic primary productivity of 16 % during a Heinrich event, in agreement with independent modeling studies (Schmittner, 2005; Menviel et al., 2008; Schmittner and Galbraith, 2008) and more important

than the one in terrestrial GPP (3.5 %). Because $\delta^{18}O_{\text{mar}}$ is larger than $\delta^{18}O_{\text{terr}}$, this decrease in marine productivity would lead to a decrease in global $\delta^{18}O_{atm}$ during the HS, opposite to the observation. We simulated a change in the marine production to assess its impact on $\delta^{18}O_{atm}$ signal. With a change of 10 % in marine export, $\delta^{18}O_{atm}$ varies by 0.05 ‰. However this result needs to be treated with caution for two main reasons. (i) The fraction of land versus ocean production is strongly affecting $\delta^{18}O_{atm}$ if the isotope fractionation factors associated with the terrestrial and marine production are not similar. Pioneer studies on the Dole effect often invoked the marine-to-terrestrial production ratio to explain the observed variations. Though it is not the case in our model, recent studies suggest their magnitude to be very close, with $\delta^{18}O_{\text{mar}}$ 1.8 ‰ higher than $\delta^{18}O_{\text{terr}}$. The change in $\delta^{18}O_{atm}$ is thus likely to be smaller in the real world. (ii) Recent studies (eg. Mariotti et al., 2012) rather suggest a decrease in marine export after a Heinrich event. This would lead to a decrease in $\delta^{18}O_{atm}$ signal that is in opposition to the observations as mentioned in Section 5.5.1. We conclude that marine productivity is not the driver for $\delta^{18}O_{atm}$ increase during HS.

5.5.2 Disentangling the influences of climate, hydrology and vegetation on $\delta^{18}O_{atm}$: sensitivity experiments.

In order to assess the robustness of our conclusion stating that the low-latitude hydrological cycle is the driver of $\delta^{18}O_{atm}$ changes, we have run three different experiments:

- In HSclim we test the impact of the climatic conditions. This simulation is similar to LGM-ctrl, except that the temperature and relative humidity from HS_exp are prescribed as boundary conditions.
- In HShydro we test the impact of the hydrological cycle. This simulation is similar to LGM-ctrl, except that $\delta^{18}O_p$ and $\delta^{18}O_{\text{vap}}$ from HS_exp are prescribed as boundary conditions.
- In HSveget we test the impact of the vegetation. This simulation is similar to LGM-ctrl, except that the vegetation production and distribution from HS_exp are prescribed as boundary conditions.

Figure 5.11 summarizes the results of the sensitivity analysis in terms of temperature, humidity, and oxygen isotopic composition of $\delta^{18}O_p$, $\delta^{18}O_{\text{lw}}$ and $\delta^{18}O_{\text{terr}}$. The sensitivity tests show that the implementation of one parameter from HS_exp (HSclim, HShydro and HSveget) leads to a simulated $\delta^{18}O_{\text{terr}}$ anomaly similar to or higher than in the full HS_exp.

In HSclim, $\delta^{18}O_{\text{terr}}$ enrichment is mostly caused by the 0.3 % decrease in relative humidity over the LGM vegetated areas after the AMOC collapse, since $\delta^{18}O_p$ and $\delta^{18}O_{\text{lw}}$ are not modified by definition. This global decrease in GPP_O_2 -weighted relative humidity is not visible in the global HS_exp (Fig. 5.8) and hence does not explain the $\delta^{18}O_{\text{terr}}$ increase in HS_exp. In HSveget, the southward shift of HS_exp vegetation leads to a global GPP_O_2 weighted relative humidity decrease by 0.5 %. As in

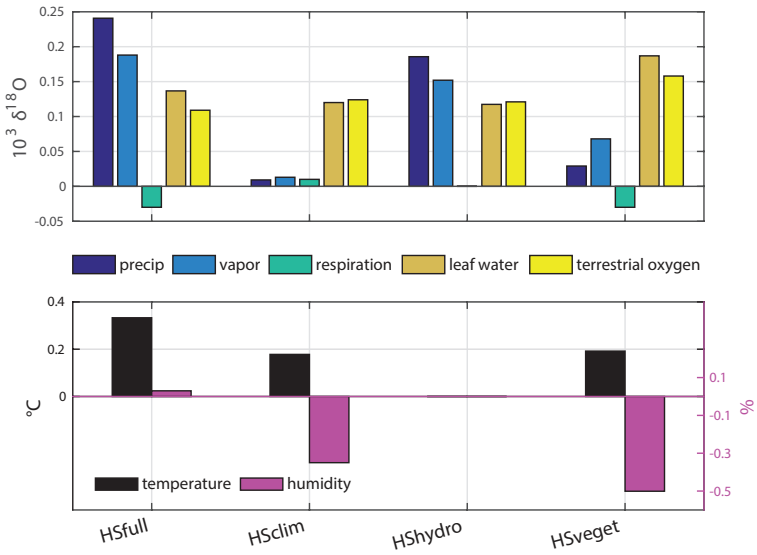

Figure 5.11 – Summary of sensitivity study experiments. HSfull uses the same settings as HS_exp, while HSclim, HShydro and HSveget experiments are identical to LGM_ctrl, except for meteoric water isotopic composition, climatic conditions, or vegetation production and distribution, respectively, originating from HS_exp. For each of the experiments, an annual-mean anomaly (experiment – LGM_ctrl) of oxygen-production-weighted temperature, relative humidity, $\delta^{18}O_p$, water vapor $\delta^{18}O$, $\delta^{18}O_{\mathrm{lw}}$, ${}^{18}\varepsilon_{\mathrm{resp}}$ and $\delta^{18}O_{\mathrm{terr}}$ is presented.

HSclim, this leads to a high $\delta^{18}O_{\mathrm{terr}}$ positive anomaly. The effect of relative humidity on $\delta^{18}O_{\mathrm{terr}}$ is minimized in HS_exp, as the southward shift in vegetation counterbalances the change in climatic conditions. This compensation explains why the final GPP_O_2 weighted relative humidity does not vary.

In HShydro, the $\delta^{18}O_p$ increase explains the whole $\delta^{18}O_{\mathrm{terr}}$ increase. This increase in GPP_O_2 -weighted $\delta^{18}O_p$ is similar in HShydro and HS_exp, which confirms that the $\delta^{18}O_{\mathrm{terr}}$ simulated by the model in the full experiment HS_exp is arising from a change intrinsic to the hydrological cycle, only slightly affected by vegetation distribution.

In addition, note that a weakening of $\delta^{18}O_{\mathrm{lw}}$ only occurs with HS vegetation (HS_exp, HSveget), regardless of the climatic conditions. Moreover, HSclim depicts a stronger $\delta^{18}O_{\mathrm{lw}}$, caused by a higher temperature increase over HS, leading to an enhanced photorespiration fraction among C3 plants. However, the temperature effect on $\delta^{18}O_{\mathrm{lw}}$ remains minor.

The global impact of ${}^{18}\varepsilon_{\mathrm{resp}}$ is negligible in all experiments, with variations 1 order of magnitude lower than $\delta^{18}O_p$.

Finally, these tests confirm the strong control of hydrological processes on $\delta^{18}O_{\mathrm{terr}}$,

and highlight the role of the vegetation distribution in defining $\delta^{18}O_p$ and climatic conditions recorded by $\delta^{18}O_{\text{terr}}$.

5.6 Conclusions and perspective

Our study first aimed at quantitatively testing the driving of $\delta^{18}O_{atm}$ by tropical hydrology as suggested by the strong correlation between local records of $\delta^{18}O_c$ and global record of $\delta^{18}O_{atm}$ on the millennial scale. For this we used a HS-type simulation under LGM background conditions with an oxygen isotope mass balance model using spatial and temporal fields of (i) temperature and relative humidity from the AOGCM IPSL-CM4, (ii) PFT distribution and GPP provided by the dynamic global vegetation model ORCHIDEE, (iii) oxygen isotope composition of water vapor and precipitation from the AOGCM LMDZ-iso, and (iv) the latest isotope fractionation factor measurements involved in respiratory and photosynthetic processes.

Validation of AOGCM outputs feeding the oxygen isotope mass balance model was performed through a model–data comparison of the main drivers of $\delta^{18}O_{\text{terr}}$: (i) simulated $\delta^{18}O_p$ was compared to speleothem's calcite $\delta^{18}O$ anomalies, and in most sites showed excellent agreement despite the complexity of the $\delta^{18}O_c$ signal; (ii) simulated HS humidity was compared to the reconstructed ones, broadly agreeing with paleodata; and (iii) simulated vegetation was compared with palynological reconstructions for LGM and HS, and was qualitatively consistent.

The model simulates a terrestrial enrichment of $\delta^{18}O_{\text{terr}}$ of 0.11 ‰, which mostly arises from the $\delta^{18}O_p$ signal. On a global scale, respiration fractionation only plays a minor role in the anomaly observed during HS, and slightly decreases $\delta^{18}O_{\text{terr}}$ in our simulation, driven by a weaker isotope fractionation of soil respiration during HS that masks the effect of increased photorespiration. Accounting for the effect of soil aeration on ${}^{18}\alpha_{\text{dark\_soil}}$ modifies the ${}^{18}\varepsilon_{\text{resp}}$ anomaly by 0.05 ‰, a change too small to challenge $\delta^{18}O_p$ main control on $\delta^{18}O_{\text{terr}}$. However, the simplicity of our approach to model soil moisture content and the GPP_O_2 weighting of ${}^{18}\alpha_{\text{dark\_soil}}$ favoring Southern Hemisphere tropics are likely to explain this result. In order to precisely evaluate the uncertainty associated with ${}^{18}\varepsilon_{\text{resp}}$, an improved parameterization of soil aeration will be needed. This limitation of the model must thus be kept in mind when considering the conclusion of this study.

The strong control of the low-latitude hydrological cycle on simulated $\delta^{18}O_{atm}$ on millennial timescales suggests that $\delta^{18}O_{atm}$ records, at first order, changes in monsoonal activity on millennial timescales, in agreement with CH_4 mixing ratio variations. Indeed, rapid CH_4 variations during the last glacial period are generally attributed to changes in the low-latitude water cycle (Baumgartner et al., 2014; Brook et al., 2000; Chappellaz et al., 1993) driven by latitudinal shifts of the ITCZ and the monsoon systems (e.g., Chiang, 2009). Such a signal can also be used for exploring the low-latitude hydrological cycle characteristic of Heinrich events. Indeed, the re-

cent study of Rhodes et al. (2015) suggests that observed CH_4 spikes in WAIS Divide ice core during the cold phases of HSs represent the hydrological signature of Heinrich events, through activation of Southern Hemisphere wetlands. The Guillevic et al. (2014) multi-ice-core proxies approach over GS9–HS4 also suggests a decoupling between changes in Greenland temperatures and low-latitude hydrology identified in both CH_4 and $\delta^{18}O_{atm}$, and demonstrates the need for high-resolution data with common precise chronology to explore submillennial variations.

$\delta^{18}O_{atm}$ is a valuable tool to assess the validity of Earth system model simulations, as it integrates a combination of hydrological, climatic and biological processes. Furthermore, $\delta^{18}O_{atm}$ is a global signal, which mostly arises from the tropics and integrates all vegetated areas. Therefore, the ability of a model to catch $\delta^{18}O_{atm}$ millennial-scale variations implies a correct spatial representation of an ensemble of processes. The comparison of Earth system model outputs with global proxies such as $\delta^{18}O_{atm}$, involving the main components of the climatic system, is crucial for gaining confidence in their ability to represent the real world. Our approach is mainly restricted to terrestrial contribution, but future modeling exercises should also include the oceanic $\delta^{18}O_{atm}$ signal.

Acknowledgements

Thanks go to the Marie Curie Initial Training Network INTRAMIF (FP7), which has funded C. Reutenauer's PhD at CIC; to the CIC, for their full support; and to the ANR EL PASO (no. 2010 BLANC 608 01). The climate model simulations were run on CEA supercomputers, and we thank GENCI and TECC for computer time and storage. We are also very grateful for the detailed and constructive comments of Jeff Severinghaus and an anonymous reviewer, which greatly helped in improving the manuscript.

Edited by: E. Wolff

Bibliography

Ahn, J. and Brook, E. J. (2014). Siple dome ice reveals two modes of millennial co2 change during the last ice age. *Nature communications*, 5.

Ahn, J., Brook, E. J., Schmittner, A., and Kreutz, K. (2012). Abrupt change in atmospheric co2 during the last ice age. *Geophysical Research Letters*, 39(18). L18711.

Allison, G., Gat, J., and Leaney, F. (1985). The relationship between deuterium and oxygen-18 delta values in leaf water. *Chemical Geology: Isotope Geoscience section*, 58(1–2):145–156.

Alvarez-Solas, J., Robinson, A., Montoya, M., and Ritz, C. (2013). Iceberg discharges of the last glacial period driven by oceanic circulation changes. *Proceedings of the National Academy of Sciences*, 110(41):16350–16354.

Angert, A., Barkan, E., Barnett, B., Brugnoli, E., Davidson, E. A., Fessenden, J., Maneepong, S., Panapitukkul, N., Randerson, J. T., Savage, K., Yakir, D., and Luz, B. (2003). Contribution of soil respiration in tropical, temperate, and boreal forests to the ^{18}o enrichment of atmospheric o_2. *Global Biogeochemical Cycles*, 17(3):1089.

Asmerom, Y., Polyak, V. J., and Burns, S. J. (2010). Variable winter moisture in the southwestern united states linked to rapid glacial climate shifts. *Nature Geoscience*, 3(2):114–117.

Aumont, O. and Bopp, L. (2006). Globalizing results from ocean in situ iron fertilization studies. *Global Biogeochemical Cycles*, 20(2):GB2017.

Badger, M. R., von Caemmerer, S., Ruuska, S., and Nakano, H. (2000). Electron flow to oxygen in higher plants and algae: rates and control of direct photoreduction (mehler reaction) and rubisco oxygenase. *Philosophical Transactions of the Royal Society of London B: Biological Sciences*, 355(1402):1433–1446.

Bariac, T., Rambal, S., Jusserand, C., and Berger, A. (1989). Evaluating water fluxes of field-grown alfalfa from diurnal observations of natural isotope concentrations, energy budget and ecophysiological parameters. *Agricultural and Forest Meteorology*, 48(3–4):263–283.

Barker, S., Diz, P., Vautravers, M. J., Pike, J., Knorr, G., Hall, I. R., and Broecker, W. S. (2009). Interhemispheric atlantic seesaw response during the last deglaciation. *Nature*, 457(7233):1097–1102.

Baumgartner, M., Kindler, P., Eicher, O., Floch, G., Schilt, A., Schwander, J., Spahni, R., Capron, E., Chappellaz, J., Leuenberger, M., Fischer, H., and Stocker, T. F. (2014). Ngrip ch4 concentration from 120 to 10 kyr before present and its relation to a $\delta^{15}n$ temperature reconstruction from the same ice core. *Climate of the Past*, 10(2):903–920.

Bazin, L., Lemieux-Dudon, B., Landais, A., Guillevic, M., Kindler, P., Parrenin, F., and Martinerie, P. (2014). Optimisation of glaciological parameters for ice core chronology by implementing counted layers between identified depth levels. *Climate of the Past Discussions*, 10(4):3585–3616.

Bender, M., Sowers, T., and Labeyrie, L. (1994). The dole effect and its variations during the last 130,000 years as measured in the vostok ice core. *Global Biogeochemical Cycles*, 8(3):363–376.

Bender, M. L. (2002). Orbital tuning chronology for the vostok climate record supported by trapped gas composition. *Earth and Planetary Science Letters*, 204(1):275–289.

Blunier, T., Barnett, B., Bender, M. L., and Hendricks, M. B. (2002). Biological oxygen productivity during the last 60,000 years from triple oxygen isotope measurements. *Global Biogeochemical Cycles*, 16(3):3–1–3–13.

Blunier, T., Bender, M. L., Barnett, B., and von Fischer, J. C. (2012). Planetary fertility during the past 400 ka based on the triple isotope composition of o_2 in trapped gases from the vostok ice core. *Climate of the Past*, 8(5):1509–1526.

Bond, G., Broecker, W., Johnsen, S., McManus, J., Labeyrie, L., Jouzel, J., and Bonani, G. (1993). Correlations between climate records from north atlantic sediments and greenland ice. *Nature*, 365(6442):143–147.

Bony, S. and Emanuel, K. A. (2001). A Parameterization of the Cloudiness Associated with Cumulus Convection; Evaluation Using TOGA COARE Data. *Journal of Atmospheric Sciences*, 58:3158–3183.

Bopp, L., Kohfeld, K. E., Le Quere, C., and Aumont, O. (2003). Dust impact on marine biota and atmospheric co2 during glacial periods. *Paleoceanography*, 18(2). 1046.

Broccoli, A. J., Dahl, K. A., and Stouffer, R. J. (2006). Response of the itcz to northern hemisphere cooling. *Geophysical Research Letters*, 33(1). L01702.

Broecker, W. (2000). Abrupt climate change: causal constraints provided by the paleoclimate record. *Earth–Science Reviews*, 51(1–4):137–154.

Broecker, W. S., Bond, G., Klas, M., Bonani, G., and Wolfli, W. (1990). A salt oscillator in the glacial atlantic? the concept. *Paleoceanography*, 5(4):469–477.

Brook, E. J., Harder, S., Severinghaus, J., Steig, E. J., and Sucher, C. M. (2000). On the origin and timing of rapid changes in atmospheric methane during the last glacial period. *Global Biogeochemical Cycles*, 14(2):559–572.

Brook, E. J., White, J. W., Schilla, A. S., Bender, M. L., Barnett, B., Severinghaus, J. P., Taylor, K. C., Alley, R. B., and Steig, E. J. (2005). Timing of millennial-scale climate change at siple dome, west antarctica, during the last glacial period. *Quaternary Science Reviews*, 24(12–13):1333–1343.

Caley, T., Roche, D. M., Waelbroeck, C., and Michel, E. (2014). Oxygen stable isotopes during the last glacial maximum climate: perspectives from data-model (iloveclim) comparison. *Climate of the Past*, 10(6):1939–1955.

Cappa, C. D., Hendricks, M. B., DePaolo, D. J., and Cohen, R. C. (2003). Isotopic fractionation of water during evaporation. *Journal of Geophysical Research: Atmospheres*, 108(D16):4525.

Chappellaz, J., Blunier, T., Raynaud, D., Barnola, J., Schwander, J., and Stauffer, B. (1993). Synchronous changes in atmospheric ch4 and greenland climate between 40-kyr and 8-kyr bp. *Nature*, 366(6454):443–445.

Chappellaz, J., Stowasser, C., Blunier, T., Baslev-Clausen, D., Brook, E. J., Dallmayr, R., Faïn, X., Lee, J. E., Mitchell, L. E., Pascual, O., Romanini, D., Rosen, J., and Schüpbach, S. (2013). High-resolution glacial and deglacial record of atmospheric methane by continuous-flow and laser spectrometer analysis along the neem ice core. *Climate of the Past*, 9(6):2579–2593.

Cheng, H., Sinha, A., Wang, X., Cruz, F. W., and Edwards, R. L. (2012). The global paleomonsoon as seen through speleothem records from asia and the americas. *Climate Dynamics*, 39(5):1045–1062.

Chiang, J. C. (2009). The tropics in paleoclimate. *Annual Review of Earth and Planetary Sciences*, 37(1):263–297.

Ciais, P., Tagliabue, A., Cuntz, M., Bopp, L., Scholze, M., Hoffmann, G., Lourantou, A., Harrison, S. P., Prentice, I., Kelley, D., et al. (2012). Large inert carbon pool in the terrestrial biosphere during the last glacial maximum. *Nature Geoscience*, 5(1):74–79.

Clement, A. C. and Peterson, L. C. (2008). Mechanisms of abrupt climate change of the last glacial period. *Reviews of Geophysics*, 46(4). RG4002.

Craig, H. and Gordon, L. (1965). Deuterium and oxygen 18 variations in the ocean and the marine atmosphere. In *Stable Isotopes in Oceanographic Studies and Paleotemperatures, July 26-30 1965, Spoleto, Italy*. Tongiorgi, E.

Cvijanovic, I. and Chiang, J. (2013). Global energy budget changes to high latitude north atlantic cooling and the tropical itcz response. *Climate Dynamics*, 40(5–6):1435–1452.

Dahl, K., Broccoli, A., and Stouffer, R. (2005). Assessing the role of north atlantic freshwater forcing in millennial scale climate variability: a tropical atlantic perspective. *Climate Dynamics*, 24(4):325–346.

Dällenbach, A., Blunier, T., Flückiger, J., Stauffer, B., Chappellaz, J., and Raynaud, D. (2000). Changes in the atmospheric ch4 gradient between greenland and antarctica during the last glacial and the transition to the holocene. *Geophysical Research Letters*, 27(7):1005–1008.

Deplazes, G., Lückge, A., Stuut, J.-B. W., Pätzold, J., Kuhlmann, H., Husson, D., Fant, M., and Haug, G. H. (2014). Weakening and strengthening of the indian monsoon during heinrich events and dansgaard-oeschger oscillations. *Paleoceanography*, 29(2):99–114.

Dokken, T. M., Nisancioglu, K. H., Li, C., Battisti, D. S., and Kissel, C. (2013). Dansgaard–oeschger cycles: Interactions between ocean and sea ice intrinsic to the nordic seas. *Paleoceanography*, 28(3):491–502.

Dongmann, G. (1974). The contribution of land photosynthesis to the stationary enrichment of ^{18}o in the atmosphere. *Radiation and Environmental Biophysics*, 11(3):219–225.

Dreyfus, G. B., Parrenin, F., Lemieux-Dudon, B., Durand, G., Masson-Delmotte, V., Jouzel, J., Barnola, J.-M., Panno, L., Spahni, R., Tisserand, A., Siegenthaler, U., and Leuenberger, M. (2007). Anomalous flow below 2700 m in the epica dome c ice core detected using δ^{18}o of atmospheric oxygen measurements. *Climate of the Past*, 3(2):341–353.

Eisenstadt, D., Barkan, E., Luz, B., and Kaplan, A. (2010). Enrichment of oxygen heavy isotopes during photosynthesis in phytoplankton. *Photosynthesis Research*, 103(2):97–103.

Elliot, M., Labeyrie, L., and Duplessy, J.-C. (2002). Changes in north atlantic deep-water formation associated with the dansgaard-oeschger temperature oscillations (60-10 ka). *Quaternary Science Reviews*, 21(10):1153 – 1165.

Emanuel, K. A. (1991). A scheme for representing cumulus convection in large-scale models. *Journal of the Atmospheric Sciences*, 48(21):2313–2329.

Farquhar, G., von Caemmerer, S. v., and Berry, J. (1980). A biochemical model of photosynthetic co2 assimilation in leaves of c3 species. *Planta*, 149(1):78–90.

Farquhar, G. D., Cernusak, L. A., and Barnes, B. (2007). Heavy water fractionation during transpiration. *Plant Physiology*, 143(1):11–18.

Farquhar, G. D., Ehleringer, J. R., , and T., H. K. (1989). Carbon isotope discrimination and photosynthesis. *Annual Review of Plant Physiology and Plant Molecular Biology*, 40(1):503–537.

Farquhar, G. D. and Lloyd, J. (1993). Carbon and oxygen isotope effects in the exchange of carbon dioxide between terrestrial plants and the atmosphere. In Farquhar, G. D., Ehleringer, J. R., and Hall, A. E., editors, *Stable Isotopes and Plant Carbon-water Relations*, pages 47–70. Academic Press, San Diego.

Flanagan, L. B., Bain, J. F., and Ehleringer, J. R. (1991a). Stable oxygen and hydrogen isotope composition of leaf water in c3 and c4 plant species under field conditions. *Oecologia*, 88(3):394–400.

Flanagan, L. B., Comstock, J. P., and Ehleringer, J. R. (1991b). Comparison of modeled and observed environmental influences on the stable oxygen and hydrogen isotope composition of leaf water in phaseolus vulgaris l. *Plant Physiology*, 96(2):588–596.

Flanagan, L. B., Marshall, J. D., and Ehleringer, J. R. (1993). Photosynthetic gas exchange and the stable isotope composition of leaf water: comparison of a xylem-tapping mistletoe and its host. *Plant, Cell & Environment*, 16(6):623–631.

Flanagan, L. B., Phillips, S. L., Ehleringer, J. R., Lloyd, J., and Farquhar, G. D. (1994). Effect of changes in leaf water oxygen isotopic composition on discrimination against c180160 during photosynthetic gas exchange. *Functional Plant Biology*, 21(2):221–234.

Fleitmann, D., Cheng, H., Badertscher, S., Edwards, R. L., Mudelsee, M., Gktürk, O. M., Fankhauser, A., Pickering, R., Raible, C. C., Matter, A., Kramers, J., and Tüysüz, O. (2009). Timing and climatic impact of greenland interstadials recorded in stalagmites from northern turkey. *Geophysical Research Letters*, 36(19). L19707.

Fletcher, W. J., Goni, M. F. S., Allen, J. R., Cheddadi, R., Combourieu-Nebout, N., Huntley, B., Lawson, I., Londeix, L., Magri, D., Margari, V., Muuller, U. C., Naughton, F., Novenko, E., Roucoux, K., and Tzedakis, P. (2010). Millennial-scale variability during the last glacial in vegetation records from europe. *Quaternary Science Reviews*, 29(21–22):2839–2864.

Flückiger, J., Dällenbach, A., Blunier, T., Stauffer, B., Stocker, T. F., Raynaud, D., and Barnola, J.-M. (1999). Variations in atmospheric n20 concentration during abrupt climatic changes. *Science*, 285(5425):227–230.

Genty, D., Blamart, D., Ouahdi, R., Gilmour, M., Baker, A., Jouzel, J., and Van-Exter, S. (2003). Precise dating of dansgaard–oeschger climate oscillations in western europe from stalagmite data. *Nature*, 421(6925):833–837.

Gillon, J. and Yakir, D. (2001). Influence of carbonic anhydrase activity in terrestrial vegetation on the 180 content of atmospheric c02. *Science*, 291(5513):2584–2587.

Grandpeix, J.-Y., Phillips, V., and Tailleux, R. (2004). Improved mixing representation in emanuel's convection scheme. *Quarterly Journal of the Royal Meteorological Society*, 130(604):3207–3222.

Grootes, P. M. and Stuiver, M. (1997). Oxygen 18/16 variability in greenland snow and ice with 1000 to 10000 year time resolution. *Journal of Geophysical Research: Oceans*, 102(C12):26455–26470.

Grousset, F., Labeyrie, L., Sinko, J., Cremer, M., Bond, G., Duprat, J., Cortijo, E., and Huon, S. (1993). Patterns of ice-rafted detritus in the glacial north atlantic (40–55 n). *Paleoceanography*, 8(2):175–192.

Guillevic, M. (2013). *Characterisation of rapid climate changes through isotope analyses of ice and entrapped air in the NEEM ice core*. PhD thesis, Versailles-St Quentin en Yvelines.

Guillevic, M., Bazin, L., Landais, A., Stowasser, C., Masson-Delmotte, V., Blunier, T., Eynaud, F., Falourd, S., Michel, E., Minster, B., Popp, T., Prie, F., and Vinther, B. M. (2014). Multi-proxy fingerprint of heinrich event 4 in greenland ice core records. *Climate of the Past Discussions*, 10(2):1179–1222.

Guy, R. D., Fogel, M. L., and Berry, J. A. (1993). Photosynthetic fractionation of the stable isotopes of oxygen and carbon. *Plant Physiology*, 101(1):37–47.

Handiani, D., Paul, A., and Dupont, L. (2012). Tropical climate and vegetation changes during heinrich event 1: a model-data comparison. *Climate of the Past*, 8(1):37–57.

Harrison, S. and Goni, M. S. (2010). Global patterns of vegetation response to millennial-scale variability and rapid climate change during the last glacial period. *Quaternary Science Reviews*, 29(21⊠-22):2957–2980.

Heinrich, H. (1988). Origin and consequences of cyclic ice rafting in the northeast Atlantic Ocean during the past 130,000 years. *Quaternary Research*, 29:142–152.

Helman, Y., Barkan, E., Eisenstadt, D., Luz, B., and Kaplan, A. (2005). Fractionation of the three stable oxygen isotopes by oxygen-producing and oxygen-consuming reactions in photosynthetic organisms. *Plant Physiology*, 138(4):2292–2298.

Hendricks, M. B., Bender, M. L., and Barnett, B. A. (2004). Net and gross o2 production in the southern ocean from measurements of biological o2 saturation and its triple isotope composition. *Deep Sea Research Part I: Oceanographic Research Papers*, 51(11):1541 – 1561.

Hessler, I., Dupont, L., Bonnefille, R., Behling, H., Gonzalez, C., Helmens, K. F., Hooghiemstra, H., Lebamba, J., Ledru, M.-P., Lezine, A.-M., Maley, J., Marret, F., and Vincens, A. (2010). Millennial-scale changes in vegetation records from tropical africa and south america during the last glacial. *Quaternary Science Reviews*, 29(21–22):2882–2899.

Hoffmann, G., Cuntz, M., Weber, C., Ciais, P., Friedlingstein, P., Heimann, M., Jouzel, J., Kaduk, J., Maier-Reimer, E., Seibt, U., and Six, K. (2004). A model of the earth's dole effect. *Global Biogeochemical Cycles*, 18(1). GB1008.

Hourdin, F., Musat, I., Bony, S., Braconnot, P., Codron, F., Dufresne, J.-L., Fairhead, L., Filiberti, M.-A., Friedlingstein, P., Grandpeix, J.-Y., Krinner, G., LeVan, P., Li, Z.-X., and Lott, F. (2006). The lmdz4 general circulation model: climate performance and sensitivity to parametrized physics with emphasis on tropical convection. *Climate Dynamics*, 27(7–8):787–813.

Huber, C., Leuenberger, M., Spahni, R., Flückiger, J., Schwander, J., Stocker, T., Johnsen, S., Landais, A., and Jouzel, J. (2006). Isotope calibrated Greenland temperature record over Marine Isotope Stage 3 and its relation to CH4. *Earth and Planetary Science Letters*, 243(3–4):504–519.

Jimenez-Moreno, G., Anderson, R. S., Desprat, S., Grigg, L. D., Grimm, E. C., Heusser, L. E., Jacobs, B. F., Lopez-Martinez, C., Whitlock, C. L., and Willard, D. A. (2010). Millennial-scale variability during the last glacial in vegetation records from north america. *Quaternary Science Reviews*, 29(21–22):2865 – 2881.

Joos, F., Gerber, S., Prentice, I. C., Otto-Bliesner, B. L., and Valdes, P. J. (2004). Transient simulations of holocene atmospheric carbon dioxide and terrestrial carbon since the last glacial maximum. *Global Biogeochemical Cycles*, 18(2):n/a–n/a. GB2002.

Kageyama, M., Merkel, U., Otto-Bliesner, B., Prange, M., Abe-Ouchi, A., Lohmann, G., Ohgaito, R., Roche, D. M., Singarayer, J., Swingedouw, D., and Zhang, X. (2013). Climatic impacts of fresh water hosing under last glacial maximum conditions: a multi-model study. *Climate of the Past*, 9(2):935–953.

Kageyama, M., Mignot, J., Swingedouw, D., Marzin, C., Alkama, R., and Marti, O. (2009). Glacial climate sensitivity to different states of the atlantic meridional overturning circulation: results from the ipsl model. *Climate of the Past*, 5(3):551–570.

Kageyama, M., Paul, A., Roche, D. M., and Meerbeeck, C. J. V. (2010). Modelling glacial climatic millennial–scale variability related to changes in the atlantic meridional overturning circulation, a review. *Quaternary Science Reviews*, 29(21–22):2931–2956.

Kanner, L. C., Buenning, N. H., Stott, L. D., Timmermann, A., and Noone, D. (2014). The role of soil processes in d180 terrestrial climate proxies. *Global Biogeochemical Cycles*, 28(3):239–252.

Kanner, L. C., Burns, S. J., Cheng, H., and Edwards, R. L. (2012). High-latitude forcing of the south american summer monsoon during the last glacial. *Science*, 335(6068):570–573.

Kawamura, K., Parrenin, F., Lisiecki, L., Uemura, R., Vimeux, F., Severinghaus, J. P., Hutterli, M. A., Nakazawa, T., Aoki, S., Jouzel, J., Raymo, M. E., Matsumoto, K., Nakata, H., Motoyama, H., Fujita, S., Goto-Azuma, K., Fujii, Y., and Watanabe, O. (2007). Northern hemisphere forcing of climatic cycles in antarctica over the past 360,000 years. *Nature*, 448(7156):912–U4.

Keeling, R. F. (1988). *Development of an interferometric oxygen analyzer for precise measurement of the atmospheric O2 mole fraction*. PhD thesis, Harvard University.

Kindler, P., Guillevic, M., Baumgartner, M., Schwander, J., Landais, A., and Leuenberger, M. (2014). Temperature reconstruction from 10 to 120 kyr b2k from the ngrip ice core. *Climate of the Past*, 10(2):887–902.

Kleppin, H., Jochum, M., Otto-Bliesner, B., Shields, C. A., and Yeager, S. (2015). Stochastic atmospheric forcing as a cause of greenland climate transitions. *Journal of Climate*, (2015).

Kohfeld, K. E., Quere, C. L., Harrison, S. P., and Anderson, R. F. (2005). Role of marine biology in glacial-interglacial co_2 cycles. *Science*, 308(5718):74–78.

Krebs, U. and Timmermann, A. (2007). Tropical air-sea interactions accelerate the recovery of the atlantic meridional overturning circulation after a major shutdown. *Journal of Climate*, 20(19):4940–4956.

Krinner, G., Viovy, N., de Noblet-Ducoudre, N., Ogee, J., Polcher, J., Friedlingstein, P., Ciais, P., Sitch, S., and Prentice, I. C. (2005). A dynamic global vegetation model for studies of the coupled atmosphere-biosphere system. *Global Biogeochemical Cycles*, 19(1). GB1015.

Landais, A., Barnola, J. M., Masson-Delmotte, V., Jouzel, J., Chappellaz, J., Caillon, N., Huber, C., Leuenberger, M., and Johnsen, S. J. (2004). A continuous record of temperature evolution over a sequence of dansgaard-oeschger events during marine isotopic stage 4 (76 to 62 kyr bp). *Geophysical Research Letters*, 31(22):n/a–n/a. L22211.

Landais, A., Dreyfus, G., Capron, E., Masson-Delmotte, V., ni, M. S.-G., Desprat, S., Hoffmann, G., Jouzel, J., Leuenberger, M., and Johnsen, S. (2010). What drives the millennial and orbital variations of $\delta^{18}o_{atm}$? *Quaternary Science Reviews*, 29(1–2):235 – 246.

Landais, A., Dreyfus, G., Capron, E., Pol, K., Loutre, M. F., Raynaud, D., Lipenkov, V. Y., Arnaud, L., Masson-Delmotte, V., Paillard, D., Jouzel, J., and Leuenberger, M. (2012). Towards orbital dating of the epica dome c ice core using delta o_2/n_2. *Climate of the Past*, 8(1):191–203.

Landais, A., Lathiere, J., Barkan, E., and Luz, B. (2007a). Reconsidering the change in global biosphere productivity between the last glacial maximum and present day from the triple oxygen isotopic composition of air trapped in ice cores. *Global Biogeochemical Cycles*, 21(1):n/a–n/a. GB1025.

Landais, A., Masson-Delmotte, V., Nebout, N. C., Jouzel, J., Blunier, T., Leuenberger, M., Dahl-Jensen, D., and Johnsen, S. (2007b). Millenial scale variations of the isotopic composition of atmospheric oxygen over marine isotopic stage 4. *Earth and Planetary Science Letters*, 258(1–2):101 – 113.

LeGrande, A. N. and Schmidt, G. A. (2008). Ensemble, water isotope-enabled, coupled general circulation modeling insights into the 8.2 ka event. *Paleoceanography*, 23(3):n/a–n/a. PA3207.

Lewis, S. C., LeGrande, A. N., Kelley, M., and Schmidt, G. A. (2010). Water vapour source impacts on oxygen isotope variability in tropical precipitation during heinrich events. *Climate of the Past*, 6(3):325–343.

Li, C., Battisti, D. S., and Bitz, C. M. (2010). Can north atlantic sea ice anomalies account for dansgaard–oeschger climate signals? *Journal of Climate*, 23(20):5457–5475.

Li, C., Battisti, D. S., Schrag, D. P., and Tziperman, E. (2005). Abrupt climate shifts in greenland due to displacements of the sea ice edge. *Geophysical Research Letters*, 32(19). L19702.

Liu, Z., Otto-Bliesner, B. L., He, F., Brady, E. C., Tomas, R., Clark, P. U., Carlson, A. E., Lynch-Stieglitz, J., Curry, W., Brook, E., Erickson, D., Jacob, R., Kutzbach, J., and Cheng, J. (2009). Transient simulation of last deglaciation with a new mechanism for bolling-allerod warming. *Science*, 325(5938):310–314.

Lloyd, J. and Farquhar, G. (1994). 13c discrimination during co2 assimilation by the terrestrial biosphere. *Oecologia*, 99(3–4):201–215.

Luz, B. and Barkan, E. (2011). The isotopic composition of atmospheric oxygen. *Global Biogeochemical Cycles*, 25(3):n/a–n/a. GB3001.

Luz, B., Barkan, E., Bender, M., Thiemens, M., and Boering, K. (1999). Triple-isotope composition of atmospheric oxygen as a tracer of biosphere productivity. *Nature*, 400(6744):547–550.

Luz, B., Barkan, E., and Severinghaus, J. (2014). 5.14 - the stable isotopic composition of atmospheric o_2. In Holland, H. D. and Turekian, K. K., editors, *Treatise on Geochemistry (Second Edition)*, pages 363 – 383. Elsevier, Oxford, second edition edition.

Luz, B., Barkan, E., Yam, R., and Shemesh, A. (2009). Fractionation of oxygen and hydrogen isotopes in evaporating water. *Geochimica et Cosmochimica Acta*, 73(22):6697–6703.

Majoube, M. (1971). Fractionnement en oxygene-18 et en deuterium entre l'eau et sa vapeur. *J. Chim. phys*, 68(10):1423–1436.

Marcott, S. A., Clark, P. U., Padman, L., Klinkhammer, G. P., Springer, S. R., Liu, Z., Otto-Bliesner, B. L., Carlson, A. E., Ungerer, A., Padman, J., He, F., Cheng, J., and Schmittner, A. (2011). Ice–shelf collapse from subsurface warming as a trigger for heinrich events. *Proceedings of the National Academy of Sciences*, 108(33):13415–13419.

Mariotti, V., Bopp, L., Tagliabue, A., Kageyama, M., and Swingedouw, D. (2012). Marine productivity response to heinrich events: a model-data comparison. *Climate of the Past*, 8(5):1581–1598.

Marti, O., Braconnot, P., Dufresne, J.-L., Bellier, J., Benshila, R., Bony, S., Brockmann, P., Cadule, P., Caubel, A., Codron, F., de Noblet, N., Denvil, S., Fairhead, L.,

Fichefet, T., Foujols, M.-A., Friedlingstein, P., Goosse, H., Grandpeix, J.-Y., Guilyardi, E., Hourdin, F., Idelkadi, A., Kageyama, M., Krinner, G., L⊠vy, C., Madec, G., Mignot, J., Musat, I., Swingedouw, D., and Talandier, C. (2010). Key features of the ipsl ocean atmosphere model and its sensitivity to atmospheric resolution. *Climate Dynamics*, 34(1):1–26.

McGuire, K., DeWalle, D., and Gburek, W. (2002). Evaluation of mean residence time in subsurface waters using oxygen-18 fluctuations during drought conditions in the mid-appalachians. *Journal of Hydrology*, 261(1–4):132 – 149.

Menviel, L., Timmermann, A., Friedrich, T., and England, M. H. (2014). Hindcasting the continuum of dansgaard-oeschger variability: mechanisms, patterns and timing. *Climate of the Past*, 10(1):63–77.

Menviel, L., Timmermann, A., Mouchet, A., and Timm, O. (2008). Meridional reorganizations of marine and terrestrial productivity during heinrich events. *Paleoceanography*, 23(1):n/a–n/a.

Merlivat, L. (1978). Molecular diffusivities of $h_2^{16}o$, $hd^{16}o$, and $h_2^{18}o$ in gases. *The Journal of Chemical Physics*, 69(6):2864–2871.

Mohtadi, M., Oppo, D. W., Steinke, S., Stuut, J.-B. W., De Pol-Holz, R., Hebbeln, D., and Lückge, A. (2011). Glacial to holocene swings of the australian-indonesian monsoon. *Nature Geoscience*, 4(8):540–544.

Monnin, E., Indermühle, A., Dällenbach, A., Flückiger, J., Stauffer, B., Stocker, T. F., Raynaud, D., and Barnola, J.-M. (2001). Atmospheric co_2 concentrations over the last glacial termination. *Science*, 291(5501):112–114.

NGRIP members (2004). High-resolution record of Northern Hemisphere climate extending into the last interglacial period. *Nature*, 431(7005):147–151.

Otto-Bliesner, B. L. and Brady, E. C. (2010). The sensitivity of the climate response to the magnitude and location of freshwater forcing: last glacial maximum experiments. *Quaternary Science Reviews*, 29(1–2):56–73.

Pausata, F. S., Battisti, D. S., Nisancioglu, K. H., and Bitz, C. M. (2011). Chinese stalagmite [delta] 18o controlled by changes in the indian monsoon during a simulated heinrich event. *Nature Geoscience*, 4(7):474–480.

Peltier, W. (2004). Global glacial isostasy and the surface of the ice-age earth: the ice-5g (vm2) model and grace. *Annu. Rev. Earth Planet. Sci.*, 32:111–149.

Peterson, L. C. and Haug, G. H. (2006). Variability in the mean latitude of the atlantic intertropical convergence zone as recorded by riverine input of sediments to the cariaco basin (venezuela). *Palaeogeography, Palaeoclimatology, Palaeoecology*, 234(1):97 – 113.

Prentice, I. C., Jolly, D., and participants, B. . (2000). Mid-holocene and glacial-maximum vegetation geography of the northern continents and africa. *Journal of Biogeography*, 27(3):507–519.

Raich, J. W. and Potter, C. S. (1995). Global patterns of carbon dioxide emissions from soils. *Global Biogeochemical Cycles*, 9(1):23–36.

Rasmussen, S. O., Abbott, P. M., Blunier, T., Bourne, A. J., Brook, E., Buchardt, S. L., Buizert, C., Chappellaz, J., Clausen, H. B., Cook, E., Dahl-Jensen, D., Davies, S. M., Guillevic, M., Kipfstuhl, S., Laepple, T., Seierstad, I. K., Severinghaus, J. P., Steffensen, J. P., Stowasser, C., Svensson, A., Vallelonga, P., Vinther, B. M., Wilhelms, F., and Winstrup, M. (2013). A first chronology for the north greenland eemian ice drilling (neem) ice core. *Climate of the Past*, 9(6):2713–2730.

Rhodes, R. H., Brook, E. J., Chiang, J. C. H., Blunier, T., Maselli, O. J., McConnell, J. R., Romanini, D., and Severinghaus, J. P. (2015). Enhanced tropical methane production in response to iceberg discharge in the north atlantic. *Science*, 348(6238):1016–1019.

Risi, C., Bony, S., Vimeux, F., and Jouzel, J. (2010). Water-stable isotopes in the lmdz4 general circulation model: Model evaluation for present-day and past climates and applications to climatic interpretations of tropical isotopic records. *Journal of Geophysical Research: Atmospheres*, 115(D12):n/a–n/a.

Roche, D., Wiersma, A., and Renssen, H. (2010). A systematic study of the impact of freshwater pulses with respect to different geographical locations. *Climate Dynamics*, 34(7–8):997–1013.

Ruddiman, W. F. (1977). Late quaternary deposition of ice-rafted sand in the subpolar north atlantic (lat 40 to 65 n). *Geological Society of America Bulletin*, 88(12):1813–1827.

Sanchez Goni, M. F. and Harrison, S. P. (2010). Millennial–scale climate variability and vegetation changes during the last glacial: Concepts and terminology. *Quaternary Science Reviews*, 29(21–22):2823–2827.

Schilt, A., Brook, E. J., Bauska, T. K., Baggenstos, D., Fischer, H., Joos, F., Petrenko, V. V., Schaefer, H., Schmitt, J., Severinghaus, J. P., et al. (2014). Isotopic constraints on marine and terrestrial n20 emissions during the last deglaciation. *Nature*, 516(7530):234–237.

Schlesinger, W. H. and Andrews, J. A. (2000). Soil respiration and the global carbon cycle. *Biogeochemistry*, 48(1):7–20.

Schmittner, A. (2005). Decline of the marine ecosystem caused by a reduction in the atlantic overturning circulation. *Nature*, 434(7033):628–633.

Schmittner, A. and Galbraith, E. D. (2008). Glacial greenhouse-gas fluctuations controlled by ocean circulation changes. *Nature*, 456(7220):373–376.

Severinghaus, J. P. (1995). Studies of the terrestrial o_2 and carbon cycles in sand dune gases and in biosphere 2. Technical report, Oak Ridge Associated Universities, Inc., TN (United States).

Severinghaus, J. P., Beaudette, R., Headly, M. A., Taylor, K., and Brook, E. J. (2009). Oxygen-18 of 02 records the impact of abrupt climate change on the terrestrial biosphere. *Science*, 324(5933):1431–1434.

Stocker, B. D., Roth, R., Joos, F., Spahni, R., Steinacher, M., Zaehle, S., Bouwman, L., Prentice, I. C., et al. (2013). Multiple greenhouse-gas feedbacks from the land biosphere under future climate change scenarios. *Nature Climate Change*, 3(7):666–672.

Stouffer, R. J., Yin, J., Gregory, J. M., Dixon, K. W., Spelman, M. J., Hurlin, W., Weaver, A. J., Eby, M., Flato, G. M., Hasumi, H., Hu, A., Jungclaus, J. H., Kamenkovich, I. V., Levermann, A., Montoya, M., Murakami, S., Nawrath, S., Oka, A., Peltier, W. R., Robitaille, D. Y., Sokolov, A., Vettoretti, G., and Weber, S. L. (2006). Investigating the causes of the response of the thermohaline circulation to past and future climate changes. *Journal of Climate*, 19(8):1365–1387.

Swingedouw, D., Mignot, J., Braconnot, P., Mosquet, E., Kageyama, M., and Alkama, R. (2009). Impact of freshwater release in the north atlantic under different climate conditions in an oagcm. *Journal of Climate*, 22(23):6377–6403.

Tagliabue, A., Bopp, L., and Aumont, O. (2009). Evaluating the importance of atmospheric and sedimentary iron sources to southern ocean biogeochemistry. *Geophysical Research Letters*, 36(13):n/a–n/a.

Takahara, H., Igarashi, Y., Hayashi, R., Kumon, F., Liew, P.-M., Yamamoto, M., Kawai, S., Oba, T., and Irino, T. (2010). Millennial-scale variability in vegetation records from the east asian islands: Taiwan, japan and sakhalin. *Quaternary Science Reviews*, 29(21–22):2900–2917.

Von Caemmerer, S. (2000). *Biochemical models of leaf photosynthesis*. Number 2. Csiro publishing.

Waelbroeck, C., Labeyrie, L., Michel, E., Duplessy, J., McManus, J., Lambeck, K., Balbon, E., and Labracherie, M. (2002). Sea-level and deep water temperature changes derived from benthic foraminifera isotopic records. *Quaternary Science Reviews*, 21(1–3):295–305.

Walker, C. and Brunel, J.-P. (1990). Examining evapotranspiration in a semi-arid region using stable isotopes of hydrogen and oxygen. *Journal of Hydrology*, 118(1–4):55 – 75.

Walker, C. D., Leaney, F. W., Dighton, J. C., and Allison, G. B. (1989). The influence of transpiration on the equilibration of leaf water with atmospheric water vapour. *Plant, Cell & Environment*, 12(3):221–234.

Wang, L., Good, S. P., Caylor, K. K., and Cernusak, L. A. (2012). Direct quantification of leaf transpiration isotopic composition. *Agricultural and Forest Meteorology*, 154-155(0):127–135.

Wang, Y., Cheng, H., Edwards, R. L., He, Y., Kong, X., An, Z., Wu, J., Kelly, M. J., Dykoski, C. A., and Li, X. (2005). The holocene asian monsoon: Links to solar changes and north atlantic climate. *Science*, 308(5723):854–857.

Wang, Y., Cheng, H., Edwards, R. L., Kong, X., Shao, X., Chen, S., Wu, J., Jiang, X., Wang, X., and An, Z. (2008). Millennial- and orbital-scale changes in the east asian monsoon over the past 224,000 years. *Nature*, 451(7182):1090–1093.

Wang, Y. J., Cheng, H., Edwards, R. L., An, Z. S., Wu, J. Y., Shen, C.-C., and Dorale, J. A. (2001). A high-resolution absolute-dated late pleistocene monsoon record from hulu cave, china. *Science*, 294(5550):2345–2348.

Weldeab, S. (2012). Bipolar modulation of millennial-scale west african monsoon variability during the last glacial (75,000-25,000 years ago). *Quaternary Science Reviews*, 40(0):21–29.

Welp, L. R., Keeling, R. F., Meijer, H. A., Bollenbacher, A. F., Piper, S. C., Yoshimura, K., Francey, R. J., Allison, C. E., and Wahlen, M. (2011). Interannual variability in the oxygen isotopes of atmospheric co2 driven by el nino. *Nature*, 477(7366):579–582.

Woillez, M.-N. (2012). *Modellisation des variations rapides du systeme atmospherere-ocean-vegetation-cryosphere en climats glaciaires*. PhD thesis, Paris Versailles St-Quentin.

Woillez, M.-N., Kageyama, M., Combourieu-Nebout, N., and Krinner, G. (2013). Simulating the vegetation response in western europe to abrupt climate changes under glacial background conditions. *Biogeosciences*, 10(3):1561–1582.

Woillez, M.-N., Kageyama, M., Krinner, G., de Noblet-Ducoudre, N., Viovy, N., and Mancip, M. (2011). Impact of co_2 and climate on the last glacial maximum vegetation: results from the orchidee/ipsl models. *Climate of the Past*, 7(2):557–577.

Yakir, D., D., DeNiro, M. J., and Gat, J. R. (1990). Natural deuterium and oxygen–18 enrichment in leaf water of cotton plants grown under wet and dry conditions: evidence for water compartmentation and its dynamics. *Plant, Cell & Environment*, 13(1):49–56.

6 Conclusions and perspectives

This thesis addresses (i) the technical aspects of O_2 isotope ratio measurements from ice core samples, and (ii) our ability to model the observed variations of $\delta^{18}O_{atm}$ during a Heinrich Stadial. In the following we summarize our findings.

Can the perovskite membrane be applied to ice core science?

Improving the precision of $^{17}\Delta_{atm}$ measurements is a crucial requirement to further explore millennial scale variations and confirm the 10 permeg variation observed over DO 19 (Landais et al., 2007). Indeed, $^{17}\Delta_{atm}$ millennial scale variations hardly exceed the precision of the measurements (currently between 5 and 10 per meg). In line with this observation, Chapter 2 presented the development and testing of a new method of O_2 separation from other atmospheric constituents in order to measure a pure O_2 , as isotope ratio determination in a gas mixture requires corrections and therefore decrease precision. It is based on a perovskite membrane ($BaCo_xFe_yZr_{1-x-y}O_{3-d}$), the transport mechanism of which is based on mixed-ionic-electronic technology: at high temperature (typically around 800 °C), permeation of O_2 across the membrane occurs in 3 steps, driven by the O_2 partial pressure gradient: reduction of O_2 molecules adsorbed at the surface with high O_2 partial pressure, counter diffusion of O_2 ions and electrons through the bulk of the membrane and oxidation of O_2 ions (loss of electron) desorbed at the surface with low O_2 partial pressure. The 100 % selectivity and high O_2 permeability of the membrane to O_2 was confirmed, ranging from 0.5 to 3.5 $ml \cdot cm^{-2} \cdot s^{-1}$. However, constant sealing issues, related to the rough and porous surface of the membrane, and variable mass-dependent fractionation, likely related to the fact that O_2 is not quantitatively released from the membrane, precludes high-precision $^{17}\Delta_{atm}$ measurements. The use of the hollow tube fiber in ice core sciences primarily requires a long-lasting gas-tight sealing. If this condition is met, the membrane can be used in applications where removal of O_2 is required, taking profit of its 100 % selectivity to O_2 . Indeed, for such applications, the fractionation of the membrane caused by O_2 segregation is not relevant. Besides, a career gas can be used to create a low O_2 partial pressure in the permeate side, hence ensuring a fast and efficient O_2 permeation. Additionally, pure O_2 standards can be produced in large amounts from e.g. atmospheric O_2 given the large permeability of the membrane.

Does the analytical system developed at CIC enable precise and accurate $\delta^{18}O_{atm}$ and $^{17}\Delta_{atm}$ measurements?

Chapter 3 described the semi-automated, offline experimental setup to extract O_2 from air preserved in ice core bubbles. The developed extraction line is based on the conventional Barkan and Luz's method, relying on GC separation of O_2 and N_2 . Minor changes were made to the original method: a closed-He cryocooler is used to collect O_2 samples at 12 K instead of liquid He, and the gas flow to the GC column is

directed with Valco valves. The setup includes air extraction from ice, standard introduction and cryo-collection in a sample manifold. As for $^{17}\Delta_{atm}$ measurements, an O_2 /Ar mixture is collected after separation from H_2O , CO_2 and N_2 . As for $\delta^{18}O_{atm}$, measured in a dried and CO_2 -free air mixture, the GC unit is bypassed as no N_2 separation is required.

We gave an overview of the units and controls of the experimental setup and presented the developed routine associated with the extraction-purification-collection of $\delta^{18}O_{atm}$ and $^{17}\Delta_{atm}$. We showed that it is critical to condition the extraction line, the collection manifold and the lines of the DI system with standard gas prior a sequence of measurements to obtain a good reproducibility of ice core measurements.

Chapter 4 showed that successful IRMS measurements of $\delta^{18}O_{atm}$ from ice core samples can be performed with the developed analytical setup at CIC. Using a wet-extraction method, $\delta^{18}O_{atm}$ from 21 NEEM Late Holocene shallow ice core samples from the same depth was measured by Grzymala-Lubanski (2015) to control the stability of the analytical system during a RICE ice core measurement campaign. These large samples ($\simeq$ 30 g) were collected offline and $\delta^{18}O_{atm}$, $\delta O_2/N_2$ and $\delta^{15}N$ were measured in an O_2 /N_2 /Ar mixture by IRMS in DI mode. The complete automation of a DI measuring sequence of ten ice core samples using a custom-based isl script was described. The scatter observed in $\delta^{18}O_{atm}$ and $\delta O_2/N_2$ of the replicate NEEM samples underlines the occurrence of gas loss fractionation processes, causing $\delta^{18}O_{atm}$ to increase by $\simeq$ 0.01 ‰ for 1 ‰ change in $\delta O_2/N_2$, as described in the literature.

We detailed the method of data-processing, its associated uncertainty and the strategy employed to correct $\delta^{18}O_{atm}$ for non climatic effects, including effects of sample and standard beam voltage imbalance on the measured O_2 ratio, dependence of $\delta^{18}O_{atm}$ on the O_2 /N_2 ratio (chemical slope), of gravitational settling in the firn, and of gas loss processes associated with bubble close-off, coring and post-coring processes.

Based on zero-enrichment tests, the internal precision of DI measurements of $\delta^{18}O$ and $\delta^{15}N$ is 0.008 ‰ (1 σ) and 0.005 ‰ (1 σ). A similar precision is reached with individual ice core sample measurements, in the range of what can be found in the literature. Based on the 21 NEEM samples, the ability of the analytical system to reproduce $\delta^{18}O_{atm}$ and $\delta O_2/N_2$ ice core measurements is estimated as 0.028 ‰ (1 σ) and 0.021 ‰ (1 σ), respectively.

In contrast, the level of precision ($<$ 10 permeg) required for $^{17}\Delta_{atm}$ measurements is not reached in the current configuration of the experimental setup. Critical improvements are required, in particular the ability of the analytical system to reproduce measurements of standard gas introduced over BFI to fully respect the IT principle.

Improvement in the ice core reproducibility of the analytical setup can be achieved by:

- Melting BFI before standard introduction in order to avoid sample contamination by dissolved gases. As long as this step is not reproducible, the Identical Treatment principle cannot be respected, and precludes very high-precision $\delta^{18}O_{atm}$ and especially $^{17}\Delta_{atm}$ measurements.

- A full automation of the extraction line in order to maintain similar conditions for each sample and avoid operator-related error, in particular in terms of timing (e.g. switching valves).

- A collector configuration of the MS enabling simultaneous collection of air isotopologues, i.e. m/z 28, 29, 32, 33, 34, 36 and 40. We are currently measuring $\delta O_2/N_2$ with a modified peak jumping procedure, obtaining a precision ranging from 0.1 to 0.4 ‰ for an individual ice core sample. Simultaneous measurements of O_2 , N_2 (and Ar) would enhance the overall precision of the measurements by avoiding corrections related to the time delay between the integration of ion currents m/z 28 and m/z 32.

What drives $\delta^{18}O_{atm}$ variations during Heinrich stadials?

Finally, chapter 5 explores the causes of $\delta^{18}O_{atm}$ millennial scale variations during the last glacial period, with a focus on Heinrich Stadials, where a systematic $\delta^{18}O_{atm}$ increase is recorded. We quantified the response of $\delta^{18}O_{atm}$ to such millennial events with an oxygen isotope mass balance model using spatial and temporal fields of (i) temperature and relative humidity from a freshwater hosing simulation performed under glacial boundary conditions with the AOGCM IPSL-CM4, (ii) PFT distribution and GPP provided by the dynamic global vegetation model ORCHIDEE, (iii) oxygen isotope composition of water vapor and precipitation from the AOGCM LMDZ-iso, and (iv) the latest isotope fractionation factor measurements involved in respiratory and photosynthetic processes. AOGCM outputs (precipitation, vegetation cover and humidity) were compared with paleodata for validation and show in general a good agreement. The model simulated a terrestrial enrichment of $\delta^{18}O_{\text{terr}}$ of 0.11 ‰, which mostly arises from the $\delta^{18}O_p$ signal. On a global scale, respiration fractionation only plays a minor role in the anomaly observed during HS, and slightly decreases $\delta^{18}O_{\text{terr}}$ in our simulation, driven by a weaker isotope fractionation of soil respiration during HS that masks the effect of increased photorespiration. Our results confirmed the strong control of the low-latitude hydrological cycle on $\delta^{18}O_{atm}$ as suggested by the strong correlation between local records of $\delta^{18}O_c$ and global record of $\delta^{18}O_{atm}$ on the millennial scale.

The O_2 isotopic mass balance model could be improved by including:

- The dependence of ${}^{18}\varepsilon_{\text{resp}}$ on soil aeration. Variations in the water content of soils modify the effective fractionation ${}^{18}\varepsilon_{\text{resp}}$, because diffusion of O_2 in water is slower than diffusion in air. It causes a drop in concentration at the site of soil respiration, which translates into a weaker back flux to the atmosphere of the $\delta^{18}O$ -enriched residual O_2 after partial respiration. In order to precisely evaluate the uncertainty associated with ${}^{18}\varepsilon_{\text{resp}}$, an improved parameterization of soil aeration is needed.

- A model of the marine component (DE_{mar}) of the Dole effect, as it has been suggested that changes of fractionations in the marine biosphere are more im-

portant than the land-sea control in regulating the magnitude of the Dole effect and its past variations.

Additionally, future research should focus on $^{17}\Delta_{atm}$ by:

- Quantifying the contribution of the processes controlling $^{17}\Delta_{atm}$ changes, using a similar modeling approach as for $\delta^{18}O_{atm}$. Subsequently, comparing the different sensitivities of $\delta^{18}O_{atm}$ and $^{17}\Delta_{atm}$ to these controlling processes should help constrain the causes of the observed O_2 isotope variations. This work is well advanced as the modeling of $^{17}\Delta_{atm}$ is already integrated in the O_2 mass balance model.

- Modeling the stratospheric photochemistry, following Young et al. (2014), to account for the numerous reactions that affect the magnitude of stratospheric ^{17}O depletion in O_2 .

- Exploring the possibility to use carbonyl sulfide as a tracer of CO_2 uptake, and thereby obtain valuable information on ecosystem photosynthesis and on the time of photosynthesis. Such constraints would enable a more precise estimation of e.g. $\delta^{18}O_{lw}$ as humidity and temperature conditions could be better estimated if the time of photosynthesis is known.

- High-resolution $^{17}\Delta_{atm}$ measurements from ice core samples to characterize its past millennial time-scale variations. So far, only one study has combined high resolution $\delta^{18}O_{atm}$ and $^{17}\Delta_{atm}$ measurements (Landais et al., 2007 over DO 19).

Bibliography

Barkan, E. and Luz, B. (2003). High-precision measurements of 170/160 and 180/160 of 02 and 02/ar ratio in air. *Rapid Communications in Mass Spectrometry*, 17(24):2809–2814.

Grzymala-Lubanski, I. (2015). $\delta^{18}o$ of o_2 in rice ice core. Master's thesis, Centre for Ice and Climate.

Landais, A., Masson-Delmotte, V., Nebout, N. C., Jouzel, J., Blunier, T., Leuenberger, M., Dahl-Jensen, D., and Johnsen, S. (2007). Millenial scale variations of the isotopic composition of atmospheric oxygen over marine isotopic stage 4. *Earth and Planetary Science Letters*, 258(1–2):101 – 113.

Young, E. D., Yeung, L. Y., and Kohl, I. E. (2014). On the d170 budget of atmospheric o_2. *Geochimica et Cosmochimica Acta*, 135:102 – 125.

A Isl scripts for automated $\delta^{18}O_{atm}$ measurements

1 Main script: lynnoax_automated_d18o2n2.isl

```

//
    ==========================================================================
//ISODAT NT SCRIPT LANGUAGE (ISL) : Dual Inlet Basic Script
//
    ==========================================================================
//
//
//   History list
//
//   Author                    Date                    Reason
            changes
//
    ------------------------------------------------------------------------------
//     hjs                          novembre 2005         created
//     hjs                          December 2005      modified and
    extended for Jeff Severinghaus, Scripps
//     hjs                          april 2006            other
    modifcations, now universally applicable for any gas jumps
//     okt/fth                   Dec 2008              refinement for
    Bern university
//     okt/fth                   Sept 2009                adjusted for
    Bern university
////  C. Reutenauer         18.10.2012            adjusted for CPH to
     be integrated to the main acquisition file
//     I. Lubanski           07.08.2015            Argon 40 removed
    from the Peak jumping
//
    ------------------------------------------------------------------------------


///
    ##############################################################################

//   DEAR DELTA/MAT253 USER !!!

///
    ##############################################################################
// Script for performing a dual inlet peak jump acquisition.
```

```
// replace default acquisition.isl with this script in dual inlet method.
// Start a jump measurement between two gases as dual inlet measurement using
// some  parameters as defined in dual inlet method.
// The scripts writes results into a comma separated *.txt file (can be imported and subsequently evaluated in Excel).
// The default folder is: c:\\jump_results. This folder must be created by the user !!!
// To change the folder name and path go to xxx
// Background is determined for each gas individually if checked in the sequence line
// Press adjust is done for the first gas to be measured when checked in the sequence line
//
// Parameters to be modified by user are at the end of the script.
// Please find more info at the bottom of the script.

external array  g_nInties  of number [10];
//external array  g_n1Inties  of number [10];
external array  g_nCurrInties  of number [10];
external array  g_nBackgrounds  of number [10];
external array  g_nBgd of number [10];   //added
external array  g_sBgd of string [10];  //added
external number g_NumberOfCurrInties = 0;
external array  g_ChannelArr  of channel [10];
external array  g_sLastIntiesStr of string [10];  //added
//external array  g_sInties of string [10];  //added
external string g_sInties="";
external string g_resultstr="";
external string g_sOldGasConf="";
external string g_sFileName="";
external string g_sSection="";
external number g_n1Inties=0;
external number g_n2Inties=0;
external number g_nNumCycle=0;
external number g_nBackgroundDelay = 60; //must be defined here in the script. Method value ignored. Value in seconds.
external number g_nPressAdjustDelay = 10;//second

script DualInletPeakJumpAcquisitionLynnOax
{
   const number NUM_CHANNELS=10; // see above!

   const number KEEP_GC=0;     // gas configuration
   const number CHANGE_GC=1;
   const number NO_PC=0;          // peak center
   const number YES_PC=1;
   const number NO_BGD=0;      // background
   const number YES_BGD=1;
   const number NO_PA=0;          // press adjust
   const number YES_PA=1;
}
```

```
//
include "lib\math.isl"
include "lib\stdisl.isl"
include "lib\instrument.isl"
include "lib\DualInlet_lib.isl"
include "lib\LynnOax_lib_waterMS.isl"
include "lib\InterferingMassLynnOax.isl"


//
function ConvertIntyStr (string sIntyStr)
{
   g_NumberOfCurrInties = 0;
   number nCnt = 0;
   string sSubStr;
   string sHlpStr;
   number nStrLen = _strlen (sIntyStr);
   number nPos = 0;

   if (nStrLen > 0)
   {
      nPos = _strstr (sIntyStr, ",");
      while ((nPos>=0) && (nCnt<10))
      {
         sSubStr = _strleft (sIntyStr, nPos);
         g_nCurrInties[nCnt] = _strtod (sSubStr);
         g_NumberOfCurrInties++;

         sHlpStr = _strright (sIntyStr, (nStrLen - nPos - 1));
         sIntyStr = sHlpStr;
         nStrLen = _strlen (sIntyStr);
         nPos = _strstr (sIntyStr, ",");

         nCnt++;
      }

      if ((nStrLen>0) && (nCnt<10))
      {
         g_nCurrInties[nCnt] = _strtod (sIntyStr);
         g_NumberOfCurrInties++;
      }
   }
}
//

function AppendIntensities (string sIntyStr)
{
   call ConvertIntyStr (sIntyStr);
```

```
    number nCnt = 0;
    for (nCnt=0; nCnt<g_NumberOfCurrInties; nCnt++;)
    {
        g_nInties[nCnt] = g_nInties[nCnt] + g_nCurrInties[nCnt];
    }
}

//
    ------------------------------------------------------------------------
function MyBackground(channel nChan, number nIntegrationTime)
{
   string csResult="?";
    string csInfo="Background: ";
    number nBGDDelay = g_nBackgroundDelay * 1000;
    string sLastIntiesStr;
    string sTransition
    number nNumDigits=3;
    number nChanIdx=0;   //added
    number nCnt = 0;
    number nMaxChan=NUM_CHANNELS;

    bool bBackground=_GetSequenceFlag("Background",TRUE);
   if (bBackground==TRUE)
   {
    _UserInfo("Start Background",0,1);
    call ChangeOverClose();
    _Delay (nBGDDelay);

        _ResetLastAcqInty ();
        number nIntyEx = _GetIntensityEx(nChan,nIntegrationTime);
//      sLastIntiesStr = _GetLastAcqInty (nNumDigits);
        sLastIntiesStr= _strFromNumber(nIntyEx);
        call AppendIntensities (sLastIntiesStr);
        for (nCnt=0; nCnt<g_NumberOfCurrInties; nCnt++;)
        {
            g_nBackgrounds[nCnt] = g_nInties[nCnt];
            g_nInties[nCnt] = 0;
        }
   }
}

//
    ------------------------------------------------------------------------
function sci2str(number in):string   //converts scientific format into string
{
    number i;
    string out;

    for(i=0;in<1;i++;)
    {
         in=in*10;
```

```
    }
    out=_strFormat("%1.3fe-%1.0f",in,i);
    return out;
}
//
function Inty_Mass(channel chan, number mass):number
{
    number int_time=10000;  // integration time default
    number inty;

    number Dac=0;
    Dac=_SetMassViaDac(1,mass);
    _PeakCenter(1);
    _Delay(int_time);_Delay(int_time);//_Delay(int_time);_Delay(int_time);
    inty=_GetIntensityEx(chan,int_time);

    return inty;
}
//
function Jump2Mass(string GasConfigGasX, channel measchannel, number mass,  string& csOld, bool ChangeGasConfig, bool DoPeakCenter):number
    // jump to desired mass
{
    bool bPeakCenterOn=_GetSequenceFlag("Peak Center",FALSE);
    number Dac;
    number ActMass;
    number MassAcurr=0.3;
    // magnet is switched only if mass difference is greater than MassAcurr
    // otherwhise mass will be corrected by peakcenter
    if (ChangeGasConfig==TRUE)
    {
        _SetGasConfiguration(GasConfigGasX,csOld);
    }
    ActMass=_GetMass(measchannel);
    if (abs(mass-ActMass) > MassAcurr)
    {
        Dac=_SetMassViaDac(measchannel,mass);
    }
    if ((DoPeakCenter==TRUE) && (bPeakCenterOn==TRUE))
    {
        _UserInfo("Start Peak Center after jump to mass",0,1);
        number nResult=_PeakCenter(measchannel);

        if (nResult<0)
        {
            _ScriptError("Peak Center failed <%0.0f>", ERROR_TYPE_SCR_SEQ, nResult);
```

```
        }
      else
      {
          _UserInfo("Peak Center found at [%0.0f]",0,0,nResult);
        }

        _Delay(Ms_PeakCenterPostDelay);
    }
    return Dac;
}
//
function Delay_Sec(number time)
{
    number delay_msec=time*1000;
    _Delay(delay_msec);
}
//
function ResetChannelArr ()
{
    number nChanIdx=0;
    for (nChanIdx=0; nChanIdx<NUM_CHANNELS; nChanIdx++;)
    {
        g_ChannelArr[nChanIdx]=-1;
    }
}
//
function MeasureGas (string sGasConfName, string SampleName, number
     mass, channel nChan, number nIntegrationTime, number
    nSampleSide, bool ChangeGasConfig, bool DoPeakCenter, bool
    bDoBackground, bool bDoPressAdjust): number
{
    number IntRepGas2=1; // how often is integration repeated with
        Integrationtime, result is mean value (not to mix with cycle
         times)

    number nResult=0;
    string sOld;
    string helpstr;
    string resultstr;
   //number nPreDelay=Dual_Inlet_Idle;
   number time_sec=0;
   number nLen=0;
   number nPressAdjustDelay = g_nPressAdjustDelay * 1000;

    if (ChangeGasConfig)
    {
        nResult=call Jump2Mass(sGasConfName,nChan,mass,sOld,
            ChangeGasConfig,DoPeakCenter);
```

```
256         nLen=_strlen(g_sOldGasConf);
257         if (nLen == 0)
258         {
259             g_sOldGasConf = sOld;
260         }
261     }
262 
263     number nChanIdx=0;
264     string sLastIntiesStr;
265     string sTransInties
266     for (nChanIdx=0; nChanIdx<NUM_CHANNELS; nChanIdx++;)
267     {
268         g_nInties[nChanIdx]=0;
269         g_nBackgrounds[nChanIdx]=0;
270     }
271 
272     if (bDoBackground)
273     {
274         call MyBackground(nChan, nIntegrationTime);
275     }
276 
277     if (bDoPressAdjust)
278     {
279         _Delay(nPressAdjustDelay);
280         call Pressureadjust();
281     }
282 
283     call SwitchChangeOver(nSampleSide);
284     resultstr=_strFromNumber(g_nNumCycle);
285     helpstr=",";
286     resultstr+= helpstr;
287 
288     time_sec=_ElapsedTime()/1000;
289     helpstr=_strFromNumber(time_sec);
290     resultstr+= helpstr;
291 
292     helpstr=",";
293     resultstr+= helpstr;
294     helpstr=SampleName;//", Sample, ";
295     resultstr+= helpstr;
296 
297     helpstr=",";
298     resultstr+= helpstr;
299     helpstr=sGasConfName;
300     resultstr+= helpstr;
301 
302     helpstr=",";
303     resultstr+= helpstr;
304     helpstr=_strFromNumber(mass);
305     resultstr+= helpstr;
306 
307     helpstr=",";
308     resultstr+= helpstr;
309     _Delay(Dual_Inlet_Idle);
```

```
310
311     number nDefault=(-1000);
312     number inty=0;
313     number k=0;
314     number nMaxChan=NUM_CHANNELS;
315     nChanIdx=0;
316     for (nChanIdx=0; nChanIdx<NUM_CHANNELS; nChanIdx++;)
317     {
318     g_nInties[nChanIdx]=0;
319     } // removed
320
321     nDefault=(-999);
322
323     number nNumDigits = 3;
324     number ff = 15000;
325
326     for (k=0;k<IntRepGas2;k++;)
327     {
328         _ResetLastAcqInty ();
329         _GetIntensityEx(nChan,nIntegrationTime);
330 //      sLastIntiesStr = _GetLastAcqInty (nNumDigits);
331         number nIntyEx = _GetIntensityEx(nChan,nIntegrationTime);
332         sLastIntiesStr= _strFromNumber(nIntyEx);
333
334         call AppendIntensities (sLastIntiesStr);
335     }
336
337     for (nChanIdx=0; nChanIdx<nMaxChan; nChanIdx++;)
338     {
339         if (g_ChannelArr[nChanIdx]<0)
340         {
341             nMaxChan = nChanIdx;
342         }
343         else
344         {
345             g_nInties[nChanIdx] = g_nInties[nChanIdx] / IntRepGas2;
346             g_nInties[nChanIdx] = g_nInties[nChanIdx] - g_nBackgrounds
                    [nChanIdx];
347             inty=g_nInties[nChanIdx];
348             helpstr=_strFromNumber(inty);
349             resultstr+=helpstr;
350             helpstr=" , ";
351             resultstr+= helpstr;
352         }
353     }
354
355     helpstr=_strFromNumber(nIntegrationTime);
356     helpstr+=" ,";
357     resultstr+= helpstr;
358
359     _Write(g_sFileName,g_sSection,resultstr," , line end,");
360     _UserInfo(resultstr,0,0);
361     _Trace(resultstr,g_nNumCycle);
362     g_resultstr=resultstr;
```

```
363
364     return nResult;
365 }
366
367 //
    ------------------------------------------------------------------------------------------
368 //
    ------------------------------------------------------------------------------------------
369 //
    ------------------------------------------------------------------------------------------
370 function CleanUp()
371 {
372 }
373 //
    ------------------------------------------------------------------------------------------
374 function InitScript()
375 {
376   OnBreak CleanUp;
377 }
378 //
    ------------------------------------------------------------------------------------------
379 main()
380 {
381     bool DoPeakCenter=TRUE;
382
383     string NameGas1="Default1";
384     string GasConfigGas1="O2_gaslab"//"AA";        // Default
385     string NameGas2="Default2";
386     string GasConfigGas2="O2_gaslab"//"BB";        // Default
387     channel cChannel=1;                            // Default
388     number  nIntegrationTime=16000; //Integration time default value
        . Can be set individually for each gas below.
389
390     string helpstr;
391     string helpstr2;
392     string infodefault="line,Sa_";
393     string section="header";
394     string userinfo;
395   string filename_default;
396   string filename=filename_default;
397   string resultstr;
398   string i_as_str;
399   string csOld;
400     number i;
401     number j;
402     number k;
403     number line;
404     number strpos;
405     number nResult;
```

```
    bool bOK;
    number inty;
    number nSampleSide=Dual_Inlet_Sample;
   number nStandardSide=Dual_Inlet_Standard;
   number nPreDelay=Dual_Inlet_Idle;
   number time_sec;
   number helpnumber;
   bool ChangeGasConfig=TRUE;

    string sGasName="";
    number nMassSelect=0;
    number nSaStartPressure;
    number nStdStartPressure;

    call InitScript();

   if (_stricmp(GasConfigGas1,GasConfigGas2)==0)
   {
    ChangeGasConfig=FALSE;
   }

   _Set("Dual Inlet System/Valve 15",1); //open valve 15
    _Set("Dual Inlet System/Valve 25",1); //open valve 25

    bool bEvacuateSa     =_GetSequenceFlag("Evacuate Sa",FALSE); //
        evacuate sample side
    bool bEvacuateStd    =_GetSequenceFlag("Evacuate Std",FALSE); //
        evacuate std side
    bool bMonitormass =_GetSequenceFlag("MonitorMass",FALSE);
    bool bPressAdjustOn=_GetSequenceFlag("Pressadjust",FALSE);    //
        <---.press adjust if checked in sequence
    bool bPeakCenterOn=_GetSequenceFlag("Peak Center",FALSE);
    bool bPILeft=_GetSequenceFlag("Pleft+",FALSE);
    bool bPIRight=_GetSequenceFlag("Pright+",FALSE);

    //added april 2013, used for correction, tuning, what needs to
        be monitored on the MS
g_sMeasType =_GetSequenceText("Measurement Type","none");
g_sStdInj = _GetSequenceText("Standard Injection","none");
g_sChecks = _GetSequenceText("Checks","none");
g_nAmountBellow = _GetSequenceNumber("AmountBellow",0.0);
g_nPercentBellow = _GetSequenceNumber("Preparation",1000);
g_sEquilTime = _GetSequenceText("Preparation","");


// if first run and first row of the sequence
//if (_GetSequenceInfo(IS_FIRST_SAMPLE_RUNNING,-1))
//     {
       if ((bEvacuateSa==TRUE) && (bEvacuateStd==TRUE))
          {
          call Preparation_DualInletSystem();
          }
//     }

```

```
456    g_sPortName=_GetSequenceText("Lynn Oax Inlet","none");
457    string sSampleIDstring=_strleft(g_sPortName,(_strlen("sample")))
       ;
458
459    // check if std signal is higher than 10mbar  at full expansion
460
461 if (_strcmp(sSampleIDstring,"sample")==0) //depending on the string
       on Lynn Oax Inlet sequence's column, switch from script
462 {
463
464     if (bEvacuateSa==TRUE) // if box checked, means sample needs to
           be transferred
465     {
466     _UserInfo("Vacuuming Sample Side",0,1);
467       if (bEvacuateStd==TRUE) {call StdTransferDIRIGHT();}//if (
           _GetSequenceInfo(IS_FIRST_SAMPLE_RUNNING,FALSE)) {call
           StdTransferDIRIGHT();}
468       if (bEvacuateStd==FALSE)   {call StdRefill();}
469
470     g_sPortName=_GetSequenceText("Lynn Oax Inlet","none");//get
           column string from attached sequence
471    channel chPA_channel = chPa; //_GetChannelForCup(PAcup);
472    call SwitchChangeOver(Dual_Inlet_Standard); //switch changeover
       to std side
473    call MpTransfer();//call DiSwitchX(nside,nNo,bOpen,delay) first
       close valve 11 and open 15
474                                //if port recognized, starts
                                      MpTransferMp
475    call PeakCenter();
476     //    call GetIntPress_Introduction();
477
478         if (bPressAdjustOn==TRUE)
479         {
480         nStdStartPressure = call GetIntPressStd_Introduction();
481         nSaStartPressure  = call GetIntPressSa_Introduction();
482         }
483
484     call Background();
485    //call DiSetVolume(Dual_Inlet_Standard,100); // to remove if PA
       manual !!as Sample is Master, Standard pressure in bellow
       has to be lower than sample pressure. Can be improved
486    call Pressureadjust_LynnOaxd18O2N2();
487    call GetVoltage_Pressure_diff(nSaStartPressure,nStdStartPressure
       );
488    call Acquisition();
489    call MonitorMass();
490     //    call MagnetScan();
491
492         if (_GetSequenceInfo(IS_LAST_SAMPLE_RUNNING,TRUE))
493         {
494         call ChangeOverClose();
495         }
496
497   }
```

```
498   else
499   {
500    _UserInfo("Skip Sample Side Evacuation",0,1);
501    call StdRefill();
502    // call DiBellowAdjust_Increase(Dual_Inlet_Sample,
         nMaxContractionTries);
503    call PeakCenter();
504
505       if (bPressAdjustOn==TRUE)
506       {
507       nStdStartPressure = call GetIntPressStd_Introduction();
508       nSaStartPressure  = call GetIntPressSa_Introduction();
509       }
510
511    call Background();
512    call Pressureadjust_LynnOaxd18O2N2();
513    call GetVoltage_Pressure_diff(nSaStartPressure,nStdStartPressure
         );
514    call Acquisition();
515    call MonitorMass();
516     //    call MagnetScan();
517
518       if (_GetSequenceInfo(IS_LAST_SAMPLE_RUNNING,TRUE))
519       {
520         call ChangeOverClose();
521       }
522   }
523
524 }
525 else
526 {
527   if (_strcmp(g_sPortName,"none")==0)
528   {
529     if (bEvacuateSa==TRUE)
530    {
531       _UserInfo("Vacuuming Sample Side for Zero-enrichment test"
             ,0,1);
532    g_sPortName=_GetSequenceText("Lynn Oax Inlet","none");//get
         column string from attached sequence"
533    g_nSeqRowNumber = _GetSequenceNumber("Row",0);
534       channel chPA_channel = chPa; //channel chPA_channel =
             _GetChannelForCup(PAcup);
535         //  call SwitchChangeOver(Dual_Inlet_Standard); //switch
               changeover to std side
536
537
538         //  if (g_nSeqRowNumber = 1) {call StdTransferDIRIGHT();}
539         if (bEvacuateStd==TRUE) {call StdTransferDIRIGHT();}//if (
               _GetSequenceInfo(IS_FIRST_SAMPLE_RUNNING,FALSE)) {call
               StdTransferDIRIGHT();}
540         if (bEvacuateStd==FALSE) {call StdRefill();}
541         // call Flushing(1); added in StdTransferDILEFT //
               FlushingCycles=3   flush std line 3 times by default
542    call StdTransferDILEFT();
```

```
543     call DiSwitchX(Dual_Inlet_Sample,2,0,DI_DEFAULT_VALVE_DELAY);
544     call DiSwitchX(Dual_Inlet_Sample,3,0,DI_DEFAULT_VALVE_DELAY);
545     call DiSwitchX(Dual_Inlet_Standard,2,0,DI_DEFAULT_VALVE_DELAY);
546     call CheckVacuum(Dual_Inlet_Standard,3,Press_read_waiting_time);
            // close vac pumps, open specified valve and check vacuum
547
548     call PeakCenter();
549          if (bPressAdjustOn==TRUE)
550          {
551          nStdStartPressure = call GetIntPressStd_Introduction();
552          nSaStartPressure  = call GetIntPressSa_Introduction();
553          }
554
555     call Background();
556
557     call Pressureadjust_LynnOaxd18O2N2();
558     call GetVoltage_Pressure_diff(nSaStartPressure,nStdStartPressure
            );
559     call Acquisition();
560     call MonitorMass();
561 //  call MagnetScan();
562
563     }
564     else
565     {
566     _UserInfo("Skip Sample Side Evacuation",0,1);
567     call StdRefill();
568      //    call DiBellowAdjust_Increase(Dual_Inlet_Sample,
            nMaxContractionTries);
569     call PeakCenter();
570          if (bPressAdjustOn==TRUE)
571          {
572          nStdStartPressure = call GetIntPressStd_Introduction();
573          nSaStartPressure  = call GetIntPressSa_Introduction();
574          }
575
576     call Background();
577     call Pressureadjust_LynnOaxd18O2N2();
578     call GetVoltage_Pressure_diff(nSaStartPressure,nStdStartPressure
            );
579     call Acquisition();
580     call MonitorMass();
581      //    call MagnetScan();
582
583          if (_GetSequenceInfo(IS_LAST_SAMPLE_RUNNING,TRUE))
584          {
585          call ChangeOverClose();
586          }
587      }
588     }
589 }
590
591 // Start peak jumps
592
```

```
593     bool bMagnetScan  =_GetSequenceFlag("MagnetScan",FALSE);
594
595  if (bMagnetScan==TRUE)
596 {
597   filename_default="C:\Thermo\Isodat NT\Global\User\Dual Inlet
        System\Results\ACQ_O2_Results\jump_results";
598   //<=  define your result folder here, make sure it exists !!
599   filename_default+="O2_N2_Ar";                          // <=  define
        your filename here
600   filename_default+="__000.txt";
601   filename=filename_default;
602
603    // check for next free file
604    //_Write(filename,section,infodefault,"header");
605
606    for (i=1;i<999;i++;)
607    {
608       strpos=_strstr (filename,"__");
609       strpos=strpos+2;
610       helpstr=_strleft(filename,strpos);
611       filename=helpstr;
612       i_as_str="00";
613       i_as_str+=_strFromNumber(i);
614       helpstr=_strright(i_as_str,7);
615       helpstr=_strleft(helpstr,3);
616       filename+=helpstr;
617       filename+=".txt";
618       bOK=_ExistFile(filename);
619       if(bOK==FALSE){i=999;}
620    }
621
622 // helpstr = _GetDate();
623 // helpstr2 = _GetTime();
624   infodefault = "Date: ";
625 //  infodefault += helpstr;
626   infodefault += "  Time: ";
627 //  infodefault += helpstr2;
628       _Write(filename,section,infodefault,"header");
629
630    section="greetings_from_bremen";
631   infodefault="line, time/sec,  Std/Sa,  Gas,  Mass/Da, Inty/mV,
        Inty mV, Inty mV, Intytime/msec "; // time/sec is related to
        acquisition start after each integration.
632
633    _Write(filename,section,infodefault,"info");
634
635    g_sFileName=filename;
636    g_sSection=section;
637
638    helpstr = "Analysis started. Result file is ";
639    helpstr += g_sFileName;
640    _UserInfo (helpstr,0,1);
641
642    //Acquisition starts here
```

```
643
644     call SwitchChangeOver(nStandardSide);
645     helpnumber=i*4;
646
647     _ResetTimer();
648
649     for (i=0;i<3;i++;)    //the measurement cycles start here
        Dual_Inlet_Cycles
650     {
651        g_nNumCycle = i+1;
652
653
654 //     Measurement sequence example:    (IN CASE OF Kr/Ar, see
        Severinghaus 2003, p. 333)
655 //           jump to 84
656 //           peak center
657 //           switch changeover to sample
658 //           idle 10 sec
659 //           integrate 16 sec
660 //           switch changeover to standard
661 //           idle 10 sec
662 //           integrate 16 sec
663 //
664 //           jump to 36
665 //           peak center
666 //           switch changeover to sample
667 //           idle 10 sec
668 //           integrate 8 sec
669 //           switch changeover to standard
670 //           idle 10 sec
671 //           integrate 8 sec
672
673             // start FIRST GAS
                ////////////////////////////////////////////////////////////////////////////////
674 //     nIntegrationTime=16000; // integration time in milliseconds
675 //     sGasName="N2/O2/Ar";             // set the gas configuration
        name (must be identical to name in GasConfiguration!!!)
676 //
677 //     nMassSelect=33;               // select this mass on "
        cChannel", next line
678 //     cChannel=1;                 // channel for mass select
679 //
680 //     call ResetChannelArr(); // clear array for channel in use
681 //     g_ChannelArr[0]=1;//40  // define channels in use; always
        begin with g_ChannelArr[0]
682 //
683 //     if (i==0)
684 //     {
685 //        call MeasureGas (sGasName, "Pre", nMassSelect, cChannel,
        nIntegrationTime, nStandardSide, CHANGE_GC, YES_PC, YES_BGD,
        NO_PA);
686 //     }
```

```
687 //      call MeasureGas (sGasName, "Sample", nMassSelect, cChannel,
    nIntegrationTime, nSampleSide, CHANGE_GC, NO_PC, NO_BGD, NO_PA)
    ;
688 //      call MeasureGas (sGasName, "Standard", nMassSelect, cChannel,
     nIntegrationTime, nStandardSide, KEEP_GC, NO_PC, NO_BGD, NO_PA
    );
689       // end FIRST GAS
          ////////////////////////////////////////////////////////////////////

690
691  // start THIRD GAS
     ////////////////////////////////////////////////////////////////////

692       nIntegrationTime=16000; // integration time in milliseconds
693       sGasName="O2_gaslab";                // set the gas
          configuration name (must be identical to name in
          GasConfiguration!!!)
694
695       nMassSelect=18;                // select this mass on "
          cChannel", next line
696       cChannel=1;                 // channel for mass select
697
698       call ResetChannelArr(); // clear array for channel in use
699       g_ChannelArr[0]=1;//3;//28 // define channels in use; always
          begin with g_ChannelArr[0]
700       //g_ChannelArr[1]=1;//29    // add or delete Channels
          depending on number of masses to be recorded
701       //g_ChannelArr[2]=2;//30
702
703       if (i==0)
704       {
705       //call MeasureGas (sGasName, "Pre", nMassSelect, cChannel,
          nIntegrationTime, nStandardSide, CHANGE_GC, YES_PC,
          NO_BGD, NO_PA);
706       call MeasureGas (sGasName, "Sample", nMassSelect, cChannel,
          nIntegrationTime, nSampleSide, CHANGE_GC, NO_PC, NO_BGD,
          NO_PA);
707       call MeasureGas (sGasName, "Standard", nMassSelect, cChannel,
           nIntegrationTime, nStandardSide, CHANGE_GC, NO_PC,
          NO_BGD, NO_PA);
708       }
709       // end THIRD GAS
          ////////////////////////////////////////////////////////////////////

710
711
712    // start FOURTH GAS
       ////////////////////////////////////////////////////////////////////

713       nIntegrationTime=16000; // integration time in milliseconds
714       sGasName="O2_gaslab";                // set the gas
          configuration name (must be identical to name in
          GasConfiguration!!!)
715
```

```
716         nMassSelect=44;                    // select this mass on "
            cChannel", next line
717         cChannel=1;                    // channel for mass select
718
719         call ResetChannelArr(); // clear array for channel in use
720         g_ChannelArr[0]=1;//3;//28 // define channels in use; always
            begin with g_ChannelArr[0]
721         //g_ChannelArr[1]=1;//29    // add or delete Channels
            depending on number of masses to be recorded
722         //g_ChannelArr[2]=2;//30
723
724         if (i==0)
725         {
726         //call MeasureGas (sGasName, "Pre", nMassSelect, cChannel,
            nIntegrationTime, nStandardSide, CHANGE_GC, YES_PC,
            NO_BGD, NO_PA);
727         call MeasureGas (sGasName, "Sample", nMassSelect, cChannel,
            nIntegrationTime, nSampleSide, CHANGE_GC, NO_PC, NO_BGD,
            NO_PA);
728         call MeasureGas (sGasName, "Standard", nMassSelect, cChannel,
             nIntegrationTime, nStandardSide, CHANGE_GC, NO_PC,
            NO_BGD, NO_PA);
729         }
730         // end FOURTH GAS
            ////////////////////////////////////////////////////////////////////////
731
732 // start FIRST GAS
    ////////////////////////////////////////////////////////////////////////
733         nIntegrationTime=16000; // integration time in milliseconds
734         sGasName="O2_gaslab";                    // set the gas
            configuration name (must be identical to name in
            GasConfiguration!!!)/\
735
736         nMassSelect=32;                    // select this mass on "
            cChannel", next line
737         cChannel=0;                    // channel for mass select
738
739         call ResetChannelArr(); // clear array for channel in use
740         g_ChannelArr[0]=0;//40  // define channels in use; always
            begin with g_ChannelArr[0]
741
742         //if (i==0)
743         //{
744         // call MeasureGas (sGasName, "Pre", nMassSelect, cChannel,
            nIntegrationTime, nStandardSide, CHANGE_GC, NO_PC, NO_BGD
            , NO_PA);
745         //}
746         call MeasureGas (sGasName, "Sample", nMassSelect, cChannel,
            nIntegrationTime, nSampleSide, CHANGE_GC, NO_PC, NO_BGD,
            NO_PA);
747         call MeasureGas (sGasName, "Standard", nMassSelect, cChannel,
             nIntegrationTime, nStandardSide, CHANGE_GC, NO_PC,
```

```
        NO_BGD, NO_PA);
    // end FIRST GAS //////////////////////////////////////////////////////////////////////

        // start SECOND GAS ////////////////////////////////////////////////////////////////////

    nIntegrationTime=16000; // integration time in milliseconds
    sGasName="O2_gaslab" //"N2/O2/Ar";          // set the gas configuration name (must be identical to name in GasConfiguration!!!)

    nMassSelect=28;              // select this mass on "cChannel", next line
    cChannel=0;                  // channel for mass select

    call ResetChannelArr(); // clear array for channel in use
    g_ChannelArr[0]=0;//40  // define channels in use; always begin with g_ChannelArr[0]

    //if (i==0)
    //{
    // call MeasureGas (sGasName, "Pre", nMassSelect, cChannel, nIntegrationTime, nStandardSide, CHANGE_GC, NO_PC, NO_BGD, NO_PA);
    //}
    if (i<3)
    {
    call MeasureGas (sGasName, "Sample", nMassSelect, cChannel, nIntegrationTime, nSampleSide, CHANGE_GC, NO_PC, NO_BGD, NO_PA);
    call MeasureGas (sGasName, "Standard", nMassSelect, cChannel, nIntegrationTime, nStandardSide, CHANGE_GC, NO_PC, NO_BGD, NO_PA);
    }
    // end SECOND GAS //////////////////////////////////////////////////////////////////////


//      start THIRD GAS ////////////////////////////////////////////////////////////////////////

//    nIntegrationTime=16000; // integration time in milliseconds
//    sGasName="N2";               // set the gas configuration name (must be identical to name in GasConfiguration!!!)/\
//
//    nMassSelect=40;              // select this mass on "cChannel", next line
//    cChannel=1;                  // channel for mass select
//
//    call ResetChannelArr(); // clear array for channel in use
```

```
//      g_ChannelArr[0]=1;//40   // define channels in use; always begin with g_ChannelArr[0]
//
//      if (i==0)
//      {
//          call MeasureGas (sGasName, "Pre", nMassSelect, cChannel, nIntegrationTime, nStandardSide, CHANGE_GC, YES_PC, YES_BGD, NO_PA);
//      }
//      call MeasureGas (sGasName, "Sample", nMassSelect, cChannel, nIntegrationTime, nSampleSide, CHANGE_GC, NO_PC, NO_BGD, NO_PA);
//      call MeasureGas (sGasName, "Standard", nMassSelect, cChannel, nIntegrationTime, nStandardSide, KEEP_GC, NO_PC, NO_BGD, NO_PA);

//      end THIRD GAS //////////////////////////////////////////////////////////////////////



    }       // end of loop, measurement cycle ends here
}

        if (_GetSequenceInfo(IS_LAST_SAMPLE_RUNNING,FALSE))
  {
   call ChangeOverClose();
  }

}
//________________________________________________________________________________
```

II Library: LynnOax_lib_waterMS.isl

```
//===========================================================================
//ISODAT NT SCRIPT LANGUAGE (ISL) : Dual Inlet Basic Script
//===========================================================================
//
//   History list
//
//   Author                    Date                    Reason changes
//________________________________________________________________________________
```

```
9  //   C. Reutenauer            18.10.2012            Created
10 //
11 //
12 //
13 //
   ------------------------------------------------------------------------------------------
14 //place your includes here
15 //
   ------------------------------------------------------------------------------------------
16 include "lib\stdisl.isl"
17 include "lib\instrument.isl"
18 include "lib\DualInlet_lib.isl"
19 include "lib\math.isl"
20 include "lib\InterferingMassLynnOax.isl"
21
22 //LynnOax
23 const number nMaxContractionTries    =10;
24 const number FlushingCycles             =3;
25 external number Success                =0;
26 //
   ------------------------------------------------------------------------------------------
27 external string   sMultiportName          ="Lynn Oax";
28 external string   sTubeCrackerName       ="Tube Cracker";
29 external string   sLoadStd                  ="Lynn Oax/load O2std"
   ;
30 external string   sInjectStd                 ="Lynn Oax/inject
   O2std";
31
32 external number   LynnOax_SampleTransferTime =180000;
33 external number   LynnOax_PressureThreshold  =75; //for pure O2 40
34 //
   ------------------------------------------------------------------------------------------
35 external string   g_sPortName                ="";
36 external string   g_sIdentifier1Name      ="";
37 external string g_sMeasType               ="";
38 external string g_sStdInj                 ="";
39 external string g_sChecks                 ="";
40 external string g_sEquilTime              ="";
41
42 external number g_nAmountBellow        =0.0;
43 external number g_nPercentBellow        =1000;
44 external number nPa                              =0;
45 external number PAfinalIntyStd             =0;
46 external number   g_nSeqRowNumber             =0;
47 external number g_ExpansionDelay        =5000;
48 external number Press_read_waiting_time = 3000;
49 external number Flushing_Delay_Min =60000; //
50 external number Flushing_Delay_10s = 10000;
51 external number Flushing_Delay_30s =30000; //
52 external number   Dual_Inlet_Fore_Vacuum_Threshold_LynnOax =0.008;
```

```
53 external number Dual_Inlet_High_Vacuum_Threshold =0.0015;
54 external number Dual_Inlet_System_High_Vacuum_Threshold =0.0015;
55 external number Dual_Inlet_Standard_filling_High_Vacuum_Threshold
    =0.0015;
56 external number Dual_Inlet_System_High_Vacuum_Pump_Time =120000;
57 external number Dual_Inlet_StandardFilling_High_Vacuum_Pump_Time
    =30000;
58 external number nMaxPumpCycles_LynnOax        =1000;
59 external number nStdFlushingDelay = 60000; //
60 external number StdMinVolt =5000; //for O2 in air //8000 for pure
    O2!! to ensure viscous flow
61
62 //Press Adjust related
63 const number PAinitial  = 20000;
64 const number PAinitiald18O2N2  = 10000;
65 const number PAinitiald29N2  = 32000;
66 const number PAinterval  =5000;
67 const number PAmax = 45000;
68 const number PAtolerance  = 30;
69 const number PAcup = 2; //m32
70 const channel chPa = 0; //m32
71 const number nMinPress = 55; //mbar
72 const number nMinPressd18O2N2 = 81; //mbar too reach 12000 mV(
73 const number nMinPressd29N2 = 30; //mbar 19 before amplifier added,
     10G 02/2015
74 const number nMaxPressd29N2 = 60; //mbar 20 before amplifier added,
     10G 02/2015
75 //
    ------------------------------------------------------------------------------------------
76 //this is the main point entry - this function is essential
77 //
    ------------------------------------------------------------------------------------------
78
79 function EquilibrationTime() //(string sEquilTime)
80 {
81 if (_strcmp(g_sEquilTime,"cinq_s")==0)          {Flushing_Delay_Min
     =5000;}
82 if (_strcmp(g_sEquilTime,"dix_s")==0)           {Flushing_Delay_Min
     =1000;}
83 if (_strcmp(g_sEquilTime,"trente_s")==0)      {Flushing_Delay_Min
    =30000;}
84 if (_strcmp(g_sEquilTime,"soixante_s")==0)    {Flushing_Delay_Min
    =60000;}
85 if (_strcmp(g_sEquilTime,"troiscents_s")==0){Flushing_Delay_Min
    =300000;}
86 _UserInfo("equilibration time is set to %0.2f s",0,0, (
    Flushing_Delay_Min/1000));
87
88 }
89 //
    ------------------------------------------------------------------------------------------
```

```
90 function GetIntPressStd_Introduction() : number
91 {
92     bool success;
93     channel chPA_channel = chPa;
94     call DiSetVolume(Dual_Inlet_Standard,100.0); //set the volume to
           100%
95 //  call DiSetVolume(Dual_Inlet_Standard,100); //set the volume to
       100%
96
97     call DiSwitchX(Dual_Inlet_Standard,5,1,0);//
98     call SwitchChangeOver(Dual_Inlet_Standard);
99     _Delay(10000,1,"Reaching constant voltage");
100    number nStdStartPressure = call DiReadVolumePressure(
           Dual_Inlet_Standard);
101    number nStdIntro = _GetIntensityEx(chPA_channel,8000);// replace
           m32 channel by Dual_Inlet_g_nPaChannel ?
102    number nBVright = _GetCalc("Dual Inlet System/VolumeControl
           Right");
103    _UserInfo("Fully expanded after intro, Standard Intensity %0.2f
           mV, pressure in bellow is %0.2f mbar at %0.2f percent",0,0,
           nStdIntro,nStdStartPressure,nBVright);
104    return nStdStartPressure;
105 }
106 //
       ------------------------------------------------------------------------------------------------------------------------------------------------------
107 function GetIntPressSa_Introduction() : number
108 {
109    bool success;
110    channel chPA_channel = chPa;
111    call DiSetVolume(Dual_Inlet_Sample,100.0); //set the volume to
           100%
112 //  call DiSetVolume(Dual_Inlet_Standard,100); //set the volume to
       100%
113
114    call DiSwitchX(Dual_Inlet_Sample,5,1,0);//
115    call SwitchChangeOver(Dual_Inlet_Sample);
116    _Delay(10000,1,"Reaching constant voltage");
117       number nSaStartPressure = call DiReadVolumePressure(
              Dual_Inlet_Sample);
118    number nSaIntro = _GetIntensityEx(chPA_channel,8000);// replace
           m32 channel by Dual_Inlet_g_nPaChannel ?
119    number nBVleft = _GetCalc("Dual Inlet System/VolumeControl Left"
           );
120
121    _UserInfo("Fully expanded after intro, Sample Intensity %0.2f mV
           , pressure in bellow is %0.2f mbar at %0.2f percent",0,0,
           nSaIntro,nSaStartPressure,nBVleft);
122    return nSaStartPressure;
123 }
124 //
       ------------------------------------------------------------------------------------------------------------------------------------------------------
125 function GetIntPressStd_AfterPA_d29N2() : number
```

```
{
   bool success;
   channel chPA_channel = chPa;
   call DiSetVolume(Dual_Inlet_Standard,100.0); //set the volume to 100%
// call DiSetVolume(Dual_Inlet_Standard,100); //set the volume to 100%

   call DiSwitchX(Dual_Inlet_Standard,5,1,0);//
   call SwitchChangeOver(Dual_Inlet_Standard);
   _Delay(10000,1,”Reaching constant voltage”);
   number nStdPAPressure = call DiReadVolumePressure(Dual_Inlet_Standard);
   number nStdIntro = _GetIntensityEx(chPA_channel,8000);// replace m32 channel by Dual_Inlet_g_nPaChannel ?
   number nBVright = _GetCalc(”Dual Inlet System/VolumeControl Right”);
   _UserInfo(”After N2 Press Adjust, Standard Intensity %0.2f mV, pressure in bellow is %0.2f mbar at %0.2f percent”,0,0,nStdIntro,nStdPAPressure,nBVright);
   return nStdPAPressure;
}
//--------------------------------------------------------------------------------

function GetIntPressSa_AfterPA_d29N2() : number
{
   bool success;
   channel chPA_channel = chPa;
   call DiSetVolume(Dual_Inlet_Sample,100.0); //set the volume to 100%
// call DiSetVolume(Dual_Inlet_Standard,100); //set the volume to 100%

   call DiSwitchX(Dual_Inlet_Sample,5,1,0);//
   call SwitchChangeOver(Dual_Inlet_Sample);
   _Delay(10000,1,”Reaching constant voltage”);
      number nSaPAPressure = call DiReadVolumePressure(Dual_Inlet_Sample);
   number nSaIntro = _GetIntensityEx(chPA_channel,8000);// replace m32 channel by Dual_Inlet_g_nPaChannel ?
   number nBVleft = _GetCalc(”Dual Inlet System/VolumeControl Left”);

   _UserInfo(”After N2 Press Adjust, Sample Intensity %0.2f mV, pressure in bellow is %0.2f mbar at %0.2f percent”,0,0,nSaIntro,nSaPAPressure,nBVleft);
   return nSaPAPressure;
}
//--------------------------------------------------------------------------------


function DiWaitForHighVacuum(number nThreshold, number nPumpTime)
```

```
    {
        number nVacuum=0.009;
        number nCycle=0;
        while (nVacuum>nThreshold)
        {
            nVacuum=_GetCalc("Dual Inlet System/Fore Vacuum");

            _Delay(500);

        _UserInfo("DI: Waiting to reach Threshold %0.4f mBar [ %0.0f s ] : Pressure %0.4f mBar",19,3,nThreshold,nCycle,nVacuum);

            nCycle++;

            if (nCycle>nMaxPumpCycles_LynnOax)
            {
                string sInfo=_strFormat("DI: Pressure Threshold %0.4f mBar not reached : %0.4f mBar",nThreshold,nVacuum);

            _ScriptError(sInfo,ERROR_TYPE_SCR_SEQ);
            }
        }
            _Delay(nPumpTime,1,"Pump Multiport with Turbo Pump");
    }
//
    ------------------------------------------------------------------------------------------------------------------------------------------------------
function DiOpenHighVacPumpCR()
{
// _Set("Dual Inlet System/Valve 39",0); //check if I really need this redondance
    call Switch_Valve39(0);
    _Delay(DI_DEFAULT_VALVE_DELAY);
    _Set("Dual Inlet System/Valve 40",1);
}
//
    ------------------------------------------------------------------------------------------------------------------------------------------------------
function OpenSide(int nSide)
{
call DiSwitchX(nSide,3,1,200);
call DiSwitchX(nSide,4,1,200);
call DiSwitchX(nSide,6,1,200);
call DiSwitchX(nSide,5,1,200);

}
//
    ------------------------------------------------------------------------------------------------------------------------------------------------------
function OpenAllValves()
{
call OpenSide(Dual_Inlet_Sample);
call DiSwitchX(Dual_Inlet_Sample,2,1,0);
```

```
call OpenSide(Dual_Inlet_Standard);
call DiSwitchX(Dual_Inlet_Standard,2,1,0);

}
//------------------------------------------------------------------------
function PumpHighVacuum(number nThreshold, number nPumpTime)
{
    call DiOpenHighVacPumpCR();
    call DiWaitForHighVacuum(nThreshold,nPumpTime);
}


//------------------------------------------------------------------------
function CheckVacuum(int nSide, number nValveID, number nDelay): bool
{
    bool bOk=FALSE;
    call CloseVacPumps();
    call DiSwitchX(nSide,nValveID,1,nDelay); //opens valve depending on the sample side
    _Delay(Press_read_waiting_time,1,”Pump Flushed Standard with Rough Pump”);

            if (_GetCalc(”Dual Inlet System/Fore Vacuum”)>Dual_Inlet_Fore_Vacuum_Threshold_LynnOax)
            {
            call DiOpenForeVacPump();
            call DiWaitForForeVacuum(Dual_Inlet_Fore_Vacuum_Threshold_LynnOax);
            _Delay(Press_read_waiting_time,1,”4 s to get the right DI pressure”);
            }
    call PumpHighVacuum(Dual_Inlet_Standard_filling_High_Vacuum_Threshold, Dual_Inlet_StandardFilling_High_Vacuum_Pump_Time);
    bool bOK=TRUE;
    return bOk;
}

//------------------------------------------------------------------------
function DiExpandLynnOax(int nSide,number nThreshold,number nMaxTries) : bool
{
    number    nPressure;
    number    nTries;
    bool      bOk=FALSE;
    string csSaStd;

```

```
245     call DiSetVolume(nSide,100);
246     for (nTries=0;nTries<nMaxTries;nTries++;)
247     {
248         nPressure=call DiReadVolumePressure(nSide);
249
250
251
252     if (nSide    == Dual_Inlet_Sample)  {    csSaStd=_strFormat("
            DiExpand Sample Pressure %0.2f mBar",nPressure);}
253     if (nSide    == Dual_Inlet_Standard){    csSaStd=_strFormat("
            DiExpand Standard Pressure %0.2f mBar",nPressure);}
254
255         _UserInfo(csSaStd,0,0);
256         if (nPressure<=nThreshold){bOk=TRUE;break;}
257
258         _UserInfo("Expand Sample Cycle (%0.0f)",0,0,(nTries+1));
259         call DiSwitchX(nSide,4,0,0);
260         call DiSwitchX(nSide,2,0,0);
261         call DiSwitchX(nSide,1,0,0); //valve needs to be closed to
                expand sample in cross and not in the whole LynnOax line
262         call CheckVacuum(nSide,3,5000); // close vac pumps, open
                specified valve and check vacuum
263
264         call DiSwitchX(nSide,3,0,0);
265         call DiSetVolume(nSide,50);
266         call DiSwitchX(nSide,4,1,0);
267
268         _Delay(30000,1,"Expand Sample - Equilibration");
269         call DiSwitchX(nSide,4,0,0); // added August2015 to isolate
                again the bellow (maybe there was a reason??)
270         call DiSetVolume(nSide,100); //added August 2015 to read new
                pressure after expansion at 100%!!!
271         _Delay(10000,1,"Wait a bit before reading new pressure"); //
                added August2015
272     }
273
274     return bOk;
275 }
276 //
    ------------------------------------------------------------------------------------------------------------------------------------------------------
277 function DiBellowAdjust_Decrease(int nSide,number nThreshold,number
        nMaxTries) : bool
278 { // contracts progressively bellow to expand more gas in the cross
        .. Aim is to loose as little gas as possible, we may think
        about dicarding it. The threshold is 75 mbar
279     number    nPressure;
280     number    nTries;
281     number   nVolTries;
282     bool      bOk=FALSE;
283     string csSaStd;
284
285     call DiSwitchX(nSide,4,0,0);
286     call DiSwitchX(nSide,2,1,0);
```

```
    call DiSwitchX(nSide,3,1,0);
    call DiSwitchX(nSide,1,0,0);
    call CheckVacuum(nSide,3,Press_read_waiting_time); // close vac pumps, open specified valve and check vacuum
    call DiSwitchX(nSide,2,0,0);
    call DiSwitchX(nSide,3,0,0);
    call DiSwitchX(nSide,1,0,0);

    for (nTries=0;nTries<nMaxTries;nTries++;)
    {
        nVolTries = (100-(50*nTries)); //modified August2015, changed 10 by 50 to reduce cycle numbers that take time here
        nPressure=call DiReadVolumePressure(nSide);

        if (nSide   == Dual_Inlet_Sample)  {   csSaStd=_strFormat(”Sample Pressure %0.2f mBar”,nPressure);}
        if (nSide   == Dual_Inlet_Standard){   csSaStd=_strFormat(”Standard Pressure %0.2f mBar”,nPressure);}

        _UserInfo(csSaStd,0,0);

        if (nPressure<=nThreshold){bOk=TRUE;break;}

        _UserInfo(”Contract Bellow Cycle (%0.0f)”,0,1,(nTries+1));
        call DiSwitchX(nSide,4,1,0); //first loop shouldn't open this valve
        call DiSetVolume(nSide,nVolTries);
       _Delay(30000,1,”Bellow just contracted - Wait a little bit”);
        call DiSwitchX(nSide,4,0,0);
        call DiSetVolume(nSide,100);
        _Delay(30000,1,”Bellow just expanded - Wait a little bit more”);
    }
        return bOk;
}
//

// un peu tire par les cheveux, mais ca devrait fonctionner
function DiBellowAdjust_DecreaseN2(int nSide,number nThreshold, number nMaxTries) : bool
{
    number    nPressure;
    number    nTries;
    number   nVolTries;
    bool      bOk=FALSE;
    string  csSaStd;

    call DiSwitchX(nSide,4,0,0);
    call DiSwitchX(nSide,2,1,0);
    call DiSwitchX(nSide,3,1,0);
    call DiSwitchX(nSide,1,0,0);
    call CheckVacuum(nSide,3,Press_read_waiting_time); // close vac pumps, open specified valve and check vacuum
```

```
    call DiSwitchX(nSide,2,0,0);
    call DiSwitchX(nSide,3,0,0);
    call DiSwitchX(nSide,1,0,0);

    for (nTries=0;nTries<nMaxTries;nTries++;)
    {
        nVolTries = (100-(50*nTries));
        nPressure=call DiReadVolumePressure(nSide);

        if (nSide    == Dual_Inlet_Sample)  {    csSaStd=_strFormat("Sample Pressure %0.2f mBar",nPressure);}
        if (nSide    == Dual_Inlet_Standard){    csSaStd=_strFormat("Standard Pressure %0.2f mBar",nPressure);}

        _UserInfo(csSaStd,0,0);

        if (nPressure<=nThreshold){bOk=TRUE;break;}

        _UserInfo("Contract Bellow Cycle (%0.0f)",0,1,(nTries+1));
        call DiSwitchX(nSide,4,1,0); //first loop shouldn't open this valve
        call DiSetVolume(nSide,nVolTries);
       _Delay(10000,1,"Bellow just contracted - Wait a little bit");
        call DiSwitchX(nSide,4,0,0);
        call DiSetVolume(nSide,100);
        _Delay(10000,1,"Bellow just expanded - Wait a little bit more");
    }

if (nPressure>=nThreshold)
{
call DiSwitchX(nSide,2,0,0);
call DiSwitchX(nSide,3,0,0);
call CheckVacuum(nSide,3,Press_read_waiting_time); // close vac pumps, open specified valve and check vacuum
call DiSwitchX(nSide,3,0,0);

number nTries2=0;
    for (nTries2=0;nTries2<nMaxTries;nTries2++;)
    {
        nVolTries = (100-(50*nTries2));
        nPressure=call DiReadVolumePressure(nSide);

        if (nSide    == Dual_Inlet_Sample)  {    csSaStd=_strFormat("Sample Pressure %0.2f mBar",nPressure);}
        if (nSide    == Dual_Inlet_Standard){    csSaStd=_strFormat("Standard Pressure %0.2f mBar",nPressure);}

        _UserInfo(csSaStd,0,0);

        if (nPressure<=nThreshold){bOk=TRUE;break;}

        _UserInfo("Contract Bellow Cycle (%0.0f)",0,1,(nTries+1));
```

```
        call DiSwitchX(nSide,4,1,0); //first loop shouldn't open this valve
        call DiSetVolume(nSide,nVolTries);
       _Delay(10000,1,"Bellow just contracted - Wait a little bit");
        call DiSwitchX(nSide,4,0,0);
        call DiSetVolume(nSide,100);
        _Delay(10000,1,"Bellow just contracted - Wait a little bit more");
    }
}

if (nPressure>=nThreshold)
{
call DiSwitchX(nSide,2,0,0);
call DiSwitchX(nSide,3,0,0);
call CheckVacuum(nSide,3,Press_read_waiting_time); // close vac pumps, open specified valve and check vacuum
call DiSwitchX(nSide,3,0,0);
number nTries3=0;
    for (nTries3=0;nTries3<nMaxTries;nTries3++;)
    {
        nVolTries = (100-(50*nTries));
        nPressure=call DiReadVolumePressure(nSide);

        if (nSide   == Dual_Inlet_Sample)  {   csSaStd=_strFormat("Sample Pressure %0.2f mBar",nPressure);}
        if (nSide   == Dual_Inlet_Standard){   csSaStd=_strFormat("Standard Pressure %0.2f mBar",nPressure);}

        _UserInfo(csSaStd,0,0);

        if (nPressure<=nThreshold){bOk=TRUE;break;}

        _UserInfo("Contract Bellow Cycle (%0.0f)",0,1,(nTries+1));
        call DiSwitchX(nSide,4,1,0); //first loop shouldn't open this valve
        call DiSetVolume(nSide,nVolTries);
       _Delay(10000,1,"Bellow just contracted - Wait a little bit");
        call DiSwitchX(nSide,4,0,0);
        call DiSetVolume(nSide,100);
        _Delay(10000,1,"Bellow just contracted - Wait a little bit more");
    }
}
    call DiSwitchX(nSide,2,0,0);
    call DiSwitchX(nSide,3,0,0);
    call CheckVacuum(nSide,3,Press_read_waiting_time); // close vac pumps, open specified valve and check vacuum
    call DiSwitchX(nSide,3,0,0);
    return bOk;
}
//
```

```
function DiBellowAdjust_Increase(int nSide,number nMaxTries) : bool
{
   number    nPressure;
   number   nStdPressure;
   number nStdStartPressure;
   number    nTries;
   number nVolTries;
   number nStdInt;
   number nSaInt;
   number nBellowVolt;
   bool      bOk=FALSE;
   string csSaStd;

// this function is only use for the sample bellow in the current scripts last modifiedMay2016. Not part of standard refill for instance. It makes sure that the sample pressure will be higher than the standard one so a press adjust with sample as master is possible. IT SHOULD INCLUDE A STANDARD REFILL PROCEDURE in case Istd<2000 but that should not occur.

// channel chPA_channel = _GetChannelForCup(PAcup); //only exists with Isodat3.0
   channel chPA_channel = chPa;
   call DiSetVolume(Dual_Inlet_Sample,100.0); //set the volume to 100%
   call DiSetVolume(Dual_Inlet_Standard,100.0); //set the volume to 100%

   call DiSwitchX(Dual_Inlet_Standard,5,1,0);//
   call SwitchChangeOver(Dual_Inlet_Standard);
   _Delay(10000,1,"Reaching constant voltage");
   nStdStartPressure = call DiReadVolumePressure(Dual_Inlet_Standard);
   nStdInt = _GetIntensityEx(chPA_channel,8000);// replace m32 channel by Dual_Inlet_g_nPaChannel ?
   _UserInfo("Start of DIBellowIncrease, Standard Intensity %0.2f mV, pressure in bellow is %0.2f at 100 percent",0,0, nStdInt,nStdStartPressure);

 if (nStdInt<StdMinVolt) //8000mV but should be above 20mbar for viscous flow
   {
   nStdInt = _SetBellowVolt(Dual_Inlet_Standard,StdMinVolt,chPA_channel,500);
         if (nStdInt<2000)
         {
               _UserInfo("Skip preliminary bellow adjustment cause standard has not been introduced yet. Standard intensisty is %0.2f mV",0,0,nStdInt);
         }
   }

//else
// {
```

```
459     nStdPressure = call DiReadVolumePressure(Dual_Inlet_Standard);
460     for (nTries=0;nTries<nMaxTries;nTries++;)
461     {
462        nVolTries = (100-(10*(nTries+1)));
463
464        call DiSwitchX(nSide,5,1,0);// 15
465        call SwitchChangeOver(nSide);
466        _Delay(5000,1,"Reaching constant voltage");
467        nSaInt = _GetIntensityEx(chPA_channel,8000);
468        nPressure=call DiReadVolumePressure(nSide);
469 //     if (nSaInt==0) {nSaInt = nStdInt;}
470              if (nSide   == Dual_Inlet_Sample)  {csSaStd=_strFormat(
                    "After DIBellowIncrease, Sample Intensity %4.2f mV
                    Pressure %4.2f mBar, bellow contraction %0.0f (
                    cycle %0.0f)", nSaInt, nPressure ,(nVolTries+10), (
                    nTries));}
471              if (nSide   == Dual_Inlet_Standard){csSaStd=_strFormat(
                    "After DIBellowIncrease, Standard Intensity %4.2f
                    mV Pressure %4.2f mBar, bellow contraction %0.0f (
                    cycle %0.0f)", nSaInt, nPressure ,(nVolTries+10), (
                    nTries));}
472          _UserInfo(csSaStd,0,1);
473
474
475             if (nPressure>=nStdPressure)
476             {
477                      call DiSwitchX(nSide,5,1,0);// 15
478                      call SwitchChangeOver(nSide);
479                      _Delay(3000,1,"Reaching constant voltage"); //
                            modifiedMay2016 from 10000 to 3000 ms
480                      nSaInt = _GetIntensityEx(chPA_channel,8000);
481                      nPressure=call DiReadVolumePressure(nSide);
482                  if (nSide   == Dual_Inlet_Sample)  {csSaStd=
                        _strFormat("After DIBellowIncrease, Sample
                        Intensity %4.2f mV Pressure %4.2f mBar, bellow
                        contraction %0.0f ( cycle %0.0f)", nSaInt,
                        nPressure ,(nVolTries+10), (nTries));}
483                  if (nSide   == Dual_Inlet_Standard){csSaStd=
                        _strFormat("After DIBellowIncrease, Standard
                        Intensity %4.2f mV Pressure %4.2f mBar, bellow
                        contraction %0.0f ( cycle %0.0f)", nSaInt,
                        nPressure ,(nVolTries+10), (nTries));}
484                  _UserInfo(csSaStd,6,0);
485                  _UserInfo("Bellow contracted to %0.0f (Cycle %0.0f)
                        ",0,0,(nVolTries+10),(nTries));
486
487                 call SwitchChangeOver(Dual_Inlet_Standard);
488                 bOk=TRUE;
489                 break;
490             }
491             // to avoid expanding bellow to 100%
492             call DiSetVolume(nSide,nVolTries);
493             _UserInfo("Contract Bellow to %0.0f (Cycle %0.0f)",0,1,
                    nVolTries,(nTries+1));
```

```
494                 _Delay(2000,1,"Be patient");
495
496         }
497
498 //  _UserInfo("After DIBellowIncrease, Sample Intensity %0.2f mV
        Pressure %0.2f mBar, bellow contraction %0.0f ( cycle %0.0f)
        ",0,0, nSaInt, nPressure ,nVolTries, (nTries+1));
499 //      _UserInfo(csSaStd,0,0);
500
501 //}
502     return bOk;
503 }
504
505 //
        ------------------------------------------------------------------------------------------------------------------------------------
506 function Pressureadjust_LynnOax() :number
507 {
508 bool bPressAdjust=_GetSequenceFlag("Pressadjust",FALSE);
509 //bool bPressAdjustOn=TRUE;
510 number nSaInt;
511 number nSaIntfullycompressed;
512 number nPressure;
513
514 channel chPA_channel = chPa;//_GetChannelForCup(PAcup);
515 call DiSwitchX(Dual_Inlet_Sample,5,1,0);
516 call ChangeOverLeft();
517 call SwitchChangeOver(Dual_Inlet_Sample);
518 nPressure=call DiReadVolumePressure(Dual_Inlet_Sample);
519 nSaInt=_GetIntensityEx(chPA_channel,8000); //should be at 100%
520 number nBVleft = _GetCalc("Dual Inlet System/VolumeControl Left");
521 number nBVright = _GetCalc("Dual Inlet System/VolumeControl Right")
        ;
522
523 _UserInfo("After introduction and before pressAdjust, Sample
        Intensity %0.2f mV, Pressure in bellow %0.2f at %0.2f ",0,1,
        nSaInt,nPressure,nBVleft);
524 // consider to remove the upper line as it will be anyway measured
        in the IntPress_Intro function
525
526  if (bPressAdjust==TRUE)
527  {
528     call DiSwitchX(Dual_Inlet_Standard,5,1,0);
529     call SwitchChangeOver(Dual_Inlet_Standard);
530
531     _UserInfo("Start Pressure Adjustment",0,1);
532   string     csResult="?";
533     string csInfo="";
534     nPa=PAinitial;
535
536         if ((nSaInt>nPa)==TRUE)
537         {
538         _UserInfo("Sample intensity too high for Manual Press Adjust
                at %0.0f mV, swiched to PA with master as sample",0,0,
```

```
            PAinitial);
539         _ChangePaMode(PRESS_AD_RIGHT); //so needs to be in manual
                first !!!
540         _ObjectPressAdjust(DualInlet_PressAdjust,csResult)
541         csInfo="Master is Sample PressAdjust: ";
542         csInfo+=csResult;
543         _UserInfo(csInfo,0,0);
544
545     }
546
547     else
548     {
549     // alternative : use pressure instead of voltage in order not to
            affect filament with too high amount
550         call DiSetVolume(Dual_Inlet_Sample,0);
551         number nCurrPress=call DiReadVolumePressure(Dual_Inlet_Sample
                );
552
553
554         if ((nCurrPress<nMinPress)==TRUE) //2
555             {
556             _UserInfo("Sample intensity too low at full expansion for
                    Manual Pressure Adjustment at %0.0f mV ; swiched to PA
                     with master as sample",0,0,PAinitial);
557             call DiBellowAdjust_Increase(Dual_Inlet_Sample,
                    nMaxContractionTries);
558             _ChangePaMode(PRESS_AD_RIGHT); //so needs to be in manual
                    first !!!
559             _ObjectPressAdjust(DualInlet_PressAdjust,csResult)
560             csInfo="Master is Sample PressAdjust: ";
561             csInfo+=csResult;
562             _UserInfo(csInfo,0,0);
563
564             }
565       else
566       {
567
568     call DiSetVolume(Dual_Inlet_Sample,100.0);
569     _ObjectPressAdjust(DualInlet_PressAdjust,csResult)
570     csInfo="Manual PressAdjust: ";
571     csInfo+=csResult;
572     _UserInfo(csInfo,0,0);
573
574             }
575         }
576     }
577     else
578     {
579      _UserInfo("Pressure Adjustment skipped",1,0);
580     }
581
582 return TRUE;
583 }
```

```
584 //
    ------------------------------------------------------------------------------------------------------------------------------
585 function Pressureadjust_LynnOaxd18O2N2() :number
586 {
587 bool bPressAdjust=_GetSequenceFlag("Pressadjust",FALSE);
588 //bool bPressAdjustOn=TRUE;
589 number nSaInt;
590 number nSaIntfullycompressed;
591 number nPressure;
592
593 channel chPA_channel = chPa;//_GetChannelForCup(PAcup);
594 call DiSwitchX(Dual_Inlet_Sample,5,1,0);
595 call ChangeOverLeft();
596 call SwitchChangeOver(Dual_Inlet_Sample);
597 nPressure=call DiReadVolumePressure(Dual_Inlet_Sample);
598 nSaInt=_GetIntensityEx(chPA_channel,8000); //should be at 100%
599 number nBVleft = _GetCalc("Dual Inlet System/VolumeControl Left");
600 number nBVright = _GetCalc("Dual Inlet System/VolumeControl Right")
    ;
601
602 _UserInfo("After introduction and before pressAdjust, Sample
    Intensity %0.2f mV, Pressure in bellow %0.2f at %0.2f ",0,1,
    nSaInt,nPressure,nBVleft);
603 // consider to remove the upper line as it will be anyway measured
    in the IntPress_Intro function
604
605  if (bPressAdjust==TRUE)
606  {
607    call DiSwitchX(Dual_Inlet_Standard,5,1,0);
608    call SwitchChangeOver(Dual_Inlet_Standard);
609
610    _UserInfo("Start Pressure Adjustment",0,1);
611   string     csResult="?";
612    string csInfo="";
613    nPa=PAinitiald18O2N2;
614
615     if ((nSaInt>nPa)==TRUE)
616     {
617       _UserInfo("Sample intensity too high for Manual Press Adjust
            at %0.0f mV, swiched to PA with master as sample",0,0,
            PAinitiald18O2N2);
618
619       //_ChangePaMode(PRESS_AD_RIGHT); //so needs to be in manual
            first !!!
620         call DiBellowAdjust_Increase(Dual_Inlet_Sample,
              nMaxContractionTries);// added line but should not
              happen that  modifiedMay2016 CR
621               _ChangePaMode(PRESS_AD_LEFT);// modifiedMay2016 CR to
                  LEFT
622       _ObjectPressAdjust(DualInlet_PressAdjust,csResult)
623       csInfo="Master is Sample PressAdjust: ";
624       csInfo+=csResult;
625       _UserInfo(csInfo,0,0);
```

```
626
627     }
628
629     else
630     {
631     // alternative : use pressure instead of voltage in order not to
          affect filament with too high amount
632        call DiSetVolume(Dual_Inlet_Sample,0);
633        number nCurrPress=call DiReadVolumePressure(Dual_Inlet_Sample
            );
634
635
636          if ((nCurrPress<nMinPressd18O2N2)==TRUE) //2
637          {
638           _UserInfo("Sample intensity too low at full expansion for
               Manual Pressure Adjustment at %0.0f mV ; swiched to PA
                with master as sample",0,0,PAinitiald18O2N2);
639           call DiBellowAdjust_Increase(Dual_Inlet_Sample,
               nMaxContractionTries); //some time may be gained here
               as the called function expands bellow to 100% while it
                should not be needed. On the other hand
640           //_ChangePaMode(PRESS_AD_RIGHT); //so needs to be in
               manual first !!!
641              _ChangePaMode(PRESS_AD_LEFT); //so needs to be in
                  manual first !!! changed to left on 100815 by
                  Isabell
642           _ObjectPressAdjust(DualInlet_PressAdjust,csResult)
643           csInfo="Master is Sample PressAdjust: ";
644           csInfo+=csResult;
645           _UserInfo(csInfo,0,0);
646           }
647           else
648          {
649                call DiSetVolume(Dual_Inlet_Sample,100.0);
650                _ObjectPressAdjust(DualInlet_PressAdjust,csResult)
651                csInfo="Manual PressAdjust: ";
652                csInfo+=csResult;
653                _UserInfo(csInfo,0,0);
654           }
655          }
656  }
657 // this function requires Standard Intensity to be always lower
      than PAinitiald1802n2 at 100 % otherwise PA manual or PA with
      sample as master will fail.
658  else
659  {
660   _UserInfo("Pressure Adjustment skipped",1,0);
661  }
662
663 return TRUE;
664 }
665 //
      ------------------------------------------------------------------------------------------
```

```
666 function Pressureadjust_LynnOaxd29N2() :number
667 {
668 bool bPressAdjust=_GetSequenceFlag("Pressadjust",FALSE);
669 //bool bPressAdjustOn=TRUE;
670 number nSaInt;
671 number nStdInt;
672 number nSaIntfullycompressed;
673 number nPressure;
674 number nStdPAPressure;
675 number nSaPAPressure;
676
677 channel chPA_channel = chPa;//_GetChannelForCup(PAcup);
678 call DiSwitchX(Dual_Inlet_Sample,5,1,0);
679 call ChangeOverLeft();
680 call SwitchChangeOver(Dual_Inlet_Sample);
681 nPressure=call DiReadVolumePressure(Dual_Inlet_Sample);
682 nSaInt=_GetIntensityEx(chPA_channel,8000); //should be at 100%
683 number nBVleft = _GetCalc("Dual Inlet System/VolumeControl Left");
684 number nBVright = _GetCalc("Dual Inlet System/VolumeControl Right")
      ;
685
686 _UserInfo("After introduction and before pressAdjust, Sample
      Intensity %0.2f mV, Pressure in bellow %0.2f at %0.2f ",0,1,
      nSaInt,nPressure,nBVleft);
687 // consider to remove the upper line as it will be anyway measured
      in the IntPress_Intro function
688
689  if (bPressAdjust==TRUE)
690  {
691    call DiSwitchX(Dual_Inlet_Standard,5,1,0);
692    call SwitchChangeOver(Dual_Inlet_Standard);
693    nStdInt=_GetIntensityEx(chPA_channel,8000); //should be at 100%
694
695    _UserInfo("Start Pressure Adjustment",0,1);
696   string     csResult="?";
697    string csInfo="";
698    nPa=PAinitiald29N2;
699
700        if ((nStdInt>nPa)==TRUE)
701        {
702        _UserInfo("Standard intensity too high for Manual Press
            Adjust at %0.0f mV, check if gas needs to be removed from
             bellow",0,0,PAinitiald29N2);
703        call DiBellowAdjust_DecreaseN2(Dual_Inlet_Standard,
            nMaxPressd29N2,3);
704
705           nPressure=call DiReadVolumePressure(Dual_Inlet_Standard);
706           if nPressure>nMaxPressd29N2
707           {
708           call DiBellowAdjust_DecreaseN2(Dual_Inlet_Standard,
               nMaxPressd29N2,3);
709           }
710           nPressure=call DiReadVolumePressure(Dual_Inlet_Standard);
711           if nPressure>nMaxPressd29N2
```

```
712            {
713            call DiBellowAdjust_DecreaseN2(Dual_Inlet_Standard,
                   nMaxPressd29N2,3);
714            }
715          nStdPAPressure = call GetIntPressStd_AfterPA_d29N2();
716         }
717
718        if ((nSaInt>nPa)==TRUE)
719        {
720            _UserInfo("Sample intensity too high for Manual Press
                   Adjust at %0.of mV, check if gas needs to be removed
                   from bellow",0,0,PAinitiald29N2);
721            call DiBellowAdjust_DecreaseN2(Dual_Inlet_Sample,
                   nMaxPressd29N2,3);
722
723            nPressure=call DiReadVolumePressure(Dual_Inlet_Sample);
724            if nPressure>nMaxPressd29N2
725            {
726            call DiBellowAdjust_DecreaseN2(Dual_Inlet_Sample,
                   nMaxPressd29N2,3);
727            }
728            nPressure=call DiReadVolumePressure(Dual_Inlet_Sample);
729            if nPressure>nMaxPressd29N2
730            {
731            call DiBellowAdjust_DecreaseN2(Dual_Inlet_Sample,
                   nMaxPressd29N2,3);
732            }
733
734            call DiSwitchX(Dual_Inlet_Sample,5,1,0);
735            //call ChangeOverLeft();
736            call SwitchChangeOver(Dual_Inlet_Sample);
737            nSaPAPressure = call GetIntPressSa_AfterPA_d29N2();
738
739        call DiSetVolume(Dual_Inlet_Sample,100.0);
740        _ObjectPressAdjust(DualInlet_PressAdjust,csResult)
741        csInfo="Manual PressAdjust: ";
742        csInfo+=csResult;
743        _UserInfo(csInfo,0,0);
744        }
745
746    else
747    {
748    // alternative : use pressure instead of voltage in order not to
           affect filament with too high amount
749        call DiSetVolume(Dual_Inlet_Sample,0);
750        number nCurrPress=call DiReadVolumePressure(Dual_Inlet_Sample
               );
751
752
753        if ((nCurrPress<nMinPressd29N2)==TRUE) //2
754            {
755            _UserInfo("Sample intensity too low at full contraction
                   for Manual Pressure Adjustment at %0.of mV ; swiched
                   to PA with master as sample",0,0,PAinitial);
```

```
            call DiBellowAdjust_Increase(Dual_Inlet_Sample, nMaxContractionTries);
            _ChangePaMode(PRESS_AD_RIGHT); //so needs to be in manual first !!!
            _ObjectPressAdjust(DualInlet_PressAdjust, csResult)
            csInfo="Master is Sample PressAdjust: ";
            csInfo+=csResult;
            _UserInfo(csInfo,0,0);

            }
       else
       {

            call DiSetVolume(Dual_Inlet_Sample,100.0);
            _ObjectPressAdjust(DualInlet_PressAdjust, csResult)
            csInfo="Manual PressAdjust: ";
            csInfo+=csResult;
            _UserInfo(csInfo,0,0);
            }
        }
    }
    else
    {
      _UserInfo("Pressure Adjustment skipped",1,0);
    }

return TRUE;
}
//
function WaitForScanEnd() :bool
{
    while(_IsScanning()==TRUE)
    {
        _Delay(1000);
    }
    return FALSE;
}
//


function MassScanning() : bool
{
bool sOK = _StartDACScan(MAGNET,2000,12000,100);
call WaitForScanEnd();
// sOK=_SaveFile("C:\Thermo\Isodat NT\Global\User\Dual Inlet System\Results\ACQ_O2_Results\Scans"


return sOK;
}
```

```
802 //
    ------------------------------------------------------------------------------------------------------------
803 //function InfoMCR
804 //_GetGasConfMass
805 //_GetResistor
806 //_GetChannelForCup
807 //_GetConfigurationName
808 //
    ------------------------------------------------------------------------------------------------------------
809
810 function MpReadMultiportPressure() : number
811 {
812
813     string sGauge="Isotope MS/";
814     sGauge+=sMSInstMultiportName;
815     number nPressure=_GetCalc(sGauge);
816
817     return nPressure;
818 }
819 //
    ------------------------------------------------------------------------------------------------------------
820 function MpSwitchValve(string sValveName,int nState)
821 {
822     string sValve=sMultiportName;
823     sValve+="/";
824     sValve+=sValveName;
825
826     _Set(sValve,nState);
827 }
828 //
    ------------------------------------------------------------------------------------------------------------
829 function MpCrackTube(string sPort)
830 {
831     string sNumber=_strright(sPort,(_strlen(sPort) - 6));
832
833     string sCracker=sTubeCrackerName;
834     sCracker+="/Cracker";
835     sCracker+=sNumber;
836
837     _Set(sCracker,1);
838     _Delay(1000);
839     _Set(sCracker,0);
840 }
841 //
    ------------------------------------------------------------------------------------------------------------
842 function MpSampleValve(string sPort,int nState)
843 {
844     string sNumber=_strright(sPort,(_strlen(sPort) - 6)); //get rid
        of sample string and keeps number
```

```
845
846     string sSwitch=sMultiportName;
847     sSwitch+="/Valve";
848     sSwitch+=sNumber;
849
850     _Set(sSwitch,nState);
851 }
852 //
    ------------------------------------------------------------------------------------------------------------------------------------------
853 function MpConnect(bool bConnect)
854 {
855     int nState=bConnect;
856
857     _ConnectDev("Lynn Oax",bConnect);
858     call MpSwitchValve("Dual Inlet System/Valve 11",nState);
859 }
860 //
    ------------------------------------------------------------------------------------------------------------------------------------------
861
862 function MpPump()
863 {
864     _UserInfo("Pump Sample Side",0,1);
865
866     //
        ..............................................................................................................
867     //Multiport
868     //
        ..............................................................................................................
869     call DiSetVolume(Dual_Inlet_Sample,100.0); //set the volume to
            100%
870
871     //call MpConnect(1); see below for substitution
872    call DiSwitchX(Dual_Inlet_Sample,1,1,0); //opens either 11 or 21
          depending on the sample side
873
874        if (_GetCalc("Dual Inlet System/Fore Vacuum")>
               Dual_Inlet_Fore_Vacuum_Threshold_LynnOax)
875        {       call DiPumpSide(Dual_Inlet_Sample,
               Dual_Inlet_Fore_Vacuum_Threshold_LynnOax);
876                _Delay(Dual_Inlet_Fore_Vacuum_Pump_Time,1,"Pump
                      Multiport with Rough Pump");}
877        else
878        {
879        call DiOpenHighVacPumpCR();
880        call OpenSide(Dual_Inlet_Sample); //opens 13 14 15 16
881        }
882        call PumpHighVacuum(Dual_Inlet_High_Vacuum_Threshold,
               Dual_Inlet_System_High_Vacuum_Pump_Time);
883
884     //call MpSwitchValve("Waste",0);  not needed
```

```
885
886     //call MpConnect(0);
887     call DiSwitchX(Dual_Inlet_Sample,1,0,0); //closes either 11 or
            21 depending on the sample side
888     call DiCloseSide(Dual_Inlet_Sample); //13, 14, 15 , and 16
            closed
889
890     _Delay(DI_DEFAULT_VALVE_DELAY);
891 }
892 //
        ------------------------------------------------------------------------------------------
893 //
        ------------------------------------------------------------------------------------------
894
895 function Vacuuming()
896 {
897     _UserInfo("Pump Dual Inlet System yeah",0,1);
898
899     call ChangeOverClose();
900     call DiSetVolume(Dual_Inlet_Sample,100.0); //set the volume to
            100%
901     call DiSetVolume(Dual_Inlet_Standard,100.0); //set the volume to
             100%
902     call CloseVacPumps();
903     call OpenAllValves();
904     _Delay(Press_read_waiting_time,1,"4 s to get the right DI
            pressure");
905
906
907         if (_GetCalc("Dual Inlet System/Fore Vacuum")>
                Dual_Inlet_Fore_Vacuum_Threshold_LynnOax)
908         {
909                 call DiOpenForeVacPump();
910                 call DiWaitForForeVacuum(
                        Dual_Inlet_Fore_Vacuum_Threshold_LynnOax);
911                 _Delay(Dual_Inlet_Fore_Vacuum_Pump_Time,1,"Pumping Dual
                         Inlet System with Rough Pump");
912         }
913
914     call PumpHighVacuum(Dual_Inlet_System_High_Vacuum_Threshold,
            Dual_Inlet_High_Vacuum_Pump_Time);
915     _Delay(DI_DEFAULT_VALVE_DELAY);
916 }
917
918 //
        ------------------------------------------------------------------------------------------
919 function GetPortName() : bool
920 {
921     bool bResult=TRUE; // Do I need to add IsDeviceAvailable ?
922     g_sPortName=_GetSequenceText("Lynn Oax Inlet","none");
923     g_sIdentifier1Name=_GetSequenceText("Identifier 1","none");
```

```
924     string sSampleIDnumber=_strright(g_sPortName,(_strlen(
            g_sPortName) - _strlen("sample"))); //get rid of sample
            string and keeps number
925     string sSampleIDstring=_strleft(g_sPortName,(_strlen(g_sPortName
            ) - (_strlen(sSampleIDnumber) )));
926     string sSampleID="ID of measured sample is ";
927     if (_strcmp(sSampleIDstring,"sample")==0){sSampleID+=
            sSampleIDnumber;}
928     else{sSampleID+="none";} //mars2013 : replaced standard by none,
             does not make sense to keep standard here as there is
            another column for identification
929     sSampleID+=": ";
930     sSampleID+=g_sIdentifier1Name;
931    _UserInfo(sSampleID,0,0);
932
933     return bResult;
934 }
935 //
        ------------------------------------------------------------------------------------------
936 function MpTransferMp() : bool
937 {
938     call SwitchChangeOver(Dual_Inlet_Standard);
939
940     call MpPump();
941
942     bool bOk=FALSE;
943
944         call DiSetVolume(Dual_Inlet_Sample,100.0);
945         call DiSwitchX(Dual_Inlet_Sample,1,1,0); //11  call MpConnect
                (1);
946
947         call DiSwitchX(Dual_Inlet_Sample,4,1,0);// 14
948         call DiSwitchX(Dual_Inlet_Sample,2,0,0);// 12 to be safe
949
950         call MpSampleValve(g_sPortName,0); //open Lynn Oax valve (0
                cause inversed normal state)
951         _Delay(LynnOax_SampleTransferTime,1,"Sample Transfertime");
952         bOk = call DiBellowAdjust_Decrease(Dual_Inlet_Sample,
                LynnOax_PressureThreshold,3); //modified August2015
953         if (bOk==FALSE)
954         {
955         call DiSetVolume(Dual_Inlet_Sample,100); //put the bellow
                back to 100% before press adjust
956         call CloseVacPumps();
957         bOk= call DiExpandLynnOax(Dual_Inlet_Sample,
                LynnOax_PressureThreshold,nMaxContractionTries); //
                modified August2015
958         call DiSwitchX(Dual_Inlet_Sample,4,0,0); // close 14
959             if (bOk==FALSE){ _ScriptError("Multiport Expansion failed!
                    ",ERROR_TYPE_SCR_SEQ);}
960         }
961         call MpSampleValve(g_sPortName,1); //close Lynn Oax valve (1
                cause inversed normal state)
```

```
        call DiSwitchX(Dual_Inlet_Sample,1,0,0); //close 11  call MpConnect(0);
        call DiSwitchX(Dual_Inlet_Sample,4,0,0); //close 14  call MpConnect(0); should already be closed
//      bOk=call DiBellowAdjust_Increase(Dual_Inlet_Sample, nMaxContractionTries);
        call DiSwitchX(Dual_Inlet_Sample,5,1,0); // why 15 ?
    return bOk;
}
//
function MpTransfer() : bool
{
    call DiSwitchX(Dual_Inlet_Sample,1,0,0);
    call CloseVacPumps();
    call DiSwitchX(Dual_Inlet_Sample,4,1,0);
    call DiSwitchX(Dual_Inlet_Sample,3,1,0);
    _Delay(1000,1,"Check if bellow is empty");
    call DiSwitchX(Dual_Inlet_Sample,4,0,0);

    bool bMeasure=call GetPortName();
    if (bMeasure){call MpTransferMp();}

    return 1;
}
//

function checkVacStdAA() : bool
{
        bool bOk=FALSE;
    call CloseVacPumps();
    //isolate standard aliquot line to pump
    call DiSwitchX(Dual_Inlet_Standard,2,0,DI_DEFAULT_VALVE_DELAY);
    call DiSwitchX(Dual_Inlet_Standard,4,0,DI_DEFAULT_VALVE_DELAY);
    call DiSwitchX(Dual_Inlet_Standard,6,0,DI_DEFAULT_VALVE_DELAY);
    call DiSwitchX(Dual_Inlet_Sample,3,0,DI_DEFAULT_VALVE_DELAY);
    call DiSwitchX(Dual_Inlet_Sample,6,0,DI_DEFAULT_VALVE_DELAY);
    call DiSwitchX(Dual_Inlet_Standard,1,1,DI_DEFAULT_VALVE_DELAY);
    call DiSwitchX(Dual_Inlet_Standard,3,1,DI_DEFAULT_VALVE_DELAY);
    _Set(sLoadStd,1); //closing Std upstream
    _Set(sInjectStd,0); //opening aliquot StdAA
    _Delay(Press_read_waiting_time,1,"Be patient, getting the right pressure");

            if (_GetCalc("Dual Inlet System/Fore Vacuum")>Dual_Inlet_Fore_Vacuum_Threshold_LynnOax)
            {
            call DiOpenForeVacPump();
            call DiWaitForForeVacuum(Dual_Inlet_Fore_Vacuum_Threshold_LynnOax);
```

```
1005            _Delay(Press_read_waiting_time,1,"4 s to get the right DI
                    pressure");
1006            }
1007    call PumpHighVacuum(
            Dual_Inlet_Standard_filling_High_Vacuum_Threshold,
            Dual_Inlet_StandardFilling_High_Vacuum_Pump_Time);
1008    //back to initial valve configuration. Better to ensure v4's and
            v6's are still closed
1009    _Set(sInjectStd,1); //closing (inversed too?)
1010    call CloseVacPumps(); //added cause comes before checking inner
            lines
1011    call DiSwitchX(Dual_Inlet_Standard,1,0,DI_DEFAULT_VALVE_DELAY);
1012
1013    return bOk;
1014
1015 }
1016
1017 //
        ------------------------------------------------------------------------------------------------------------
1018 function StdAA_introduction(number eq_delay) : bool
1019 {
1020 bool bintOk=FALSE;
1021
1022    _Set(sInjectStd,1); //closing
1023    _Set(sLoadStd,1);     //closing
1024    _Delay(1000);
1025    _Set(sLoadStd,0);     //opening
1026    _Delay(eq_delay,1,"Loading Standard to StdAA");
1027    _Set(sLoadStd,1);     //closing
1028    _Delay(eq_delay,1,"Standard equilibrating in StdAA");
1029    return bintOk;
1030 }
1031 //
        ------------------------------------------------------------------------------------------------------------
1032
1033 function Flushing(number nMaxFlush) : bool
1034 {
1035
1036    number    nFlush;
1037    bool      bOk=FALSE;
1038
1039    //1.
1040 // string szActionMessage = "Please open the standard line (3 SS4H
        valves, one is upstream the pressure regulator ) and make sure
        P regulator not above .2 bar overpressure";
1041 // _MessageBox(szActionMessage,MB_OK,MB_ICONEXCLAMATION);
1042
1043        _UserInfo("Hope you didn't forget to open the standard line,
                check that pressure is at 1.2bar overpressure",0,1);
1044
1045
1046    for (nFlush=0;nFlush<nMaxFlush;nFlush++;)
```

```
1047    {
1048        call DiSwitchX(Dual_Inlet_Sample,1,0,0);
1049        call DiSwitchX(Dual_Inlet_Sample,4,0,0);
1050        call DiSwitchX(Dual_Inlet_Sample,2,1,0);
1051        call DiSwitchX(Dual_Inlet_Standard,2,1,0);
1052        //make sure DI ext right is evacuated
1053        _Set(sLoadStd,1); //closing Std upstream
1054        _Set(sInjectStd,0); //opening aliquot StdAA
1055        call DiSwitchX(Dual_Inlet_Standard,1,1,0);
1056        bool boOk = call CheckVacuum(Dual_Inlet_Standard,3,
            DI_DEFAULT_VALVE_DELAY); // close vac pumps, open
            specified valve and check vacuum
1057
1058        call DiSwitchX(Dual_Inlet_Standard,4,0,0);
1059        call DiSwitchX(Dual_Inlet_Standard,6,0,0);
1060        call DiSwitchX(Dual_Inlet_Sample,6,0,0);
1061        call DiSwitchX(Dual_Inlet_Sample,3,0,0);
1062        call DiSwitchX(Dual_Inlet_Standard,3,0,0);
1063        call StdAA_introduction(Flushing_Delay_10s);
1064        _Set(sInjectStd,0);      //opening StdAA to MS
1065        string sFlushMessage = _strFormat("Std Wall Equilibration
            cycle %0.0f",(nFlush+1));
1066        call CloseVacPumps();
1067        _Delay(Flushing_Delay_10s,1,sFlushMessage);
1068        call CloseVacPumps();
1069        //call DiSwitchX(Dual_Inlet_Standard,1,0,0);
1070        call DiSwitchX(Dual_Inlet_Standard,3,1,
            Press_read_waiting_time);
1071        _Delay(Press_read_waiting_time,1,"3 s to get the right DI
            pressure");
1072
1073            if (_GetCalc("Dual Inlet System/Fore Vacuum")>
                Dual_Inlet_Fore_Vacuum_Threshold_LynnOax)
1074            {
1075            call DiOpenForeVacPump();
1076            call DiWaitForForeVacuum(
                Dual_Inlet_Fore_Vacuum_Threshold_LynnOax);
1077            _Delay(Dual_Inlet_Fore_Vacuum_Threshold_LynnOax,1,"Pumping
                Flushed Standard with Rough Pump");
1078            }
1079            else
1080            {
1081            _MessageBox("You probably forgot to introduce the standard
                in the line... Try again",MB_OK,MB_ICONEXCLAMATION);
1082            call Flushing(nMaxFlush);
1083            }
1084            call PumpHighVacuum(
                Dual_Inlet_Standard_filling_High_Vacuum_Threshold,
                Dual_Inlet_StandardFilling_High_Vacuum_Pump_Time);
1085        }
1086        call DiSwitchX(Dual_Inlet_Standard,1,0,0);
1087        _Set(sInjectStd,1);      //closing
1088
1089    return bOk;
```

```
}
//
function CompressBellowOption(int nSide,number nCompression) : bool
{
bool bOk = FALSE;
bool bPILeft=_GetSequenceFlag("Pleft+",FALSE);
bool bPIRight=_GetSequenceFlag("Pright+",FALSE);

      if bPILeft
      {
      call DiSetVolume(Dual_Inlet_Sample,nCompression);
      _UserInfo("Left (Sa) Bellow has been set to %0.2f percent",0,0,nCompression);
      }
      if bPIRight
      {
      call DiSetVolume(Dual_Inlet_Standard,nCompression);
      _UserInfo("Right (Std) Bellow has been set to %0.2f percent",0,0,nCompression);
      }
return bOk;
}
//
function StdTransferDIRIGHT() : bool
{

   bool bOk = FALSE;
   bool boOk = FALSE;

    call Flushing(1); // line added to ensure flushing at each std introduction
   call DiSetVolume(Dual_Inlet_Standard,100.0);

   call DiSwitchX(Dual_Inlet_Sample,4,0,0); //should be closed
   call DiSwitchX(Dual_Inlet_Sample,1,0,0); //should be closed
   call DiSwitchX(Dual_Inlet_Sample,6,0,0); //should be closed

   call CloseVacPumps();
   call DiSwitchX(Dual_Inlet_Sample,2,1,0);
   call OpenSide(Dual_Inlet_Standard);
   call DiSwitchX(Dual_Inlet_Sample,3,1,0);
   //make sure DI ext right is evacuated
   _Set(sLoadStd,1); //closing Std upstream
   _Delay(1000);
   _Set(sInjectStd,0); //opening aliquot StdAA
   call DiSwitchX(Dual_Inlet_Standard,1,1,0);

   // call checkVacStdAA();
   boOk = call CheckVacuum(Dual_Inlet_Standard,2,Press_read_waiting_time); // close vac pumps, open specified
```

```
        valve and check vacuum
//***** currently 1 2 3 4 5 6 std side and 2 3 sample side opened ****//


    //Amount in bellow

    if (g_nAmountBellow == 0.5) //16mbar
    {
        call DiSwitchX(Dual_Inlet_Standard,2,0,0);
    }

        if (g_nAmountBellow==0.6)
    {
        call DiSetVolume(Dual_Inlet_Standard,80.0);
    }

    if (g_nAmountBellow == 1.0)  //28 mbar
    {
        call DiSetVolume(Dual_Inlet_Standard,100.0);
    }

    if (g_nAmountBellow == 1.3)  //34 mbar
    {
        call DiSetVolume(Dual_Inlet_Standard,100.0);
    }

    if ((g_nAmountBellow == 0.0) || (g_nAmountBellow == 0.1) || (
        g_nAmountBellow == 0.2) || (g_nAmountBellow == 0.3) ||(
        g_nAmountBellow == 0.4) ||(g_nAmountBellow == 0.7) ||(
        g_nAmountBellow == 0.8) ||(g_nAmountBellow == 0.9) ||(
        g_nAmountBellow == 1.1) ||(g_nAmountBellow == 1.2) ||(
        g_nAmountBellow == 1.4) ||(g_nAmountBellow == 1.5) ||(
        g_nAmountBellow == 1.6) ||(g_nAmountBellow == 1.7) ||(
        g_nAmountBellow == 1.8))
    {
        call DiSetVolume(Dual_Inlet_Standard,8.0);
        call DiSetVolume(Dual_Inlet_Sample,8.0);
    _UserInfo("this amount hasn't been stricto sensu defined "
        ,0,1);

    }

 // common introduction
            // call at last to respect equilibration time between
                runs
        if (g_nPercentBellow!=1000) {call CompressBellowOption(
            Dual_Inlet_Standard,g_nPercentBellow);}
        call StdAA_introduction(Flushing_Delay_Min);
    //isolate standard aliquot line to pump
    call DiSwitchX(Dual_Inlet_Sample,3,0,1000);
    call DiSwitchX(Dual_Inlet_Standard,4,0,DI_DEFAULT_VALVE_DELAY
        );
```

```
        call DiSwitchX(Dual_Inlet_Standard,3,0,DI_DEFAULT_VALVE_DELAY);
        _Set(sInjectStd,0); //opening (inversed too)
        _Delay(Flushing_Delay_Min,1,"Standard Transfer to Standard, Sample Cross and inner line, IT as good as it can be in separate filling");

    _UserInfo("amount introduced in right standard bellow is roughly %0.2f cc",0,1,g_nAmountBellow);
    call DiSwitchX(Dual_Inlet_Standard,1,0,DI_DEFAULT_VALVE_DELAY);
    _Set(sInjectStd,1); //closing
    _Delay(Flushing_Delay_Min,1,"DI Ext right closed");
    call DiSwitchX(Dual_Inlet_Standard,5,0,1000);
    call DiSwitchX(Dual_Inlet_Standard,4,1,DI_DEFAULT_VALVE_DELAY);
    _Delay(Flushing_Delay_Min,1,"Standard Transfer to Bellows");
    call DiSwitchX(Dual_Inlet_Standard,4,0,DI_DEFAULT_VALVE_DELAY);
    call DiSetVolume(Dual_Inlet_Standard,100.0);
    _Delay(Flushing_Delay_Min,1,"Standard Equilibration Bellows");
    call DiSwitchX(Dual_Inlet_Standard,6,0,1000);

// call CloseVacPumps(); done with DiExpand
    bOk= call DiExpandLynnOax(Dual_Inlet_Standard, LynnOax_PressureThreshold,nMaxExpansionTries);
    call DiSwitchX(Dual_Inlet_Standard,4,0,DI_DEFAULT_VALVE_DELAY);

// bOkbis=call DiBellowAdjust_Increase(Dual_Inlet_Standard, nMaxContractionTries);
    call DiSwitchX(Dual_Inlet_Standard,5,1,DI_DEFAULT_VALVE_DELAY);
    return bOk;
}
//
    ------------------------------------------------------------------------------------------------------------------------------------------------------

function StdRefill() : bool
{
bool bOk = FALSE;
g_sPortName=_GetSequenceText("Lynn Oax Inlet","none");
channel chPA_channel = chPa;

call DiSetVolume(Dual_Inlet_Standard,100.0);
//call DiSwitchX(Dual_Inlet_Standard,5,1,0);
//call SwitchChangeOver(Dual_Inlet_Standard);
number nRefill = call DiReadVolumePressure(Dual_Inlet_Standard);
if (nRefill<25)
    {
    //call Flushing(1); // FlushingCycles default =3  Line removed modifiedMay2016
    call StdTransferDIRIGHT();
    }
return bOk;
}

//
    ------------------------------------------------------------------------------------------------------------------------------------------------------
```

```
function StdTransferDILEFT() : bool
{

   bool bOk = FALSE;
   bool bOkbis = FALSE;
   bool boOk = FALSE;

    call Flushing(1);
   call DiSetVolume(Dual_Inlet_Sample,100.0); //put the bellow back to 100% before press adjust

   call DiSwitchX(Dual_Inlet_Standard,3,0,0);
   call DiSwitchX(Dual_Inlet_Standard,4,0,0);
   call DiSwitchX(Dual_Inlet_Sample,1,0,0);
   call DiSwitchX(Dual_Inlet_Standard,6,0,0);

   call CloseVacPumps();
   call DiSwitchX(Dual_Inlet_Standard,2,1,0);
   call OpenSide(Dual_Inlet_Sample); // 3 4 5 6
   call DiSwitchX(Dual_Inlet_Standard,3,1,0);
   //make sure DI ext right is evacuated
   _Set(sLoadStd,1); //closing Std upstream
   _Delay(1000);
   _Set(sInjectStd,0); //opening aliquot StdAA
   call DiSwitchX(Dual_Inlet_Standard,1,1,0);
   boOk = call CheckVacuum(Dual_Inlet_Sample,2,Press_read_waiting_time); // close vac pumps, open specified valve and check vacuum
  //***** currently 2 3 4 5 6 sample side and 1 2 3 standard side opened ****//


          //Amount in bellow
//      if (_strcmp(g_sAmountBellow,"na")==0)
       if (g_nAmountBellow == 0.6) //16mbar
       {
       call DiSetVolume(Dual_Inlet_Sample,80.0);
       }
       if (g_nAmountBellow == 1.0)  //28 mbar
       {
          call DiSetVolume(Dual_Inlet_Sample,100.0);
       }
       if (g_nAmountBellow == 1.3)  //34 mbar
       {
          call DiSetVolume(Dual_Inlet_Sample,100.0);
       }
          if ((g_nAmountBellow == 0.0) || (g_nAmountBellow == 0.1) || (g_nAmountBellow == 0.2) || (g_nAmountBellow == 0.3) ||(g_nAmountBellow == 0.4)||(g_nAmountBellow == 0.5) ||(g_nAmountBellow == 0.7) ||(g_nAmountBellow == 0.8) ||(g_nAmountBellow == 0.9) ||(g_nAmountBellow == 1.1) ||(g_nAmountBellow == 1.2) ||(g_nAmountBellow == 1.4) ||(g_nAmountBellow == 1.5) ||(g_nAmountBellow ==
```

```
                1.6) ||(g_nAmountBellow == 1.7) ||(g_nAmountBellow ==
                1.8))
        {
            call DiSetVolume(Dual_Inlet_Sample,8.0);
            call DiSetVolume(Dual_Inlet_Sample,8.0);
            _UserInfo("this amount hasn't been defined yet",0,1);
        }

    // common introduction
    // call at last to respect equilibration time between runs
    if (g_nPercentBellow!=1000) {call CompressBellowOption(
        Dual_Inlet_Sample,g_nPercentBellow);}
    call StdAA_introduction(Flushing_Delay_Min);
    //isolate standard aliquot line to pump
    call DiSwitchX(Dual_Inlet_Standard,3,0,1000);
    call DiSwitchX(Dual_Inlet_Sample,4,0,DI_DEFAULT_VALVE_DELAY);
    call DiSwitchX(Dual_Inlet_Sample,3,0,DI_DEFAULT_VALVE_DELAY);
    _Set(sInjectStd,0); //opening (inversed too)
    _Delay(Flushing_Delay_Min,1,"Standard Transfer to Standard,
        Sample Cross and inner line, IT as good as it can be in
        separate filling");

// _Set(sInjectStd,1); //closing (inversed too?)
    call DiSwitchX(Dual_Inlet_Standard,1,0,DI_DEFAULT_VALVE_DELAY);
    _Set(sInjectStd,1); //closing
    _UserInfo("amount introduced in left sample bellow is roughly
        %0.2f cc",0,1,g_nAmountBellow);
    _Delay(Flushing_Delay_Min,1,"DI Ext right closed");
    call DiSwitchX(Dual_Inlet_Sample,5,0,1000);
    call DiSwitchX(Dual_Inlet_Sample,4,1,DI_DEFAULT_VALVE_DELAY);
    _Delay(Flushing_Delay_Min,1,"Standard Transfer to left Bellow");
    call DiSwitchX(Dual_Inlet_Sample,4,0,DI_DEFAULT_VALVE_DELAY);
    call DiSetVolume(Dual_Inlet_Standard,100.0);
    _Delay(Flushing_Delay_Min,1,"Standard Equilibration in left
        Bellow");
    call DiSwitchX(Dual_Inlet_Sample,6,0,1000);

    bOkbis= call DiExpandLynnOax(Dual_Inlet_Sample,
        LynnOax_PressureThreshold,nMaxExpansionTries);
    call DiSwitchX(Dual_Inlet_Sample,4,0,DI_DEFAULT_VALVE_DELAY);
// bOkbis=call DiBellowAdjust_Increase(Dual_Inlet_Sample,
    nMaxContractionTries);
    call DiSwitchX(Dual_Inlet_Sample,5,1,DI_DEFAULT_VALVE_DELAY);

    return bOkbis;
    return bOk;

//****  Mass Spec Droite ****//
/* call DiSwitchX(Dual_Inlet_Standard,1,1,DI_DEFAULT_VALVE_DELAY);
    _Delay(Flushing_Delay_Min,1,"Standard Transfer to Standard Cross
        ");
    call DiSwitchX(Dual_Inlet_Standard,1,0,0);
    call DiSwitchX(Dual_Inlet_Sample,4,0,0);
    call DiSwitchX(Dual_Inlet_Sample,3,0,DI_DEFAULT_VALVE_DELAY);
```

```
    call DiSwitchX(Dual_Inlet_Standard,2,1,DI_DEFAULT_VALVE_DELAY);
    _Delay(Flushing_Delay_Min,1,"Standard Transfer to Innerline and Sample Cross");
    call DiSetVolume(Dual_Inlet_Sample,10);
    call DiSwitchX(Dual_Inlet_Sample,5,0,0);
    call DiSwitchX(Dual_Inlet_Sample,6,0,DI_DEFAULT_VALVE_DELAY);
    call DiSwitchX(Dual_Inlet_Sample,4,1,0);
    _Delay(Flushing_Delay_Min,1,"Standard Transfer to Bellows");
    call DiSwitchX(Dual_Inlet_Sample,4,0,DI_DEFAULT_VALVE_DELAY);
    call DiSetVolume(Dual_Inlet_Sample,100);
    _Delay(Flushing_Delay_Min,1,"Standard Equilibration Bellows");
*/

}
//
function LinearityBellowImbalance() : bool
{

bool bOk = FALSE;
bool bPILeft=_GetSequenceFlag("Pleft+",FALSE);
bool bPIRight=_GetSequenceFlag("Pright+",FALSE);
number nSigInt;
channel chPA_channel = chPa;


/*
if (bPILeft) //alternative 1
{
call DiSwitchX(Dual_Inlet_Standard,5,1,0); //actually decrease on std side
}
if (bPIRight) //alternative 1
{
call DiSwitchX(Dual_Inlet_Sample,5,1,0);
}
*/

if (bPILeft) //alternative 2
{

    call DiSwitchX(Dual_Inlet_Standard,5,1,0);//
    call DiSwitchX(Dual_Inlet_Sample,5,1,0);//
    call SwitchChangeOver(Dual_Inlet_Standard);
    _Delay(10000,1,"Reaching constant voltage");
    nSigInt = _GetIntensityEx(chPA_channel,8000);// replace m32 channel by Dual_Inlet_g_nPaChannel ?
// if (nStdInt<StdMinVolt)
// {
// nStdInt = _SetBellowVolt(Dual_Inlet_Standard,StdMinVolt,chPA_channel,50);
// }
// if (nStdInt<2000)
```

```
//   {
//         _UserInfo(”Skip preliminary bellow adjustment cause standard has not been introduced yet. Standard intensisty is %0.2f mV”,0,0,nStdInt);
//   }
    call DiSwitchX(Dual_Inlet_Standard,4,0,0);
    call DiSwitchX(Dual_Inlet_Sample,4,0,0);
    call SwitchChangeOver(Dual_Inlet_Sample);

    number deltaVoltage = 1000;
    number VoltTarget = (nSigInt+deltaVoltage);
    number nSaInt_linearity = _SetBellowVolt(Dual_Inlet_Sample, VoltTarget,chPA_channel,50);


}
if (bPIRight)
{

    call DiSwitchX(Dual_Inlet_Standard,5,1,0);
    call DiSwitchX(Dual_Inlet_Sample,5,1,0);//
    call SwitchChangeOver(Dual_Inlet_Sample);
    _Delay(10000,1,”Reaching constant voltage”)
    nSigInt = _GetIntensityEx(chPA_channel,8000);// replace m32 channel by Dual_Inlet_g_nPaChannel ?
    call DiSwitchX(Dual_Inlet_Standard,4,0,0);
    call DiSwitchX(Dual_Inlet_Sample,4,0,0);
    call SwitchChangeOver(Dual_Inlet_Standard);


    number deltaVoltage = 1000;
    number VoltTarget = (nSigInt+deltaVoltage);
    number nStdInt_linearity = _SetBellowVolt(Dual_Inlet_Standard, VoltTarget,chPA_channel,50);
}

return bOk;
}
//----------------------------------------------------------------------------------

function StdTransferEQINNERLINE() : bool
{

    bool bOk = FALSE;
    bool bOkbis = FALSE;
    bool boOk = FALSE;
    number nStdInt;
    number nSaInt;
     _UserInfo(”You are currently in simultanuous introduction, with equilibration in inner line”,0,0);

    call DiSetVolume(Dual_Inlet_Sample,100.0); //put the bellow back to 100% before press adjust
```

```
    call DiSetVolume(Dual_Inlet_Standard,100.0); //put the bellow back to 100% before press adjust
    call DiSwitchX(Dual_Inlet_Sample,1,0,0);
    call CloseVacPumps();
    call DiSwitchX(Dual_Inlet_Standard,1,1,0);
    _Set(sInjectStd,0); //opening (inversed too?)
    call DiSwitchX(Dual_Inlet_Standard,2,1,0);
    call OpenSide(Dual_Inlet_Standard); // 3 4 5 6
    call OpenSide(Dual_Inlet_Sample); // 3 4 5 6
    boOk = call CheckVacuum(Dual_Inlet_Sample,2,Press_read_waiting_time); // close vac pumps, open specified valve and check vacuum
// here we need to make sure 13 15 23 25 are closed
    call DiSwitchX(Dual_Inlet_Sample,3,0,0);
    call DiSwitchX(Dual_Inlet_Standard,3,0,0);

//Amount in bellow

if (g_nAmountBellow == 1.0)
{
    call DiSetVolume(Dual_Inlet_Standard,6.0);
    call DiSetVolume(Dual_Inlet_Sample,6.0);
}

if (g_nAmountBellow == 0.8)
{
    call DiSetVolume(Dual_Inlet_Standard,4.0);
    call DiSetVolume(Dual_Inlet_Sample,4.0);
}
if (g_nAmountBellow == 0.4)
{
    call DiSetVolume(Dual_Inlet_Standard,2.0);
    call DiSetVolume(Dual_Inlet_Sample,2.0);
}

if ((g_nAmountBellow == 0.0) || (g_nAmountBellow == 0.1) || (g_nAmountBellow == 0.2) || (g_nAmountBellow == 0.3) ||(g_nAmountBellow == 0.5) || (g_nAmountBellow == 0.6)||(g_nAmountBellow == 0.7)  ||(g_nAmountBellow == 0.9) ||(g_nAmountBellow == 1.1) ||(g_nAmountBellow == 1.2)||(g_nAmountBellow == 1.3)||(g_nAmountBellow == 1.4) ||(g_nAmountBellow == 1.5) ||(g_nAmountBellow == 1.6) ||(g_nAmountBellow == 1.7) ||(g_nAmountBellow == 1.8))

{
    call DiSetVolume(Dual_Inlet_Standard,100.0);
    call DiSetVolume(Dual_Inlet_Sample,100.0);
}


    // common introduction with stdAA
    call StdAA_introduction(Flushing_Delay_Min); // introduction to stdAA
   call DiSwitchX(Dual_Inlet_Sample,4,0,0);
```

```
  call DiSwitchX(Dual_Inlet_Standard,4,0,0);
  _UserInfo("amount introduced in left sample bellow is roughly %0.2f cc",0,1,g_nAmountBellow);
  _Set(sInjectStd,0); //opening StdAA to MS
  _Delay(Flushing_Delay_Min,1,"Equilibrating in inner line and StdAA");
   _Set(sInjectStd,1); //closing (inversed too?)
   call DiSwitchX(Dual_Inlet_Standard,1,0,DI_DEFAULT_VALVE_DELAY);
   _Delay(Flushing_Delay_Min,1,"Equilibrating in inner line, DI Ext right closed");
   call DiSwitchX(Dual_Inlet_Standard,5,0,DI_DEFAULT_VALVE_DELAY);
   call DiSwitchX(Dual_Inlet_Sample,5,0,DI_DEFAULT_VALVE_DELAY);
   call DiSwitchX(Dual_Inlet_Sample,4,1,0);
   call DiSwitchX(Dual_Inlet_Standard,4,1,0);
 _Delay(Flushing_Delay_Min,1,"Equilibrating in inner line and bellows");

   call DiSwitchX(Dual_Inlet_Sample,4,0,0);
   call DiSwitchX(Dual_Inlet_Standard,4,0,0);
   call DiSetVolume(Dual_Inlet_Standard,100.0);
   call DiSetVolume(Dual_Inlet_Sample,100.0);
   call DiSwitchX(Dual_Inlet_Sample,6,0,DI_DEFAULT_VALVE_DELAY);
   call DiSwitchX(Dual_Inlet_Standard,6,0,DI_DEFAULT_VALVE_DELAY);

   bOkbis= call DiExpandLynnOax(Dual_Inlet_Sample,LynnOax_PressureThreshold,nMaxExpansionTries);
   call DiSwitchX(Dual_Inlet_Sample,4,0,DI_DEFAULT_VALVE_DELAY);

   return bOk;
}
//

function GetVoltage_Pressure_diff(number nSaStartPressure,number nStdStartPressure)
{
//      number nSaStartPressure;
//      number nStdStartPressure;
        channel chPA_channel = chPa;
        call DiSwitchX(Dual_Inlet_Standard,5,1,0);
        call ChangeOverRight();
        call SwitchChangeOver(Dual_Inlet_Standard);
        call DiSwitchX(Dual_Inlet_Standard,5,1,0);
//      call PeakCenter();
        _Delay(10000,1,"Reaching constant voltage Std");
        number StdSig = _GetIntensityEx(chPA_channel,8000); //
        call SwitchChangeOver(Dual_Inlet_Sample);
        call DiSwitchX(Dual_Inlet_Sample,5,1,0);
        _Delay(10000,1,"Reaching constant voltage Sa");
        number SaSig = _GetIntensityEx(chPA_channel,8000); //chPA_channel
        call ChangeOverClose();
        number diffVolt = (SaSig - StdSig);

```

```
1488        number nRPress = call DiReadVolumePressure(
                Dual_Inlet_Standard);
1489        number nLPress = call DiReadVolumePressure(Dual_Inlet_Sample)
                ;
1490        number nLRpress = (nLPress - nRPress); //always sample -
                standard
1491        number nVleft = _GetCalc("Dual Inlet System/VolumeControl
                Left");
1492        number nVright = _GetCalc("Dual Inlet System/VolumeControl
                Right");
1493        number nLRV     = (nVleft-nVright);
1494 //     number BelVolDiff = ((38*nSaStartPressure/nLPress)-(38*
        nStdStartPressure/nRPress));
1495 //     number LBelVol = (38*nSaStartPressure/nLPress);
1496
1497        _UserInfo("Voltage difference (Sa-Std) at acquisition start
                %4.1f mV: Sa:%4.1f mV Std:%4.1f mV",3,0,diffVolt,SaSig,
                StdSig);
1498        _UserInfo("Pressure difference (Sa-Std) at acquisition start
                %4.1f mbar: Sa:%4.1f mbar Std:%4.1f mbar",3,0,nLRpress,
                nLPress,nRPress);
1499        _UserInfo("Bellow percentage difference (Left-Right) at
                acquisition start %4.1f : Sa:%4.1f  Std:%4.1f ",3,0,nLRV,
                nVleft,nVright);
1500 if ((_GetSequenceFlag("Pressadjust",FALSE))==TRUE)
1501    {
1502        _UserInfo("Bellow volume difference (Left-Right) at
                acquisition start %4.2f cc: Sa:%4.2f cc Std:%4.2f cc"
                ,3,0,((38*nSaStartPressure/nLPress)-(38*nStdStartPressure
                /nRPress)),(38*nSaStartPressure/nLPress),(38*
                nStdStartPressure/nRPress));
1503        _UserInfo("Amount difference (STP) (Left-Right) in bellow at
                acquisition start %4.3f cc: Sa:%4.3f cc Std:%4.3f cc"
                ,3,0,((38*nSaStartPressure/1013.15)-(38*nStdStartPressure
                /1013.15)),(38*nSaStartPressure/1013.15),(38*
                nStdStartPressure/1013.15));
1504    }
1505    if ((_GetSequenceFlag("Pressadjust",FALSE))==FALSE)
1506    {
1507 _UserInfo("work in progress, bellow calib needed",3,0);
1508 _UserInfo("work in progress, bellow calib needed",3,0);
1509 //     _UserInfo("Bellow volume difference (Left-Right) at
        acquisition start %4.2f cc: Sa:%4.2f cc Std:%4.2f cc",3,0,((38*
        nSaStartPressure/nLPress)-(38*nStdStartPressure/nRPress)),(38*
        nSaStartPressure/nLPress),(38*nStdStartPressure/nRPress));
1510 //     _UserInfo("Amount difference (STP) (Left-Right) in bellow at
        acquisition start %4.3f cc: Sa:%4.3f cc Std:%4.3f cc",3,0,((38*
        nSaStartPressure/1013.15)-(38*nStdStartPressure/1013.15)),(38*
        nSaStartPressure/1013.15),(38*nStdStartPressure/1013.15));
1511    }
1512
1513 }
1514
```

```
//
function Preparation_DualInletSystem() : bool
{
    call checkVacStdAA();
    call DiSwitchX(Dual_Inlet_Standard,1,0,0);//
    call DiSwitchX(Dual_Inlet_Sample,1,0,0);//
    call Vacuuming();
    call Flushing(FlushingCycles); //FlushingCycles=3   flush std line 3 times by default

    return 1;
}
//
function MonitorMass()
{
        bool bMonitormass =_GetSequenceFlag("MonitorMass",FALSE);

       if (bMonitormass==TRUE)
   {
        _UserInfo("Mass Monitoring",0,1);
        call DiMeasureInterferingMasses(Ms_PeakCenterChannel, Ms_IntegrationTime);
   }
}
//
function MagnetScan()
{
bool bMagnetScan  =_GetSequenceFlag("MagnetScan",FALSE);

      if (bMagnetScan==TRUE)
   {
        _UserInfo("Mass scanning",0,1);
        call MassScanning();
   }
}
//
```

B Python code to calculate $\delta O_2/N_2$ obtained by peak jumping

```python

#!/usr/bin/env python

# ------------------------------------------------------------------ #
#  Simple python script to calculate delta O2/N2 (peak jumping).
#
#  Author: Isabell Lubanski
#  Date:   15-09-2015
# ------------------------------------------------------------------ #
from ROOT import *          # Import ROOT libraries (to use ROOT)
import math                 # Import MATH libraries (for extended MATH functions)
from array import array     # Import the concept of arrays (needed in TGraphErrors)

import fileinput

SavePlots = True           # Determining if plots are saved or not

gStyle.SetOptStat("emr")
gStyle.SetOptFit(1111)


# ------------------------------------------------------------------ #
# Read the data:
# ------------------------------------------------------------------ #

# Define eight arrays containing 16O and 15N values for both sample and standard gas:

T_16O_sample  = array("f")
V_16O_sample = array("f")
T_16O_standard  = array("f")
V_16O_standard  = array("f")
T_14N_sample  = array("f")
V_14N_sample = array("f")
T_14N_standard  = array("f")
V_14N_standard  = array("f")


content = []
for line in fileinput.input():
    content.append(line)


for blokNo in range(1,6+1) : #Reads 6 blocks (+1 because the last is not included) Change here you want e.g. 3 instead of 6 runs
```

```
    line1 = content[4*blokNo+4].split(",") #line1 = 16O_sample and so forth. This splits the line at all ",", so that we now have a list of numbers in "content" that consist of a block
    line2 = content[4*blokNo+5].split(",")
    line3 = content[4*blokNo+6].split(",")
    line4 = content[4*blokNo+7].split(",")

    T_16O_sample.append(float(line1[1])) #Here we fill in the times where 16O is measured into the already defined array 'T_16O_sample' and so forth. Entry [1] corresponds to number two entry because the first is 0
    V_16O_sample.append(float(line1[5]))
    T_16O_standard.append(float(line2[1]))
    V_16O_standard.append(float(line2[5]))
    T_14N_sample.append(float(line3[1]))
    V_14N_sample.append(float(line3[5]))
    T_14N_standard.append(float(line4[1]))
    V_14N_standard.append(float(line4[5]))

# Fit the linearity of 16O sample:
canvas_16O_standard = TCanvas( "canvas_O16_standard", "canvas_O16_standard", 50, 50, 1200, 600 )

graph_16O_standard = TGraph(len(T_16O_standard), T_16O_standard, V_16O_standard)
graph_16O_standard.SetMarkerStyle(2)

fit_16O_standard = TF1("fit_16O_standard", "1.0 ++ x", 0, T_16O_standard[-1])     # A line as fitting function.
#fit_16O_standard = TF1("fit_16O_standard", "[0] + [1]*x", 0, T_16O_standard[-1])     # A line as fitting function.
#fit_16O_standard.SetParameters(7000.0, -0.2)          # Set the starting values of [0] and [1] to 7000 and -0,2
fit_16O_standard.SetLineColor(kRed)                # Set the line color to red.
fit_16O_standard.SetLineWidth(2)                   # Set the line width to 4.

graph_16O_standard.Fit("fit_16O_standard", "R")              # Make the fit with the range as set.
graph_16O_standard.Draw("AP")                      # Draw the axis and points of the graph.

#print fit_16O_standard.GetParameter(0)
#print fit_16O_standard.GetParameter(1)
#print fit_16O_standard.Eval(800)

if (SavePlots):
    canvas_16O_standard.SaveAs("fit_16O_standard.png")         # Save plot as "fit_16O_standard.png" (format follow extension name)

# Fit the linearity of 14N sample:
```

```
canvas_14N_sample = TCanvas( "canvas_14N_sample", "canvas_14N_sample", 50, 50, 1200, 600 )

graph_14N_sample = TGraph(len(T_14N_sample), T_14N_sample, V_14N_sample)
graph_14N_sample.SetMarkerStyle(2)

fit_14N_sample = TF1("fit_14N_sample", "1.0 ++ x", 0, T_14N_sample[-1])     # A line as fitting function.
fit_14N_sample.SetLineColor(kRed)                # Set the line color to red.
fit_14N_sample.SetLineWidth(2)                   # Set the line width to 4.

graph_14N_sample.Fit("fit_14N_sample", "R")             # Make the fit with the range as set.
graph_14N_sample.Draw("AP")                      # Draw the axis and points of the graph.

if (SavePlots):
    canvas_14N_sample.SaveAs("fit_14N_sample.png")        # Save plot as "fit_16O_standard.png" (format follow extension name)


# Fit the linearity of 14N standard:
canvas_14N_standard = TCanvas( "canvas_14N_standard", "canvas_14N_standard", 50, 50, 1200, 600 )

graph_14N_standard = TGraph(len(T_14N_standard), T_14N_standard, V_14N_standard)
graph_14N_standard.SetMarkerStyle(2)

fit_14N_standard = TF1("fit_14N_standard", "1.0 ++ x", 0, T_14N_standard[-1])     # A line as fitting function.
fit_14N_standard.SetLineColor(kRed)                # Set the line color to red.
fit_14N_standard.SetLineWidth(2)                   # Set the line width to 4.

graph_14N_standard.Fit("fit_14N_standard", "R")             # Make the fit with the range as set.
graph_14N_standard.Draw("AP")                      # Draw the axis and points of the graph.

if (SavePlots):
    canvas_14N_standard.SaveAs("fit_14N_standard.png")        # Save plot as "fit_16O_standard.png" (format follow extension name)

Delta_O2_N2 = array("f")

for blokNo in range(1,6+1) : #Reads 6 blocks (+1 because the last is not included). Change here if less cycles
```

```
    Time_of_sample_16O = T_16O_sample[blokNo-1]
    Numerator = V_16O_sample[blokNo-1]/fit_14N_sample.Eval(Time_of_sample_16O)
    #print fit_14N_standard.Eval(Time_of_sample_16O)
    Denominator = fit_16O_standard.Eval(Time_of_sample_16O)/fit_14N_standard.Eval(Time_of_sample_16O)
    Delta_O2_N2.append(((Numerator/Denominator)-1)*1000.0)

print Delta_O2_N2

#print sum(Delta_O2_N2)
#print len(Delta_O2_N2)

Delta_O2_N2_average = sum(Delta_O2_N2)/len(Delta_O2_N2)

Sum_of_squares = 0.0
for blokNo in range(1,6+1) : #Reads 6 blocks (+1 because the last is not included). Change here!! if less cycles
    Sum_of_squares = Sum_of_squares + ((Delta_O2_N2_average - Delta_O2_N2[blokNo-1])**2)/len(Delta_O2_N2)

Delta_O2_N2_std_dev = math.sqrt(Sum_of_squares)

print Delta_O2_N2_average
print Delta_O2_N2_std_dev

raw_input('Press Enter to exit')
```

Acknowledgements

The Center for Ice and Climate is like a small family, and I have been honored to be a member of this beautiful group. The CIC always provided me optimal conditions to work on my project, and offered me the opportunity to spend a month at Neem in 2010, just when the bedrock was reached. I want to deeply thank my supervisor Amaelle Landais, without which I would never have finished this PhD thesis. Your knowledge and efficiency, but also your enthusiasm, your dynamism, your positive attitude and your moral support have been essential. I would like also to thank my supervisor, Thomas, for giving me the possibility to do my PhD in Copenhagen within the frame of the Intramif network. I have always felt your moral support, and can only be grateful for the trust and the patience you had for me, even when no outcome was foreseeable. I really enjoyed to be so independent and responsible for the success or failure of my project, to learn how to run a laboratory on my own, from the daily maintenance of a mass spectrometer to the design of an analytical setup from scratch. It was a tough but enriching journey.

I have met great people during my extended time at CIC. Peter (Sperlich), I lost more than a friend when you left the gaslab. Not only your experimental skills, but also the positive waves that were radiating from you. Your empathy and your generosity. Thinking of your wonderful family fills me with happiness. I hope to see you soon down under. Myriam (Guillevic), your kindness, your altruism and your open-minded attitude have been such a privilege to experience. I really wish you the best in your life, you just deserve happiness. Ivana, I remember the wonderful hikes, bike ride, and deep discussion we had together. I was happy to share your friendship for a couple of years. Jesper, your dry humor, your human qualities and your guitar skills are impressive, but the fact that you appreciate Dagerman is a huge bonus. Paul, without you I would never have started to climb, I wouldn't have enjoyed this great climbing trip in Göteborg with Alex, Felicia and you. I know I can always rely on you, I know you'll always have some activities in mind, and I would like to thank you for that. Ali, you are just so funny, smiling most of the time, I should have stayed longer with you in the Danish courses. Alex, you are just great, full of energy, jokes, and attention. I got so many nice presents from you, and to participate to the breathing of the world, it is now my turn It is a shame I haven't seen you since more than 6 months. The same holds true for Felicia. Are they gonna fix Banana park one day? Malte, you're just the cool guy, always in good mood, relax, fun, what else? I am super happy to be working with you. Trevor, I hope that one day we'll do a bike trip together. Gabriela, I was happy to share my office with you for a while, that made the hard days in the lab much

nicer when nothing was working with the experiments. Mai, the time seemed to stop when you were playing the piano during the long evenings at CIC. I would lie on the coach, close my eyes and let the music rock me. Lone, thank you for your permanent good mood, you can't imagine how your smile helped me to survive the dark days. And Michele, I almost forgot you! Your were so full of life, funny, and able to listen to people. I really enjoyed your stay here. I could say the same for you, Helen and Kaitlin. And so many others, Christo, I enjoyed as much as you our stay in Karthaus, thanks for having taught me tango! Anne-so, Bernhard, Torsten, James, it was so great to get to know you. Thanks Renato, Carl, Roselyn, Denise, and the rest of the Intramif crew for the good moments we spent together in various summerschools. Elisa, our weekend in Paris was really wonderful. Too bad we lost contact afterwards. And thank you Simon, for our discussions at 5 am at CIC. Then I would like to thank maman, Martin, Jo, Cap, Lisa. You can't imagine how important you have been for me during these tough years, despite the lack of contact. And Kamanyn, Naim, Eva, I would like to spend every day with you. Thank you Lisa to offer me so amazing nephews. I probably forgot many others, starting with Arianna, Niccolo, Christopher and Olivia, David, Mads, our great glassblower Svenn Pantmann, Vasilis, etc, but I can't go on ad aeternam. I would like to conclude with you Hannah, because I owe you this thesis. Thank you for supporting me without conditions. Thank you for bringing some light in this last year's darkness. Thank you for preparing me all these delicious dishes while I had my head stuck in the computer, thank you for sharing the same desire of large spaces and liberty. I can't wait for being on the road with you, leaving the past in our back and aiming for the sun.